

Fall 12-2010

A Comprehensive Uncertainty Analysis and Method of Geometric Calibration for a Circular Scanning Airborne Lidar

Michael Oliver Gonsalves
University of Southern Mississippi

Follow this and additional works at: <https://aquila.usm.edu/dissertations>



Part of the [Applied Mathematics Commons](#), [Biology Commons](#), [Earth Sciences Commons](#), [Marine Biology Commons](#), and the [Oceanography Commons](#)

Recommended Citation

Gonsalves, Michael Oliver, "A Comprehensive Uncertainty Analysis and Method of Geometric Calibration for a Circular Scanning Airborne Lidar" (2010). *Dissertations*. 679.
<https://aquila.usm.edu/dissertations/679>

This Dissertation is brought to you for free and open access by The Aquila Digital Community. It has been accepted for inclusion in Dissertations by an authorized administrator of The Aquila Digital Community. For more information, please contact Joshua.Cromwell@usm.edu.

The University of Southern Mississippi

A COMPREHENSIVE UNCERTAINTY ANALYSIS AND METHOD OF
GEOMETRIC CALIBRATION FOR A CIRCULAR SCANNING AIRBORNE LIDAR

by

Michael Oliver Gonsalves

Abstract of a Dissertation
Submitted to the Graduate School
of The University of Southern Mississippi
in Partial Fulfillment of the Requirements
for the Degree of Doctor of Philosophy

December 2010

ABSTRACT

A COMPREHENSIVE UNCERTAINTY ANALYSIS AND METHOD OF GEOMETRIC CALIBRATION FOR A CIRCULAR SCANNING AIRBORNE LIDAR

by Michael Oliver Gonsalves

December 2010

This dissertation describes an automated technique for ascertaining the values of the geometric calibration parameters of an airborne lidar. A least squares approach is employed that adjusts the point cloud to a single planar surface which could be either a narrow airport runway or a dynamic sea surface. Going beyond the customary three boresight angles, the proposed adjustment can determine up to eleven calibration parameters to a precision that renders a negligible contribution to the point cloud's positional uncertainty.

Presently under development is the Coastal Zone Mapping and Imaging Lidar (CZMIL), which, unlike most contemporary systems that use oscillating mirrors to reflect the beam, will use a circular spinning prism to refract the laser in the desired direction. This departure from the traditional scanner presents the potential for internal geometric misalignments not previously experienced. Rather than relying on past calibration practices (like requiring data be acquired over a pitched-roof), a more robust method of calibration is established which does not depend on the presence of any cultural features.

To develop this new method of calibration, the laser point positioning equation for this lidar was developed first. The system was then simulated in the MATLAB environment. Using these artificial datasets, the behavior of each geometric parameter

was systematically manipulated, understood and calibrated, while an optimal flight strategy for the calibration acquisition was simultaneously developed. Finally, the total propagated uncertainty (TPU) of the point cloud was determined using a propagation of variances. Using this TPU module, the strength of the calibration solution was assessed. For example, four flight lines each of 20 seconds in duration contained sufficient information to determine the calibration parameters to such a degree of confidence that their contribution to the final point cloud uncertainty was only 0.012m in the horizontal and 0.002m in the vertical (1σ).

COPYRIGHT BY
MICHAEL OLIVER GONSALVES
2010

The University of Southern Mississippi

A COMPREHENSIVE UNCERTAINTY ANALYSIS AND METHOD OF
GEOMETRIC CALIBRATION FOR A CIRCULAR SCANNING AIRBORNE LIDAR

by

Michael Oliver Gonsalves

A Dissertation
Submitted to the Graduate School
of The University of Southern Mississippi
in Partial Fulfillment of the Requirements
for the Degree of Doctor of Philosophy

Approved:

Stephan Howden
Director

David Wells

Steven Lohrenz

Grady Tuell

Chris Parrish

Susan A. Siltanen
Dean of the Graduate School

December 2010

ACKNOWLEDGMENTS

The author wishes to acknowledge several groups of people who each played an important role in the synthesis of this work:

- My command, Mike Aslaksen, Jr., CDR Eric Berkowitz and the staff of NOAA's Remote Sensing Division for both their financial and professional support over the past three-and-a-half years.
- My colleagues of the Joint Airborne Lidar Bathymetry Technical Center of Expertise (JALBTCX), particularly Jennifer Wozencraft, Christopher Macon and Bill Elenbaas, who have been particularly understanding of my often being the silent partner of our "Joint" center.
- My committee members, Drs. David Dodd, Stephan Howden, Steven Lohrenz, Chris Parrish and Grady Tuell, who have been very encouraging and have offered invaluable feedback in the final stages of research.
- Jessica Burt and Jennifer Dowling, who rose beyond the call of duty by agreeing to take on the unenviable roles of being the first to edit this document for grammar.
- Above all, the author wishes to acknowledge Dr. David Wells who, but for a technicality in the paperwork, was the true Director of my dissertation committee. From the inception of the original concept, through the sensor models, through the linear algebra, through the least squares, through the uncertainty propagation, every section of this document bears Dr. Wells' influence. While this work may have persevered without amenable bosses, coworkers or friends; without Dr. Wells this research would – not – have – happened.

TABLE OF CONTENTS

ABSTRACT	ii
ACKNOWLEDGMENTS	iv
LIST OF ILLUSTRATIONS	vii
LIST OF ABBREVIATIONS	xx
LIST OF SYMBOLS	xxii
CHAPTER	
I. INTRODUCTION	1
1.1 - Problem Statement	
1.2 - Proposed Approach	
1.3 - Dissertation Contributions	
1.4 - Outline of Dissertation	
II. REVIEW OF PREVIOUS WORK	16
2.1 - Introduction	
2.2 - Strip Adjustment	
2.3 - Feature Extraction	
2.4 - Adjustment Procedures	
2.5 - Uncertainty Analysis	
2.6 - Over-Constrained Systems	
2.7 - Summary	
III. THE LASER LOCATION EQUATION	36
3.1 - Component Analysis	
3.2 - Preliminary Sensitivity Analysis	
3.3 - Summary of Key Results	
IV. THE LIDAR SIMULATION MODULE	76
4.1 - Module Overview	
4.2 - Advanced Simulation Options	
4.3 - Summary of Key Results	

V.	THE ADJUSTMENT ALGORITHM.....	113
	5.1 - Theory of a Least Squares Adjustment	
	5.2 - The Adjustment Model	
	5.3 - Improving Memory Usage for the Least Squares Partitioning	
	5.4 - Summary of Key Results	
VI.	THE LIDAR CALIBRATION MODULE.....	153
	6.1 - Geometric Impacts of Boresight Misalignments and Signature Analysis	
	6.2 - The Calibration Module	
	6.3 - Signature Analysis of the Remaining Calibration Parameters	
	6.4 - Impacts of Survey Site Selection on the Calibration Module	
	6.5 - Summary of Key Results	
VII.	TOTAL PROPAGATED UNCERTAINTY	283
	7.1 - Background	
	7.2 - Total Propagated Uncertainty Visualization Module	
	7.3 - Relative Contributions to TPU of Observed and Calculated Parameters' Uncertainties	
	7.4 - Summary of Key Results	
VIII.	CONCLUSIONS.....	367
	8.1 - Results	
	8.2 - Recommendations for Future Work	
	APPENDIX.....	374
	REFERENCES	381

LIST OF ILLUSTRATIONS

Figure

1.	Chapter I outline.	1
2.	The path of a laser as it travels between the vehicle and the ground.	2
3.	A lidar system with some of its many components, each with its own reference frame and displacement vector.	3
4.	Rather than relying on reflective surfaces, the CZMIL system will use a Fresnel prism to steer the laser beam via refraction.	6
5.	Basic scan pattern of present generation lidar system (SHOALS) and proposed CZMIL scanner (direction of flight is from bottom to top).	7
6.	Chapter II outline.	16
7.	Chapter III outline.	36
8.	Components of the CZMIL system to be incorporated into the laser location equation for a geometric calibrator.	38
9.	The laser-prism-scanner assembly, showing the laser reference point which is the point of origin for computations within this dissertation (left), shown along with the scanner's right-handed forward-starboard-down coordinate system (right).	39
10.	Tracking a laser pulse as it moves from one medium to another, showing the angles of incidence and refraction ($\eta_2 > \eta_1$)	40
11.	Tracking a laser pulse as it moves from one medium to another, showing the angles of incidence and refraction.	42
12.	Trigonometric relation of θ_3 and θ_4	44
13.	Tracking the laser pulses' path in, through and out of the Fresnel prism.	46
14.	The Fresnel prism's slope, θ_{FR} , is the angle of incidence, θ_1 , for the Snell's Law refraction problem.	48
15.	CZMIL scan patterns for various Fresnel prism slopes.	49
16.	A well-aligned prism-scanner assembly in which the scanner's axis of rotation, z_s , is parallel to the prism base's normal vector, \vec{P}_2	50

17.	The effects of rotating the Fresnel prism about the scanner's y-axis (top) and x-axis (bottom).	51
18.	Rotating the Fresnel prism about the scanner's y-axis, y_s , by angle $PS\theta_y$, increases the radius of the circular scan pattern (blue trace).	51
19.	Orienting the laser to the scanner's reference frame through spherical coordinates.	53
20.	Tilting the laser from vertical (increasing ϕ_{LS}) will alter the scan pattern from its intended circular scan pattern (shown in blue) to produce a teardrop-shaped pattern.	55
21.	The rotating prism shown in its forward and backward position along with a "well-aligned" laser (red).....	56
22.	By rotating the prism (but holding the laser fixed with respect to the scanner reference frame), the laser's exit angle, θ_4 , actually decreases with respect to the lower face of the prism, but (including the rotation of the prism) the exit angle actually increases with respect to nadir.....	56
23.	The relationship between the SRF and the IRF, showing the boresight misalignments, $BS\theta_x$, $BS\theta_y$ and $BS\theta_z$, and the SRF to IRF offset vector, $[\Delta x_{IL} \quad \Delta y_{IL} \quad \Delta z_{IL}]$	58
24.	A pair of laser scans with a known (red) and unknown (black) pitch boresight misalignment.....	60
25.	Two flight lines with a misalignment in the yaw boresight angle: the left is from a level flight, while the right is from a flight line in which the plane had a 10° pitch.	60
26.	Three different sets of scan patterns (looking from above) induced by rotating different system components with respect to one another.	61
27.	An illustration of a potential heading misalignment between the vehicle reference frame and the INS reference frame.	63
28.	An Applanix POS AV Ver. 5 indicates which way should be pointed "forward." Sketch modified from Applanix (2007).	64
29.	The effects of crosstalk in a poorly mounted INS.	65

30.	A radiometric bias or a linear scale factor in the laser range computation would create a geometric bias in the point cloud that would not be identified if these parameters were not included in the calibration.	66
31.	The Fresnel prism's slope, θ_{FR} , is the angle of incidence, θ_i , for the Snell's law refraction problem.	71
32.	Table of laser point biases induced by a 1 mrad (0.06°) and 1° bias in each calibration parameter, where Δz = vertical bias and $\Delta(x, y)$ = horizontal displacement.	73
33.	Chapter IV outline.	76
34.	Solving for the parameter, t , where a line intersects a plane.	79
35.	The lidar simulator interface.	81
36.	A closer view of the left panel of the lidar simulator.	82
37.	A closer view of the center panel of the lidar simulator.	82
38.	A closer view of the right panel of the lidar simulator.	83
39.	Examples of flights in which the vehicle experiences static (left) and dynamic (right) changes in attitude.	84
40.	A rolling vehicle with a delay in the attitude time stamping will result a potentially incoherent point cloud (black).	86
41.	The same point cloud with variance display options: the default (upper-left), with the laser beams displayed (upper-right), suppressing the vehicle (lower-left) and suppressing the ground (lower-right).	88
42.	Simulations of various lidar scan patterns: the circular scanning CZMIL, the rectangular grid producing LADS, and the forward arcing SHOALS.	89
43.	Two revolutions of a lidar with no geometric misalignments (left) and the same point cloud with an unknown 10° forward (i.e., towards the nose) pitch boresight bias (right).	90
44.	Three survey lines are simulated and two regions are selected by the subset editor (left).	93
45.	A simulation of a lidar survey across the land-water boundary.	94
46.	Pseudocode (left) and visual decision tree (right) used for rendering the perimeter of the water surface in the presence of a sloping seafloor.	95

47.	A sample water surface polygon along with the associated nodes needed for its derivation.	96
48.	A combination of low-amplitude, high-frequency waves and high-amplitude, low-frequency swell are used to create an idealized sea surface.	100
49.	A view of a point cloud acquired over a calm sea surface (top) and the effects when a swell is added (bottom).	102
50.	Relating the height of a wave with the induced uncertainty in the laser range measurement.	104
51.	When a sea wave's wavelength is much smaller than the lidar spot size (left), the dynamics of the wave height are averaged out.	105
52.	The behavior of a laser pulse as it crosses the air-water interface in the presence of surface waves.	107
53.	Top-down view of distribution of lidar points on the seafloor acquired in the presence of surface swell.	108
54.	Distribution of one cluster of laser strikes on the seafloor in the presence of a 1m swell with a 50m wavelength, as highlighted in Figure 53.	108
55.	The different tidal interfaces within the simulator.	109
56.	Side views of a point cloud with four different tidal models applied: no tides (upper-left), a linear tidal model (upper-right), a sinusoidal tidal model (lower-right) and loading a user-defined tide from a file (lower-left)	110
57.	Chapter V outline.	113
58.	Determining the equation of a plane that best fits a collection of laser observations.	128
59.	A modified spherical coordinate representation of the planar normal vector (pink) referenced to a locally level plane (grey).	133
60.	A simplified laser scanner with three observables: the laser range, ρ , the laser nadir angle, α , and the laser azimuth angle, β	134
61.	The chain tree showing the variables on which the laser vector exiting the prism, \vec{L}_2 , is dependent (and their associated inter-dependencies).	139

62.	Table of number of entries contained within the four primary matrices that are declared during the least squares adjustment (assuming five adjusting parameters and three observables).....	143
63.	Chapter VI outline.....	153
64.	Two revolutions of the laser scanner with no boresight misalignments – notice both circular traces are coplanar (left).	156
65.	Visualization of a point cloud generated from a lidar with an unidentified 1° pitch boresight misalignment (top), and a point cloud from the same system as it experiences an increase in altitude (bottom).....	158
66.	Signature analysis plots for a lidar with a 1° pitch boresight misalignment in the presence of a rolling (top), pitching (middle) and yawing (bottom) vehicle.	159
67.	A sample signature analysis plot that compares each laser point’s associated pitch with their calculated z-coordinate.	160
68.	Visualization of a point cloud generated from a lidar with an unidentified 1° roll boresight misalignment (top), and a point cloud from the same system as it experiences an increase in altitude (bottom).....	162
69.	Signature analysis plots for a lidar with a 1° roll boresight misalignment in the presence of a rolling (top), pitching (middle) and yawing (bottom) vehicle.	163
70.	With a misalignment in the roll boresight angle, the best flight configuration for calibration is produced by flight lines in opposing directions.	164
71.	Visualization of a point cloud generated from a lidar with an unidentified 1° yaw boresight misalignment (top), and a point cloud from the same system as it experiences an increase in altitude (bottom).....	165
72.	Top-down view of a point cloud (red) and its biased counterpart which contains an unidentified boresight yaw misalignment (black).....	166
73.	Signature analysis plots for a lidar with a 1° yaw boresight misalignment in the presence of a rolling (top), pitching (middle) and yawing (bottom) vehicle.	167
74.	A vehicle pitching nose-up will measure the longest slant range in its forward-most beam (red arrow).	168
75.	The lidar calibration interface.....	170
76.	A closer view of the left panel of the lidar calibrator.	171
77.	A closer view of the right panel of the lidar calibrator.	172

78.	A closer view of the interface for a single parameter within the calibration module.....	174
79.	Proposed flight pattern for simplified (boresight) calibration.	180
80.	Output of calibration module: the boresight angles were recovered and the point cloud was successfully fit to the planar surface shown in Figure 79.....	181
81.	Table of results of boresight calibration trials under a number of different acquisition scenarios: increasing data density (A), increasing vehicle attitude (B), adding a reciprocal flight line (C) and adding a geographically separated line (D).	182
82.	Overhead view of the cloverleaf acquisition flight plan designed to best determine the boresight misalignments.	187
83.	Table of results of boresight calibration trials along the cloverleaf flight pattern.	188
84.	Variance-covariance visualization module.....	190
85.	Correlation coefficient visualization module.....	191
86.	Variance-covariance visualization module for a poorly designed flight.	192
87.	Correlation coefficient visualization module for a poorly designed flight.	193
88.	Visualization of a point cloud generated from a lidar with an unidentified 0.1° prism slope misalignment(top), and a point cloud from the same system as it experiences an increase in altitude (bottom).....	196
89.	Signature analysis plots for a lidar with a 0.1° prism slope misalignment in the presence of a rolling (top), pitching (middle) and yawing (bottom) vehicle.	197
90.	Visualization of a point cloud generated from a lidar with known non-zero boresight angles and an unidentified 0.1° prism slope misalignment.....	198
91.	Table of results of prism slope calibration trials under a number of different acquisition scenarios: increasing data density (A), increasing the vehicle's dynamic motion (B), and adding a geographically separated line (C).	199
92.	Correlation coefficients from a single flight line (shown in Figure 80) in which the three boresight angles and prism slope are adjusted.	201
93.	Two attempts at calibrated point clouds produced when the prism slope was held fixed at an incorrect value and only the pitch boresight angle (red) and yaw boresight angle (black) were adjusted.....	202

94.	Visualization of a point cloud generated from a lidar with an unidentified 1° laser-to-scanner phi-angle misalignment (top), and a point cloud from the same system as it experiences an increase in altitude (bottom).	204
95.	Signature analysis plots for a lidar with a 1° laser-to-scanner phi-angle misalignment in the presence of a rolling (top), pitching (middle) and yawing (bottom) vehicle.	205
96.	Signature analysis plots for a lidar with a $\pm 1^\circ$, $\pm 90^\circ$ and 180° laser-to-scanner theta-angle misalignment for a level flight.	207
97.	Visualization of a point cloud generated from a lidar with an unidentified 180° laser-to-scanner theta-angle misalignment (top), and a point cloud from the same system as it experiences an increase in altitude (bottom).	209
98.	Signature analysis plots for a lidar with a 180° laser-to-scanner theta-angle misalignment in the presence of a rolling (top), pitching (middle) and yawing (bottom) vehicle.	210
99.	Table of results of six-parameter calibration trials under a number of different acquisition scenarios: increasing data density (A), increasing vehicle attitude (B), adding a reciprocal and parallel flight lines (C) adopting a cloverleaf pattern (D) and crossing pattern (E).	211
100.	Correlation coefficients from a single flight line (shown in Figure 80) of a six parameter adjustment (boresight angles, prism slope and laser/scanner alignment).	213
101.	Proposed crossing flight plan which features survey lines at two different acquisition altitudes and the intersection of all lines over a common point (adapted from Morin 2002).	216
102.	Visualization of a point cloud generated from a lidar with an unidentified 1° VRF/IRF heading misalignment (top), and a point cloud from the same system as it experiences an increase in altitude (bottom).	218
103.	Signature analysis plots for a lidar with a 1° VRF/IRF heading misalignment in the presence of a rolling (top), pitching (middle) and yawing (bottom) vehicle.	219
104.	Table of results of seven-parameter calibration trials.	221
105.	Correlation coefficients from a single flight line (shown in Figure 80) of a seven-parameter adjustment (only boresight angles, VRF/IRF alignment shown).	221
106.	Visualization of a point cloud generated from a lidar with an 1° VRF/IRF heading misalignment that is misidentified as a -1° yaw boresight angle (top),	

and a point cloud from the same system as it experiences an increase in altitude (bottom).....	224
107. Signature analysis plots for a lidar with a 1° VRF/IRF heading misalignment that is misidentified as a -1° yaw boresight angle in the presence of a rolling (top), pitching (middle), and yawing (bottom) vehicle.....	225
108. When a VRF/IRF heading misalignment is incorrectly identified as a yaw boresight misalignment, a vertical bias in the point cloud will result.	226
109. Top-down view of a point cloud (red) and its biased counterpart which contains an unidentified forward Δx_{IL} (black).....	228
110. Signature analysis plots for a lidar with a 1m starboard IMU offset bias in the presence of a vehicle rolling (top), and a lidar with a 1m forward IMU offset bias in the presence of a vehicle pitching (bottom).	229
111. Table of results of different combinations of a 9-parameter calibration where the INS offset vector was held constant (A), no parameters were held constant (B) and only Δy_{IL} was held constant (C).	230
112. Covariances from a 9-parameter adjustment (boresight angles, prism slope, VRF/IRF heading alignment, INS offset vector and laser/scanner alignment).	231
113. Correlation coefficients from a 9-parameter adjustment (only the boresight angles, prism slope, VRF/IRF heading alignment and INS offset vector are shown).....	231
114. Two valid definitions of a vehicle reference frame: one oriented at an angle (left) and the other oriented towards the nose of the aircraft (right).....	234
115. Signature analysis plots for a lidar with a 1m vertical IMU offset bias (top), in the presence of a rolling vehicle (middle), and pitching vehicle (bottom).	238
116. Table of results of a 9-parameter calibration (including the vertical INS offset) both without (A) and with (B) ground control.....	239
117. Visualization of a point cloud generated from a lidar with an unidentified $1^\circ PS\theta_y$ misalignment (top), and a point cloud from the same system as it experiences an increase in altitude (bottom). The red points indicate the true laser strikes, while the black are the miscalculated biased points. All units in meters.	243
118. Signature analysis plots for a lidar with a $1^\circ PS\theta_y$ misalignment in the presence of a rolling (top), pitching (middle), and yawing (bottom) vehicle.	244

119. Comparison of signature plots for two level flight lines with an unidentified rotation of 1° between the prism and scanner about two different axes, $PS\theta_x$ (left) and $PS\theta_y$ (right).	245
120. Comparison of signature plots for a level flight with an unidentified rotation of 1° prism/scanner x -axis alignment (1) and same incrementally more complicated point cloud, introducing known biases to the roll boresight (2), pitch boresight (3) and laser/scanner alignments (4). The red points indicate the true laser strikes, while the black are the miscalculated biased points.	246
121. Table of results of an 11-parameter calibration trial with ground control (1σ uncertainties shown).	247
122. An 11-parameter calibration in which the scanner azimuth bias is held fixed at 0° .	250
123. A second attempt at an 11-parameter calibration of the same point cloud as in Figure 122, this time holding the scanner azimuth bias fixed at 10° .	250
124. Visualization of a point cloud generated from a lidar with an unidentified laser range scale factor of 1.01 (top), and a point cloud from the same system as it experiences an increase in altitude (bottom).	256
125. Signature analysis plots for a lidar with a 1m laser range bias for a level flight (top) and in the presence of a rolling (middle) and pitching (bottom) vehicle.	257
126. Table of confidences of an 11-parameter calibration trial including the laser range bias and scale factor (1σ uncertainties shown).	258
127. Correlation coefficients of the final 11-parameter calibration using the crossing flight pattern of Figure 101.	261
128. From the crossing flight pattern, a swath of data 50m wide, to simulate an airport runway, is extracted using the simulator's subset tool.	265
129. Both the uncalibrated (black) and calibrated point cloud (green) based on the data limited to the width of an airport runway.	265
130. Table of confidences of an 11-parameter calibration trial over a 50m runway with ground control (1σ uncertainties shown).	266
131. Calibrated point cloud when acquired over a dynamic sea with a 1m swell height.	270
132. Table of confidences of an 11-parameter calibration trial over a dynamic sea surface (1σ uncertainties shown).	271

133. Table of confidences of an 11-parameter calibration trial over a narrow runway versus a dynamic sea surface (1σ uncertainties shown).	272
134. Crossing pattern point cloud in the presence of a tidal effect.....	274
135. Table of confidences of an 11-parameter calibration trial in the presence of tides (1σ uncertainties shown).....	275
136. Side view of attempts to calibrate a point cloud in the presence of tides in which a tidal signature is erroneously believed to not be present.	276
137. Side view of attempts to calibrate a point cloud in the presence of tides in which the tidal signature is approximated with a linear model.	277
138. Table summary of the 15 proposed calibration parameters: including the vehicle maneuver that yields the most confident result in the calibration, which other parameters have a high correlation, identifies the 2 groups of parameters that are linearly dependent, and other calibration notes.	278
139. Chapter VII outline.	283
140. A simplified laser scanner with only three inputs, a laser range ρ , azimuth angle θ and elevation angle ϕ	294
141. Determining the area (and associated uncertainty) of a rectangle whose dimensions are determined by wrapping a 10-meter tape measure along the rectangle's half-perimeter.	301
142. The total propagated uncertainty interface.	305
143. A closer view of the parameter select screen within the TPU module.	306
144. A closer view of the point cloud spatial view within the TPU module.	307
145. A closer view of the TPU module's control panel.....	307
146. Table of predicted horizontal (2D) and vertical uncertainties of the CZMIL point cloud (1σ) with different models of Applanix POS AV.....	308
147. The net contribution to the horizontal and vertical TPU, sorted by parameter (left) and the percent contribution (right).	310
148. Point cloud colored by horizontal uncertainty (top).	312
149. The same point cloud in Figure 148, this time colored by TVU.	313

150. Dataset viewed from the front (vehicle traveling towards viewer) with vertical error bars shown with two standard deviations.....	314
151. Horizontal TPU where horizontal error bars are exaggerated at 10 times the scale used for the data points.	315
152. Horizontal (black) and vertical (red) propagated uncertainty (1σ) plotted versus the vehicle roll.....	316
153. Vertical propagated uncertainty (1σ) plotted versus vehicle roll.....	317
154. Vertical propagated uncertainty (1σ) plotted versus the laser range.	318
155. Horizontal propagated uncertainty (1σ) plotted versus the laser range.	318
156. Vertical (red) and horizontal (black) point cloud TPU (1σ) plotted versus the laser scanner's azimuth.	319
157. Horizontal (top) and vertical (bottom) point cloud TPU (1σ) plotted for various vehicle altitudes (from left-to-right: 1200, 1000, 800, 600, 400 and 200 meters).	321
158. Horizontal point cloud TPU (1σ) plotted against scanner azimuth for flight lines of various altitudes (0° = forward, 90° = starboard, etc.).	323
159. Horizontal point cloud TPU (1σ) for a vehicle steadily gaining altitude (200m left side to 600m right side).	324
160. Horizontal point cloud TPU (1σ) for a vehicle with boresight angles tilting the laser scanner forward and to port.....	325
161. Horizontal point cloud TPU (1σ) compared to laser azimuth (0° = forward, 90° = starboard, etc.).	326
162. Horizontal (left) and vertical (right) TPU (1σ) compared to laser range for a vehicle experiencing no dynamic roll, pitch or yaw.	326
163. Horizontal point cloud TPU (1σ) for a vehicle with boresight angles tilting the laser scanner forward and to port.....	327
164. Total horizontal uncertainty (1σ) for a rolling vehicle (black) plotted versus laser range.	328
165. Total horizontal uncertainty (1σ) for a rolling vehicle plotted versus vehicle's attitude.....	329
166. Total horizontal uncertainty (1σ) for a rolling vehicle plotted versus scanner azimuth (0° = forward, 90° = starboard, etc.).	330

167. The TPU module's interface as called from the calibration module.	332
168. Covariance panel within the propagated uncertainty interface, allowing the user the option of including covariance in uncertainty calculations.	333
169. Flight plan used to illustrate covariance.	337
170. Horizontal propagated uncertainty (1σ) with covariance included error calculation (all units in meters).	337
171. Horizontal propagated uncertainty (1σ) with covariance not included in error calculations (all units in meters).	338
172. Horizontal TPU (1σ) versus scanner azimuth (0° = forward, 90° = starboard, etc.) for a point cloud both including (top) and not including (bottom) covariance in the computation.	339
173. Table of reported confidences (1σ) from two calibration routines attempting to determine 4 (calibration #1) and 5 (calibration #2) parameters.	340
174. Horizontal TPU (1σ), in meters, when a fifth parameter (ϕ_{LS}) is included in the calibration.	342
175. Horizontal TPU (1σ), in meters, when a fifth parameter (ϕ_{LS}) is included in the calibration.	343
176. Visualization module of the variance-covariance matrix for the five parameter calibration run.	343
177. Visualization module of the correlation coefficients for the five parameter calibration run.	344
178. Horizontal TPU (1σ), in meters, for a point cloud which has both large uncertainties in its input parameters and large correlations among said parameters.	347
179. Horizontal TPU (1σ), in meters, for a point cloud which has both large uncertainties in its input parameters and large correlations among said parameters.	347
180. Table of changes in point cloud vertical TPU (1σ), in meters, depending on when the vertical GPS uncertainty is updated: in just the TPU module or both the TPU and calibration modules.	351

181.	For a point cloud with 8 observed parameters and 5 calibrated parameters (1σ uncertainties shown), table of the horizontal and vertical TPU (1σ) of the point cloud is presented for a variety of inputs into the TPU module.	352
182.	Table of calibration results from an 11-parameter calibration including prism/scanner alignments (1σ uncertainties shown).	354
183.	Horizontal (left) and vertical (right) TPU (1σ) versus scanner azimuth (0° = forward, 90° = starboard, etc.) for the calibrated point cloud depicted in Figure 182 – column 2.	355
184.	Table of calibration results from an 9-parameter calibration including the scanner azimuth bias (1σ uncertainties shown).	357
185.	Table of anticipated calibration and point cloud uncertainties (1σ) for the final proposed calibration procedure.	358
186.	Table of point cloud uncertainties (1σ) induced by the observed parameters (column 1), the calibration parameters derived from the LSA (column 2), the combined observed and LSA-calibrated parameters (column 3) and the combined uncertainty when the calibration parameters are determined by a method other than the LSA (column 4).	362
187.	Table of the true and adjusted values of the calibration parameters used to render the point cloud in Figure 188.	363
188.	An independent flight line was simulated (left).	364
A1.	An aircraft's roll (x-axis), pitch (y-axis) and yaw (z-axis) axes, where the arrow indicates the positive direction (from Grewal, Weill, & Andrews, 2007).	374
A2.	An aircraft's three orthogonal axes and the corresponding direction of a positive rotation.	375
A3.	The Tait-Bryan rotation sequence (ECEF to VRF): (a) align vehicle to ECEF, (b) rotate yaw angle, κ , about VRF z-axis, (c) rotate pitch angle, ψ , about once-rotated VRF y-axis, (d) rotate roll angle, ω , about twice-rotated VRF x-axis.	376
A4.	By reversing the order of rotations prescribed by the Tait-Bryan convention, an equivalent transformation can be performed by rotating about the fixed (non-rotating) Earth-centered Earth-fixed (ECEF) coordinate axes.	380

LIST OF ABBREVIATIONS

BAIM	Block Adjustment of Independent Models
CHARTS	Compact Hydrographic Airborne Rapid Total Survey
CZMIL	Coastal Zone Mapping and Imaging Lidar
DTM	Digital Terrain Model
ECEF	Earth-centered Earth-fixed
GPS	Global Positioning System
GUI	Graphical User Interface
ICP	Iterated Closest Point
IMU	Inertial Measurement Unit
INS	Inertial Navigation System
IRF	INS Reference Frame
LADS	Laser Airborne Depth Sounder
LiDAR	Light Detection and Ranging
LLRF	Locally-level Reference Frame
LPS	Laser-prism-scanner
LSA	Least-Squares Adjustment
NOAA	National Oceanic and Atmospheric Administration
QA/QC	Quality Control / Quality Assurance
SBET	Smoothed Best Estimated Trajectory
SHOALS	Scanning Hydrographic Operational Airborne Lidar Survey
SRF	Scanner Reference Frame
T-B	Tait-Bryan

THU	Total Horizontal Uncertainty
TPU	Total Propagated Uncertainty
TVU	Total Vertical Uncertainty
USACE	U.S. Army Corps of Engineers
USM	University of Southern Mississippi
VRF	Vehicle Reference Frame

LIST OF SYMBOLS

A	first-order design matrix for \vec{x} in LSA
B	first-order design matrix for $\vec{\ell}$ in LSA
$BS\theta_x$	SRF-to-IRF boresight (roll) misalignment
$BS\theta_y$	SRF-to-IRF boresight (pitch) misalignment
$BS\theta_z$	SRF-to-IRF boresight (yaw) misalignment
C_ℓ	a priori covariance matrix of the observations, $\vec{\ell}$
C_x	a priori covariance matrix of the parameters, \vec{x}
$\vec{\ell}$	observables within the LSA
\vec{L}_0	direction of laser pulse entering Fresnel prism
\vec{L}_1	direction of laser pulse within Fresnel prism
\vec{L}_2	direction of laser pulse exiting Fresnel prism
\vec{n}	normal vector for a planar surface used in the LSA
\vec{n}_{ECEF}	arbitrary vector in ECEF reference frame
\vec{n}_{VRF}	arbitrary vector in vehicle reference frame
\vec{P}	normal vector of interface between media (Snell's Law)
\vec{P}_1	normal vector to upper face of Fresnel prism
\vec{P}'_1	normal vector to upper face of Fresnel prism after rotations applied
\vec{P}_2	normal vector to lower face of Fresnel prism
\vec{P}'_2	normal vector to upper face of Fresnel prism after rotations applied

$PS\theta_x$	prism-to-scanner rotation angle about x_s
$PS\theta_y$	prism-to-scanner rotation angle about y_s
$PS\theta_z$	prism-to-scanner rotation angle about z_s
r	vector of correctors (residuals) to $\vec{\ell}$
\mathbb{R}_{BS}	rotation matrix based on vehicle boresight angles
\mathbb{R}_{ECEF}^{IRF}	rotation matrix from IRF to ECEF
\mathbb{R}_{LRF}	rotation matrix from nadir to LRF
\mathbb{R}_{IRF}^{LRF}	rotation matrix from LRF to IRF
$\mathbb{R}_{PS\theta_x}$	prism-to-scanner rotation matrix about x_s
$\mathbb{R}_{PS\theta_y}$	prism-to-scanner rotation matrix about y_s
$\mathbb{R}_{PS\theta_z}$	prism-to-scanner rotation matrix about z_s
\mathbb{R}_V	rotation matrix based upon vehicle attitude
\mathbb{R}_x	Tait-Bryan rotation about x-axis (roll)
$\mathbb{R}_{x''}$	Tait-Bryan rotation about twice-rotated x-axis (roll)
\mathbb{R}_y	Tait-Bryan rotation about y-axis (pitch)
$\mathbb{R}_{y'}$	Tait-Bryan rotation about once-rotated y-axis (pitch)
\mathbb{R}_z	Tait-Bryan rotation about z-axis (yaw)
$\mathbb{R}_{\theta_{zs}}$	rotation matrix to account for scanner azimuth
w	the misclosure of the LSA observation equation
\vec{x}	adjusting parameters within the LSA

\vec{x}'	once-rotated x-axis in Tait-Bryan
\vec{x}''	twice-rotated x-axis in Tait-Bryan
\vec{x}_{ECEF}	position of INS in ECEF reference frame
\vec{x}_G	coordinates of laser points on ground in ECEF reference frame
x_I	x-axis of INS reference frame
\vec{x}_{ECEF}^{IRF}	offset vector from IRF to ECEF
\vec{x}_{IRF}^{LRF}	offset vector from LRF to IRF
\vec{x}_{OBS}	coordinates of laser points within the LSA
\vec{x}_p	coordinates of reference point on planar surface used in the LSA
x_s	x-axis of scanner reference frame
\vec{y}'	once-rotated y-axis in Tait-Bryan
\vec{y}''	twice-rotated y-axis in Tait-Bryan
y_I	y-axis of INS reference frame
y_s	y-axis of scanner reference frame
\vec{z}'	once-rotated z-axis in Tait-Bryan
\vec{z}''	twice-rotated z-axis in Tait-Bryan
z_I	z-axis of INS reference frame
z_s	z-axis of scanner reference frame
δ	vector of correctors (adjustments) to \vec{x} used in the LSA
Δx_{IL}	x-component of offset vector from SRF to IRF

Δy_{IL}	y-component of offset vector from SRF to IRF
Δz_{IL}	z-component of offset vector from SRF to IRF
η_a	refractive index of air
η_s	refractive index of fused silica
η_w	refractive index of water
θ_1	angle of incidence (Snell's Law)
θ_2	angle of refraction (Snell's Law)
θ_{FR}	Fresnel prism slope
θ_{GR}	theta-angle describing ground normal in spherical coordinates
θ_{LS}	azimuth angle for laser vector $\overrightarrow{L_0}$ measured from x_s
θ_{VI}	heading misalignment between VRF and IRF
θ_{zs}	scanner azimuth angle
κ	vehicle yaw
μ_x	mean value of random variable x
ρ	laser range
ρ_0	laser range bias
ρ_1	laser range scale factor
$\rho_{x,y}$	correlation coefficient of random variables x and y
σ_x	standard deviation of random variable x
$\sigma_{x,y}$	covariance of random variables x and y

σ_x^2	variance of random variable x
ϕ_{LS}	zenith angle measured between laser vector $\overrightarrow{L_0}$ and z_s
ϕ_{GR}	phi-angle describing ground normal in spherical coordinates
ψ	vehicle pitch
ω	vehicle roll

CHAPTER I

INTRODUCTION

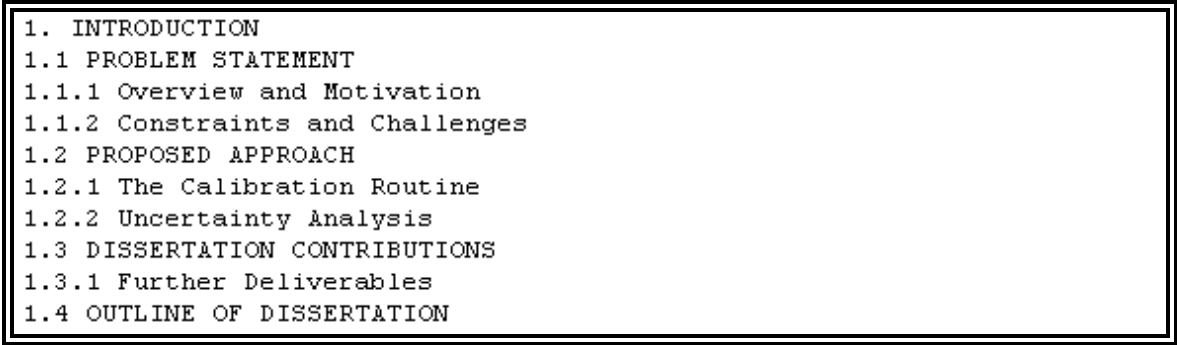
- 
- 1. INTRODUCTION
 - 1.1 PROBLEM STATEMENT
 - 1.1.1 Overview and Motivation
 - 1.1.2 Constraints and Challenges
 - 1.2 PROPOSED APPROACH
 - 1.2.1 The Calibration Routine
 - 1.2.2 Uncertainty Analysis
 - 1.3 DISSERTATION CONTRIBUTIONS
 - 1.3.1 Further Deliverables
 - 1.4 OUTLINE OF DISSERTATION

Figure 1. Chapter I outline.

1.1 – Problem Statement

1.1.1 – Overview and Motivation

This dissertation seeks to develop the acquisition procedures and data processing algorithms which are necessary for the determination of the angular misalignments and other geometric parameters associated with a bathymetric lidar; specifically, for the Coastal Zone Mapping and Imaging Lidar (CZMIL) system presently under development by Optech International, in collaboration with The University of Southern Mississippi, for the U.S. Army Corps of Engineers (USACE) in Kiln, MS (Tuell, Barbor & Wozencraft, 2010). More concisely, this dissertation will present a geometric calibrator for the CZMIL system. With a well-defined geometric calibration routine internal inconsistencies of the solutions to the laser location equation can be minimized, horizontal and vertical uncertainties of the laser footprints can be quantified and propagated into derived products, and a sensitivity analysis can be performed to understand what factors are the largest contributors to error in the sensor. Future work

could include incorporating results of the sensitivity analysis into a refined design of the CZMIL scanner.

This dissertation, to paraphrase Schenk (2001), proposes to close the gap between the accuracy potential and the actual accuracy achieved by today's airborne lidar systems. This can only be achieved through the development of a rigorous error model and a rigorous calibration procedure. A poor error model that does not sufficiently explain the measured discrepancies can lead to a lack of confidence in the system, which can be as damaging to the perceived value of a lidar than the magnitude of any actual errors.

In general terms, a bathymetric lidar (sometimes written "LiDAR" for Light Detection and Ranging) fires a laser pulse from an airborne platform, while a detector then measures the diffusely reflected energy from both the sea surface and the sea floor. Based upon the known speed of light in air and water and a finely measured two-way travel time of the laser pulse, the distances among the aircraft, the water's surface and the seafloor can be determined. Differencing the surface and bottom then yield a depth for a given location (Figure 2).

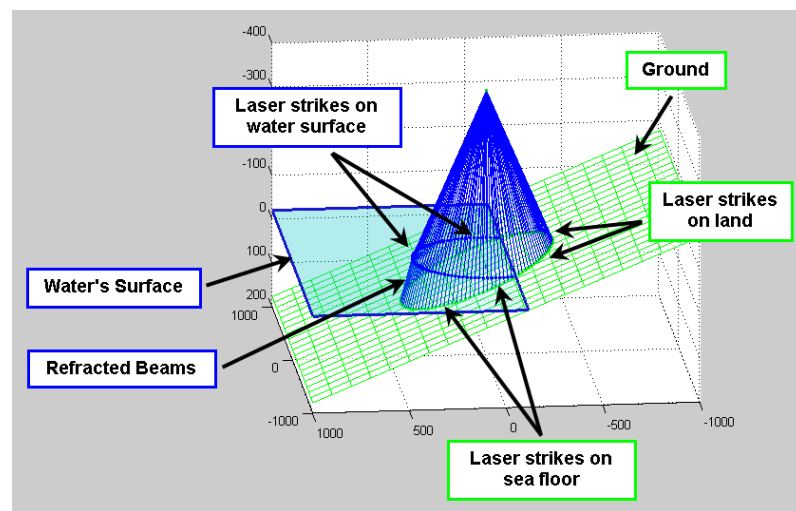


Figure 2. The path of a laser as it travels between the vehicle and the ground. Every ray shown in blue is traversed in both directions. Should the laser encounter the water, it is refracted and follows a new path.

One of the principle challenges of a bathymetric lidar (or, for that matter, a topographic lidar which measures elevations rather than depths) is accurately determining the three-dimensional position of this laser spot on the surface of the earth. To collect a swath of data coverage, the laser pulse itself must be constantly redirected across the ground in the form of some scan pattern (rectilinear, circular arc) through the use of a scanning device (e.g. precisely-synchronized mirrors or a rotating prism) (Figure 3).

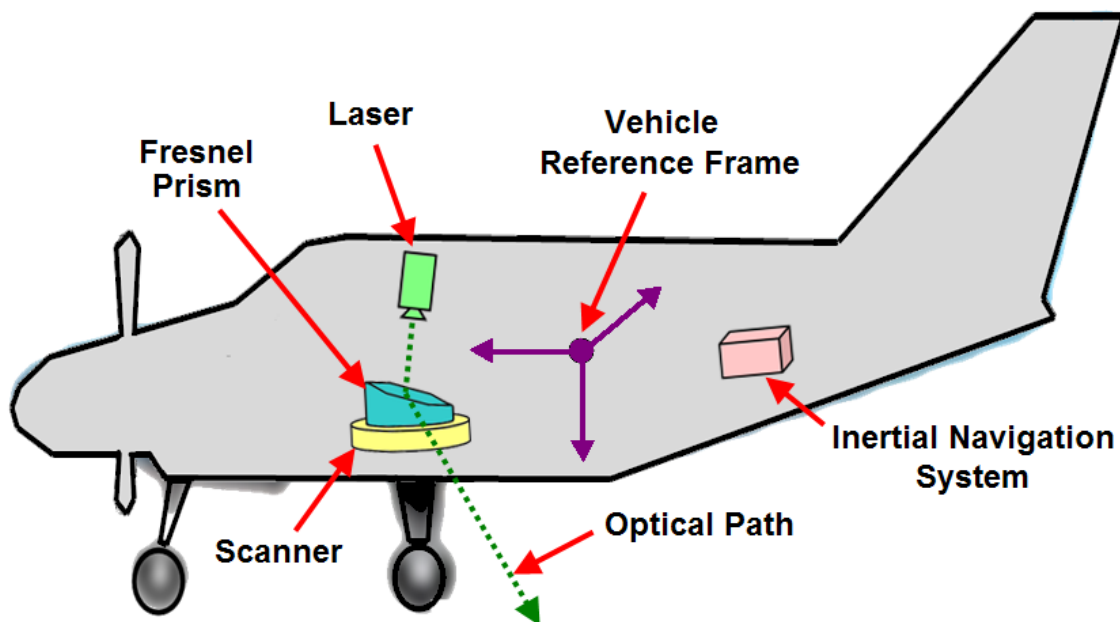


Figure 3. A lidar system with some of its many components, each with its own reference frame and displacement vector.

The aircraft from which the lidar is deployed is a dynamic environment that is subject to pitch, roll and yaw. Additional sensors, such as an Inertial Measurement Unit (IMU) and Global Positioning System (GPS) antenna are needed to determine the position and orientation of the aircraft. In a perfectly aligned system, one in which the reference frame of the laser is coincident with the reference frames of the scanner, IMU and aircraft, changes in orientation of the aircraft (and sensors) will be precisely

determined by the IMU and directly converted to changes in the laser's orientation. Thus these orientation parameters must be measured and accounted for in the geometric problem of tracing the laser pulse to the ground. More likely, the various reference frames will be slightly out of alignment. In an exaggerated case, if a laser system were to be incorrectly mounted with a 90° rotation, then any aircraft pitch measured by the IMU would actually be interpreted as a systematic roll bias in the laser, and vice versa. The misalignments between laser and IMU (the boresight angles) must be determined so the proper orientation parameters measured in the IMU's reference frame can be propagated to the laser.

Lastly, the precise position of these aircraft-fixed reference frames must be known with respect to the eventual charting reference frame. It does no good to know the depth directly below the aircraft if, in turn, one does not know where the aircraft is. Further, because the laser and the GPS antenna will be at different physical locations on the aircraft, offsets between the two instruments must be measured (likely in the IMU's reference frame). In this way, the position of the antenna can then be translated to the laser.

It is only through an exact determination of the scanning device's pointing vector; the alignment of the laser with respect to the IMU; the offsets among the laser, scanner, GPS antenna, and IMU; and the orientation/position of the IMU with respect to a reference datum that one can compute a precise location of the laser footprint. The greater the uncertainty in any of the preceding input parameters, the greater the uncertainty (and induced error) in the location of the ultimate laser footprint. The

preceding parameters can only be estimated through a rigorous geometric calibration routine, which is the goal of this study.

1.1.2 – Constraints and Challenges

The development of a geometric calibrator must take the following constraints and challenges into consideration:

1. The scanner design: The proposed CZMIL scanner, a fixed-elevation, circular-spinning scanner is a departure from designs employed in previous systems developed by Optech (SHOALS and CHARTS with their forward-looking fixed-arc scanners). While earlier generation commercial bathymetric lidars have employed servo-based scanners to direct the beam, CZMIL employs a constantly rotating Fresnel prism that will refract the laser pulses to a constant off-nadir angle (Figure 4) (Fuchs & Mathur, 2010; Fuchs & Tuell, 2010). The continuous uni-directional movement has an advantage over other scanner designs because it is thought to be a more mechanically stable system and permits a faster scanning rate. While used in the military for the detection of power lines, they are not routinely used in airborne surveying (Wehr, 2009). Due to this dearth of operational deployment, one of the largest potential contributions of this research is a full parameterization of the movement of such a scanner. This could include such attributes as the angles of refraction, potential misalignment between the prism and the scanner's axis of rotation, and identifying time latencies with regard to the prism's radial orientation.

2. Optical path alignment: The orientation of the laser/scanner assembly with respect to the IMU, and any biases/misalignments must be established. Further, there may be misalignments between the laser and scanner (i.e., the laser is not fired

orthogonal to the prism or the laser is not centered on the prism) (Figure 3). It is conceivable these internal misalignments between laser and scanner may have to be determined during a factory calibration (where the proposed geometric calibrator can estimate the uncertainties of these parameters). Some may have concerns about the alignment of the optical receptors as well, but this dissertation is geared only towards aligning the outgoing signal. As will be discussed, the top of the prism is considered the origin of this particular lidar, and in that respect, the optical paths of both the transmitted and received pulses are equivalent. Any further misalignments of the receiving optics will result in no waveforms being detected (a situation that will hopefully be quickly recognized while still in the hands of Optech).

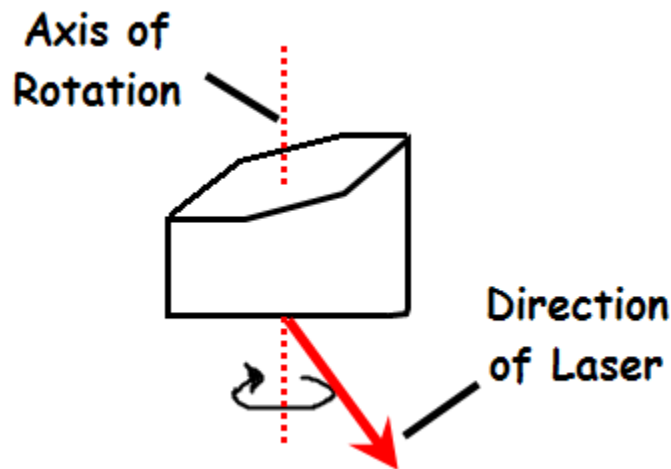


Figure 4. Rather than relying on reflective surfaces, the CZMIL system will use a Fresnel prism to steer the laser beam via refraction.

3. Discrete sampling pattern: Lidar yields a discrete sample of postings from a continuous world. Even were the same area to be flown several times, it is unlikely a laser spot will strike the exact same footprint a second time. This irregular spatial distribution must be overcome if one hopes to compare one dataset to another in an

attempt to extract calibration parameters. Herein, we adopt an approach to this correspondence problem based on the fitting of the lidar point cloud to planar surfaces.

4. Non-uniform scanning pattern: The circular scanner employed on the CZMIL system will result in a helical scan pattern on the ground (Figure 5). This non-uniform data will result in a relative abundance of laser strikes to either side of the aircraft as opposed to directly ahead or behind. Further, unique to a circular scanner is that it is a multi-look system; that is, some areas will be illuminated more than once on a single pass. This non-uniform scanning pattern will present both challenges and opportunities with respect to a geometric calibrator.

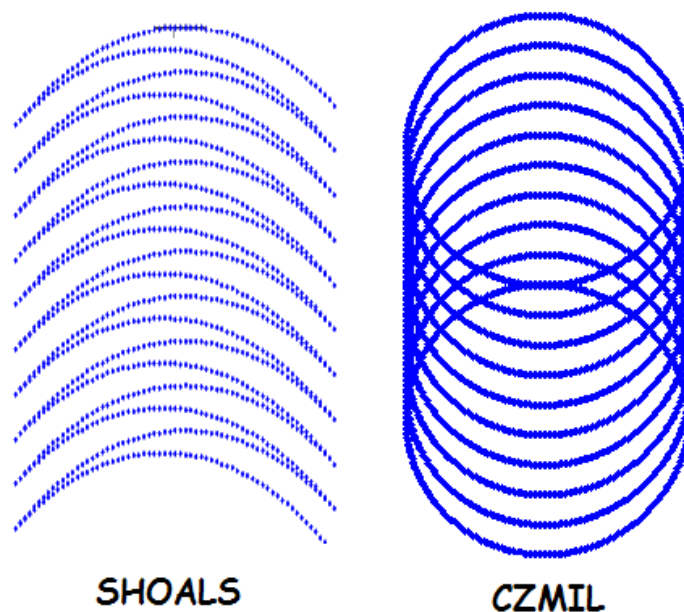


Figure 5. Basic scan pattern of present generation lidar system (SHOALS) and proposed CZMIL scanner (direction of flight is from bottom to top).

5. Working in a simulated environment: The first flights of the CZMIL system are scheduled for the spring of 2011. Therefore, the calibrator developed in this work has been based on data generated with a geometric simulator of the CZMIL scan pattern. Through dialog with the engineers building the system, every effort has been made to

assure the accuracy and validity of the point cloud simulator. It is based on these simulated datasets that the calibration routines and algorithms have been developed. It must be examined to what extent the artificial errors introduced in such a controlled environment will accurately reflect the uncertainties that will be experienced in the field. On the other hand, there are advantages to working with a digital model. In theory, a complete calibration flight-plan can be designed, acquired and processed without an actual aircraft ever leaving the ground. Analyzing this virtual data set will provide an estimate on the confidence in the extracted parameters. Additionally, any fault (from a geometric standpoint) can be simulated to establish the impacts on the point cloud (with the intent of constructing a catalog for real-world failures). “Point cloud” being a generic term to describe the collection of (x,y,z) laser spots located in space.

Finally, a complete production model of the CZMIL system is not necessary to examine the behavior of the individual components. As modules of the CZMIL system are constructed (particularly the scanner), the simulated errors can be tested and refined against the actual components.

1.2 – Proposed Approach

This research is divided into three principal components: a simulation of the point cloud, the development of a calibration algorithm, and an assessment of the uncertainty in both the calibrated parameters and the resulting point cloud. Through the development of the equation, a sensitivity analysis is then performed on each parameter to assess how small changes in a given parameter manifest themselves as changes to the point cloud. In the execution of the calibration algorithm, various flight characteristics

are then examined to assess how unidentified system misalignments manifest themselves in the biased point cloud via signature analysis plots.

1.2.1 – The Calibration Routine

The adjustment is based upon a least-squares model similar to one employed by Freiss (2006), with an observation equation given as:

$$f(\vec{\ell}, \vec{x}) = \vec{n} \cdot (\vec{x}_{OBS} - \vec{x}_p) \quad (1.1)$$

$\vec{\ell}$ = the observations (laser range, scanner azimuth, etc.)

\vec{x} = adjusting parameters of planar surface and laser

\vec{n} = normal vector of the planar surface

\vec{x}_{OBS} = coordinates of laser point

\vec{x}_p = coordinates of reference point on planar surface

In words, the model performs an adjustment that minimizes the perpendicular distance between a collective set of data points and the planar surface which they describe. The advantage is this model allows for a simultaneous adjustment in determining the parameters of the planar surface as well as the calibration values of the lidar system.

Through linearization, the observation equation takes the form:

$$w + A \cdot \delta + B \cdot r = 0 \quad (1.2)$$

w = the misclosure of f

A = the first-order design matrix for \vec{x} , the parameters

δ = vector of correctors (adjustments) to \vec{x}

B = the first-order design matrix for $\vec{\ell}$, the observations

r = vector of correctors (residuals) to $\vec{\ell}$

A modification to the traditional least-squares will be employed using the weighted constraint normal equations (Wells, 1999):

$$\begin{bmatrix} C_\ell^{-1} & B^T & 0 \\ B & 0 & A \\ 0 & A^T & C_x^{-1} \end{bmatrix} \cdot \begin{bmatrix} r \\ k \\ \delta \end{bmatrix} + \begin{bmatrix} 0 \\ w \\ 0 \end{bmatrix} = \vec{0} \quad (1.3)$$

C_ℓ = the a priori covariance matrix of the observations, $\vec{\ell}$

C_x = the a priori covariance matrix of the parameters, \vec{x}

The difference between this model and the one employed by Freiss (2006) is the Bayesian inference applied through the weighting of the initial estimates of the parameters, the C_x . Using Bayesian decision theory, by making some a priori assumptions about the uncertainties of the estimated parameters, the model can be “steered” to an appropriate solution (Martin, 1967). Through judicious monitoring of the weights on the parameters to be estimated, singularities that could arise in solving for δ can be averted. In this way, the Hough Transform used by some authors (Freiss 2006; Lee & Schenk, 2001; Vosselman & Dijkman, 2001) can be circumvented. The disadvantage of the traditional implementation of the Hough transform is that the performance deteriorates as the planar surfaces approach vertical; with weighted constraints, it is believed both horizontal and vertical planes can be captured. This would imply that the sides of buildings can be captured in addition to just the roofs, relaxing the requirements that are placed on field units with regard to the type of cultural features required to be in a survey area to perform a successful calibration. Further, linear feature extraction could be achieved through the intersection of a building’s wall and roof (alleviating the necessity of gabled roofs).

A future planned modification to the least-squares model is to pursue a sequential strategy. Data points will be processed in clusters, in which the estimated parameters

from the first cluster will be used as the initial estimate for the second cluster, and so on until the entire data set is processed. Such an approach will reduce the computational load at any given step, particularly with regard to the necessary matrix inversions, and facilitate the processing of extremely dense datasets.

1.2.2 – Uncertainty and Analysis

The uncertainty analysis begins with the results of the calibration routine. The uncertainty analysis of this project will begin with the statistical confidence that can be placed in the values of the calibrated parameters. An advantage to using a least-squares approach for the calibration is that the output yields both calibration values and a variance-covariance matrix of the same parameters. Examination of the covariance matrix will yield both the estimated uncertainties of the parameters, and an indication of any cross-correlations (which will aid in identifying whether the calibration routine is properly isolating all the parameters of interest). After repeated executions of the calibration routine on a variety of datasets, the estimated calibration parameters and their associated estimated uncertainties can be examined to determine whether they are statistically compatible with the “known” calibration values.

From there, the reported uncertainties of the calibration parameters can be coupled with the uncertainties of the observed parameters to determine the net uncertainty in the point cloud positions. This will be performed via the general law of the propagation of variances.

1.3 – Dissertation Contributions

The ultimate goal of this dissertation is to deliver the framework of a geometric calibrator for the CZMIL system. This framework includes guidelines on an optimized

flight plan to be used during acquisition to collect the needed calibration data and a set of software tools that can be used to extract the calibration parameters (boresight misalignments, laser/navigation timing, a parameterization of the prism and its axis of rotation, lever arm offsets, and inconsistencies in the IMU and GPS). An ancillary product of the calibration routine are the uncertainty estimates in each of these geometric parameters. These uncertainties can be used to feed an uncertainty analysis model derived from a propagation of variances, yielding both a horizontal and vertical uncertainty of each laser footprint. Finally, a sensitivity analysis for the CZMIL system is presented. With this information, the coupling of the uncertainties are better understood and more informed decisions can be made with regard to any future system refinements with the aim of minimizing the uncertainties of the laser footprint locations, and improving the efficiencies of the calibration process as a whole.

1.3.1 – Further Deliverables

In addition to addressing the preceding considerations, the following items are natural requirements and products of a geometric calibrator:

1. Efficient field calibration: This calibration routine should be designed in such a way that it can easily be performed by a technician in the field with minimal acquisition time invested.

2. Patch test analog: In the world of acoustic sonar, the determination of offset and orientation parameters is done through a calibration routine called a ‘patch test’. In a patch test, a series of data strips (oriented in a predetermined way, sometimes involving the use of special geometric targets) are collected and then compared to one another to assess the magnitude of the internal biases. This dissertation seeks to find a calibration

line plan for the CZMIL system that can (ideally) be performed in as generic a landscape as possible (i.e. requiring gabled roofs = bad; flat runways = better).

3. Sensitivity analysis: With a fully-developed set of uncertainty propagation equations, a sensitivity analysis can then be performed to establish which input parameters have the greatest effect on the final horizontal and vertical uncertainties of the laser footprints. In an ideal world, this analysis would be performed early enough in the CZMIL development cycle that resources could be appropriately invested to address the more egregious parameters. For example, should more effort be expended making sure the prism spins at a uniform rate, or that the prism is well-aligned with the scanner?

1.4 – Outline of Dissertation

The overall structure of this dissertation is as follows:

- Chapter II is a literature review that seeks to summarize the key work others have done as related to this dissertation. This literature review not only touches on how these previous works are important to this current research, but establish how this particular dissertation is unique to the scholarly works that have preceded it.
- Chapter III presents the laser location equation. It spells out in full detail how to take all of the lidar's input parameters and create a geometrically correct point cloud.
- With the laser equation developed, Chapter IV encodes the equation within MATLAB to permit the simulation of a point cloud. A simulation is the only means of generating datasets for use in testing the calibrator given the lidar itself has not yet been constructed. Other advantages to having a point cloud simulator are discussed in Chapter IV.

- Chapter V presents the theoretical framework for the development of a least squares adjustment. The method of least squares is derived from first principles and then applied to an observation equation that will result in fitting the lidar point cloud to a single planar surface.
- Where Chapter V is theoretical, Chapter VI is practical. Chapter VI examines all of the input parameters of the laser equation developed in Chapter III and examines how they impact the point cloud. Particular attention is given to what flight characteristics are necessary to calibrate any given parameter. Then the least squares algorithms developed in Chapter V are applied to the system calibration under a variety of calibration conditions (including over narrow runways and a dynamic sea surface). The confidence of the solution of the calibration algorithm will also be discussed. Chapter VI will describe the precise recommendations for conducting an in-field calibration exercise.
- Chapter VII then takes the uncertainties of the calibration parameters and parlays them into a full total propagated uncertainty model for the point cloud. Using a general law for the propagation of variances, the predicted confidence in the positioning of the laser points can be assessed. The relative contributions of uncertainty by the manufactured components and the calibration module; the effects of ground control; and the effects of flight characteristics will all be considered.
- Finally, Chapter VIII contains a summary of all key findings from previous chapters. Additionally, Chapter IX presents recommendations for future work, which would include both refinements of the present techniques and an expansion towards other bathymetric systems.

Each chapter begins with a short summary outlining the material that follows, and each chapter will end with a summary statement that encapsulates the most important take-home messages from the preceding material.

CHAPTER II

REVIEW OF PREVIOUS WORK

2.1 INTRODUCTION
2.2 STRIP ADJUSTMENT
2.3 FEATURE EXTRACTION
2.3.1 Planar Patches
2.3.2 Linear Features
2.3.2.1 Intersection of planes
2.3.2.2 Covariance of points
2.4 ADJUSTMENT PROCEDURES
2.4.1 Feature Adjustment
2.4.2 Point-Set Registration
2.4.3 Grid Surface Matching
2.4.4 Calibration Targets
2.5 UNCERTAINTY ANALYSIS
2.6 OVER-CONSTRAINED SYSTEMS
2.7 SUMMARY

Figure 6. Chapter II outline.

2.1 – Introduction

Before rushing headlong into the development of a geometric calibration tool, a brief summary of some of the related literature on airborne calibration is presented. The methods include manually adjusting adjacent strips of data until the two datasets appear internally consistent (Section 2.2); extracting linear or planar features from the point clouds, which are then adjusted to one another (Section 2.3) – this adjustment may be performed through a least squares algorithm (Section 2.4.1); fitting the points of each swath to each other via an iterated closest point algorithm (Section 2.4.2); deriving gridded surfaces from the data (Section 2.4.3); or setting targets of known location through the survey area (Section 2.4.4). In addition to calibration, articles were also consulted on the present techniques for computing the uncertainty of a point cloud (Sections 2.5 & 2.6). Finally, all of the previous techniques are objectively assessed for

their applicability to this study as a decision to employ a least squares adjustment is made (Section 2.7).

2.2 – Strip Adjustment

Lidar data acquisition is typically done from an airborne platform that flies back and forth over a given survey area, acquiring alternating swaths, or strips, of data. A “strip adjustment” is a generic term that refers to a technique used to identify and reduce (or eliminate) any positional discrepancies in the lidar point cloud as observed between adjacent strips of lidar data (Habib, Kersting, Ruifang, Al-Durgham, Kim & Lee, 2008b). This is achieved by improving the compatibility among neighboring strips. The technique is similar, in principle, to the Block Adjustment of Independent Models (BAIM) developed for use in photogrammetry.

An adjustment in photogrammetry largely depends on the identification of prominent control points in overlapping photographs. These control points can then be used to estimate the mounting parameters (offset and orientation) of the camera with respect to the aircraft’s reference frame. Kilian, Haala, & Englich (1996) were the first to describe a procedure openly modeled after the photogrammetric strip adjustment that was designed to determine the systematic errors in the GPS and INS sensors of a “laser scanner system.” With lidar, however, due to the sparse nature of the lidar footprints, even were one to survey a given area several times, it is unlikely two laser footprints will be exactly coincident on the surface scanned (Freiss, 2006). This suggests that a calibration routine based on point-to-point comparisons of overlapping swaths may be difficult to implement.

To overcome the challenge to the correspondence problem presented by matching individual points, photogrammetrists have adopted object-based matching techniques, wherein spatial objects were extracted from the imagery or point clouds. The most frequently extracted features are either planar patches (Freiss, 2006; Lee & Schenk, 2001; Vosselman & Dijkman, 2001) or linear features (Habib et al., 2008b). The extracted planes and lines will then act as proxies for the control points in the BAIM of photogrammetry. On some occasions, digital terrain models (DTMs) of the point clouds are constructed, then corresponding areas within DTMs are compared (Kilian et al., 1996). Working with DTMs, however, presents the same problem as working with the point data, it is difficult to truly determine what areas are conjugate; moreover, the original data set is altered in the DTM through the interpolation that must occur in the conversion to a grid (Gross & Thoennessen, 2006).

It must be noted that some strip adjustments, particularly when performed in the context of lidar, only have the stated goal of making sure the point clouds from each strip are consistent with each other. Not only must the data be internally consistent, this dissertation has the added requirement that the final point cloud must be consistent with the real-world (i.e., though the lidar point cloud may look good on its own, it must also be consistent when compared to an outside data source, like another survey). Further, the goal is to solve for physically-meaningful calibration parameters associated with a well-designed sensor model; not to just make the data from overlapping swaths “fit.”

2.3 – Feature Extraction

2.3.1 – Planar Patches

Vosselman and Dijkman (2001) wrote, “due to the overwhelming evidence provided by the large number of points, the detection of planar roof faces is quite reliable” (p. 37). The extraction of planar patches from laser scanner data has been used extensively for urban planning, the construction of 3D city models and to promote enhanced navigation (Gross & Thoennessen, 2006). One method employed for the planar extraction is the Hough transform (extended into three dimensions). The advantage of the Hough transform is that it does not require the computation of a normal vector to the plane, which can be noisy with laser data (Vosselman & Dijkman, 2001). With the Hough transform, each laser point in real space corresponds to a plane in a parameter space (these being the parameters of a potential plane in real space). Any laser points that are coplanar in real space will have planes in the parameter space that intersect at a point (the coordinates of this point being the planar parameters).

Lee and Schenk (2001) found the Hough transform to be lacking because it did not account for the spatial relationship of the laser points. That is, a collection of points that happen to occupy the same plane may not necessarily be part of the same physical space (consider separate roofs of adjacent buildings). Thus Lee and Schenk offered a refined approach to the Hough transform based on the concept of surface growing. For each laser strike, a small patch is constructed from neighboring points based on the spanning tree of a Delaunay triangulation network. A plane is fitted to each patch (using a least-squares approach) and the patches are then sorted by a fitting error associated with each plane. Each patch then acts as a seed as one-by-one, adjacent laser points are tested

whether they also fit the associated plane (to a prescribed tolerance). With a successful fit, the point is added to the patch and the parameters of the best-fit plane are recomputed. This modified version of the Hough transform is commonly used for extracting planar surfaces from lidar data (Freiss, 2006)

While determining the orientation and altitude of the planar patches is a relatively easy matter, the sparse laser footprints makes determining the perimeter of the planes more difficult. To augment their extraction algorithms, some researchers (Kilian et al., 1996; Vosselman & Dijkman, 2001) would consult the ground plans of the buildings surveyed. These plans would reveal the precise locations of all building walls and the extents of roof faces. Additionally, ground plans would reveal any elaborate features (e.g. gables) that could be difficult to discern from the point data.

2.3.2 – *Linear Features*

2.3.2.1 – *Intersection of planes.* While planar patches are the most prominent feature to be found in the surveyed terrain (Freiss, 2006), linear features also bear investigation. Vosselman and Dijkman (2001) used linear features as a supplement to their extracted planar patches. All of the (non-parallel) planes were extended until they intersected in a line object. It was argued that these detected ridge lines in the roofs would have a “very high” (p. 40) accuracy as they are derived from two planes which are both determined through many lidar points (Vosselman & Dijkman, 2001). The larger source planes would incorporate more laser footprints and thus be less susceptible to point cloud noise (Habib et al., 2008b).

Habib et al. (2008b) also used the intersection of extracted planar surfaces for the purposes of identifying linear features in the dataset. The intersections of neighboring

planes will produce a theoretically infinite line; endpoints to the line segments are determined based upon the dimensions of the planar patches and user-defined buffers. These endpoints are then used for the purposes of performing the adjustment in later steps (see “Least-Squares Adjustment” in next section). Conjugate linear features from different swaths are then identified based upon the normal distance between lines, the degree of parallelism and the percentage of overlap.

2.3.2.2 – Covariance of points. An alternative method of extracting linear features from point data (that does not depend on the intersection of planes) instead focuses on the neighborhood of each laser point (Gross & Thoennessen, 2006). A sphere is circumscribed around each laser footprint (the radius of the sphere being a function of the lidar spot spacing). For each sphere, a covariance matrix is constructed based upon the centralized moments of the enclosed points. Finally, the eigenvalues and eigenvectors of the covariance matrices are computed. Based on the ratios of the eigenvalues, the object characteristics of the point can be deduced with respect to its neighbors (i.e., whether the point lies on a edge, corner, plane, etc.).

After every point is categorized into its appropriate “situation type” (Gross & Thoennessen, 2006), all the points that lie on an edge are collected and examined. For a point on a line, the eigenvector associated with the largest eigenvalues is oriented in the direction of the line. The inner product of eigenvectors of points within a given proximity of this line are then computed with respect to the original eigenvector (with a given threshold) to determine whether they lie on the same line. Finally, there is some deconfliction of line segments based on a prescribed minimum gap in the data (to separate features like collinear edges of different buildings in a row).

In implementations of the covariance method, datasets were derived from terrestrial laser scanners, not airborne lidar systems. The data density exhibited in Gross and Thoennessen (2006) is nearly two orders of magnitude larger than any presently available airborne system. The extraction algorithms may not be robust enough to work on a single swath of data collected from an airborne platform.

2.4 – Adjustment Procedures

2.4.1 – Feature Adjustment

Be it points, lines or planes, once the desired features have been parameterized, an adjustment method is needed to determine the calibration parameters that lead to an optimal alignment of the extracted features. Whether deriving a calibration routine or performing an adjustment for some other purpose, the literature is abound with variations of the least-squares adjustment (LSA) (Bang, Kersting, Habib & Lee, 2009; Habib et al., 2008b; May, 2009; Vosselman & Dijkman, 2001). In some cases (Freiss, 2006), several least-squares adjustments are performed within a single study; for example, in a strip adjustment, one adjustment would be necessary for the extraction of the planar patches within each strip, and a second adjustment would be needed to align the patches from strip to strip.

The most robust LSA model, particularly with regard to what this dissertation is proposing, is the model employed by Freiss (2006). Freiss, who was using conjugate planar patches as his seed, developed a model that adjusted for the planar patch's normal vector, a correction factor for the laser range, a single scan angle scaling and offset correction, a set of corrections for the GPS antenna to laser scanner offset and orientation

corrections. The input parameters are the laser range and angle, the GPS antenna position and the IMU attitude (pitch, roll, heading).

There are several advantages to the use of a LSA in this application. Not only will the adjustment identify any systematic errors for removal, producing a geometrically-correct point cloud, but analysis of the covariance matrix will provide estimates of the random uncertainty of each input parameter (Freiss, 2006). What is more, through manipulation of the weights in the covariance matrix the degree to which a given observation affects the final calibration parameters can be estimated – this is the essence of sensitivity analysis. Finally, the uncertainty of the point cloud positioning can be determined through error propagation, by substituting the uncertainties derived through the covariance matrices.

A potential alternative to using planar patches as a seed in the LSA is instead using linear features (which are typically, but not always, derived from the intersection of the neighboring planes). Both Habib et al. (2008b) and Bang et al. (2009) used extracted line segments in their adjustment; however, because of the sparse nature of the data, the endpoints of these line segments could not be expected to coincide from swath to swath. To compensate for non-conjugate end points, a new coordinate system was defined with one axis oriented along the line segment. Then, as the adjustment is performed, a suitably large variance is introduced along this axis to permit the end points to “wander.”

2.4.2 – Point-Set Registration

There are several disadvantages in trying to adjust a lidar point cloud based upon using extracted features. For one, it is computationally non-trivial to extract and coregister objects from different swaths. In working with extracted planar patches and

line segments, one isn't working with the actual observables, thus the uncertainties of the adjustment are compounded. Finally, making lines and planes a prerequisite for a calibration routine will fundamentally limit the number of areas where a calibration can be performed: buildings and structures may not be present in a survey area and adequate ground control may not be established near the airport. Thus, an ideal registration might be performed with several overlapping data sets collected over a generic surface by adjusting the laser footprints themselves.

In Besl and McKay (1992), one of the earliest descriptions of the registration of point sets is presented. It was presented as a computer visualization problem in which a model, existing in its own model space, has a 3D representation of data points (presumably collected in some separate sensor space). The problem was to determine the optimum rotation, translation and scaling that would align the model and geographic spaces and thus minimize the distances between the two data sets. The optimization method used was the Iterated Closest Point (ICP) algorithm.

The ICP is robust enough to work on point sets, line segments, curves, faceted surfaces, and others (thus it could be utilized on the extracted features described in the previous section). Further, no derivatives or finite elements are needed. Requiring an initial guess of the 6-parameter transformation (three rotations, three translations, no scaling), an LSA is performed, adjusting for the sum of the minimum distances from one point set to the other. The registration from the LSA is applied to one of the data sets and the process is repeated, monotonically converging on an optimal solution. When multiple scans of the same area were available, Gross and Thoennessen (2006) used an ICP algorithm to resolve discrepancies between datasets.

There are two drawbacks to the ICP. First, the algorithm is highly susceptible to outliers. The ICP was not developed with lidar data sets in mind, thus a filtering procedure would need to be placed on the front end of the data. Second, while the algorithm converges rapidly at first, it is very slow in converging to a final optimal solution. Both of these short-comings are addressed in a modified version of the ICP called the Levenberg-Marquardt ICP (Fitzgibbon, 2003).

The Levenberg-Marquardt ICP, replaces the LSA in the traditional ICP approach with a non-linear 2nd order series expansion of the point-to-point uncertainties. The technique is still iterative, following a Gauss-Newton approximation model, but an extra parameter is added to the iteration step. This extra parameter can be used to fine-tune the convergence rate of the algorithm. In this way, Fitzgibbon (2003) was able to overcome the relative slow convergence near the optimal registration and created a technique less dependent on the quality of the initial guess.

2.4.3 – Grid Surface Matching

May (2008) also recognized the difficulties in trying to establish correspondence between objects acquired in overlapping strips. To overcome this, she would construct an interpolated grid of each swath. Then choosing an appropriate patch (avoiding forests or densely built-up areas), the distances from all the laser points in one swath would be compared to a collection of virtual points on the interpolated grid of the other swath. These distances would be the observations to be minimized via a LSA based on a Gauss-Markov model. Intensity information would also sometimes be used to augment the identification of segments.

In this way, using only two to three overlapping flight lines, May (2008) was able to estimate the three boresight misalignments. Patches were chosen for comparison such that they were as far from nadir as possible – outer swaths being preferable because boresight misalignments would be most magnified there. The proposed flight pattern had two flights flown in opposite directions, overlapping along their outerbeams, and one crossline flown perpendicular to the other two. This proposed flight pattern is very similar to the acquisition lines suggested by NOAA when performing a multibeam calibration (NOAA, 2008).

Bang et al. (2009) performed a similar point-to-virtual point matching. Rather than comparing laser points from one swath to the interpolated grid of another, they compared the points of one swath to the extracted planar patches of the other (and vice versa). This maintained a level of integrity with respect to working directly with the original observations.

2.4.4 – Calibration Targets

An alternative to having to develop algorithms designed to extract planar patches or linear features from (often) irregular objects that exist in the real world is to instead import some mobile lidar targets. In Csanyi, Toth, Grejner-Brzezinska and Ray (2005), a study was conducted to determine what characteristics would make for the best ground-based deployable lidar target. It was found a circular disk (circular, to be directionally independent), raised from the ground (so it could be identified from the elevation data), with two concentric circles of contrasting reflectance. By using the highly contrasting colors, the targets can be identified with an automated algorithm that uses a histogram-based adaptive threshold based on the intensity of the returns.

When deployed, the targets are leveled, thus when the targets are identified in the point cloud, a horizontal plane is fitted to the data. This fitted plane can then be one of the observations in the calibration adjustment. Further, the center of each target can be surveyed in using precise ground control, which will aid in shifting the lidar data into the proper mapping frame. The horizontal adjustment is aided by the Hough transform. The center of the target is estimated in the lidar data based upon the known radius of target. A locus of all the possible locations of the center is determined, and then the center is assumed to be at the centroid of this region.

Using the targets and procedures described above, reported discrepancies of as little as 2-3 cm in the horizontal and 1.3 cm in the vertical were detected. The accuracy is highly dependent on the density of the postings, with the previous accuracy being quoted at a data density of 16 points/m². This could be an instance where CZMIL could take advantage of its circular scanner design, which is anticipated to have a high density of points at the outer edges of each swath.

The advantage to using the lidar targets is it provides the closest analog to the photogrammetric control points used in the BAIM. Without control points, the surveyor is depending on the local geography of the survey area to provide features (buildings, roads, broad flat patches) that can be used for registration. One disadvantage is the size of the targets. The optimal size was found to have a radius of 1 meter. Unless a collapsible alternative is constructed, these targets may prove difficult for field crews to transport from project to project. Another major drawback is requiring the presence of a field survey crew to support operations on the ground.

2.5 – Uncertainty Analysis

A point cloud simulator provides a simple tool for a preliminary sensitivity analysis. Most authors (Freiss, 2006; Habib et al., 2008b; Schenk, 2001) who developed a simulator took advantage of their encoded lidar equations to assess the impacts of systematic biases in the lidar location equation. They would begin with a defined set of trajectories, scan angles, position and orientation information to be used as a reference. Biases would then be systematically added to each parameter and the impact between the bias-contaminated and the true coordinates of the laser footprints would be assessed. In this way, Habib et al. (2008b) confirmed any biases between adjacent lidar strips could be modeled with a six-parameter rigid-body transformation (three translations and three rotations); and Freiss (2006) could derive a correlation between vertical uncertainty and scan angle.

There have been several comprehensive approaches to uncertainty analysis of lidar data, two of which originated within The Ohio State University, Schenk (2001) and May (2008). Both studies consider a vertical lidar scanner, though Schenk does briefly touch on a circular scanner. Schenk is meticulous in his derivation of a pristine (error-free) lidar positioning equation and equally thorough in developing a positioning equation that contains each conceivable type of error source.

Both authors, once their error sources have been identified, proceed with considering the individual impact of each input parameter on the final point positioning accuracy. By working with one parameter at a time, it was easier to assess the individual effect of each input parameter under various conditions (different altitudes, scan angles, or magnitudes of random error). May (2008) subdivides the uncertainty analysis into

both systematic bias and random errors which are both considered through a propagation of variances based on a first-order Taylor series expansion; whereas Schenk (2001) uses geometric arguments to derive explicit expressions for the error model.

In addition to examining individual errors, May (2008) performed a comprehensive accuracy assessment through the analytic derivation of the error formulas from a rigorous error propagation of the lidar location equation. This error propagation only considered random errors and thus had assumed a proper calibration routine had already been performed to remove (or at least quantify) any systematic bias.

Through the derived error equations, May (2008) was also able to perform a sensitivity analysis by examining how multiplying the uncertainty of a given input parameter would propagate through to final accuracy of the point positioning. These calculations could be used to determine the dominant error source under various flight conditions (altitude, ground speed, etc.).

2.6 – Over-Constrained Systems

Schenk (2001), with his rigorous derivation of a lidar observation equation with error terms, took a different approach to a calibration routine. He considered a calibration routine to be a two-phase problem: first derive an error model, then proceed with a methodology for parameter recovery. Schenk considered the error model key, finding it “impossible to correct errors from analyzing individual error vectors without an error model” (2001, p.1). Through a tight scrutiny of the derived error equation, direct recovery of systematic errors, either individually or in groups (if errors are not separable), could be achieved using a specific flight pattern. It is worth emphasizing that no adjustments are necessary in this technique, just a measurement of the planimetric

elevation differences of chosen primitives. As far as what objects to use as a reference between swaths, Schenk suggests the usual suspects of extracted planar surfaces and their lines of intersection, referred to as an “abstract edge” (p.34).

By measuring nothing more than elevation differences, Schenk proposed a methodology that determines the systematic biases in the INS, the lateral scan angle, the ranging bias and the mounting offset vector between the laser and GPS. Additionally, it determines some coupled errors like the boresight misalignments and the laser mounting parameters. These biases can be determined through the observation that if flight lines are conducted in a certain configuration, then it can be arranged that all but one error term would result in being canceled. The drawback to this method is that it assumed any planimetric offsets are due to the systematic biases, while there is likely to also be a random error component. To isolate the bias, it is likely that several trials would need to be conducted (or several primitives identified).

Bang et al. (2009) conducted a study similar to Schenk (2001) with regard to extracting boresight misalignments through the measurement of primitive offsets in overlapping swaths. They even proposed a basic flight plan that could yield the boresight misalignments plus the planimetric offsets (two flights in opposite directions with 100% overlap repeated at two different heights). Their primitives, planar patches and line segments, were extracted using the technique identical to Habib et al. (2008b). However, Bang et al.’s lidar error equation was highly simplified and assumed no uncertainties in either the laser range or scan angle measurements. Introducing these extra error sources makes it that much harder to attempt to decouple errors through just a few flight lines.

Schenk (2001) also observes that most errors within the input parameters will lead to a non-linear distortion of the surveyed area, thus one cannot hope to reconstruct the true surface from a collection of observed points through a similarity transformation.

2.7 – Summary

Creating an artificial data set for the purposes of developing and testing calibration algorithms for a lidar system has proven successful in the past (Freiss, 2006; Gross & Thoennessen, 2006; Habib et al., 2008b). One fundamental difference between this dissertation and all previous simulations is the construction of a different sensor model due to the different scanner design being implemented in CZMIL. CZMIL's circular scanner requires parameterization of the rotational bias in the prism, in addition to the prism's axis of rotation and refractive angles.

In performing the adjustment, techniques are available to work directly with the point data (Besl & McKay, 1992; Fitzgibbon, 2003), rather than extracted features. However, the literature review thus far has only revealed studies where one data set is held as the “truth” and the second set is registered to the first. No guidance was found with regard to adjusting several data sets simultaneously, nor to distributing the uncertainty. The Levenberg-Marquardt ICP could be used as an analog for a strip adjustment (where one strip is held fixed and adjacent strips are adjusted to this reference); but, without further research, a point-set registration will not be the best suited technique for deriving a geometric calibrator. A post-calibration point-wise adjustment might prove to be useful as a QC tool.

In Vosselman and Dijkman (2001), referring to the ground plans of the structures surveyed provided a clever method of extracting extra constraints for their least squares

problem. However, no mention was made to how data extracted from a set of structural plans can be translated into the point cloud's reference frame. Further, having to track down ground plans of any structure illuminated during a calibration survey (a) may not be possible and (b) puts an excessive burden on the field crew. Thus, the inclusion of ground plans will not be further considered in this work.

Deriving linear features from the point cloud does have some advantages. While there are the same number of parameters that determine a line and a plane (both requiring a point and a vector), a line creates a more distinct locus in space. However, most implementations (Habib et al, 2008b; Vosselman & Dijkman, 2001) call for the construction of lines through a set of extracted planar patches. Given there is an uncertainty in the orientation of the planar patches, it is expected this uncertainty will then propagate to any derived objects. Further, the adjustment technique of Habib et al. (2008b) introduces an artificially large variance along the axis that contains the line segment (to accommodate the non-conjugate end points). This large variance will also propagate through to the final point cloud. Linear features will be secondary to planar patches as a method of determining calibration coefficients, and will unlikely be used for the uncertainty analysis. The covariance of points used by Gross and Thoennessen (2006) for the extraction of linear features is untested on less-dense airborne data. However, because the line segments are derived in such a unique way (i.e. without a dependency on a LSA), they may prove to be useful as a QC tool of the final adjusted point cloud.

As compared to linear features, algorithms for the extraction of planar patches appear more robust and have been used with greater frequency with regard to lidar data.

The modified Hough algorithm with the connectivity model and surface growing algorithm (Lee & Schenk, 2001) could be further explored as a method of distinguishing multiple planar patches within one scene, but is not further investigated in this dissertation given the use of only a single planar calibration surface.

An ancillary product of the point cloud simulator, is a simple tool for evaluating the sensitivity of the input parameters. By starting with a control dataset, both systematic biases and random uncertainties can be introduced into the alignment of the laser, the pointing vector, the position or orientation of the aircraft. In so doing, the introduced horizontal and vertical errors can be assessed on a pulse-by-pulse basis. This simple form of error propagation (which is available early in the synthesis of this dissertation) can be used to provide a preliminary assessment of the impact of input uncertainties on the final point cloud. Further, a simulated swath can be used to check the results of a more robust uncertainty model upon completion of the project.

The more robust propagation of variances employed by May (2008) and the explicit error formulae derived by Schenk (2001) will be an ancillary step for this dissertation. A rigorous understanding of the geometric influence of each parameter in the laser geolocation equation must be pursued in order to design a flight line plan that will properly isolate each variable. While the mathematical procedure is the same, May and Schenk focused on a vertical laser scanner (which had issues of a scan angle bias and varying beam footprints). The circular scanner design will have a constant scan angle and beam footprint (over level ground), thus avoiding some of their complications; but instead this dissertation has incorporated a model for the rate of the prism's spin and its axis of rotation. These changes at the origin of the lidar observation equation will yield

an entirely different set of error formulas. A different set of error equations may make Schenk's method of the recovery of systematic errors inapplicable.

Freiss' (2006) generic least-squares adjustment model appears to be the best point of origin for this research. The model simultaneously addresses the issues of calibration, uncertainty analysis and sensitivity analysis. However, as promising as this model is, results of Freiss' subsequent work had not been made publically available. This dissertation will build upon Freiss' work by determining a set of calibration parameters for a simulated data set.

While May (2008) did develop an automated calibration routine, it only adjusted for the three boresight misalignments. Scan angle and GPS-IMU-laser lever arms were considered to be addressed in separate tests. The inclusion of special purpose lidar targets appeared to greatly improve the quality of the calibration, while simultaneously providing a ready feature to be identified in overlapping swaths. While the results (horizontal accuracy: 5-10cm, vertical accuracy 2.5 cm with 4 points/m² spot density) associated with the lidar targets are hard to deny, there are logistical considerations with respect to hauling around a 1m radius disc (particularly given CZMIL will spend roughly 50% of its time outside the contiguous U.S.). A lidar target may be considered to be part of an initial (factory) QC check, but would preferably not be a requirement for the geometric calibrator.

The technique of determining systematic uncertainties by directly measuring the offsets of conjugate primitives flown in the same or opposite directions (Bang et al., 2009; Schenk, 2001) appears promising. However, both authors neglected the impact of the random errors in the measurement when measuring their offsets, suggesting the need

for several flights. Bang et al. overcomes this need by acquiring data over a region that contains many features to extract (21 lines and 34 planes); however, this level of civilization may not be available at a typical survey site.

One parameter that has been missing from most contemporary lidar uncertainty models, but was included in early models (Kilian et al., 1996), is the concept of a linear drift model for the calibration parameters. Likely, the linear drift was dropped due to improvements over the past decade in hardware (GPS, INS), but some parameters in the circular scanner (an encoder bias) may benefit from the inclusion of a linear drift parameter.

CHAPTER III

THE LASER LOCATION EQUATION

3. THE LASER LOCATION EQUATION
3.1 COMPONENT ANALYSIS
3.1.1 Snell's Law
3.1.1.1 Two-dimensional and vector versions
3.1.1.2 Prism slope and the laser elevation angle
3.1.1.3 Path of a laser pulse through the Fresnel prism
3.1.2 Prism Slope
3.1.3 Laser-Prism-Scanner Assembly
3.1.3.1 Prism-scanner alignment
3.1.3.2 Laser-scanner alignment
3.1.4 Vehicle Reference Frame, INS and Laser-Prism-Scanner Assembly
3.1.4.1 INS reference frame and laser-prism-scanner alignment
3.1.4.2 INS reference frame and vehicle reference frame alignment
3.1.5 Laser Range and Scale Factor
3.1.6 The Laser Location Equation
3.2 PRELIMINARY SENSITIVITY ANALYSIS
3.3 SUMMARY OF KEY RESULTS

Figure 7. Chapter III outline.

Before any discussion of calibration can begin, one must first endeavor to understand the process that is being calibrated. If a given parameter in a process is not allocated proper consideration, the calibration routine may produce nonsensical results or, worse yet, produce an erroneous result with a high degree of confidence.

As an example from hydrography, consider someone who is designing a prototype sound speed profiler which measures the water column's temperature and salinity and then computes a predicted speed of sound. A (seemingly) meticulous calibration can be performed in a laboratory setting by immersing the instrument in water and then calculating the sound speed under innumerable salinity and temperature regimes. What the designer does not realize is that the device will not perform as intended as soon as it is deployed at any depth (other than that of the calibration tank), because sound speed is also a function of pressure, which was not controlled for in the calibration routine. There are two lessons to extrapolate from this example:

- A sensor calibration may be valid only so long as the sensor is deployed under conditions identical to those under which the calibration was performed (thus the calibration routine must be performed under as varied a set of acquisition conditions as possible).
- Without a rigorous (and correct) mathematical model of the sensor, any attempt at sensor calibration may prove fruitless.

It is upon the second bullet item that this chapter focuses: seeking to determine what parameters affect the positioning of a laser point on the ground. Once identified, a calibration routine can be developed.

3.1 – Component Analysis

A cursory review of the relevant literature will reveal an abundance of examples of generic laser point equations (Freiss, 2006; Habib, 2008a; Skaloud & Schaer, 2007).

Most equations take the form:

$$\vec{x}_G = \mathbb{R}_{ECEF}^{IRF} \cdot \left(\mathbb{R}_{IRF}^{LRF} \cdot \mathbb{R}_{LRF} \cdot \vec{\rho} + \vec{x}_{IRF}^{LRF} \right) + \vec{x}_{ECEF}^{IRF} \quad (3.1)$$

where:

\vec{x}_G = coordinates of laser point on ground in ECEF reference frame

\mathbb{R}_{ECEF}^{IRF} = rotation matrix from INS reference frame (IRF) to Earth-centered Earth-fixed reference frame (ECEF) (i.e. vessel pitch, roll and yaw)

\mathbb{R}_{IRF}^{LRF} = rotation matrix from laser reference frame (LRF) to IRF (i.e. laser boresight misalignments)

\mathbb{R}_{LRF} = rotation matrix from nadir-looking to laser reference frame (i.e. laser azimuth and elevation angles)

$\vec{\rho}$ = laser range

\vec{x}_{IRF}^{LRF} = offset vector from LRF to IRF

\vec{x}_{ECEF}^{IRF} = offset vector from IRF to ECEF

While the terms of (3.1) hold true for nearly all lidar systems, this general lidar equation can be made specific to a particular lidar system through the inclusion of the appropriate sensor model describing the ranging and scanning strategy.

Figure 8 shows a simplified sketch of the CZMIL system design, highlighting the components that relate to the system's geometric calibration which will be examined in this study. The Fresnel prism refracts the laser beam from nadir; the scanner motor rotates the Fresnel prism and generates the scan pattern on the ground; the INS measures the sensor's orientation and position information (note: the GPS antennas are considered to be bundled within the INS for the purposes of this study); and the vehicle reference frame (VRF) provides a framework to orient the previous components. Each component, and their relationship to one another, will be discussed in the following sections.

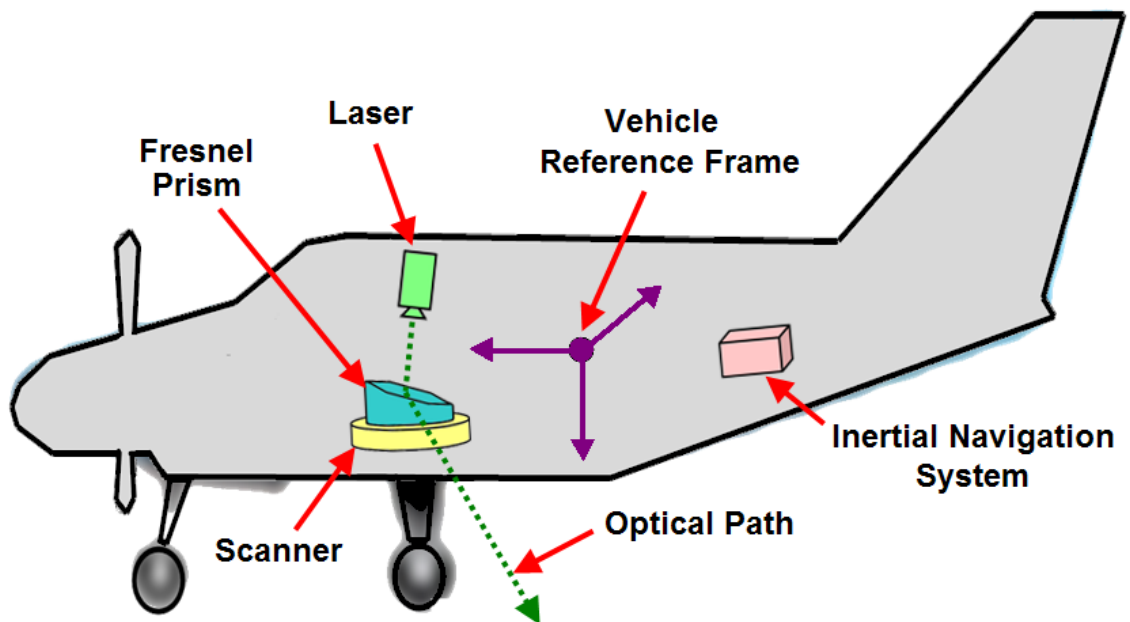


Figure 8. Components of the CZMIL system to be incorporated into the laser location equation for a geometric calibrator.

For the purposes of convention, this dissertation will use a right-handed, forward-starboard-down coordinate system (Figure 9) and the zero angle for the scanner azimuth will direct the laser forward (+x direction). The reference point of the laser-prism-scanner assembly (the point from which all measurements will be computed) will be located on the upper face of the prism, where the outgoing laser beam strikes the Fresnel prism. For the purposes of ray tracing, all refraction will be reduced to this reference point; that is, the prism will be thought of as infinitely thin. This assumption will lead to a very minor (approximately 0.001m) horizontal bias in the laser point.

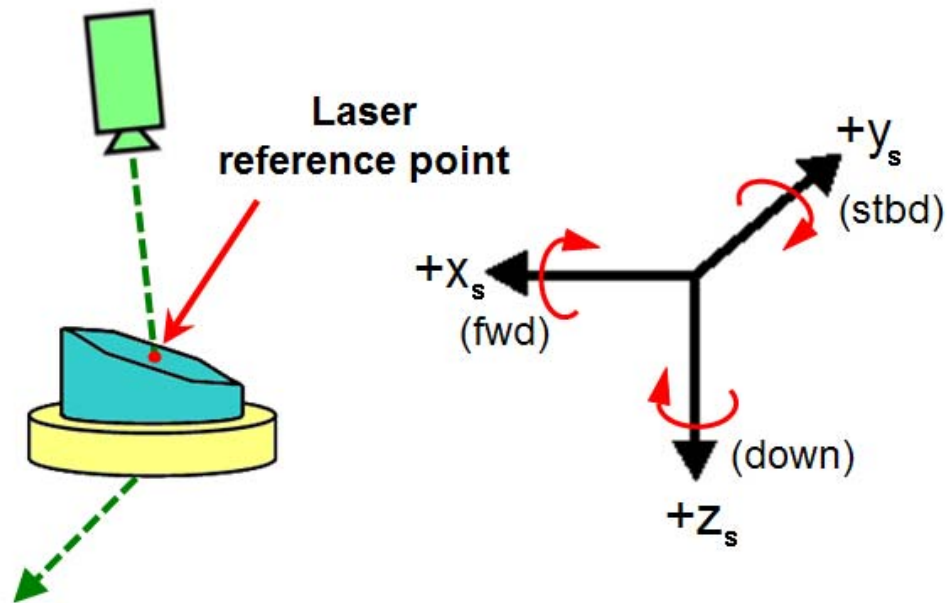


Figure 9. The laser-prism-scanner assembly, showing the laser reference point which is the point of origin for computations within this dissertation (left), shown along with the scanner's right-handed forward-starboard-down coordinate system (right).

3.1.1 – Snell's Law: Two-dimensional and Vector Versions

3.1.1.1 – Two-dimensional and vector versions. Before discussing the behavior of the prism slope, an understanding of vector version of Snell's Law is required. Snell's Law describes the path light (or other types of waves) will take as it passes between two

different media. Of interest to this study is understanding the path the laser will take as it travels through the Fresnel prism, composed of fused silica, and the behavior of the laser pulse when it strikes the water surface.

Classically stated, Snell's Law gives (see Figure 10):

$$\frac{\sin \theta_1}{\sin \theta_2} = \frac{\eta_2}{\eta_1} \quad (3.2)$$

where:

η_1 = refractive index of upper medium (dimensionless)

η_2 = refractive index of lower medium (dimensionless)

θ_1 = angle of incidence

θ_2 = angle of refraction

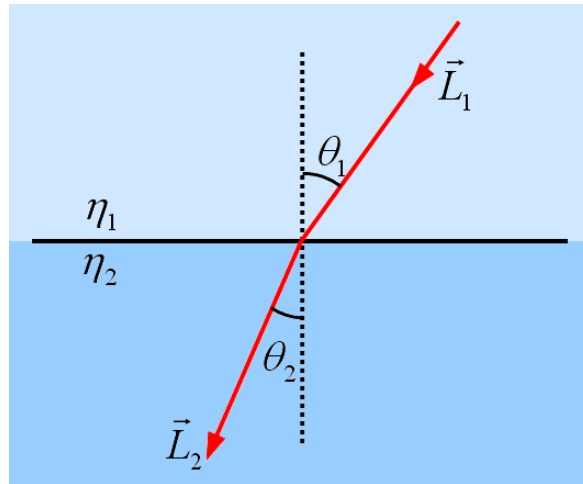


Figure 10. Tracking a laser pulse as it moves from one medium to another, showing the angles of incidence and refraction ($\eta_2 > \eta_1$).

where the indices of refraction are a function of the light's wavelength. Glassner (1989)

offers a vector version of Snell's Law:

$$\cos \theta_1 = -\vec{P} \cdot \vec{L}_1 \quad (3.3)$$

$$\cos \theta_2 = \sqrt{1 - \left(\frac{\eta_1}{\eta_2}\right)^2 \sin^2 \theta_1} \quad (3.4)$$

$$\begin{aligned}
\vec{L}_2 &= \left(\frac{n_1}{n_2}\right)\vec{L}_1 + \left(\frac{n_1}{n_2}\cos\theta_1 - \cos\theta_2\right)\vec{P}, \text{ if } (-\vec{P} \cdot \vec{L}_1) > 0 \\
\vec{L}_2 &= \left(\frac{n_1}{n_2}\right)\vec{L}_1 + \left(\frac{n_1}{n_2}\cos\theta_1 + \cos\theta_2\right)\vec{P}, \text{ if } (-\vec{P} \cdot \vec{L}_1) < 0
\end{aligned} \tag{3.5}$$

where:

\vec{L}_1 = incident light ray (unit vector)

\vec{L}_2 = refracted light ray (unit vector)

\vec{P} = normal vector of interface between media (unit vector)

By inspection of Figure 10 (considering down and right to be positive):

$$\vec{L}_1 = (-\sin\theta_1)\hat{i} + (\cos\theta_1)\hat{j} \tag{3.6}$$

$$\vec{L}_2 = (-\sin\theta_2)\hat{i} + (\cos\theta_2)\hat{j} \tag{3.7}$$

$$\vec{P} = 0\hat{i} - 1\hat{j} \tag{3.8}$$

which can be used to verify equations (3.3) through (3.5). Substituting (3.6) and (3.8)

into (3.3) yields:

$$\begin{aligned}
\cos\theta_1 &= -\langle 0, -1 \rangle \cdot \langle -\sin\theta_1, \cos\theta_1 \rangle \\
&= -(0 - \cos\theta_1) \\
&= \cos\theta_1
\end{aligned} \tag{3.9}$$

Solving (3.2) for $\sin\theta_1$ and substituting into (3.4) yields:

$$\begin{aligned}
\cos\theta_2 &= \sqrt{1 - \left(\frac{n_1}{n_2}\right)^2 (\sin\theta_1)^2} \\
&= \sqrt{1 - \left(\frac{n_1}{n_2}\right)^2 \left(\frac{n_2}{n_1} \sin\theta_2\right)^2} \\
&= \sqrt{1 - (\sin\theta_2)^2} = \sqrt{\cos^2\theta_2} = \cos\theta_2
\end{aligned} \tag{3.10}$$

Lastly, substituting (3.6) and (3.8) into (3.5) yields:

$$\begin{aligned}
\vec{L}_2 &= \left(\frac{n_1}{n_2}\right)\langle -\sin\theta_1, \cos\theta_1 \rangle + \left(\frac{n_1}{n_2}\cos\theta_1 - \cos\theta_2\right) \cdot \langle 0, -1 \rangle \\
&= \left(\frac{\sin\theta_2}{\sin\theta_1}\right)\langle -\sin\theta_1, \cos\theta_1 \rangle + \left(\frac{\sin\theta_2}{\sin\theta_1}\cos\theta_1 - \cos\theta_2\right) \cdot \langle 0, -1 \rangle \\
&= \left\langle -\sin\theta_2, \frac{\sin\theta_2 \cos\theta_1}{\sin\theta_1} \right\rangle + \left\langle 0, -\frac{\sin\theta_2 \cos\theta_1}{\sin\theta_1} + \cos\theta_2 \right\rangle \\
&= \langle -\sin\theta_2, \cos\theta_2 \rangle
\end{aligned} \tag{3.11}$$

which agrees with (3.7). Thus the vector version of Snell's Law agrees with the simpler stated case.

3.1.1.2 – Prism slope and the laser elevation angle. Depending on the user's perspective, there are two angles that are of interest with respect to the Fresnel prism. The hardware team needs to know the slope of the prism's refracting surface (θ_1 in Figure 11); whereas, the software team will need to know the angle at which the laser pulse is exiting the prism (θ_4 in Figure 11).

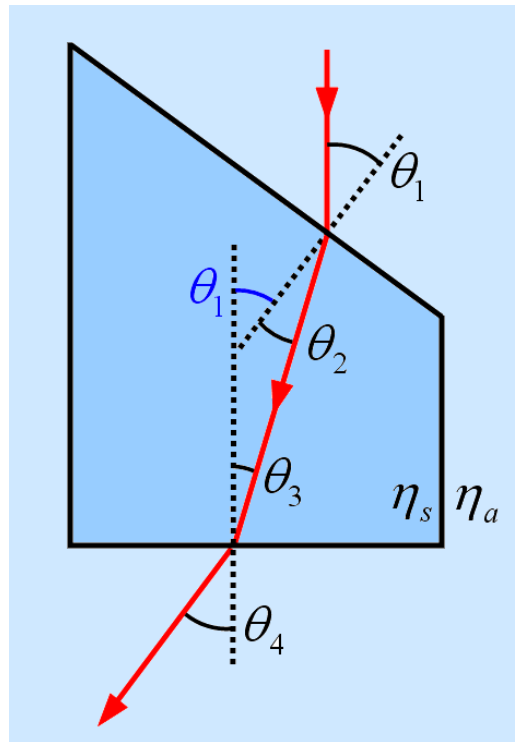


Figure 11. Tracking a laser pulse as it moves from one medium to another, showing the angles of incidence and refraction. Note: θ_1 is also the Fresnel prism slope.

From Figure 11, the angular relationship $\theta_1 = \theta_2 + \theta_3$ is observed (an external angle of a triangle is equal in measure to the sum of its two interior angles), which can be substituted into (3.2) (as applied at the upper facet in Figure 11)

$$\sin \theta_1 = \frac{\eta_s}{\eta_a} \sin(\theta_1 - \theta_3) \quad (3.12)$$

where:

η_a = refractive index of air

η_s = refractive index of fused silica

Applying an angle summation formula and simplifying:

$$\sin \theta_1 = \frac{\eta_s}{\eta_a} (\sin \theta_1 \cos \theta_3 - \cos \theta_1 \sin \theta_3) \quad (3.13)$$

$$\sin \theta_1 - \frac{\eta_s}{\eta_a} \sin \theta_1 \cos \theta_3 = -\frac{\eta_s}{\eta_a} \cos \theta_1 \sin \theta_3 \quad (3.14)$$

$$\sin \theta_1 (1 - \frac{\eta_s}{\eta_a} \cos \theta_3) = -\frac{\eta_s}{\eta_a} \cos \theta_1 \sin \theta_3 \quad (3.15)$$

$$\frac{\sin \theta_1}{\cos \theta_1} = \frac{-\frac{\eta_s}{\eta_a} \sin \theta_3}{1 - \frac{\eta_s}{\eta_a} \cos \theta_3} \quad (3.16)$$

$$\tan \theta_1 = \frac{-\eta_s \sin \theta_3}{\eta_a - \eta_s \cos \theta_3} \quad (3.17)$$

From (3.2) applied to the lower facet in Figure 11:

$$\sin \theta_3 = \frac{\eta_a}{\eta_s} \sin \theta_4 \quad (3.18)$$

A reverse trigonometric substitution can then be performed using (3.18), to define $\cos \theta_3$,

from (3.17), in terms of θ_4 .

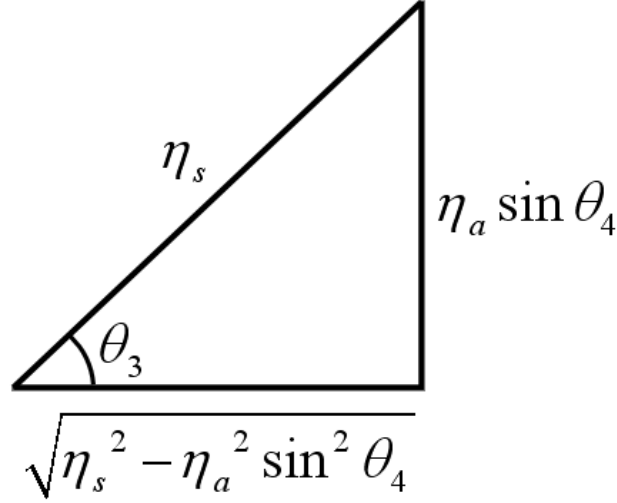


Figure 12. Trigonometric relation of θ_3 and θ_4 .

From Figure 12, an expression for $\cos \theta_3$ can be derived:

$$\cos \theta_3 = \frac{\sqrt{\eta_s^2 - \eta_a^2 \sin^2 \theta_4}}{\eta_s} \quad (3.19)$$

Substituting (3.19) and (3.18) into (3.17) and again simplifying:

$$\tan \theta_1 = \frac{-\eta_s \left(\frac{\eta_a}{\eta_s} \sin \theta_4 \right)}{\eta_a - \eta_s \left(\frac{\sqrt{\eta_s^2 - \eta_a^2 \sin^2 \theta_4}}{\eta_s} \right)} \quad (3.20)$$

$$\boxed{\tan \theta_1 = \frac{-(\eta_a \sin \theta_4)}{\eta_a - \sqrt{\eta_s^2 - \eta_a^2 \sin^2 \theta_4}}} \quad (3.21)$$

Using (3.21), the slope of the prism can be determined for a given desired laser elevation angle. For example, a laser elevation angle of 20° implies a prism slope of 39.16° .

Aside: the refractive indices used are $\eta_{\text{air}} = 1.0003$ (Feynman, 1963), $\eta_{\text{silica}} = 1.461$ (532 nm wavelength) (Del Mar Ventures, 2007).

Conversely, if the prism slope is known and the laser elevation angle is desired, again, referring to (3.18) and observing $\theta_1 = \theta_2 + \theta_3$ yields:

$$\sin \theta_4 = \frac{\eta_s}{\eta_a} \sin(\theta_1 - \theta_2) \quad (3.22)$$

But, from (3.2):

$$\theta_2 = \arcsin\left(\frac{\eta_a}{\eta_s} \sin \theta_1\right) \quad (3.23)$$

Substituting (3.23) into (3.22) and simplifying:

$$\sin \theta_4 = \frac{\eta_s}{\eta_a} \sin\left(\theta_1 - \arcsin\left(\frac{\eta_a}{\eta_s} \sin \theta_1\right)\right) \quad (3.24)$$

$$\boxed{\sin \theta_4 = -\sin \theta_1 \left(\cos \theta_1 - \frac{\sqrt{\eta_s^2 - \eta_a^2 \sin^2 \theta_1}}{\eta_a} \right)} \quad (3.25)$$

3.1.1.3 – Path of a laser pulse through the Fresnel prism. Finally, combining the vector version of Snell's Law (3.3) to (3.5) with the shape of the Fresnel prism (Figure 13) the path of the laser can be traced through the Fresnel prism. Given:

\vec{P}_1 = normal vector of upper facet of prism

\vec{P}_2 = normal vector of lower facet of prism

\vec{L}_0 = direction of laser entering prism

\vec{L}_1 = direction of laser within prism

\vec{L}_2 = direction of laser exiting prism

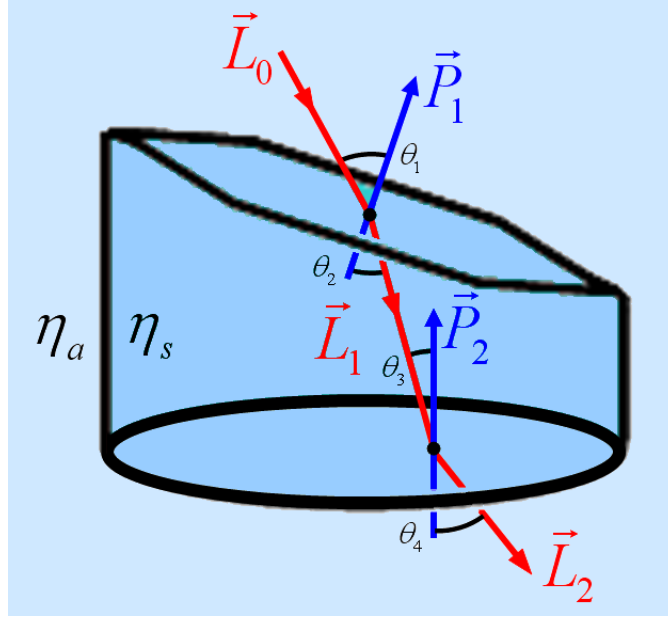


Figure 13. Tracking the laser pulses' path in, through and out of the Fresnel prism.

From (3.5) and (3.4):

$$\vec{L}_1 = \frac{\eta_a}{\eta_s} \vec{L}_0 + \left(\frac{\eta_a}{\eta_s} \cos \theta_1 - \cos \theta_2 \right) \vec{P}_1 \quad (3.26)$$

$$\cos \theta_2 = \sqrt{1 - \left(\frac{\eta_a}{\eta_s} \right)^2 \sin^2 \theta_1} \quad (3.27)$$

Substituting (3.27) into (3.26) and simplifying:

$$\vec{L}_1 = \frac{\eta_a}{\eta_s} \vec{L}_0 + \left(\frac{\eta_a}{\eta_s} \cos \theta_1 - \sqrt{1 - \left(\frac{\eta_a}{\eta_s} \right)^2 \sin^2 \theta_1} \right) \vec{P}_1 \quad (3.28)$$

$$\vec{L}_1 = \frac{\eta_a}{\eta_s} \vec{L}_0 + \left(\frac{\eta_a}{\eta_s} \cos \theta_1 - \sqrt{1 - \left(\frac{\eta_a}{\eta_s} \right)^2 (1 - \cos^2 \theta_1)} \right) \vec{P}_1 \quad (3.29)$$

Substituting for $\cos \theta_1$ from (3.3) into (3.29)

$$\boxed{\vec{L}_1 = \frac{\eta_a}{\eta_s} \vec{L}_0 + \left(-\frac{\eta_a}{\eta_s} (\vec{P}_1 \cdot \vec{L}_0) - \sqrt{1 - \left(\frac{\eta_a}{\eta_s} \right)^2 \left(1 - (\vec{P}_1 \cdot \vec{L}_0)^2 \right)} \right) \vec{P}_1} \quad (3.30)$$

Applying (3.3) through (3.5) to the lower face of the prism:

$$\cos \theta_3 = -\vec{P}_2 \cdot \vec{L}_1 \quad (3.31)$$

$$\cos \theta_4 = \sqrt{1 - \left(\frac{\eta_s}{\eta_a} \right)^2 \sin^2 \theta_3} \quad (3.32)$$

$$\vec{L}_2 = \frac{\eta_s}{\eta_a} \vec{L}_1 + \left(\frac{\eta_s}{\eta_a} \cos \theta_3 - \cos \theta_4 \right) \vec{P}_2 \quad (3.33)$$

Finally, substituting (3.31) and (3.32) into (3.33) yields an expression for the laser pulse exiting the prism (where \vec{L}_1 is defined as in (3.30)):

$$\boxed{\vec{L}_2 = \frac{\eta_s}{\eta_a} \vec{L}_1 + \left(-\frac{\eta_s}{\eta_a} (\vec{P}_2 \cdot \vec{L}_1) - \sqrt{1 - \left(\frac{\eta_s}{\eta_a} \right)^2 \left(1 - (\vec{P}_2 \cdot \vec{L}_1)^2 \right)} \right) \vec{P}_2} \quad (3.34)$$

3.1.2 – Prism Slope

As shown in the previous section the slope of the Fresnel prism, θ_{FR} , dictates the elevation angle of the outgoing laser shot, θ_4 (Figure 14). As the slope of the prism increases, so too does the laser elevation angle and the radius of circular ground scan pattern (Figure 15). Under anticipated CZMIL acquisition parameters (altitude = 400 meters, laser elevation angle = 20°), the prism slope will be 39.2° with a scanning swath width of 300 meters (Tuell et al., 2010), as computed using (3.21).

The slope of the Fresnel prism is not expected to change through the operating life of the instrument, unlike the boresight calibration values which will change with each installation. Without relying on the Fresnel prism fabricator to know the precise milling of the prism slope, the prudent lidar operator should know how to determine this value to a high degree of accuracy.

The prism slope will be simulated through the declaration of the two surface normal vectors for the upper and lower facets of the Fresnel prism, \vec{P}_1 and \vec{P}_2 , which in the scanner reference frame are:

$$\vec{P}_1 = [-\sin \theta_{FR} \quad 0 \quad -\cos \theta_{FR}]^T \quad (3.35)$$

$$\vec{P}_2 = [0 \quad 0 \quad -1]^T \quad (3.36)$$

where:

θ_{FR} = slope of the Fresnel prism upper facet.

The definition of \vec{P}_1 and \vec{P}_2 will be the seeds for the Snell's Law refraction computation.

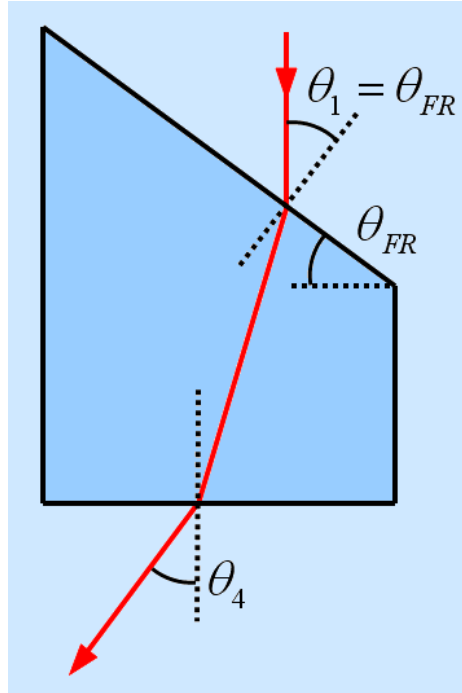


Figure 14. The Fresnel prism's slope, θ_{FR} , is the angle of incidence, θ_1 , for the Snell's Law refraction problem.

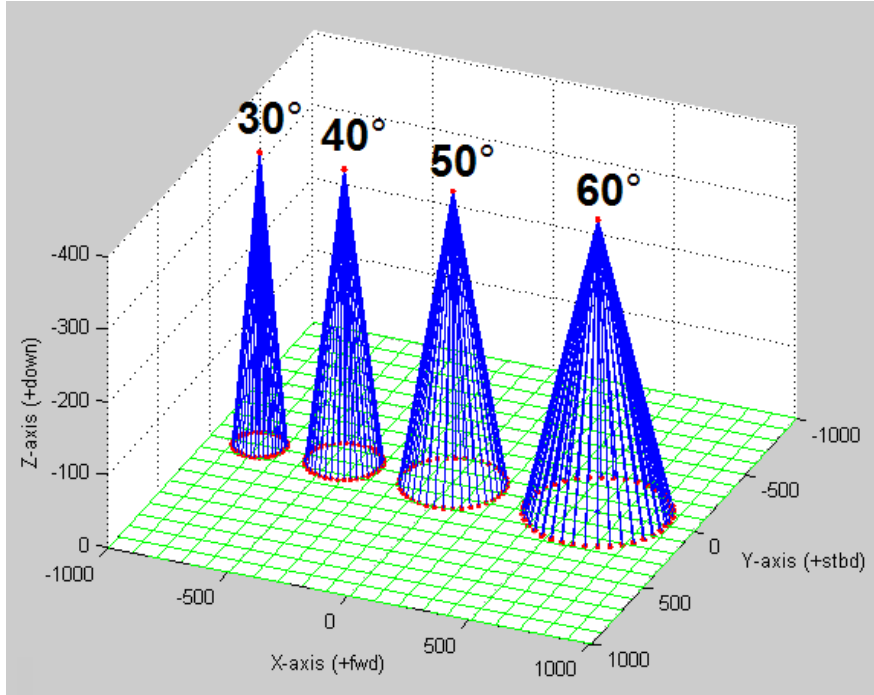


Figure 15. CZMIL scan patterns for various Fresnel prism slopes. The system is being designed with a $\theta_{FR} \approx 39.2^\circ$. All units shown in meters.

3.1.3 – Laser-Prism-Scanner Assembly

3.1.3.1 – Prism-scanner alignment. In a well-aligned system, the scanner's axis of rotation, z_s , will be orthogonal to the lower face of the prism (and therefore parallel to \vec{P}_2), see Figure 16. If the prism is not properly set in the scanner, rather than spinning flat (like a turn table), the prism will nutate (like a spinning coin). Such a behavior could be caused by a faulty ball bearing in the scanner (random error) or a poor mounting of the prism (systematic bias). Conceivably, the prism could also jostle within the scanner, but any translation of the prism will have an equivalent translation on the point cloud. It is not anticipated the prism will translate more than a millimeter – the greater concern are angular rotations of the prism which will have a magnified effect on the computed ground coordinates.

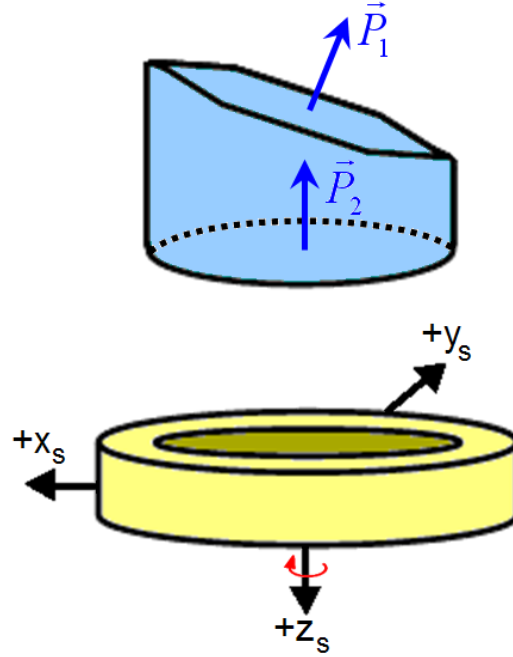


Figure 16. A well-aligned prism-scanner assembly in which the scanner's axis of rotation, z_s , is parallel to the prism base's normal vector, \vec{P}_2 .

In the case of a systematic bias, there are three possible rotations which the prism can undergo: rotations about the scanner's x, y and z-axes (x_s, y_s and z_s) by angles respectively called $PS\theta_x, PS\theta_y$ and $PS\theta_z$ (Figure 17). The misalignments $PS\theta_x$ and $PS\theta_y$ will be mathematically accounted for as rotational matrices as applied to the normal vectors \vec{P}_1 and \vec{P}_2 , affecting the solution to Snell's Law. The rotational matrices will have the form:

$$\mathbb{R}_{PS\theta_x} = \begin{bmatrix} 1 & 0 & 0 \\ 0 & \cos PS\theta_x & -\sin PS\theta_x \\ 0 & \sin PS\theta_x & \cos PS\theta_x \end{bmatrix} \quad (3.37)$$

$$\mathbb{R}_{PS\theta_y} = \begin{bmatrix} \cos PS\theta_y & 0 & \sin PS\theta_y \\ 0 & 1 & 0 \\ -\sin PS\theta_y & 0 & \cos PS\theta_y \end{bmatrix} \quad (3.38)$$

In the case of $PS\theta_x$ and $PS\theta_y$, the ultimate effect on the ground scan pattern will be to enlarge the radius of the circular trace (Figure 18).

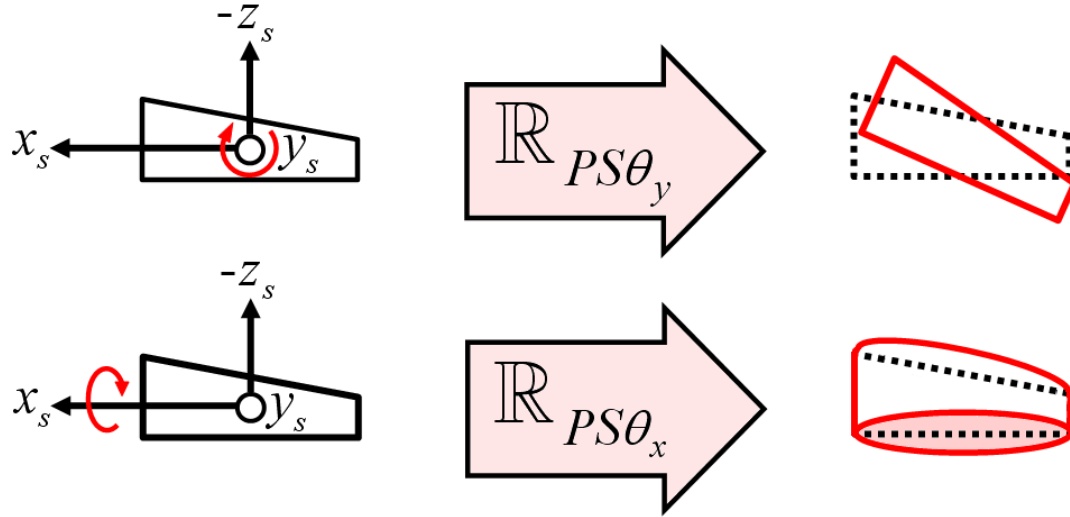


Figure 17. The effects of rotating the Fresnel prism about the scanner's y-axis (top) and x-axis (bottom).

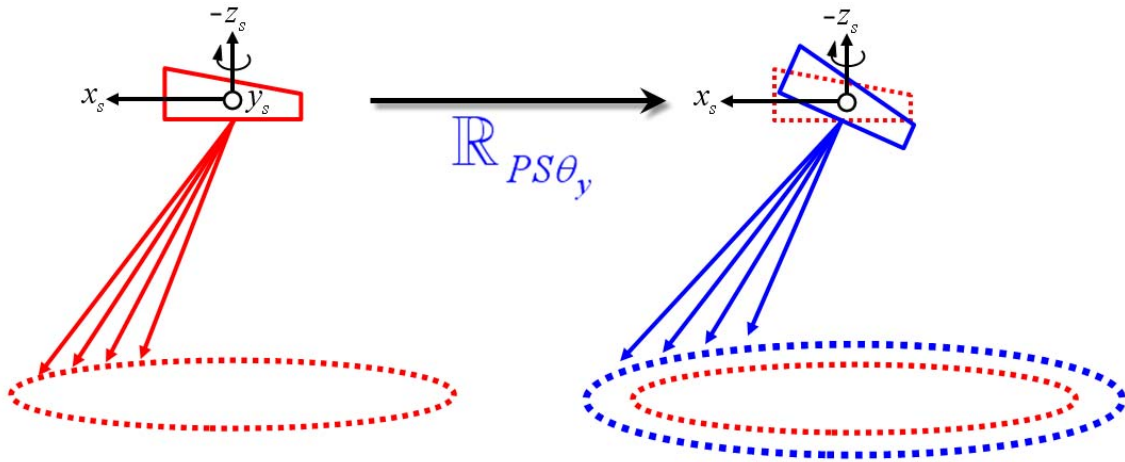


Figure 18. Rotating the Fresnel prism about the scanner's y-axis, y_s , by angle $PS\theta_y$, increases the radius of the circular scan pattern (blue trace). Similar effects are observed with a rotation about x_s (though not as large an increase in radius).

Because the scanner rotates the prism about its z-axis, z_s , any misalignment of the Fresnel prism about z_s would be interpreted as a bias in the scanner's azimuth measurement, θ_{zs} . Algebraically:

$$\mathbb{R}_{PS\theta_z} = \begin{bmatrix} \cos PS\theta_z & -\sin PS\theta_z & 0 \\ \sin PS\theta_z & \cos PS\theta_z & 0 \\ 0 & 0 & 1 \end{bmatrix} \quad (3.39)$$

$$\mathbb{R}_{\theta_{zs}} = \begin{bmatrix} \cos \theta_{zs} & -\sin \theta_{zs} & 0 \\ \sin \theta_{zs} & \cos \theta_{zs} & 0 \\ 0 & 0 & 1 \end{bmatrix} \quad (3.40)$$

and when multiplied together:

$$\mathbb{R}_{\theta_{zs}} \cdot \mathbb{R}_{PS\theta_z} = \begin{bmatrix} \cos(\theta_{zs} + PS\theta_z) & -\sin(\theta_{zs} + PS\theta_z) & 0 \\ \sin(\theta_{zs} + PS\theta_z) & \cos(\theta_{zs} + PS\theta_z) & 0 \\ 0 & 0 & 1 \end{bmatrix} \quad (3.41)$$

confirming $PS\theta_z$ is merely a bias in θ_{zs} (so long as this order of multiplication is preserved).

As discussed in the Appendix, the Tait-Bryan convention will be followed when multiplying several rotation matrices. Thus, the prism normal vectors, from (3.35) and (3.36), as applied to Snell's Law, (3.30) and (3.34), will have the form:

$$\begin{aligned} \vec{P}'_1 &= \mathbb{R}_{\theta_{zs}} \cdot \mathbb{R}_{PS\theta_z} \cdot \mathbb{R}_{PS\theta_y} \cdot \mathbb{R}_{PS\theta_x} \cdot \vec{P}_1 \\ \vec{P}'_2 &= \mathbb{R}_{\theta_{zs}} \cdot \mathbb{R}_{PS\theta_z} \cdot \mathbb{R}_{PS\theta_y} \cdot \mathbb{R}_{PS\theta_x} \cdot \vec{P}_2 \end{aligned} \quad (3.42)$$

where:

\vec{P}_1 = normal vector of upper face of prism (before rotation)

\vec{P}_2 = normal vector of lower face of prism (before rotation)

\vec{P}'_1 = normal vector of upper face of prism (after rotation)

\vec{P}'_2 = normal vector of lower face of prism (after rotation)

3.1.3.2 – *Laser-scanner alignment.* With the orientation of the prism determined with respect to the scanner, the laser can be incorporated. Figure 19 shows the laser in the scanner's reference frame. In a well-aligned system, the laser beam will be pointed orthogonal to the scanner; that is, \vec{L}_0 will be parallel to z_s (shown in Figure 19, and also parallel to the prism's lower face's normal vector, \vec{P}_2 , shown in Figure 16).

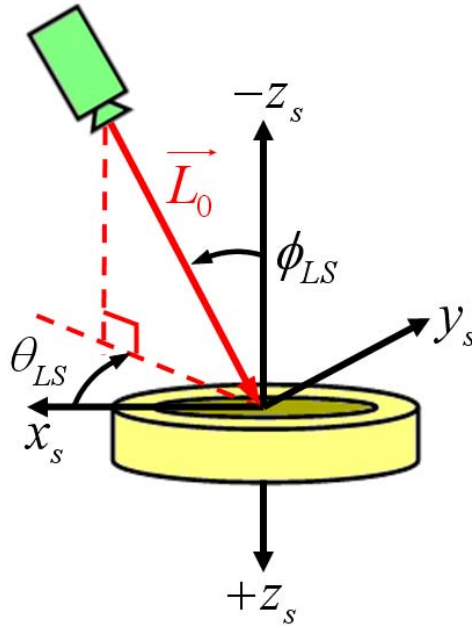


Figure 19. Orienting the laser to the scanner's reference frame through spherical coordinates.

If the laser and scanner are not so oriented, the laser-to-scanner vector, \vec{L}_0 , is parameterized using the angles:

ϕ_{LS} = zenith angle measured from scanner's $-z_s$ axis ($0 \leq \phi_{LS} \leq \pi$)

θ_{LS} = azimuth angle measured from scanner's $+x_s$ axis in clockwise direction ($-\pi < \theta_{LS} \leq \pi$)

The formulation of \vec{L}_0 can be expressed in terms of rotational matrices:

$$\begin{aligned}
\vec{L}_0 &= \begin{bmatrix} \cos \theta_{LS} & -\sin \theta_{LS} & 0 \\ \sin \theta_{LS} & \cos \theta_{LS} & 0 \\ 0 & 0 & 1 \end{bmatrix} \cdot \begin{bmatrix} \cos \phi_{LS} & 0 & \sin \phi_{LS} \\ 0 & 1 & 0 \\ -\sin \phi_{LS} & 0 & \cos \phi_{LS} \end{bmatrix} \cdot \begin{bmatrix} 0 \\ 0 \\ 1 \end{bmatrix} \\
&= \begin{bmatrix} -\cos \theta_{LS} \sin \phi_{LS} \\ -\sin \theta_{LS} \sin \phi_{LS} \\ \cos \phi_{LS} \end{bmatrix}
\end{aligned} \tag{3.43}$$

Notice the z-component of \vec{L}_0 should always be positive to indicate that the laser is firing down, into the Fresnel prism. Two advantages of parameterizing \vec{L}_0 in this fashion (versus a form like $[L_x \ L_y \ L_z]^T$) are that: first, it guarantees \vec{L}_0 will take the form of a unit vector, which is necessary for the refractive equations (3.30) and (3.34); and second, using two variables instead of three is computationally more efficient.

Equation (3.43) is equivalent to the spherical-to-Cartesian coordinate transformation equations, $(\rho, \theta, \phi) \rightarrow (x, y, z)$ (Anton, Bivens & Davis, 2002), where $\rho = 1$. This is not a coincidence.

Altering the laser-to-scanner vector has the effect of producing a teardrop-like scan pattern (Figure 20). The larger the value of ϕ_{LS} , the more elongated the teardrop. The drop will point in the direction opposite θ_{LS} . For example, if $\theta_{LS} = 0^\circ$, then the laser will be located in the +x direction (forward of) the scanner and the beam pattern will be pointing in the -x direction (backwards).

Figure 21 offers a pictorial demonstration of why tilting the laser with respect to the scanner leads to the teardrop-shaped scan pattern. By either increasing or decreasing the angle of incidence of the prism's upper face (depending on the orientation of the prism), the exiting angle either decreases or increases, respectively. By way of comparison, Figure 22 shows the effect of rotating the prism and holding the laser and

scanner fixed. As depicted in the figure, the angle of incidence increases with the rotation of the prism, which (as in Figure 21) leads to a decrease in the angle between the prism and the exiting laser. Interestingly, this decrease is less in magnitude than the amount by which the prism was rotated, thus there is a net increase in the angle with respect to nadir. The end result is a circular scan pattern with a larger radius than previous (as depicted in Figure 18). If the prism is rotated in the opposite direction than depicted in Figure 22, the scan pattern will have a smaller radius.

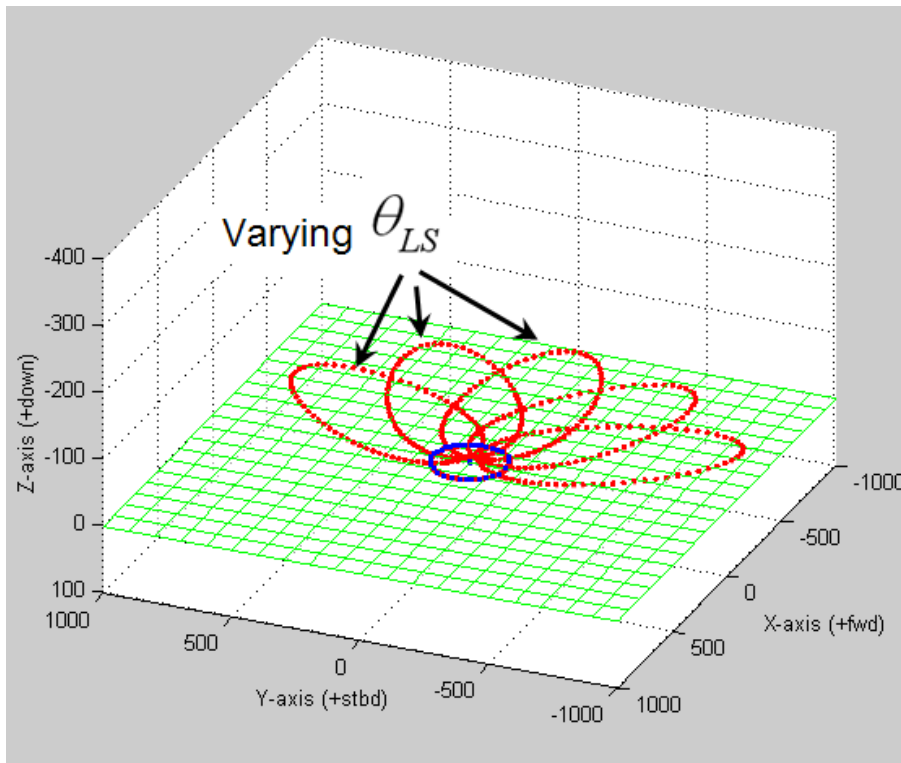


Figure 20. Tilting the laser from vertical (increasing ϕ_{LS}) will alter the scan pattern from its intended circular scan pattern (shown in blue) to produce a teardrop-shaped pattern. Changing values for θ_{LS} will result in rotating this pattern about nadir (shown in red).

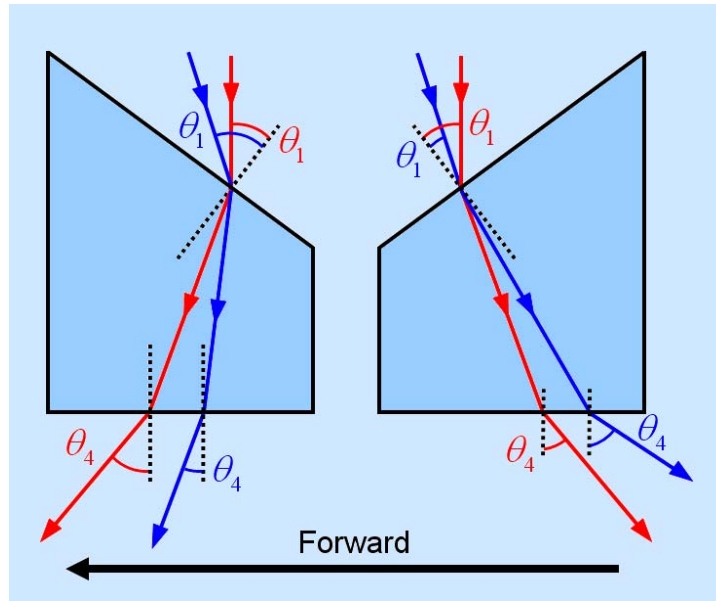


Figure 21. The rotating prism shown in its forward and backward position along with a “well-aligned” laser (red). By tilting the laser forward (shown in blue) the laser exiting the prism will be directed further aft than before, regardless of prism orientation.

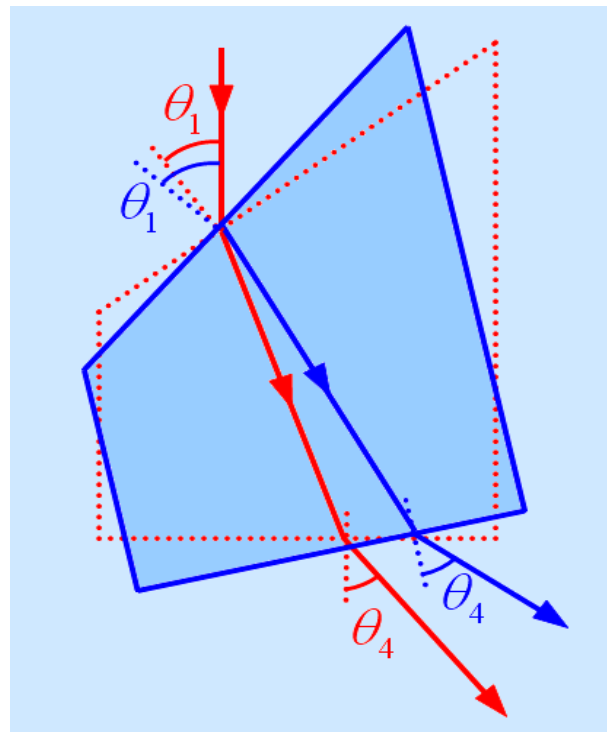


Figure 22. By rotating the prism (but holding the laser fixed with respect to the scanner reference frame), the laser’s exit angle, θ_4 , actually decreases with respect to the lower face of the prism, but (including the rotation of the prism) the exit angle actually increases with respect to nadir.

3.1.4 – Vehicle Reference Frame, INS and Laser-Prism-Scanner Assembly

3.1.4.1 – INS reference frame and laser-prism-scanner alignment. The preceding sections on the laser-prism-scanner (LPS) assembly, when coupled with the discussion of the vector version of Snell's Law are sufficient to determine the direction of the laser as it exits the scanner reference frame (SRF). The next step is to convert this vector from the SRF into the INS Reference Frame (IRF). Once in the IRF, it is a matter of applying the appropriate geodetic equations to reproject the vector in the user's preferred Earth-fixed coordinate system.

For the moment, let us assume that the INS has been mounted in such a way that the vehicle reference frame (VRF) and IRF are co-located and co-aligned. In and of itself, this is not an unreasonable assumption in the world of multibeam sonar if one follows the techniques of Hughes Clark (2003) or de Hilster (2008). It is unclear if these methods have been applied to aircraft. The topic of the subtle difference between the VRF and IRF will be addressed in the following section. For the purposes of this section the VRF and IRF will be considered to be coincident.

A six parameter transformation (three rotations and three translations) is required to convert the laser pointing vector from the SRF to the IRF (Figure 23). The rotations are the angles commonly referred to as the boresight misalignments: the roll bias ($BS\theta_x$), the pitch bias ($BS\theta_y$), and the heading/yaw bias ($BS\theta_z$). As with the previous sets of rotations, the Tait-Bryan convention will be followed.

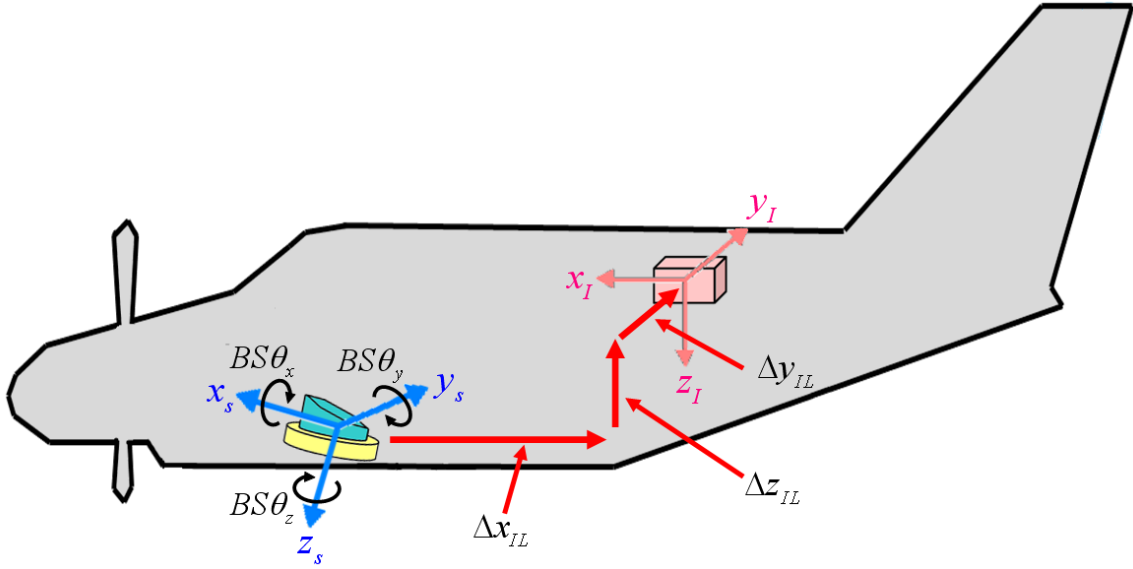


Figure 23. The relationship between the SRF and the IRF, showing the boresight misalignments, $BS\theta_x$, $BS\theta_y$ and $BS\theta_z$, and the SRF to IRF offset vector, $[\Delta x_{IL} \quad \Delta y_{IL} \quad \Delta z_{IL}]$

The rotation matrices for Tait-Bryan are given in (9.12):

$$\begin{aligned} \mathbb{R}_z \cdot \mathbb{R}_y \cdot \mathbb{R}_x &= \begin{bmatrix} \cos \kappa & -\sin \kappa & 0 \\ \sin \kappa & \cos \kappa & 0 \\ 0 & 0 & 1 \end{bmatrix} \cdot \begin{bmatrix} \cos \psi & 0 & \sin \psi \\ 0 & 1 & 0 \\ -\sin \psi & 0 & \cos \psi \end{bmatrix} \cdot \begin{bmatrix} 1 & 0 & 0 \\ 0 & \cos \omega & -\sin \omega \\ 0 & \sin \omega & \cos \omega \end{bmatrix} \\ &= \begin{bmatrix} \cos \kappa \cos \psi & -\cos \omega \sin \kappa + \sin \omega \cos \kappa \sin \psi & \sin \omega \sin \kappa + \cos \omega \cos \kappa \sin \psi \\ \sin \kappa \cos \psi & \cos \omega \cos \kappa + \sin \omega \sin \kappa \sin \psi & -\sin \omega \cos \kappa + \cos \omega \sin \kappa \sin \psi \\ -\sin \psi & \sin \omega \cos \psi & \cos \omega \cos \psi \end{bmatrix} \end{aligned} \quad (3.44)$$

where:

κ = the vessel roll ($BS\theta_x$)

ψ = the vessel pitch ($BS\theta_y$)

ω = the vessel yaw ($BS\theta_z$)

Unlike the slope of the Fresnel prism or the prism-to-scanner misalignments, (which yield a vertical bias in their associated point clouds), a bias in the roll or pitch boresight alignment ($BS\theta_x$ or $BS\theta_y$) produces a variable vertical error. Referring to

Figure 24, a vehicle with a positive pitch bias will have a negative vertical bias for the forward portion of the swath and a positive vertical bias for the aft portion (for a level flight). Similar results are observed with respect to a roll boresight misalignment.

For a level flight over level ground, a yaw boresight misalignment will not lead to any vertical discrepancies from the “true” ground; though there will clearly be a horizontal shift (Figure 25, left). If the aircraft experiences any change in attitude (a vehicle pitch or roll), or if the ground is no longer flat, an error in the vertical position of the laser points will become apparent (Figure 25, right).

Each misalignment discussed so far has been addressed through a rotational matrix, which at first glance appears to perform identical manipulations. Figure 26 offers a quick visual dictionary that illustrates how the different parameters affect the final point cloud. Perturbing the laser-to-scanner alignments results in an almost teardrop-shaped scan pattern (Figure 26, left); changing the boresight angles yield an elliptical scan pattern (Figure 26, center); and altering the prism-to-scanner angles, or the Fresnel prism slope will produce concentric circular scan patterns (Figure 26, right). That each parameter affects the point cloud differently (i.e., has a different “signature”) will play an important role when attempting to decouple the effects of two different parameters on the point cloud. Conversely, should two parameters affect the point cloud in an identical way, the parameters will be linearly dependent on one another and only one will be capable of being ascertained through calibration.

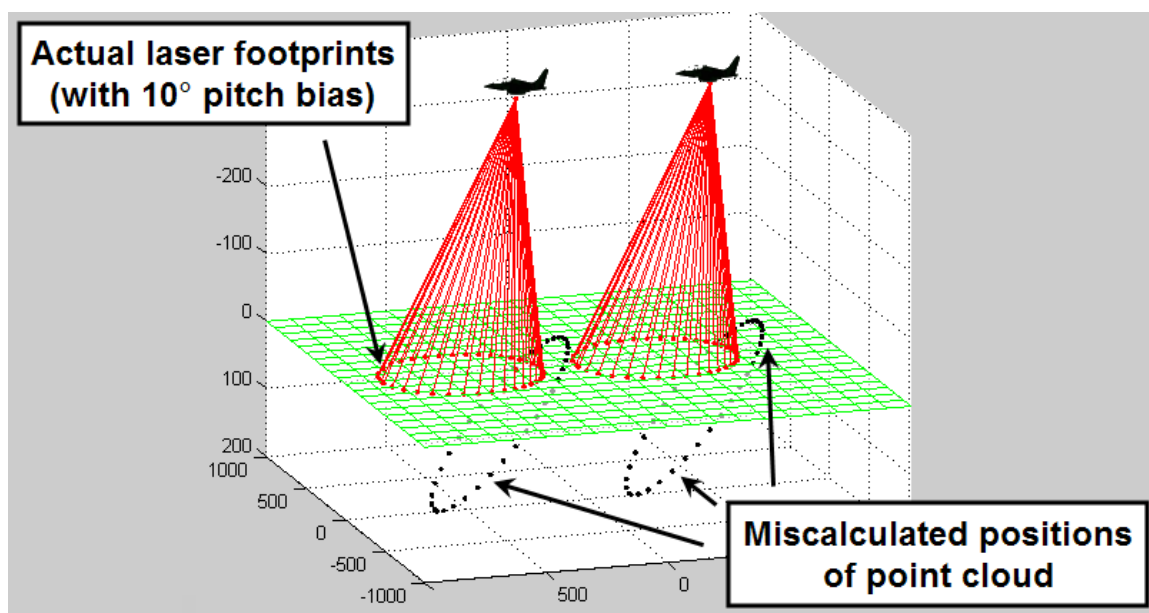


Figure 24. A pair of laser scans with a known (red) and unknown (black) pitch boresight misalignment.

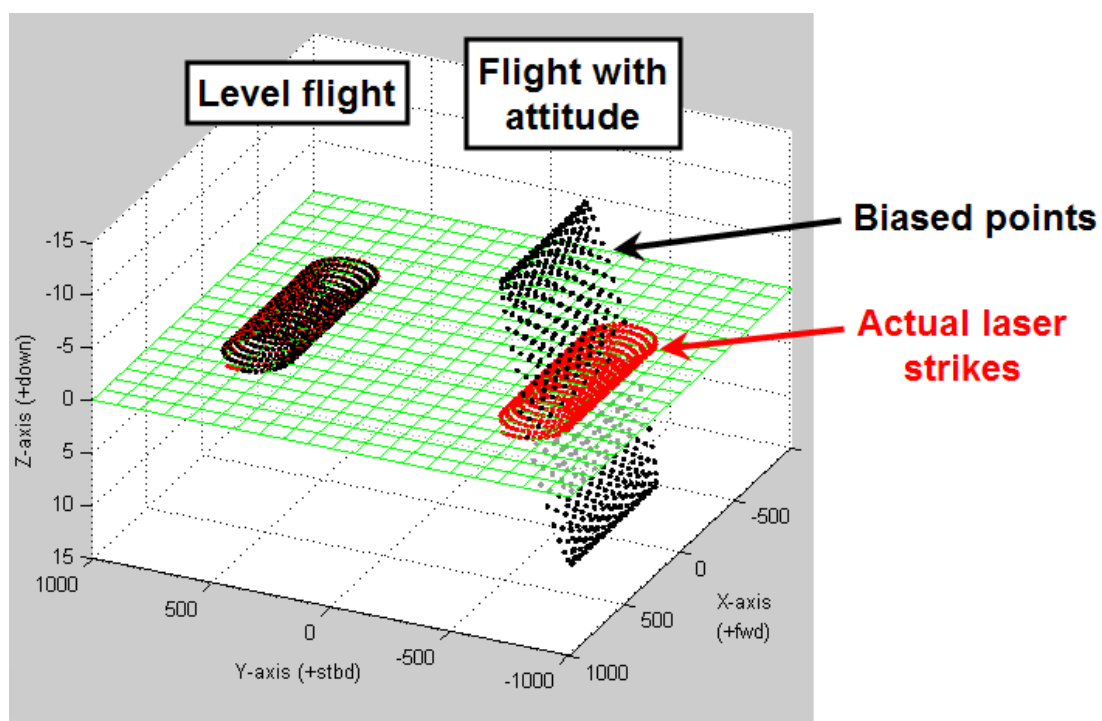


Figure 25. Two flight lines with a misalignment in the yaw boresight angle: the left is from a level flight, while the right is from a flight line in which the plane had a 10° pitch.

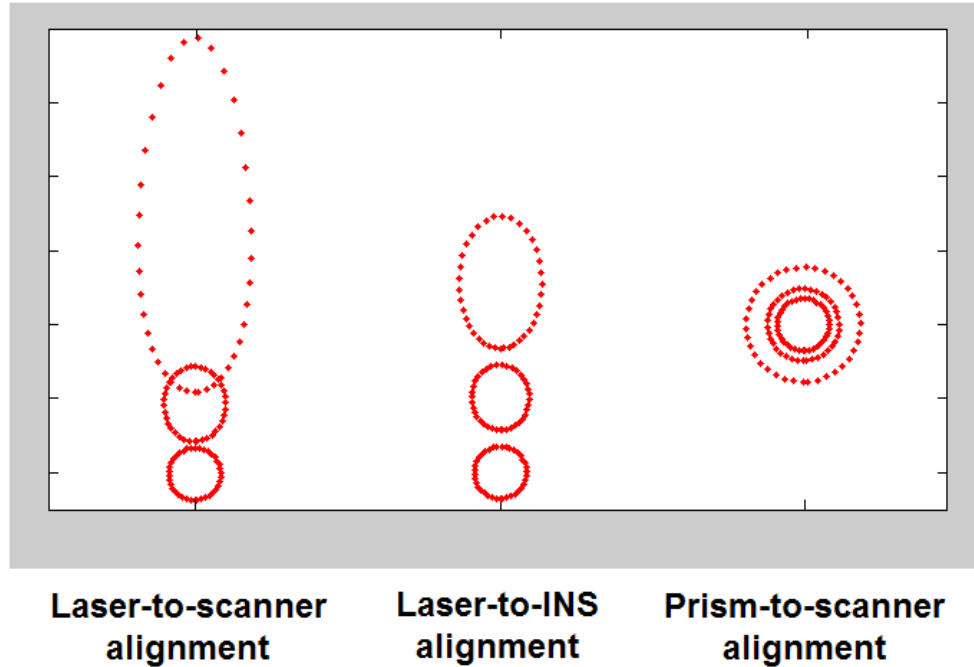


Figure 26. Three different sets of scan patterns (looking from above) induced by rotating different system components with respect to one another. Teardrop (left), elliptical (center) or circular (right) scan patterns are all possible.

The second-half of the six parameter transformation mentioned earlier is the translation of the laser pointing vector by the SRF to the IRF (Figure 23). This lever arm can be manually measured in the field with equipment as simple as a tape measure and plumb bob. Such a low-tech solution may prove more accurate than attempting to determine the vector, $[\Delta x_{IL} \quad \Delta y_{IL} \quad \Delta z_{IL}]$, by examining the point cloud. To best estimate the SRF to IRF vector, a full vehicle survey using a total station and adjustment software package should be pursued.

By convention, a SRF to IRF vector with all positive values $[+\Delta x_{IL} \quad +\Delta y_{IL} \quad +\Delta z_{IL}]$ implies that the reference point of the LPS assembly (located on the upper facet of the Fresnel prism, shown in Figure 9) is forward, to starboard and below the INS reference point.

3.1.4.2 – *INS reference frame and vehicle reference frame alignment.* With the laser pointing vector expressed with respect to IRF, the vehicle's attitude data (vehicle roll - ω , pitch - ψ , and yaw - κ) and INS-reported positions can be applied to reduce the system to a locally-level reference frame. While the Tait-Bryan convention was previously chosen for convenience, it *must* be followed in rectifying the vehicle orientation because T-B is the convention followed by the INS manufacturer employed in CZMIL (Applanix Corporation, 2007).

Collecting all the terms discussed so far, the generic laser equation given in (3.1) can now be written out more adapted to CZMIL:

$$\vec{x}_G = \mathbb{R}_{ECEF}^{IRF} \cdot \left(\mathbb{R}_{IRF}^{LRF} \cdot \mathbb{R}_{LRF} \cdot \vec{\rho} + \vec{x}_{IRF}^{LRF} \right) + \vec{x}_{ECEF}^{IRF}$$

Becoming:

$$\vec{x}_G = \mathbb{R}_V \cdot \left(\mathbb{R}_{BS} \cdot \vec{L}_2 \cdot \rho + \vec{x}_{IL} \right) + \vec{x}_{ECEF} \quad (3.45)$$

where:

\vec{x}_G = coordinates of laser point on ground in ECEF reference frame

\mathbb{R}_V = rotation matrix for vessel orientation

\mathbb{R}_{BS} = rotation matrix for boresight misalignments

\vec{L}_2 = direction of laser exiting LPS assembly (unit vector)

ρ = laser range (scalar quantity)

\vec{x}_{IL} = INS-to-laser offset vector

\vec{x}_{ECEF} = Earth-centered Earth-fixed position

A few final modifications can now be made to (3.45) by revisiting the concept of the vehicle reference frame (VRF). The VRF is simply a reference frame that is associated with the aircraft, rather than any other sensor. To simplify the problem (and to minimize the number of reference frames used), the VRF should be defined to be coincident with another reference frame, the IRF.

The IRF already has a convenient reference point (usually marked on the surface of the INS), which can also serve as the reference point of the VRF. Lastly, the VRF must be oriented to the IRF. Local gravity will serve to align the respective z-axes of the two coordinate systems, leaving only the problem of aligning the respective x-y planes. The concern is that a heading misalignment between the VRF and IRF, θ_{VI} in Figure 27, would lead to cross talk in the INS's sensed-pitch and roll.

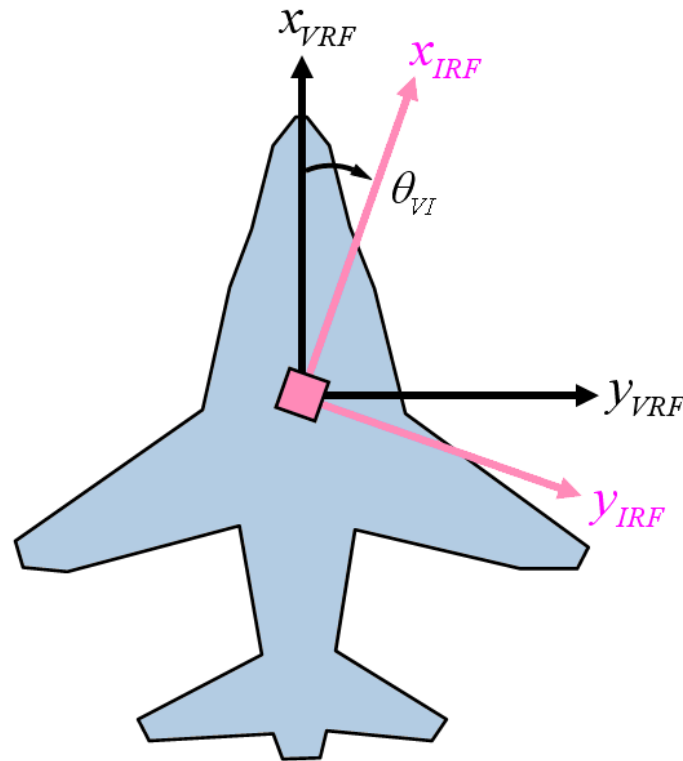


Figure 27. An illustration of a potential heading misalignment between the vehicle reference frame and the INS reference frame.

For example, consider a plane with a laser mounted one meter forward of the INS. In this case, the term “forward” is ambiguous as it does not identify which reference frame is being used. It is assumed that when individuals make offset measurements in a given vehicle, they are doing so with respect to the vehicle’s reference frame (e.g., measuring forward-aft distances relative to an aircraft’s centerline or lateral port-

starboard distances relative to a ship's frame). Survey vehicles can have convenient reference points, with long baselines, surveyed into vehicles frame; whereas, an INS is small box with arrows painted on it indicating forward (Figure 28).

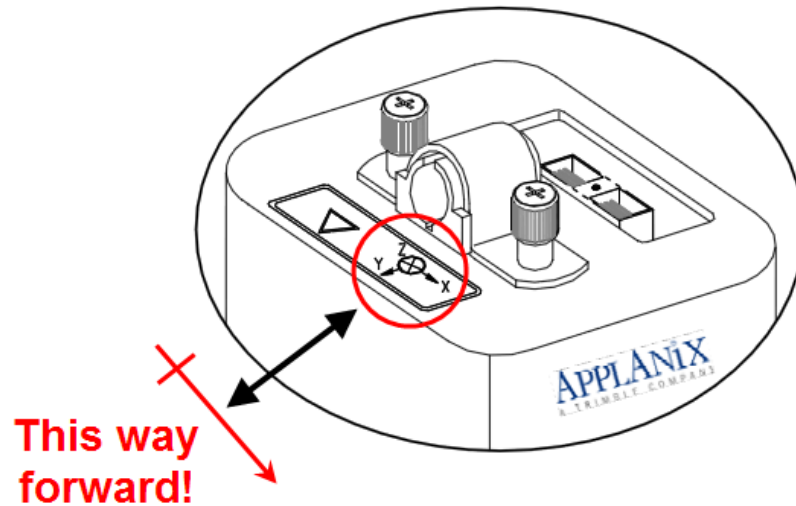


Figure 28. An Applanix POS AV Ver. 5 indicates which way should be pointed “forward.” Sketch modified from Applanix (2007).

Returning to the example, a plane has a laser mounted one meter forward (with respect to the VRF) of the IMU (Figure 29 - #1). Assuming the INS sticker was not consulted during mounting, so there is a slight offset between the VRF and IRF headings. Now, if this vehicle were to strictly pitch, then the laser head would pivot up towards the INS (Figure 29 - #2). However, because the INS is misaligned, while the plane is pitching, the INS is sensing that it is mostly pitching along with a slight roll (Figure 29 - #3). This sensed data is recorded and later applied when the plane's trajectory is computed. By applying these incorrect rotations to the laser head it (a) is computed to be in the wrong spot and (b) will have an incorrectly computed orientation (Figure 29 - #4).

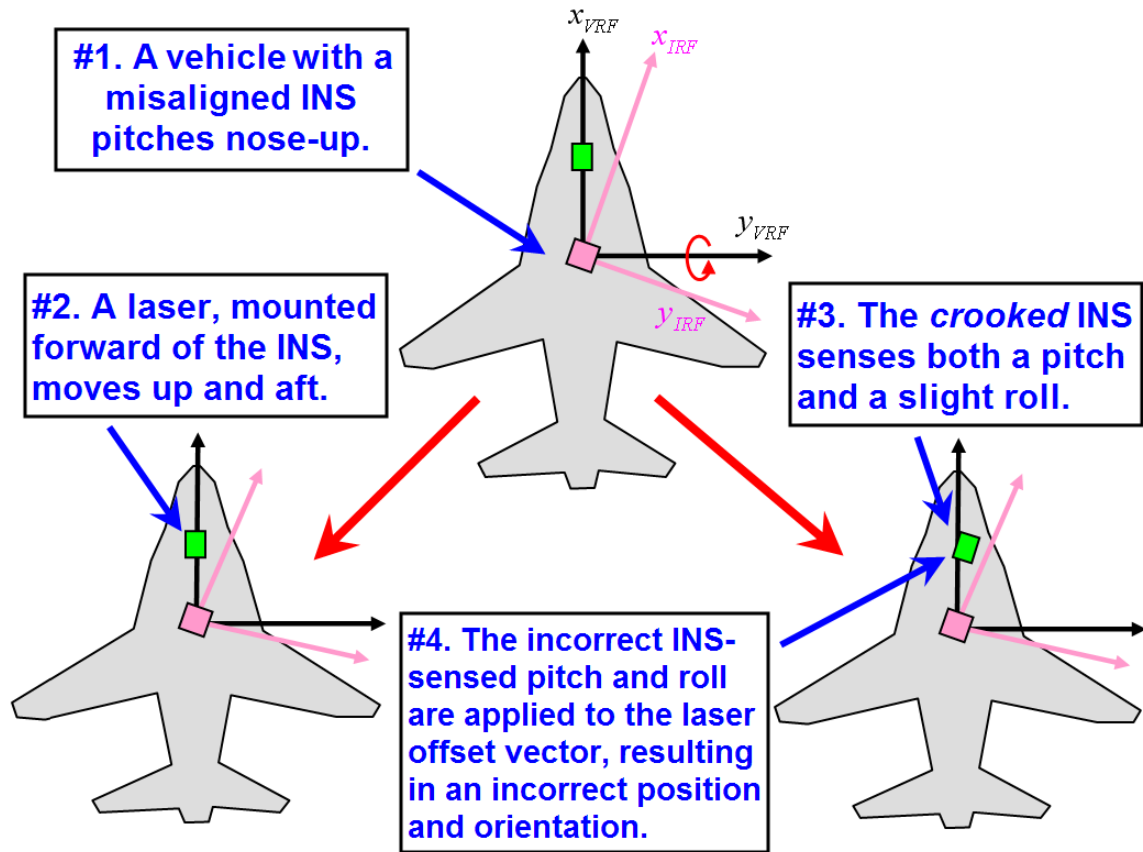


Figure 29. The effects of crosstalk in a poorly mounted INS. Incorrect rotations are applied to the lever arms resulting in both translational shifts and angular biases.

These induced errors are relatively minor and until recently, with system noise and poor GPS resolution have been considered inconsequential (Hughes Clark, 2003).

With improved positioning techniques (real-time kinematic), which can achieve positional accuracies on the order of centimeters, these errors are rising above the noise.

This leaves the surveyor with the conundrum of how to solve for a misalignment when all the conventional calibration routines do not address alignments between the VRF and any sensors (de Hilster, 2008, Hughes Clark, 2003).

Recent attempts in the marine environment to solve for θ_{VI} include using multiple GPS antennas to survey extra marks into the deck of the ship and then incrementally tilt the vehicle while it is tied up alongside a pier, called the “Dutch Method” in the literature

(yielding an accuracy of 0.03° ; de Hilster, 2008). Unfortunately, an airplane on the ground cannot be manipulated in the same way as a boat alongside a pier. Further an airplane's fuselage does not afford as many points to install extra GPS antennas as a ship.

An attempt to identify and remove the artifact caused by a heading misalignment between the vehicle reference frame and the INS reference frame will also be addressed in this dissertation.

3.1.5 – Laser Range and Scale Factor

The final pair of calibration values refer to the algorithms that are used to compute the laser range based on the intensity of the returning waveform (Figure 30). This is largely a radiometric problem and may be beyond the scope of this dissertation.

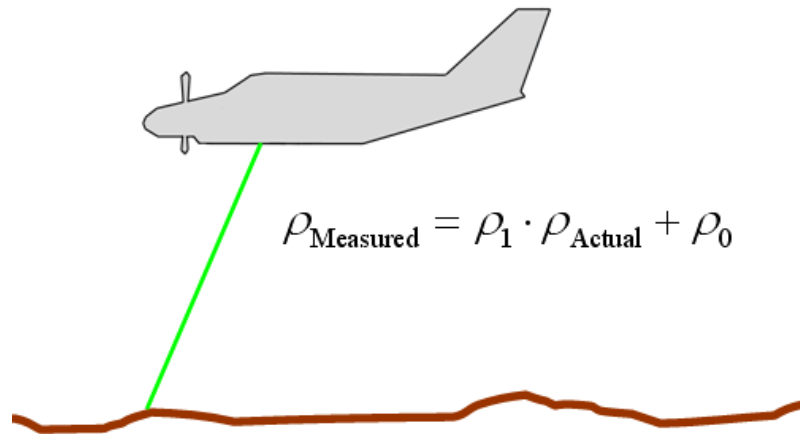


Figure 30. A radiometric bias or a linear scale factor in the laser range computation would create a geometric bias in the point cloud that would not be identified if these parameters were not included in the calibration.

These two parameters are a laser range bias, ρ_0 , and a laser range scale factor, ρ_1 . A laser range bias could manifest in something as simple as an encoder timing error. For all its advanced technology, a lidar is still computing two-way travel times; if there is a bias in these times, then there will be an associated bias in the range measurement.

Different surfaces that may be interrogated by the lidar (a metal roof, a shingled-roof, a paved road, a dirt road, the water's surface) will have different reflective properties (depending on surface roughness, albedo, etc.). In a poorly trained lidar waveform analysis program, an object with high reflectivity will be erroneously identified as being slightly closer than a second, less reflective object that is an equivalent distance away. Incorporating a laser range scale factor in the list of considered parameters will help mitigate these radiometric issues. In the end, the operator can always choose to not include these values in the calibration procedure.

3.1.6 – The Laser Location Equation

To summarize the previous sections, the following is a list of the lidar observables (values which CZMIL will measure on its own):

- ρ = laser range (m)
- θ_{zs} = scanner azimuth (deg)
- ω = vehicle roll (deg)
- ψ = vehicle pitch (deg)
- κ = vehicle heading (deg)
- x_I = INS position, x-coordinate (m)
- y_I = INS position, y-coordinate (m)
- z_I = INS position, z-coordinate (m)

The parameters that will be considered in the lidar point positioning equation (and later incorporated into the geometric calibrator are as follows:

- θ_{FR} = Fresnel element slope
- $PS\theta_x$ = Prism-to-scanner alignment (x-axis)
- $PS\theta_y$ = Prism-to-scanner alignment (y-axis)
- $PS\theta_z$ = Prism-to-scanner alignment (z-axis)
- ϕ_{LS} = Laser-to-scanner phi-angle
- θ_{LS} = Laser-to-scanner theta-angle
- $BS\theta_x$ = Boresight alignment (x-axis)
- $BS\theta_y$ = Boresight alignment (y-axis)
- $BS\theta_z$ = Boresight alignment (z-axis)
- Δx_{IL} = INS-to-LPS offset (x-axis)
- Δy_{IL} = INS-to-LPS offset (y-axis)
- Δz_{IL} = INS-to-LPS offset (z-axis)
- θ_{VI} = Vehicle-to-INS heading alignment
- ρ_0 = Laser range bias
- ρ_1 = Laser range scale factor

Finally, we are in a position to write out the full laser location for the CZMIL system. From (3.45):

$$\vec{x}_G = \mathbb{R}_V \cdot \mathbb{R}_{VI} \left(\mathbb{R}_{BS} \cdot \vec{L}_2 \cdot \left(\frac{\rho - \rho_0}{\rho_1} \right) + \vec{x}_{IL} \right) + \vec{x}_{ECEF} \quad (3.46)$$

where:

$$\begin{aligned} \vec{x}_G &= \text{coordinates of laser point on ground in ECEF reference frame} \\ \mathbb{R}_V &= \underbrace{\begin{bmatrix} \cos \kappa & -\sin \kappa & 0 \\ \sin \kappa & \cos \kappa & 0 \\ 0 & 0 & 1 \end{bmatrix}}_{\text{Vehicle yaw}} \cdot \underbrace{\begin{bmatrix} \cos \psi & 0 & \sin \psi \\ 0 & 1 & 0 \\ -\sin \psi & 0 & \cos \psi \end{bmatrix}}_{\text{Vehicle pitch}} \cdot \underbrace{\begin{bmatrix} 1 & 0 & 0 \\ 0 & \cos \omega & -\sin \omega \\ 0 & \sin \omega & \cos \omega \end{bmatrix}}_{\text{Vehicle roll}} \\ \mathbb{R}_{VI} &= \underbrace{\begin{bmatrix} \cos \theta_{VI} & \sin \theta_{VI} & 0 \\ -\sin \theta_{VI} & \cos \theta_{VI} & 0 \\ 0 & 0 & 1 \end{bmatrix}}_{\text{Vehicle-INS heading misalignment}} \\ \mathbb{R}_{BS} &= \underbrace{\begin{bmatrix} \cos BS\theta_z & -\sin BS\theta_z & 0 \\ \sin BS\theta_z & \cos BS\theta_z & 0 \\ 0 & 0 & 1 \end{bmatrix}}_{\text{Yaw boresight angle}} \cdot \underbrace{\begin{bmatrix} \cos BS\theta_y & 0 & \sin BS\theta_y \\ 0 & 1 & 0 \\ -\sin BS\theta_y & 0 & \cos BS\theta_y \end{bmatrix}}_{\text{Pitch boresight angle}} \cdot \underbrace{\begin{bmatrix} 1 & 0 & 0 \\ 0 & \cos BS\theta_x & -\sin BS\theta_x \\ 0 & \sin BS\theta_x & \cos BS\theta_x \end{bmatrix}}_{\text{Roll boresight angle}} \\ \vec{L}_2 &= \text{direction of laser exiting LPS assembly (unit vector)} \\ \rho &= \text{laser range (measured)} \\ \rho_0 &= \text{laser range bias (scalar quantity)} \\ \rho_1 &= \text{laser range scale factor (scalar quantity)} \\ \vec{x}_{IL} &= \underbrace{[\Delta x_{IL} \quad \Delta y_{IL} \quad \Delta z_{IL}]^T}_{\text{INS-to-Laser offset}} \\ \vec{x}_{ECEF} &= \underbrace{[x_{LL} \quad y_{LL} \quad z_{LL}]^T}_{\text{GPS position in ECEF}} \end{aligned} \quad (3.47)$$

Further, the laser vector exiting the LPS assembly, \vec{L}_2 , is defined in terms of the laser vector entering the LPS assembly (\vec{L}_0), the laser vector within the Fresnel prism (\vec{L}_1), the slope of the Fresnel prism (θ_{FR}), the orientation of the vectors normal to the upper

and lower faces of the Fresnel prism (\vec{P}_1 and \vec{P}_2), and the refractive coefficients for both air and fused silica (η_a and η_s). Thus:

$$\begin{aligned}
 \mathbb{R}_{\theta_{zs}} &= \underbrace{\begin{bmatrix} \cos \theta_{zs} & -\sin \theta_{zs} & 0 \\ \sin \theta_{zs} & \cos \theta_{zs} & 0 \\ 0 & 0 & 1 \end{bmatrix}}_{\text{Rotation by scanner motion}} \\
 \mathbb{R}_{PS\theta} &= \underbrace{\begin{bmatrix} \cos PS\theta_z & -\sin PS\theta_z & 0 \\ \sin PS\theta_z & \cos PS\theta_z & 0 \\ 0 & 0 & 1 \end{bmatrix} \begin{bmatrix} \cos PS\theta_y & 0 & \sin PS\theta_y \\ 0 & 1 & 0 \\ -\sin PS\theta_y & 0 & \cos PS\theta_y \end{bmatrix} \begin{bmatrix} 1 & 0 & 0 \\ 0 & \cos PS\theta_x & -\sin PS\theta_x \\ 0 & \sin PS\theta_x & \cos PS\theta_x \end{bmatrix}}_{\text{Prism-to-Scanner misalignments}} \\
 \vec{P}_1 &= \mathbb{R}_{\theta_{zs}} \cdot \mathbb{R}_{PS\theta} \cdot \underbrace{\begin{bmatrix} -\sin \theta_{FR} \\ 0 \\ -\cos \theta_{FR} \end{bmatrix}}_{\text{Upper normal}}; \quad \vec{P}_2 = \mathbb{R}_{\theta_{zs}} \cdot \mathbb{R}_{PS\theta} \cdot \underbrace{\begin{bmatrix} 0 \\ 0 \\ -1 \end{bmatrix}}_{\text{Lower normal}} \\
 \vec{L}_0 &= \underbrace{\begin{bmatrix} -\cos \theta_{LS} \sin \phi_{LS} \\ -\sin \theta_{LS} \sin \phi_{LS} \\ \cos \phi_{LS} \end{bmatrix}}_{\text{Vector entering prism}} \\
 \vec{L}_1 &= \underbrace{\frac{\eta_a}{\eta_s} \vec{L}_0 + \left(-\frac{\eta_a}{\eta_s} (\vec{P}_1 \cdot \vec{L}_0) - \sqrt{1 - \left(\frac{\eta_a}{\eta_s} \right)^2 \left(1 - (\vec{P}_1 \cdot \vec{L}_0)^2 \right)} \right) \vec{P}_1}_{\text{Vector inside prism}} \\
 \vec{L}_2 &= \underbrace{\frac{\eta_s}{\eta_a} \vec{L}_1 + \left(-\frac{\eta_s}{\eta_a} (\vec{P}_2 \cdot \vec{L}_1) - \sqrt{1 - \left(\frac{\eta_s}{\eta_a} \right)^2 \left(1 - (\vec{P}_2 \cdot \vec{L}_1)^2 \right)} \right) \vec{P}_2}_{\text{Vector exiting prism}}
 \end{aligned}$$

(3.48)

3.2 – Preliminary Sensitivity Analysis

Having identified the CZMIL parameters that will be investigated in this dissertation, it is necessary to establish an association of these parameters to each other. A simple comparison of how a small bias in each parameter will affect the location of the

laser point cloud will reveal which are the more “sensitive.” Parameters with a high sensitivity could potentially lead to large biases in the final point cloud, and thus warrant the closest scrutiny in a calibration procedure.

For example: if the prism slope were smaller than the manufacturer advertised, then the scan pattern would have a slightly smaller radius than anticipated (red points in Figure 31). The result of this narrower swath would be a set of laser ranges that would be shorter than expected resulting in a vertical bias to the data. Under anticipated CZMIL acquisition parameters (altitude = 400 meters, prism slope 39.2°), an error of 1 mrad (0.06°) in the prism slope would cause a 9 cm vertical bias and a 25 cm horizontal offset in the final point cloud (for a level flight). Armed with the foreknowledge of a user’s desired laser point accuracy, the Fresnel prism’s surface slope can be monitored for the appropriate accuracy during fabrication.

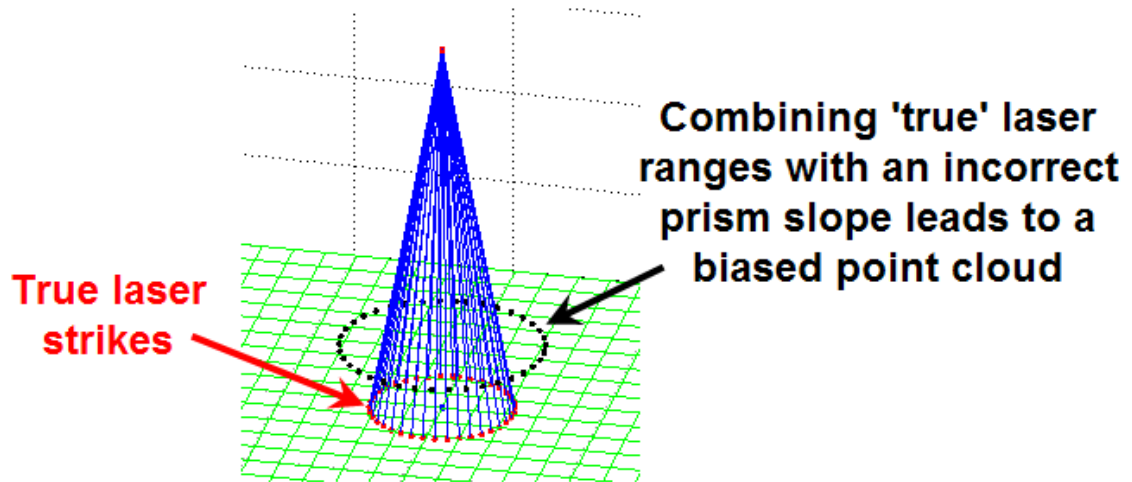


Figure 31. The Fresnel prism’s slope, θ_{FR} , is the angle of incidence, θ_i , for the Snell’s law refraction problem.

The magnitude of the induced bias in the final point cloud caused by a miscalculation of $PS\theta_x$ or $PS\theta_y$ will not be as large in comparison to a comparable error

in the Fresnel slope. As described earlier, a 1 mrad bias in θ_{FR} leads to a 25 cm horizontal error and 9 cm vertical bias of the laser point computations (for a level flight). A 1 mrad bias in $PS\theta_x$ would lead to a 3 cm horizontal error and a vertical bias of less than 1 cm; a similar bias in $PS\theta_y$ would lead to horizontal and vertical errors of 4 cm and 2 cm, respectively.

The preceding comparison between the Fresnel slope and the prism-to-scanner misalignments demonstrates a simplified sensitivity analysis. In the case of the Fresnel slope, because equivalent changes in the calibration parameters led to a much larger effect on the final point cloud, the system could be thought to be more “sensitive” to the Fresnel slope. This implies that greater attention should be paid to the slope of the Fresnel prism in the development of CZMIL (as compared to the prism-to-scanner alignments) if the manufacturer seeks to minimize positional errors in the point cloud. A second, though less intuitive implication is that because the system is not as sensitive to the prism-to-scanner alignments, these parameters will be more difficult to determine in any calibration procedure. This point will be revisited in the calibration chapter, but it is worth noting that parameters with the greatest effect on the point cloud will be the easiest to ascertain in the calibration routine and vice versa.

A sample list of biases induced by uncertainties in all the discussed laser parameters is provided in Figure 32. The parameters that have the greatest impact on the final point cloud are the pitch and roll boresight angles, $BS\theta_x$ and $BS\theta_y$. These values have historically been determined through some calibration routine and will be done so in this study as well.

Parameter type	Symbol	1 mrad bias		1.0° bias	
		Δz	$\Delta(x,y)$	Δz	$\Delta(x,y)$
Fresnel slope	θ_{FR}	9 cm	25 cm	160 cm	450 cm
Prism-to-Scanner alignment	$PS\theta_x$	< 1 cm	3 cm	1 cm	45 cm
Prism-to-Scanner alignment	$PS\theta_y$	2 cm	4 cm	30 cm	80 cm
Prism-to-Scanner alignment	$PS\theta_z$	0 cm	15 cm	0 cm	250 cm
Laser-to-Scanner vector	ϕ_{LS}	± 14 cm	40 cm	± 240 cm	600 cm
* Laser-to-Scanner vector	θ_{LS}	± 14 cm	40 cm	± 240 cm	750 cm
Boresight roll	$BS\theta_x$	± 15 cm	40 cm	± 250 cm	720 cm
Boresight pitch	$BS\theta_y$	± 15 cm	40 cm	± 250 cm	720 cm
Boresight yaw	$BS\theta_z$	0 cm	15 cm	0 cm	250 cm
** Vehicle heading alignment	θ_{VI}	± 3 cm	100 cm	± 45 cm	280 cm

* - in the presence of an equivalent ϕ_{LS} bias

** - where INS is mounted 1-meter to side of laser,
and vehicle experiences a 10-degree pitch

Figure 32. Table of laser point biases induced by a 1 mrad (0.06°) and 1° bias in each calibration parameter, where Δz = vertical bias and $\Delta(x,y)$ = horizontal displacement. Data based upon a 400m altitude and 20° laser elevation angle with no other biases (unless noted).

After the boresight angles, the laser-to-scanner vector is the next most critical value to be accurately determined. Specifically, ϕ_{LS} is of greater consequence since the entries in Figure 32 for θ_{LS} assume misalignments in both the laser-to-scanner parameters (and the magnitude of the point cloud biases do not appreciably worsen by the addition of a θ_{LS} misalignment). The ϕ_{LS} angle must be carefully measured on the system itself and included in a geometric calibration routine.

Caution must be used when interpreting the biases induced by the heading misalignment between the vehicle and the INS, θ_{VI} . While it is true changing θ_{VI} by 1 mrad will induce a 1 meter horizontal offset in the final point cloud, such a scenario is

unlikely to exist after any calibration routine. This is because there is a correlation among the different parameters. If the vehicle-to-INS heading misalignment was held fixed (at 0° , which is often the assumption), the other calibration parameters could be adjusted in an attempt to compensate for this error. “Compensate,” but not eliminate. It is a mathematical case of several wrongs (incorrect calibration values) trying to make a right (a coherent point cloud). A more detailed discussion of the correlation and linear dependence of parameters is presented in Chapter VI.

As a final observation from Figure 32, the least sensitive parameters (the ones that least affect the laser point accuracy) are the three prism-to-scanner alignment angles. This suggests fewer resources need to be expended to determine these angles. Nevertheless, the angles $PS\theta_x$, $PS\theta_y$, and $PS\theta_z$ will be included in the calibrator development (and the operator will be given the option whether to include these parameters in their own calibration).

3.3 – Summary of Key Results

This chapter endeavored to take the eight observed quantities (laser range, scanner azimuth, GPS position and vehicle orientation) and the five CZMIL system components (laser, prism, scanner, INS, vehicle) along with their respective reference frames and fuse them into a single equation which described the location of a laser point on the ground. That equation culminated in the development of (3.46).

In addition to the eight aforementioned observed quantities, thirteen calibration parameters were identified to describe the alignments among the system components (3 boresight angles, the prism slope, the VRF/IRF heading bias, the 3 components of the offset vector between the IRF and SRF, 2 angles to describe the laser-to-scanner

alignment, and 3 angles to describe the prism-to-scanner alignment. Additionally, two radiometric parameters were added to correct for any errors that may exist within the laser range computation (both a bias and scaling factor), bringing the total number of inputs for any point in the laser equation to 23.

To understand the propagation of the laser through the Fresnel prism, the vector version of Snell's Law was investigated (Sections 3.1.1 through 3.1.1.3).

Throughout, renderings of the point cloud were provided to demonstrate how each of the proposed calibration parameters affect the final point cloud (Sections 3.1.2 through 3.1.4.1). A preliminary sensitivity analysis was also presented for all of the angular parameters to demonstrate how large of a change there would be in the point cloud positions were there to be a change in one of the calibration values (Section 3.2). The roll and pitch boresight angles, along with the laser-to-scanner Φ -angle, induced the largest changes in the point cloud. The prism-to-scanner alignments yielded the least change in the point cloud. The concept of a small change in a calibration parameter leading to a large change in the point cloud will be revisited in Chapter VI (where it will be demonstrated such parameters will be calibrated to a higher degree of confidence than those who produce only minimal changes in the point cloud).

CHAPTER IV

THE LIDAR SIMULATION MODULE

4. THE LIDAR SIMULATION MODULE
4.1 MODULE OVERVIEW
4.1.1 The Intersection of Lines and Planes
4.1.2 Adjusting Acquisition and System Parameters
4.1.3 Navigation Time Error
4.1.4 Simulation Display Options
4.1.5 Displaying Point Cloud Biases
4.2 ADVANCED SIMULATION CONTROLS
4.2.1 Appending and Subsetting the Point Cloud
4.2.2 Simulating the Interaction of the Laser and the Water Surface
4.2.2.1 Rendering the land-water interface
4.2.2.2 Propagating the laser through the water column
4.2.2.3 Simulating surface waves and swell
4.2.2.4 Wave-induced uncertainty in the laser range
4.2.2.5 A dynamic ocean surface and beam steering
4.2.2.6 A simulated tidal model
4.3 SUMMARY OF KEY RESULTS

Figure 33. Chapter IV outline.

The previous chapter was devoted to deriving the laser location equation using all the inputs, both static (calibration values) and dynamic (quantities like the laser range), of the lidar to generate a geometrically-correct point cloud. While having the laser equation is sufficient to immediately proceed with the development of the calibration routine, without a working lidar, any calibrator utility will have to sit idle and untested until the system's delivery and actual test flights are flown. Instead, the laser equation is encoded in Matlab and affixed to a virtual aircraft to generate data streams equivalent to those that would be created during an actual flight.

Along with theory and experimentation, simulation has been characterized as a third avenue of scientific pursuit. Simulations can be used to garner insights, validate models, support statistical analysis, predict potential outcomes, test and evaluate new systems, and support what-if analyses (Reynolds, 2009). Here, if the laser equation of

Chapter III is taken to be correct, the simulation will allow us to gain insight into the behavior of the scan pattern, as well as the performance of the calibrator.

In addition to being able to test and validate the calibrator sooner, there are several other advantages to constructing an independent point cloud simulator. Through simulation, the flight characteristics can be precisely controlled to test vehicle maneuvering impacts on both the calibration's performance and the point cloud's propagated uncertainty – flights can be rerun without any cost to staffing, fuel or hardware fatigue. Different flight patterns can be tested to determine which best decouples the calibration parameters. Basic lidar coverage maps (both topographic and bathymetric) can be generated should the flight crew wish to alter the vehicle's speed or altitude. Different sea states or long period swell can be introduced to assess the impacts of beam steering. Datasets can be cropped to evaluate the impacts on the calibration routine for runways of differing sizes. What makes a lidar point cloud simulator most beneficial to a lidar point cloud calibrator is that the calibration parameters used to generate the point cloud will be exactly known, so there will be no doubt whether the proposed values of the calibrator are correct or not.

The principle drawback to any simulation is that it may not accurately represent the system being modeled. In such a case, the user must not rely too heavily on the model's conclusions until the simulation can be verified to be accurately reflect reality.

4.1 – Module Overview

4.1.1 – The Intersection of Lines and Planes

The construction of a lidar simulator comes down to the simple problem of determining the point at which a line (a laser beam) intersects a plane (the ground). The

laser beam will be defined from Chapter III, while the ground will be defined in the context of the simulator. First consider the purely geometric problem.

A line in 3D space is defined parametrically as:

$$\begin{aligned}x &= x_L + a_L t \\y &= y_L + b_L t \\z &= z_L + c_L t\end{aligned}\tag{4.1}$$

where:

(x, y, z) = 3D Cartesian coordinates
 $\langle x_L, y_L, z_L \rangle$ = 3D coordinates of an arbitrary point on line
 $\langle a_L, b_L, c_L \rangle$ = vector parallel to line
 t = free parameter.

A plane is defined as:

$$a_p x + b_p y + c_p z = d\tag{4.2}$$

where:

(x, y, z) = 3D Cartesian coordinates
 $\langle a_p, b_p, c_p \rangle$ = vector normal to plane
 d = constant.

If the plane is defined in such a way that it passes through the point $\langle x_p, y_p, z_p \rangle$, then we

can solve for d . Substituting into (4.2):

$$a_p x_p + b_p y_p + c_p z_p = d.\tag{4.3}$$

So any point (x, y, z) that satisfies the equation:

$$a_p x + b_p y + c_p z = a_p x_p + b_p y_p + c_p z_p,\tag{4.4}$$

lies on the plane (see Figure 34). Specifically, we wish to find a value of t in (4.1), if it exists, that will produce such an (x, y, z) .

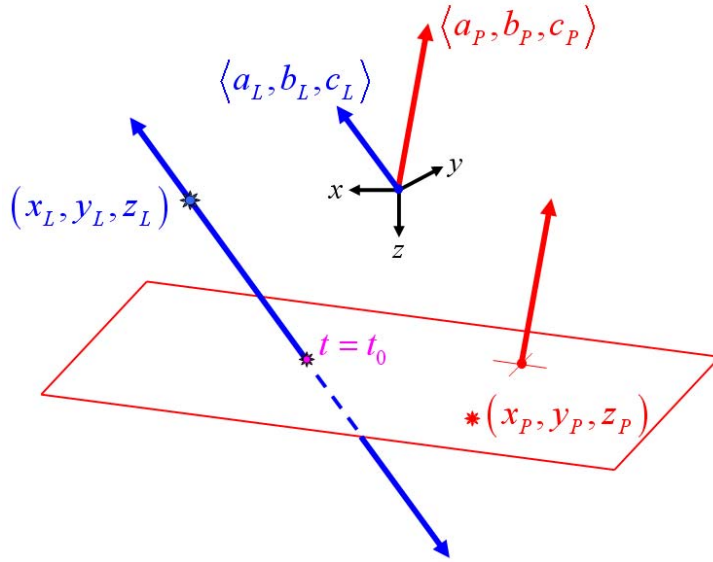


Figure 34. Solving for the parameter, t , where a line intersects a plane.

Substituting the parameterized coordinates of the line (4.1) into the equation for the plane (4.4) yield:

$$a_P(x_L + a_L t_0) + b_P(y_L + b_L t_0) + c_P(z_L + c_L t_0) = a_P x_P + b_P y_P + c_P z_P. \quad (4.5)$$

Then, solving for t_0 :

$$\begin{aligned} a_P x_L + a_P a_L t_0 + b_P y_L + b_P b_L t_0 + c_P z_L + c_P c_L t_0 &= a_P x_P + b_P y_P + c_P z_P \\ a_P a_L t_0 + b_P b_L t_0 + c_P c_L t_0 + a_P x_L + b_P y_L + c_P z_L &= a_P x_P + b_P y_P + c_P z_P \\ t_0(a_P a_L + b_P b_L + c_P c_L) + a_P x_L + b_P y_L + c_P z_L &= a_P x_P + b_P y_P + c_P z_P \end{aligned} \quad (4.6)$$

$$t_0 = \frac{a_P x_P + b_P y_P + c_P z_P - (a_P x_L + b_P y_L + c_P z_L)}{a_P a_L + b_P b_L + c_P c_L}. \quad (4.7)$$

Rewriting (4.7) in terms of dot products yields:

$$t_0 = \frac{\langle a_P, b_P, c_P \rangle \langle x_P, y_P, z_P \rangle - \langle a_P, b_P, c_P \rangle \langle x_L, y_L, z_L \rangle}{\langle a_P, b_P, c_P \rangle \langle a_L, b_L, c_L \rangle}. \quad (4.8)$$

Substituting t_0 into (4.1) will then give the (x, y, z) coordinates of the line-plane intersection.

In the context of a laser striking the ground, (4.8) becomes:

$$t_0 = \frac{\langle \text{ground_norm} \rangle \langle \text{nadir_pt} \rangle - \langle \text{ground_norm} \rangle \langle \text{laser_node_pt} \rangle}{\langle \text{ground_norm} \rangle \langle \text{laser_unit} \rangle} \quad (4.9)$$

where:

ground_norm = vector normal to the ground

nadir_pt = point on the ground (taken as point directly below aircraft)

laser_node_pt = origin of laser (taken as point on top of prism)

laser_unit = direction of laser as it departs vessel.

The ground normal, represented in spherical coordinates with angles (ϕ_{GR}, θ_{GR}) , will be defined as:

$$\text{ground_norm} = \begin{bmatrix} \sin \phi_{GR} \cos \theta_{GR} \\ \sin \phi_{GR} \sin \theta_{GR} \\ -\cos \phi_{GR} \end{bmatrix}. \quad (4.10)$$

When the simulated vehicle begins its trajectory, the point at nadir is defined as the origin of the coordinate system. That is:

$$\text{nadir_pt} = \begin{bmatrix} 0 \\ 0 \\ 0 \end{bmatrix}. \quad (4.11)$$

Equation (3.46) gives a generic laser equation:

$$\vec{x}_G = \mathbb{R}_V \cdot \mathbb{R}_{VI} \left(\mathbb{R}_{BS} \cdot \vec{L}_2 \cdot \left(\frac{\rho - \rho_0}{\rho_1} \right) + \vec{x}_{IL} \right) + \vec{x}_{ECEF}$$

The preceding equation can be split into two components to find both the origin of the laser and its direction (the requisite point and vector needed to define a line). The top of the prism is defined as:

$$\text{laser_node_pt} = \mathbb{R}_V \cdot \mathbb{R}_{VI} \cdot \vec{x}_{IL} + \vec{x}_{ECEF}, \quad (4.12)$$

and the direction of the laser as it departs the vehicle is given by:

$$\text{laser_unit} = \mathbb{R}_V \cdot \mathbb{R}_{VI} \cdot \mathbb{R}_{BS} \cdot \vec{L}_2. \quad (4.13)$$

Should the operator wish to simulate a laser striking a surface other than the ground (a building roof, a runway, a sloping sea surface, etc.), it would only be necessary to define this new surface's normal vector and an included point.

Once the coordinates of where the laser strikes the ground are known, \vec{x}_G , the distance formula can be applied to this point and the laser's origin, laser_node_pt, to calculate the laser range of the lidar.

4.1.2 – Adjusting Acquisition and System Parameters

A rendering of the overall lidar simulation module interface is shown in Figure 35 (along with more detailed views shown in Figure 36, Figure 37 and Figure 38).

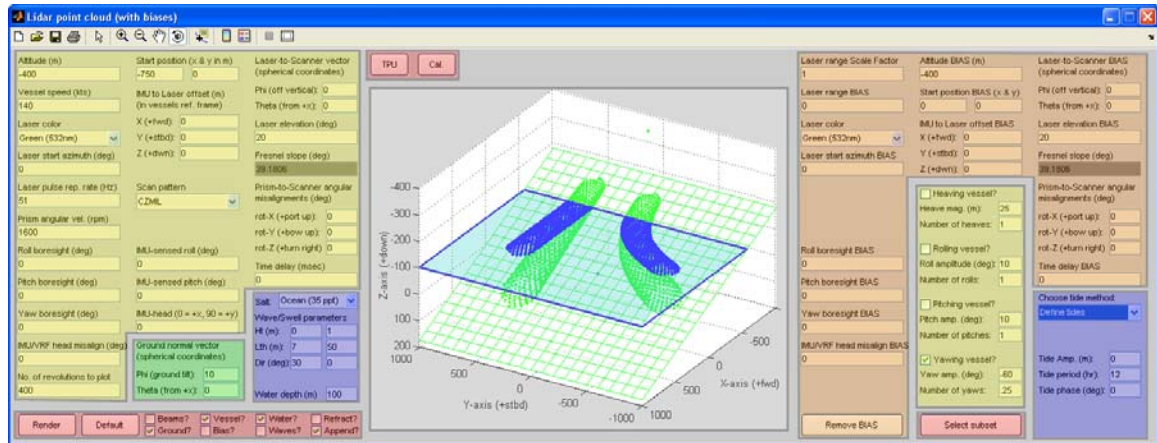


Figure 35. The lidar simulator interface. Close up views of the left, middle and right portions are shown in the following figures.

Altitude (m) -400	Start position (x & y in m) -750 0	Laser-to-Scanner vector (spherical coordinates)
Vessel speed (kts) 140	IMU to Laser offset (m) (in vessels ref. frame)	Phi (off vertical): 0
Laser color Green (532nm) ▼	X (+fwd): 0	Theta (from +x): 0
Laser start azimuth (deg) 0	Y (+stbd): 0	Laser elevation (deg) 20
Laser pulse rep. rate (Hz) 51	Z (+dwn): 0	Fresnel slope (deg) 39.1806
Prism angular vel. (rpm) 1600	Scan pattern CZMIL ▼	Prism-to-Scanner angular misalignments (deg)
Roll boresight (deg) 0	IMU-sensed roll (deg) 0	rot-X (+port up): 0
Pitch boresight (deg) 0	IMU-sensed pitch (deg) 0	rot-Y (+bow up): 0
Yaw boresight (deg) 0	IMU-head (0 = +x, 90 = +y) 0	rot-Z (+turn right) 0
IMU/VRF head misalign (deg) 0	Ground normal vector (spherical coordinates)	Time delay (msec) 0
No. of revolutions to plot 400	Phi (ground tilt): 10	Salt: Ocean (35 ppt) ▼
	Theta (from +x): 0	Wave/Swell parameters
		Ht (m): 0 1
		Lth (m): 7 50
		Dir (deg): 30 0
		Water depth (m) 100
<div>Render Default <input type="checkbox"/> Beams? <input checked="" type="checkbox"/> Vessel? <input checked="" type="checkbox"/> Water? <input type="checkbox"/> Refract?</div> <div><input checked="" type="checkbox"/> Ground? <input type="checkbox"/> Bias? <input type="checkbox"/> Waves? <input checked="" type="checkbox"/> Append?</div>		

Figure 36. A closer view of the left panel of the lidar simulator. The flight and lidar parameters are highlighted in yellow; the orientation of the ground is in green; controls for the ocean surface are in blue; and the GUI's control panel is in red.

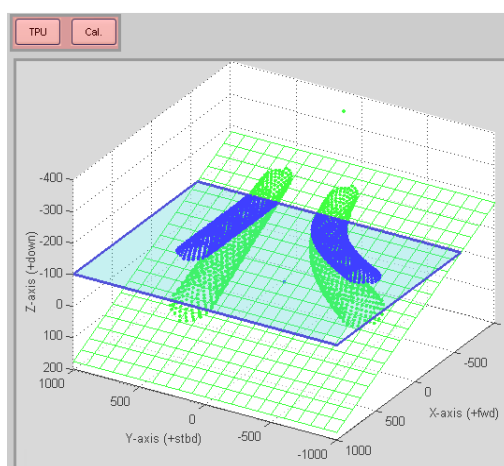


Figure 37. A closer view of the center panel of the lidar simulator. The panel is dominated by a plot of the point cloud (shown with two flight lines surveying across the land-sea boundary), but the buttons for launching the uncertainty and calibration modules are also present (highlighted in red).

Laser range Scale Factor 1	Altitude BIAS (m) -400	Laser-to-Scanner BIAS (spherical coordinates)
Laser range BIAS 0	Start position BIAS (x & y) 0 0	Phi (off vertical): 0
Laser color Green (532nm)	IMU to Laser offset BIAS	Theta (from +x): 0
Laser start azimuth BIAS 0	X (+fwd): 0	Laser elevation BIAS 20
	Y (+stbd): 0	Fresnel slope (deg) 39.1806
	Z (+dwn): 0	Prism-to-Scanner angular misalignments (deg)
	<input type="checkbox"/> Heaving vessel?	rot-X (+port up): 0
	Heave mag. (m): 25	rot-Y (+bow up): 0
	Number of heaves: 1	rot-Z (+turn right): 0
	<input type="checkbox"/> Rolling vessel?	Time delay BIAS 0
	Roll amplitude (deg): 10	
	Number of rolls: 1	
	<input type="checkbox"/> Pitching vessel?	
	Pitch amp. (deg): 10	
	Number of pitches: 1	
	<input checked="" type="checkbox"/> Yawing vessel?	
	Yaw amp. (deg): -60	
	Number of yaws: .25	
Roll boresight BIAS 0		Choose tide method: Define tides
Pitch boresight BIAS 0		Tide Amp. (m): 0
Yaw boresight BIAS 0		Tide period (hr): 12
IMU/VRF head misalign BIAS 0		Tide phase (deg): 0
Remove BIAS	Select subset	

Figure 38. A closer view of the right panel of the lidar simulator. Sensor misalignments can be introduced to the point cloud (orange); the vehicle's attitude can be varied during flight (yellow); a tidal model can be introduced (blue) and a subset of the data can be highlighted for further analysis (red)

To simulate a lidar flight, more information is needed than just the geometric alignments (boresight angles, IMU-to-laser offset, etc.) of the lidar. The characteristics of the laser/scanner assembly and the trajectory of the aircraft must also be fully described. For the laser/scanner, the user must specify values for: the laser's wavelength (needed for determining the refractive coefficients) and pulse repetition rate, the prism's rate of rotation and starting azimuth, and the number of revolutions to plot (Figure 36 – yellow). For the vehicle, the user must specify: the acquisition altitude, the starting position, and the vehicle's speed and base course. A fixed set in the vehicle's orientation can also be added (for example, if the airplane is heeling with the nose up at a constant 10°) (Figure 36 – yellow). In addition, the vehicle's attitude can be adjusted dynamically

to simulate a vehicle pitching, rolling or yawing during flight (Figure 38 – yellow).

Examples of both a static and dynamic change in roll are shown in Figure 39. The dynamic attitude is based only on a sinusoidal curve, that is, the vehicle's roll at any time is defined by (terms in red can be specified in simulator):

$$\omega(t) = \omega_0 + A_\omega \sin\left(\frac{2\pi t}{t_{\text{TOTAL}}} N_\omega\right), \quad (4.14)$$

where:

$\omega(t)$ = vessel roll at time t

ω_0 = static vessel roll

A_ω = amplitude of dynamic vessel roll

t = time of observation

t_{TOTAL} = elapsed time of entire rolling flight line

N_ω = number of rolls experienced.

Though this model is simplistic, the goal is not to recreate an actual vehicle's flight characteristics, but to provide a “dynamic-enough” dataset to test the calibration module.

Dynamic heave can also be simulated with the above model. Once all acquisition and system parameters are specified, the “Render” button (Figure 36 – red) will synthesize the point cloud.

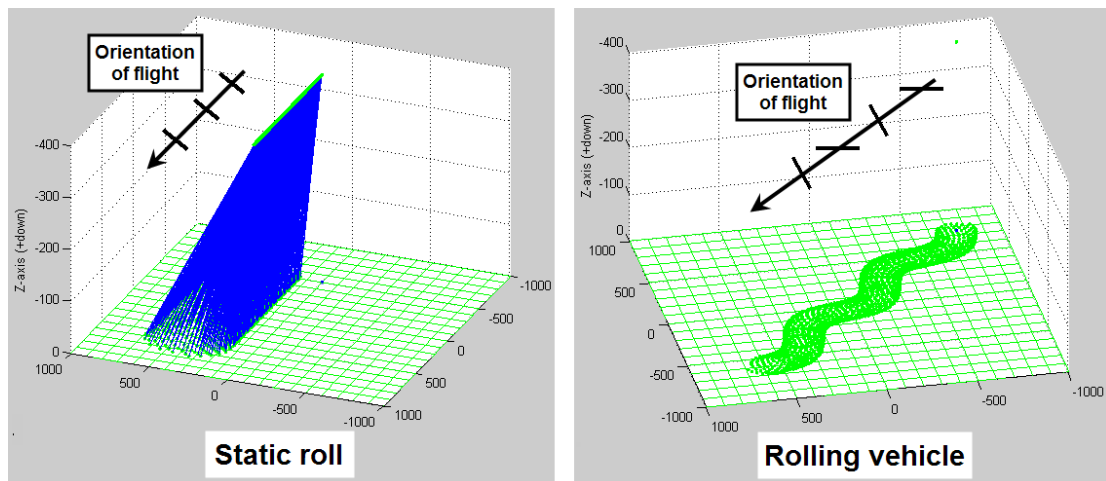


Figure 39. Examples of flights in which the vehicle experiences static (left) and dynamic (right) changes in attitude.

4.1.3 – Navigation Time Error

The simulator not only renders the point cloud, but also creates an output file containing the eight raw measurements used to create each point: the laser range, the scanner azimuth, the three-dimensional location of the IMU and the three angles that describe the vehicle's attitude. These eight measurements and the laser equation are sufficient information to recreate the point cloud. A ninth measurement, the time stamp, is also output with each point for organizational purposes, with the first point in the simulation given a time tag of zero. The inclusion of dynamic vehicle motion, coupled with time stamping, means a navigation timing error can also be modeled.

A navigation timing error, also referred to as a “time delay” or “time synchronization error,” results when measurements simultaneously recorded by different acquisition systems (e.g., the INS, the laser encoder) are associated with differing time stamps. Calder and McLeod (2007) discuss methods of preventing such an error from ever manifesting during acquisition; however, the lidar simulator still provides a field for editing this time delay (Figure 36 – yellow). For example, a one millisecond delay in the vehicle's attitude, applied to a 20 second flight line that experiences one roll oscillation of 10° , will have up to 1cm of vertical error on the reconstructed point cloud (Figure 40).

Entering a positive value for the time latency within the simulation implies that the laser encoder is receiving “old” information from the INS (i.e., the laser is ahead in time). A negative value can also be entered, thereby making the INS the master clock and instead retarding the laser. In the module's present implementation, editing the time delay only affects the time stamps associated with the attitude information; the INS-reported positions are not modified.

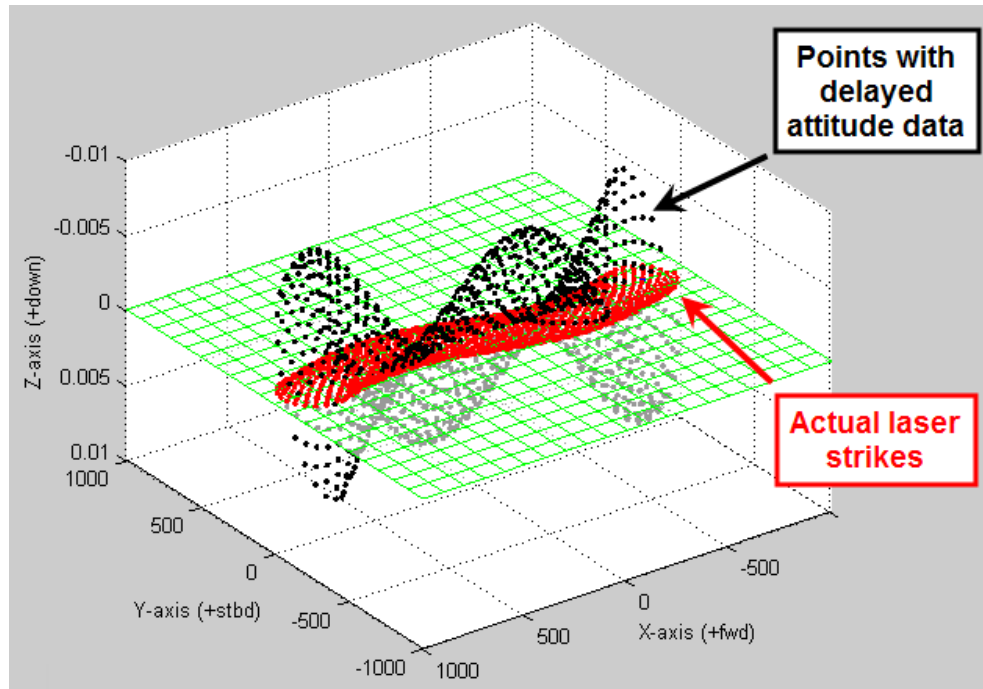


Figure 40. A rolling vehicle with a delay in the attitude time stamping will result a potentially incoherent point cloud (black).

The output file of the simulator is indexed by shot number. Due to the laser's steady pulse repetition rate each laser point is temporally separated from its neighbors by a fixed increment of time. If a one kilohertz laser is simulated, then each shot will be separated by a one millisecond time stamp, and the vehicle attitude will be logged accordingly. Should there be an integer number of milliseconds time delay applied, then the attitude data is read from the appropriate field in the array. For example, if there is a two millisecond delay, then the laser range associated with time $t = 5$ seconds would use the attitude information associated with the laser point time stamped $t = 5.002$ seconds. However, if the time delay results in the needed information being situated chronologically between two laser shots, then a linear interpolation is used to estimate the attitude. For example, if the previous example has a 2.3ms delay, then the attitude

associated with the laser range at time $t = 5$ would be between the attitude measured 2ms and 3ms ago:

$$attitude_5 = 0.7 * attitude_{5.002} + 0.3 * attitude_{5.003}. \quad (4.15)$$

4.1.4 – Simulation Display Options

The point cloud is oriented in a right-handed forward-starboard-down coordinate system. Once rendered, there are a number of plot features that may be toggled to aid with the interpretation of the data (Figure 36 – red). At the user’s discretion, the laser beams, the vehicle and the ground plane can be displayed or hidden. By default, the point cloud is rendered over a 2km×2km ground plane with the vehicle’s starting position for reference (Figure 41 – upper-left). By toggling on the laser beams a better representation of the vehicle’s trajectory is seen, here shown with a large heave (Figure 41 – upper-right). Also the rendering of the vehicle (Figure 41 – lower-left) and ground (Figure 41 – lower-right) can be suppressed to exaggerate the vertical and horizontal scales respectively.

The orientation of the ground plane is controlled by editing the orientation of its normal vector (Figure 36 – green). The user can specify the grade of the ground, ϕ_{GR} , as well as which direction is “down-hill,” θ_{GR} , (both expressed in spherical coordinates), see (4.10).

Subtle changes in the execution of the laser equation can produce the scan pattern of several other lidar sensors. Preliminary rendering of point clouds from three types of scanners are shown in Figure 42. These different patterns can be selected from the “Scan Pattern” drop down menu (Figure 36 – yellow). It must be emphasized that these visualizations are only preliminary in nature, and the simulator does not yet model the

full laser equations of any lidar other than CZMIL. Proposed future work should include a further investigation of these alternative laser equations. These equations will not only permit the rendering of synthetic point clouds, but expand the use of the calibration, covariance and uncertainty modules presented in this dissertation to the larger suite of laser scanners presently deployed.

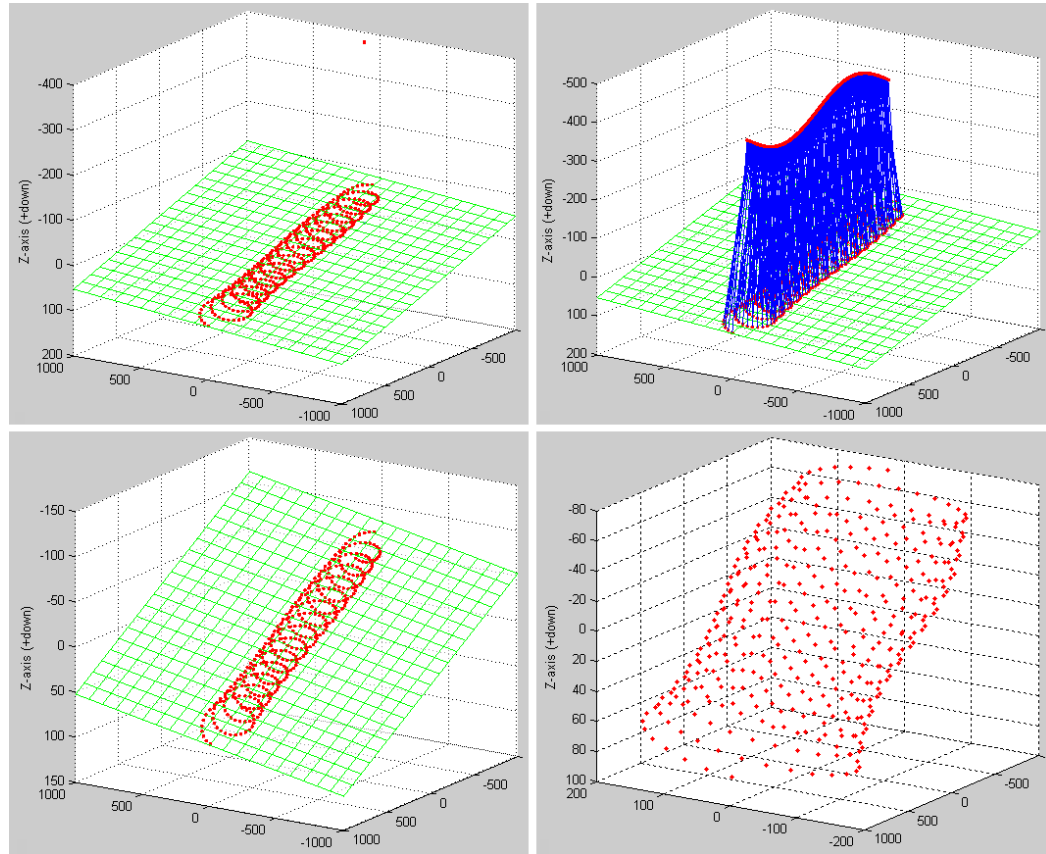


Figure 41. The same point cloud with variance display options: the default (upper-left), with the laser beams displayed (upper-right), suppressing the vehicle (lower-left) and suppressing the ground (lower-right).

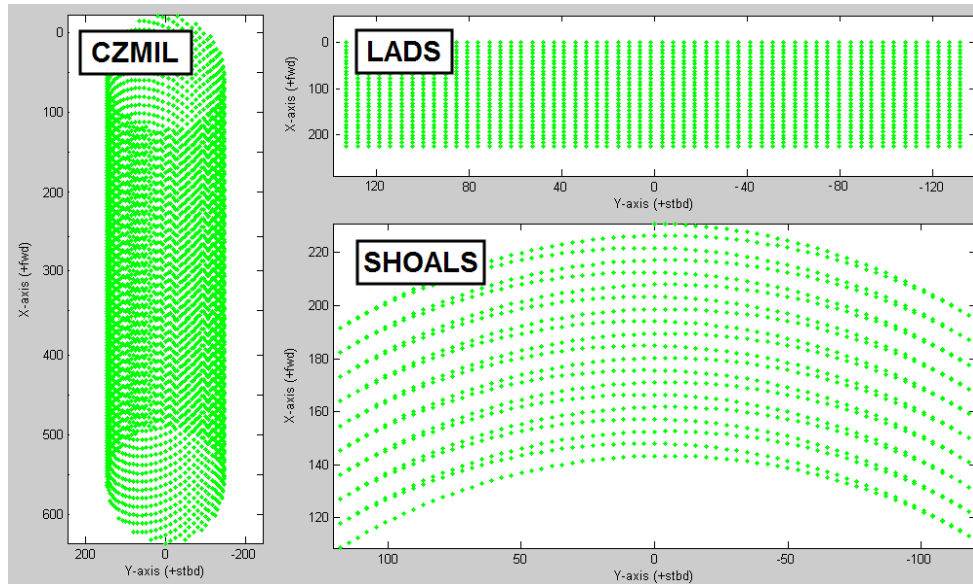


Figure 42. Simulations of various lidar scan patterns: the circular scanning CZMIL, the rectangular grid producing LADS, and the forward arcing SHOALS.

4.1.5 – Displaying Point Cloud Biases

There have already been several examples in this document of what a point cloud would look like were there an undetected misalignment within the lidar (e.g. Figure 24, Figure 25, Figure 31 and Figure 40). All these figures were created using controls available within the simulator. The left side of the simulator (Figure 36) can be thought of as the “truth”. Given the provided system parameters, the program will determine the point where the laser strikes the ground and correctly report the laser range. The right side of the simulator (Figure 38 – orange) can then be interpreted as the “perceived truth.” The user may take the correct laser ranges and then re-render the point cloud using a laser equation that is filled with incorrect system parameters.

An example of how this bias visualization tool performs is shown in Figure 43. On the left are two revolutions of a circular scanning lidar with no boresight misalignments (i.e., all beams are angled 20° from nadir). In such a case, the forward, aft, port and starboard-looking beams will all have the same computed range. Should the

lidar have a positive boresight misalignment of 10° in the pitch angle (Figure 43), then the forward-oriented beams will have a relatively longer range and the aft-oriented beams will have a shorter range. Should the lidar operator incorrectly believe there to be no pitch boresight misalignment (i.e., possess the geometry of Figure 43 – left), then the longer forward beams will lead the operator to believe the laser pulses are located below the actual ground plane and the shorter aft beams are located above the ground (Figure 43 – right). Within the simulator, the pitch boresight angle was entered as 10° while the pitch boresight bias was entered as 0° . The rendering of the biases can be toggled on by selecting the “Bias?” switch (Figure 36 – red).

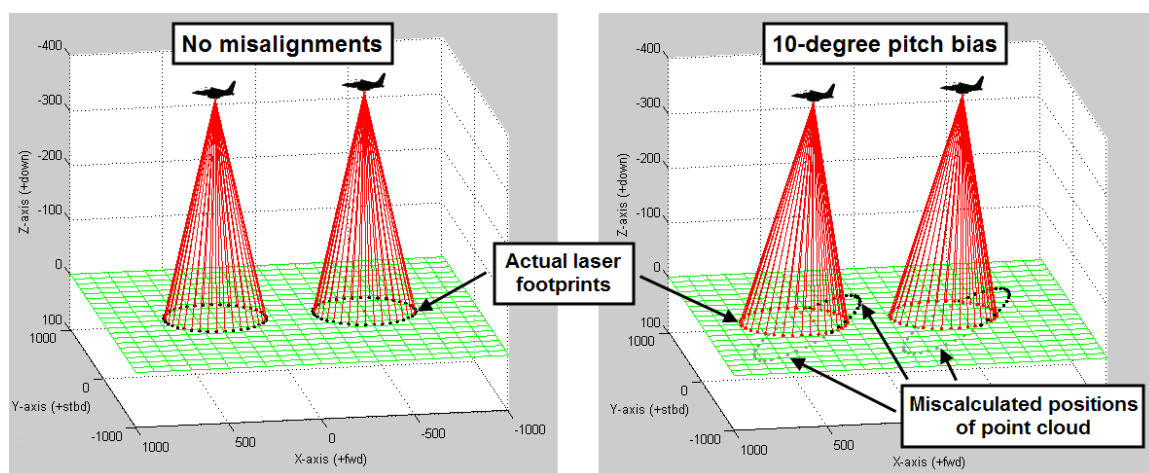


Figure 43. Two revolutions of a lidar with no geometric misalignments (left) and the same point cloud with an unknown 10° forward (i.e., towards the nose) pitch boresight bias (right). The actual laser footprints are shown in red and the miscalculated point clouds are shown in black.

The ability to preview a geometrically-biased point cloud has several advantages. First, an easily visualized sensitivity analysis can be performed (as shown in Figure 32) to assess how any error in a calibration parameter will translate to an error in the reported positions of the laser points. Second, the ability to view biased point clouds lays the ground work for a signature analysis utility to assess potential misalignments within a

point cloud just by examining the clouds geometric characteristics (presently proposed as future work). Finally, from a calibration perspective, different flight line strategies can be simulated to establish what maneuvers must be performed to decouple the many calibration parameters. The topic of how the flight lines characteristics relate to the ability to determine the calibration parameters is further discussed in Chapter VI.

4.2 – Advanced Simulation Controls

4.2.1 – Appending and Subsetting the Point Cloud

The lidar simulation program is not meant to be a stand-alone package. Rather, it was created to generate test datasets for other modules, in particular the calibration module but also the total propagated uncertainty (TPU) module. Provided a point cloud has been created, both the calibrator and TPU modules can be immediately launched from within the simulator (Figure 37 – red). Launching the calibrator will only cause the output of the nine observed quantities associated with each laser spot (the laser range, the scanner azimuth, etc.). No information regarding the position of the laser points or the system parameters used to create the point cloud is passed to the calibrator. In contrast, all the parameters (both observables and system alignments) are passed to the TPU module. Further details of the calibration module are presented in Chapter 6, while the TPU module is discussed in Chapter VII.

Each time the “Render” button within the simulator is pushed one flight line is synthesized; however, these auxiliary modules are not limited to working with only a single line of data. By toggling on the “Append” feature (Figure 36 – red), a user may simulate an entire day’s worth of flights. This means that several flights acquired at different altitudes, orientations or sampling densities can all be used simultaneously in

the calibration procedure. One could also use this feature to assess data coverage rates between overlapping swaths. The append tool has already been demonstrated repeatedly within this dissertation including in Figure 43 which illustrated the appending of two flights, each consisting of a single revolution of the scanner.

Note that each time a new flight line is appended to the point cloud, the time stamp of the first laser pulse is advanced six minutes from the time of the last pulse on the previous flight line. This time lag was added to approximate the time necessary to turn the vehicle and line up for the next pass. These steps in time will be of consequence later in this chapter when we introduce wave and tidal models into the point cloud.

While the append feature allows the user to increase the size of the point cloud, the subset feature (Figure 38 – red) allows the user to narrow the points sent to the calibration and TPU modules. Pressing the subset button will turn the user's cursor into a lasso tool to highlight only a portion of the data for further analysis. Figure 44 shows an example where three flight lines are simulated over a sloping surface. Imagine the user is only interested in the center flight and the downslope portion of all three lines (perhaps representing the intersection of two paved surfaces). Using the lasso tool twice, the two areas of interest are highlighted (left) and exported to other modules (right). This subset tool will be critical when trying to assess the viability of performing a calibration on land using only the narrow strip of data that would be available over an airport runway.

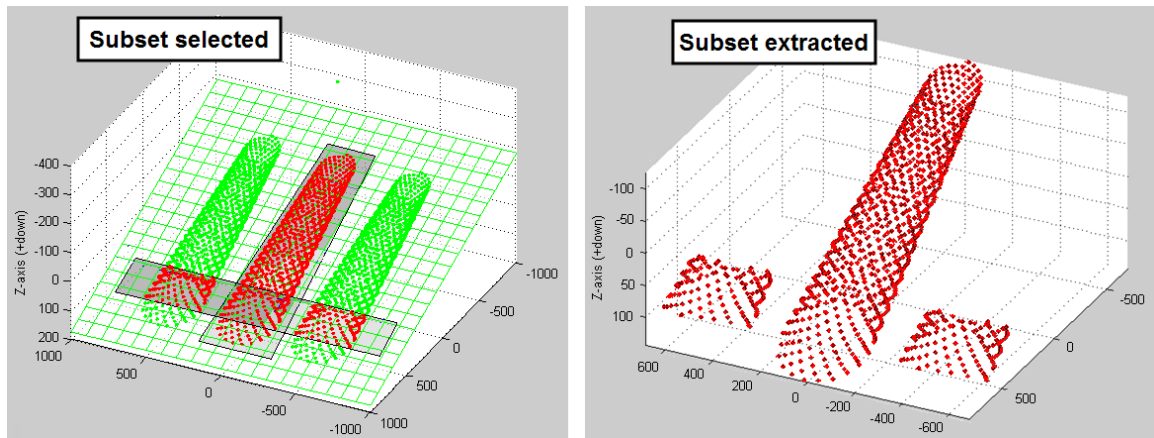


Figure 44. Three survey lines are simulated and two regions are selected by the subset editor (left). Only the selected points are exported to other modules.

4.2.2 – Simulating the Interaction of the Laser and the Water Surface

Given that this dissertation is dedicated towards the calibration of a bathymetric lidar, incorporating a water surface into the simulation is a crucial step. Figure 45 highlights some of the challenges that must be confronted when surveying across a virtual shoreline: the intersection of the land-water boundary must be defined; the laser pulses must be recorded from both the water surface and the seafloor; and the physical properties of the water mass must be simulated to determine the laser's refraction. This dissertation proposes to use the water surface as a potential calibration site. Because tidal and sea swell may affect the feasibility of such a choice, both tides and waves and their associated impact on the laser must also be considered.

Note that this dissertation is not unique in the use of a sea surface return as part of the calibration routine. Conversations with Eric Yang of Optech have revealed the SHOALS system has long employed a sea surface detection strategy as a part of their calibration methodology. This dissertation is unique in proposing to use the sea surface return exclusively for the calibration routine. The methodology employed for SHOALS

also requires additional flight lines over airport runways and buildings with particular sloped roofs.

The remainder of this chapter will focus on the preceding list of challenges associated with the water surface. Some topics (like the rendering of the water boundary) present algorithmic challenges that should be understood by anyone trying to modify the program. Such topics, however, have little impact on the ultimate calibration routine. Those strictly interested in material of relevance to the calibrator may wish to skip to the final two sections of this chapter regarding the inclusion of waves and tide.

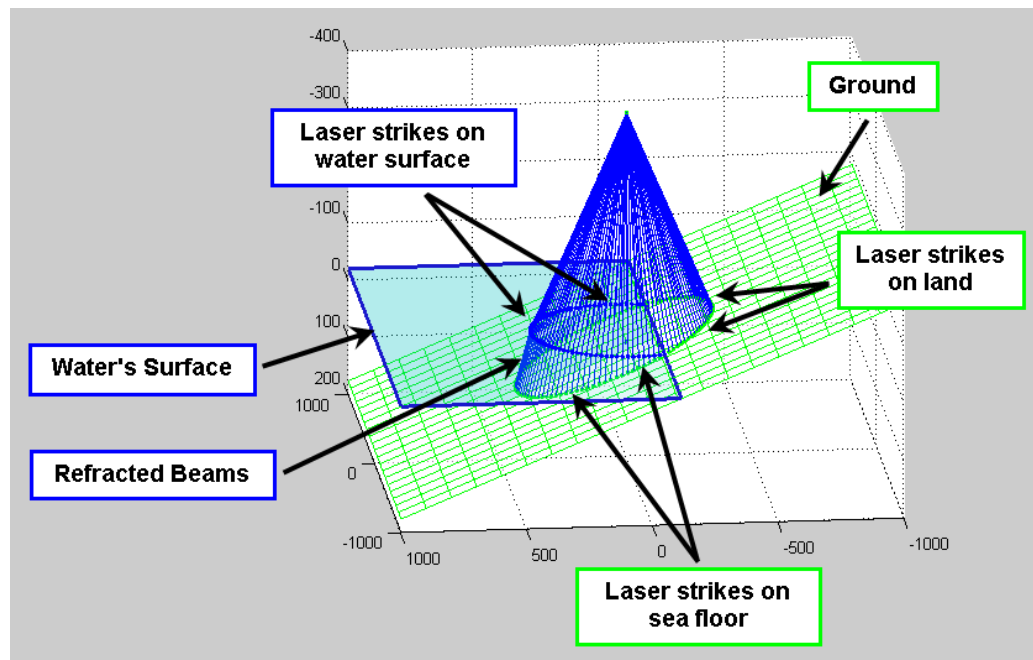
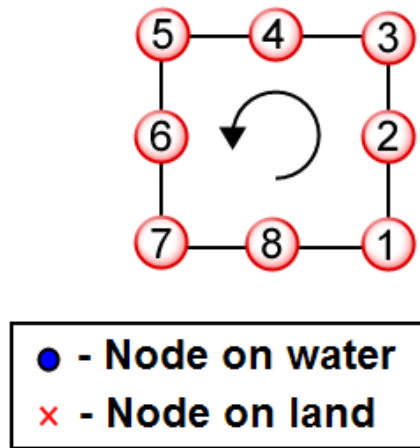


Figure 45. A simulation of a lidar survey across the land-water boundary.

4.2.2.1 – Rendering the land-water interface. The aquatic features are toggled on or off via the control panel (shown in red in Figure 36) and interacted with the fields shown in blue. Should the seafloor be horizontal, then the water surface will fill the entire plot area. If, however, the seafloor is sloping, a decision tree must be employed to

determine whether a given (x,y) location is over land or water (see Figure 46 for a visual representation of the algorithm).



The goal is to draw the perimeter of the water surface:

Check whether node 1 is above or below the water surface.

- If node 1 is wet, check node 3. (I)
- If node 3 is wet, continue checking corners. (II)
- If node 3 is dry, solve for node 2 shoreline. (III)
- Etcetera...

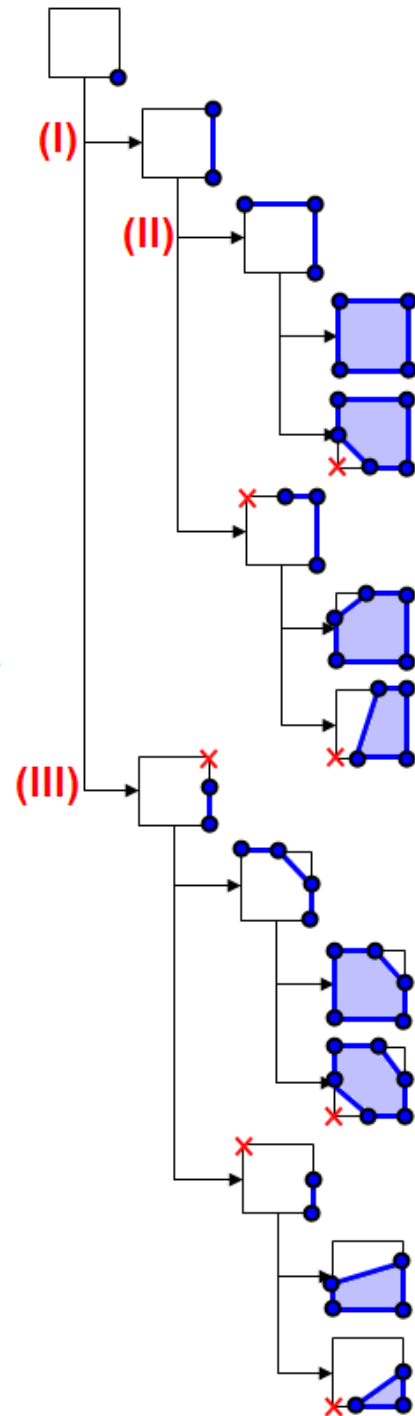


Figure 46. Pseudocode (left) and visual decision tree (right) used for rendering the perimeter of the water surface in the presence of a sloping seafloor. See discussion in text.

A polygon representing the water surface must be solved for algorithmically to determine whether the laser will strike land, or strike the water, refract through the water column and then strike the seafloor. For one corner of the area of interest (node 1 in Figure 46), the elevation of the ground plane is compared to that of sea level. If the z -value is below sea level, then node 1 becomes the first vertex of the water surface polygon. If node 1 is underwater, node 3 is then checked. Should node 3 also be underwater, then the edge comprised of nodes 1 and 3 is an edge in the water surface polygon, (I) in Figure 46. On the other hand, if node 3 is above sea level, then there must be some point (node 2) between nodes 1 and 3 where the ground plane and water surface intersect. Solving for this point is a simple matter and yields an edge in the water surface polygon spanning from node 1 to node 2, (III) in Figure 46. The process is repeated around the perimeter of the area of interest until the full water surface polygon is defined. A sample water surface and its associated nodes are shown in Figure 47.

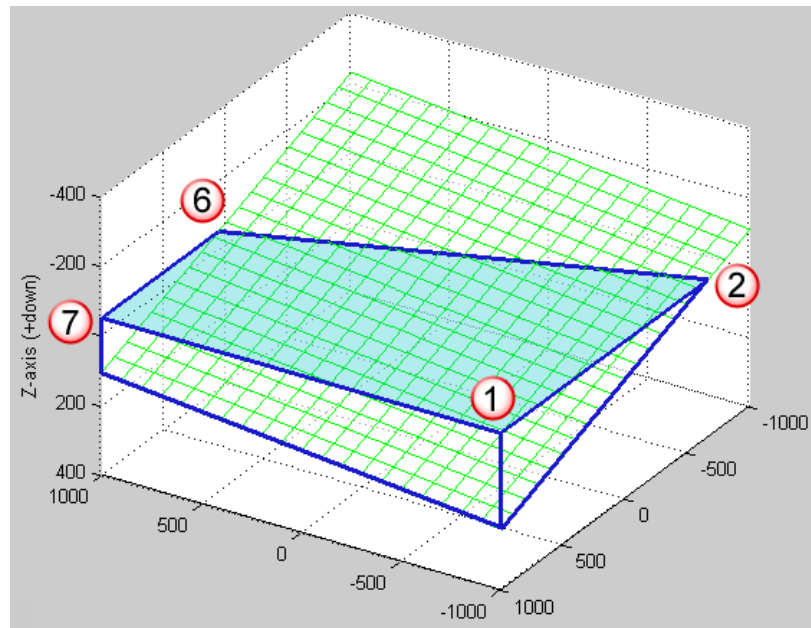


Figure 47. A sample water surface polygon along with the associated nodes needed for its derivation. Vertical edges and lines along the seafloor have been added for clarity.

With the water surface polygon defined, the point of intersection between the laser and the ground plane is computed. If the (x,y) projection of this point onto the water plane is not contained within the water surface polygon, then the point is logged as a strike on dry land and the algorithm concludes. Conversely, should the point's projection be within the water surface polygon, then the first calculated point is discarded as erroneous (because it neglected refraction at the air-water interface) and instead the intersection of the laser and the water surface is computed (yielding the coordinates of the laser spot on the water surface). The next section discusses how the laser is then propagated through the water column to get the coordinates of the laser strike on the seafloor.

4.2.2.2 – Propagating the laser through the water column. The physics of a laser pulse as it propagates through the water column are complicated; particularly if one considers that the laser will not be a point, but a spot 3m in diameter at the sea surface (Fuchs & Mathur, 2010). For the purposes of tracking the theoretical center of the laser spot on the seafloor, the laser beam is assumed to be a low divergence beam entering a homogenous water mass.

In its simplified form, the problem is again one of determining the intersection of a line and a plane, which can be solved using (4.7) and (4.1). In this case, the plane is the same ground plane as before, leaving the line, which is the laser beam traveling through the water column to be determined. Again, a line is defined by a contained point and a parallel vector. The point was found in the previous section where the laser struck the water surface, leaving only the direction of the laser within the water column. To

determine the direction of the laser within the water column, we return to the vector version of Snell's Law, specifically (3.30):

$$\vec{L}_w = \frac{\eta_a}{\eta_w} \vec{L}_a + \left(-\frac{\eta_a}{\eta_w} (\vec{w} \cdot \vec{L}_a) - \sqrt{1 - \left(\frac{\eta_a}{\eta_w} \right)^2 (1 - (\vec{w} \cdot \vec{L}_a)^2)} \right) \vec{w} \quad (4.16)$$

where:

\vec{L}_w = direction of laser pulse in water column

\vec{L}_a = direction of laser pulse in air

η_a = refractive index of laser (532nm) in air

η_w = refractive index of laser (532nm) in water

\vec{w} = vector normal to water surface.

If the water surface is horizontal, the normal vector is simply:

$$\vec{w} = [0 \quad 0 \quad -1]. \quad (4.17)$$

Neglecting atmospheric refraction, the direction of the laser pulse entering the water column is equivalent to the direction of the laser pulse exiting the aircraft. From (4.13):

$$\vec{L}_a = \mathbb{R}_V \cdot \mathbb{R}_{VI} \cdot \mathbb{R}_{BS} \cdot \vec{L}_2.$$

An atmospheric index of refraction of $\eta_a = 1.0003$ is used from Feynman (1963). The refractive index for the water column is slightly more complicated, being a function of the laser's wavelength, the absolute temperature of the water and the water's density (where density is further a function of the water's salinity). The equation used for calculating the refractive index was provided by the International Association for the Properties of Water and Steam (1997). Refractive indices for the green laser (assuming a water temperature of 20°C) were computed for three water types: fresh (0 psu), brackish (10 psu) and oceanic (35 psu). For fresh, brackish and oceanic waters, the refractive indices are computed to be 1.3354, 1.3387 and 1.3468 respectively. Putting these

refractive indices in perspective, should the incoming laser pulse have an incidence angle of 20° , then the refracted angle will range between 14.84° (fresh) and 14.72° (oceanic). Referencing back to Figure 45, one can see the subtle bending of the laser beams towards the water surface normal as it enters the water surface.

To summarize, using Snell's Law will give the direction of laser pulse within the water column. When this vector is combined with the coordinates of the laser point on the water surface (found from the intersection of the laser exiting the vehicle and the water surface), the intersection of the laser within the water column and the seafloor can be computed.

4.2.2.3 – Simulating surface waves and swell. Sea waves and long period swell may adversely affect the point cloud in a number of ways. From the perspective of rendering the point cloud, the changing slope of the sea surface may lead to unanticipated beam steering at the air-water interface. From the perspective of the calibration, the changing sea surface height might make the water too poor a proxy for a flat surface to be used as a reference for calibration. Further, the variation in the sea height for any given location will lead to a variation in the measured laser range for that same location. This uncertainty will have to be accounted for and propagated within the calibration module. But before we can examine the impacts of waves on calibration or beam steering, we must first simulate it.

It should be emphasized that we are not attempting to construct a model of the sea surface that will satisfy the most exacting of physical oceanographers. Instead, we are just trying to distill some of the key behaviors of the sea surface that will affect a lidar and its calibration. In the context of this dissertation, “sea waves” will be used to model

the small amplitude, high frequency waves that lead to a checkerboard-like confused sea surface (Figure 48 – upper-left). In contrast, “sea swell” will be used to model the larger amplitude, long period linear wave fronts (Figure 48 – lower-left). The two phenomena will then be added together to produce the net “sea state” (Figure 48 – right). To enable the wave model within the simulator, check the “Waves?” button (Figure 36 – red).

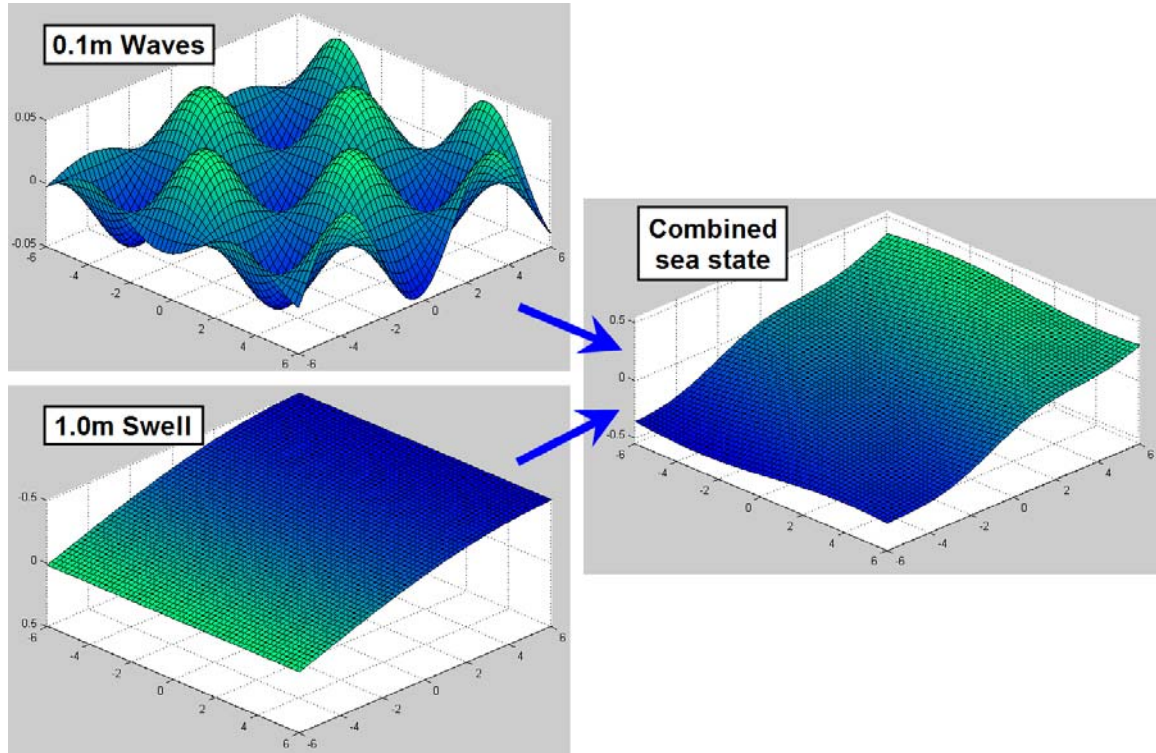


Figure 48. A combination of low-amplitude, high-frequency waves and high-amplitude, low-frequency swell are used to create an idealized sea surface.

For both the waves, W , and swell, S , the user may specify the wavelength, λ , the peak-to-peak wave height, h , and the direction of propagation, θ (Figure 36 – blue). With the previous parameters defined, the wave’s speed, c , will be given by (Pond & Pickard, 2000):

$$c = \sqrt{\frac{g\lambda}{2\pi} \tanh\left(\frac{2\pi D}{\lambda}\right)}. \quad (4.18)$$

where:

g = acceleration due to gravity (9.8 m/s^2)

D = water depth.

Making the assumption that the water depth is greater than half the wave length, (4.18)

simplifies to:

$$c = \sqrt{\frac{g\lambda}{2\pi}}, \quad (4.19)$$

with an associated wave period, T , of:

$$T = \lambda / c. \quad (4.20)$$

So, a point (x,y) at time t will have sea surface height due to the sea waves, z_w , defined as:

$$z_w(x, y, t) = \frac{h_w}{2} \sin\left(\frac{2\pi x}{\lambda_w} + \frac{t}{T_w} \cos \theta_w\right) \sin\left(\frac{2\pi y}{\lambda_w} + \frac{t}{T_w} \sin \theta_w\right). \quad (4.21)$$

Similarly, the sea surface height due to swell, z_s , is defined as:

$$z_s(x, y, t) = \frac{h_s}{2} \sin\left(\frac{2\pi(x \cos \theta_s + y \sin \theta_s)}{\lambda_s} + \frac{t}{T_s}\right). \quad (4.22)$$

Notice the convention of the above two definitions preclude the possibility of the wavelength being set to zero. It should also be stated that (4.21) and (4.22) are not advertised to be the formal solutions to the two-dimensional wave equation. Instead they were simply constructed to produce the behavior that is demonstrated in Figure 48. Should a user wish to remove either the sea waves or swell from the model, the associated height should be set to zero.

Programmatically the simulator determines the z -value for the waves and/or swell which shifts the entire water plane by the appropriate amount. This shifted surface is then used in the calculation of the intersection of the laser beam and the water plane.

Rather than getting entrenched in the details of (4.21) and (4.22), the reader may content themselves with the fact that the preceding equations were used to generate the surfaces shown in Figure 48. Recall the goal is not to create a perfect physical model of the sea surface, but a surface that exhibits the general behavior of the sea surface (which is demonstrated in Figure 48). Referring to Figure 49, we see that the introduction of a dynamic sea surface has an effect that looks like noise in the vertical component of the point cloud. This noise is the precise phenomenon we wish to understand as it later relates to the calibration module.

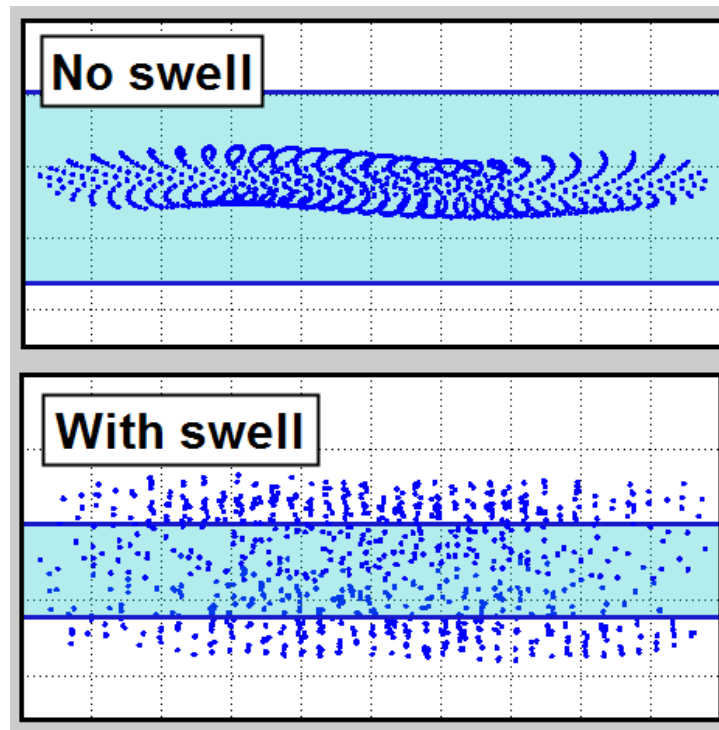


Figure 49. A view of a point cloud acquired over a calm sea surface (top) and the effects when a swell is added (bottom).

4.2.2.4 – *Wave-induced uncertainty in the laser range.* A laser directed at the same spot on a dynamic sea surface, can yield a large variation in the reported laser range (Figure 50). A geometric relationship is required to describe how the uncertainty is

propagated from wave to laser. For a wave with a peak-to-peak height of h , the standard deviation in the height is given by (Smith, 1997):

$$\sigma_h = \frac{h}{2\sqrt{2}}. \quad (4.23)$$

Studying Figure 50, should the laser make a 20° angle with the mean sea surface normal, then the uncertainty in the wave height, σ_h , will be related to the contributed uncertainty to the laser range, σ_{ρ_h} by:

$$\sigma_{\rho_h} = \sigma_h \sec 20^\circ \quad (4.24)$$

or:

$$\sigma_{\rho_h}^2 = \sigma_h^2 \sec^2 20^\circ. \quad (4.25)$$

Thus the new uncertainty in the laser range, σ_{ρ^*} , can be expressed as the sum of squares of the old uncertainty in the laser range, σ_{ρ} (associated with the laser manufacturer's specifications), plus the uncertainty induced by the waves, σ_{ρ_w} , and swell, σ_{ρ_s} :

$$\begin{aligned} \sigma_{\rho^*}^2 &= \sigma_{\rho}^2 + \sigma_{\rho_w}^2 + \sigma_{\rho_s}^2 \\ &= \sigma_{\rho}^2 + (\sigma_{h_w}^2 + \sigma_{h_s}^2) \sec^2 20^\circ. \end{aligned} \quad (4.26)$$

Finally, substituting from (4.23) yields:

$$\sigma_{\rho^*}^2 = \sigma_{\rho}^2 + \left(\frac{h_w^2 + h_s^2}{8} \right) \sec^2 20^\circ. \quad (4.27)$$

If the calibration adjustment is performed over the water surface, (4.27) will be used to describe the variability of the laser range.

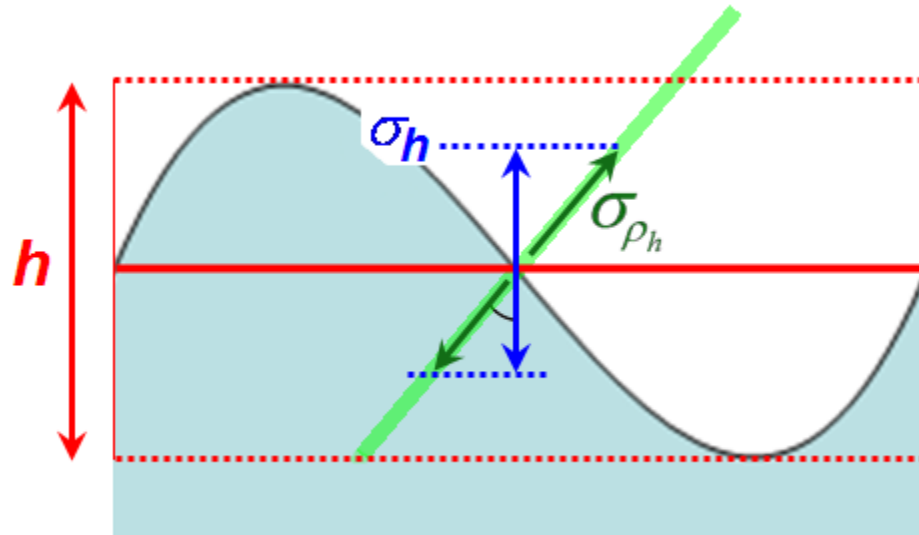


Figure 50. Relating the height of a wave with the induced uncertainty in the laser range measurement.

4.2.2.5 – *A dynamic ocean surface and beam steering.* In reality, the large spot size of the laser (estimated at a 3m diameter for CZMIL) will serve to dampen the effects of any waves or swell that are present. So long as the wavelength of the sea waves is less than the diameter of the laser spot, the effects of the dynamic sea surface will average out (Figure 51 – left). Problems may arise however in the presence of sufficiently long period swell (Figure 51 – right). If the period is long enough, then the entire laser spot may be focused on just the crest or the trough of the wave. This will cause variability in the vertical position of the point on the sea surface, but may also change the average sea slope causing the laser beam to refract further or nearer than anticipated from (4.16).

Because the simulator treats the laser as an infinitely narrow beam, high frequency waves will never be averaged out (as shown in Figure 49). This implies the simulator will represent a worst-case scenario as far as generating datasets for the calibrator. If the calibrator can work with datasets with no spot averaging, then it should

perform better on an actual data. The problem of beam refraction induced by long period swell will now be investigated further.

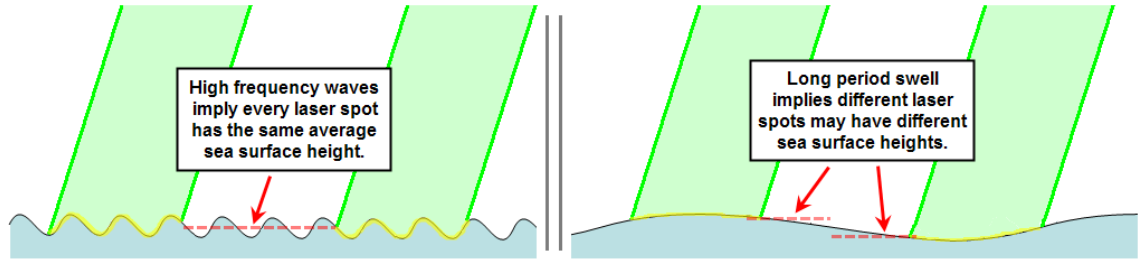


Figure 51. When a sea wave's wavelength is much smaller than the lidar spot size (left), the dynamics of the wave height are averaged out. In the presence of long period swell (right), a lidar's entire spot may be focused on the wave's crest or trough, resulting in different estimates of the sea surface height from shot-to-shot.

As discussed earlier in the chapter, the path the laser takes when entering the water column is subject to Snell's law and is a function of the normal vector of the sea surface. Previously, this vector was assumed to be vertical, see (4.17), but with long period swell, this will not necessarily be the case. For an arbitrary function, $f(x,y)$, the surface normal vector, \vec{w} , is given by:

$$\vec{w} = \left[\frac{\partial f}{\partial x} \quad \frac{\partial f}{\partial y} \quad -1 \right]^T. \quad (4.28)$$

Thus, the surface normal vector at any point on the sea surface can be found by applying (4.28) to the equations for the wave and swell height, (4.21) and (4.22). This normal vector is then substituted into the equation representing Snell's Law, (4.16), and the location of the laser spot on the seafloor is then solved for as before.

To enable or disable the beam steering due to the dynamic sea surface slope, the user may toggle the "Refract?" button (Figure 36 – red). Examples are shown below of the behavior a lidar pulse both with and without beam steering. In Figure 52, a laser is repeatedly fired at the same location as the sea surface moves up and down. The upper

portion of the figure assumes the sea surface normal is vertical, and thus neglects beam steering, applying a constant angle of refraction once the laser enters the water. Notice that when beam steering is neglected, all the theoretical paths of the laser are parallel. Figure 52 (bottom) shows what happens to the laser should the changing slope of the sea surface be included; the result is a larger distribution of points on the seafloor. Note the maximum refraction occurs when the wave height is near zero (i.e., where the wave has maximum slope).

A top-down view of a point cloud collected from a stationary vehicle is shown in Figure 53. Data are repeatedly collected from the same locations as the sea surface is free to change beneath it. In this case, only a swell front is present moving from the top of the image to the bottom. Beams oriented directly into the swell (at the top of the image) only have their points on the seafloor slide forward and back. However, as the angle the laser makes with the direction of the wave front increases, there is a larger spread in the distribution of points. One such cluster of points, highlighted with a blue rectangle in Figure 53, is shown in Figure 54. Given a water column depth of 10m, the points on the seafloor demonstrate a distribution of 2m in the fore-aft direction and 1m laterally. Again, in reality, the laser will be subject to beam spreading throughout the water column: Figure 54 just demonstrates how large the distribution of the center of that spreading beam will be.

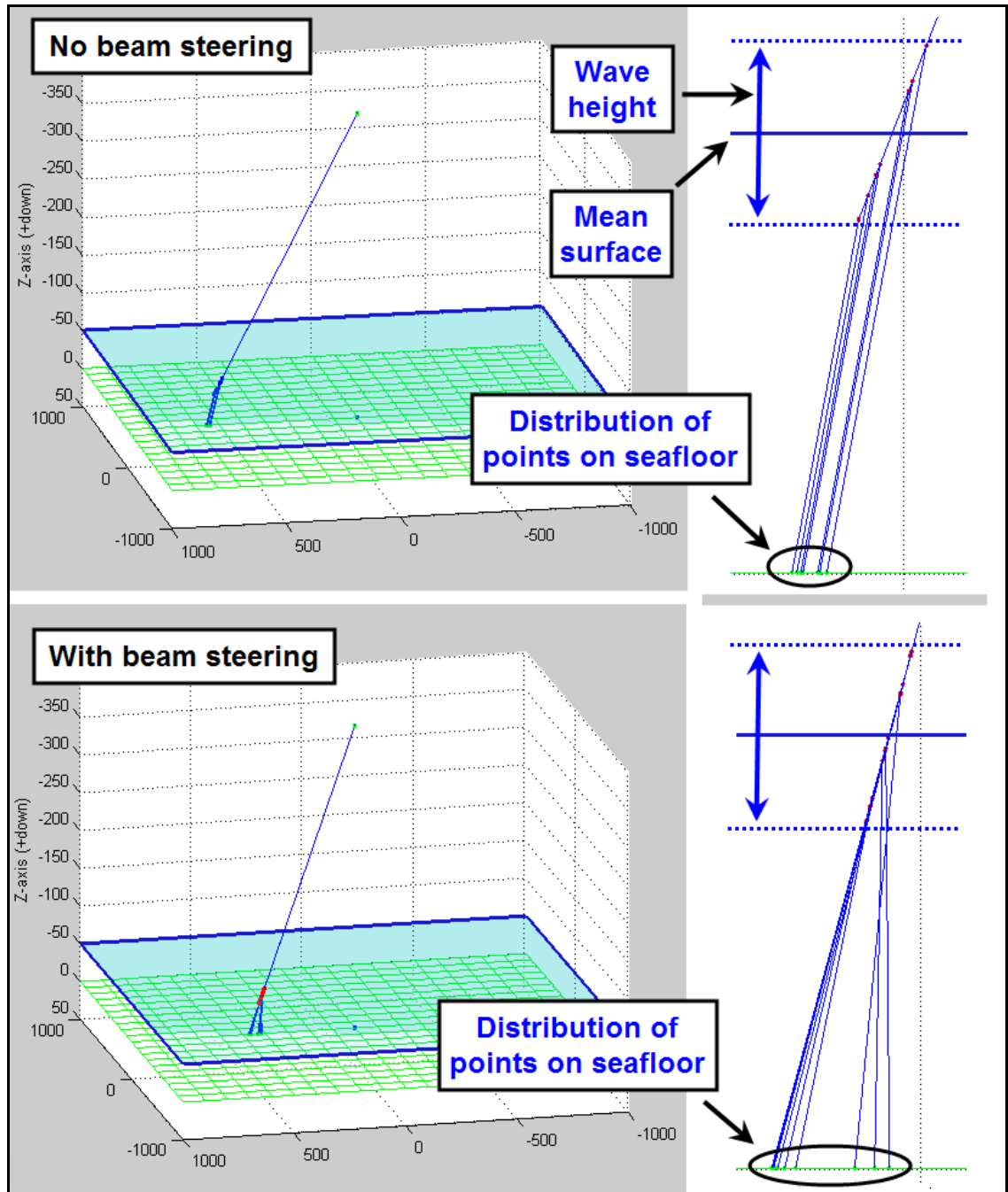


Figure 52. The behavior of a laser pulse as it crosses the air-water interface in the presence of surface waves. Examples are shown both without (top) and with (bottom) the inclusion of beam steering caused by a sloping sea surface.

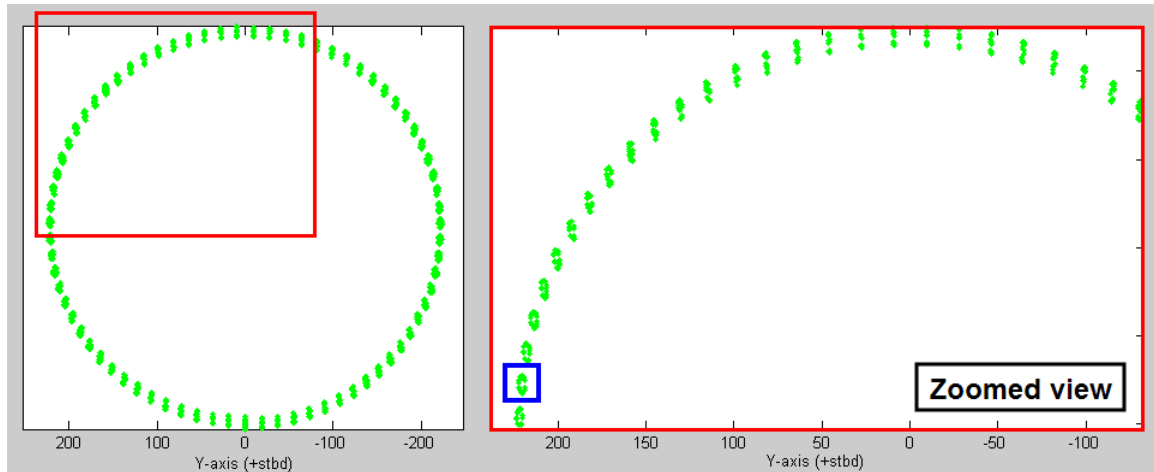


Figure 53. Top-down view of distribution of lidar points on the seafloor acquired in the presence of surface swell. Swell traveling from top to bottom of image. Right panel is a close-up view of left panel. The blue rectangle is shown in Figure 54.

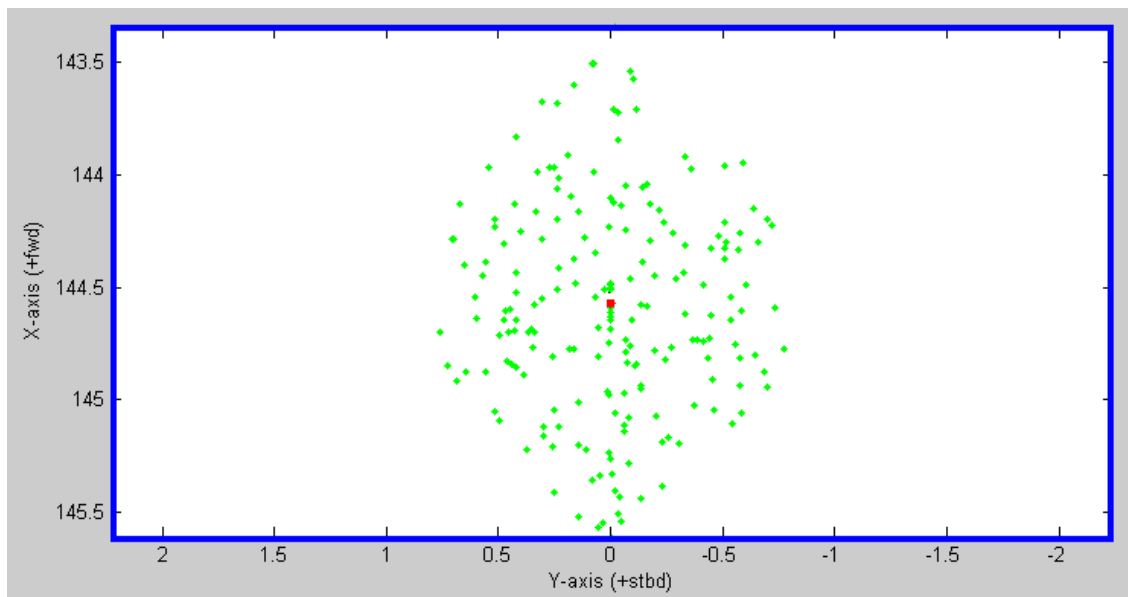


Figure 54. Distribution of one cluster of laser strikes on the seafloor in the presence of a 1m swell with a 50m wavelength, as highlighted in Figure 53. Acquisition altitude was 400m while the water depth was 10m. Theoretical footprint shown in red. All units in meters.

4.2.2.6 – A simulated tidal model. The last feature contained within the point cloud simulation is the ability to introduce a tidal model to the water surface (Figure 38 – blue). There are four different options given with respect to tides: no tides, a linear tidal

model, a sinusoidal tidal model, or incorporating tides from a file. The tidal option chosen will dictate the form of the tidal interface (Figure 55).

Figure 55. The different tidal interfaces within the simulator.

As was the case with simulating sea waves and sea swell, the goal of the simulator is not to produce a perfect tidal model complete with all the principal tidal constituents. The simulator will only attempt to replicate the possible effects on the point cloud that may occur over the course of a single survey mission.

The simulator merely determines the z -value for the tides at the time the laser is fired and then shifts the water plane up or down appropriately. This shifted surface is used in the calculation of the intersection of the laser beam and water plane. Selecting “no tides” merely removes any tidal artifacts that were previously introduced. The linear tide model is provided as a trouble-shooting tool for the calibrator, which has the ability to approximate the changing tides with a linear model (this topic will be further discussed in Chapter VI). The models of greatest relevance are the last two options: the sinusoidal tide model and reading the tides from an external file.

As the name suggests, the sinusoidal tide model permits the user to apply a simple sinusoidal tide curve to the point cloud. Specifying the peak-to-peak tidal range, R , the tidal period, T , and the present phase of the tides, ϕ , the tide value, z , at time t is given by:

$$z(t) = \frac{R}{2} \sin\left(\frac{2\pi}{T}t + \phi\right). \quad (4.29)$$

Setting a phase of 0° will assure the tide is changing at the maximum rate at the beginning of survey; however, this can be set to any value. A sinusoidal model is good enough for the purposes of simulating the behavior of tides through an entire sortie of flight lines. How the calibrator will handle this model is discussed in later chapters.

The final tidal option is the ability to read the tide values from an external file. Either spreadsheet or text formats are acceptable and require only two columns of data: the time tags in seconds and the tide values in meters. Through a separate file, the user may create as complicated (or as simple) a tidal model as they desire (bearing in mind the simulator time tags its first laser point as $t = 0$). Thinking ahead with regard to using the sea surface for a calibrator, a predicted tide file could be downloaded from NOAA and be used to remove the tidal signal, leaving only the mean water surface. For illustrative purposes, examples of a flight line acquired over (very exaggerated) tidal regimes are shown in Figure 56.

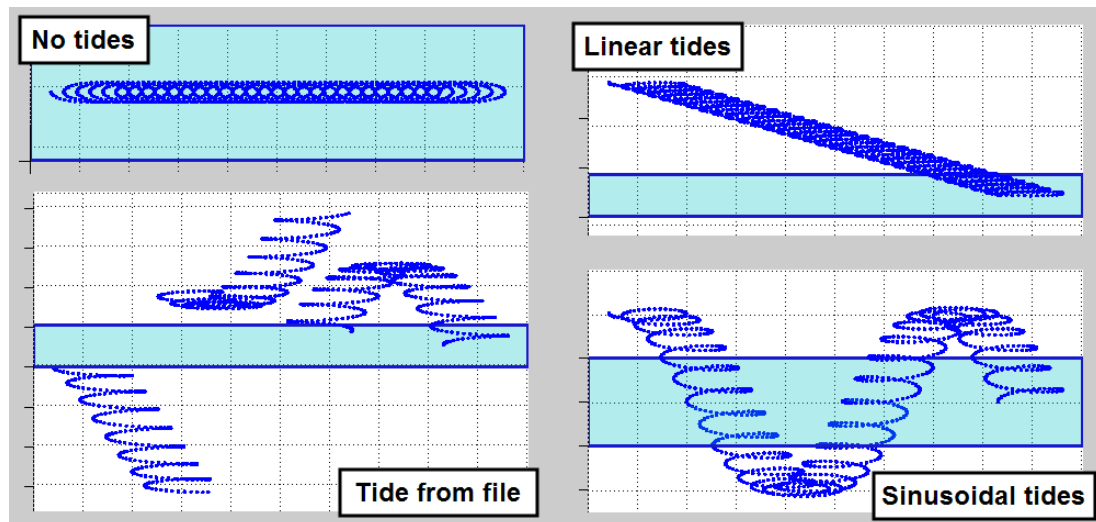


Figure 56. Side views of a point cloud with four different tidal models applied: no tides (upper-left), a linear tidal model (upper-right), a sinusoidal tidal model (lower-right) and loading a user-defined tide from a file (lower-left) .

4.3 – Summary of Key Results

This chapter was devoted entirely to the lidar simulation module. The following is a bulleted list of the key aspects of the simulation. When possible, the relevant section(s) that offer a more detailed explanation are indicated.

- The module provides the ability to visualize any biases in the point cloud based on an incorrect assumption about one of the lidar's calibration values (Section 4.1.5). The ability to visualize biases is key in conducting a sensitivity analysis as all the biases displayed in Figure 32 were generated using this feature.
- The simulation is based on the intersection of a line (the laser beam) and a plane, the ground, water surface or sea floor (Sections 4.1.1, 4.2.2.1 & 4.2.2.2).
- For each flight line, up to 22 parameters can be specified to describe the lidar configuration, in addition to the ability to have the vehicle experience dynamic changes in altitude and attitude mid-flight (Section 4.1.2).
- The module provides the ability to select just a subset of the data for further analysis (Section 4.2.1): a tool that will be useful in Section 6.4.1 – Calibration on a narrow runway.
- A water interface has been added to the simulation which includes the ability to generate sea waves and tidal effects (Sections 4.2.2.3 & 4.2.2.6): a tool that will be useful in Section 6.4.2 – Calibration on a dynamic sea surface. In addition surface refraction and swell-induced beam steering has been implemented to visualize the scan pattern on the seafloor (Sections 4.2.2.2 & 4.2.2.5).

Having now constructed this robust lidar point cloud simulator, we may now turn our attention to the thrust of this dissertation, a method of determining the lidar's system parameters which produced the aforementioned point clouds.

CHAPTER V

THE ADJUSTMENT ALGORITHM

5. THE ADJUSTMENT ALGORITHM
5.1 THEORY OF A LEAST SQUARES ADJUSTMENT
5.1.1 Sample System of Linear Equations
5.1.2 General System of Linear Equations
5.1.3 A Weighted Constraint Least Squares Model
5.1.3.1 Adjusting a non-linear equation
5.1.3.2 The Lagrange correlate
5.1.4 Solving a Linear System Through Matrix Partitioning
5.2 THE ADJUSTMENT MODEL
5.2.1 Parameterizing the Planar Surface
5.2.2 A Simplified Adjustment Example
5.2.2.1 The full-form partial derivatives
5.3 IMPROVING MEMORY USAGE FOR THE LEAST SQUARES ALGORITHM
5.4 SUMMARY OF KEY RESULTS

Figure 57. Chapter V outline.

Now that the frame work for synthesizing a point cloud is complete, the focus can shift to the methodology for calibrating said point cloud. The discussion of calibration is divided into two chapters: this chapter is more theoretical in nature, developing the theory necessary for the development of a calibration module; whereas the following chapter then takes said module and performs the adjustment. There are three key goals to this chapter:

- To provide the mathematical framework and derivation for the type of adjustment model (a weighted constraint, linearized least squares model solved through matrix partitioning) used in this dissertation (Section 5.1)
- To present the equation used to calibrate the point cloud – fitting the data to a single planar surface (Section 5.2.1).
- To provide both simplified and advanced examples of how a theoretical adjustment model can be applied to a lidar calibration (Sections 5.2.2 & 5.2.2.1).

As its name implies, the first section of this chapter is focused on the theory of least squares adjustments. This material is provided both for completeness and for the benefit of the uninitiated with regard to adjustment algorithms. This information will be valuable to anyone seeking either to modify the proposed algorithms or to develop an adjustment algorithm unique to their own lidar. Those already possessing a firm understanding of the principles of the least squares may wish to skip ahead to Section 5.2 which presents the proposed adjustment equation for the CZMIL system.

5.1 – Theory of a Least Squares Adjustment

5.1.1 – Sample System of Linear Equations

Before discussing the details of the least squares model, first a simplified problem is presented. Note: for a more complete discussion of the least squares adjustment than what is presented in this paper, the reader is directed to either Ghilani & Wolf (2006) or Wells (1999), who were heavily referenced in the development of this chapter.

Consider an error-free system of linear equations:

$$\begin{aligned} x_1 + x_2 &= 2 \\ x_1 - x_2 &= 0 \end{aligned} \tag{5.1}$$

which is of the form:

$$\begin{aligned} a_{11}x_1 + a_{12}x_2 &= \ell_1 \\ a_{21}x_1 + a_{22}x_2 &= \ell_2 \end{aligned} \tag{5.2}$$

where:

a_{ii} = constants

x_i = unknowns

ℓ_i = observations.

The equations represented in (5.1) are simple and straight-forward to solve, yielding the unknowns as $x_1=1$ and $x_2=1$. As an aside, so long as the number of

equations matches the number of unknowns, a unique solution exists (assuming the linear independence of the equations). Any additional equation would be necessarily redundant (linearly dependent) and contain no new information (for example: $2x_1 + 2x_2 = 4$).

A better analog for the real world is found if we permit there to be some uncertainty in the observations. Take the system of equations:

$$\begin{aligned}x_1 + x_2 &= 1.9 \\x_1 - x_2 &= 0.1 \\2x_1 + x_2 &= 3.2\end{aligned}\tag{5.3}$$

which are of the form:

$$\begin{aligned}a_{11}x_1 + a_{12}x_2 &= \ell_1 + r_1 \\a_{21}x_1 + a_{22}x_2 &= \ell_2 + r_2 \\a_{31}x_1 + a_{32}x_2 &= \ell_3 + r_3\end{aligned}\tag{5.4}$$

where r_i are the residuals or misclosures of ℓ_i .

The determination of x_1 and x_2 is no longer so obvious (and impossible if the residuals are not acknowledged). The first two equations of (5.3) suggest $x_1=1$ and $x_2 = 0.9$; whereas the last two equations present an inconsistent solution of $x_1=1.1$ and $x_2 = 1$. In the presence of uncertainty, the problem must be redefined: rather than finding the unique solution set, instead the unknowns must be selected in such a way so as to minimize the misclosures of the observation equations. Rewriting (5.3) as:

$$\begin{aligned}x_1 + x_2 &= 1.9 + r_1 \\x_1 - x_2 &= 0.1 + r_2 \\2x_1 + x_2 &= 3.2 + r_3\end{aligned}\tag{5.5}$$

the goal is to choose x_1 and x_2 that “best fit” the equations of (5.5). We would like to minimize $r_1 + r_2 + r_3$ (the L^1 norm). However, to avoid the trivial case created by

allowing the residuals to grow unbounded towards negative infinity, we shall instead minimize the sum of the squares of the residual (the L^2 norm). That is, minimize:

$$\phi(x_1, x_2) = r_1^2 + r_2^2 + r_3^2. \quad (5.6)$$

From calculus, a potential minimum is identified by taking the first-derivative and equating it to zero. In the case of (5.5):

$$\phi(x_1, x_2) = (x_1 + x_2 - 1.9)^2 + (x_1 - x_2 - 0.1)^2 + (2x_1 + x_2 - 3.2)^2 \quad (5.7)$$

has partial derivatives:

$$\begin{aligned} \frac{\partial \phi}{\partial x_1} &= 2(x_1 + x_2 - 1.9) + 2(x_1 - x_2 - 0.1) + 2(2x_1 + x_2 - 3.2)(2) = 0 \\ \frac{\partial \phi}{\partial x_2} &= 2(x_1 + x_2 - 1.9) + 2(x_1 - x_2 - 0.1)(-1) + 2(2x_1 + x_2 - 3.2) = 0 \end{aligned} \quad (5.8)$$

which simplifies to the normal equations:

$$\begin{aligned} 12x_1 + 4x_2 - 16.8 &= 0 \\ 4x_1 + 6x_2 - 10 &= 0. \end{aligned} \quad (5.9)$$

The linear system given in (5.9) has a solution of $x_1 = 1.0857$ and $x_2 = 0.9429$. The preceding solution then has associated residuals given by (5.5) of

$r_1 = 0.129$, $r_2 = 0.043$, $r_3 = -0.086$, which when substituted into (5.6) yields a sum of

squares of 0.026. Contrast that with the residuals associated with the somewhat

capriciously chosen solution $x_1 = 1$ and $x_2 = 1$, which has a larger sum of squares total of

0.06. The solution to (5.9) represents the best possible choice for x_1 and x_2 that yields

the least sum of the residuals' squares.

5.1.2 – General System of Linear Equations

In a more general case, we have:

$$\begin{aligned}
 a_{11}x_1 + a_{12}x_2 + \dots + a_{1n}x_n &= \ell_1 + r_1 \\
 a_{21}x_1 + a_{22}x_2 + \dots + a_{2n}x_n &= \ell_2 + r_2 \\
 &\vdots \\
 a_{m1}x_1 + a_{m2}x_2 + \dots + a_{mn}x_n &= \ell_m + r_m
 \end{aligned} \tag{5.10}$$

where we wish to minimize the function:

$$\phi(x_1, x_2, \dots, x_n) = r_1^2 + r_2^2 + \dots + r_m^2 \tag{5.11}$$

$$\begin{aligned}
 \phi &= \sum_{i=1}^m r_i^2 = (a_{11}x_1 + a_{12}x_2 + \dots + a_{1n}x_n - \ell_1)^2 + \dots \\
 &\quad (a_{21}x_1 + a_{22}x_2 + \dots + a_{2n}x_n - \ell_2)^2 + \dots + \dots \\
 &\quad (a_{m1}x_1 + a_{m2}x_2 + \dots + a_{mn}x_n - \ell_m)^2.
 \end{aligned} \tag{5.12}$$

The minimum is again found through computing the partial derivatives and equating each to zero.

$$\begin{aligned}
 \frac{\partial \phi}{\partial x_1} &= 2(a_{11}x_1 + a_{12}x_2 + \dots + a_{1n}x_n - \ell_1)(a_{11}) + \dots \\
 &\quad 2(a_{21}x_1 + a_{22}x_2 + \dots + a_{2n}x_n - \ell_2)(a_{21}) + \dots + \dots \\
 &\quad 2(a_{m1}x_1 + a_{m2}x_2 + \dots + a_{mn}x_n - \ell_m)(a_{m1}) = 0 \\
 \frac{\partial \phi}{\partial x_2} &= 2(a_{11}x_1 + a_{12}x_2 + \dots + a_{1n}x_n - \ell_1)(a_{12}) + \dots \\
 &\quad 2(a_{21}x_1 + a_{22}x_2 + \dots + a_{2n}x_n - \ell_2)(a_{22}) + \dots + \dots \\
 &\quad 2(a_{m1}x_1 + a_{m2}x_2 + \dots + a_{mn}x_n - \ell_m)(a_{m2}) = 0 \\
 &\quad \vdots \\
 \frac{\partial \phi}{\partial x_n} &= 2(a_{11}x_1 + a_{12}x_2 + \dots + a_{1n}x_n - \ell_1)(a_{1n}) + \dots \\
 &\quad 2(a_{21}x_1 + a_{22}x_2 + \dots + a_{2n}x_n - \ell_2)(a_{2n}) + \dots + \dots \\
 &\quad 2(a_{m1}x_1 + a_{m2}x_2 + \dots + a_{mn}x_n - \ell_m)(a_{mn}) = 0
 \end{aligned} \tag{5.13}$$

Multiplying and collecting like terms:

$$\begin{aligned}
& (a_{11}a_{11} + a_{21}a_{21} + \dots + a_{m1}a_{m1})x_1 + \dots \\
& (a_{12}a_{11} + a_{22}a_{21} + \dots + a_{m2}a_{m1})x_2 + \dots + \dots \\
& (a_{1n}a_{11} + a_{2n}a_{21} + \dots + a_{mn}a_{m1})x_n = a_{11}\ell_1 + a_{21}\ell_2 + \dots + a_{m1}\ell_m \\
& (a_{11}a_{12} + a_{21}a_{22} + \dots + a_{m1}a_{m2})x_1 + \dots \\
& (a_{12}a_{12} + a_{22}a_{22} + \dots + a_{m2}a_{m2})x_2 + \dots + \dots \\
& (a_{1n}a_{12} + a_{2n}a_{22} + \dots + a_{mn}a_{m2})x_n = a_{12}\ell_1 + a_{22}\ell_2 + \dots + a_{m2}\ell_m \\
& \vdots \\
& (a_{11}a_{1n} + a_{21}a_{2n} + \dots + a_{m1}a_{mn})x_1 + \dots \\
& (a_{12}a_{1n} + a_{22}a_{2n} + \dots + a_{m2}a_{mn})x_2 + \dots + \dots \\
& (a_{1n}a_{1n} + a_{2n}a_{2n} + \dots + a_{mn}a_{mn})x_n = a_{1n}\ell_1 + a_{2n}\ell_2 + \dots + a_{mn}\ell_m
\end{aligned} \tag{5.14}$$

or in sigma notation:

$$\begin{aligned}
& \left(\sum_{i=1}^m a_{i1}a_{i1} \right) x_1 + \left(\sum_{i=1}^m a_{i2}a_{i1} \right) x_2 + \dots + \left(\sum_{i=1}^m a_{in}a_{i1} \right) x_n = \sum_{i=1}^m a_{i1}\ell_i \\
& \left(\sum_{i=1}^m a_{i1}a_{i2} \right) x_1 + \left(\sum_{i=1}^m a_{i2}a_{i2} \right) x_2 + \dots + \left(\sum_{i=1}^m a_{in}a_{i2} \right) x_n = \sum_{i=1}^m a_{i2}\ell_i \\
& \vdots \\
& \left(\sum_{i=1}^m a_{i1}a_{in} \right) x_1 + \left(\sum_{i=1}^m a_{i2}a_{in} \right) x_2 + \dots + \left(\sum_{i=1}^m a_{in}a_{in} \right) x_n = \sum_{i=1}^m a_{in}\ell_i.
\end{aligned} \tag{5.15}$$

However, if we let:

$$\mathbf{A} = \begin{bmatrix} a_{11} & a_{12} & \cdots & a_{1n} \\ a_{21} & a_{22} & \cdots & a_{2n} \\ \vdots & \vdots & \ddots & \vdots \\ a_{m1} & a_{m2} & \cdots & a_{mn} \end{bmatrix}; \mathbf{x} = \begin{bmatrix} x_1 \\ x_2 \\ \vdots \\ x_n \end{bmatrix}; \text{ and } \mathbf{L} = \begin{bmatrix} \ell_1 \\ \ell_2 \\ \vdots \\ \ell_n \end{bmatrix}, \tag{5.16}$$

then the original problem stated in (5.10) becomes:

$$\mathbf{Ax} = \mathbf{L} \tag{5.17}$$

and (5.15) can be rewritten as:

$$\mathbf{A}^T \mathbf{Ax} = \mathbf{A}^T \mathbf{L} \tag{5.18}$$

which has the solution:

$$\mathbf{x} = (\mathbf{A}^T \mathbf{A})^{-1} \mathbf{A}^T \mathbf{L}. \quad (5.19)$$

5.1.3 – A Weighted Constraint Least Squares Model

The sum of the residuals' squares,

$$\phi = r_1^2 + r_2^2 + r_3^2 + \dots + r_m^2 \quad (5.20)$$

can be expressed in matrix form:

$$\phi = \mathbf{r}^T \mathbf{r} \quad (5.21)$$

where:

$$\mathbf{r} = [r_1 \quad r_2 \quad r_3 \quad \dots \quad r_m]$$

But not all observations are necessarily of equal merit, and there may be less confidence in some measurements; therefore, these observations should be allocated less weight in the adjustment. If each observation, ℓ_i , were to have a known variance of $\sigma_{\ell_i}^2$, then a covariance matrix is constructed as:

$$\mathbf{C}_\ell = \begin{bmatrix} \sigma_{\ell_1}^2 & 0 & \dots & 0 \\ 0 & \sigma_{\ell_2}^2 & \dots & 0 \\ \vdots & \vdots & \ddots & \vdots \\ 0 & 0 & \dots & \sigma_{\ell_m}^2 \end{bmatrix}. \quad (5.22)$$

Note: in the case of (5.22), all the cross-covariances are assumed to be zero and only the variances are included. Given \mathbf{C}_ℓ is a diagonal matrix, its inverse is the reciprocal of the diagonal elements. The reciprocals are defined as:

$$\omega_i = \frac{1}{(\sigma_{\ell_i}^2)} \quad (5.23)$$

where ω_i represents the desired weighting for each observation. Under this scheme, an observation with a large variance will have an appropriately small weight and vice-versa. So the weighting matrix is given by:

$$\mathbf{C}_\ell^{-1} = \begin{bmatrix} \omega_1 & 0 & \cdots & 0 \\ 0 & \omega_2 & \cdots & 0 \\ \vdots & \vdots & \ddots & \vdots \\ 0 & 0 & \cdots & \omega_m \end{bmatrix} \quad (5.24)$$

and the new function to be minimized is:

$$\phi = \omega_1 r_1^2 + \omega_2 r_2^2 + \omega_3 r_3^2 + \dots + \omega_m r_m^2 \quad (5.25)$$

or:

$$\phi = \mathbf{r}^T \mathbf{C}_\ell^{-1} \mathbf{r}. \quad (5.26)$$

There may not only be misclosures in the observations, ℓ , (written as r); there may also be misclosures in the adjusting parameters, \mathbf{x} , which are denoted by $\boldsymbol{\delta}$. These misclosures in the adjusting parameters should also be minimized in the adjustment. Further, these misclosures, $\boldsymbol{\delta}$, can also be weighted with an a priori knowledge of their uncertainties, \mathbf{C}_x^{-1} (defined in a similar manner to that shown in (5.22) through (5.24)), yielding:

$$\phi = \mathbf{r}^T \mathbf{C}_\ell^{-1} \mathbf{r} + \boldsymbol{\delta}^T \mathbf{C}_x^{-1} \boldsymbol{\delta}. \quad (5.27)$$

The inclusion of the a priori weighting of the adjusting parameters, also referred to as a Bayesian inference (Martin, 1967), offers several advantages. By manipulating the weights, the operator can dictate which parameters have the greatest amount of flexibility in the adjustment. For example, if parameter X has a high confidence (low standard deviation) and parameter Y has a low confidence (high standard deviation), then

the user would want any misclosures in the observations to be more heavily attributed to parameter Y. The \mathbf{C}_x^{-1} matrix provides the means of having the least squares preferentially adjust the parameters with the lesser confidences.

Secondly, a weighting of the adjusting parameters will aid in the prevention of the least squares algorithm iterating off towards infinite values or converging towards physically nonsensical values. For example, if the actual pitch bias were to be 10° , then, while 370° , 730° or 1090° are also mathematically valid answers, they are unpalatable answers from the perspective of the system operator. Also, if too much freedom is given to the system parameters, the virtual components might start flipping upside down or aligning themselves in ways not physically possible. Through a sufficiently small a priori weighting on a given parameter, the operator can prevent the least squares algorithm from wildly iterating; instead, keeping each parameter in the neighborhood of the initial guesses.

5.1.3.1 – Adjusting a non-linear equation. Equation (5.17) can be rewritten as:

$$\mathbf{Ax} - \mathbf{L} = \mathbf{0} \quad (5.28)$$

which is of the form:

$$f(\ell, x) = 0 \quad (5.29)$$

where ℓ represent the measured quantities and x represent the unknowns.

Should the function shown in (5.29) be non-linear, then a Taylor Series expansion is performed. The expanded model is given by:

$$f(\ell, x) = f(\ell_0, x_0) + (\ell - \ell_0) \left. \frac{\partial f}{\partial \ell} \right|_{\ell=\ell_0, x=x_0} + (x - x_0) \left. \frac{\partial f}{\partial x} \right|_{\ell=\ell_0, x=x_0} + \text{higher-order terms} \quad (5.30)$$

which, when truncated yields a first-order linear approximation:

$$f(\ell, x) \approx \underbrace{f(\ell_0, x_0)}_g + \underbrace{(\ell - \ell_0)}_r \underbrace{\frac{\partial f}{\partial \ell} \Big|_{\ell=\ell_0, x=x_0}}_D + \underbrace{(x - x_0)}_{\delta} \underbrace{\frac{\partial f}{\partial x} \Big|_{\ell=\ell_0, x=x_0}}_A \approx 0 \quad (5.31)$$

where:

g = initial approximation of model

\mathbf{r} = corrections to the measured quantities, ℓ (residuals)

δ = corrections to the unknowns x (adjustments)

\mathbf{D} = design matrix with respect to observations

\mathbf{A} = design matrix with respect to adjusting parameters.

Thus:

$$f \approx g + \mathbf{D}\mathbf{r} + \mathbf{A}\delta = 0. \quad (5.32)$$

5.1.3.2 – *The Lagrange correlate.* Using the above-stated linearized model, the equation to be optimized (5.27) can be visited one more time as:

$$\phi(\mathbf{r}, \delta) = \mathbf{r}^T \mathbf{C}_\ell^{-1} \mathbf{r} + 2\mathbf{k}^T (g + \mathbf{D}\mathbf{r} + \mathbf{A}\delta) + \delta^T \mathbf{C}_x^{-1} \delta. \quad (5.33)$$

Notice the term in parenthesis in (5.33) is the expression from (5.32), which is equal to zero. Thus, mathematically, the expression for ϕ has not changed. The extra term, \mathbf{k} , is called a Lagrange correlate and aids in steering the overall convergence of the least squares algorithm. The Lagrange correlate can be thought of as a weighting for each entire observation equation (versus the individual observations, ℓ weighted through \mathbf{C}_ℓ , or the adjusting parameters, x weighted through \mathbf{C}_x). For further information on the Lagrange correlate, the reader is referred to Wells (1999). What follows is a demonstration of how the Lagrange correlate is used in practice.

As before, (5.33) can be optimized by setting its first-partial derivatives equal to zero.

$$\frac{\partial \phi}{\partial \mathbf{r}} = \mathbf{r}^T \mathbf{C}_\ell^{-1} + \mathbf{k}^T (\mathbf{D}) + \mathbf{0} = \mathbf{0} \quad (5.34)$$

$$\frac{\partial \phi}{\partial \delta} = \mathbf{0} + \mathbf{\lambda} \mathbf{k}^T (\mathbf{A}) + \mathbf{\lambda} \delta^T \mathbf{C}_x^{-1} = \mathbf{0} \quad (5.35)$$

which are both valid, provided:

$$\mathbf{g} + \mathbf{D} \mathbf{r} + \mathbf{A} \delta = \mathbf{0} \quad (5.36)$$

The above three equations can then be condensed into a single matrix equation:

$$\begin{bmatrix} \mathbf{C}_\ell^{-1} & \mathbf{D}^T & \mathbf{0} \\ \mathbf{D} & \mathbf{0} & \mathbf{A} \\ \mathbf{0} & \mathbf{A}^T & \mathbf{C}_x^{-1} \end{bmatrix} \begin{bmatrix} \mathbf{r} \\ \mathbf{k} \\ \delta \end{bmatrix} + \begin{bmatrix} \mathbf{0} \\ \mathbf{g} \\ \mathbf{0} \end{bmatrix} = \begin{bmatrix} \mathbf{0} \\ \mathbf{0} \\ \mathbf{0} \end{bmatrix} \quad (5.37)$$

As an aside, Equation (5.37) can be checked as follows, multiplying through the first row of the 3×3 matrix yields:

$$\begin{aligned} \mathbf{C}_\ell^{-1} \mathbf{r} + \mathbf{D}^T \mathbf{k} &= \mathbf{0} \\ (\mathbf{C}_\ell^{-1} \mathbf{r})^T + (\mathbf{D}^T \mathbf{k})^T &= \mathbf{0}^T \text{ (where } \mathbf{C}_\ell^{-1} \text{ is symmetric)} \\ \mathbf{r}^T \mathbf{C}_\ell^{-1} + \mathbf{k}^T \mathbf{D} &= \mathbf{0} \end{aligned}$$

which matches (5.34). Multiplying out the second row yields:

$$\mathbf{D} \mathbf{r} + \mathbf{A} \delta + \mathbf{g} = \mathbf{0}$$

which matches (5.36); and checking the third row yields:

$$\begin{aligned} \mathbf{A}^T \mathbf{k} + \mathbf{C}_x^{-1} \delta &= \mathbf{0} \\ (\mathbf{A}^T \mathbf{k})^T + (\mathbf{C}_x^{-1} \delta)^T &= \mathbf{0}^T \text{ (where } \mathbf{C}_x^{-1} \text{ is symmetric)} \\ \mathbf{k}^T \mathbf{A} + \delta^T \mathbf{C}_x^{-1} &= \mathbf{0} \end{aligned}$$

which matches (5.35).

5.1.4 – Solving a Linear System Through Matrix Partitioning

We are now in a position to begin solving (5.37), bearing in mind the goal is to solve for δ ; that is, to determine how far off are the adjusting parameters from the initial

estimates. To solve this linear system, the matrix will be partitioned in the manner discussed in Wells (1999) to isolate δ . First, consider the simpler linear system:

$$\begin{bmatrix} N_{11} & N_{12} \\ N_{21} & N_{22} \end{bmatrix} \begin{bmatrix} y_1 \\ y_2 \end{bmatrix} + \begin{bmatrix} u_1 \\ u_2 \end{bmatrix} = \begin{bmatrix} 0 \\ 0 \end{bmatrix} \quad (5.38)$$

for which the goal is to solve for y_1 and y_2 . Multiplying out the matrix equation yields:

$$N_{11}y_1 + N_{12}y_2 + u_1 = 0 \quad (5.39)$$

$$N_{21}y_1 + N_{22}y_2 + u_2 = 0. \quad (5.40)$$

Assuming N_{11} is non-singular, (5.39) can be solved for y_1

$$y_1 = -N_{11}^{-1} (N_{12}y_2 + u_1) \quad (5.41)$$

Substituting y_1 into (5.40) yields:

$$N_{21}(-N_{11}^{-1}(N_{12}y_2 + u_1)) + N_{22}y_2 + u_2 = 0. \quad (5.42)$$

Simplifying and solving for y_2 yields:

$$y_2 = \left[-N_{21}N_{11}^{-1}N_{12} + N_{22} \right]^{-1} \left[N_{21}N_{11}^{-1}u_1 - u_2 \right], \quad (5.43)$$

and back-substituting (5.43) into (5.41) gives an expression for y_1 :

$$y_1 = -N_{11}^{-1} \left(N_{12} \left[-N_{21}N_{11}^{-1}N_{12} + N_{22} \right]^{-1} \left[N_{21}N_{11}^{-1}u_1 - u_2 \right] + u_1 \right). \quad (5.44)$$

Returning to (5.37), the system can be partitioned as follows:

$$\left[\begin{array}{c|cc} \mathbf{C}_\ell^{-1} & \mathbf{D}^T & \mathbf{0} \\ \hline \mathbf{D} & \mathbf{0} & \mathbf{A} \\ \hline \mathbf{0} & \mathbf{A}^T & \mathbf{C}_x^{-1} \end{array} \right] \begin{bmatrix} \mathbf{r} \\ \mathbf{k} \\ \delta \end{bmatrix} + \begin{bmatrix} \mathbf{0} \\ \mathbf{g} \\ \mathbf{0} \end{bmatrix} = \begin{bmatrix} \mathbf{0} \\ \mathbf{0} \\ \mathbf{0} \end{bmatrix} \quad (5.45)$$

where: $y_1 = \mathbf{r}$ and $y_2 = \begin{bmatrix} \mathbf{k} \\ \delta \end{bmatrix}$ in equations (5.44) and (5.43), respectively. Applying (5.43)

yields:

$$\begin{aligned}
\begin{bmatrix} \mathbf{k} \\ \boldsymbol{\delta} \end{bmatrix} &= \begin{bmatrix} -\begin{bmatrix} \mathbf{D} \\ \mathbf{0} \end{bmatrix} \mathbf{C}_\ell \begin{bmatrix} \mathbf{D}^T & \mathbf{0} \end{bmatrix} \begin{bmatrix} \mathbf{0} & \mathbf{A} \\ \mathbf{A}^T & \mathbf{C}_x^{-1} \end{bmatrix}^{-1} \begin{bmatrix} \mathbf{D} \\ \mathbf{0} \end{bmatrix} \mathbf{C}_\ell \cdot \mathbf{0} - \begin{bmatrix} \mathbf{g} \\ \mathbf{0} \end{bmatrix} \end{bmatrix} \\
&= \begin{bmatrix} -\mathbf{D} \mathbf{C}_\ell \mathbf{D}^T & \mathbf{0} \\ \mathbf{0} & \mathbf{0} \end{bmatrix} + \begin{bmatrix} \mathbf{0} & \mathbf{A} \\ \mathbf{A}^T & \mathbf{C}_x^{-1} \end{bmatrix}^{-1} \begin{bmatrix} -\mathbf{g} \\ \mathbf{0} \end{bmatrix} \\
&= \begin{bmatrix} -\mathbf{D} \mathbf{C}_\ell \mathbf{D}^T & \mathbf{A} \\ \mathbf{A}^T & \mathbf{C}_x^{-1} \end{bmatrix}^{-1} \begin{bmatrix} -\mathbf{g} \\ \mathbf{0} \end{bmatrix}.
\end{aligned} \tag{5.46}$$

The terms of the preceding equation are then rearranged to match the form of (5.38), whose solution was previously identified:

$$\begin{bmatrix} -\mathbf{D} \mathbf{C}_\ell \mathbf{D}^T & \mathbf{A} \\ \mathbf{A}^T & \mathbf{C}_x^{-1} \end{bmatrix} \begin{bmatrix} \mathbf{k} \\ \boldsymbol{\delta} \end{bmatrix} + \begin{bmatrix} \mathbf{g} \\ \mathbf{0} \end{bmatrix} = \begin{bmatrix} \mathbf{0} \\ \mathbf{0} \end{bmatrix} \tag{5.47}$$

where $y_1^* = \mathbf{k}$ and $y_2^* = \boldsymbol{\delta}$. Thus, a second application of (5.43) yields:

$$\boldsymbol{\delta} = \begin{bmatrix} -\mathbf{A}^T (-\mathbf{D} \mathbf{C}_\ell \mathbf{D}^T)^{-1} \mathbf{A} + \mathbf{C}_x^{-1} \end{bmatrix}^{-1} \begin{bmatrix} \mathbf{A}^T (-\mathbf{D} \mathbf{C}_\ell \mathbf{D}^T)^{-1} \mathbf{g} - \mathbf{0} \end{bmatrix}. \tag{5.48}$$

$$\boxed{\boldsymbol{\delta} = - \begin{bmatrix} \mathbf{C}_x^{-1} + \mathbf{A}^T (\mathbf{D} \mathbf{C}_\ell \mathbf{D}^T)^{-1} \mathbf{A} \end{bmatrix} \mathbf{A}^T (\mathbf{D} \mathbf{C}_\ell \mathbf{D}^T)^{-1} \mathbf{g}} \tag{5.49}$$

Equation (5.49) is the key iterative equation that will be used in the least squares adjustment. To find the residuals of the observations, ℓ , (helpful in the identification of data outliers), one must first solve for \mathbf{k} . Applying (5.41) to (5.47) yields:

$$\begin{aligned}
\mathbf{k} &= -N_{11}^{-1} (N_{12} y_2 + u_1) \\
&= -(-\mathbf{D} \mathbf{C}_\ell \mathbf{D}^T)^{-1} (\mathbf{A} \boldsymbol{\delta} + \mathbf{g}) \\
&= (\mathbf{D} \mathbf{C}_\ell \mathbf{D}^T)^{-1} (\mathbf{A} \boldsymbol{\delta} + \mathbf{g}).
\end{aligned} \tag{5.50}$$

Back-substituting a second time by applying (5.41) to (5.45) yields:

$$\begin{aligned}
\mathbf{r} &= -N_{11}^{-1} (N_{12}y_2 + u_1) \\
&= -(\mathbf{C}_\ell^{-1})^{-1} \left(\begin{bmatrix} \mathbf{D}^T & \mathbf{0} \end{bmatrix} \begin{bmatrix} \mathbf{k} \\ \delta \end{bmatrix} + \begin{bmatrix} \mathbf{0} \end{bmatrix} \right) \\
&= -\mathbf{C}_\ell \mathbf{D}^T \mathbf{k} \\
&= -\mathbf{C}_\ell \mathbf{D}^T (\mathbf{D} \mathbf{C}_\ell \mathbf{D}^T)^{-1} (\mathbf{A} \delta + g) \\
&= -\mathbf{C}_\ell \mathbf{D}^T (\mathbf{D} \mathbf{C}_\ell \mathbf{D}^T)^{-1} \left(\mathbf{A} \left(-\left[\mathbf{C}_x^{-1} + \mathbf{A}^T (-\mathbf{D} \mathbf{C}_\ell \mathbf{D}^T)^{-1} \mathbf{A} \right] \mathbf{A}^T (\mathbf{D} \mathbf{C}_\ell \mathbf{D}^T)^{-1} g \right) + g \right) \\
&= -\mathbf{C}_\ell \mathbf{D}^T (\mathbf{D} \mathbf{C}_\ell \mathbf{D}^T)^{-1} \left(\mathbf{I} - \mathbf{A} \left[\mathbf{C}_x^{-1} + \mathbf{A}^T (-\mathbf{D} \mathbf{C}_\ell \mathbf{D}^T)^{-1} \mathbf{A} \right] \mathbf{A}^T (\mathbf{D} \mathbf{C}_\ell \mathbf{D}^T)^{-1} \right) g.
\end{aligned} \tag{5.51}$$

The preceding equation can be simplified computationally if the following identity is observed:

$$\begin{aligned}
&(\mathbf{S} + \mathbf{A}^T \mathbf{R} \mathbf{A})^{-1} \mathbf{A}^T \mathbf{R} = \mathbf{S}^{-1} \mathbf{A}^T (\mathbf{R}^{-1} + \mathbf{A} \mathbf{S}^{-1} \mathbf{A}^T)^{-1} \\
&\mathbf{I} \cdot (\mathbf{S} + \mathbf{A}^T \mathbf{R} \mathbf{A})^{-1} \mathbf{A}^T \mathbf{R} = \mathbf{S}^{-1} \mathbf{A}^T (\mathbf{R}^{-1} + \mathbf{A} \mathbf{S}^{-1} \mathbf{A}^T)^{-1} \cdot \mathbf{I} \\
&(\mathbf{S}^{-1} \mathbf{A}^T (\mathbf{A}^T)^{-1} \mathbf{S}) (\mathbf{S} + \mathbf{A}^T \mathbf{R} \mathbf{A})^{-1} \mathbf{A}^T \mathbf{R} = \mathbf{S}^{-1} \mathbf{A}^T (\mathbf{R}^{-1} + \mathbf{A} \mathbf{S}^{-1} \mathbf{A}^T)^{-1} (\mathbf{R}^{-1} (\mathbf{A}^T)^{-1} \mathbf{A}^T \mathbf{R}) \\
&(\mathbf{S}^{-1} \mathbf{A}^T (\mathbf{A}^T)^{-1} \mathbf{S}) (\mathbf{S} + \mathbf{A}^T \mathbf{R} \mathbf{A})^{-1} \mathbf{A}^T \mathbf{R} = \mathbf{S}^{-1} \mathbf{A}^T (\mathbf{R}^{-1} + \mathbf{A} \mathbf{S}^{-1} \mathbf{A}^T)^{-1} (\mathbf{R}^{-1} (\mathbf{A}^T)^{-1} \mathbf{A}^T \mathbf{R}) \\
&(\mathbf{A}^T)^{-1} \mathbf{S} (\mathbf{S} + \mathbf{A}^T \mathbf{R} \mathbf{A})^{-1} = (\mathbf{R}^{-1} + \mathbf{A} \mathbf{S}^{-1} \mathbf{A}^T)^{-1} \mathbf{R}^{-1} (\mathbf{A}^T)^{-1} \\
&\left[(\mathbf{A}^T)^{-1} \mathbf{S} (\mathbf{S} + \mathbf{A}^T \mathbf{R} \mathbf{A})^{-1} \right]^{-1} = \left[(\mathbf{R}^{-1} + \mathbf{A} \mathbf{S}^{-1} \mathbf{A}^T)^{-1} \mathbf{R}^{-1} (\mathbf{A}^T)^{-1} \right]^{-1} \\
&(\mathbf{S} + \mathbf{A}^T \mathbf{R} \mathbf{A}) \mathbf{S}^{-1} \mathbf{A}^T = \mathbf{A}^T \mathbf{R} (\mathbf{R}^{-1} + \mathbf{A} \mathbf{S}^{-1} \mathbf{A}^T) \\
&\mathbf{S} \mathbf{S}^{-1} \mathbf{A}^T + \mathbf{A}^T \mathbf{R} \mathbf{A} \mathbf{S}^{-1} \mathbf{A}^T = \mathbf{A}^T \mathbf{R} \mathbf{R}^{-1} + \mathbf{A}^T \mathbf{R} \mathbf{A} \mathbf{S}^{-1} \mathbf{A}^T \\
&\mathbf{I} \mathbf{A}^T + \mathbf{A}^T \mathbf{R} \mathbf{A} \mathbf{S}^{-1} \mathbf{A}^T = \mathbf{A}^T \mathbf{I} + \mathbf{A}^T \mathbf{R} \mathbf{A} \mathbf{S}^{-1} \mathbf{A}^T \\
&\mathbf{I} = \mathbf{I}.
\end{aligned} \tag{5.52}$$

As applied to (5.51),

$$\mathbf{r} = -\mathbf{C}_\ell \mathbf{D}^T (\mathbf{D} \mathbf{C}_\ell \mathbf{D}^T)^{-1} \left(\mathbf{I} - \mathbf{A} \left[\underbrace{\mathbf{C}_x^{-1}}_{\mathbf{S}} + \underbrace{\mathbf{A}^T}_{\mathbf{A}^T} \underbrace{(-\mathbf{D} \mathbf{C}_\ell \mathbf{D}^T)^{-1}}_{\mathbf{R}} \underbrace{\mathbf{A}}_{\mathbf{A}} \right] \underbrace{\mathbf{A}^T}_{\mathbf{A}^T} \underbrace{(\mathbf{D} \mathbf{C}_\ell \mathbf{D}^T)^{-1}}_{\mathbf{R}} \right) g. \tag{5.53}$$

$$\boxed{\mathbf{r} = -\mathbf{C}_\ell \mathbf{D}^T (\mathbf{D} \mathbf{C}_\ell \mathbf{D}^T)^{-1} \left(\mathbf{I} - \mathbf{A} \mathbf{C}_x \mathbf{A}^T (\mathbf{D} \mathbf{C}_\ell \mathbf{D}^T + \mathbf{A} \mathbf{C}_x \mathbf{A}^T)^{-1} \right) g}, \tag{5.54}$$

the misclosures of the observations.

Finally, an updated variance-covariance matrix can be computed for the calibration parameters:

$$\mathbf{C}_x = \left(\mathbf{A}^T (\mathbf{D}\mathbf{C}_\ell \mathbf{D}^T)^{-1} \mathbf{A} \right)^{-1}. \quad (5.55)$$

This matrix will be instrumental in assessing the quality of a proposed calibration solution (Section 6.2.1.3), the linear dependence of the calibration variables (6.2.2) and the total propagated uncertainty of the point cloud (Chapter VII).

5.2 – The Adjustment Model

The adjustment model employed in this dissertation seeks to fit the laser point cloud to a single planar surface. This represents a divergence from such adjustment procedures of Alharthy and Bethel (2004) or Vosselman and Dijkman (2001) who use several planar surfaces (i.e., building roofs) in their calculations. To mathematically derive the plane that best fits the point cloud, the same equation as employed by Freiss (2006) is used:

$$f = \vec{n} \cdot (\vec{x}_{OBS} - \vec{x}_{PLANE}) \quad (5.56)$$

where:

\vec{n} = normal vector of the planar surface

\vec{x}_{OBS} = 3D coordinates of the laser observations being fit to the plane.

\vec{x}_{PLANE} = 3D coordinates of an arbitrary point located on the planar surface.

Referring to Figure 58, $(\vec{x}_{OBS} - \vec{x}_{PLANE})$ describes the vector from point \vec{x}_{PLANE} to point \vec{x}_{OBS} (highlighted in blue).

One definition of the dot product is given by:

$$a \cdot b = \|a\| \|b\| \cos \theta \quad (5.57)$$

where a and b are arbitrary vectors and θ is the included angle between the two.

Assuming both a and b to be non-zero vectors, then the dot product (5.57) can only be

zero if $\cos \theta = 0$. Or, in other words, if $\theta = 90^\circ$. In the case of the vectors n and

$(\vec{x}_{OBS} - \vec{x}_{PLANE})$, should their included angle equal 90° , then that would imply the vector

$(\vec{x}_{OBS} - \vec{x}_{PLANE})$ lies within the plane, and thus, the point \vec{x}_{OBS} also lies within the plane.

In this way, every laser point observation which is given by the laser location equation

(3.46) is substituted into (5.56). Each equation, once linearized, then forms a single

observation in the system of linear equations discussed in (5.10).

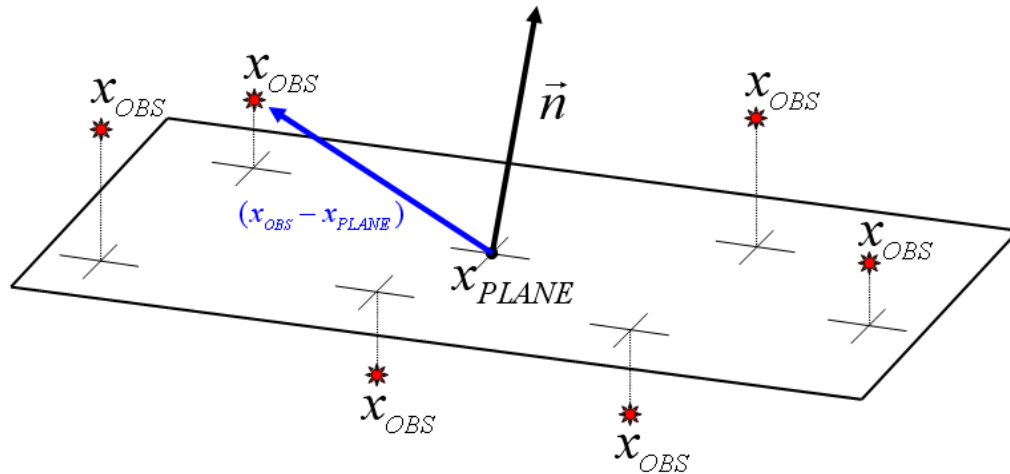


Figure 58. Determining the equation of a plane that best fits a collection of laser observations.

Should an ideal plane be found that fits all of the laser points, then each equation would be of the form (5.10) with all misclosures, r , being zero. However, if no plane fits perfectly, then each equation will have a non-zero misclosure. As discussed previously, the least squares adjustment will be used to minimize the collective sum of the squares of these misclosures. It should be emphasized that not only will the parameters of the planar surface be adjusted (i.e. n and \vec{x}_{PLANE}), but also the parameters

within the laser location equation. In this way, rather than stating that the planar surface is being fitted to the laser point cloud, it is more accurate to state that both the plane and the point cloud are being adjusted to each other.

5.2.1 – Parameterizing the Planar Surface

There are two over-arching objects that must be parameterized with respect to the planar surface (each of which has three components): the normal vector, n , and the included point, \vec{x}_{PLANE} . Unfortunately, from the perspective of the least squares method which seeks the one optimal solution, both the vector and point have an infinite number of solutions. As such, care must be taken in the representation of these parameters to facilitate the convergence of the least squares (versus an infinite oscillation among several suboptimal solutions).

In general, a plane can be represented by the equation:

$$n_x(x - x_p) + n_y(y - y_p) + n_z(z - z_p) = 0 \quad (5.58)$$

where:

$$\vec{n} = \begin{bmatrix} n_x & n_y & n_z \end{bmatrix} = \text{planar normal vector}$$

$$\vec{x}_{PLANE} = \begin{pmatrix} x_p & y_p & z_p \end{pmatrix} = \text{point contained in plane.}$$

In this form, the least squares algorithm must solve for 6 parameters. Vosselman and Dijkman (2001) propose a modified three-dimensional Hough transform to describe the plane:

$$z = n_x x + n_y y + z_p \quad (5.59)$$

where (as defined above in (5.58)):

n_x = slope of plane in x -direction

n_y = slope of plane in y -direction

z_p = vertical distance of plane to origin.

Effectively, Vosselman & Dijkman acknowledge there are an infinite number of ways to parameterize a single plane. So long as the plane in question is not vertical, they state that there must be some point that passes above/below the origin (i.e., $x_p = 0$ and $y_p = 0$). Further, by setting $n_z = 1$, the normal vector is prohibited from scaling (i.e. if $[1 \ -1 \ 2]$ is a correct normal vector, so is any constant multiple, like $[2 \ -2 \ 4]$ or $[\frac{1}{2} \ -\frac{1}{2} \ 1]$).

Regarding the least squares algorithm, the advantage to the Hough transform is that the planar surface can be represented with three parameters (rather than the full six), which is computationally more efficient. The disadvantage is that it prevents the inclusion of any vertical planar surfaces, which may be of interest in the case modeling the sides of buildings. In the interest of keeping the adjustment algorithm as general as possible, the Hough transform will not be used in this document. Instead, as discussed earlier in this chapter, an a priori weighted least squares adjustment will be performed (here the emphasis is on the a priori weighting). None of the planar parameters will be fixed (as is done with Hough); rather the observations that $x_p = 0$, $y_p = 0$ and $n_z = 1$ will be used as the initialization of the least squares. So long as the planar surface is not thought to be vertical, the above three guesses will be given large weights (small standard deviations) through the C_x matrix in (5.33). Should a vertical plane need to be modeled, the weights and initial guesses will need to be adjusted accordingly (such adjustments must be viewed on a case-by-case basis, depending on the orientation of the plane).

If the scale of the planar normal vector is not fixed, then the algorithm risks convergence to a trivial solution. Examining (5.56):

$$f = \vec{n} \cdot (\vec{x}_{OBS} - \vec{x}_{PLANE})$$

where the goal is to make $f=0$ for all observations, choosing a planar normal vector, $n=[0 \ 0 \ 0]$, will result in a trivial solution; since every dot product will be zero; this is clearly a minimum in the eyes of the least squares. Without hard coding the planar parameters (as is done in the case of Hough), there are three methods for preventing the normal vector from scaling to zero:

- Using an appropriate weighting in the covariance matrix, C_x . The weighting on n_z could be set prohibitively large to prevent its elements from converging to zero.

However, so long as n_z remains a stochastic variable, the least squares will slowly increment the normal vector to zero. Placing a large weight on any element of the normal vector is just a round-about method of recreating the Hough transform and should not be used.

- Defining the normal vector as a unit vector. Rather than having a three parameter normal vector of the form shown in (5.58), instead, n , can be defined as:

$$n = \begin{bmatrix} \frac{n_x}{\sqrt{n_x^2 + n_y^2 + n_z^2}} & \frac{n_y}{\sqrt{n_x^2 + n_y^2 + n_z^2}} & \frac{n_z}{\sqrt{n_x^2 + n_y^2 + n_z^2}} \end{bmatrix}. \quad (5.60)$$

Here, by scaling the normal vector, the magnitude is forced to of unit length, and thus prevents n from scaling to zero. While having a unit vector does have its appeals (for example: the vector version of Snell's Law used in this document demands that all vectors be of unit length), the above definition can be computationally cumbersome.

Both the fractions and square roots introduce potential domain concerns that could derail the least squares algorithm. Further, the square roots make for awkward partial derivatives that are computationally expensive. Having a unit vector without the square roots brings us to our third option.

▪ Defining the normal vector in spherical coordinates. The classic equations for the transformation from rectangular to spherical coordinates is given as:

$$\begin{aligned}x &= \rho \cos \theta \sin \phi \\y &= \rho \sin \theta \sin \phi \\z &= \rho \cos \phi\end{aligned}\tag{5.61}$$

where:

ρ = radial distance of vector

θ = azimuth angle, measured from $+x$

ϕ = zenith angle, measured from $+z$.

For the planar normal vector, a slight modification is made to the spherical transformation listed above, Figure 59. The length of the vector, ρ , is set to 1, and the z -component is reversed to account for a positive-down nomenclature. This leaves a proposed representation of the normal vector as:

$$n = \begin{bmatrix} \cos \theta_p \sin \phi_p \\ \sin \theta_p \sin \phi_p \\ -\cos \phi_p \end{bmatrix}.\tag{5.62}$$

This representation has several advantages: it guarantees the vector is of unit length, it has none of the domain or differentiability concerns of (5.60), and it reduces the number of adjustment parameters from three to two.

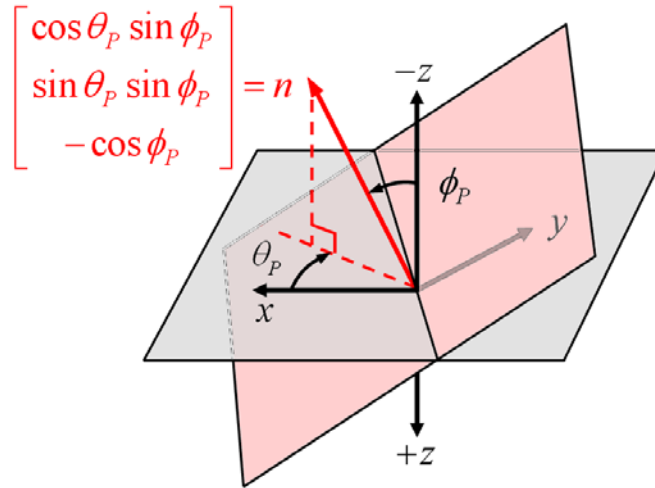


Figure 59. A modified spherical coordinate representation of the planar normal vector (pink) referenced to a locally level plane (grey).

5.2.2 – A Simplified Adjustment Example

A fully-developed transcription of the least squares adjustment is prohibitively large to include in this document (the MATLAB code is over 4,000 lines). For the purposes of illustrating the form of the least squares (other than through the generic equations offered to this point), a simplified laser scanner is presented. Consider a stationary platform housing a laser scanner with two degrees of freedom: a nadir angle, α , and an azimuth angle, β , Figure 60.

In this simplified case of fitting the point cloud to a plane, there are three observables: the laser range, nadir angle and azimuth angle (ρ , α , and β respectively); and there are five unknowns: the five parameters associated with the ground plane ($\phi_p, \theta_p, x_p, y_p, z_p$). Writing out (5.56) for this particular system, the observation equation becomes:

$$f = \begin{bmatrix} \cos \theta_p \sin \phi_p \\ \sin \theta_p \sin \phi_p \\ -\cos \phi_p \end{bmatrix} \cdot \left(\begin{bmatrix} \rho \cos \beta \sin \alpha \\ \rho \sin \beta \sin \alpha \\ \rho \cos \alpha \end{bmatrix} - \begin{bmatrix} x_p \\ y_p \\ z_p \end{bmatrix} \right) = 0. \quad (5.63)$$

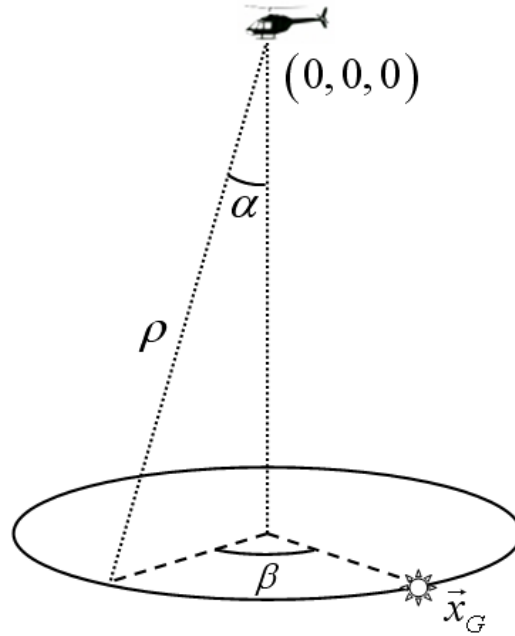


Figure 60. A simplified laser scanner with three observables: the laser range, ρ , the laser nadir angle, α , and the laser azimuth angle, β .

Recalling the nomenclature of the linearization presented in (5.31):

$$f(\ell, x) \approx \underbrace{f(\ell_0, x_0)}_g + \underbrace{(\ell - \ell_0)}_r \underbrace{\frac{\partial f}{\partial \ell} \Big|_{\ell=\ell_0, x=x_0}}_D + \underbrace{(x - x_0)}_{\delta} \underbrace{\frac{\partial f}{\partial x} \Big|_{\ell=\ell_0, x=x_0}}_A \approx 0$$

where:

g = initial approximation of model

r = corrections to the observations (residuals)

δ = corrections to the unknowns (adjustments)

D = design matrix with respect to observations

A = design matrix with respect to adjusting parameters.

The initialization of the model will simply be:

$$g = \begin{bmatrix} \cos \theta_{p0} \sin \phi_{p0} \\ \sin \theta_{p0} \sin \phi_{p0} \\ -\cos \phi_{p0} \end{bmatrix} \cdot \left(\begin{bmatrix} \rho_0 \cos \beta_0 \sin \alpha_0 \\ \rho_0 \sin \beta_0 \sin \alpha_0 \\ \rho_0 \cos \alpha_0 \end{bmatrix} - \begin{bmatrix} x_{p0} \\ y_{p0} \\ z_{p0} \end{bmatrix} \right). \quad (5.64)$$

Given n observations, the design matrix, \mathbf{D} , will have the form:

$$\mathbf{D} = \frac{\partial f}{\partial \ell} = \begin{bmatrix} \frac{\partial f_1}{\partial \rho_1} & \frac{\partial f_1}{\partial \alpha_1} & \frac{\partial f_1}{\partial \beta_1} & \frac{\partial f_1}{\partial \rho_2} & \frac{\partial f_1}{\partial \alpha_2} & \frac{\partial f_1}{\partial \beta_2} & \dots & \frac{\partial f_1}{\partial \rho_n} & \frac{\partial f_1}{\partial \alpha_n} & \frac{\partial f_1}{\partial \beta_n} \\ \frac{\partial f_2}{\partial \rho_1} & \frac{\partial f_2}{\partial \alpha_1} & \frac{\partial f_2}{\partial \beta_1} & \frac{\partial f_2}{\partial \rho_2} & \frac{\partial f_2}{\partial \alpha_2} & \frac{\partial f_2}{\partial \beta_2} & \dots & \frac{\partial f_2}{\partial \rho_n} & \frac{\partial f_2}{\partial \alpha_n} & \frac{\partial f_2}{\partial \beta_n} \\ \vdots & & & & \vdots & & \ddots & & \vdots & \\ \frac{\partial f_n}{\partial \rho_1} & \frac{\partial f_n}{\partial \alpha_1} & \frac{\partial f_n}{\partial \beta_1} & \frac{\partial f_n}{\partial \rho_2} & \frac{\partial f_n}{\partial \alpha_2} & \frac{\partial f_n}{\partial \beta_2} & \dots & \frac{\partial f_n}{\partial \rho_n} & \frac{\partial f_n}{\partial \alpha_n} & \frac{\partial f_n}{\partial \beta_n} \end{bmatrix}. \quad (5.65)$$

Assuming each laser shot is independent of the others, each element in the above matrix will be zero provided the indices of a given fraction are unequal. For example, $\partial f_1 / \partial \rho_2$ is a measure of how the first laser strike observation changes with respect to the second measured laser range. Again, if we assume independence from shot-to-shot, the first observation will not vary with respect to a parameter from the second observation; thus $\partial f_1 / \partial \rho_2 = 0$. So, (5.65) can be simplified to the more sparse

$$\mathbf{D} = \frac{\partial f}{\partial \ell} = \begin{bmatrix} \frac{\partial f_1}{\partial \rho_1} & \frac{\partial f_1}{\partial \alpha_1} & \frac{\partial f_1}{\partial \beta_1} & 0 & 0 & 0 & \dots & 0 & 0 & 0 \\ 0 & 0 & 0 & \frac{\partial f_2}{\partial \rho_2} & \frac{\partial f_2}{\partial \alpha_2} & \frac{\partial f_2}{\partial \beta_2} & \dots & 0 & 0 & 0 \\ \vdots & & & \vdots & & & \ddots & & \vdots & \\ 0 & 0 & 0 & 0 & 0 & 0 & \dots & \frac{\partial f_n}{\partial \rho_n} & \frac{\partial f_n}{\partial \alpha_n} & \frac{\partial f_n}{\partial \beta_n} \end{bmatrix}. \quad (5.66)$$

In turn, the i^{th} partial derivatives are populated as follows:

$$\frac{\partial f_i}{\partial \rho_i} = \begin{bmatrix} \cos \theta_{p_i} \sin \phi_{p_i} \\ \sin \theta_{p_i} \sin \phi_{p_i} \\ -\cos \phi_{p_i} \end{bmatrix} \cdot \begin{bmatrix} \cos \beta_i \sin \alpha_i \\ \sin \beta_i \sin \alpha_i \\ \cos \alpha_i \end{bmatrix} \quad (5.67)$$

$$\frac{\partial f_i}{\partial \alpha_i} = \begin{bmatrix} \cos \theta_{p_i} \sin \phi_{p_i} \\ \sin \theta_{p_i} \sin \phi_{p_i} \\ -\cos \phi_{p_i} \end{bmatrix} \cdot \begin{bmatrix} \rho_i \cos \beta_i \cos \alpha_i \\ \rho_i \sin \beta_i \cos \alpha_i \\ -\rho_i \sin \alpha_i \end{bmatrix} \quad (5.68)$$

$$\frac{\partial f_i}{\partial \beta_i} = \begin{bmatrix} \cos \theta_{p_i} \sin \phi_{p_i} \\ \sin \theta_{p_i} \sin \phi_{p_i} \\ -\cos \phi_{p_i} \end{bmatrix} \cdot \begin{bmatrix} -\rho_i \sin \beta_i \sin \alpha_i \\ \rho_i \cos \beta_i \sin \alpha_i \\ 0 \end{bmatrix}. \quad (5.69)$$

The residual vector will have the form:

$$\mathbf{r} = \begin{bmatrix} r_{\rho_1} & r_{\alpha_1} & r_{\beta_1} & r_{\rho_2} & r_{\alpha_2} & r_{\beta_2} & \cdots & r_{\rho_n} & r_{\alpha_n} & r_{\beta_n} \end{bmatrix}^T \quad (5.70)$$

and the covariance matrix (again assuming no cross-correlation among observations) will

be the sparse diagonal matrix:

$$\mathbf{C}_\ell = \begin{bmatrix} \sigma_{\rho_1}^2 & 0 & 0 & 0 & 0 & 0 & 0 & 0 & 0 & 0 \\ 0 & \sigma_{\alpha_1}^2 & 0 & 0 & 0 & 0 & 0 & 0 & 0 & 0 \\ 0 & 0 & \sigma_{\beta_1}^2 & 0 & 0 & 0 & 0 & 0 & 0 & 0 \\ 0 & 0 & 0 & \sigma_{\rho_2}^2 & 0 & 0 & 0 & 0 & 0 & 0 \\ 0 & 0 & 0 & 0 & \sigma_{\alpha_2}^2 & 0 & 0 & 0 & 0 & 0 \\ 0 & 0 & 0 & 0 & 0 & \sigma_{\beta_2}^2 & 0 & 0 & 0 & 0 \\ 0 & 0 & 0 & 0 & 0 & 0 & \ddots & 0 & 0 & 0 \\ 0 & 0 & 0 & 0 & 0 & 0 & 0 & \sigma_{\rho_n}^2 & 0 & 0 \\ 0 & 0 & 0 & 0 & 0 & 0 & 0 & 0 & \sigma_{\alpha_n}^2 & 0 \\ 0 & 0 & 0 & 0 & 0 & 0 & 0 & 0 & 0 & \sigma_{\beta_n}^2 \end{bmatrix}. \quad (5.71)$$

The second design matrix, \mathbf{A} , is given by:

$$\mathbf{A} = \frac{\partial f}{\partial \mathbf{x}} = \begin{bmatrix} \frac{\partial f_1}{\partial \phi_{p_1}} & \frac{\partial f_1}{\partial \theta_{p_1}} & \frac{\partial f_1}{\partial x_{p_1}} & \frac{\partial f_1}{\partial y_{p_1}} & \frac{\partial f_1}{\partial z_{p_1}} \\ \frac{\partial f_2}{\partial \phi_{p_2}} & \frac{\partial f_2}{\partial \theta_{p_2}} & \frac{\partial f_2}{\partial x_{p_2}} & \frac{\partial f_2}{\partial y_{p_2}} & \frac{\partial f_2}{\partial z_{p_2}} \\ \vdots & \vdots & \vdots & \vdots & \vdots \\ \frac{\partial f_n}{\partial \phi_{p_n}} & \frac{\partial f_n}{\partial \theta_{p_n}} & \frac{\partial f_n}{\partial x_{p_n}} & \frac{\partial f_n}{\partial y_{p_n}} & \frac{\partial f_n}{\partial z_{p_n}} \end{bmatrix}, \quad (5.72)$$

which is populated with the following partial derivatives:

$$\frac{\partial f_i}{\partial \phi_{Pi}} = \begin{bmatrix} \cos \theta_{Pi} \cos \phi_{Pi} \\ \sin \theta_{Pi} \cos \phi_{Pi} \\ -\sin \phi_{Pi} \end{bmatrix} \cdot \left(\begin{bmatrix} \rho_i \cos \beta_i \sin \alpha_i \\ \rho_i \sin \beta_i \sin \alpha_i \\ \rho_i \cos \alpha_i \end{bmatrix} - \begin{bmatrix} x_{Pi} \\ y_{Pi} \\ z_{Pi} \end{bmatrix} \right) \quad (5.73)$$

$$\frac{\partial f_i}{\partial \theta_{Pi}} = \begin{bmatrix} -\sin \theta_{Pi} \sin \phi_{Pi} \\ \cos \theta_{Pi} \sin \phi_{Pi} \\ 0 \end{bmatrix} \cdot \left(\begin{bmatrix} \rho_i \cos \beta_i \sin \alpha_i \\ \rho_i \sin \beta_i \sin \alpha_i \\ \rho_i \cos \alpha_i \end{bmatrix} - \begin{bmatrix} x_{Pi} \\ y_{Pi} \\ z_{Pi} \end{bmatrix} \right) \quad (5.74)$$

$$\frac{\partial f_i}{\partial x_{Pi}} = -\cos \theta_{Pi} \sin \phi_{Pi} \quad (5.75)$$

$$\frac{\partial f_i}{\partial y_{Pi}} = -\sin \theta_{Pi} \sin \phi_{Pi} \quad (5.76)$$

$$\frac{\partial f_i}{\partial z_{Pi}} = \cos \phi_{Pi}. \quad (5.77)$$

The adjustment vector is given by:

$$\delta = [\delta_{\phi_p} \quad \delta_{\theta_p} \quad \delta_{x_p} \quad \delta_{y_p} \quad \delta_{z_p}]^T \quad (5.78)$$

with an associated covariance matrix (assuming no cross-correlation among parameters)

of:

$$\mathbf{C}_x = \begin{bmatrix} \sigma_{\phi_p}^2 & 0 & 0 & 0 & 0 \\ 0 & \sigma_{\theta_p}^2 & 0 & 0 & 0 \\ 0 & 0 & \sigma_{x_p}^2 & 0 & 0 \\ 0 & 0 & 0 & \sigma_{y_p}^2 & 0 \\ 0 & 0 & 0 & 0 & \sigma_{z_p}^2 \end{bmatrix}. \quad (5.79)$$

Piecing together all the components between (5.63) and (5.79), the solution to the least squares problem is given by (5.49):

$$\delta = -\left[\mathbf{C}_x^{-1} + \mathbf{A}^T (\mathbf{D} \mathbf{C}_\ell \mathbf{D}^T)^{-1} \mathbf{A} \right] \mathbf{A}^T (\mathbf{D} \mathbf{C}_\ell \mathbf{D}^T)^{-1} \mathbf{g}.$$

5.2.2.1 – *The full-form partial derivatives.* Returning to the observation equation, (5.56), with the full laser location equation, (3.46), we have:

$$f = n \cdot \left(\left(\mathbb{R}_V \cdot \mathbb{R}_{VI} \left(\mathbb{R}_{BS} \cdot \vec{L}_2 \cdot \left(\frac{\rho - \rho_0}{\rho_1} \right) + \vec{x}_{IL} \right) + \vec{x}_{ECEF} \right) - \vec{x}_{PLANE} \right). \quad (5.80)$$

The scope of the ensuing partial derivatives needed for the least squares are largely a function of whether or not \vec{L}_2 , the laser vector exiting the prism, is a function of a particular variable. An example of a partial derivative of a variable that is independent of \vec{L}_2 :

$$\frac{\partial f}{\partial \rho} = n \cdot \left(\left(\mathbb{R}_V \cdot \mathbb{R}_{VI} \left(\mathbb{R}_{BS} \cdot \vec{L}_2 \cdot \left(\frac{1-0}{\rho_1} \right) + \mathbf{0} \right) + \mathbf{0} \right) - \mathbf{0} \right). \quad (5.81)$$

To compute the partial derivatives of a variable on which \vec{L}_2 is dependent ($PS\theta_x$, $PS\theta_y$, $PS\theta_z$, θ_{zs} , ϕ_{LS} , θ_{LS} , and θ_{FR}), one must navigate the chain rule, Figure 61.

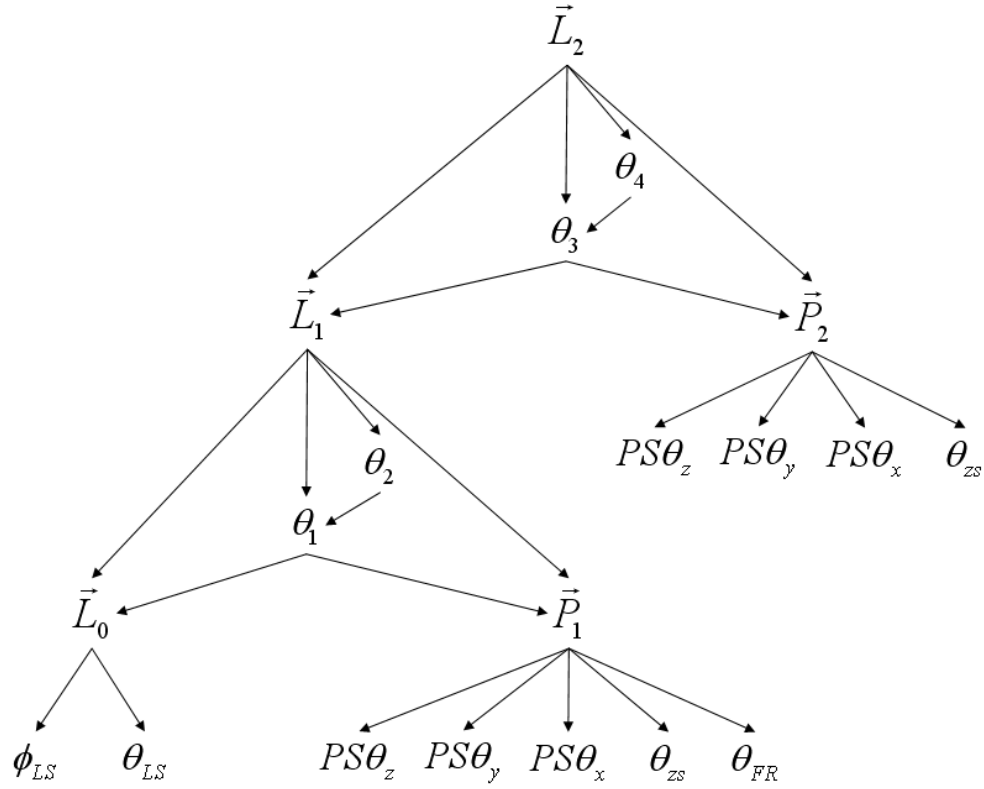


Figure 61. The chain tree showing the variables on which the laser vector exiting the prism, \vec{L}_2 , is dependent (and their associated inter-dependencies).

Where, as a reminder (see Figure 13):

\vec{L}_0 = direction of laser pulse entering Fresnel prism

\vec{L}_1 = direction of laser pulse within Fresnel prism

\vec{L}_2 = direction of laser pulse exiting Fresnel prism

\vec{P}_1 = normal vector to upper face of Fresnel prism

\vec{P}_2 = normal vector to lower face of Fresnel prism

θ_1 = angle of incidence at upper face of Fresnel prism

θ_2 = angle of refraction at upper face of Fresnel prism

θ_3 = angle of incidence at lower face of Fresnel prism

θ_4 = angle of refraction at lower face of Fresnel prism

To illustrate, the partial derivative (and the many sub-derivatives) are shown with respect to the scanner angle, θ_{zs} . From (3.48):

$$\frac{\partial \vec{P}_1}{\partial \theta_{zs}} = \begin{bmatrix} -\sin \theta_{zs} & -\cos \theta_{zs} & 0 \\ \cos \theta_{zs} & -\sin \theta_{zs} & 0 \\ 0 & 0 & 0 \end{bmatrix} \cdot \mathbb{R}_{PS\theta} \cdot \begin{bmatrix} -\sin \theta_{FR} \\ 0 \\ -\cos \theta_{FR} \end{bmatrix} \quad (5.82)$$

$$\text{and } \frac{\partial \vec{L}_0}{\partial \theta_{zs}} = \begin{bmatrix} 0 \\ 0 \\ 0 \end{bmatrix}, \quad (5.83)$$

from (3.3) (terms equaling zero marked in red):

$$\begin{aligned} \frac{\partial \theta_1}{\partial \theta_{zs}} &= \frac{-1}{\sqrt{1 - (\vec{P}_1 \cdot -\vec{L}_0)^2}} \left(\frac{\partial \vec{P}_1}{\partial \theta_{zs}} \cdot -\vec{L}_0 \right) + \frac{-1}{\sqrt{1 - (\vec{P}_1 \cdot -\vec{L}_0)^2}} \left(\vec{P}_1 \cdot \frac{-\partial \vec{L}_0}{\partial \theta_{zs}} \right) \\ &= \frac{-1}{\sqrt{1 - (\vec{P}_1 \cdot -\vec{L}_0)^2}} \left(\frac{\partial \vec{P}_1}{\partial \theta_{zs}} \cdot -\vec{L}_0 \right), \end{aligned} \quad (5.84)$$

from (3.4):

$$\frac{\partial \theta_2}{\partial \theta_1} = \frac{-1}{\sqrt{1 - \left(1 - \left(\frac{\eta_A}{\eta_S}\right)^2 \sin^2 \theta_1\right)}} \frac{1}{2\sqrt{1 - \left(\frac{\eta_A}{\eta_S}\right)^2 \sin^2 \theta_1}} \left(-\left(\frac{\eta_A}{\eta_S}\right)^2 2 \sin \theta_1 \cos \theta_1 \right), \quad (5.85)$$

from the chain rule:

$$\frac{\partial \theta_2}{\partial \theta_{zs}} = \frac{\partial \theta_2}{\partial \theta_1} \frac{\partial \theta_1}{\partial \theta_{zs}}, \quad (5.86)$$

from (3.48):

$$\frac{\partial \vec{P}_2}{\partial \theta_{zs}} = \begin{bmatrix} -\sin \theta_{zs} & -\cos \theta_{zs} & 0 \\ \cos \theta_{zs} & -\sin \theta_{zs} & 0 \\ 0 & 0 & 0 \end{bmatrix} \cdot \mathbb{R}_{PS\theta} \cdot \begin{bmatrix} 0 \\ 0 \\ -1 \end{bmatrix}, \quad (5.87)$$

and, finally, recalling (3.26) which states:

$$\vec{L}_1 = \left(\frac{\eta_A}{\eta_s}\right) \vec{L}_0 + \left(\frac{\eta_A}{\eta_s} \cos \theta_1 - \cos \theta_2\right) \vec{P}_1,$$

we have (terms equaling zero marked in red):

$$\begin{aligned} \frac{\partial \vec{L}_1}{\partial \theta_{zs}} &= \left(\frac{\eta_A}{\eta_s}\right) \frac{\partial \vec{L}_0}{\partial \theta_{zs}} + \left(\frac{\eta_A}{\eta_s} (-\sin \theta_1) \left(\frac{\partial \theta_1}{\partial \theta_{zs}}\right) + (\sin \theta_2) \left(\frac{\partial \theta_2}{\partial \theta_{zs}}\right)\right) \vec{P}_1 + \left(\frac{\eta_A}{\eta_s} \cos \theta_1 - \cos \theta_2\right) \frac{\partial \vec{P}_1}{\partial \theta_{zs}} \\ &= \left(\frac{\eta_A}{\eta_s} (-\sin \theta_1) \left(\frac{\partial \theta_1}{\partial \theta_{zs}}\right) + (\sin \theta_2) \left(\frac{\partial \theta_2}{\partial \theta_{zs}}\right)\right) \vec{P}_1 + \left(\frac{\eta_A}{\eta_s} \cos \theta_1 - \cos \theta_2\right) \frac{\partial \vec{P}_1}{\partial \theta_{zs}} \end{aligned} \quad (5.88)$$

where the partials given in (5.84), (5.86) and (5.82) are substituted where needed.

As an alternative to (5.88), a version of (3.26) that circumvents the internal angles

$(\theta_1 - \theta_4)$ can be used, namely, (3.48), which states:

$$\vec{L}_1 = \frac{\eta_A}{\eta_s} \vec{L}_0 + \left(-\frac{\eta_A}{\eta_s} (\vec{P}_1 \cdot \vec{L}_0) - \sqrt{1 - \left(\frac{\eta_A}{\eta_s}\right)^2 \left(1 - (\vec{P}_1 \cdot \vec{L}_0)^2\right)}\right) \vec{P}_1. \quad (5.89)$$

Computing the partial derivative of (5.89) yields (terms equaling zero marked in red):

$$\begin{aligned} \frac{\partial \vec{L}_1}{\partial \theta_{zs}} &= \left(\frac{\eta_A}{\eta_s}\right) \frac{\partial \vec{L}_0}{\partial \theta_{zs}} + \dots \\ &\quad \left(-\frac{\eta_A}{\eta_s} \left(\frac{\partial \vec{P}_1}{\partial \theta_{zs}} \cdot \vec{L}_0 + \vec{P}_1 \cdot \frac{\partial \vec{L}_0}{\partial \theta_{zs}}\right) - \frac{-\left(\frac{\eta_A}{\eta_s}\right)^2 (-2) (\vec{P}_1 \cdot \vec{L}_0) \left(\frac{-\partial \vec{P}_1}{\partial \theta_{zs}} \cdot \vec{L}_0 - \vec{P}_1 \cdot \frac{\partial \vec{L}_0}{\partial \theta_{zs}}\right)}{2\sqrt{1 - \left(\frac{\eta_A}{\eta_s}\right)^2 \left(1 - (\vec{P}_1 \cdot \vec{L}_0)^2\right)}}\right) \vec{P}_1 + \dots \\ &\quad \left(-\frac{\eta_A}{\eta_s} (\vec{P}_1 \cdot \vec{L}_0) - \sqrt{1 - \left(\frac{\eta_A}{\eta_s}\right)^2 \left(1 - (\vec{P}_1 \cdot \vec{L}_0)^2\right)}\right) \frac{\partial \vec{P}_1}{\partial \theta_{zs}} \\ &= \left(-\frac{\eta_A}{\eta_s} \left(\frac{\partial \vec{P}_1}{\partial \theta_{zs}} \cdot \vec{L}_0\right) - \frac{-\left(\frac{\eta_A}{\eta_s}\right)^2 (-2) (\vec{P}_1 \cdot \vec{L}_0) \left(\frac{-\partial \vec{P}_1}{\partial \theta_{zs}} \cdot \vec{L}_0\right)}{2\sqrt{1 - \left(\frac{\eta_A}{\eta_s}\right)^2 \left(1 - (\vec{P}_1 \cdot \vec{L}_0)^2\right)}}\right) \vec{P}_1 + \dots \\ &\quad \left(-\frac{\eta_A}{\eta_s} (\vec{P}_1 \cdot \vec{L}_0) - \sqrt{1 - \left(\frac{\eta_A}{\eta_s}\right)^2 \left(1 - (\vec{P}_1 \cdot \vec{L}_0)^2\right)}\right) \frac{\partial \vec{P}_1}{\partial \theta_{zs}}. \end{aligned} \quad (5.90)$$

By removing the internal angles, the previous equation eliminates the need for (5.84) through (5.86) and replaces (5.88).

The internal angles will be skipped for the computation of $\partial \vec{L}_2 / \partial \theta_{zs}$. Similar to (5.89):

$$\vec{L}_2 = \frac{\eta_s}{\eta_a} \vec{L}_1 + \left(-\frac{\eta_s}{\eta_a} (\vec{P}_2 \cdot \vec{L}_1) - \sqrt{1 - \left(\frac{\eta_s}{\eta_a} \right)^2 \left(1 - (\vec{P}_2 \cdot \vec{L}_1)^2 \right)} \right) \vec{P}_2. \quad (5.91)$$

So:

$$\begin{aligned} \frac{\partial \vec{L}_2}{\partial \theta_{zs}} = & \left(\frac{\eta_s}{\eta_a} \right) \frac{\partial \vec{L}_1}{\partial \theta_{zs}} + \dots \\ & \left(-\frac{\eta_s}{\eta_a} \left(\frac{\partial \vec{P}_2}{\partial \theta_{zs}} \cdot \vec{L}_1 + \vec{P}_2 \cdot \frac{\partial \vec{L}_1}{\partial \theta_{zs}} \right) - \frac{-\left(\frac{\eta_s}{\eta_a} \right)^2 (-2) (\vec{P}_2 \cdot -\vec{L}_1) \left(\frac{-\partial \vec{P}_2}{\partial \theta_{zs}} \cdot \vec{L}_1 - \vec{P}_2 \cdot \frac{\partial \vec{L}_1}{\partial \theta_{zs}} \right)}{2\sqrt{1 - \left(\frac{\eta_s}{\eta_a} \right)^2 \left(1 - (\vec{P}_2 \cdot -\vec{L}_1)^2 \right)}} \right) \vec{P}_2 + \dots \quad (5.92) \\ & \left(-\frac{\eta_s}{\eta_a} (\vec{P}_2 \cdot \vec{L}_1) - \sqrt{1 - \left(\frac{\eta_s}{\eta_a} \right)^2 \left(1 - (\vec{P}_2 \cdot -\vec{L}_1)^2 \right)} \right) \frac{\partial \vec{P}_2}{\partial \theta_{zs}}. \end{aligned}$$

Thus,

$$\frac{\partial f}{\partial \theta_{zs}} = n \cdot \left(\left(\mathbb{R}_V \cdot \mathbb{R}_{VI} \left(\mathbb{R}_{BS} \cdot \frac{\partial \vec{L}_2}{\partial \theta_{zs}} \cdot \left(\frac{\rho - \rho_0}{\rho_1} \right) + \mathbf{0} \right) + \mathbf{0} \right) - \mathbf{0} \right) \quad (5.93)$$

where $\partial \vec{L}_2 / \partial \theta_{zs}$ (5.92), $\partial \vec{L}_1 / \partial \theta_{zs}$ (5.90), $\partial \vec{P}_2 / \partial \theta_{zs}$ (5.87) and $\partial \vec{P}_1 / \partial \theta_{zs}$ (5.82) are substituted in order. The process is then repeated for the other six stated variables on which \vec{L}_2 is dependent.

5.3 – Improving Memory Usage for the Least Squares Algorithm

Inspecting the simplified adjustment procedure shown in (5.63), one can appreciate the magnitude of the memory that must be allocated for the different matrices

needed in the adjustment, Figure 62. Of primary concern is any matrix that grows by a factor of the square of the number of observations, specifically \mathbf{D} and \mathbf{C}_ℓ . To mitigate the drain on the computer's memory, the matrix algebra will be redefined in a way to take advantage of the sparse nature of the involved matrices.

Matrix	Dimensions	Number of observations		
		$n = 100$	$n = 1,000$	$n = 10,000$
\mathbf{C}_x	(5×5)	25	25	25
\mathbf{A}	$(n \times 5)$	500	5,000	50,000
\mathbf{D}	$(n \times 3n)$	30,000	3,000,000	300,000,000
\mathbf{C}_ℓ	$(3n \times 3n)$	90,000	9,000,000	900,000,000

Figure 62. Table of number of entries contained within the four primary matrices that are declared during the least squares adjustment (assuming five adjusting parameters and three observables).

Revisiting the iterative least squares formula, (5.49), the sizes of the respective matrices are indicated:

$$\delta = - \left[\underbrace{\mathbf{C}_x^{-1}}_{(5 \times 5)} - \underbrace{\mathbf{A}^T \left(\underbrace{\mathbf{D}}_{(n \times 3n)} \underbrace{\mathbf{C}_\ell}_{(3n \times 3n)} \underbrace{\mathbf{D}^T}_{(3n \times n)} \right)^{-1} \mathbf{A}}_{(n \times n)} \right] \underbrace{\mathbf{A}^T}_{(5 \times n)} \underbrace{\left(\underbrace{\mathbf{D}}_{(n \times 3n)} \underbrace{\mathbf{C}_\ell}_{(3n \times 3n)} \underbrace{\mathbf{D}^T}_{(3n \times n)} \right)^{-1} \mathbf{g}}_{(n \times n)}. \quad (5.94)$$

The above is written with the assumption that only five adjusting parameters, three observables and n -observations are given (equivalent to the simplified adjustment given earlier). For perspective, the proposed least squares adjustment will have 20 adjusting parameters and eight observables. In (5.94), not only must all matrices which contain n elements in both their rows and columns be avoided (e.g., \mathbf{D} and \mathbf{C}_ℓ), but so too must any intermediate matrices that result from the products of these matrices. By seeking a definition for $\mathbf{A}^T (\mathbf{D} \mathbf{C}_\ell \mathbf{D}^T)^{-1}$ without declaring the individual matrices, the resulting

matrix will only be $5 \times n$, which is no more than a linear problem with respect to memory.

First, \mathbf{D} and \mathbf{C}_ℓ must be redefined as \mathbf{D}^* and \mathbf{C}_ℓ^* according to their sparse nature.

$$\mathbf{D} = \left[\begin{array}{ccc|ccc|c|ccc} \frac{\partial f_1}{\partial \rho_1} & \frac{\partial f_1}{\partial \alpha_1} & \frac{\partial f_1}{\partial \beta_1} & 0 & 0 & 0 & \dots & 0 & 0 & 0 \\ 0 & 0 & 0 & \frac{\partial f_2}{\partial \rho_2} & \frac{\partial f_2}{\partial \alpha_2} & \frac{\partial f_2}{\partial \beta_1} & \dots & 0 & 0 & 0 \\ & \vdots & & & \vdots & & \ddots & & \vdots & \\ 0 & 0 & 0 & 0 & 0 & 0 & \dots & \frac{\partial f_n}{\partial \rho_n} & \frac{\partial f_n}{\partial \alpha_n} & \frac{\partial f_n}{\partial \beta_n} \end{array} \right] \text{ becomes} \quad (5.95)$$

$$\mathbf{D}^* = \left[\begin{array}{ccc|ccc|c|ccc} \frac{\partial f_1}{\partial \rho_1} & \frac{\partial f_1}{\partial \alpha_1} & \frac{\partial f_1}{\partial \beta_1} & \frac{\partial f_2}{\partial \rho_2} & \frac{\partial f_2}{\partial \alpha_2} & \frac{\partial f_2}{\partial \beta_1} & \dots & \frac{\partial f_n}{\partial \rho_n} & \frac{\partial f_n}{\partial \alpha_n} & \frac{\partial f_n}{\partial \beta_n} \end{array} \right]$$

and

$$\mathbf{C}_\ell = \left[\begin{array}{cccccccccc} \sigma_{\rho_1}^2 & 0 & 0 & 0 & 0 & 0 & 0 & 0 & 0 & 0 \\ 0 & \sigma_{\alpha_1}^2 & 0 & 0 & 0 & 0 & 0 & 0 & 0 & 0 \\ 0 & 0 & \sigma_{\beta_1}^2 & 0 & 0 & 0 & 0 & 0 & 0 & 0 \\ 0 & 0 & 0 & \sigma_{\rho_2}^2 & 0 & 0 & 0 & 0 & 0 & 0 \\ 0 & 0 & 0 & 0 & \sigma_{\alpha_2}^2 & 0 & 0 & 0 & 0 & 0 \\ 0 & 0 & 0 & 0 & 0 & \sigma_{\beta_2}^2 & 0 & 0 & 0 & 0 \\ 0 & 0 & 0 & 0 & 0 & 0 & \ddots & 0 & 0 & 0 \\ 0 & 0 & 0 & 0 & 0 & 0 & 0 & \sigma_{\rho_n}^2 & 0 & 0 \\ 0 & 0 & 0 & 0 & 0 & 0 & 0 & 0 & \sigma_{\alpha_n}^2 & 0 \\ 0 & 0 & 0 & 0 & 0 & 0 & 0 & 0 & 0 & \sigma_{\beta_n}^2 \end{array} \right] \text{ becomes} \quad (5.96)$$

$$\mathbf{C}_\ell^* = \left[\begin{array}{cccccccccc} \sigma_{\rho_1}^2 & \sigma_{\alpha_1}^2 & \sigma_{\beta_1}^2 & \sigma_{\rho_2}^2 & \sigma_{\alpha_2}^2 & \sigma_{\beta_2}^2 & \dots & \sigma_{\rho_n}^2 & \sigma_{\alpha_n}^2 & \sigma_{\beta_n}^2 \end{array} \right].$$

Notice, \mathbf{D} has gone from an $n \times 3n$ matrix to a $1 \times 3n$ matrix; and similarly, \mathbf{C}_ℓ has been reduced from $n \times n$ to $1 \times n$ – both now linear in size with respect to the number of

observations. Conceivably, \mathbf{C}_ℓ^* could be further rewritten as a 1×3 matrix if

uncertainties in the observables are assumed to be the same from shot to shot. That is:

$$\mathbf{C}_\ell^{**} = \begin{bmatrix} \sigma_\rho^2 & \sigma_\alpha^2 & \sigma_\beta^2 \end{bmatrix}. \quad (5.97)$$

For now, however, each observation will be assumed to be independent of all other observations (including their associated uncertainties).

The next task is to compute $\mathbf{A}^T(\mathbf{D}\mathbf{C}_\ell\mathbf{D}^T)^{-1}$ (a $5 \times n$ matrix) by encoding the matrix multiplication without allowing the individual matrices to be declared in memory.

First, we compute $\mathbf{D}\mathbf{C}_\ell$:

$$\begin{aligned} \mathbf{D}\mathbf{C}_\ell &= \dots \\ &= \begin{bmatrix} \frac{\partial f_1}{\partial \rho_1} & \frac{\partial f_1}{\partial \alpha_1} & \frac{\partial f_1}{\partial \beta_1} & 0 & 0 & 0 & \dots \\ 0 & 0 & 0 & \frac{\partial f_2}{\partial \rho_2} & \frac{\partial f_2}{\partial \alpha_2} & \frac{\partial f_2}{\partial \beta_1} & \dots \\ & \vdots & & & \vdots & & \ddots \\ 0 & 0 & 0 & 0 & 0 & 0 & \dots \end{bmatrix} \begin{bmatrix} \sigma_{\rho_1}^2 & 0 & 0 & 0 & 0 & 0 & 0 \\ 0 & \sigma_{\alpha_1}^2 & 0 & 0 & 0 & 0 & 0 \\ 0 & 0 & \sigma_{\beta_1}^2 & 0 & 0 & 0 & 0 \\ 0 & 0 & 0 & \sigma_{\rho_2}^2 & 0 & 0 & 0 \\ 0 & 0 & 0 & 0 & \sigma_{\alpha_2}^2 & 0 & 0 \\ 0 & 0 & 0 & 0 & 0 & \sigma_{\beta_2}^2 & 0 \\ 0 & 0 & 0 & 0 & 0 & 0 & \ddots \end{bmatrix} \\ &= \begin{bmatrix} \sigma_{\rho_1}^2 \frac{\partial f_1}{\partial \rho_1} & \sigma_{\alpha_1}^2 \frac{\partial f_1}{\partial \alpha_1} & \sigma_{\beta_1}^2 \frac{\partial f_1}{\partial \beta_1} & 0 & 0 & 0 & \dots \\ 0 & 0 & 0 & \sigma_{\rho_2}^2 \frac{\partial f_2}{\partial \rho_2} & \sigma_{\alpha_2}^2 \frac{\partial f_2}{\partial \alpha_2} & \sigma_{\beta_2}^2 \frac{\partial f_2}{\partial \beta_1} & \dots \\ & \vdots & & & \vdots & & \ddots \end{bmatrix}, \end{aligned} \quad (5.98)$$

which is then collapsed from $(n \times 3n)$ to the $(1 \times 3n)$:

$$\mathbf{D}\mathbf{C}_\ell^* = \left[\sigma_{\rho_1}^2 \frac{\partial f_1}{\partial \rho_1} \quad \sigma_{\alpha_1}^2 \frac{\partial f_1}{\partial \alpha_1} \quad \sigma_{\beta_1}^2 \frac{\partial f_1}{\partial \beta_1} \mid \sigma_{\rho_2}^2 \frac{\partial f_2}{\partial \rho_2} \quad \dots \mid \sigma_{\rho_n}^2 \frac{\partial f_n}{\partial \rho_n} \quad \sigma_{\alpha_n}^2 \frac{\partial f_n}{\partial \alpha_n} \quad \sigma_{\beta_n}^2 \frac{\partial f_n}{\partial \beta_n} \right]. \quad (5.99)$$

Continuing the multiplication, $\mathbf{DC}_\ell \mathbf{D}^T$:

$$\mathbf{DC}_\ell \mathbf{D}^T = \dots$$

$$\begin{bmatrix} \sigma_{\rho_1}^2 \frac{\partial f_1}{\partial \rho_1} & \sigma_{\alpha_1}^2 \frac{\partial f_1}{\partial \alpha_1} & \sigma_{\beta_1}^2 \frac{\partial f_1}{\partial \beta_1} & 0 & 0 & 0 & \dots & 0 & 0 \\ 0 & 0 & 0 & \sigma_{\rho_2}^2 \frac{\partial f_2}{\partial \rho_2} & \sigma_{\alpha_2}^2 \frac{\partial f_2}{\partial \alpha_2} & \sigma_{\beta_2}^2 \frac{\partial f_2}{\partial \beta_2} & \dots & 0 & 0 \\ & \vdots & & & \vdots & & \ddots & \vdots & \\ 0 & 0 & 0 & 0 & 0 & 0 & \dots & \sigma_{\alpha_n}^2 \frac{\partial f_n}{\partial \alpha_n} & \sigma_{\beta_n}^2 \frac{\partial f_n}{\partial \beta_n} \end{bmatrix} \bullet \dots$$

$$\begin{bmatrix} \frac{\partial f_1}{\partial \rho_1} & 0 & 0 \\ \frac{\partial f_1}{\partial \alpha_1} & 0 & \dots & 0 \\ \frac{\partial f_1}{\partial \beta_1} & 0 & 0 \\ 0 & \frac{\partial f_2}{\partial \rho_2} & 0 \\ 0 & \frac{\partial f_2}{\partial \alpha_2} & \dots & 0 \\ 0 & \frac{\partial f_2}{\partial \beta_1} & 0 \\ \vdots & \vdots & \ddots & \vdots \\ 0 & 0 & \frac{\partial f_n}{\partial \rho_n} \\ 0 & 0 & \dots & \frac{\partial f_n}{\partial \alpha_n} \\ 0 & 0 & \frac{\partial f_n}{\partial \beta_n} \end{bmatrix},$$

(5.100)

yielding an $(n \times n)$ diagonal matrix with diagonal entries given by:

$$\begin{aligned}
 (1,1) &= \left(\frac{\partial f_1}{\partial \rho_1} \sigma_{\rho_1} \right)^2 + \left(\frac{\partial f_1}{\partial \alpha_1} \sigma_{\alpha_1} \right)^2 + \left(\frac{\partial f_1}{\partial \beta_1} \sigma_{\beta_1} \right)^2 \\
 (2,2) &= \left(\frac{\partial f_2}{\partial \rho_2} \sigma_{\rho_2} \right)^2 + \left(\frac{\partial f_2}{\partial \alpha_2} \sigma_{\alpha_2} \right)^2 + \left(\frac{\partial f_2}{\partial \beta_2} \sigma_{\beta_2} \right)^2 \\
 &\vdots \\
 (n,n) &= \left(\frac{\partial f_n}{\partial \rho_n} \sigma_{\rho_n} \right)^2 + \left(\frac{\partial f_n}{\partial \alpha_n} \sigma_{\alpha_n} \right)^2 + \left(\frac{\partial f_n}{\partial \beta_n} \sigma_{\beta_n} \right)^2.
 \end{aligned} \tag{5.101}$$

Thus:

$$\mathbf{DC}_\ell \mathbf{D}^T = \dots \left[\begin{array}{ccc} \left(\frac{\partial f_1}{\partial \rho_1} \sigma_{\rho_1} \right)^2 + \left(\frac{\partial f_1}{\partial \alpha_1} \sigma_{\alpha_1} \right)^2 + \left(\frac{\partial f_1}{\partial \beta_1} \sigma_{\beta_1} \right)^2 & 0 & \dots \\ 0 & \left(\frac{\partial f_2}{\partial \rho_2} \sigma_{\rho_2} \right)^2 + \left(\frac{\partial f_2}{\partial \alpha_2} \sigma_{\alpha_2} \right)^2 + \left(\frac{\partial f_2}{\partial \beta_2} \sigma_{\beta_2} \right)^2 & \dots \\ \vdots & \vdots & \ddots \end{array} \right], \tag{5.102}$$

which can again be condensed to:

$$(\mathbf{DC}_\ell \mathbf{D}^T)^* = \left[\begin{array}{c} \left(\frac{\partial f_1}{\partial \rho_1} \sigma_{\rho_1} \right)^2 + \left(\frac{\partial f_1}{\partial \alpha_1} \sigma_{\alpha_1} \right)^2 + \left(\frac{\partial f_1}{\partial \beta_1} \sigma_{\beta_1} \right)^2 \\ \left(\frac{\partial f_2}{\partial \rho_2} \sigma_{\rho_2} \right)^2 + \left(\frac{\partial f_2}{\partial \alpha_2} \sigma_{\alpha_2} \right)^2 + \left(\frac{\partial f_2}{\partial \beta_2} \sigma_{\beta_2} \right)^2 \\ \vdots \\ \left(\frac{\partial f_n}{\partial \rho_n} \sigma_{\rho_n} \right)^2 + \left(\frac{\partial f_n}{\partial \alpha_n} \sigma_{\alpha_n} \right)^2 + \left(\frac{\partial f_n}{\partial \beta_n} \sigma_{\beta_n} \right)^2 \end{array} \right]^T. \tag{5.103}$$

Because $\mathbf{DC}_\ell \mathbf{D}^T$ is a square diagonal matrix, its inverse is also a square diagonal matrix, given by the relationship:

$$\mathbf{X} = \begin{bmatrix} a & 0 & 0 \\ 0 & b & 0 \\ 0 & 0 & c \end{bmatrix} \Rightarrow \mathbf{X}^{-1} = \begin{bmatrix} 1/a & 0 & 0 \\ 0 & 1/b & 0 \\ 0 & 0 & 1/c \end{bmatrix}. \quad (5.104)$$

So, $(\mathbf{DC}_\ell \mathbf{D}^T)^{-1}$ is simply given by the reciprocal of the individual diagonal elements of

$\mathbf{DC}_\ell \mathbf{D}^T$. Here we have:

$$(\mathbf{DC}_\ell \mathbf{D}^T)^{-1} = \dots \begin{bmatrix} \left(\left(\frac{\partial f_1}{\partial \rho_1} \sigma_{\rho_1} \right)^2 + \left(\frac{\partial f_1}{\partial \alpha_1} \sigma_{\alpha_1} \right)^2 + \left(\frac{\partial f_1}{\partial \beta_1} \sigma_{\beta_1} \right)^2 \right)^{-1} & 0 & \dots \\ 0 & \left(\left(\frac{\partial f_2}{\partial \rho_2} \sigma_{\rho_2} \right)^2 + \left(\frac{\partial f_2}{\partial \alpha_2} \sigma_{\alpha_2} \right)^2 + \left(\frac{\partial f_2}{\partial \beta_2} \sigma_{\beta_2} \right)^2 \right)^{-1} & \dots \\ \vdots & \vdots & \ddots \end{bmatrix} \quad (5.105)$$

which is condensed to:

$$(\mathbf{DC}_\ell \mathbf{D}^T)^{-1*} = \begin{bmatrix} \left(\left(\frac{\partial f_1}{\partial \rho_1} \sigma_{\rho_1} \right)^2 + \left(\frac{\partial f_1}{\partial \alpha_1} \sigma_{\alpha_1} \right)^2 + \left(\frac{\partial f_1}{\partial \beta_1} \sigma_{\beta_1} \right)^2 \right)^{-1} \\ \left(\left(\frac{\partial f_2}{\partial \rho_2} \sigma_{\rho_2} \right)^2 + \left(\frac{\partial f_2}{\partial \alpha_2} \sigma_{\alpha_2} \right)^2 + \left(\frac{\partial f_2}{\partial \beta_2} \sigma_{\beta_2} \right)^2 \right)^{-1} \\ \vdots \\ \left(\left(\frac{\partial f_n}{\partial \rho_n} \sigma_{\rho_n} \right)^2 + \left(\frac{\partial f_n}{\partial \alpha_n} \sigma_{\alpha_n} \right)^2 + \left(\frac{\partial f_n}{\partial \beta_n} \sigma_{\beta_n} \right)^2 \right)^{-1} \end{bmatrix}^T. \quad (5.106)$$

Finally, we can write an expression for $\mathbf{A}^T (\mathbf{D}\mathbf{C}_\ell \mathbf{D}^T)^{-1}$:

$$\mathbf{A}^T (\mathbf{D}\mathbf{C}_\ell \mathbf{D}^T)^{-1} = \dots$$

$$\begin{bmatrix} \frac{\partial f_1}{\partial \phi_p} & \frac{\partial f_2}{\partial \phi_p} & \dots & \frac{\partial f_n}{\partial \phi_p} \\ \frac{\partial f_1}{\partial \theta_p} & \frac{\partial f_2}{\partial \theta_p} & \dots & \frac{\partial f_n}{\partial \theta_p} \\ \frac{\partial f_1}{\partial x_p} & \frac{\partial f_2}{\partial x_p} & \dots & \frac{\partial f_n}{\partial x_p} \\ \frac{\partial f_1}{\partial y_p} & \frac{\partial f_2}{\partial y_p} & \dots & \frac{\partial f_n}{\partial y_p} \\ \frac{\partial f_1}{\partial z_p} & \frac{\partial f_2}{\partial z_p} & \dots & \frac{\partial f_n}{\partial z_p} \end{bmatrix} \bullet \dots$$

$$\begin{bmatrix} \left(\left(\frac{\partial f_1}{\partial \rho_1} \sigma_{\rho_1} \right)^2 + \left(\frac{\partial f_1}{\partial \alpha_1} \sigma_{\alpha_1} \right)^2 + \left(\frac{\partial f_1}{\partial \beta_1} \sigma_{\beta_1} \right)^2 \right)^{-1} & 0 & \dots \\ 0 & \left(\left(\frac{\partial f_2}{\partial \rho_2} \sigma_{\rho_2} \right)^2 + \left(\frac{\partial f_2}{\partial \alpha_2} \sigma_{\alpha_2} \right)^2 + \left(\frac{\partial f_2}{\partial \beta_2} \sigma_{\beta_2} \right)^2 \right)^{-1} & \dots \\ \vdots & \vdots & \ddots \end{bmatrix}.$$

(5.107)

Which can be simplified to:

$$\mathbf{A}^T (\mathbf{DC}_\ell \mathbf{D}^T)^{-1} = \dots$$

$$\begin{bmatrix} \frac{\partial f_1}{\partial \phi_p} \left(\left(\frac{\partial f_1}{\partial \rho_1} \sigma_{\rho_1} \right)^2 + \left(\frac{\partial f_1}{\partial \alpha_1} \sigma_{\alpha_1} \right)^2 + \left(\frac{\partial f_1}{\partial \beta_1} \sigma_{\beta_1} \right)^2 \right)^{-1} & \frac{\partial f_2}{\partial \phi_p} \left(\left(\frac{\partial f_2}{\partial \rho_2} \sigma_{\rho_2} \right)^2 + \left(\frac{\partial f_2}{\partial \alpha_2} \sigma_{\alpha_2} \right)^2 + \left(\frac{\partial f_2}{\partial \beta_2} \sigma_{\beta_2} \right)^2 \right)^{-1} & \dots \\ \frac{\partial f_1}{\partial \theta_p} \left(\left(\frac{\partial f_1}{\partial \rho_1} \sigma_{\rho_1} \right)^2 + \left(\frac{\partial f_1}{\partial \alpha_1} \sigma_{\alpha_1} \right)^2 + \left(\frac{\partial f_1}{\partial \beta_1} \sigma_{\beta_1} \right)^2 \right)^{-1} & \frac{\partial f_2}{\partial \theta_p} \left(\left(\frac{\partial f_2}{\partial \rho_2} \sigma_{\rho_2} \right)^2 + \left(\frac{\partial f_2}{\partial \alpha_2} \sigma_{\alpha_2} \right)^2 + \left(\frac{\partial f_2}{\partial \beta_2} \sigma_{\beta_2} \right)^2 \right)^{-1} & \dots \\ \frac{\partial f_1}{\partial x_p} \left(\left(\frac{\partial f_1}{\partial \rho_1} \sigma_{\rho_1} \right)^2 + \left(\frac{\partial f_1}{\partial \alpha_1} \sigma_{\alpha_1} \right)^2 + \left(\frac{\partial f_1}{\partial \beta_1} \sigma_{\beta_1} \right)^2 \right)^{-1} & \frac{\partial f_2}{\partial x_p} \left(\left(\frac{\partial f_2}{\partial \rho_2} \sigma_{\rho_2} \right)^2 + \left(\frac{\partial f_2}{\partial \alpha_2} \sigma_{\alpha_2} \right)^2 + \left(\frac{\partial f_2}{\partial \beta_2} \sigma_{\beta_2} \right)^2 \right)^{-1} & \dots \\ \frac{\partial f_1}{\partial y_p} \left(\left(\frac{\partial f_1}{\partial \rho_1} \sigma_{\rho_1} \right)^2 + \left(\frac{\partial f_1}{\partial \alpha_1} \sigma_{\alpha_1} \right)^2 + \left(\frac{\partial f_1}{\partial \beta_1} \sigma_{\beta_1} \right)^2 \right)^{-1} & \frac{\partial f_2}{\partial y_p} \left(\left(\frac{\partial f_2}{\partial \rho_2} \sigma_{\rho_2} \right)^2 + \left(\frac{\partial f_2}{\partial \alpha_2} \sigma_{\alpha_2} \right)^2 + \left(\frac{\partial f_2}{\partial \beta_2} \sigma_{\beta_2} \right)^2 \right)^{-1} & \dots \\ \frac{\partial f_1}{\partial z_p} \left(\left(\frac{\partial f_1}{\partial \rho_1} \sigma_{\rho_1} \right)^2 + \left(\frac{\partial f_1}{\partial \alpha_1} \sigma_{\alpha_1} \right)^2 + \left(\frac{\partial f_1}{\partial \beta_1} \sigma_{\beta_1} \right)^2 \right)^{-1} & \frac{\partial f_2}{\partial z_p} \left(\left(\frac{\partial f_2}{\partial \rho_2} \sigma_{\rho_2} \right)^2 + \left(\frac{\partial f_2}{\partial \alpha_2} \sigma_{\alpha_2} \right)^2 + \left(\frac{\partial f_2}{\partial \beta_2} \sigma_{\beta_2} \right)^2 \right)^{-1} & \dots \end{bmatrix}.$$

(5.108)

While (5.108) is cumbersome to behold, it is worth observing that $\mathbf{A}^T (\mathbf{DC}_\ell \mathbf{D}^T)^{-1}$ has dimension of $(5 \times n)$; thus it only grows linearly with respect to the number of observations. Thus, the above matrix will be computed directly, using the indicated entries, and substituted into (5.49) as indicated below:

$$\delta = - \left[\mathbf{C}_x^{-1} + \underbrace{\mathbf{A}^T (\mathbf{DC}_\ell \mathbf{D}^T)^{-1} \mathbf{A}}_{\text{Substitute here}} \right] \underbrace{\mathbf{A}^T (\mathbf{DC}_\ell \mathbf{D}^T)^{-1} \mathbf{g}}_{\text{Substitute here}} \quad (5.109)$$

Prior to implementing the improved memory management strategy, any dataset over approximately 1,200 observations would cause the author's computer to experience a memory failure and subsequently crash. Since implementation, datasets over one hundred times as large have been processed without incident. In addition to the ability to process larger datasets, the redefinition of the matrices also leads to a faster executing algorithm. In the case of processing 750 observations, the computation time dropped

from 3 minutes 48 seconds to nine-and-a-half seconds – an improvement in processing speed of over 24 times.

5.4 – Summary of Key Results

The following is a bulleted list of the key results, concepts and contributions presented within this chapter. When possible, the relevant section(s) that offer a more detailed explanation are indicated.

- A weighted constraint least squares model was identified as the method pursued for the calibration algorithm (Section 5.1.3). In addition, the basic theory of a least squares adjustment was presented (Section 5.1.2), along with how to linearized the model (Section 5.1.3.1) and solve the systems through matrix partitioning (Section 5.1.4).
- Geometrically, the adjustment model is based upon fitting the lidar point cloud to a single planar surface (Section 5.2).
- The planar surface will be represented by 5 parameters: three for a point contained within the plane and two to describe the plane's normal vector in spherical coordinates. Spherical coordinates reduced the number of parameters included in the adjustment, prevented the vector from scaling to zero (leading to a trivial solution to the LSA), and allowed for the possibility of vertical surfaces to be used in the adjustment (Section 5.2.1).
- Both simplified and full lidar models were included as examples to demonstrate the structure of the least squares (Sections 5.2.2 & 5.2.2.1). Using these as a starting point, a reader should be able to develop an adjustment model particular to their own systems.

- Finally a method was presented to make the adjustment algorithm more efficient in both memory requirements and processing time. By taking advantage of the sparse nature of the design matrices, portions of the iterative formula for computing the corrections to the calibration parameters can be manually determined without performing the full series of matrix multiplications and inverses. By circumventing portions of the matrix algebra, both memory and processing time became linear functions of the number of datapoints being adjusted. On the main laptop used for testing, the end result was datasets over 100 times as large could be processed, and any given dataset could be processed in $1/24^{\text{th}}$ the time.

CHAPTER VI

THE LIDAR CALIBRATION MODULE

6. THE LIDAR CALIBRATION MODULE
6.1 GEOMETRIC IMPACTS OF BORESIGHT MISALIGNMENTS AND SIGNATURE ANALYSIS
6.1.1 The Boresight Angles - Pitch Axis
6.1.2 The Boresight Angles - Roll Axis
6.1.3 The Boresight Angles - Yaw Axis
6.2 THE CALIBRATION MODULE
6.2.1 Calibration Module Interface
6.2.1.1 Defining the LSA inputs
6.2.1.2 Coping with non-adjusted calibration parameters
6.2.1.3 Boresight calibration examples and improving the output's confidence
6.2.2 Covariance and Correlation Coefficients
6.3 SIGNATURE ANALYSIS OF THE REMAINING CALIBRATION PARAMETERS
6.3.1 The Prism Slope
6.3.2 Laser-to-Scanner Alignments
6.3.3 The Vehicle Reference Frame
6.3.3.1 Vehicle-to-INS Heading Alignment
6.3.3.2 Scanner-to-INS horizontal offset measurement
6.3.3.3 Scanner-to-INS vertical offset measurement
6.3.4 Prism-to-Scanner Alignments
6.3.4.1. Prism "pitch" and "roll" biases
6.3.4.2. Scanner azimuth bias
6.3.5 Laser Range Bias and Scale Factor
6.3.6 Advice on Setting Weights within the LSA
6.4 IMPACTS OF SURVEY SITE SELECTION ON CALIBRATION MODULE
6.4.1 Calibration on a Narrow Runway
6.4.2 Calibration on a Dynamic Sea Surface
6.4.2.1 Wave effects on calibration uncertainty
6.4.2.2 Tidal effects on calibration uncertainty
6.5 SUMMARY OF KEY RESULTS

Figure 63. Chapter VI outline.

While the previous chapter outlined the theory of a least squares adjustment, this chapter discusses the precise methods used to put the theory into practice, in the form of a LSA calibration module. There are three key goals to this chapter:

- To offer an intuitive explanation of what the LSA is geometrically doing and to explain the flight characteristics necessary to determine each calibration parameter through signature analysis plots (Sections 6.1 & 6.3).

- To present a “user’s guide” for the calibration module and to explain the flexibility the user has in how the LSA is implemented with regard to uncertainty propagation (Section 6.2).
- To propose various flight plans to assess which best determines the system’s calibration parameters and to show how the performance is affected by conditions at the survey site: narrow runways (Section 6.4.1), wavy water surfaces (Section 6.4.2.1) or in the presence of tides (Section 6.4.2.2).

In Chapter III, 15 lidar calibration parameters were presented: the three scanner-to-INS (boresight) angles (Section 3.1.4.1), the prism slope (Section 3.1.2), the two laser-to-scanner angles (Section 3.1.3.2), the vehicle-to-INS heading alignment (Section 3.1.4.2), the three scanner-to-INS offset measurements (Section 3.1.4.1), the three prism-to-scanner angles (Section 3.1.3.1), and the laser range bias and scale factor (Section 3.1.5). Each parameter and how it affects the point cloud will be discussed in turn.

First, only the three boresight angles will be examined to establish a foundational relationship among the types of system misalignments, the maneuvering of the vehicle, and the structure of the biased point cloud. After establishing a flight plan that contains the geometric information necessary for a successful execution of the adjustment algorithm, the calibration module is presented, offering a brief tutorial on how the software works and how to interpret the results (e.g., the variance-covariance matrix and correlation coefficients). The discussion will then return to the remaining 12 calibration parameters and how their incremental inclusion in the adjustment model affects both the design of acquisition flight plan and the performance of the LSA. Finally, this chapter will conclude by examining different calibration scenarios, varying both the flight plan

and the survey site selection (choosing among narrow airstrips or the dynamic ocean surface).

6.1 – Geometric Impacts of Boresight Misalignments and Signature Analysis

The key to the calibration routine is as follows: any sensor misalignment (when coupled with an appropriate vehicle maneuver) that results in a non-coplanar point cloud (when acquired over a planar surface) can be determined through the proposed calibration routine. Thus, for every parameter we must consider what flight characteristic (heaving, pitching, rolling or changing of direction) leads to the “least coplanar” point cloud. In this way, the maneuver that produces the least coherent point cloud becomes a page in the signature analysis handbook – geared towards designing a flight plan that best determines any given parameter (i.e., if the laser range bias produces the greatest signature when the vehicle pitches, then the vehicle should be intentionally pitched to determine the laser range bias).

For this first group of parameters, the boresight angles, a geometric argument is presented to elucidate this dissertation’s central claim that all the sensor misalignments can be assessed from a flat and featureless planar surface.

6.1.1 – The Boresight Angles – Pitch Axis

Before launching into the full suite of signature analysis plots, consider just two separate scans of a lidar with an unknown boresight misalignment in the pitch axis (Figure 64). On the left is a perfectly-oriented lidar (free of boresight misalignments) in which the scanning axis is normal to the ground plane. Under such an orientation, the forward, aft, port and starboard-oriented beams will all have the same computed range. Should the lidar have a positive boresight misalignment in the pitch angle, then the

forward-oriented beams will have a relatively longer range and the aft-oriented beams will have a shorter range. Should the lidar operator incorrectly believe there to be no pitch boresight misalignment (i.e., possess the geometry of Figure 64 – left), then the longer forward beams will lead the operator to believe these points are located below the ground plane and the shorter aft beams are located above the ground (Figure 64 – right). The key point is that what was a coplanar dataset is no longer so. The calibration module, in fitting the data to a planar surface, will thus be able to determine this pitch bias.

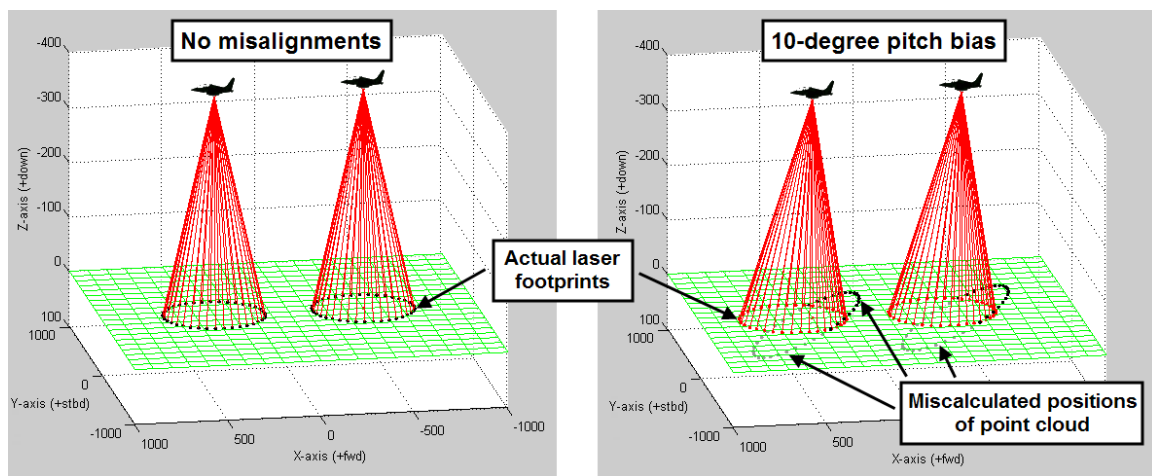


Figure 64. Two revolutions of the laser scanner with no boresight misalignments – notice both circular traces are coplanar (left). With a 10° forward (i.e. towards the nose) pitch boresight bias, two revolutions are shown with both the actual laser footprints (shown in red) along with the miscalculated point cloud (shown in black). Notice the biased points are no longer coplanar.

It should be apparent from Figure 64 (right) that no maneuvering of the vehicle beyond moving forward is necessary to yield a non-coplanar point cloud. To expand upon the previous plot, several hundred revolutions are shown in Figure 65 (top). The upper two plots show the same point cloud from two different perspectives in which there

is an unidentified 1° pitch boresight misalignment. The biased point cloud is rendered as a helical pattern with an equal distribution above and below the actual ground plane.

To further investigate how the point cloud behaves in the presence of a more dynamic vehicle trajectory, plots of the biased cloud are rendered in the presence of vehicle heave, roll, pitch and yaw. While the level flight yields a cylindrical point cloud, increasing the vehicle's altitude by heaving steadily increases the diameter of this cylinder (Figure 65 – bottom). Because the points now exhibit a larger spatial distribution, the point cloud less resembles a planar surface. This implies that increasing the acquisition altitude will make it easier to determine the pitch boresight misalignment (i.e., yield more confident results).

Figure 66 shows what happens as the vehicle's attitude is permitted to go from a level flight to a more extreme orientation. The upper plot incrementally increases the vehicle's roll from 0° to 30° . Much like increasing the altitude, a spreading of the biased points is observed; however, the spreading is not as pronounced as it is with the increasing altitude. Further, even if the spread between the altitude and roll plots was equal, one must consider which is a more feasible acquisition scenario: asking the pilot to ascend 100m or to roll the vehicle by 30° . In this case, increasing the altitude is a better method for increasing the confidence in the calibration value for the pitch boresight angle.

In contrast to both heaving and rolling, inducing a pitch has a large pronounced effect on the point cloud (Figure 66 – middle). Not only does the spread of the point cloud become more pronounced with increased vehicle pitch, but the calculated z-values of the points become lower and lower. Of all the renderings in Figure 65 and Figure 66,

the one with the pitching vehicle exhibits the greatest dispersion of its points.

Alternatively stated, the pitch boresight angle is most sensitive to the vehicle's pitch. The surveyors should induce a change in vehicle pitch to ensure the highest confidence in the calculated value for the pitch boresight misalignment.

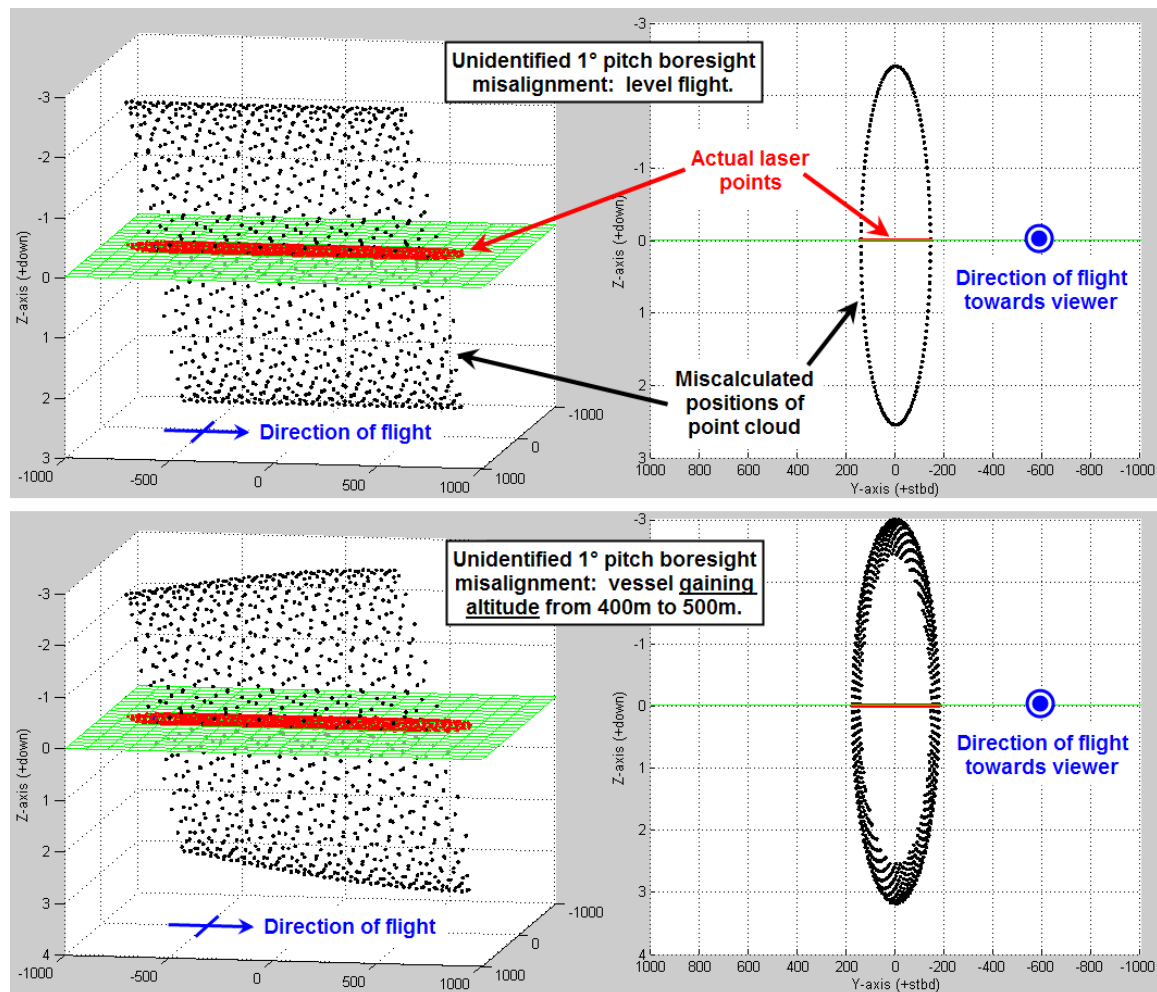


Figure 65. Visualization of a point cloud generated from a lidar with an unidentified 1° pitch boresight misalignment (top), and a point cloud from the same system as it experiences an increase in altitude (bottom). The red points indicate the true laser strikes, while the black are the miscalculated biased points. All units in meters.

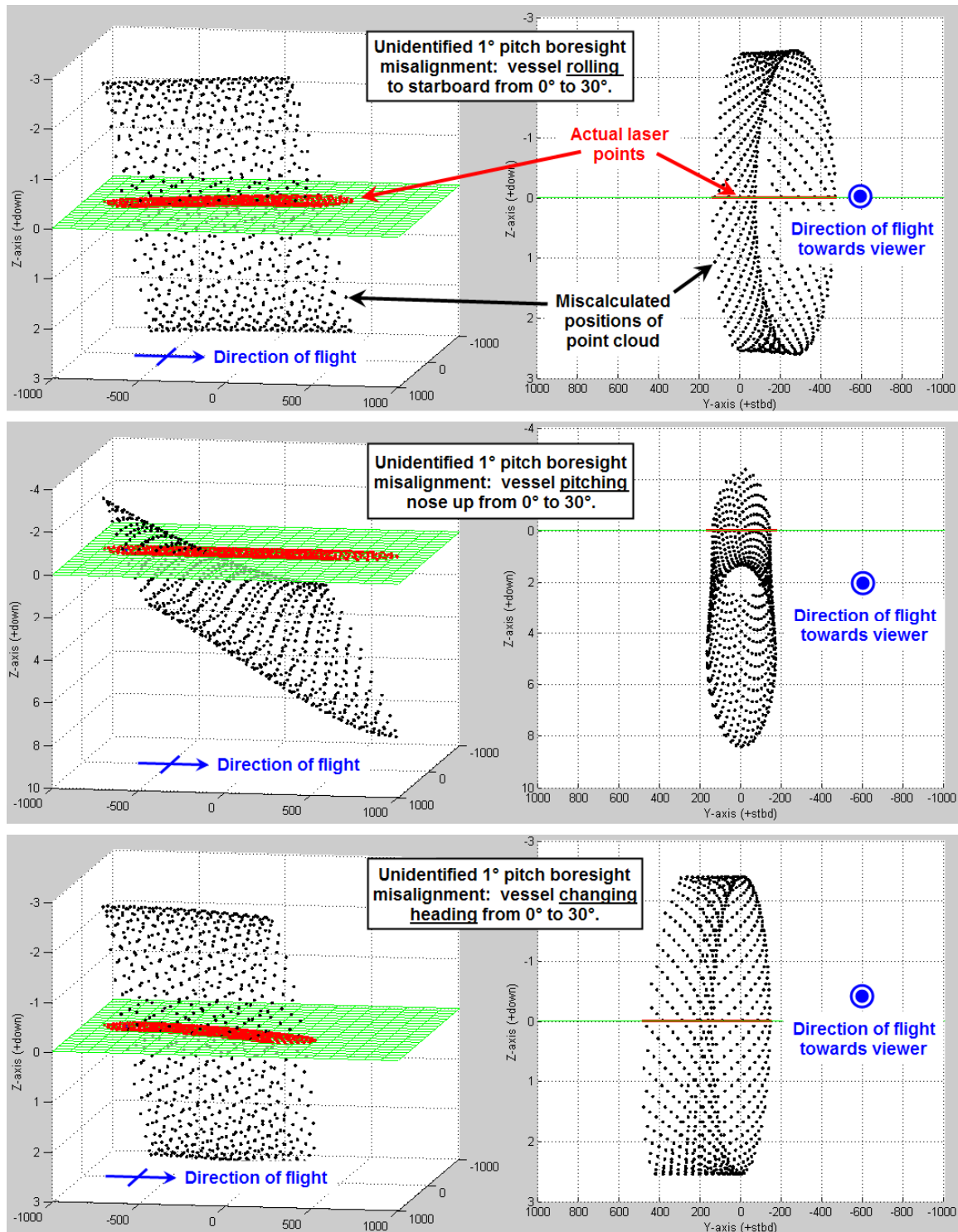


Figure 66. Signature analysis plots for a lidar with a 1° pitch boresight misalignment in the presence of a rolling (top), pitching (middle) and yawing (bottom) vehicle. The red points indicate the true laser strikes, while the black are the miscalculated biased points. All units in meters.

The renderings in (Figure 65 and Figure 66) are referred to as signature analysis plots as they can be used to assess whether a point cloud has a particular misalignment based solely on general structure, or signature, of the point cloud. For example, the middle plots of Figure 66 suggest that, in the presence of a pitch boresight misalignment, an increase in the vehicle's pitch leads to a decrease in the calculated z -values of the lidar points. Thus, as a quality control measure, each day a subset of the acquired bathy flight lines can have their points' associated vehicle pitch compared with their computed z coordinate for the sea surface height. If there is either a positive or negative correlation between the pitch and z -coordinate (as shown in Figure 67), then there is potentially a bias in the pitch boresight angle. The development of automated tools for performing such signature analyses is reserved as future work.

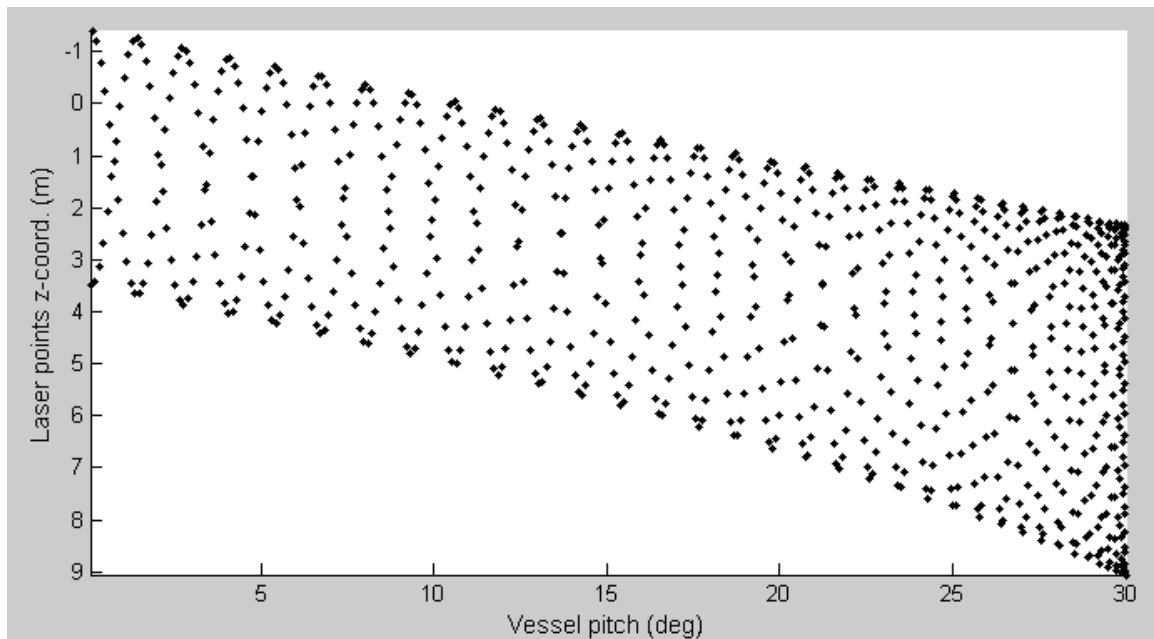


Figure 67. A sample signature analysis plot that compares each laser point's associated pitch with their calculated z -coordinate. The negative correlation between pitch and z -coordinate suggests a potential undetected pitch boresight misalignment in the lidar.

While increasing the altitude, vehicle roll or vehicle pitch will cause a biased point cloud to have a larger dispersion (and thus be easier to calibrate), the fact remains that no extraneous motion beyond the vehicle simply advancing in a straight line is necessary to determine the pitch boresight angle. A single flight line contains enough geometric information to determine the pitch boresight angle. As will be seen in the subsequent sections, the other calibration parameters are not so easily found.

6.1.2 – The Boresight Angles – Roll Axis

A misalignment in the roll boresight angle presents a unique problem with regard to this dissertation's proposed calibration strategy. The biased point cloud resulting from an unidentified error in the roll boresight angle will still be coplanar (Figure 69 – top). By introducing a roll bias, the entire point cloud, as acquired over a planar surface, is also rolled en masse. This implies it will be impossible to calibrate the roll boresight angle from a single, level flight line. Further, neither increasing the altitude (Figure 71 – bottom) nor permitting the vehicle to roll (Figure 69 – top) is a sufficient maneuver to make the biased points non-coplanar.

Allowing the vehicle to pitch does produce a very slight deviation from a coplanar point cloud (Figure 69 – middle). This minor deflection from coplanar implies that it may be possible to determine the roll boresight angle strictly with a flight line that exhibits a change in pitch; however, with system noise, the calibration routine is unlikely to produce a confident result. In this case, the roll boresight angle is said to be insensitive to the vehicle's pitch.

The only appreciable method of producing a non-coplanar point cloud is exhibited by allowing the vehicle to experience a change in heading (Figure 69 – middle). The

greater the change in heading, the less coplanar the point cloud becomes. While even a single flight line with a change in heading is sufficient, geometrically speaking, the strongest configuration for the calibration routine is provided by survey lines flown in opposing directions (Figure 70).

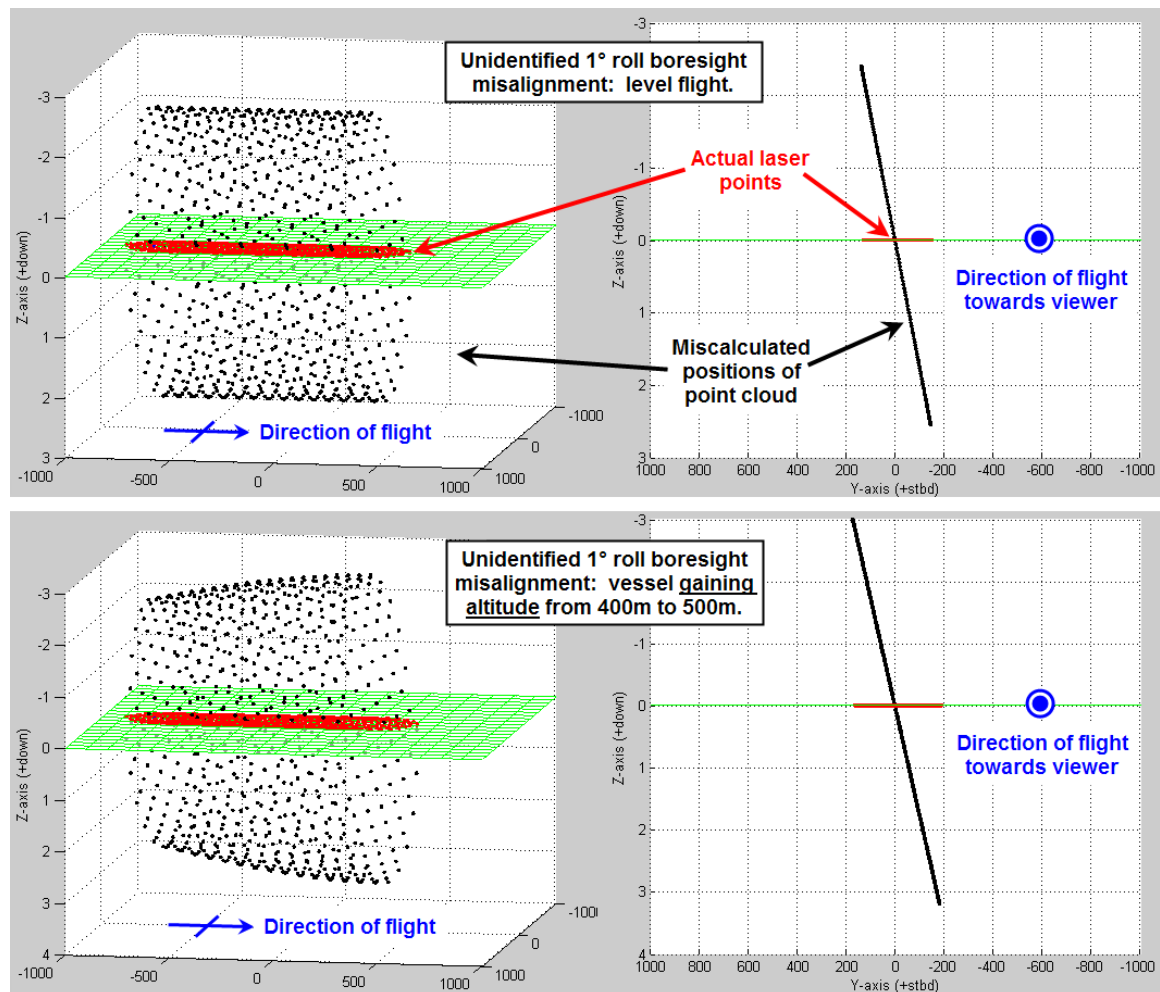


Figure 68. Visualization of a point cloud generated from a lidar with an unidentified 1° roll boresight misalignment (top), and a point cloud from the same system as it experiences an increase in altitude (bottom). The red points indicate the true laser strikes, while the black are the miscalculated biased points. All units in meters.

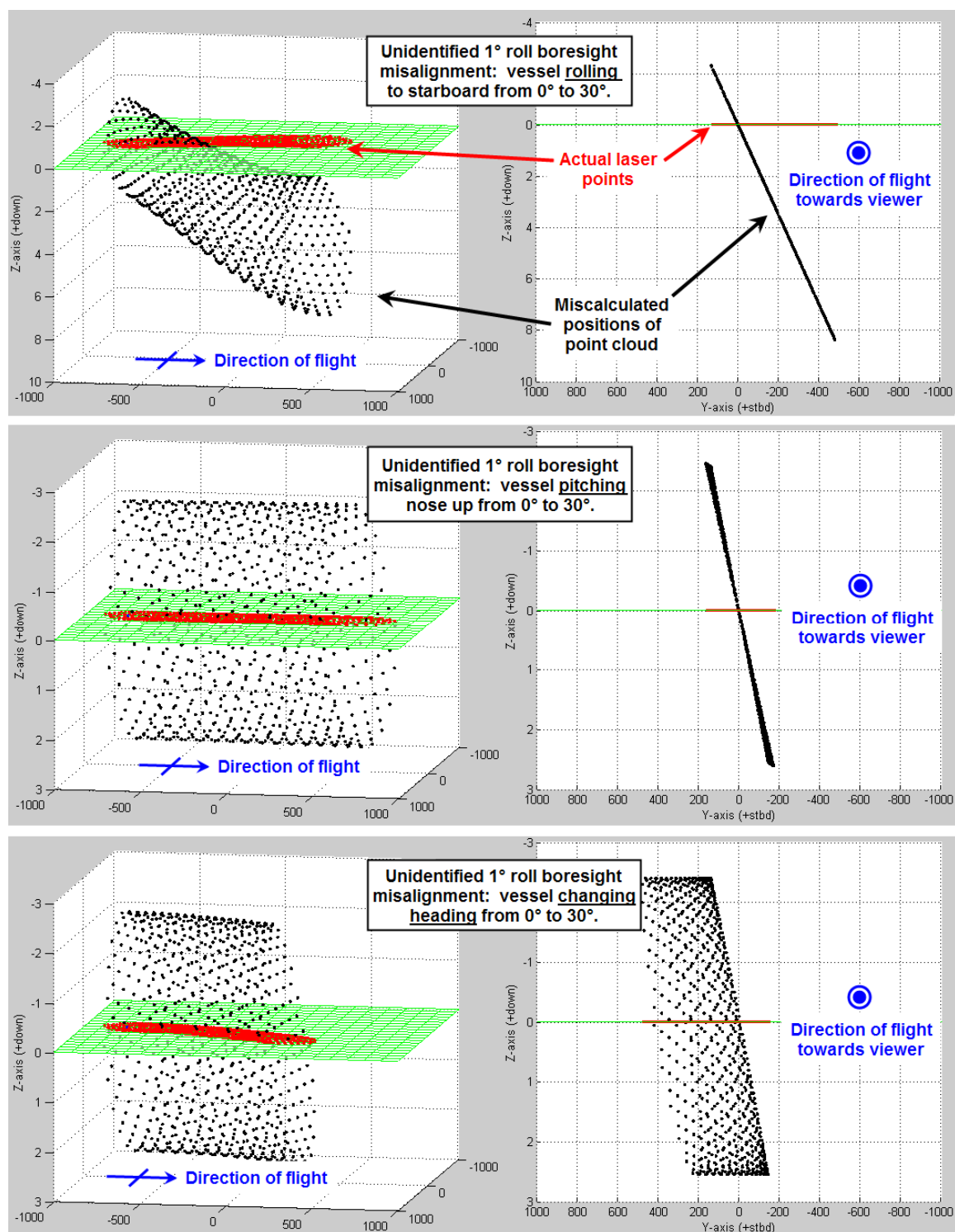


Figure 69. Signature analysis plots for a lidar with a 1° roll boresight misalignment in the presence of a rolling (top), pitching (middle) and yawing (bottom) vehicle. The red points indicate the true laser strikes, while the black are the miscalculated biased points. All units in meters.

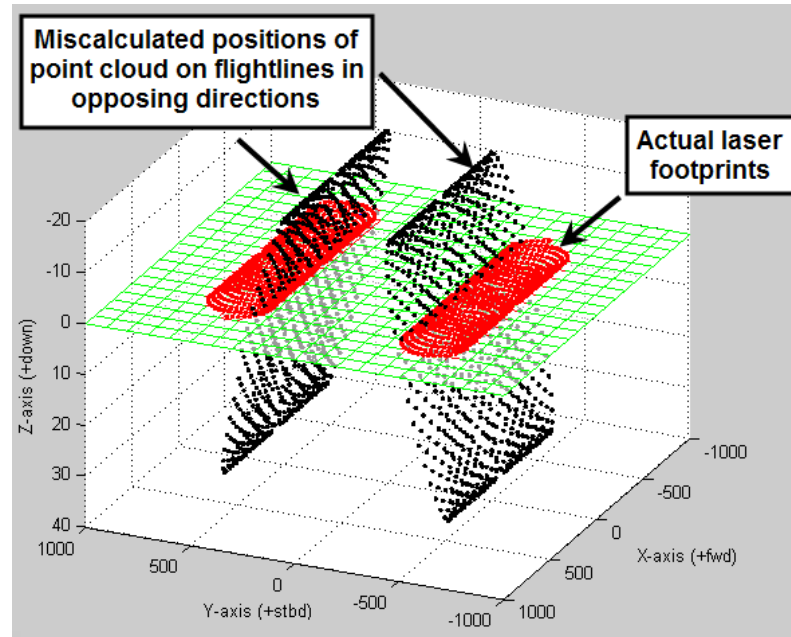


Figure 70. With a misalignment in the roll boresight angle, the best flight configuration for calibration is produced by flight lines in opposing directions. The red points indicate the true laser strikes, while the black are the miscalculated biased points. All units in meters.

As an aside, while permitting the vehicle to roll (Figure 69 – top) does not provide the geometric purchase to successfully implement the calibration LSA, one can again observe the principles of signature analysis. Much like the example in the previous section where a misalignment in the pitch boresight angle led to a strong correlation between the vehicle pitch and point cloud's z -coordinate; with a roll boresight misalignment, there appears to be a strong correlation between the vehicle roll and point cloud's z -coordinate. Further research is required to establish whether the magnitude of the roll boresight misalignment can be determined from such a signature analysis alone.

6.1.3 – The Boresight Angles – Yaw Axis

Similar to a misalignment in the boresight roll angle, a bias in the boresight yaw angle will still yield a coplanar point cloud. In contrast, however, the biased point cloud will lie within the correct ground plane (Figure 71 – top). Changing the vehicle's altitude

will also have little effect on the biased point cloud's coplanar status (Figure 71 – bottom). It should be mentioned that while the actual laser strikes and the biased points appear to be coincident in Figure 71, there is actually a horizontal shift among the points. The magnitude of this shift is a function of (among other things) the vehicle's altitude – higher altitudes leading to larger displacements (Figure 72).

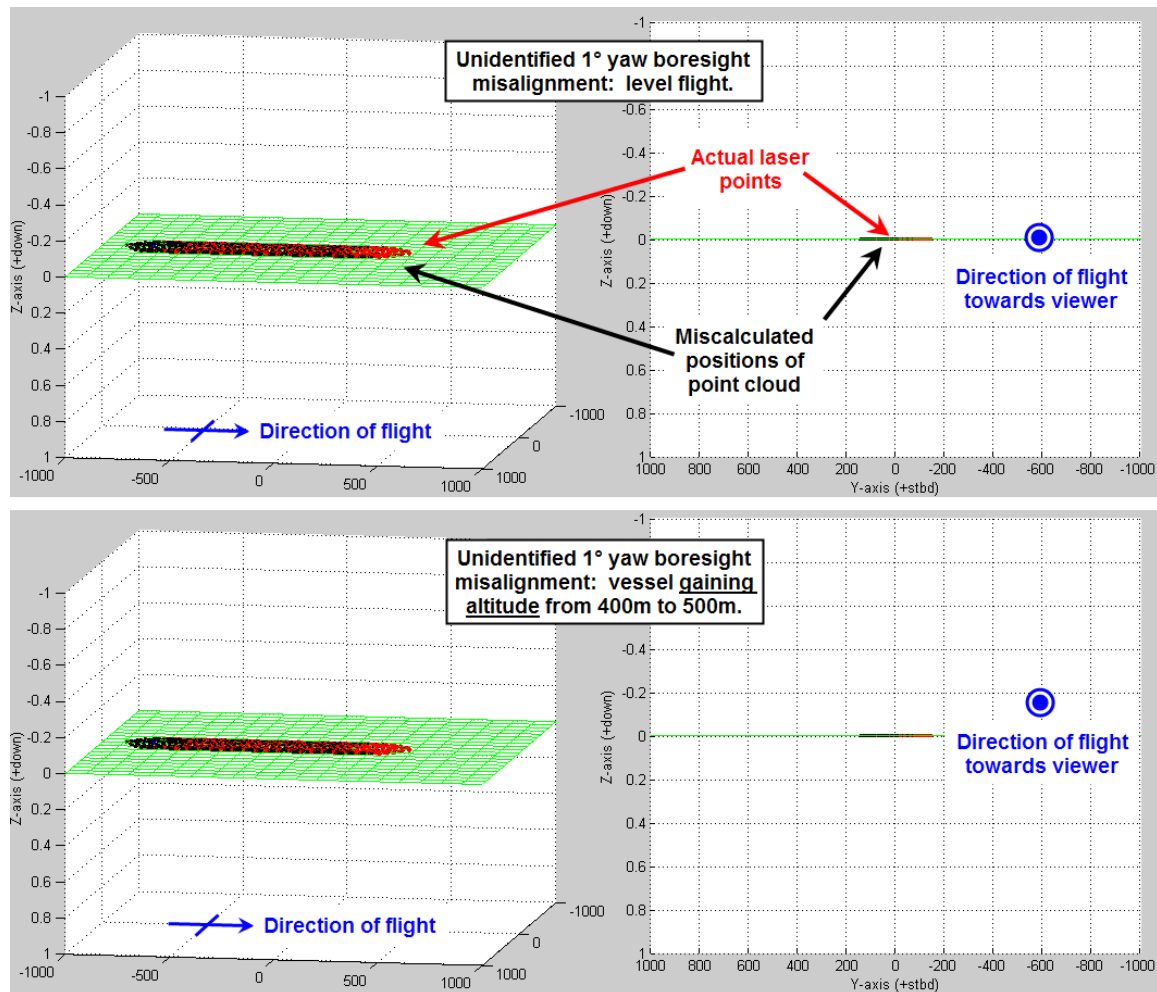


Figure 71. Visualization of a point cloud generated from a lidar with an unidentified 1° yaw boresight misalignment (top), and a point cloud from the same system as it experiences an increase in altitude (bottom). The red points indicate the true laser strikes, while the black are the miscalculated biased points. All units in meters.

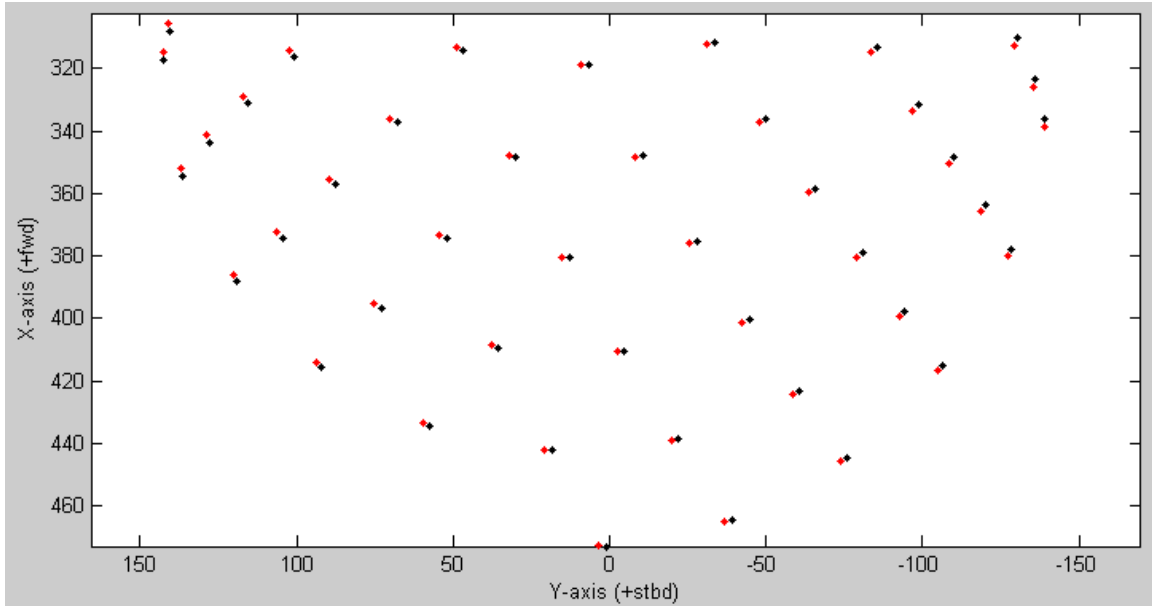


Figure 72. Top-down view of a point cloud (red) and its biased counterpart which contains an unidentified boresight yaw misalignment (black). All units in meters.

The key to determining the yaw boresight misalignment lies in having the vehicle either roll or pitch (Figure 73 – top and middle, respectively). Both changes in attitude lead to pronounced effects on the laser points, producing non-coplanar point clouds; thus, either is a candidate for inclusion in the design of a calibration flight configuration.

There is a distinct signature for the yaw boresight misalignment associated with the vehicle pitching (Figure 73 – middle). In a pitching vehicle, one side of the swath consistently has a large z -coordinate than the other side. A similar trend would also be seen were there a roll boresight misalignment (Figure 69 – middle); however, in the case of the yaw misalignment, this pattern is not exhibited in the presence of a rolling vehicle (in contrast to the roll misalignment). To summarize, if one side of the swath has a higher elevation than the other when the vehicle pitches, but not when the vehicle rolls, then the lidar may have a misalignment in the yaw boresight angle.

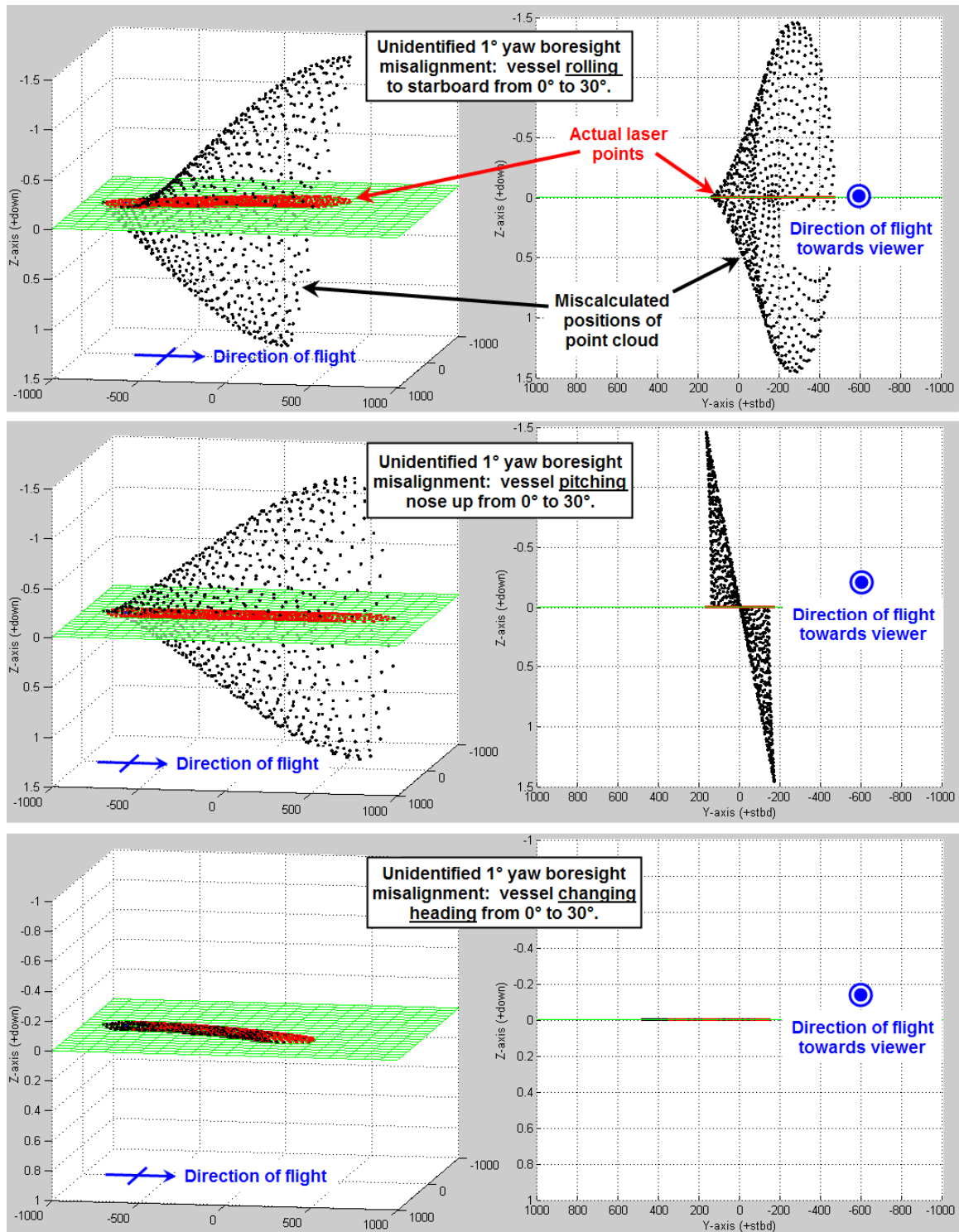


Figure 73. Signature analysis plots for a lidar with a 1° yaw boresight misalignment in the presence of a rolling (top), pitching (middle) and yawing (bottom) vehicle. The red points indicate the true laser strikes, while the black are the miscalculated biased points. All units in meters.

It may seem counterintuitive that it is possible to determine a yaw misalignment from a flat, featureless surface. In fact, so long as the vehicle has no change in attitude, it is not possible to determine a yaw misalignment; the key lies in changing the vehicle's attitude. As depicted in Figure 74, if a vehicle is pitching nose up, with no boresight misalignments, the greatest measured laser range will be produced from the forward-most beam (indicated in red). Were this same vehicle to have a yaw boresight misalignment, then the range from the forward-most beam would be erroneously assigned to an azimuth rotated about the scanner's central axis (indicated in orange) by the yaw angle from the forward direction (indicated in black). The end result would be a biased cloud that is sometimes below and sometimes above the actual ground plane. Again, the resulting non-coplanar nature of the point cloud is what permits the calibration by the least squares model.

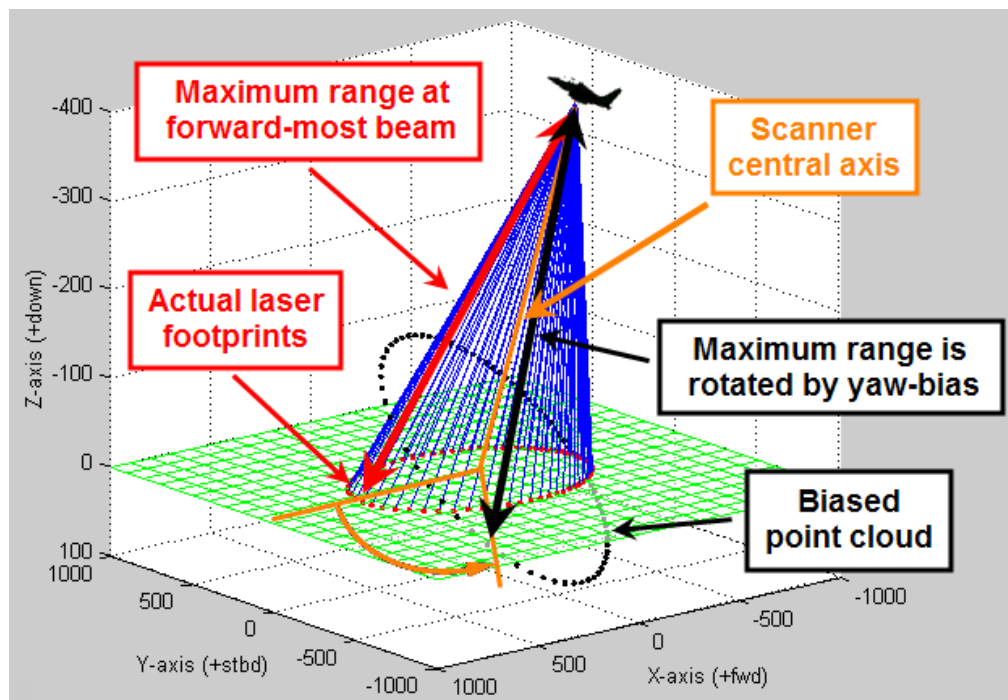


Figure 74. A vehicle pitching nose-up will measure the longest slant range in its forward-most beam (red arrow). If this same vehicle instead has a yaw misalignment, then the range previously associated with the forward-most beam will be rotated by the yaw angle bias (black arrow).

To summarize the calibration requirements for just the boresight angles: the pitch bias can be found simply by advancing the vehicle forward, the roll bias can be found with a change in vehicle heading, and the yaw bias can be found with a change in the vehicle's pitch or roll. Conceivably, all three parameters could be determined from a single flight line that exhibits both a dynamic roll and a change in heading. The greater the magnitude of the vehicle roll and the greater the change in the heading, the better the calibration routine will perform.

6.2 – The Calibration Module

Now that a basic acquisition strategy has been developed for the boresight angles, we will take a break from the signature analysis of the calibration parameters and instead introduce the calibration module. By considering the simplified calibration routine of only the three boresight angles, insights can be gained in how to interpret the algorithm's outputs; understanding topics like covariance, correlation, or the impacts of data density and vehicle dynamics. These lessons can then be applied to the incrementally more complicated calibration routine as a greater number of parameters are adjusted.

6.2.1 – Calibration Module Interface

6.2.1.1 – Defining the LSA inputs. The full graphical user interface for the calibration module is shown in Figure 75 (with close-up views shown in Figure 76 and Figure 77). Recall from Chapter V, the iterative formula for the least squares adjustment is given by (5.49):

$$\delta = - \left[\mathbf{C}_{x_0}^{-1} + \mathbf{A}^T (\mathbf{D} \mathbf{C}_\ell \mathbf{D}^T)^{-1} \mathbf{A} \right] \mathbf{A}^T (\mathbf{D} \mathbf{C}_\ell \mathbf{D}^T)^{-1} \mathbf{g}$$

where:

δ = iteration in calibration solution vector

C_{x_0} = initial estimate of uncertainties in adjusted (calibration) parameters

C_ℓ = uncertainties in observed (measured) parameters

A = design matrix with respect to observed parameters

D = design matrix with respect to adjusted parameters

g = initial guess for adjusted (calibration) parameters.

The three primary terms that must be specified by the user each time a calibration routine

is executed are the two variance-covariance matrices C_ℓ and C_{x_0} and the model

initialization, g . A and D are populated by the partial derivatives of the laser location

equation with respect to the observations and calibration parameters respectively, and one

should expect to have to modify these terms; however, it will be shown the user also has

a role in the construction of matrices. Each term's corresponding control within the

calibration interface will be illustrated in turn.

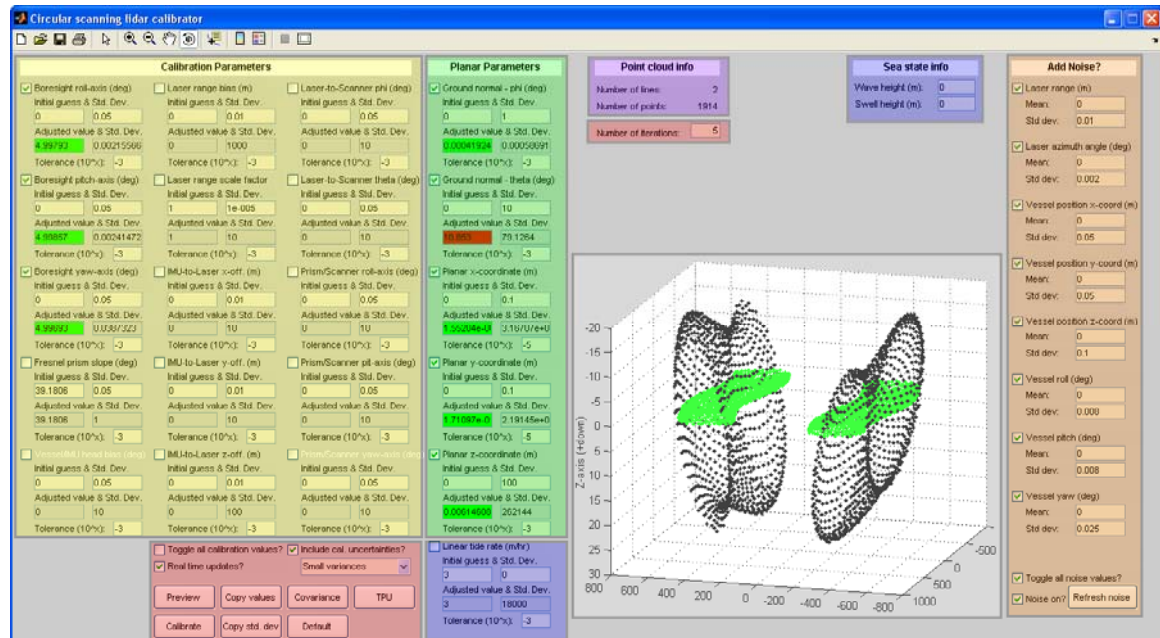


Figure 75. The lidar calibration interface. Close up views of the left and right portions are shown in the following figures.

Calibration Parameters			Planar Parameters	
<input checked="" type="checkbox"/> Boresight roll-axis (deg) Initial guess & Std. Dev. 0 0.05 Adjusted value & Std. Dev. 4.99793 0.00215566 Tolerance (10 ^x): -3	<input type="checkbox"/> Laser range bias (m) Initial guess & Std. Dev. 0 0.01 Adjusted value & Std. Dev. 0 1000 Tolerance (10 ^x): -3	<input type="checkbox"/> Laser-to-Scanner phi (deg) Initial guess & Std. Dev. 0 0.05 Adjusted value & Std. Dev. 0 10 Tolerance (10 ^x): -3	<input checked="" type="checkbox"/> Ground normal - phi (deg) Initial guess & Std. Dev. 0 1 Adjusted value & Std. Dev. 0.00041924 0.00058691 Tolerance (10 ^x): -3	
<input checked="" type="checkbox"/> Boresight pitch-axis (deg) Initial guess & Std. Dev. 0 0.05 Adjusted value & Std. Dev. 4.99857 0.00241472 Tolerance (10 ^x): -3	<input type="checkbox"/> Laser range scale factor Initial guess & Std. Dev. 1 1e-005 Adjusted value & Std. Dev. 1 10 Tolerance (10 ^x): -3	<input type="checkbox"/> Laser-to-Scanner theta (deg) Initial guess & Std. Dev. 0 0.05 Adjusted value & Std. Dev. 0 10 Tolerance (10 ^x): -3	<input checked="" type="checkbox"/> Ground normal - theta (deg) Initial guess & Std. Dev. 0 10 Adjusted value & Std. Dev. 10.853 79.1264 Tolerance (10 ^x): -3	
<input checked="" type="checkbox"/> Boresight yaw-axis (deg) Initial guess & Std. Dev. 0 0.05 Adjusted value & Std. Dev. 4.99893 0.0387323 Tolerance (10 ^x): -3	<input type="checkbox"/> IMU-to-Laser x-off. (m) Initial guess & Std. Dev. 0 0.01 Adjusted value & Std. Dev. 0 10 Tolerance (10 ^x): -3	<input type="checkbox"/> Prism/Scanner roll-axis (deg) Initial guess & Std. Dev. 0 0.05 Adjusted value & Std. Dev. 0 10 Tolerance (10 ^x): -3	<input checked="" type="checkbox"/> Planar x-coordinate (m) Initial guess & Std. Dev. 0 0.1 Adjusted value & Std. Dev. 1.55204e-01 3.16707e+0 Tolerance (10 ^x): -5	
<input type="checkbox"/> Fresnel prism slope (deg) Initial guess & Std. Dev. 39.1806 0.05 Adjusted value & Std. Dev. 39.1806 1 Tolerance (10 ^x): -3	<input type="checkbox"/> IMU-to-Laser y-off. (m) Initial guess & Std. Dev. 0 0.01 Adjusted value & Std. Dev. 0 10 Tolerance (10 ^x): -3	<input type="checkbox"/> Prism/Scanner pitch-axis (deg) Initial guess & Std. Dev. 0 0.05 Adjusted value & Std. Dev. 0 10 Tolerance (10 ^x): -3	<input checked="" type="checkbox"/> Planar y-coordinate (m) Initial guess & Std. Dev. 0 0.1 Adjusted value & Std. Dev. 1.71097e-01 2.19145e+0 Tolerance (10 ^x): -5	
<input type="checkbox"/> Vessel/IMU head bias (deg) Initial guess & Std. Dev. 0 0.05 Adjusted value & Std. Dev. 0 10 Tolerance (10 ^x): -3	<input type="checkbox"/> IMU-to-Laser z-off. (m) Initial guess & Std. Dev. 0 0.01 Adjusted value & Std. Dev. 0 100 Tolerance (10 ^x): -3	<input type="checkbox"/> Prism/Scanner yaw-axis (deg) Initial guess & Std. Dev. 0 0.05 Adjusted value & Std. Dev. 0 10 Tolerance (10 ^x): -3	<input checked="" type="checkbox"/> Planar z-coordinate (m) Initial guess & Std. Dev. 0 100 Adjusted value & Std. Dev. 0.00614608 262144 Tolerance (10 ^x): -3	
<input type="checkbox"/> Toggle all calibration values? <input checked="" type="checkbox"/> Include cal. uncertainties? <input checked="" type="checkbox"/> Real time updates? Small variances			<input type="checkbox"/> Linear tide rate (m/hr) Initial guess & Std. Dev. 3 0 Adjusted value & Std. Dev. 3 18000 Tolerance (10 ^x): -3	
Preview Copy values Covariance TPU Calibrate Copy std. dev Default				

Figure 76. A closer view of the left panel of the lidar calibrator. The calibration parameters are highlighted in yellow; the planar parameters are in green; and the GUI's control panel is in red. The tide control panel (shown in blue) will only appear if the user wishes to estimate the tide rate.

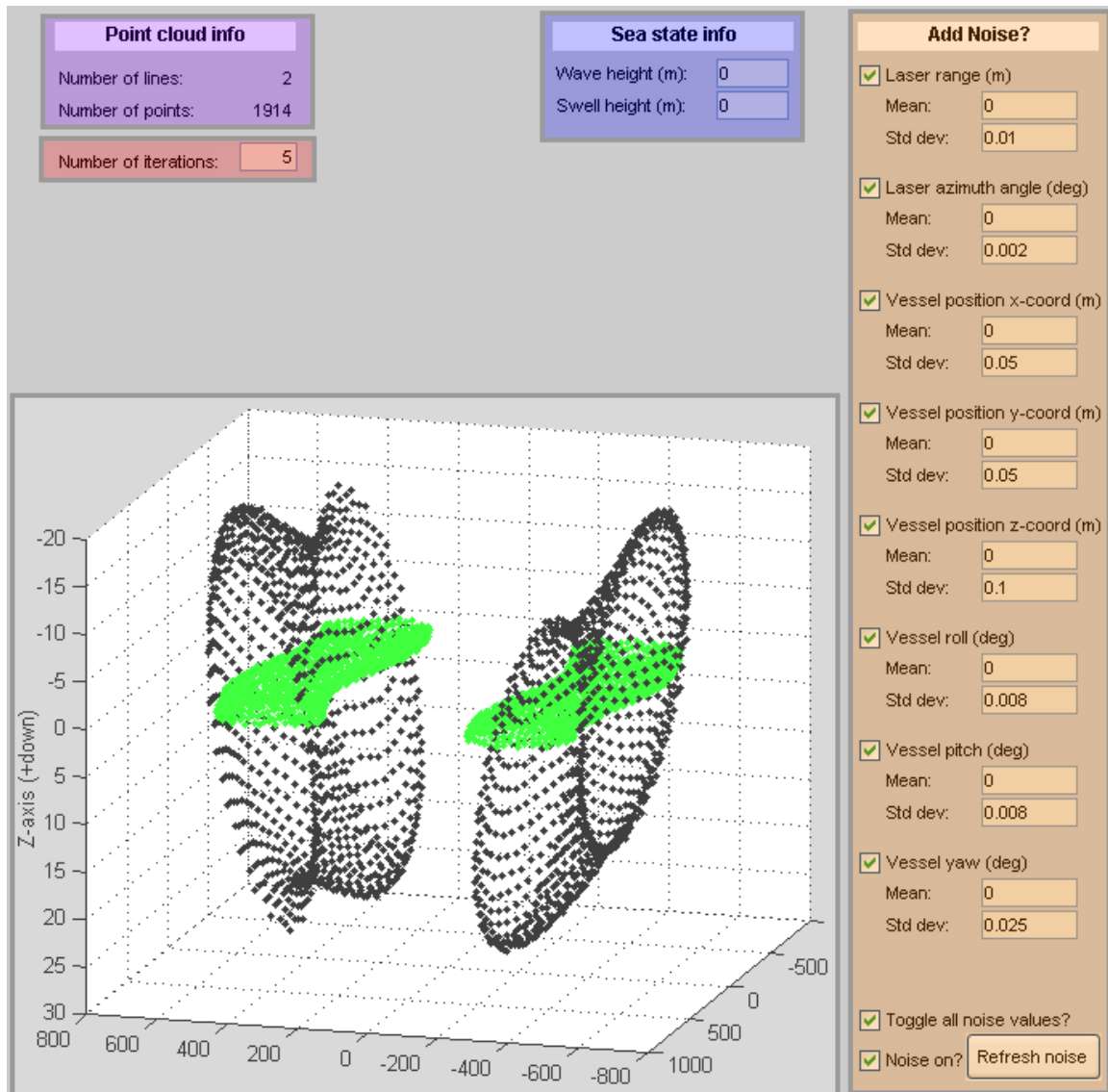


Figure 77. A closer view of the right panel of the lidar calibrator. Information about the point cloud size is highlighted in purple; input for the sea state (used for uncertainty calculations) is in blue; the uncertainty in the observables is shown in orange; the number of iterations performed by the least squares is in red; and the pre- and post-calibration point cloud is plotted in white.

The uncertainties in the measured quantities (laser range, scanner azimuth, etc.), used to populate the diagonal matrix C_ℓ , are modified under the “Std. dev.” fields for each observable (Figure 77 – orange). These values will largely be populated by the manufacturers’ specifications for the various components. As far as the calibration

routine is concerned, the greater the uncertainty of the input variables, the greater the uncertainty in the calibration solution. While the framework does exist for a different uncertainty for every single laser shot (e.g., the navigation software is capable of associating an uncertainty to each computed vehicle attitude measurement), this feature has not been implemented in the current calibration module and is recommended for future work.

The uncertainties in the observables also serve a secondary purpose within the calibrator. Because the calibration module was first designed to work with data generated by the simulation module, and because the simulator produces “error-free” datasets, a method was needed to test the calibrator’s performance on noisy datasets – given any dataset collected in the field will inherently contain some noise. By selecting the “Noise on?” switch, a normal distribution of noise is added to each of the observed parameters of the simulated point cloud (Figure 77 – orange). Not only can the user select the standard deviation of this normal distribution, but also the mean (in this way simulating the effects of biases in the system measurements). The user also has control over which parameters have noise applied by selecting the checkboxes to the left of each observable. Finally, the user may apply a new set of random values by selecting the “Refresh noise” button.

The initial guesses and the associated uncertainties for the calibration values and planar parameters are all set in the left hand side of the calibration window (Figure 76 – yellow and green, respectively). A close-up view of a single parameter is shown in Figure 78. The two white fields at the top labeled “Initial guess” and “Std. Dev.” will respectively be used to populate g and C_{x_0} . Below these fields are the “Adjusted value

& Std. Dev.” fields which display the results of the calibration. If the user wishes to see these values updated with every iteration of the LSA, then they should toggle the “Real time updates?” switch (Figure 76 – red).

<input checked="" type="checkbox"/> Boresight yaw-axis (deg)	
Initial guess & Std. Dev.	
0	0.05
Adjusted value & Std. Dev.	
4.99693	0.0387323
Tolerance (10 ^x): -3	

Figure 78. A closer view of the interface for a single parameter within the calibration module. An adjusted value highlighted in green indicates a convergence of the LSA to within the user-specified tolerance.

Because the LSA is an iterative process, it could theoretically be executed without end. The “tolerance” fields (Figure 78) are provided for the user to guide when the algorithm terminates. When successive iterations of the LSA produces a change in the adjusted calibration value that is less than the user-specified tolerance, the proposed calibration value will change from a red to green highlight. It is important to note that the LSA will not terminate its execution when all the calibration values are within tolerance; instead, it will iterate a fixed number of times as specified by the user (Figure 77 – red). A fixed number of iterations is included for two reasons: first, it prevents a poorly constructed LSA from entering an infinite loop; second, it puts the onus of interpretation of the LSA results on the user – not an algorithm. For example, consider the adjustment shown in Figure 76 in which the ground normal theta angle failed to converge to within the indicated tolerance. A human should observe that the ground normal phi angle is

nearly zero implying (in spherical coordinates) the theta angle is arbitrary, thus the LSA may be terminated, and the proposed calibration values accepted.

Should the LSA fail to converge after the first batch of iterations, the last iterated solution vector should be used as the initial guess for subsequent iterations. To quickly copy the outputs from the previous iteration, simply press the “Copy Values” button (Figure 76 – red). In a similar manner, the variances from the previous iteration can also be used to weight the confidence of these new initial guesses (the “Copy Std. Dev.” button).

6.2.1.2 – Coping with non-adjusted calibration parameters. Each parameter also has an associated checkbox which the operator may use to determine whether a given calibration parameter is included in the adjustment; however, there is a philosophical problem of what to do with the non-adjusting calibration parameters. For example, the calibration routine is capable of determining the slope of the Fresnel prism, but this slope may already be known by the prism manufacturer to a higher precision than the calibration routine is capable of estimating. Rather than wasting the computational resources on a “known” parameter, the user may wish to treat the slope as a constant and omit it entirely from the adjustment. Schmid & Schmid (1965) observe, however, that no measurement in and of itself is flawless and must therefore be included in the adjustment in such a way that the measurement’s uncertainty can contribute to the accuracy of the final result. Schmid and Schmid go on to propose that there are neither fixed variables nor free variables; there are merely variables with appropriate weights. If a user wishes to treat a variable as a constant, they should just affix an appropriately large weight to the variable. Similarly, there are not adjusted parameters and observed parameters, there are

merely “observations.” If a user wishes to treat a measurement as absolute, then they should again affix an appropriately large weight. What Schmid and Schmid neglect in their reckoning is the non-trivial cost to both the computer’s memory and processing time associated with retaining variables that might be considered nearly constant.

If a user does not wish to adjust one of the calibration parameters (because the value is presumably known from elsewhere), there are four methods for coping with the resulting non-adjusted calibration parameter. All four methods are possible to implement within the calibration module, but only the latter three are correct:

- Option A – Treat the non-adjusted calibration parameter as a constant, setting both the covariance terms and partial derivatives in \mathbf{C}_{x_0} and \mathbf{A} to zero.

To implement: Select the parameter in question and enter a standard deviation of zero.

Advantages: The “known” value will not change.

Disadvantages: Having a zero column in the design matrix, \mathbf{A} , will lead to a singular matrix within the adjustment equation which will cause the LSA to fail.

Overall assessment: This method should not be employed.

- Option B – Treat the non-adjusted calibration parameter as a constant and remove it from both the covariance and design matrices, \mathbf{C}_{x_0} and \mathbf{A} .

To implement: Deselect the parameter in question and deselect the “Include cal. uncertainties?” switch (Figure 76 – red). The latter switch has the effect of setting all unselected parameters to constants.

Advantages: The “known” value will not change. Computationally, it is the fastest method given no extraneous entries within \mathbf{C}_{x_0} and \mathbf{A} .

Disadvantages: The uncertainties of the “known” values are not carried forward.

Overall assessment: The LSA solution for the calibration parameters is unaffected by the uncertainty of non-adjusted calibration parameters (unlike the reported solution’s confidence). If the user only wishes the calibration values, but has no interest in the uncertainty, then this option is the fastest method.

- Option C – Leave the non-adjusted calibration parameters as calibration parameters and affix them with very large weights (small standard deviations).

To implement: Select the parameter in question and enter a very small (but non-zero) standard deviation.

Advantages: Uncertainties in the “known” values will be propagated forward.

Disadvantages: Because the values are being adjusted, they may wander from their “known” values. The algorithm will perform slower than Option B given the extraneous entries in \mathbf{C}_{x_0} and \mathbf{A} .

Overall assessment: Statistically speaking, this is one of the most valid approaches and provides the best estimate of the calculated uncertainties of the adjusted parameters.

- Option D – Redefine the non-adjusted calibration parameters as observed parameters and move their associated covariance and partial derivatives to \mathbf{C}_ℓ and \mathbf{D} .

To implement: Deselect the parameter in question, input the parameter’s standard deviation, and select the “Include cal. uncertainties?” switch (Figure 76 – red).

Advantages: Uncertainties in the “known” values will be propagated forward. The “known” values themselves will not change.

Disadvantages: The algorithm will perform slower than Option B given the extraneous entries in C_ℓ and **D**.

Overall assessment: This option is as statistically sound as Option C, the only difference between the two options being whether you want to allow the “known” values to also be adjusted.

By default, the calibrator uses both Options C and D (propagates the uncertainty of the “known” values) in its adjustment, depending on whether a given parameter is selected or not. Option B can also be achieved through Option D (i.e., some non-adjusted calibration parameters can be held constant while the uncertainties of the other non-adjusted calibration parameters are propagated forward); provided the “Include cal. uncertainties?” switch is selected and the non-adjusted calibration parameter is de-selected, then a standard deviation of zero may be input.

This roundabout method of Option B is mentioned because it illustrates the vast differences in the behavior of the user-defined standard deviations whether they are applied to an adjusted or non-adjusted calibration parameter. In short, the user wants to apply small uncertainties to the all the observed and non-adjusted calibration parameters (to associate a small uncertainty with the adjusted solution); however, the user wants to apply large uncertainties to the adjusted calibration parameters (to facilitate the rapid convergence of the LSA). In the extreme case, a standard deviation of zero can be applied to a non-adjusted calibration parameter which will treat the parameter like a constant. In contrast, a standard deviation of zero applied to an adjusted calibration parameter will cause the LSA to fail to converge (as in Option A). The uncertainties of all the calibration parameters (both those being adjusted and otherwise) can be quickly

toggled between “large” and “small” from the “Variances” dropdown menu (Figure 76 – red). “Large” and “small”, of course, are relative terms and set based on experience with the calibrator. For example, a “large” angular uncertainty would be 10° , while a “small” uncertainty would be 0.1° .

There is one final note regarding the handling of non-adjusted calibration parameters. It will later be shown (Sections 6.3.3.2 & 6.3.4.2) that some of the 15 proposed calibration parameters are linearly dependent upon each other. A full discussion here is unnecessary; let it be sufficient to say that if two parameters are linearly dependent upon each other, then only one may be calibrated (the other being a free parameter). Attempting to calibrate both will produce infinitely large values in the variance-covariance matrix. In such a case, Option C (holding the “known” values fixed by applying a large weight) will not work, since both of the alleged linearly dependent variables are being calibrated. Instead, the user must deselect one of the parameters in question (Option D) to allow the LSA to work.

6.2.1.3 – Boresight calibration examples and improving the output’s confidence.

In Section 6.1, a basic acquisition strategy was presented for the calibration of boresight angles based upon examination of the biased on the analysis of the signature analysis plots shown in Figure 65 through Figure 73. In short, a change in heading is necessary for the roll boresight angle, a change in vehicle pitch or roll is necessary for the yaw boresight angle, and only forward vehicle progress is needed for the pitch boresight angle. To test this calibration strategy a lidar was simulated at the anticipated acquisition speed (140kts with scanner at 1600rpms) and altitude (400m) with boresight misalignments of 5° in the pitch, roll and yaw axis and a 1m offset between the INS and

the laser reference frame in the fore-aft, port-starboard and up-down axes. The simulated laser was set to a pulse repetition rate of 51Hz (51 rather than 50 to mitigate aliasing of the scan pattern). The simulated flight lasted approximately 20 seconds (500 scanner revolutions or ~ 1000 laser points) and during the flight there was a dynamic change in the vehicle's heading and attitude; the vehicle experienced a roll oscillation, tilting from a level attitude to 5° to starboard to 5° to port and back to level (a similar $\pm 5^\circ$ sway in heading was also simulated). Finally, noise was added to all of the measured quantities using the uncertainties shown in Figure 77 (orange). An overview of the flight line is shown in Figure 79.

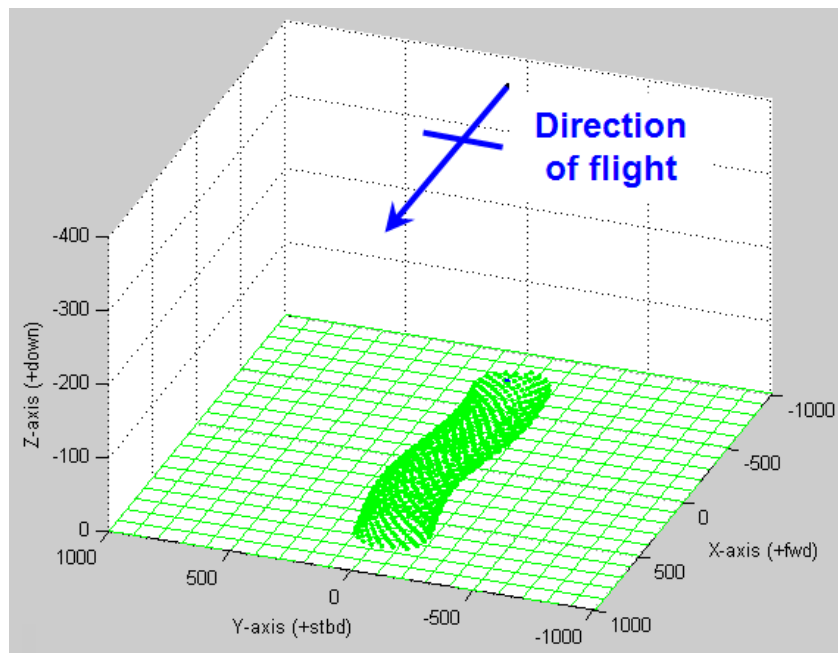


Figure 79. Proposed flight pattern for simplified (boresight) calibration. Scan pattern demonstrates both a 5° roll and 5° heading oscillation. All units in meters.

When performing the calibration of just the three boresight angles, the remaining 12 calibration parameters not being adjusted were converted to observations (Option D of Section 6.2.1.2). That is their uncertainties were propagated forward, but their values

were not allowed to change. The uncertainties used for these dozen parameters are as shown in Figure 76 (yellow) – 0.05° (1σ) for the angular measurements and 0.01m (1σ) for the range measurements. The results of the successful execution of the calibration are shown in Figure 80 (“successful” because the uncalibrated point cloud was correctly fit to the original planar surface shown in Figure 79 and the three boresight angles were properly identified to within their predicted tolerances). Given the acquisition plan and the input uncertainties, the boresight roll angle can be determined to within 0.025° , the pitch angle to within 0.004° , and the yaw angle to within 0.061° (all uncertainties reported as 1σ).

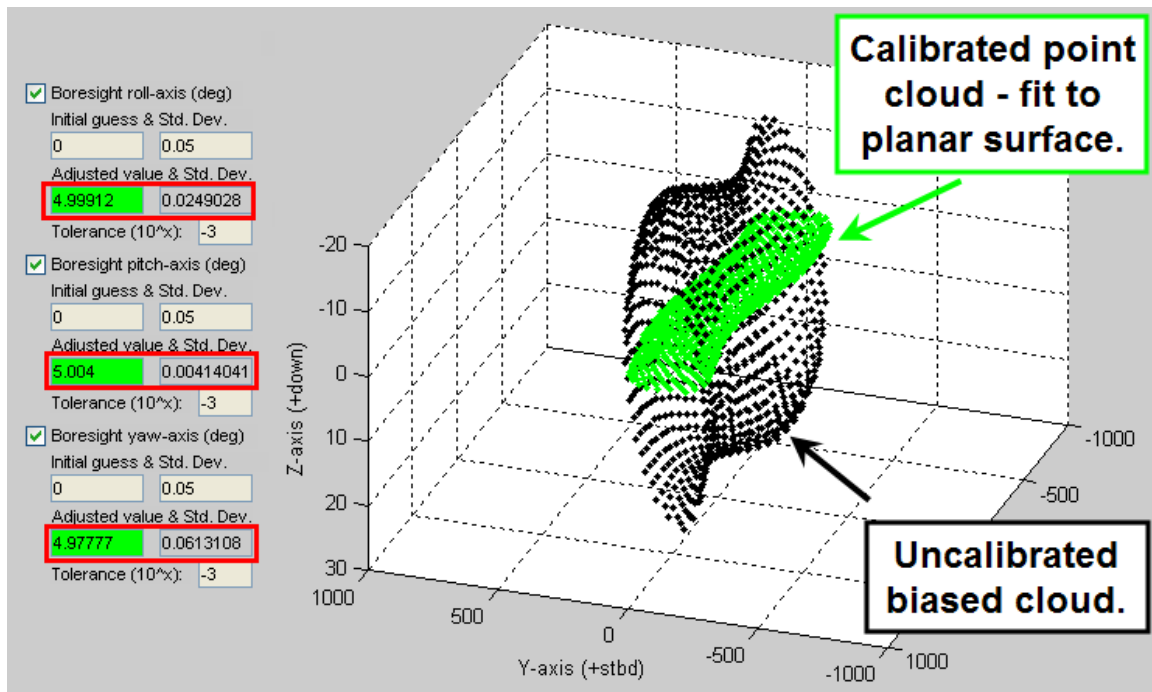


Figure 80. Output of calibration module: the boresight angles were recovered and the point cloud was successfully fit to the planar surface shown in Figure 79. All units in meters.

In the previous example, the pitch boresight angle had the highest confidence (smallest standard deviation), which should be expected after analysis of the signature

analysis plots – without any change in vehicle attitude, the pitch angle could be found while the other two require some dynamic change in vehicle orientation. Having demonstrated that the calibration routine does work, the next logical question becomes how to improve upon the confidence of the calibrator's output. Four basic strategies are proposed:

- A. Maintain the flight plan, but increase the data density.
- B. Increase the magnitude of the changes in vehicle attitude/heading.
- C. Add a second flight line with an opposing heading.
- D. Add a second flight line parallel, but separate, from the first flight line (to better describe the planar surface).

The results of all the proposed strategies are shown in Figure 81 and are discussed below.

	Acquisition Scheme	Number of data points	Confidence in solution (reported as a percentage of baseline confidence)		
			1 σ -roll	1 σ -pitch	1 σ -yaw
	Baseline (5° of dynamic vessel roll & yaw)	~950	0.025°	0.004°	0.061°
A1	2x laser repetition rate	~1,900	70.7%	70.6%	70.7%
A2	4x laser repetition rate	~3,800	50.0%	50.1%	50.0%
A3	10x laser repetition rate	~9,600	31.6%	31.6%	31.6%
A4	20x laser repetition rate	~19,000	22.4%	22.4%	22.4%
A5	40x laser repetition rate	~38,000	15.8%	15.8%	15.8%
A6	200x laser repetition rate (10Khz)	~190,000	7.1%	7.1%	7.1%
B1	Doubling the magnitude of the dynamic roll	~950	99.9%	100.9%	50.9%
B2	Doubling the magnitude of the dynamic yaw	~950	51.0%	89.4%	99.3%
C	Flying two reciprocal flight lines	~1,900	8.7%	58.3%	63.2%
D	Flying two parallel flight lines (same heading)	~1,900	9.0%	60.6%	63.5%

Figure 81. Table of results of boresight calibration trials under a number of different acquisition scenarios: increasing data density (A), increasing vehicle attitude (B), adding a reciprocal flight line (C) and adding a geographically separated line (D). All uncertainties are reported as a percentage of the baseline flight shown in Figure 80.

Strategy A – The baseline flight was simulated at 51Hz, while the hydro laser of CZMIL will be operating at 10KHz. This extra data density should help mitigate the

random noise associated with the sample measurements. Considering just flight “A1,” which had double the data density, the uncertainty of all three boresight angles was reduced to 70% of the previous levels. As the data density is increased (flights “A1” through “A6”) the confidence of the calibration values continually improves, culminating with a reduction in the baseline uncertainties by 93% at the operational speed of 10KHz. It is unequivocal; increasing the data density will improve the calibrator’s performance. The trade off to this performance in accuracy is the processing speed. All adjustments were terminated after 5 iterations. Line “A1” was processed in 20 seconds, while line “A6” took 32 minutes (and consumed over 1.3GB of the test computer’s RAM). In both cases, taking a ratio of the number of data points to the processing time reveals the algorithm can process one iteration of the LSA on 1,000 points in 2 seconds.

Strategy B – For flight “B1” the amplitude of the vehicle’s roll oscillation was increased from 5° to 10° . Under such flight conditions, there was no change in the reported confidence of the pitch and roll boresight angles; however the uncertainty in the yaw boresight was halved. None of these results should be surprising when taken in the context of the signature analysis plots of Section 6.1. Figure 73 (top) showed that the greater the change in the vehicle’s roll, the greater the dispersion of the biased point cloud in the presence of a yaw boresight misalignment (where a large dispersion implies a less coplanar state which implies an improved calibration performance). Conversely, Figure 66 (top) and Figure 69 (top) show that the biased point cloud changes very little with regard to vehicle roll in the presence of (respectively) pitch and roll boresight misalignments.

In the context of the signature analysis plots one should be able to anticipate the effect of increasing the amplitude of the vehicle's yaw oscillation (as is the case with flight "B2") on the boresight misalignments. Increasing the yaw has very little effect on a point cloud with a pitch or yaw bias (Figure 66 – bottom and Figure 73 – bottom, respectively); however, the biased point cloud displays a great deal of dispersion in the presence of a roll boresight misalignment as the vehicle experiences a larger change in heading (Figure 69 – bottom). Looking at the "B2" row of Figure 81 shows that the reported confidence in the pitch and yaw boresight angles are largely unaffected by vehicle yaw (there is a slight improvement in the pitch angle), while confidence in the roll misalignment is doubled (reduced to 51% of the baseline value). Inducing more dynamic changes in the vehicle's orientation will lead to a better determination of both the roll and yaw boresight angles.

Strategy C – Noting the marked improvement in the calibrator's performance when the attitude of the aircraft is changed, still greater changes in the vehicle's orientation can be attempted. There is a physical limit on how much a vehicle can pitch or roll (barrel rolls and loop-de-loops notwithstanding), but there is no such restriction on the vehicle heading. To test these "extreme" changes in heading, two flight lines are simulated over the same stretch of ground, but with opposite headings (Figure 81 – line "C"). Two flight lines imply twice the data coverage, so the results of this flight plan would be best compared to flight "A1" which had double the data coverage. Most notable is that the roll boresight angle has improved by a full order of magnitude over the baseline levels. Again, roll was expected to improve given how sensitive it is to the vehicle heading. The pitch boresight improves to 58.3% of the baseline level (compared

to 70.6% for flight “A1”), so the reversal of vehicle heading has also paid dividends with regard to pitch. The yaw boresight shows a slight improvement considering that twice the data of the baseline flight was acquired. This slight improvement is interesting given the yaw boresight angle is indiscriminate to changes in heading. This enhanced yaw boresight angle is possibly due to a transitive effect among the other variables; that is, because the calibrator is that much more confident in the roll boresight angle’s contribution to the misalignments there is less “doubt” with regard to the yaw boresight angle’s contribution.

Strategy D – For the final strategy, recall that the adjustment algorithm is fitting the point cloud to a planar surface. From a geometric perspective, a plane is best defined by a broad dispersion of points. For example, were all the points to lie along a single line, then there are an infinite number of planes that contain these points. As a less extreme case, a planar surface would be better defined when provided with a pair of parallel lines of data rather than just a single strip. To test the effects of “spreading” the laser points across the ground plane, two parallel flights were simulated with an 800m separation. Both flight lines still exhibited the 5° oscillation in roll and heading, but it should be emphasized that the base course for both flights were the same. That is, they were not flown in opposite directions as was the case with flight “C.” Once again, the confidence in the roll boresight angle has improved by an order of magnitude (9.0% of the baseline flight), which shows the roll boresight angle responds equally well to changes in heading or geographic distribution of points. The pitch and yaw boresight angles show slight improvements as well (about 90% of the reported confidences of the flight line with the double data density).

To summarize, all four proposed strategies showed improvements in the performance of the calibrator. Increasing the data density improved the confidence for all three boresight angles. In general, every time the number of data points is doubled, the standard deviations of the boresight angles are reduced by 29%. Increasing the vehicle's roll improved detection of the yaw boresight misalignment; whereas, increasing the vehicle's change in heading improved the confidence of the roll boresight misalignment (taking this concept to the extreme and allowing the vehicle to reverse direction led the greatest improvement of all). Finally, surveying over a broader area also improved all the boresight confidences (the roll value more than the others). Of course, the field crew is not limited to using only one of these proposed strategies. For a boresight calibration, the pilots should make an effort to create as dynamic a flight as possible acquiring at least two lines of data in opposite directions separated by some horizontal distance. Naturally, the full 10KHz data set should be used in the calibration (provided the computing resources exist).

An example of an idealized flight plan is shown in Figure 82. In anticipation of the 12 calibration parameters that have yet to be addressed, two additional flight lines have been added. Additionally, rather than require the vehicle to roll and yaw simultaneously (as in the previous example), each flight line focuses on a single maneuvering characteristics: heave, roll, pitch and yaw.

When the calibration routine is applied to the lidar from the previous example (5° boresight misalignments, 20 second flight lines, 51Hz pulse repetition rate, etc.) and is simulated navigating the cloverleaf pattern shown in Figure 82, the calibration results are

shown in Figure 83. Note the baseline flight has oscillations of 5° on the pitch, roll and yaw lines and a heave amplitude of 25m on the respective lines indicated in Figure 82.

As compared to the single flight line model “A2” of Figure 81 (which has the same number of data points as those in Figure 83), this more elaborate flight plan has a confidence in the roll boresight angle of 0.0015° (12% of “A2”) and 0.0017° in the pitch boresight angle (82% of “A2”). These improvements make sense given the cloverleaf pattern has flight lines with 4 different azimuths (and we know the roll boresight angle is very sensitive to a changing azimuth, pitch less so). Interestingly, the uncertainty in the yaw boresight misalignment is 19% larger than “A2.” It is unclear why the cloverleaf flight plan is so much worse for determining yaw. The most likely explanation is that line “A2” simultaneously rolled and yawed, creating a more extreme vehicle orientation with the cloverleaf pattern only one change in orientation occurs at a time.

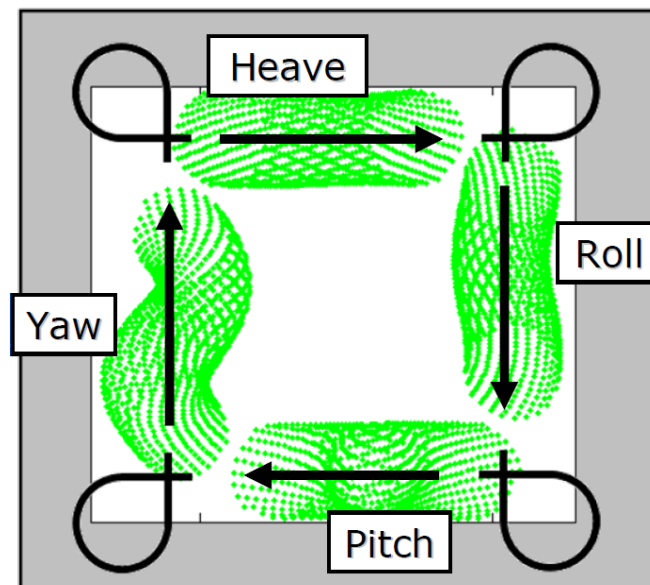


Figure 82. Overhead view of the cloverleaf acquisition flight plan designed to best determine the boresight misalignments. Each flight line has a different heading and a different dynamic vehicle characteristic.

Acquisition Scheme	Confidence in solution (reported as a percentage of baseline confidence)		
	1 σ -roll	1 σ -pitch	1 σ -yaw
Baseline (5° roll, pitch & yaw and 25m heave)	0.0015°	0.0017°	0.0363°
Doubling the laser repetition rate	70.9%	70.6%	70.7%
Doubling the magnitude of the dynamic heave	100.0%	100.0%	100.0%
Doubling the magnitude of the dynamic roll	99.2%	100.1%	65.7%
Doubling the magnitude of the dynamic pitch	100.3%	99.8%	61.9%
Doubling the magnitude of the dynamic yaw	100.0%	100.0%	100.0%

Figure 83. Table of results of boresight calibration trials along the cloverleaf flight pattern. All uncertainties are reported as a percentage of the baseline flight shown in Figure 82.

Once again, some additional maneuvers were considered to see if the reported confidence in the cloverleaf flight pattern could be improved upon. As in all the previous examples, doubling the data density reduced the uncertainty by 70%. Doubling the amplitude of the vehicle heave had no effect on improving the calibration routine (which makes sense in the context of the signature analysis plots which showed no response to heave). Doubling the magnitude of both the vehicle pitch or vehicle roll did lead to a marked improvement in the determination of the yaw boresight misalignment, which only serves to reinforce that the yaw misalignment is best served through large changes in vehicle attitude. Doubling the dynamic yaw had no effect on the boresight angles. This lack of impact due to vehicle yaw makes sense given the four flight lines already have varied headings spanning the four cardinal directions; an extra sway in heading isn't going to add anything, geometrically-speaking, to the solution.

All the flight patterns shown in Figure 81 and Figure 83 will be revisited when assessing the best method of determining the other calibration parameters.

6.2.2 – Covariance and Correlation Coefficients

Previously, when assessing the quality of a calibration solution resulting from a proposed flight plan, only the reported standard deviation of the proposed calibration

parameters was discussed: the logic being that the smaller the standard deviations, the better the calibration. This is only half of the uncertainty equation, as one must also consider the covariance entries of the variance-covariance matrix produced by the LSA. Of further importance in interpreting a flight plan are the correlation coefficients. The correlation is a measure of the dependence between two variables, x and y , and is defined by:

$$\rho_{x,y} = \frac{\sigma_{x,y}}{\sqrt{\sigma_x^2 \sigma_y^2}} \quad (6.1)$$

where:

$\rho_{x,y}$ = correlation between x and y

$\sigma_{x,y}$ = covariance between x and y

σ_x^2 = variance of x

σ_y^2 = variance of y .

All the quantities needed to compute the correlation are provided in the variance-covariance matrix \mathbf{C}_x (5.55). By nature of its definition, the correlation coefficient must assume a value between -1 and 1, where the closer the absolute value of $\rho_{x,y}$ is to 1, the greater the correlation among the parameters. In the context of the calibration, should variables have a large (positive or negative) correlation, then the calibration module was not given enough information to determine which calibration parameter to adjust to fit the point cloud to the planar surface. It should be noted that this does not imply the calibration routine was unsuccessful in fitting the point cloud to a plane, just that there was, potentially, more than one set of calibration values that would produce a coplanar point cloud.

To demonstrate how the covariance and correlation coefficient can be used in assessing the calibration, first consider the rolling/yawing line shown in Figure 80. The reported confidence in the calibration parameters, shown in Figure 81, were 0.025° , 0.004° and 0.061° (1σ) for the roll, pitch and yaw boresight angles, respectively. When the “Covariance” button (Figure 76 – red) is pressed, it launches the covariance/correlation coefficient visualization module. The default display for the module is the covariance (Figure 84).

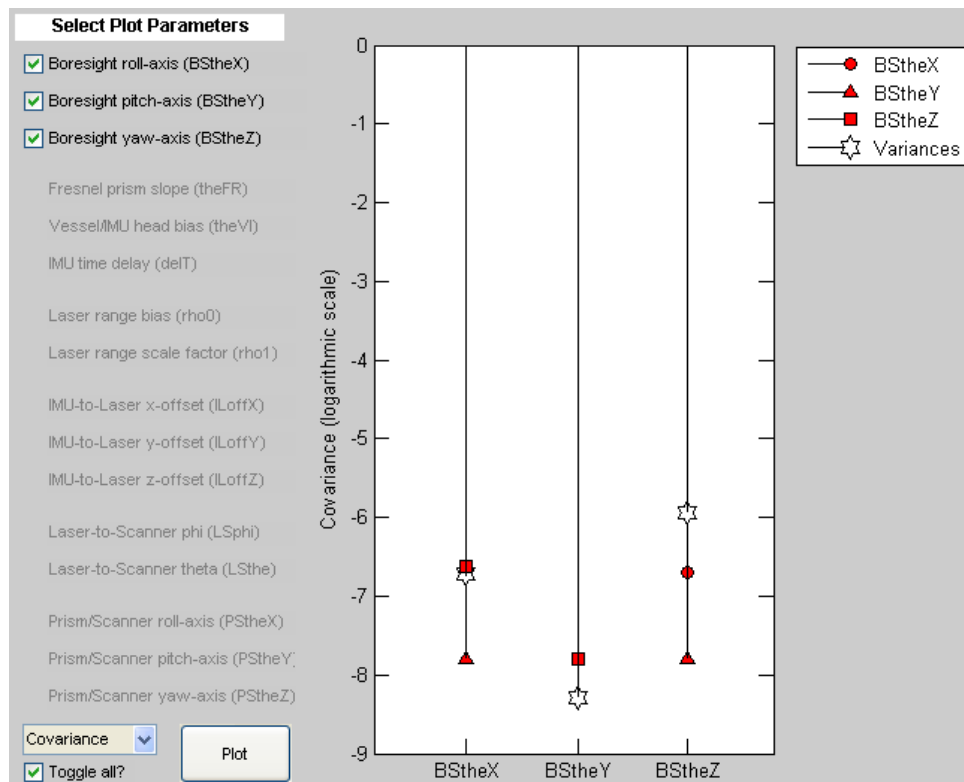


Figure 84. Variance-covariance visualization module. Variances indicated by stars and covariances by red symbols. Logarithmic scale is used.

A few notes about the covariance module: it plots the variances (not the standard deviations), all angular measurements are reported in radians (not degrees), and the vertical scale is logarithmic. The variances are indicated by stars. From the plot, we can

see the pitch boresight (BStheY) has the highest confidence (smallest variance) and the yaw boresight (BStheZ) has the least confidence (largest variance). The covariance terms are indicated by the different colored symbols. Because the yaw boresight had the largest variance, it is to be expected that the corresponding covariances with the other parameters will also be the largest (marked by the red squares). Similarly, the parameter with the smallest variance has the smallest associated covariances (marked by the red triangles). The correlation coefficient is used to normalize these covariances and see how the parameters are related. To toggle the plot to the correlation coefficient mode, select “Correlation” from the dropdown menu in the lower left and then press “Plot” to execute (Figure 85).

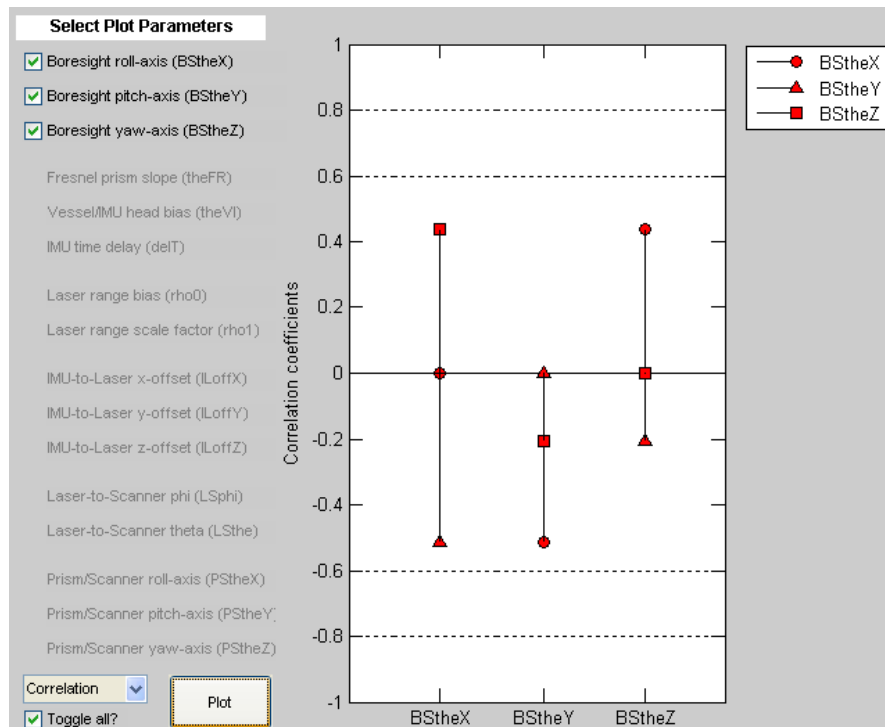


Figure 85. Correlation coefficient visualization module. No correlation had an absolute value larger than 0.5 indicating independence of the calibration values.

Interpretation of the correlation coefficients can be a subjective affair. A correlation of ± 1 indicates a dependence between the parameters, and a correlation of 0 indicates an independence of parameters. However, the cut-off between “weak” and “strong” correlations is not so well defined. That being written, such a black-and-white labeling of the correlations is not entirely necessary. For example, the correlations shown in Figure 85 seldom rise larger than 0.5; interpreted in conjunction with the covariances we can assess that the calibrator was confident in fitting the points to a plane (covariance plot) and there was no other combination of calibration parameters that could produce a planar surface (correlation plot). As an example of a poorly designed flight, consider the covariance and correlation plots shown in Figure 86 and Figure 87, respectively.

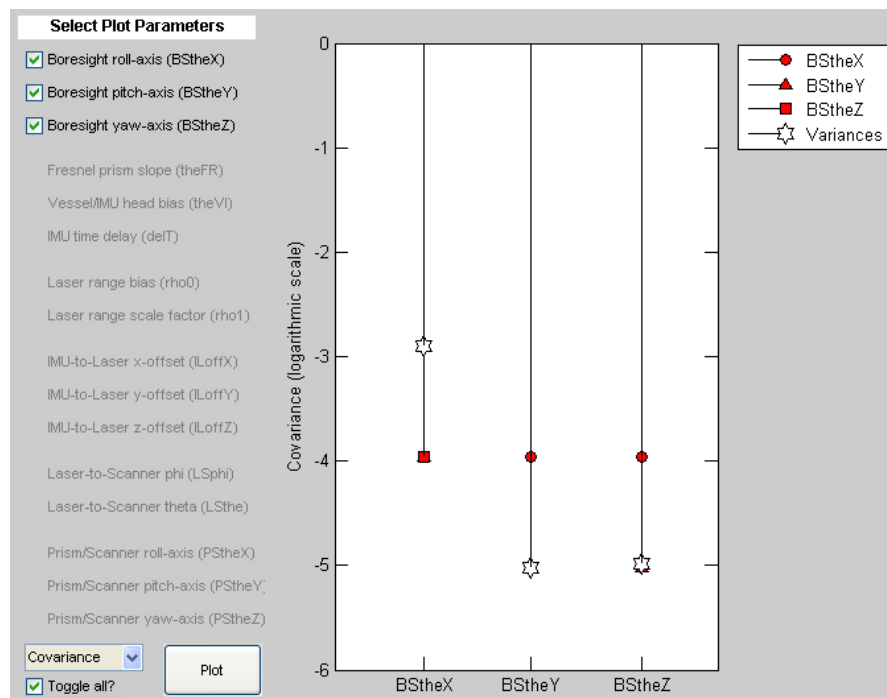


Figure 86. Variance-covariance visualization module for a poorly designed flight. Logarithmic scale is used.

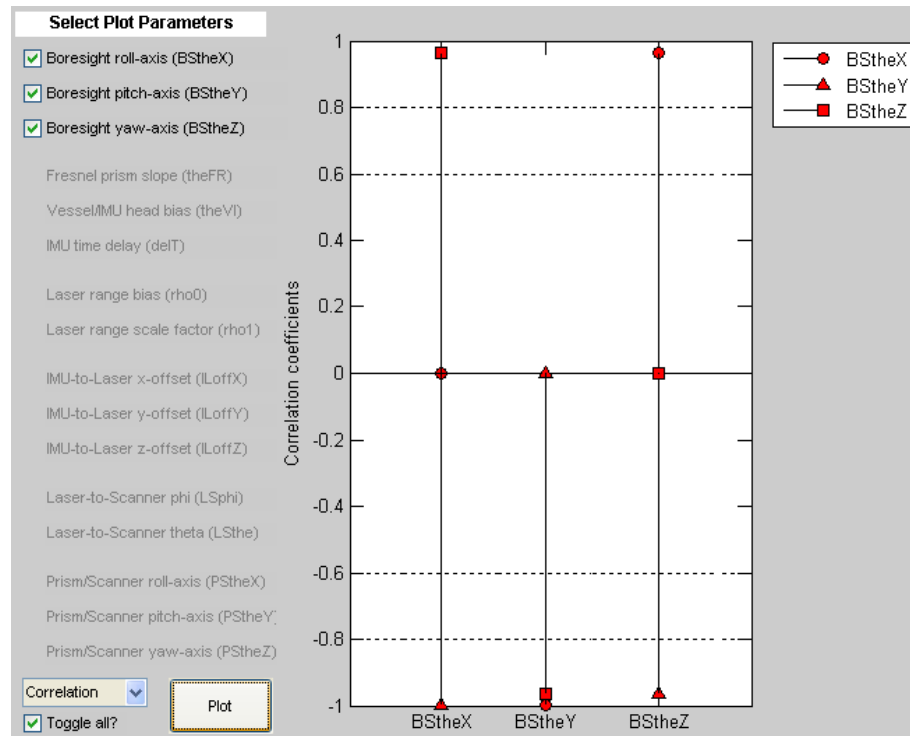


Figure 87. Correlation coefficient visualization module for a poorly designed flight. Note the positive correlation between the roll (red circle) and yaw (red square) boresight angles, and the negative correlation between the pitch boresight angle (red triangle) and both other calibration parameters.

To generate the above plots the baseline flight of Figure 81 was again simulated, only this time, rather than both rolling and yawing, the vehicle only experienced a pitch oscillation of $\pm 5^\circ$. Recall from the signature analysis plots that a pitching vehicle contains sufficient information to determine the pitch and yaw boresight angles (Figure 66 – middle and Figure 73 – middle); but will barely provide enough information for the roll boresight angle (Figure 69 – middle).

Our signature plots are confirmed in Figure 86 as the roll boresight angle has a covariance that is two orders of magnitude larger than the other two calibration parameters. Turning next to the correlation coefficients, Figure 87, we see the solution to every calibration parameter is linearly dependent on the other parameters (i.e., every parameter has a perfect positive or negative correlation). To see a correlation coefficient

of ± 1 implies that the point cloud was not geometrically “interesting enough” to reliably determine the calibration parameters involved. This could be because the vehicle’s motion was not dynamic enough (as in the previous case), because a group of parameters produce near identical effects on the point cloud (see Section 6.3.4.1), or, in the extreme case, a group of parameters are linearly dependent on each other (Section 6.3.3.2).

It is again emphasized that just because a set of calibration parameters have large covariances and high correlations among each other does not necessarily imply a “bad” calibration. While the goal of the calibrator is, naturally, to determine the lidar’s calibration parameters, the true purpose is to produce a geometrically correct point cloud with a small total propagated uncertainty. A collection of parameters with large variances, but also with large negative covariances, may still yield a point cloud with a relatively high confidence in the laser points’ positions (the ultimate measure of success for the lidar’s calibration). Such a claim, however, cannot be fully explained until topics like the point cloud total propagated uncertainty and covariance are addressed – see Section 7.2.2.2.

6.3 – Signature Analysis of the Remaining Calibration Parameters

The remaining 12 calibration parameters will now be systematically analyzed for their sensitivity to the vehicle heave, roll, pitch and yaw.

6.3.1 – *The Prism Slope*

As more non-zero misalignments are introduced in the lidar’s configuration, there will be a greater chance for interaction among the parameters. We will first consider a lidar with no misalignments other than a bias in the prism slope (i.e., all boresight angles will be 0°), to get a sense of the impact the prism slope alone. Afterwards, some

non-zero boresight angles will be included to show how/if they interact with the prism slope.

The anticipated prism slope is 39.18° , based on a desired laser nadir angle of 20° (from [3.21]). To test the structure of the biased point cloud, a misalignment of 0.1° is introduced to the prism slope (Figure 88 – top). The biased cloud does experience a vertical shift; however the point cloud itself is still coplanar, suggesting some vehicle maneuvering will be required to calibrate the prism slope.

Introducing a vehicle heave does succeed in making the point cloud non-coplanar (Figure 88 – bottom). Further a useful signature is seen with regard to a changing vehicle altitude. In the presence of an unidentified bias in the prism slope, the calculated z -values of the point cloud get successively lower.

Signature plots for the prism slope as the vehicle rolls, pitches and changes heading are shown in Figure 89 (top, middle and bottom, respectively). Changes in either the vehicle's roll or pitch attitude lead to pronounced changes in the biased point cloud. In both cases, the clouds are distinctly non-coplanar suggesting either maneuver is a viable method for determining the prism slope. Changing the vehicle heading, on the other hand, is unsuccessful in creating a non-coplanar point cloud and is of no use in calibrating the prism slope.

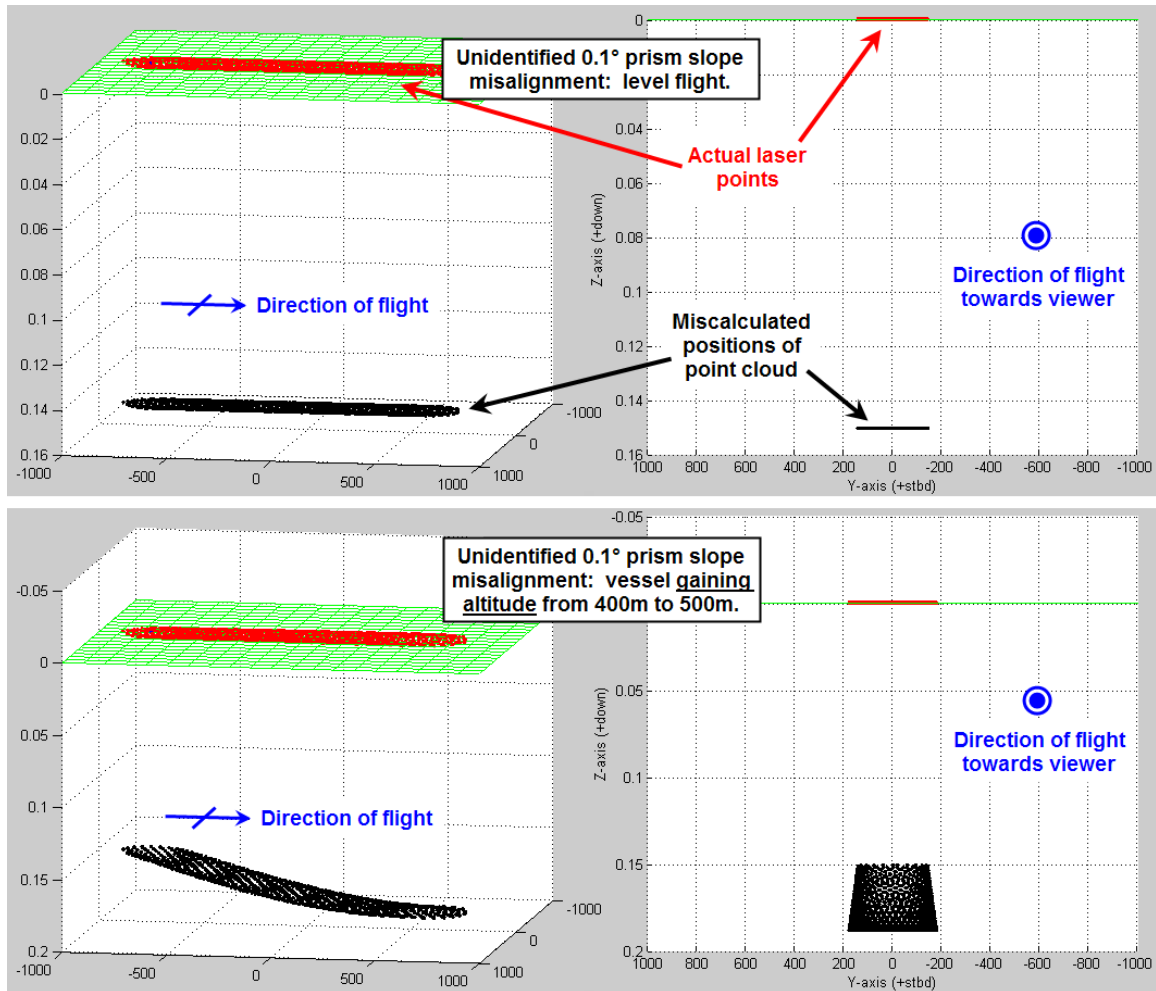


Figure 88. Visualization of a point cloud generated from a lidar with an unidentified 0.1° prism slope misalignment(top), and a point cloud from the same system as it experiences an increase in altitude (bottom). The red points indicate the true laser strikes, while the black are the miscalculated biased points. All units in meters.

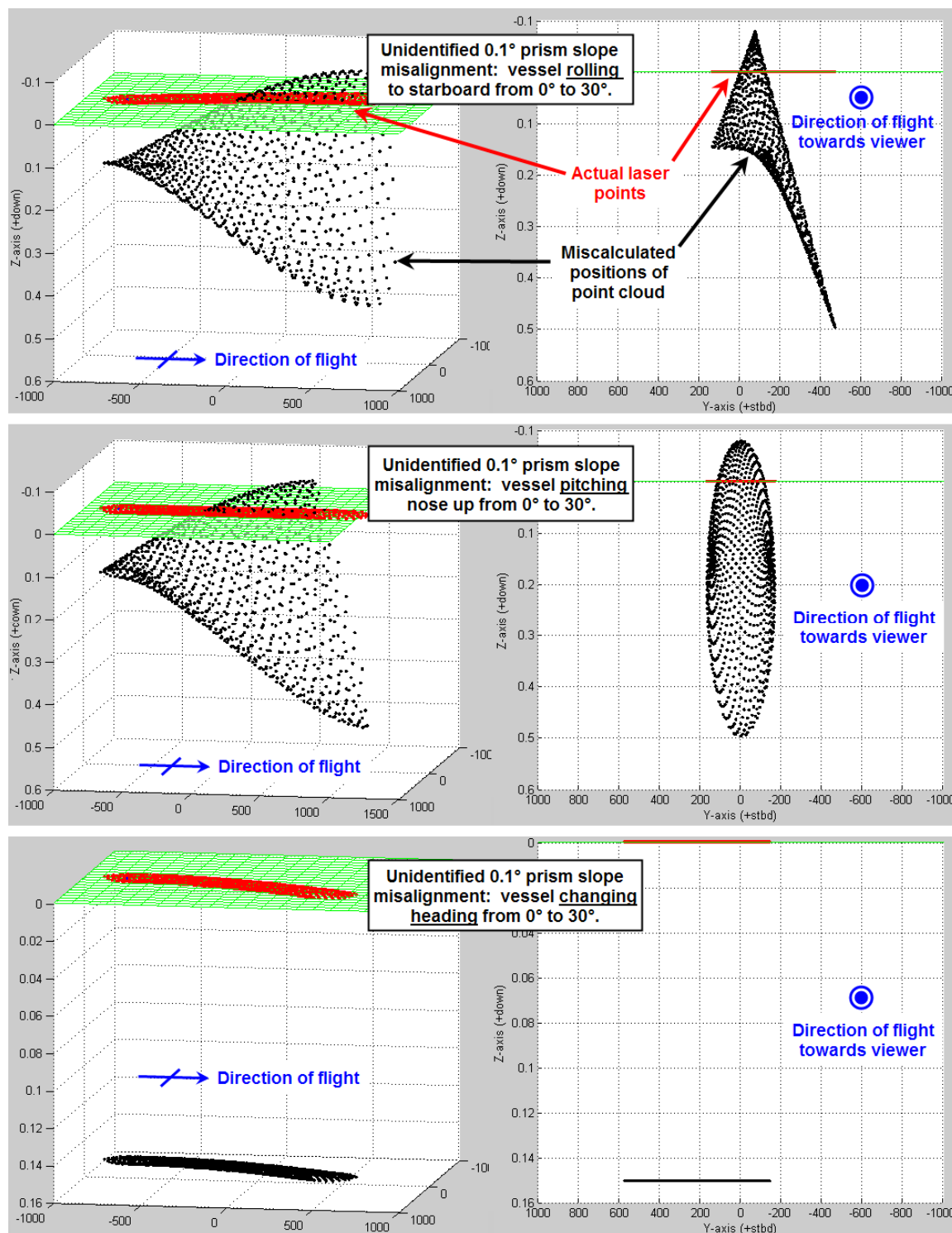


Figure 89. Signature analysis plots for a lidar with a 0.1° prism slope misalignment in the presence of a rolling (top), pitching (middle) and yawing (bottom) vehicle. The red points indicate the true laser strikes, while the black are the miscalculated biased points. All units in meters.

If one were to consider only the above signature analysis plots, then one would think the only way to calibrate the prism slope is through a heaving, rolling or pitching vehicle. However, the previous plots were rendered based upon the assumption that the lidar had an unknown bias in the prism slope, but no other system misalignments (known or unknown). Figure 90 recreates the level flight shown in Figure 88 (top), this time adding some non-zero boresight angles. It should be emphasized the boresight angles in this simulation are known, therefore the miscalculated positions of the lidar points can be attributed exclusively to the unknown bias in the prism slope. Through the addition of the non-zero boresight angles, even a level flight contains enough geometric information to calibrate the prism slope (notice the non-coplanar biased point cloud in Figure 90). Much like a change in the vehicle's attitude, the more extreme the geometry of the lidar's boresight angles, the easier it is to calibrate both the prism slope and the boresight angles themselves.

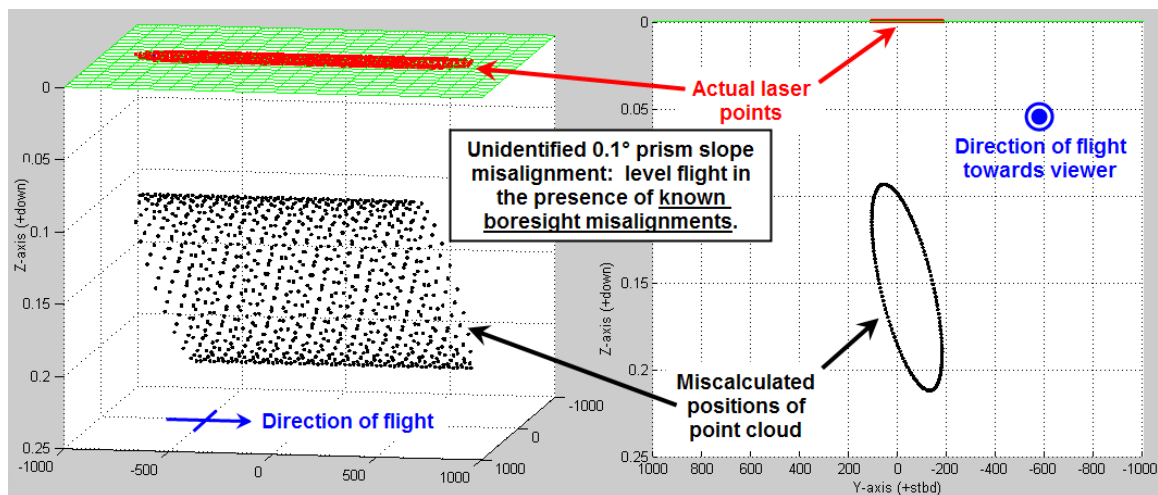


Figure 90. Visualization of a point cloud generated from a lidar with known non-zero boresight angles and an unidentified 0.1° prism slope misalignment. The red points indicate the true laser strikes, while the black are the miscalculated biased points. All units in meters.

As a baseline, when the single, straight flight shown in Figure 90 was calibrated exclusively for its prism slope, the reported confidence was 0.022° (1σ). In all previous boresight calibration trials, when the point cloud data density was doubled the reported uncertainties were reduced by approximately 30%. Doubling the data density also leads to a 30% reduction in the uncertainty for the prism slope (Figure 91 – Line “A”).

Based on the signature analysis plots in Figure 88 and Figure 89, we should anticipate a slight improvement in the prism slope calibration in the presence of vehicle heave, a large improvement in the presence of vehicle pitch or roll, and no improvement when presented with a change in heading (based on the dispersion of the point clouds). All four of these suppositions are correct (Figure 91 – Lines “B1” through “B4”).

The final technique for improving the calibration performance is adding a second set of data points geographically separated from the first, to better define the ground plane. Increasing the distribution of the data points across the ground has a greater contribution to improving the calibration routine than any of the previous suggestions (Figure 91 – Line “C”).

	Acquisition Scheme	Number of data points	Confidence in solution (reported as a percentage of baseline confidence)
			1σ - Prism slope (deg)
	Baseline (with 5° boresight angles)	~950	0.022°
A	Double data density	~1,900	70.6%
B1	Heaving vessel ($\pm 25\text{m}$)	~950	95.6%
B2	Rolling vessel ($\pm 5^\circ$)	~950	83.6%
B3	Pitching vessel ($\pm 5^\circ$)	~950	87.0%
B4	Yawing vessel ($\pm 5^\circ$)	~950	99.1%
C	Two parallel flight lines (same heading)	~1,900	52.0%

Figure 91. Table of results of prism slope calibration trials under a number of different acquisition scenarios: increasing data density (A), increasing the vehicle’s dynamic motion (B), and adding a geographically separated line (C). All uncertainties are reported as a percentage of the baseline flight shown in Figure 90.

To demonstrate how the prism slope interacts with the boresight angles within the calibrator, the baseline flight in Figure 81 (a single line with $\pm 5^\circ$ roll and yaw oscillation) is revisited. This time, the three boresight angles and the prism slope will be calibrated simultaneously. Interestingly, although the vehicle experiences a dynamic change in roll (something that should improve the confidence in the prism slope), the prism slope uncertainty actually grows by 4%. This is an example of a distributed uncertainty – the more parameters that are being adjusted, the greater the number of options the LSA has in fitting the point cloud to a planar surface, and the less confident it can be in any one solution.

Figure 92 shows the correlation among the four parameters. In this case, there is a large negative correlation between the boresight pitch angle and the prism slope. When there is a large correlation between parameters, the calibration algorithm can have difficulty distinguishing which parameter is the true culprit for the non-coplanar status of the point cloud. To put it another way, suppose a particular calibration parameter is not adjusted in the LSA and held to a fixed, but incorrect, value. Should this parameter have a large correlation with another parameter that is being adjusted, then this second parameter can compensate for the erroneous value of the first parameter. It is similar to determining the length and width of a rectangle of known area; if the length is recorded incorrectly, the width can compensate to assure that the area is correct. In the case of the calibration, we are not computing areas of rectangles, but fitting points to a planar surface; if one parameter (say the prism slope) is recorded incorrectly, then other parameters with high correlations can compensate to make sure the points will still fit to the planar surface.

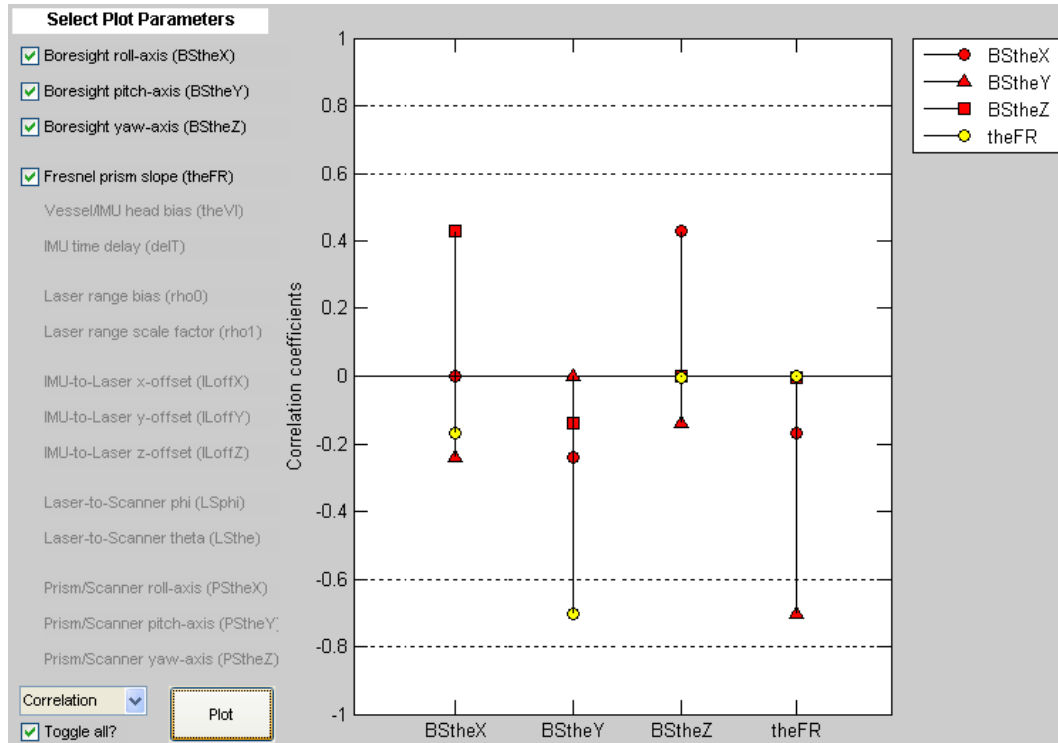


Figure 92. Correlation coefficients from a single flight line (shown in Figure 80) in which the three boresight angles and prism slope are adjusted. Note the large negative correlation between the pitch boresight (red triangle) and prism slope (yellow circle).

To illustrate the concept of compensation in the presence of correlation, consider Figure 93, which shows the results of two attempted calibrations. In both cases, the point cloud used to generate Figure 92 was employed. Also in both cases, only a single parameter was calibrated: the pitch boresight angle (in red) and the yaw boresight angle (in black). The boresight angles that were not being calibrated were fixed at their correct simulated values, while the prism slope was fixed at a value that was intentionally 0.1° smaller than its actual value. The question is then whether either the pitch or yaw boresight angles overcome this incorrect input. In Figure 93, notice that the point cloud in which the pitch boresight angle was adjusted (shown in red), both better described a planar surface (having a smaller dispersion about the proposed plane) and described a planar surface closer to the true horizontal surface. This is directly related to the fact that

pitch boresight angle had the larger correlation with the prism slope. Note also that because the two parameters were negatively correlated, holding the prism slope at a value smaller than its actual value, the pitch boresight compensated by being larger than its actual value.

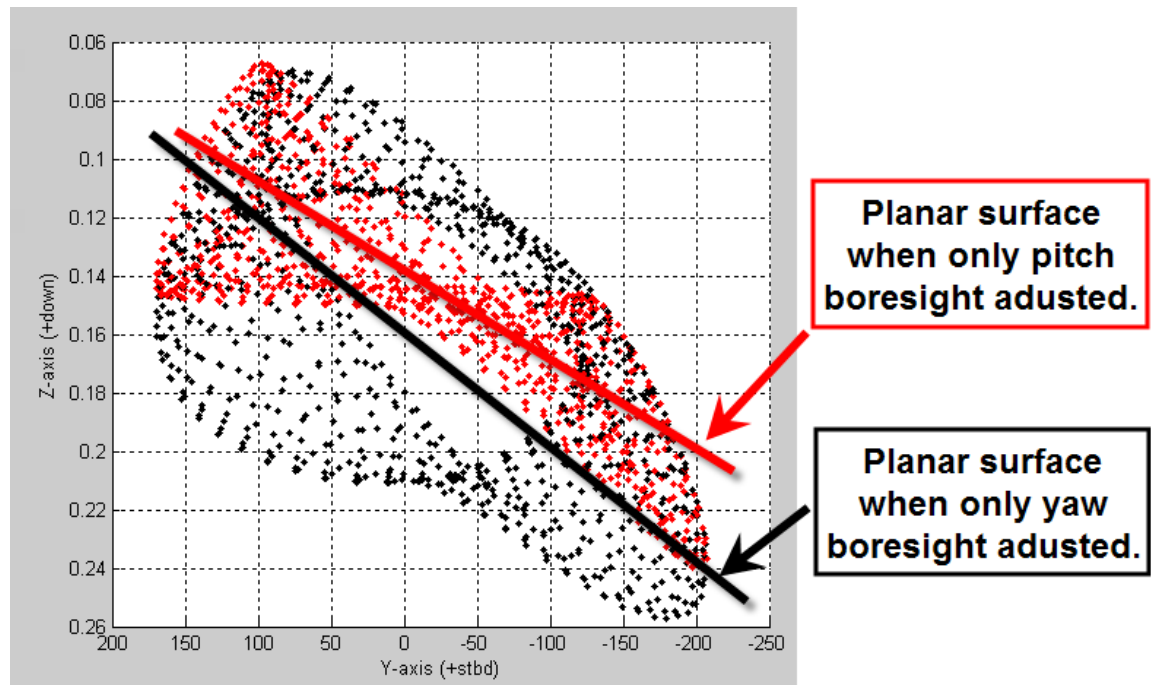


Figure 93. Two attempts at calibrated point clouds produced when the prism slope was held fixed at an incorrect value and only the pitch boresight angle (red) and yaw boresight angle (black) were adjusted. Note the pitch point cloud is slightly more coplanar and describes a plane closer to horizontal.

The ramifications for the end user are that if they ever want to withhold a parameter from the calibration routine (believing the value to be “known”), and if there is any chance the value they input for this parameter is incorrect, then they will best be served if this parameter has a high correlation with some other parameter which can compensate for the incorrect value. Conversely, parameters with high correlation coefficients can be set in advance with less risk to producing a poor calibration result.

Taken to the extreme, parameters with a perfect correlation (i.e., those that are linearly dependent on other parameters) can and should be removed from the calibration with no penalty to the quality of the calibration solution – even if the user sets these parameters to an incorrect value, the LSA will compensate. The concept of one parameter compensating for another will be revisited when discussing the VRF-to-INS heading misalignment (Section 6.3.3.1). The moral, however, should be to permit the calibration algorithm to determine all of the calibration parameters (rather than risking the input of an incorrect value).

6.3.2 – Laser-to-Scanner Alignments

The laser-to-scanner alignments describe the two angles (ϕ_{LS} and θ_{LS}) in spherical coordinates used to describe the direction in which the laser is entering the prism-scanner assembly (see Figure 19). We begin with the customary signature analysis plots given an unidentified misalignment of 1° in the ϕ_{LS} and no other non-zero calibration parameters. What is most interesting with regard to the ϕ_{LS} signature plots (Figure 94 and Figure 95) is they are mirror images (reflected about the z -plane) of the pitch boresight signature plots (Figure 65 and Figure 66). The plots would be nearly identical were a -1° ϕ_{LS} angle to be plotted instead. This similarity in signature plots suggest that the pitch boresight angle and laser-to-scanner phi-angle are going to be difficult to decouple (i.e. will have a large correlation).

All conclusions to be drawn about the signature of ϕ_{LS} are equivalent to those for the pitch boresight angle. Even for a level flight, the point cloud is largely non-coplanar, suggesting the parameter will be easy to calibrate without any excessive maneuvering of the survey vehicle. Vehicle pitch appears to create the largest dispersion in the point

cloud (Figure 95 – middle) and is thus the change in vehicle attitude that will most benefit the calibration of ϕ_{LS} .

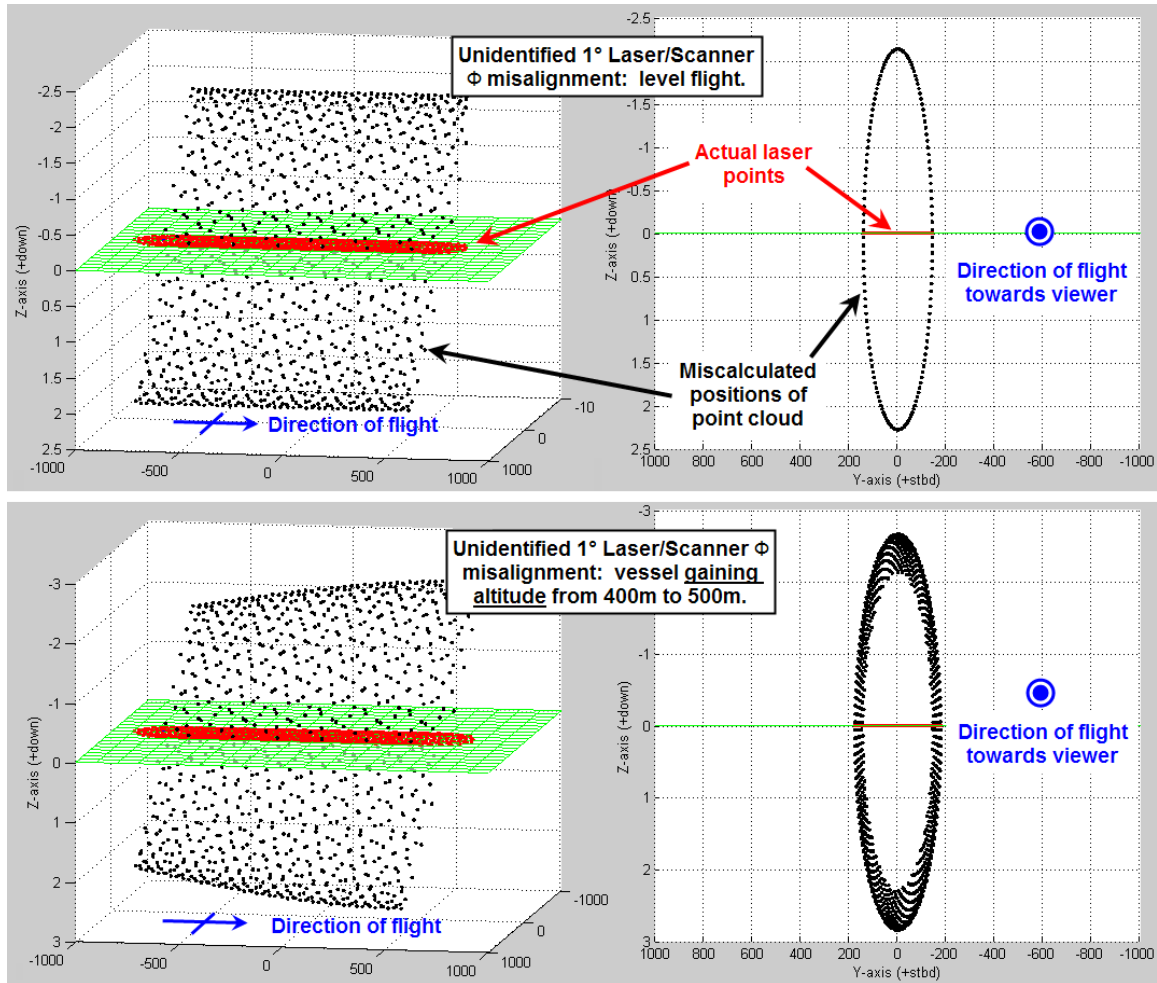


Figure 94. Visualization of a point cloud generated from a lidar with an unidentified 1° laser-to-scanner phi-angle misalignment (top), and a point cloud from the same system as it experiences an increase in altitude (bottom). The red points indicate the true laser strikes, while the black are the miscalculated biased points. All units in meters.

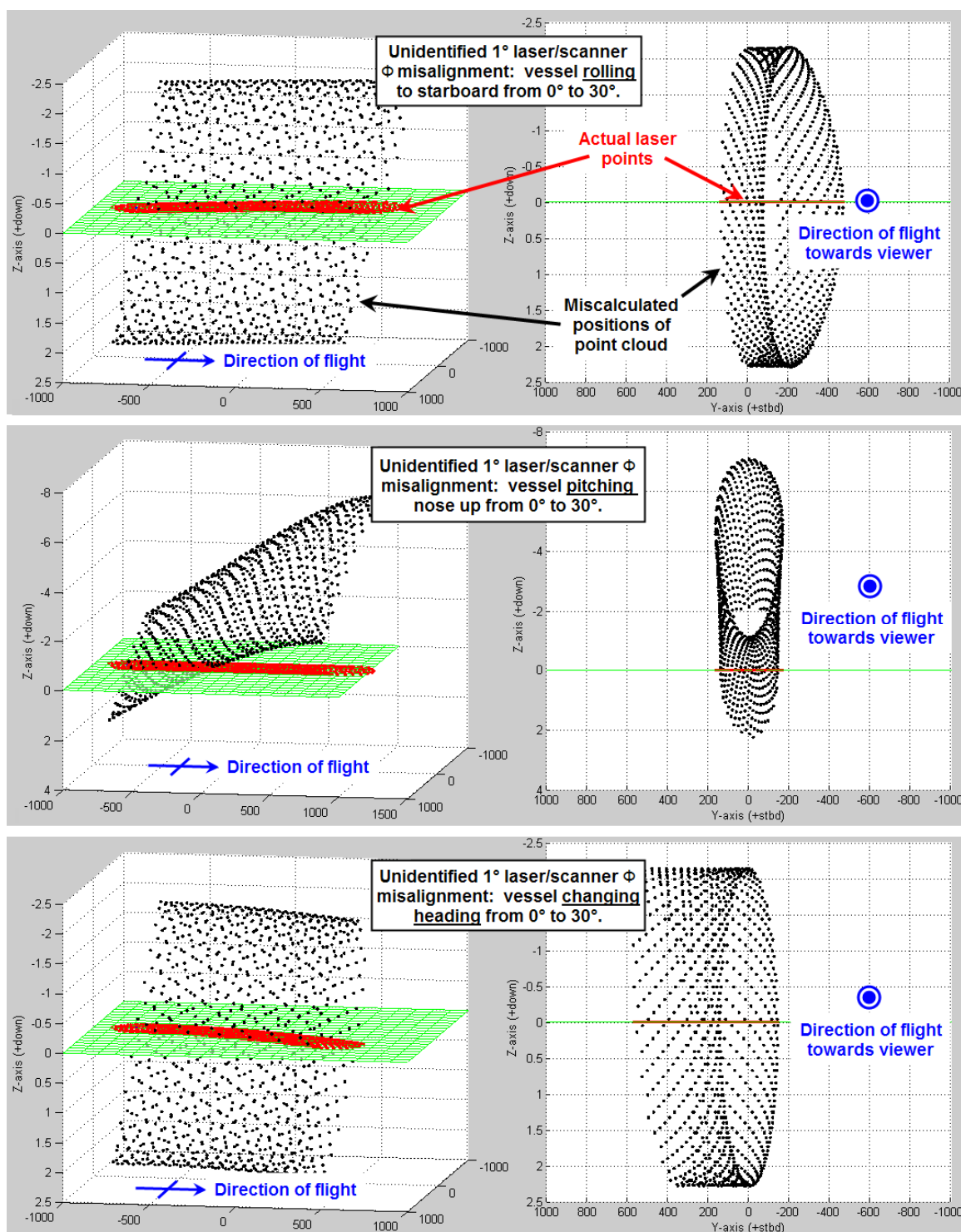


Figure 95. Signature analysis plots for a lidar with a 1° laser-to-scanner ϕ -angle misalignment in the presence of a rolling (top), pitching (middle) and yawing (bottom) vehicle. The red points indicate the true laser strikes, while the black are the miscalculated biased points. All units in meters.

The laser-to-scanner theta-angle, θ_{LS} , is unique compared to the other calibration parameters. During construction of the lidar, most of the calibration parameters will be designed to be zero. That is, the system design will call for the prism to be perfectly set within the scanner (i.e. $PS\theta_x = PS\theta_y = PS\theta_z = 0$); the scanner will not be mounted on an incline (i.e., the pitch and roll boresight angles will equal zero); and assuming the laser is oriented normal to the scanner, ϕ_{LS} will equal zero. However, if the laser is tilted just slightly away from the scanner normal, then it is equally probable to be tilted forward ($\theta_{LS} = 0^\circ$), to starboard ($\theta_{LS} = 90^\circ$), aft ($\theta_{LS} = 180^\circ$), or to port ($\theta_{LS} = 270^\circ$). If the laser is assumed to be tilted forward, but is actually tilted in some other direction, then the signature plots will have a different structure depending on the actual direction of tilt.

For example, suppose there is a known $\phi_{LS} = 1^\circ$, which is misidentified to be tilted in the forward direction (i.e. $\theta_{LS} = 0^\circ$). Figure 96 shows what the biased point clouds would look like were the θ_{LS} to have a number of different values. In the upper plots, where the assumed value for θ_{LS} is only off by 1° in either direction, the biased point clouds appear to be very coplanar. Further, there is very little vertical dispersion in the point cloud (only 0.08m). At first glance, this would imply that the laser-to-scanner theta-angle will be difficult to calibrate. However, when the assumed value for θ_{LS} is off by 90° (Figure 96 – middle), the biased point cloud is no longer coplanar looking and has a large vertical dispersion, implying the calibration routine will quickly recognize a gross error in θ_{LS} . Conversely, the LSA will have difficulty recognizing small errors in θ_{LS} . Note by the non-unique nature of spherical coordinates $\phi = 1^\circ$ and $\theta = 0^\circ$ is equivalent to $\phi = -1^\circ$ and $\theta = 180^\circ$, thus Figure 96 (bottom) is equivalent to Figure 94 (top).

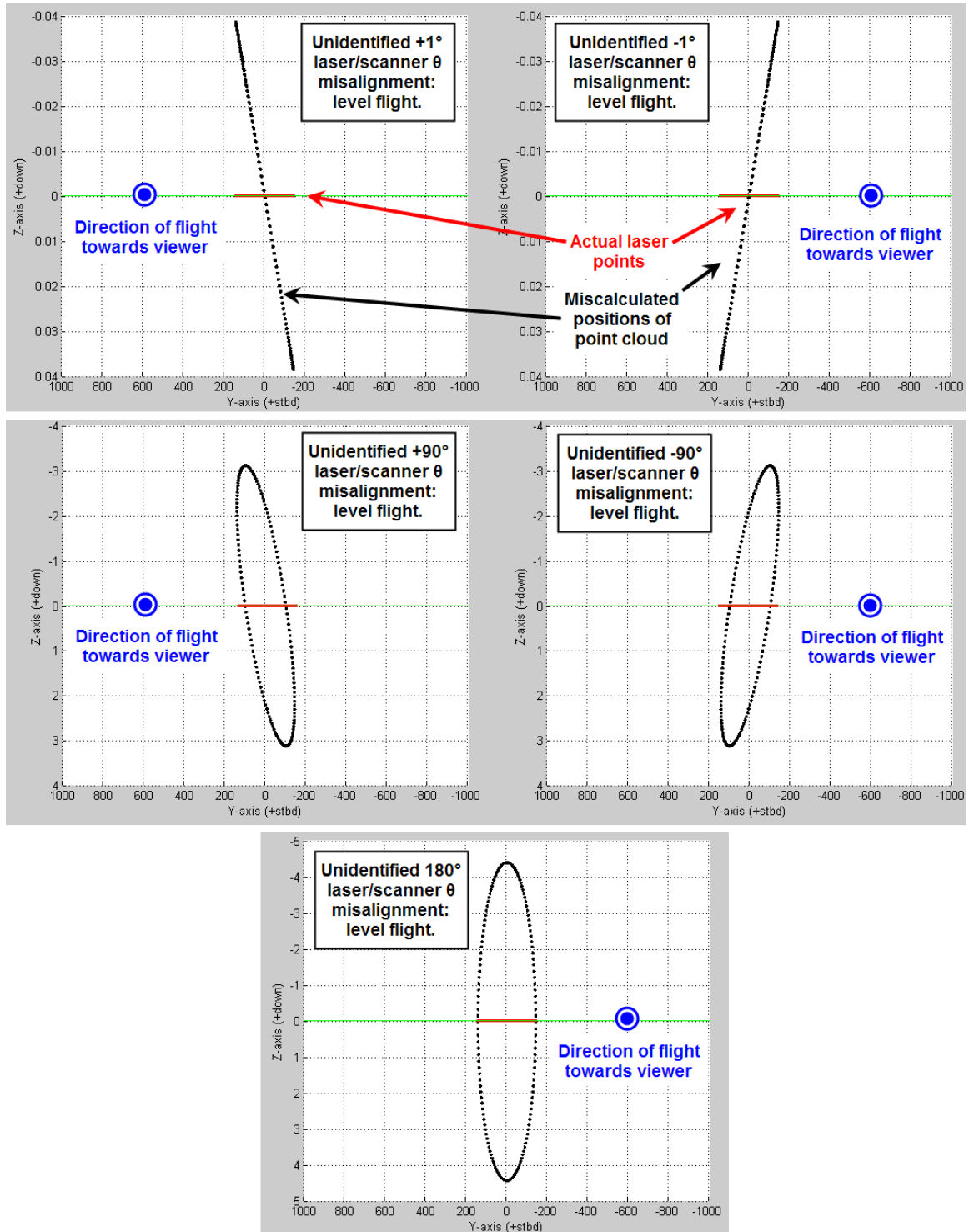


Figure 96. Signature analysis plots for a lidar with a $\pm 1^\circ$, $\pm 90^\circ$ and 180° laser-to-scanner theta-angle misalignment for a level flight. Notice the bottom plot is equivalent to a lidar with laser-to-scanner theta-angle of 0° and phi-angle of -1° (see Figure 94 – top). The red points indicate the true laser strikes, while the black are the miscalculated biased points. All units in meters.

The issue of the LSA recognizing gross, but not minor, errors in the calibration parameters raises an important philosophical point with regard to calibration. Suppose an error in parameter X causes what would otherwise be a flat, coplanar point cloud to suddenly have a vertical dispersion between $\pm 0.005\text{m}$ along a 1000m survey line. On the one hand, the point cloud is still nearly coplanar and thus the calibration routine is unlikely to identify the error in parameter X. On the other hand, the point cloud is still nearly coplanar; the data integrity is likely still good enough for most applications. In short, the parameters that are the hardest to calibrate are the ones that cause the least change to the point cloud and, thus, are the ones that matter least to the surveyor. The end goal is not to determine the precise value of all the calibration parameters (though that would be nice) – the goal is to produce a geometrically correct and consistent point cloud.

Though θ_{LS} could conceivably come from any direction, for the purposes of the sensitivity plots it will be assumed to be coming from 0° , while it is actually coming from an unknown 1° (Figure 96 – upper-left). This should represent the most difficult case with regard to attempting to calibrate θ_{LS} . Naturally, any value for θ_{LS} would be meaningless if ϕ_{LS} were to equal zero. So, ϕ_{LS} will be assumed to have a known value of 1° (“known” implying that all misalignments in the biased point clouds can be attributed exclusively to the unknown error in θ_{LS}). Using a larger value for ϕ_{LS} would only vertically amplify the signature plots.

The ϕ_{LS} signature plots are shown in Figure 97 and Figure 98. Most remarkable about the plots is their extreme resemblance to the signature plots for the roll boresight angle (Figure 68 and Figure 69). As was the case with the roll boresight angle, neither a

single level flight, nor one with a change in altitude provides sufficient geometric information to calibrate θ_{LS} , as the biased cloud is still coplanar. Similarly, were the vehicle to experience a dynamic change in either its pitch or roll (Figure 98 – top and middle) the biased point cloud would only experience minor deflections from its coplanar status, suggesting neither of these maneuvers will reliably help to determine θ_{LS} . The maneuver that shows the most promise is an oscillation in heading (Figure 98 – bottom), which is the change in attitude that results in a distinctly non-coplanar point cloud.

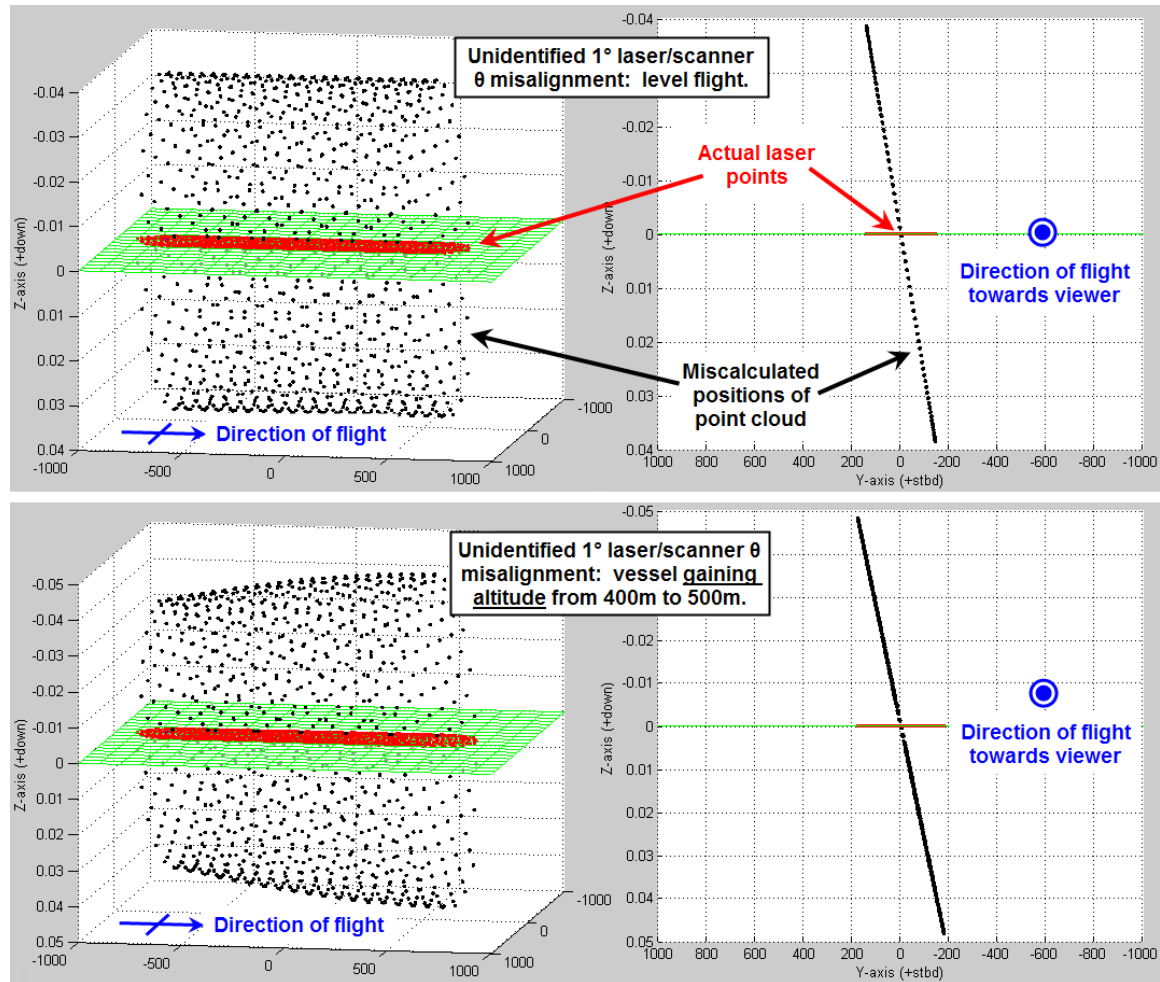


Figure 97. Visualization of a point cloud generated from a lidar with an unidentified 180° laser-to-scanner theta-angle misalignment (top), and a point cloud from the same system as it experiences an increase in altitude (bottom). The red points indicate the true laser strikes, while the black are the miscalculated biased points. All units in meters.

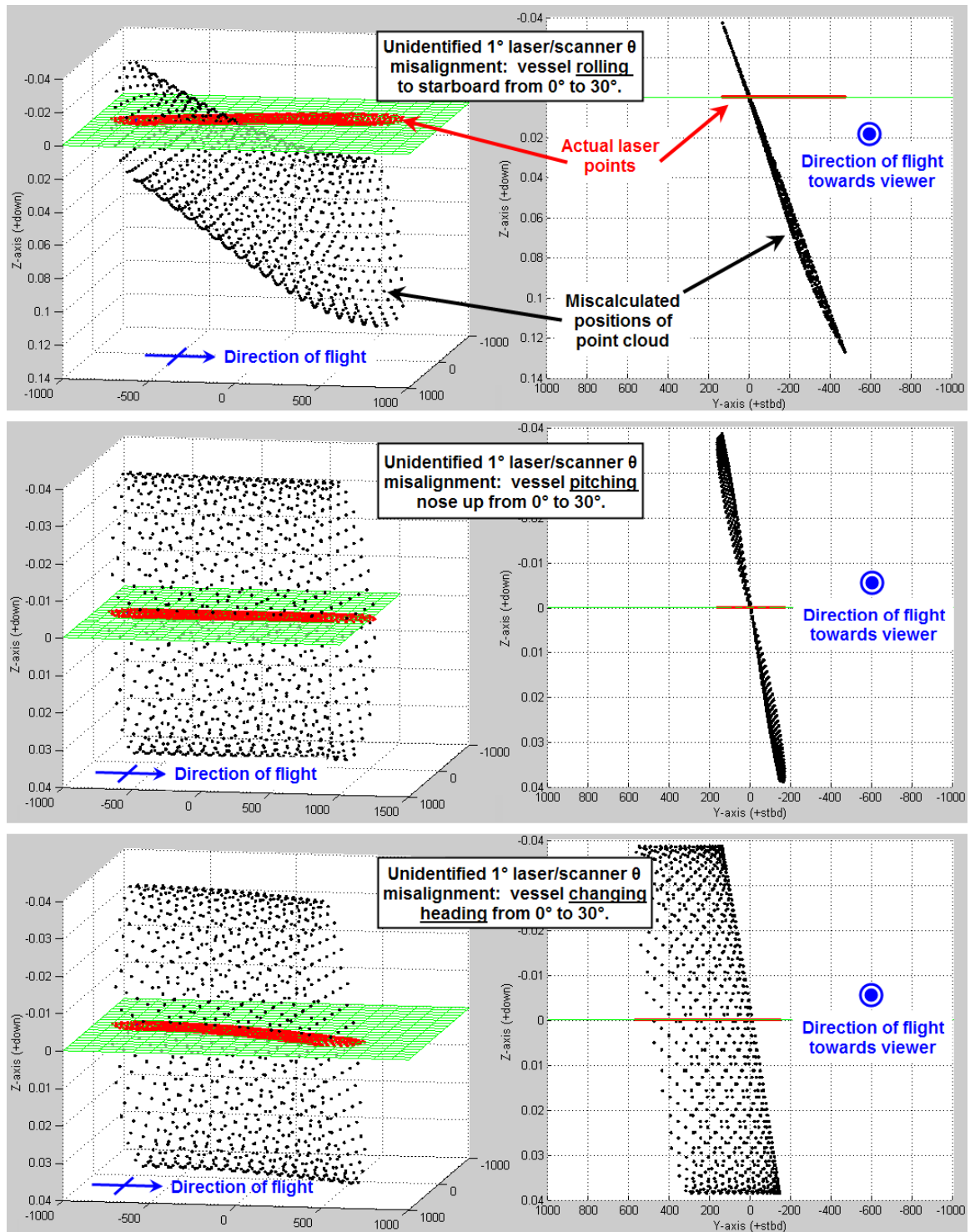


Figure 98. Signature analysis plots for a lidar with a 180° laser-to-scanner theta-angle misalignment in the presence of a rolling (top), pitching (middle) and yawing (bottom) vehicle. The red points indicate the true laser strikes, while the black are the miscalculated biased points. All units in meters.

Executing successively more complicated calibrations, the baseline flight in Figure 81 (the single line with $\pm 5^\circ$ roll and yaw oscillation) is revisited yet again, where the six parameters discussed thus far (the three boresight angles, prism slope and two laser-to-scanner angles) are calibrated simultaneously. The results of the calibration are labeled as the baseline flight in Figure 99. Looking at only the baseline flight, one should immediately notice the uncertainty for θ_{LS} is two orders of magnitude larger than any of the other calibration parameters. This large uncertainty for θ_{LS} was anticipated given the minimal dispersion of points shown in the signature analysis plots (Figure 97 and Figure 98). This large uncertainty should not be viewed with too critical an eye given that “close enough” is “good enough” regarding the point cloud positioning is concerned with the laser-to-scanner theta-angle.

	Acquisition Scheme	Number of data points	Confidence in solution (reported as a percentage of the baseline flight with same number of data points)					
			1 σ -roll	1 σ -pitch	1 σ -yaw	1 σ -prism	1 σ -LS Φ	1 σ -LS θ
	Baseline (5° of dynamic vessel roll & yaw)	~950	0.068°	0.070°	0.047°	0.021°	0.079°	4.190°
A1	2x laser repetition rate	~1,900	70.5%	70.7%	70.8%	70.7%	70.7%	70.4%
A2	4x laser repetition rate	~3,800	49.9%	50.0%	50.1%	50.0%	49.9%	48.9%
B1	Doubling the magnitude of the dynamic roll	~950	75.6%	78.5%	51.5%	50.0%	78.4%	72.5%
B2	Doubling the magnitude of the dynamic yaw	~950	35.2%	94.2%	99.2%	100.6%	93.1%	38.7%
C1	Flying reciprocal flight lines (roll/yaw both)	~1,900	88.7%	99.9%	88.2%	97.8%	99.9%	92.0%
C2	Flying parallel flight lines (same heading)	~1,900	96.1%	99.9%	88.8%	100.0%	100.0%	100.5%
D1	Clover leaf (1 heave, roll, pitch and yaw)	~3,800	103.7%	101.6%	122.9%	133.6%	101.0%	110.2%
D2	Cloverleaf configuration (2 heave/pitch, 2 roll/yaw)	~3,800	94.2%	91.7%	88.2%	99.3%	91.3%	100.0%
E	"Plus sign" (2 heave/pitch, 2 roll/yaw, 2 altitudes)	~3,800	85.4%	84.8%	81.0%	55.5%	84.7%	91.3%

Figure 99. Table of results of six-parameter calibration trials under a number of different acquisition scenarios: increasing data density (A), increasing vehicle attitude (B), adding a reciprocal and parallel flight lines (C) adopting a cloverleaf pattern (D) and crossing pattern (E). All uncertainties are reported as a percentage of the baseline flight (shown in Figure 80) with the same number of data points.

Interestingly, when only the three boresight angles were calibrated, the pitch angle was the most confident, while the yaw angle was the least confident. The magnitudes of the uncertainty for the pitch and yaw boresight angles have reversed

during this six parameter calibration. To understand this shift in uncertainty, the parameters' correlation coefficients must be considered (Figure 100). As was discussed while viewing the signature analysis plots of the two laser-to-scanner angles, ϕ_{LS} produced a biased point cloud that was very similar to those associated with the pitch boresight angle. Similarly, θ_{LS} and the roll boresight angle had similar-looking biased point clouds. These similarities have manifested themselves in the calibration routine producing near perfect correlations among the parameters. A high correlation implies the calibrator cannot determine which of the two parameters to adjust when fitting the points to the planar surface. This “indecision” causes the uncertainty of both parameters in question to be larger than they would be were the correlation not present. Specific to the baseline flight, the large correlation associated with the pitch boresight angle caused the uncertainty to grow compared to when only the three boresight angles were calibrated (from 0.004° to 0.070°). Meanwhile, the yaw boresight angle was not correlated with any other parameter in the 6-parameter calibration, and it saw its uncertainty improved as compared to the 3-parameter calibration (from 0.061° to 0.047°). Note if the correlation/covariance plots ever get too busy, then the user can choose to display only the parameters of interest by deselecting the nuisance parameters from the left side of the interface (Figure 100).

Again, striving to improve the baseline confidences of the 6-parameter calibration reported in Figure 99, the acquisition conditions are modified to see if a better flight configuration exists. Of equal interest is to uncover a flight pattern that will help decouple the parameters with the large correlations. Increasing the data density once again proves to be the guaranteed method of improving the calibrator's performance

(lines “A1” and “A2”). As before, doubling the data density reduces the uncertainty for all the parameters by about 30%. Put another way, quadrupling the data density will halve the uncertainty.

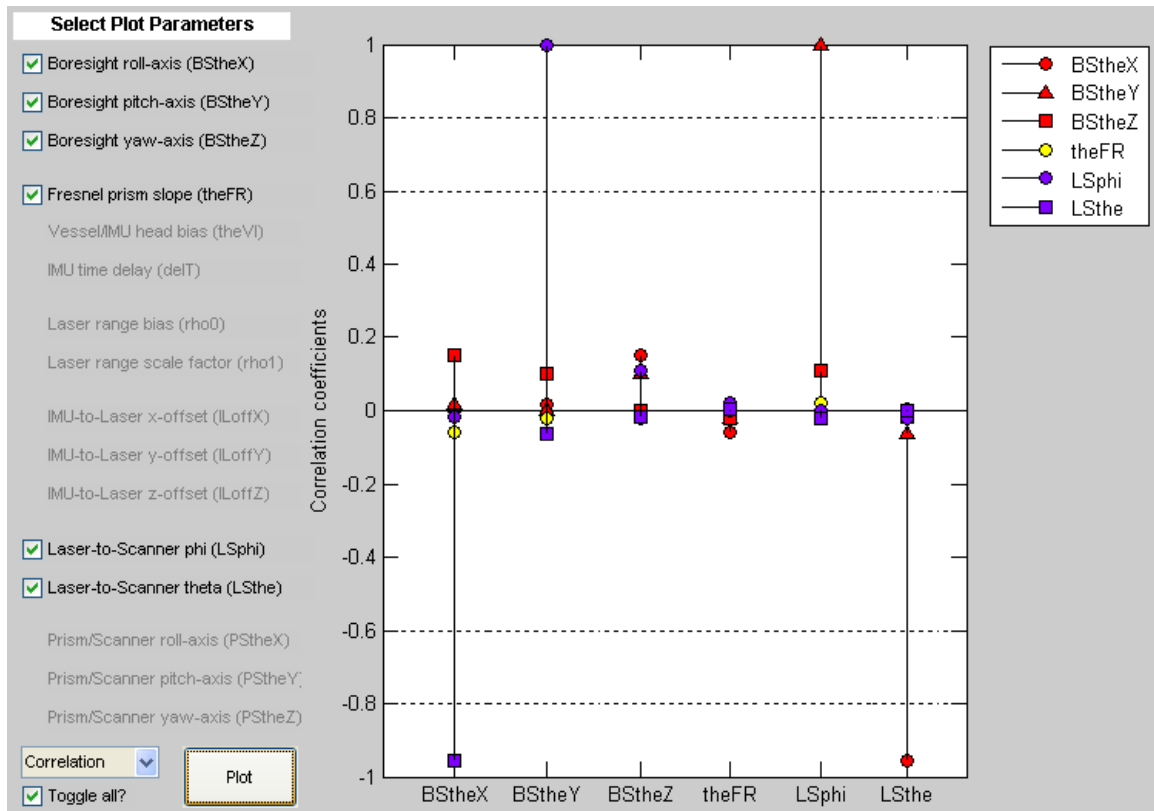


Figure 100. Correlation coefficients from a single flight line (shown in Figure 80) of a six parameter adjustment (boresight angles, prism slope and laser/scanner alignment). Notice the large correlations between the pitch boresight (red triangle) and ϕ_{LS} (purple circle) as well as between the roll boresight (red circle) and θ_{LS} (purple square).

The baseline flight experienced an oscillation in roll and heading of $\pm 5^\circ$, lines “B1” and “B2” of Figure 99 show the effect of doubling the magnitude of each of these oscillations. All of the calibration parameters benefit from an increase in the vehicle’s roll (reducing the uncertainty by at least 20%), but in particular, the prism slope’s uncertainty is halved (as is the uncertainty in the yaw boresight angle, but the relationship

between the yaw angle and vehicle roll has already been established). When the vehicle experiences a greater change in heading, the parameters as a group do not experience as large an improvement as the increased roll. The increased yaw does lead, however, to a much improved confidence in θ_{LS} (reducing the uncertainty by 59%). The roll boresight angle also has a similar improvement in confidence, but the relationship between the roll angle and the vehicle heading has also already been established.

It has been established that acquiring additional data will lead to improved calibration results; therefore all the entries in Figure 99 have been normalized to whichever baseline flight has the equivalent number of data points. For example, flight “C1” includes two survey lines acquired over the same area with a different vehicle heading. Two lines imply twice the number of postings, so its performance is assessed against flight “A1” which has twice the laser repetition rate. Interestingly, having a single flight line with a $\pm 10^\circ$ change in heading (“B2”) yields better calibration results than the two flights from opposite directions (“C1”). Also, flying two parallel lines offset by a horizontal distance offers little benefit (“C2”). From a confidence in the calibration perspective, the surveyor would be better served by just a single flight with a greater change in attitude, than by acquiring multiple flight lines (they would also save on fuel).

Speaking towards acquiring multiple survey lines, the cloverleaf pattern shown in Figure 82 was also simulated for comparison to the other flight schemes (“D1”). Amazingly, acquiring the four survey lines over the broader geometric area, while systematically varying the vehicle’s altitude, roll, pitch and yaw leads to a worse calibration than the simultaneously rolling/yawing flight line (“A2”). On a point-for-point basis, a surveyor would benefit more from investing in a denser dataset than

embarking on the full cloverleaf flight. Of course, the best of all possibilities would result from a dense dataset over the cloverleaf pattern.

One flaw with the cloverleaf pattern as it was originally proposed was that only a single change in the vehicle aspect was simulated per flight line; that is, the vehicle would just roll on one flight line (all other things being the same), and then it would change its pitch in another, etc. In reality, were an airplane to roll, it would also begin to bank and experience a corresponding change in heading. Similarly, were an airplane to pitch nose up, it would likely gain altitude. So a more realistic simulation would have a vehicle both roll and yaw simultaneously, as well as coupling any changes in pitch with heave. Simulating the cloverleaf again, only this time having two consecutive lines experience a coupled vehicle roll/yaw (with the remaining two lines experiencing a coupled pitch/heave), the calibration results are shown in Figure 99 (“D2”). Unlike the previous cloverleaf calibration, this flight strategy does produce slightly more confident calibration results than can be attributed to the increased data density alone, reducing the uncertainty by up to 9% (“A2”).

Morin (2002) also gave consideration to the design of a flight plan that would optimize the determination of the calibration parameters (though the calibration parameters under investigation were slightly different). Rather than a cloverleaf, Morin proposed two sets of survey lines, acquired at different altitudes, that would intersect at a common point (Figure 101). To modify Morin’s strategy, the dynamic changes in the vehicle’s orientation (simultaneous heave/pitch and roll/yaw) are still retained. The results of this plus-shaped flight plan are shown in Figure 99 (“E”). This crossing strategy acquired at different acquisition heights does in fact provide the best calibration

results seen so far. In particular, the uncertainty in the prism slope drops by 45%, while the other five parameters improve between 9% and 19%.

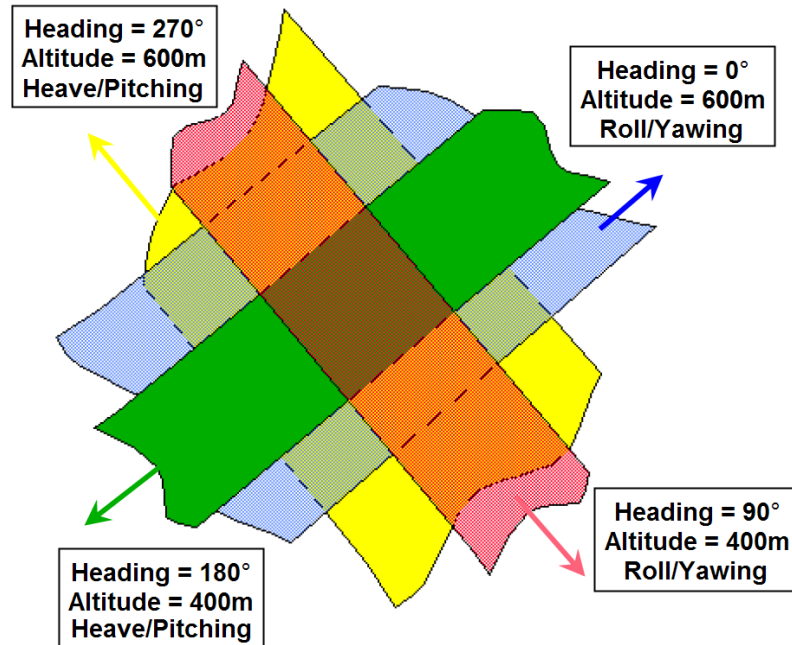


Figure 101. Proposed crossing flight plan which features survey lines at two different acquisition altitudes and the intersection of all lines over a common point (adapted from Morin 2002).

While the many previous flight strategies (increased data density, changing attitude, changing heading) did have some results in improving the confidence of one calibration parameter or another, none of them affected the correlation between the pitch boresight angle and ϕ_{LS} nor the roll boresight angle and θ_{LS} . Even with the cloverleaf and crossing flight plan the correlations could not be removed. Again, large correlations do not necessarily make for a poor calibration, they just imply that the reported uncertainties for some of the calibration parameters will be larger than the user may desire; the final point cloud will, however appear geometrically correct.

In summary, the laser-to-scanner angles, ϕ_{LS} and θ_{LS} , are almost defined by their similarities to the pitch and roll boresight angles respectively. ϕ_{LS} is easily determined

and requires no special maneuvering beyond the forward advancement of the vehicle.

θ_{LS} on the other hand, is most sensitive to changes in the vehicle heading. However, even with a change in heading this theta-angle is difficult to determine to a high precision because the point cloud is not particularly sensitive to small changes in this parameter. This has the dual implication that (a) it will not be possible to determine the value of θ_{LS} to as precise a degree as the other calibration parameters and (b) it does not need to be determined to as precise a degree as the other parameters. A corollary to any misalignment that produces only slight changes in the point cloud is that the associated parameter will be very slow to converge if included in the LSA (unless an appropriately small weight – large uncertainty is placed on the parameter).

6.3.3 – The Vehicle Reference Frame (VRF)

There are two sets of calibration parameters that are directly related to the definition of the vehicle reference frame: the VRF and IRF heading misalignment and the offset vector between the IRF and the scanner. Each will be discussed in turn. These parameters, more so than the previous six, will drive home the potential impacts of the correlation along parameters and provide the first example of a group of parameters that are completely linearly dependent on one another.

6.3.3.1 – Vehicle-to-INS heading alignment. The VRF-to-IRF heading alignment, θ_{VI} , is depicted in Figure 27. A non-zero value for θ_{VI} will result in cross-talk between the INS-sensed pitch and roll values, which must be corrected. For this set of signature analysis plots, we shall assume the lidar has 5° pitch, roll and yaw boresight angles and a 1m offset between the SRF and the VRF origins in the fore-aft, port-starboard and up-

down axes – all of these non-zero calibration parameters will be known in the signature plots implying only the error in θ_{VI} will be responsible for the biased point clouds.

The signature analysis plots for θ_{VI} (shown in Figure 102 and Figure 103) bear a striking resemblance to the signature plots for the yaw boresight angle (Figure 71 and Figure 73). Based on the discussion of previous calibration parameters, we can surmise there will likely be a high correlation between the VRF/IRF heading misalignment and the yaw boresight angle when both variables are included in the calibration routine.

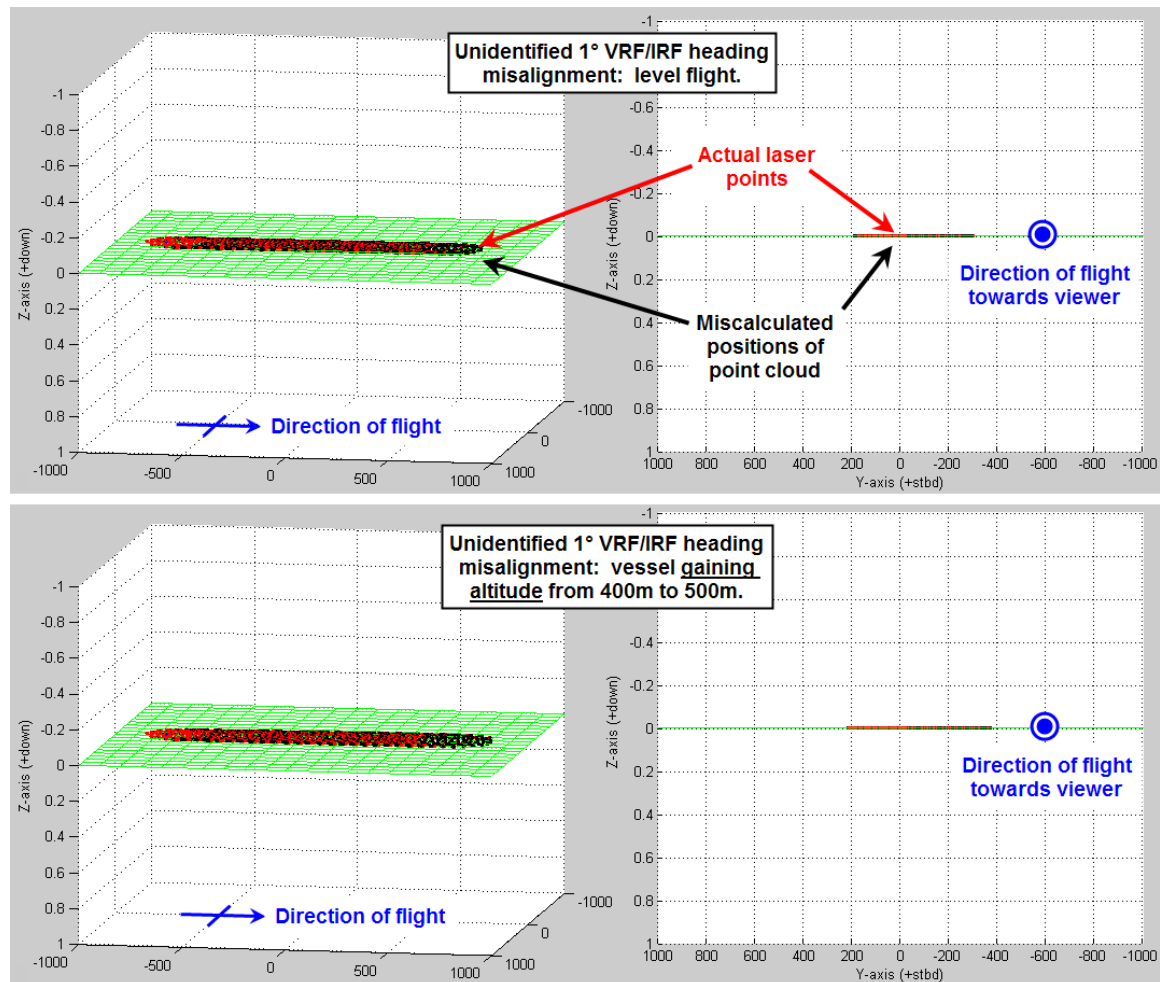


Figure 102. Visualization of a point cloud generated from a lidar with an unidentified 1° VRF/IRF heading misalignment (top), and a point cloud from the same system as it experiences an increase in altitude (bottom). The red points indicate the true laser strikes, while the black are the miscalculated biased points. All units in meters.

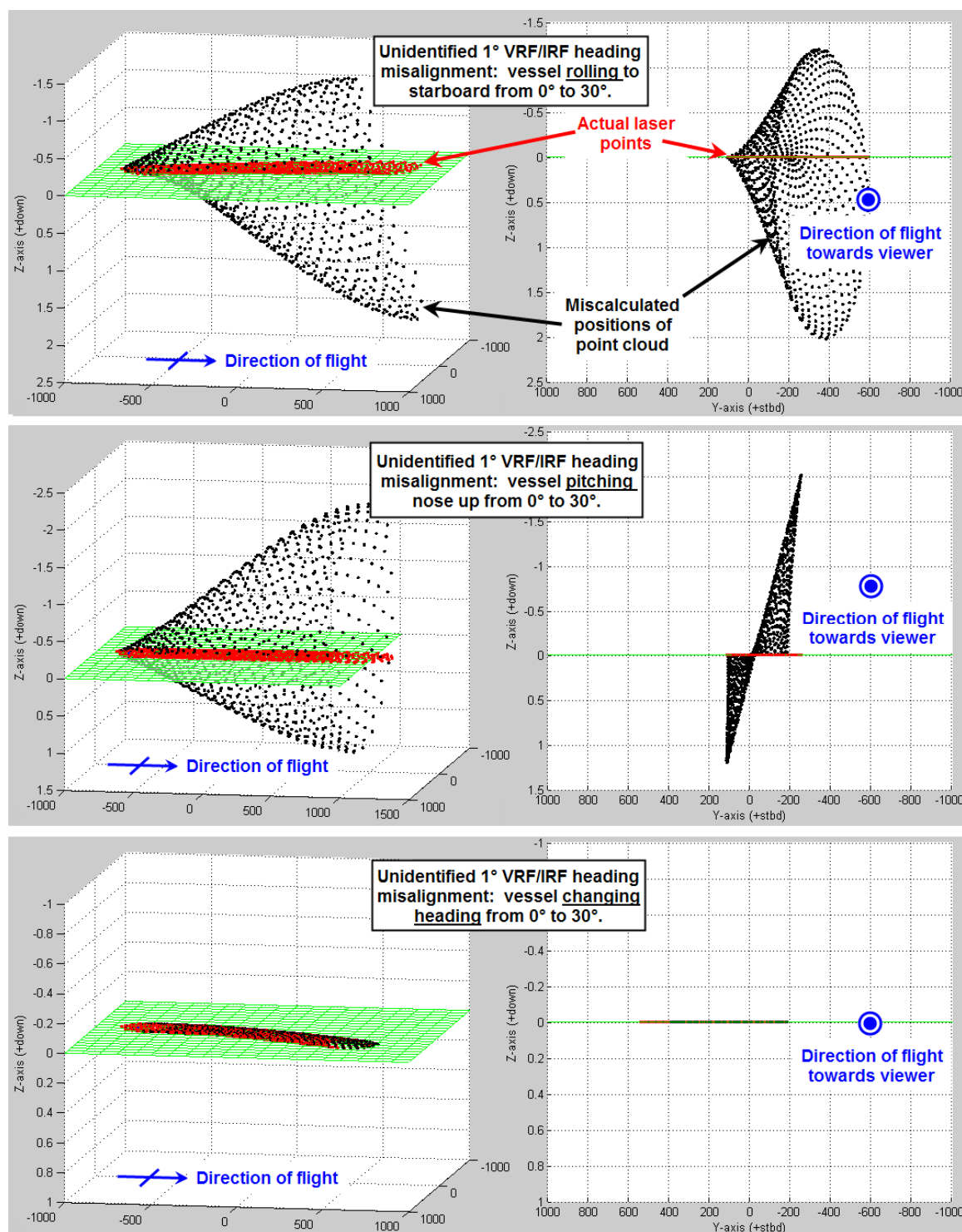


Figure 103. Signature analysis plots for a lidar with a 1° VRF/IRF heading misalignment in the presence of a rolling (top), pitching (middle) and yawing (bottom) vehicle. The red points indicate the true laser strikes, while the black are the miscalculated biased points. All units in meters.

Even with non-zero boresight angles and non-zero laser-to-scanner alignment angles, a lidar with an unidentified bias in θ_{VI} will still yield a biased point cloud that is coplanar. Further, a change in the vehicle altitude will do nothing to disturb the biased coplanar cloud (Figure 102 – bottom). This is not to imply that the true laser points and the biased points are equivalent; the biased points do experience a horizontal shift similar to that exhibited in the yaw boresight signature plot (Figure 72). The problem, from the calibrator’s point of view is that the point cloud is coplanar and thus θ_{VI} cannot be determined from the information given. To calibrate θ_{VI} requires the vehicle to either roll or pitch (Figure 103 – top and middle, respectively). The greater the change in attitude, the greater the vertical dispersion of the point cloud will be, which leads to a greater confidence in the calibrator’s ability to determine the misalignments.

The reported confidences for several calibration attempts of some 7-parameter calibrations are shown in Figure 104. The first thing to notice is that the reported uncertainty of both θ_{VI} and the yaw boresight angle are nearly 4° (1σ). For a dataset of this size, this is the largest uncertainty seen in this document thus far. To come to terms with what these large uncertainties mean, we must first examine the correlations (Figure 105).

As speculated when examining the signature analysis plots, the yaw boresight angle and the VRF/IRF heading misalignment have a near perfect correlation. Recall from Section 6.3.1 (Figure 93) that the geometric interpretation of two parameters that are highly correlated is that the error in one parameter can be compensated for by a complementary error in the other parameter. It turns out the biases in a point cloud

caused by a misalignment in the VRF/IRF heading can be almost completely eliminated by applying a correction to the yaw boresight angle.

	Acquisition Scheme	Number of data points	Confidence in solution (reported as a percentage of the baseline flight's confidence)						
			1 σ -roll	1 σ -pitch	1 σ -yaw	1 σ -prism	1 σ -VRF/IRF	1 σ -LS Φ	1 σ -LS θ
	Baseline (5° of dynamic vessel roll & yaw)	~3,800	0.036°	0.035°	3.7°	0.011°	3.7°	0.039°	2.2°
A	Cloverleaf configuration	~3,800	93.3%	94.9%	65.9%	100.0%	65.9%	94.7%	96.7%
B	"Plus sign" configuration	~3,800	85.1%	87.6%	73.5%	55.9%	73.6%	87.6%	88.6%

Figure 104. Table of results of seven-parameter calibration trials. Trials with increased data density (A), over the cloverleaf pattern (B) and crossing pattern (C) are shown. All uncertainties are reported as a percentage of the baseline flight (shown in Figure 80).

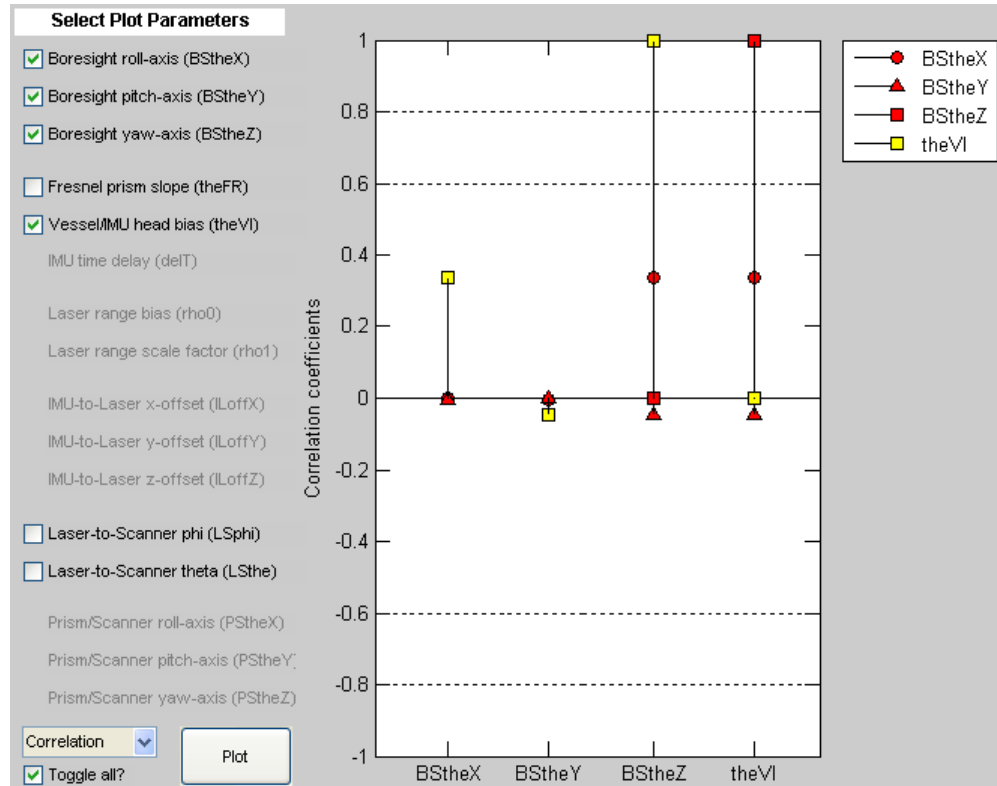


Figure 105. Correlation coefficients from a single flight line (shown in Figure 80) of a seven-parameter adjustment (only boresight angles, VRF/IRF alignment shown).

Figure 106 and Figure 107 show a second rendering of the biased point clouds resulting from a 1° bias in θ_{VI} (where the value of θ_{VI} is incorrectly assumed to be 0°).

The biased clouds are plotted, however, after intentionally setting the yaw boresight angle to an incorrect value of 4° (recall, the actual yaw boresight misalignment in this simulation is 5°). First notice that the biased point clouds resulting from the level, heaving and yawing flight lines are still coplanar; thus introducing the incorrect value for the yaw boresight angle hasn't made the problem worse when compared to Figure 102 and Figure 103. The critical observation is in the biased point clouds when the vehicle rolls and pitches (Figure 107 – top and middle). Previously, when there was only a bias in θ_{VI} such a change in vehicle attitude resulted in a vertical displacement of the point cloud by 3m to 4m (Figure 103 – top and middle). Now, with the yaw boresight angle acting as a corrector, the vertical displacement of the point cloud is on the order of 0.009m. That is, from one end of a 2,000m flight line to the other, the point cloud deviates only 9 millimeters from the true ground plane. When measurement noise is included, this deviation will be undetectable.

To summarize, if there is an unknown error in the value for the VRF/IRF heading alignment, a complementary error can be introduced into the true value of the yaw boresight angle. This complementary error will not completely remove the artifacts induced in the point cloud by the misidentified θ_{VI} angle, but it will reduce them to undetectable levels. It is not a case of two “wrongs” making a “right,” but two “wrongs” making a “right enough.”

In this way, surveyors for years might have been incorrectly mounting their IMUs to the vehicle frames. Later, when it came time to calibrate the system, the resulting biases in the point cloud resulting from the cross-talk in the IMU-sensed pitch and roll was mistakenly interpreted as a yaw boresight misalignment. Subsequently adjusting this

boresight angle would nearly remove the point cloud's artifacts to a level that would not be detectable within the system noise. The magnitude of the remaining artifact is a function of three things: the magnitude of the vehicle's pitch/roll, the length of the horizontal lever arm between the VRF and IRF, and the magnitude of θ_{VI} . Sample plots of biased clouds varying all three of the preceding items is shown in Figure 108. For the CZMIL system, a basic rule of thumb is as follows: for every 1° of θ_{VI} that is compensated by the yaw boresight angle, for every 10° of vehicle roll, for every 1m the VRF is forward of the IMU, a 0.003m vertical bias will be introduced. For example, if there is a 3° VRF/IRF misalignment with a 0.5m offset vector and 20° of roll, then there will be a vertical bias in the point cloud of $3 \times 0.5 \times 2 \times 0.003 = 0.009\text{m}$. This bias is completely independent of acquisition altitude or other calibration values.

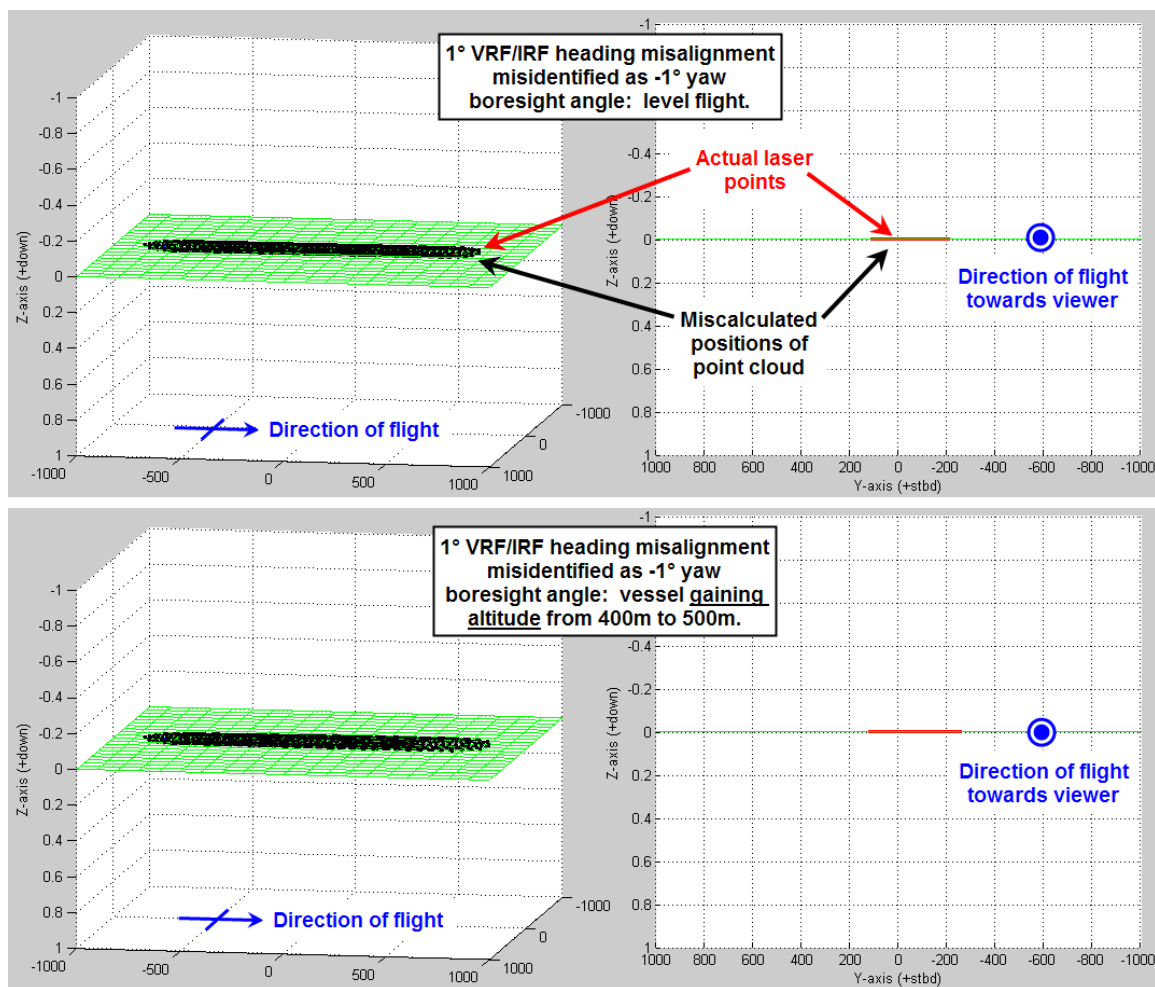


Figure 106. Visualization of a point cloud generated from a lidar with an 1° VRF/IRF heading misalignment that is misidentified as a -1° yaw boresight angle (top), and a point cloud from the same system as it experiences an increase in altitude (bottom).

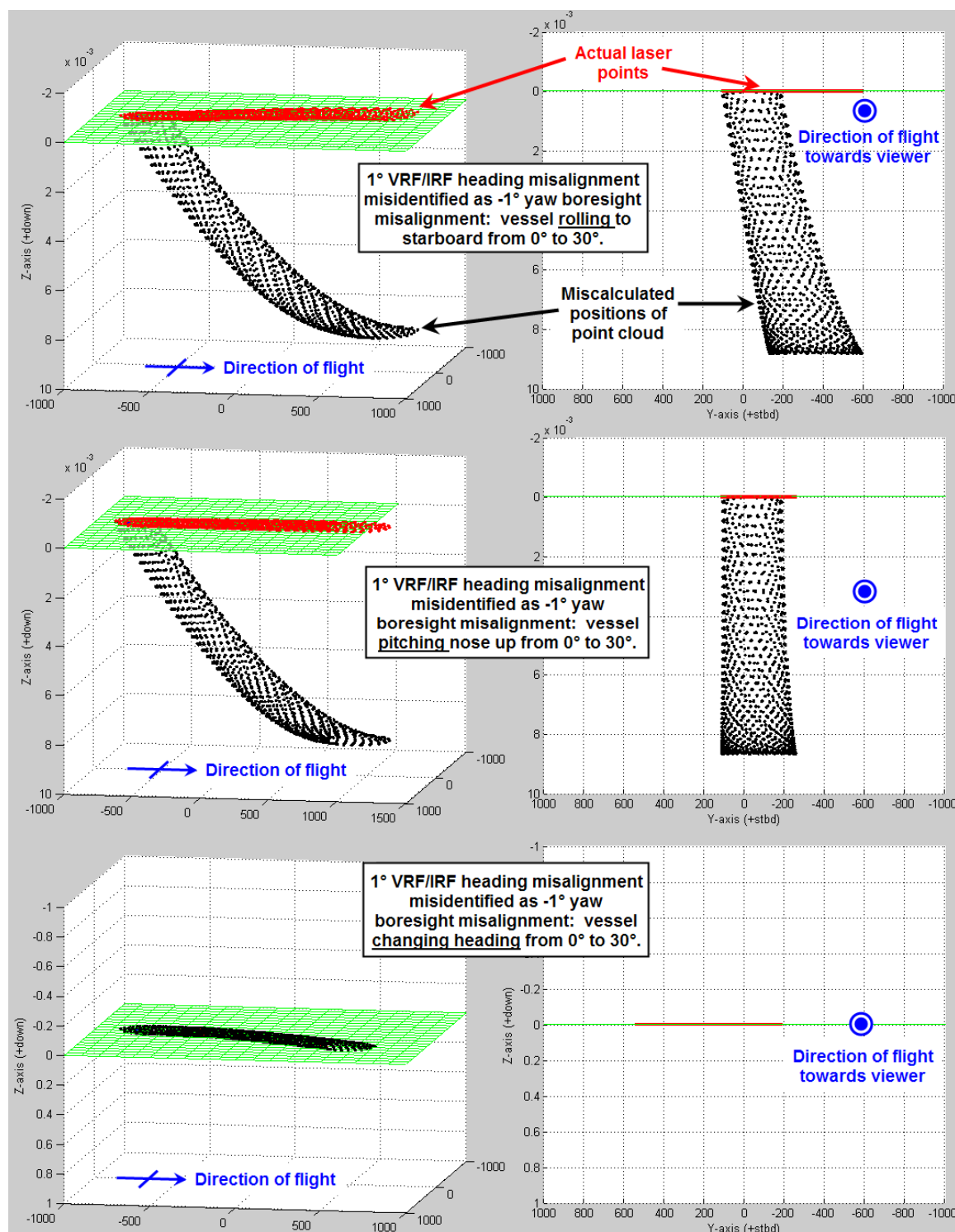


Figure 107. Signature analysis plots for a lidar with a 1° VRF/IRF heading misalignment that is misidentified as a -1° yaw boresight angle in the presence of a rolling (top), pitching (middle) and yawing (bottom) vehicle. The red points indicate the true laser strikes, while the black are the miscalculated biased points. All units in meters. Note the vertical scales are 10^{-3} m.

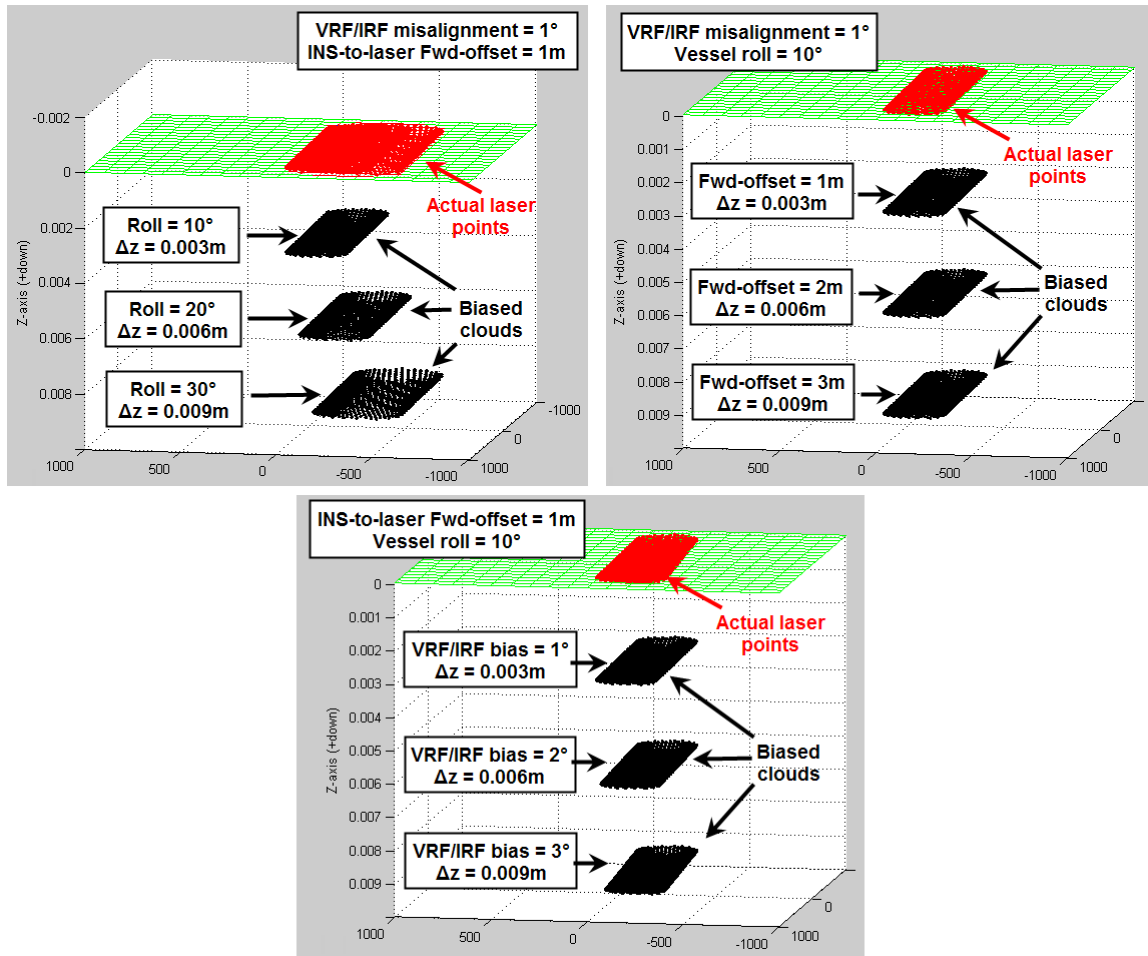


Figure 108. When a VRF/IRF heading misalignment is incorrectly identified as a yaw boresight misalignment, a vertical bias in the point cloud will result. This bias will grow by 0.003m for every 10° of vehicle roll, 1m of forward-aft offset between the INS and VRF, and 1° of θ_{VI} that is attributed to the yaw boresight.

One final point must be made with regard to VRF/IRF heading misalignment.

Recall from Figure 104 that the (1σ) confidence of θ_{VI} (and the yaw boresight angle) was nearly 4°. If the goal of the surveyor were merely to determine the system calibration values as precisely as possible, then one might be considered to label the previous calibration attempt a failure (given the inordinate uncertainty in the calibration values). However, if the goal of the surveyor is to produce a geometrically correct point cloud with a high confidence in the positions of the laser points, then the previous calibration

should not be dismissed so quickly. We have already established that the point cloud will be geometrically correct (to within a few millimeters). To see the impact of the seemingly large uncertainties of these calibration parameters on the total propagated uncertainty of the point cloud, refer to Section 7.2.2.2 where this calibration run is revisited. Not to discourage the reader from looking ahead, but the impacts of the large parameter uncertainties are very small on the propagated uncertainty.

6.3.3.2 – Scanner-to-INS horizontal offset measurement. The offset vector from the laser-prism-scanner assembly to the INS should be performed in the INS' reference frame (IRF). The problem is that it is difficult to judge relative positions in the IRF; whereas, it is easier to work in the vehicle's reference frame (VRF). The VRF is arbitrary, but is typically defined in such a way that lateral measurements are intuitive to perform – given a person has an innate appreciation for which direction is forward/aft and port/starboard when looking at a vehicle. Assuming the INS is well-mounted (i.e., $\theta_{VI} = 0$), then the VRF will coincide with the IRF and the offset measurements taken in the VRF can be used in the IRF. When there is a misalignment between the VRF and IRF, this offset vector must be rotated accordingly. The dependence of this horizontal offset measurement on an arbitrary coordinate system will prove problematic when the time comes for calibration.

First consider the horizontal bias between the two coordinate systems (denoting the forward-aft offset, Δx_{IL} , and the port-starboard offset, Δy_{IL}). A horizontal shift in the offset vector will typically just result in a horizontal shift in the point cloud (Figure 109). Such a horizontal shift still produces a coplanar point cloud and is insufficient for calibration.

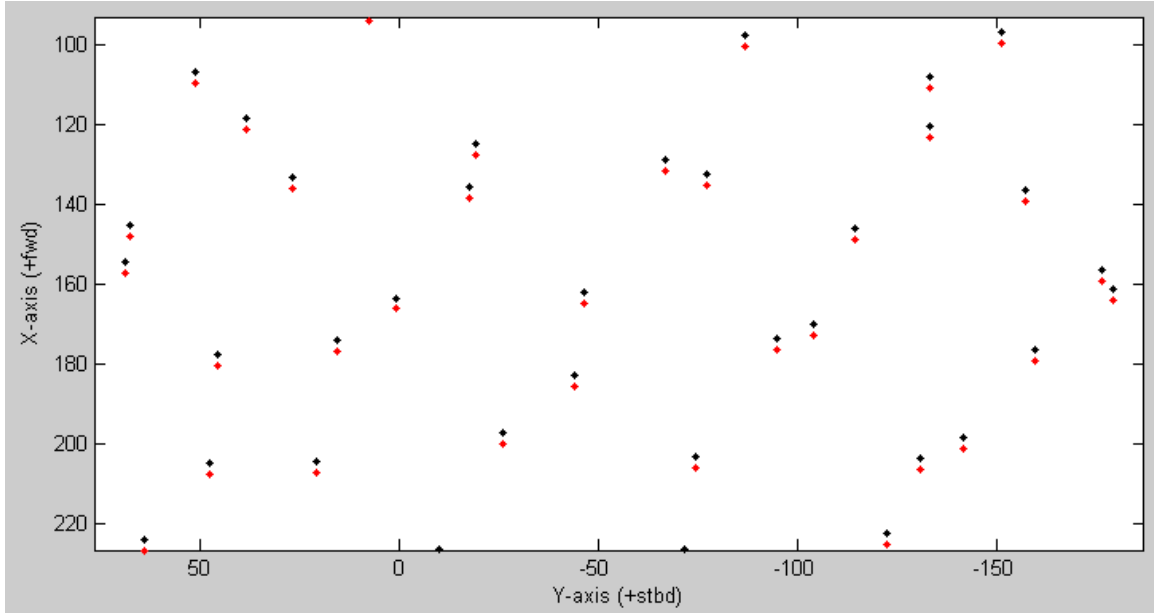


Figure 109. Top-down view of a point cloud (red) and its biased counterpart which contains an unidentified forward Δx_{IL} (black). All units in meters.

Nearly all of the signature plots for the horizontal biases in the offset vector produce a horizontal, coplanar biased point cloud. As such only the signature plots yielding a non-coplanar biased point cloud are shown below. To expose a bias in Δy_{IL} , the vehicle must experience a change in its roll aspect (Figure 110 – top). A Δx_{IL} bias requires a vehicle to pitch (Figure 110 – bottom). Δx_{IL} and Δy_{IL} are unique as calibration parameters in that having a vehicle pitch or roll is a sufficient condition for calibration. In the case of these horizontal offsets, only one change in attitude works, while the other is ineffective. Note the previous statement is not entirely true if the ground plane is tilted, but for now we will assume a horizontal planar surface.

While the signature plots shown for Δx_{IL} and Δy_{IL} do not bear an immediate resemblance to the plots of any of the preceding calibration parameters, they do look very similar to the biased point clouds resulting from misinterpreting a VHF/IHF heading bias

as a yaw boresight angle. With the exception of the vertical scale, Figure 110 appears identical to Figure 107. This suggests that Δx_{IL} and Δy_{IL} will have a high correlation with both θ_{VI} and $BS\theta_z$ in the calibration routine.

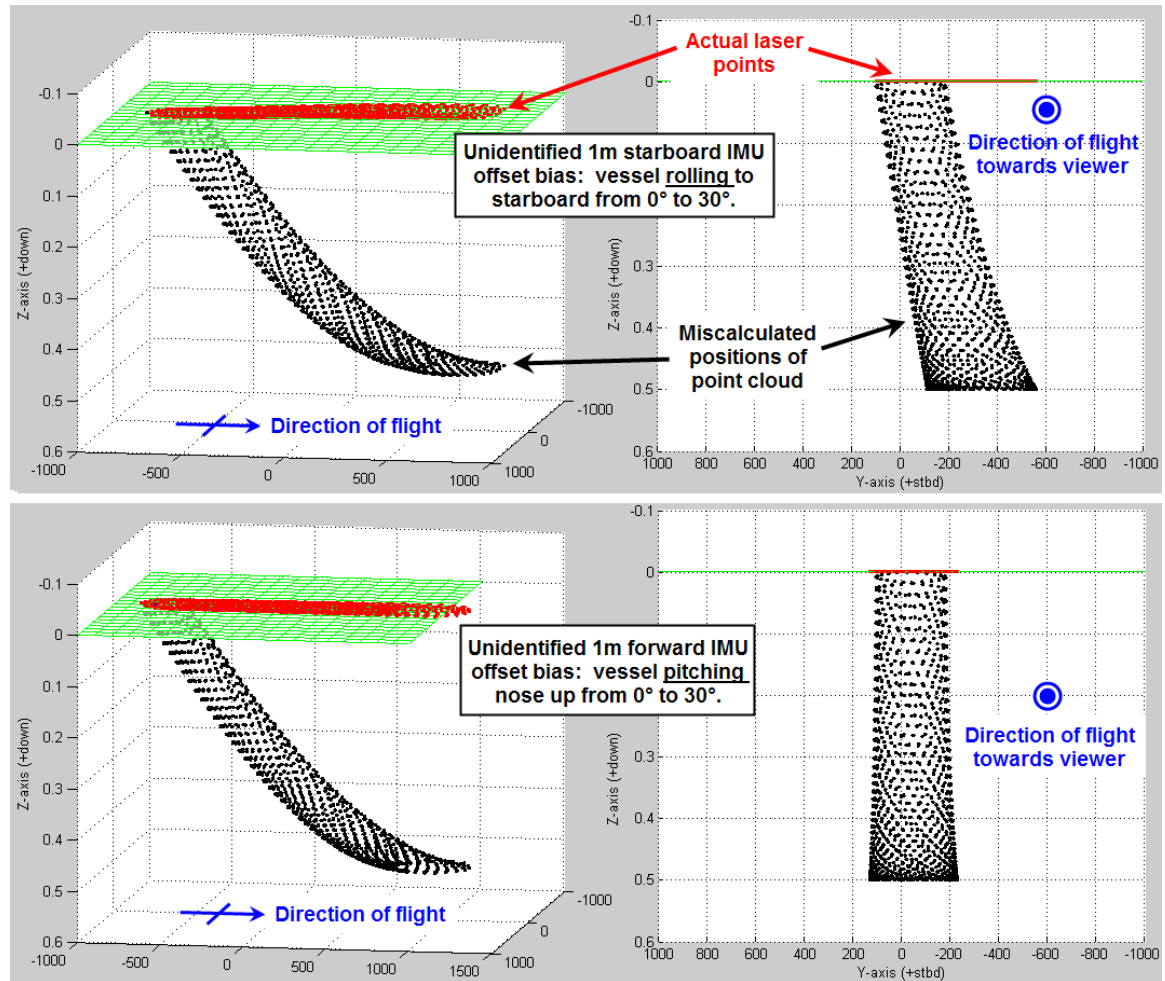


Figure 110. Signature analysis plots for a lidar with a 1m starboard IMU offset bias in the presence of a vehicle rolling (top), and a lidar with a 1m forward IMU offset bias in the presence of a vehicle pitching (bottom). The red points indicate the true laser strikes, while the black are the miscalculated biased points. All units in meters.

The crossing pattern shown in Figure 101 was simulated with non-zero values for the boresight angles, prism slope, INS offset vector and laser-to-scanner angles and subsequently calibrated. The VRF/IRF heading misalignment was set to zero, but included in the calibration. To get baseline uncertainties, the calibration was first

performed on all 9 of the preceding parameters with the exception of the INS offset vector (Figure 111 – “A”). As usual, θ_{LS} has a large uncertainty (1.939°) because this parameter is difficult to precisely calibrate (though the point cloud does not require precise calibration). $BS\theta_z$ and θ_{v1} also have large uncertainties (2.513° and 2.514° , respectively) due to their high correlation with each other.

Confidence (1σ) in calibration solution for "crossing" flight pattern where different parameters are included in adjustment (2 heave/pitch lines, 2 roll/yaw lines, 2 acquisition altitudes).									
	BS roll	BS pitch	BS yaw	Prism slope	VRF/IRF	ILoffX	ILoffY	LS Φ	LS θ
A	0.030°	0.030°	2.513°	0.006°	2.514°	-	-	0.033°	1.939°
B	0.031°	0.031°	580,000°	0.006°	580,000°	10,000m	10,000m	0.035°	1.970°
C	0.031°	0.031°	4.439°	0.006°	4.438°	0.112m	-	0.035°	1.973°

Figure 111. Table of results of different combinations of a 9-parameter calibration where the INS offset vector was held constant (A), no parameters were held constant (B) and only Δy_{IL} was held constant (C). The crossing pattern shown in Figure 101 was used to generate the data. All uncertainties are reported as 1-sigma.

When the INS offset vector is introduced into the calibration, the uncertainties grow unbounded (Figure 111 – “B”). Δx_{IL} and Δy_{IL} have uncertainties over 10 kilometers, while θ_{v1} and $BS\theta_z$ have uncertainties of nearly 600,000°. The magnitude and causes of the errors are better understood by examining the covariance (Figure 112) and correlation plots (Figure 113). The covariance plot shows that the spikes in uncertainty are limited to only four parameters in question: the rest of the calibration performed as well as normal. Turning to the correlation plot, we see that the four parameters are hopelessly entangled with each other (all having correlations of 1 or -1).

In the previous section, we saw that the large correlation between θ_{v1} and $BS\theta_z$ led to their respective increases in uncertainty. However, the extreme levels of

uncertainty here are an indication of more than just correlation – they are an indication of linear dependence.

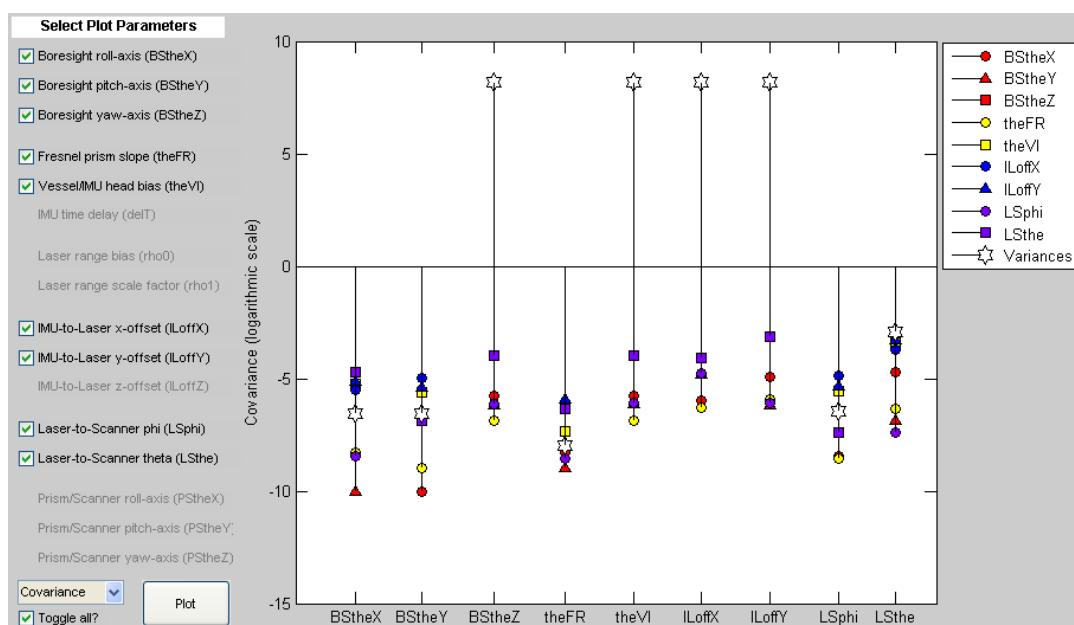


Figure 112. Covariances from a 9-parameter adjustment (boresight angles, prism slope, VRF/IRF heading alignment, INS offset vector and laser/scanner alignment). Note the logarithmic scale.

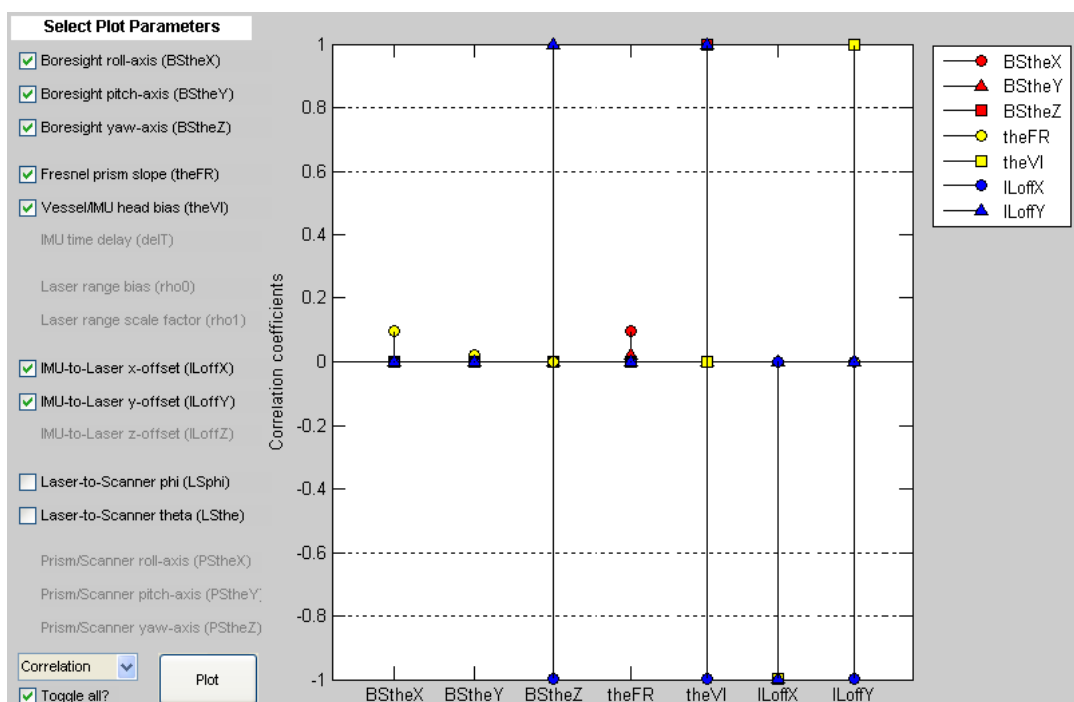


Figure 113. Correlation coefficients from a 9-parameter adjustment (only the boresight angles, prism slope, VRF/IRF heading alignment and INS offset vector are shown).

There is actually a fundamental connection among the parameters θ_{VI} , $BS\theta_z$, Δx_{IL} and Δy_{IL} which is revealed by returning to the laser location equation. Recall from (3.46) the ground coordinates of the point cloud are given by:

$$\vec{x}_G = \mathbb{R}_V \cdot \mathbb{R}_{VI} \left(\mathbb{R}_{BS} \cdot \vec{L}_2 \cdot \left(\frac{\rho - \rho_0}{\rho_1} \right) + \vec{x}_{IL} \right) + \vec{x}_{ECEF}, \quad (6.2)$$

in which the terms of particular importance are defined in (3.47):

$$\begin{aligned} \mathbb{R}_{VI} &= \underbrace{\begin{bmatrix} \cos \theta_{VI} & \sin \theta_{VI} & 0 \\ -\sin \theta_{VI} & \cos \theta_{VI} & 0 \\ 0 & 0 & 1 \end{bmatrix}}_{\text{Vehicle-INS heading misalignment}} \\ \mathbb{R}_{BS} &= \underbrace{\begin{bmatrix} \cos BS\theta_z & -\sin BS\theta_z & 0 \\ \sin BS\theta_z & \cos BS\theta_z & 0 \\ 0 & 0 & 1 \end{bmatrix}}_{\text{Yaw boresight angle}} \cdot \underbrace{\begin{bmatrix} \cos BS\theta_y & 0 & \sin BS\theta_y \\ 0 & 1 & 0 \\ -\sin BS\theta_y & 0 & \cos BS\theta_y \end{bmatrix}}_{\text{Pitch boresight angle}} \cdot \underbrace{\begin{bmatrix} 1 & 0 & 0 \\ 0 & \cos BS\theta_x & -\sin BS\theta_x \\ 0 & \sin BS\theta_x & \cos BS\theta_x \end{bmatrix}}_{\text{Roll boresight angle}} \\ \vec{x}_{IL} &= \underbrace{\begin{bmatrix} \Delta x_{IL} & \Delta y_{IL} & \Delta z_{IL} \end{bmatrix}^T}_{\text{INS-to-Laser offset}} \end{aligned} \quad (6.3)$$

It is important to note that the boresight angles are not a transformation from the laser scanner reference frame (SRF) to the INS reference frame, though they are often assumed to be due to the common practice of neglecting θ_{VI} . The boresight angles (just like \vec{x}_{IL}) are a transformation from the SRF to the VRF. The rotation matrix associated with θ_{VI} then completes the transformation from the VRF to the IRF.

Substituting (6.3) into (6.2), and temporarily disregarding the laser range bias and scale factor (ρ_0 and ρ_1), as well as the GPS position, \vec{x}_{ECEF} , we have:

$$\vec{x}_G = \mathbb{R}_V \begin{bmatrix} \cos \theta_{VI} & \sin \theta_{VI} & 0 \\ -\sin \theta_{VI} & \cos \theta_{VI} & 0 \\ 0 & 0 & 1 \end{bmatrix} \left(\begin{bmatrix} \cos BS\theta_z & -\sin BS\theta_z & 0 \\ \sin BS\theta_z & \cos BS\theta_z & 0 \\ 0 & 0 & 1 \end{bmatrix} \mathbb{R}_{BS\theta_y} \mathbb{R}_{BS\theta_x} \vec{L}_2 \rho + \begin{bmatrix} \Delta x_{IL} \\ \Delta y_{IL} \\ \Delta z_{IL} \end{bmatrix} \right). \quad (6.4)$$

The vehicle attitude (\mathbb{R}_V) and θ_{VI} rotation matrix can then be distributed inside the parenthesis:

$$\begin{aligned} \vec{x}_G = \mathbb{R}_V \begin{bmatrix} \cos \theta_{VI} & \sin \theta_{VI} & 0 \\ -\sin \theta_{VI} & \cos \theta_{VI} & 0 \\ 0 & 0 & 1 \end{bmatrix} \begin{bmatrix} \cos BS\theta_z & -\sin BS\theta_z & 0 \\ \sin BS\theta_z & \cos BS\theta_z & 0 \\ 0 & 0 & 1 \end{bmatrix} \mathbb{R}_{BS\theta_y} \mathbb{R}_{BS\theta_x} \vec{L}_2 \rho + \dots \\ + \mathbb{R}_V \begin{bmatrix} \cos \theta_{VI} & \sin \theta_{VI} & 0 \\ -\sin \theta_{VI} & \cos \theta_{VI} & 0 \\ 0 & 0 & 1 \end{bmatrix} \begin{bmatrix} \Delta x_{IL} \\ \Delta y_{IL} \\ \Delta z_{IL} \end{bmatrix}. \end{aligned} \quad (6.5)$$

Multiplying out the two θ_{VI} rotation matrices and applying some angle summation formulas then yield:

$$\begin{aligned} \vec{x}_G = \mathbb{R}_V \begin{bmatrix} \cos(BS\theta_z - \theta_{VI}) & -\sin(BS\theta_z - \theta_{VI}) & 0 \\ \sin(BS\theta_z - \theta_{VI}) & \cos(BS\theta_z - \theta_{VI}) & 0 \\ 0 & 0 & 1 \end{bmatrix} \mathbb{R}_{BS\theta_y} \mathbb{R}_{BS\theta_x} \vec{L}_2 \rho + \dots \\ + \mathbb{R}_V \begin{bmatrix} \Delta x_{IL} \cos \theta_{VI} + \Delta y_{IL} \sin \theta_{VI} \\ \Delta y_{IL} \cos \theta_{VI} - \Delta x_{IL} \sin \theta_{VI} \\ \Delta z_{IL} \end{bmatrix}. \end{aligned} \quad (6.6)$$

The preceding equation can now be put back into the form of (6.2) if we define new calibration parameters (θ_{VI}^* , $BS\theta_z^*$, Δx_{IL}^* and Δy_{IL}^*) in terms of the old parameters such that:

$$\vec{x}_G = \mathbb{R}_V \begin{bmatrix} \cos \theta_{VI}^* & \sin \theta_{VI}^* & 0 \\ -\sin \theta_{VI}^* & \cos \theta_{VI}^* & 0 \\ 0 & 0 & 1 \end{bmatrix} \left(\begin{bmatrix} \cos BS\theta_z^* & -\sin BS\theta_z^* & 0 \\ \sin BS\theta_z^* & \cos BS\theta_z^* & 0 \\ 0 & 0 & 1 \end{bmatrix} \mathbb{R}_{BS\theta_y} \mathbb{R}_{BS\theta_x} \vec{L}_2 \rho + \begin{bmatrix} \Delta x_{IL}^* \\ \Delta y_{IL}^* \\ \Delta z_{IL} \end{bmatrix} \right) \quad (6.7)$$

where:

$$\begin{aligned}\theta_{VI}^* &= 0^\circ \\ BS\theta_z^* &= (BS\theta_z - \theta_{VI}) \\ \Delta x_{IL}^* &= (\Delta x_{IL} \cos \theta_{VI} + \Delta y_{IL} \sin \theta_{VI}) \\ \Delta y_{IL}^* &= (\Delta y_{IL} \cos \theta_{VI} - \Delta x_{IL} \sin \theta_{VI}).\end{aligned}$$

In this way, the VRF/IRF heading misalignment is algebraically eliminated from the laser equation provided the value is deducted from the yaw boresight angle and the IMU offset vector is rotated. A graphical depiction of this process is shown in Figure 114.

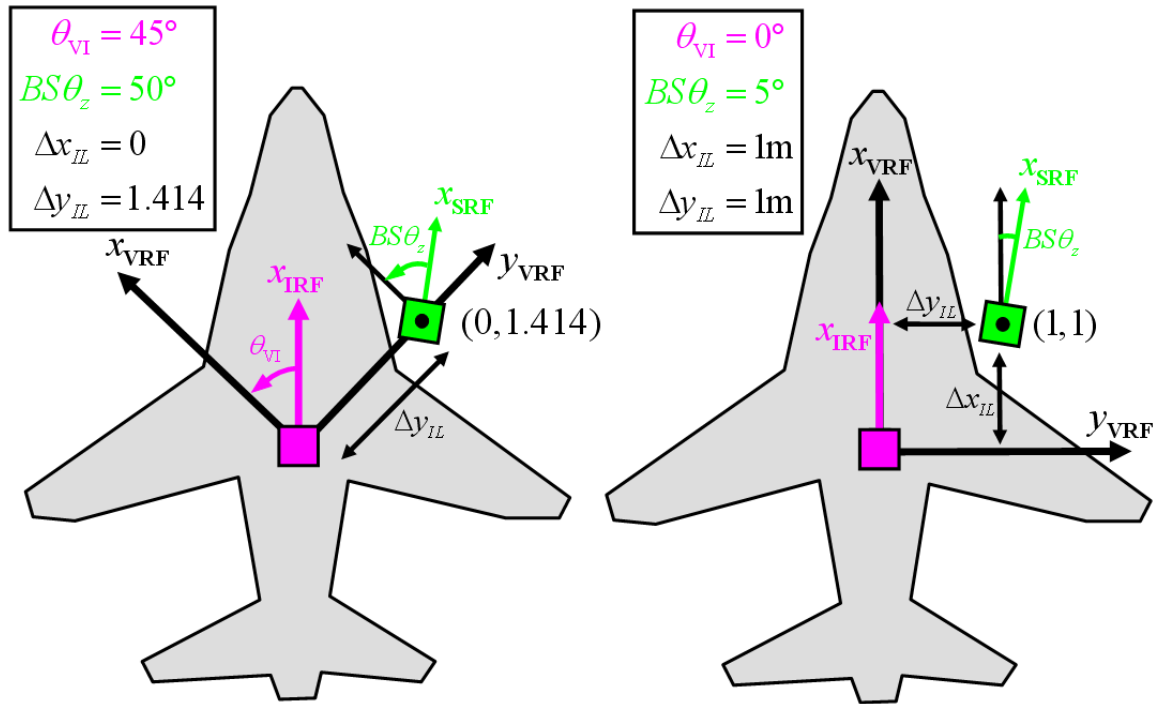


Figure 114. Two valid definitions of a vehicle reference frame: one oriented at an angle (left) and the other oriented towards the nose of the aircraft (right). Once the VRF is established, θ_{VI} , $BS\theta_z$, Δx_{IL} and Δy_{IL} are fixed accordingly. The laser scanner reference frame is indicated in green and the INS reference frame is indicated in magenta.

Suppose during a vehicle's static survey (when the offsets among the system components are measured), the surveyor capriciously decides the laser is located directly

“to the right” of the INS and proceeds to measure the distance between the two components, that is $\Delta x_{IL} = 0\text{m}$ and $\Delta y_{IL} = 1.414\text{m}$ (Figure 114 – left). So orienting the vehicle reference frame, the angular offsets between the IRF and VRF (i.e., θ_{VI}) and between the SRF and IRF (i.e., $BS\theta_z$) would then be measured as 45° and 50° , respectively. This choice of coordinate systems is not arbitrary, given it only requires the field crew to perform a single horizontal measurement (with no consideration to any angles). Within the calibrator, the INS offset vector would be set at (0,1.414) and held constant, then it will successfully determine the values for θ_{VI} and $BS\theta_z$.

Alternatively, and more likely, the surveyor would measure the horizontal offsets with respect to the airplane itself, using the vehicle’s centerline as a reference azimuth. By defining the airplane nose as “forward,” the VRF is accordingly defined and the forward and lateral offsets can be measured ($\Delta x_{IL} = 1\text{m}$ and $\Delta y_{IL} = 1\text{m}$ in this example). With these offsets input into the calibrator, it would then output the adjusted values for θ_{VI} and $BS\theta_z$ as 0° and 5° , respectively. Observe that both (0m, 1.414m, 45° , 50°) and (1m, 1m, 0° , 5°) will properly convert the point cloud into the INS’ reference frame and yield an identical point cloud.

To summarize: the four parameters θ_{VI} , $BS\theta_z$, Δx_{IL} and Δy_{IL} are linearly dependent on each other and cannot be simultaneously adjusted within the calibrator. At least one parameter must be fixed by the user in advance. Which of the four parameters to fix does not actually matter. Further, the value itself doesn’t matter either! The whole point is that we are defining an arbitrary vehicle reference frame to aid us in the measurement of the offset vector. This VRF is only temporary as no sooner are the

offsets made in the VRF that they are converted to the IRF. So, absolutely any angle can be input for θ_{VI} , and because the parameters are linearly dependent, absolutely any value can be used for one of the other parameters $BS\theta_z$, Δx_{IL} or Δy_{IL} as well. The only caveat is that neither component of the INS offset vector can be set to a value larger than the horizontal distance between the laser scanner and the INS. For example, if the two components are physically separated by 2m on a horizontal plane, then any number between +2 and -2 can be used as a fixed value for Δx_{IL} . Once Δx_{IL} is set (the thus the VRF defined), the other three parameters will align themselves accordingly.

Of course, just because something can be arbitrary doesn't mean it has to be. Surveyors can continue to declare $\theta_{VI} = 0^\circ$, but in so choosing they should not input the INS offset vector (at the risk of creating a sub-optimal calibration). Instead, the calibration routine should be permitted to solve for this offset vector. A more practical strategy, and what this dissertation recommends, is the surveyor continue to define the VRF in the intuitive manner of “forward” equals “towards the airplane’s nose.” From there, both the forward and lateral offsets can be measured, but only one should be entered into the calibrator. The other value can be held aside as a quality control check on the calibration. The results of a sample calibration, where one horizontal component of the INS offset vector is held fixed and the other is adjusted, are shown in Figure 111 (“C”). A user might have disparaging opinions about the reported uncertainty in the forward/aft INS offset of 0.112m (feeling they could measure this value more accurately by hand). There are two responses to that opinion:

1. Do not overlook the correlations – the large covariances not shown in Figure 111 that are associated with Δx_{IL} will ensure the TPU of the final point cloud is small. The

goal is not low uncertainties in the calibration parameters, but low uncertainties in the point cloud positioning.

2. The data in Figure 111 was from a simulated lidar operating at 51Hz: when the data is acquired at a full 10000Hz the expected uncertainty will be reduced from 0.112m to 0.009m (1σ).

6.3.3.2 – Scanner-to-INS vertical offset measurement. As with the horizontal biases in the INS offset vector, the presence of an unidentified vertical offset between the laser scanner and INS, Δz_{IL} , will result in a translation of the point cloud. Typically the biased point cloud will be shifted vertically by a measure equal to the magnitude of the unknown vertical offset (Figure 115 – top). Neither a change in altitude or a change in vehicle heading will produce a non-coplanar biased point cloud. The detection of a bias in Δz_{IL} is predicated on the vehicle either rolling (Figure 115 – middle) or pitching (Figure 115 – bottom). In both cases, the greater the magnitude of the vehicle's departure from a level flight, the greater the dispersion of the biased points, and the better the calibrator will perform.

The vertical INS offset is included in the calibration along with the boresight angles, prism slope, VRF/IRF heading alignment, laser/scanner angles and the INS forward offset (the INS lateral offset is held constant for reasons discussed in the previous section). Results for this 9-parameter calibration are shown in Figure 116 (“A”). As before, the usual suspects of $BS\theta_z$, θ_{VI} and θ_{LS} have relatively larger uncertainties, though none are of particular concern for the point cloud because of the large associated covariances discussed earlier. The newest parameter, Δz_{IL} , also has a large uncertainty of 1.886m (1σ) which could be problematic for the final point cloud.

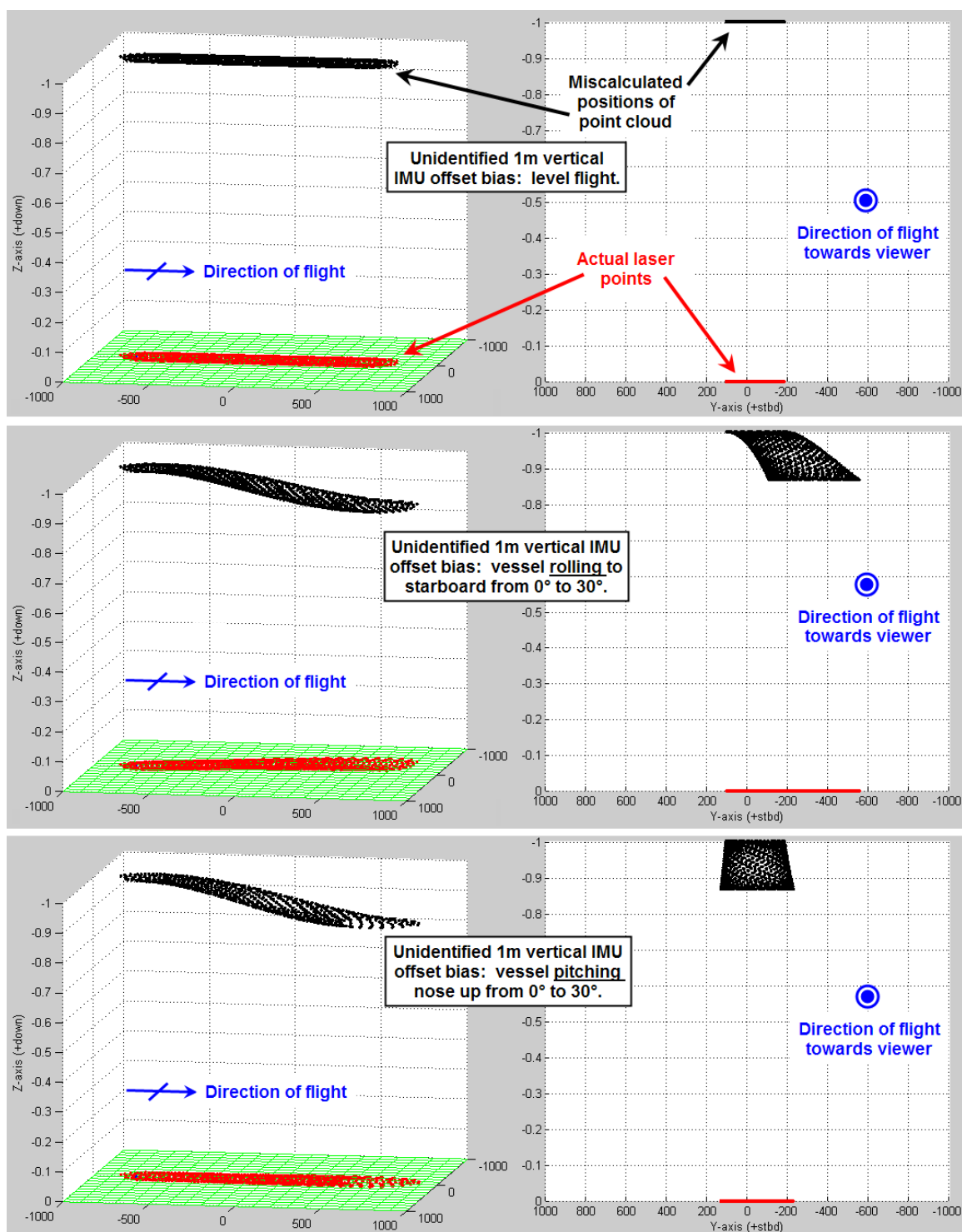


Figure 115. Signature analysis plots for a lidar with a 1m vertical IMU offset bias (top), in the presence of a rolling vehicle (middle), and pitching vehicle (bottom). The red points indicate the true laser strikes, while the black are the miscalculated biased points. All units in meters.

Confidence (1σ) in calibration solution for "crossing" flight pattern both without (A) and with (B) ground control. Average point cloud Total Vertical Uncertainty is also shown.										
	BS roll	BS pitch	BS yaw	Prism slope	VRF/IRF	ILoffX	ILoffZ	LS ϕ	LS θ	Average TVU
A	0.031°	0.032°	4.449°	0.006°	4.447°	0.121m	1.886m	0.035°	2.015°	1.88m (1σ)
B	0.031°	0.032°	4.449°	0.006°	4.447°	0.120m	0.010m	0.035°	2.015°	0.11m (1σ)

Figure 116. Table of results of a 9-parameter calibration (including the vertical INS offset) both without (A) and with (B) ground control. The vertical propagated uncertainty of the point cloud is included for reference. The crossing pattern shown in Figure 101 was used to generate the data. All uncertainties are reported as 1-sigma.

Though not shown in Figure 116, the z -coordinate of the point used to define the planar surface in the adjustment, see (5.56), also has a large uncertainty ($2.354\text{m} - 1\sigma$) and a large correlation with Δz_{IL} . As will be discussed in the Chapter VII, only the variance-covariance information associated with the lidar calibration parameters are passed to the total propagated uncertainty module. The uncertainty information as it pertains to the five planar surface parameters is not retained, which is a detriment to any calibration parameter with a high correlation to the planar parameters. For the present calibration, this implies the large variance of Δz_{IL} will be carried forward to the uncertainty module, but the large covariance of Δz_{IL} with the z -planar coordinate will not. The end result is the total vertical uncertainty (TVU) of the point cloud will be on the order of 1.88m, implying the variance of Δz_{IL} accounts for nearly 100% of the vertical uncertainty in the point cloud (see Section 7.3 for a discussion of the relative contributions to point cloud uncertainty). A nearly 2m vertical uncertainty in the point cloud is unacceptably large for most surveying applications. To control this error, two simple options exist: introduce a ground control point or measure the vertical INS offset by hand and treat it as a measured parameter in the LSA. Both options will be discussed.

To define the planar surface to which the point cloud is fit, five parameters are required (two for the planar normal vector and three for a point on the plane). All five of

these planar parameters are adjusted within the calibration routine. However, if the coordinates of any point on the planar surface are already known, three of the parameters can be removed from the adjustment. This could be achieved by performing the calibration flight in the vicinity of a known benchmark or by conducting a static GPS survey. Note, the lidar data does not have to include the reference point; that is, the lidar survey can be conducted in one spot and the reference point can be from another area (so long as both regions are coplanar with each other).

Figure 116 (“B”) shows the results of a 9-parameter calibration in which the point on the adjusted planar surface is held fixed. By adding the one ground control point, the uncertainty in the Δz_{LL} drops from 1.886m to 0.010m (1σ). Likewise, the uncertainty of vertical propagated uncertainty of the point cloud drops from 1.88m to a much more acceptable 0.11m (1σ). Of note is the confidence of the other 8 calibration parameters unaffected by the inclusion of ground control.

The other option available to the surveyor is to measure vertical INS offset manually and declare the Δz_{LL} as an “observed” rather than a “calibrated” parameter in the LSA (while the five planar parameters are again adjusted). Under such a scheme, both the confidence of the remaining eight calibration parameters and the propagated uncertainty of the final point cloud are equivalent to the calibration with the ground control.

To summarize, the vertical INS offset cannot be added to calibration algorithm (along with the other eight calibration parameters and five planar parameters) without inducing a large uncertainty in the positions of the final point cloud. To cope with this uncertainty, either a ground control point should be included or Δz_{LL} should be measured

directly by the surveyors and removed from the adjustment. Given the surveyors are already measuring the two horizontal components of the INS offset vector (of which one is required to be held fixed in the LSA), measuring the vertical offset as well does not require much additional effort. Measuring Δz_{ll} is also particularly simple in contrast to the level of effort required to survey a ground control point to the same accuracy of this vertical offset. However, by removing the planar coordinate from the adjustment, any associated covariances that would otherwise be associated with these points are eliminated (a desired feature with regard to the propagated uncertainty of the point cloud).

6.3.4 – Prism-to-Scanner Alignments

As more parameters are included in the calibration routine, the least squares adjustment has more “options” with regard to fitting the point cloud to a planar surface. Altering one combination of parameters can produce a point cloud that is similar (or identical, as was seen in with θ_{vl}) to the effect achieved by changing another parameter. Thus, as more parameters are piled on the calibrator, the expected confidences in their solution will become less and less.

The next-to-last group of calibration parameters to discuss is the prism-to-scanner angular alignments. There are three rotations to consider: the roll-like rotation of prism about the scanner’s about its x -axis ($PS\theta_x$) and pitch-like rotation about the scanner’s y -axis ($PS\theta_y$), both shown in Figure 17, and the bias in the scanner’s azimuth angle ($PS\theta_z$). The first pair of misalignments (which display a similar behavior) will be discussed in tandem in one section with the third parameter to follow in a separate section.

6.3.4.1 – *Prism “pitch” and “roll” biases.* For a lidar with no non-zero geometric alignments (i.e. boresight angles, laser/scanner angles and VRF/IRF heading are equal to 0°), a rotation of the prism with respect to either the scanner’s x or y -axis will just produce a larger circular scan pattern than what would otherwise be present (see Figure 18). This is the same effect that can be achieved were the prism slope to be increased (see Figure 15). The similarities in these plots suggest there will be a high degree of correlation both between the two parameters $PS\theta_x$ and $PS\theta_y$, and with the prism slope θ_{FR} .

To confirm the connections among θ_{FR} and the prism/scanner angles, consider the signature plots for $PS\theta_y$ shown in Figure 117 and Figure 118. The trends of the biased point clouds are all nearly identical to those shown for θ_{FR} (Figure 88 and Figure 89). Since each parameter produces such a similar effect on the point cloud, they will be very difficult to decouple in the calibration process. However, they will not be impossible to decouple, as $PS\theta_y$ cannot be algebraically eliminated from the laser equation as θ_{VI} was in (6.7).

Signature plots for $PS\theta_x$ (not shown) are also near equivalents to those for $PS\theta_y$ with two slight differences: the behavior for a rolling and pitching vehicle are reversed, and the vertical scale of the biased cloud is different. The disparity in scales between $PS\theta_x$ and $PS\theta_y$ is shown in Figure 119. An unknown bias of 1° in $PS\theta_x$ will lead to a vertical shift in the point cloud of 0.005m; whereas a similar bias in $PS\theta_y$ will lead to a 0.309m shift. This magnification effects on the biased point clouds implies that $PS\theta_y$ will be the easier parameter to determine during the calibration. For reference, a bias of

1° in the prism slope leads to a 1.54m shift (implying it will be easier to calibrate than both of the preceding parameters). The fact that an equal change in θ_{FR} and $PS\theta_x$ has an almost 300 fold difference in how it is manifested has a secondary consequence: if both parameters are calibrated, the uncertainty in $PS\theta_x$ is going to be much larger.

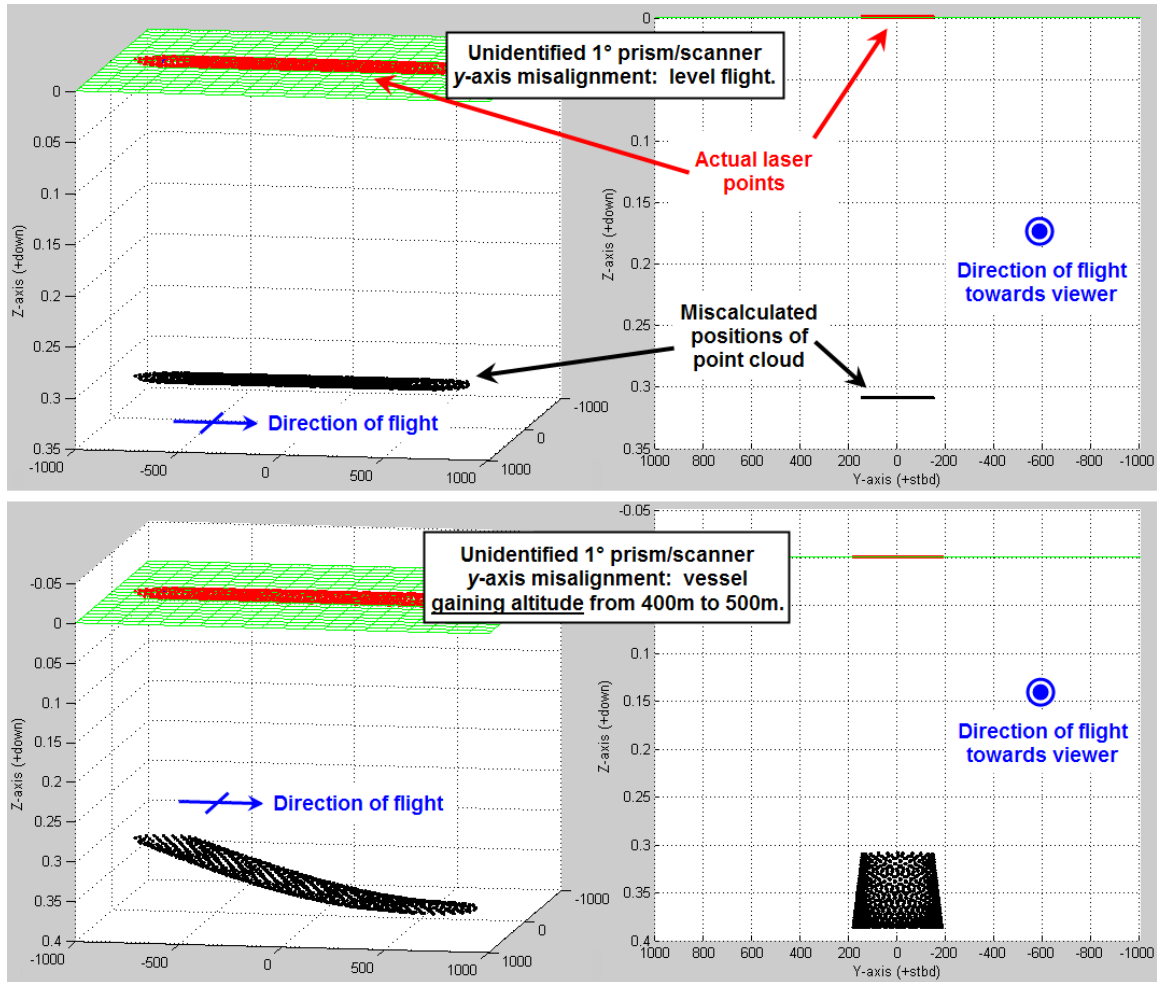


Figure 117. Visualization of a point cloud generated from a lidar with an unidentified 1° $PS\theta_y$ misalignment(top), and a point cloud from the same system as it experiences an increase in altitude (bottom). The red points indicate the true laser strikes, while the black are the miscalculated biased points. All units in meters.

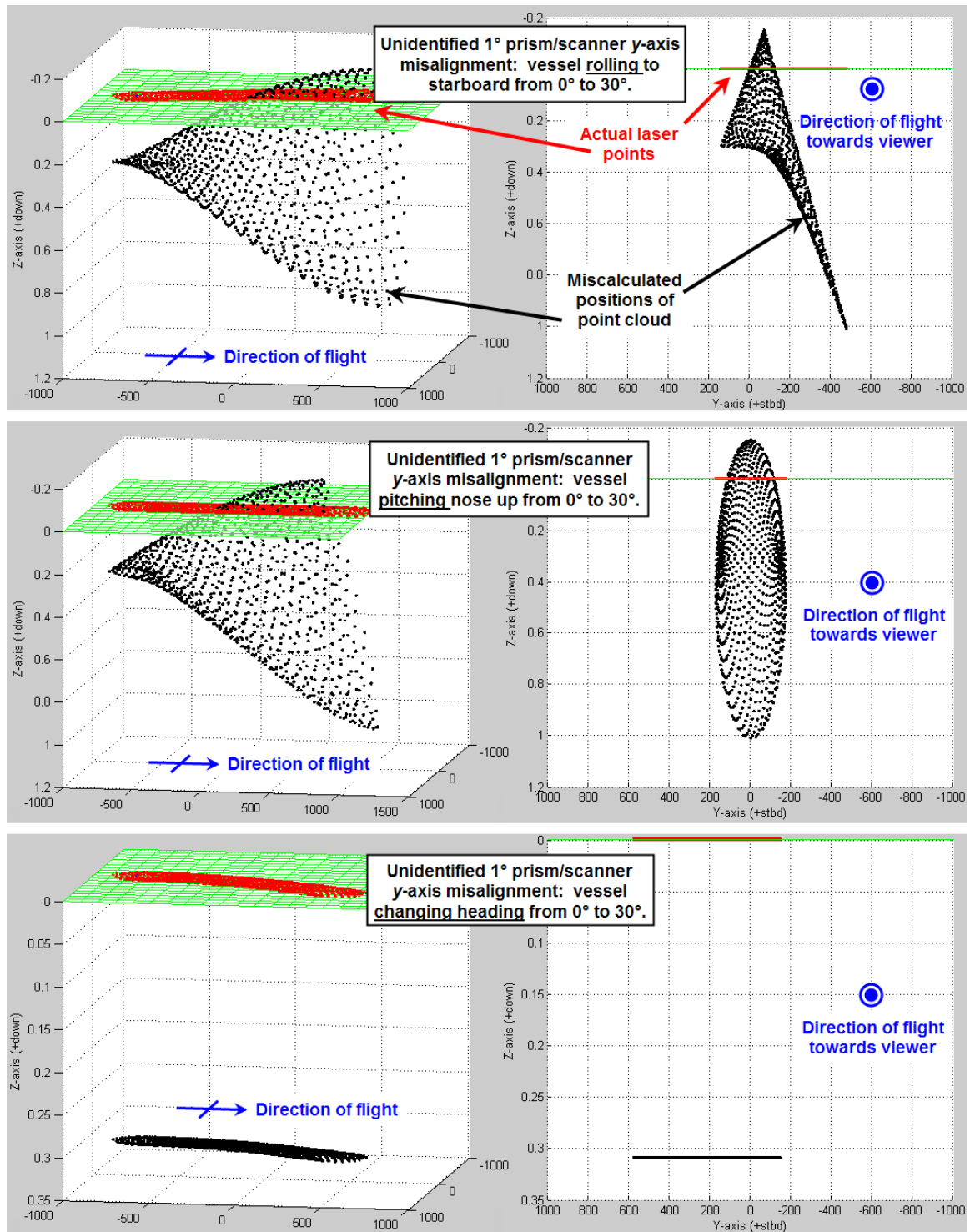


Figure 118. Signature analysis plots for a lidar with a 1° $PS\theta_y$ misalignment in the presence of a rolling (top), pitching (middle) and yawing (bottom) vehicle. The red points indicate the true laser strikes, while the black are the miscalculated biased points. All units in meters.

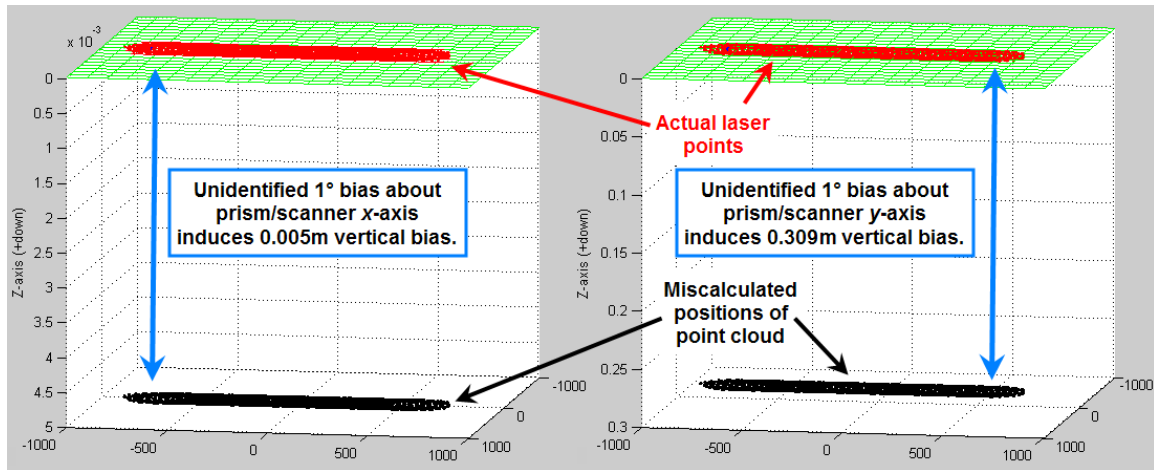


Figure 119. Comparison of signature plots for two level flight lines with an unidentified rotation of 1° between the prism and scanner about two different axes, $PS\theta_x$ (left) and $PS\theta_y$ (right). The red points indicate the true laser strikes, while the black are the miscalculated biased points. All units in meters.

It should be noted that the previous signature plots for the prism/scanner alignments were all generated with the assumption that no other non-zero system alignments are present. In the actual system, it is unlikely that every component will be so perfectly situated. Figure 120 shows what the biased point cloud would look like were there an unknown 1° bias in $PS\theta_x$ (a re-rendering of Figure 119 – left, from a different perspective) as well as that same bias in the presence of a geometrically more complicated system. Moving from left to right, new known misalignments are introduced until Figure 120 – 4 which displays a biased point cloud containing non-zero values for the pitch and roll boresight angles in addition to the laser/scanner alignments. Note, only the bias in $PS\theta_x$ is unknown, and is thus the only cause of the miscalculated positions of the point cloud. As the orientation of the system grows in complexity, the misalignment in $PS\theta_x$ induces a larger vertical displacement on the biased point cloud. Should the

vehicle experience any change in aspect (pitch or roll), then these vertical displacements are further amplified.

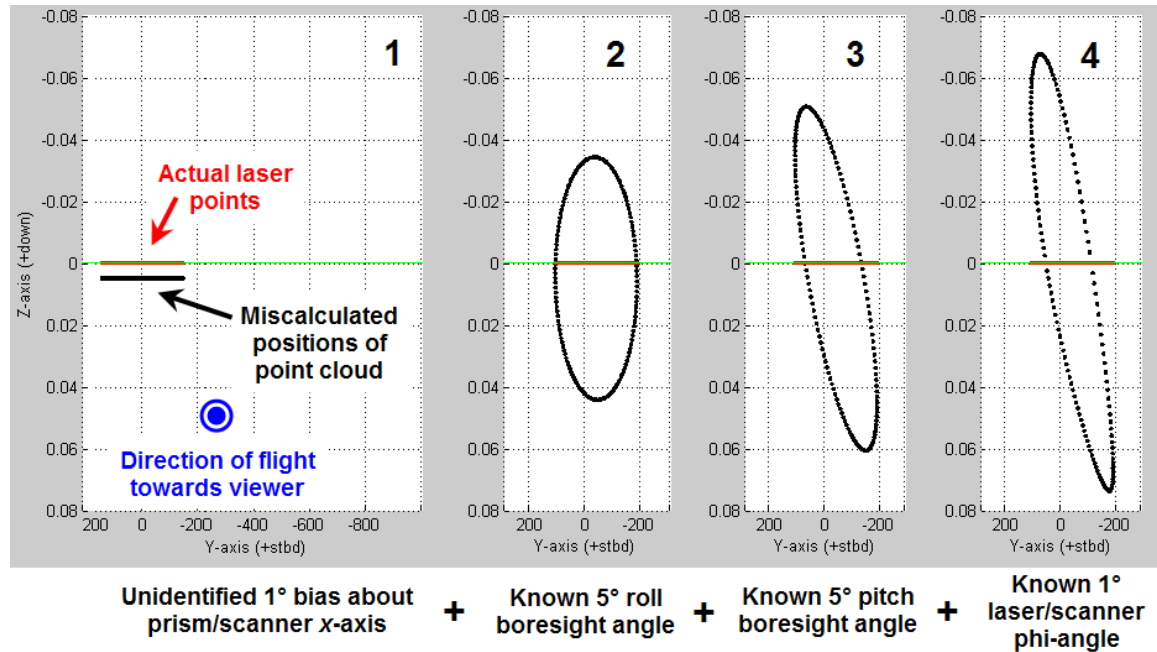


Figure 120. Comparison of signature plots for a level flight with an unidentified rotation of 1° prism/scanner x -axis alignment (1) and same incrementally more complicated point cloud, introducing known biases to the roll boresight (2), pitch boresight (3) and laser/scanner alignments (4). The red points indicate the true laser strikes, while the black are the miscalculated biased points. All units in meters.

The usual flight pattern of Figure 101 was simulated at 51Hz (3,800 data points) with an additional misalignment in $PS\theta_x$ and $PS\theta_y$. Before processing a full 11-parameter calibration (ground control was simulated, permitting the adjustment of Δz_{IL}), a 9-parameter calibration was first simulated to provide a baseline confidence (Figure 121 – Trial 1). Trial 2 includes $PS\theta_y$ in the adjustment while Trial 3 includes $PS\theta_x$. In both cases, the uncertainty for the two parameters is large (8 216° and 7.974°, respectively). Further all the calibration parameters (pitch and roll boresight, prism slope, and the two laser/scanner angles) with correlations of ± 1 with these two parameters

also wind up with inordinately large uncertainties (highlighted in bold in Figure 121).

For example, when $PS\theta_y$ is included in the calibration, the uncertainty in the prism slope increases by over 40,000%, to 1.634° (1σ). This leap in uncertainty validates the supposition from the signature plots whose similarities suggested the two parameters would be difficult to decouple.

Calibration parameter	Confidence (1σ) in calibration solution (reported as a percentage of the baseline, "Trial 1", confidence).				
Trial #	1	2	3	4	5
Prism/Scanner x-axis	-	-	7.974°	7.771°	0.379°
Prism/Scanner y-axis	-	8.216°	-	8.213°	0.046°
Boresight roll angle	0.018°	190%	1540%	1510%	-
Boresight pitch angle	0.018°	2420%	450%	2450%	-
Boresight yaw angle	3.036°	105%	128%	131%	-
Prism slope	0.004°	42600%	1330%	42600%	-
VRF/IRF heading bias	3.035°	106%	107%	112%	-
IMU x-offset	0.083m	109%	100%	109%	-
IMU z-offset	0.007m	98%	101%	99%	-
Laser/Scanner Φ -angle	0.021°	1890%	250%	1910%	-
Laser/Scanner θ -angle	1.191°	250%	1860%	1820%	-
Max. contribute to THU	0.100m	23.1m	9.7m	24.9m	0.273m
Max. contribute to TVU	0.009m	37.5m	18.9m	37.6m	0.889m

Figure 121. Table of results of an 11-parameter calibration trial with ground control (1σ uncertainties shown). Parameters marked by a '-' were not included in a given calibration trial. Trial 1 provides a baseline calibration without $PS\theta_x$ and $PS\theta_y$. The remaining trials report the parameter uncertainties as a percentage of this baseline. Parameters with ± 1 correlations to $PS\theta_x$ or $PS\theta_y$ are highlighted in bold. The maximum contribution to the propagated uncertainty of the point cloud is included for reference. The crossing pattern shown in Figure 101 was used to generate the data.

Since the inclusion of θ_{VI} in the calibration routine (Section 6.3.3.1), the uncertainties in $BS\theta_z$, θ_{VI} and θ_{LS} have had large uncertainties (see Figure 104). In spite of these large uncertainties, their covariances worked towards keeping the contribution to the propagated uncertainty in the point cloud positions relatively small. For example, the previous baseline flight contributed only 0.009m to the point cloud

vertical TPU and 0.100m to the horizontal TPU (Figure 121 – Trial 1). The addition of $PS\theta_x$ and $PS\theta_y$ to the calibration however are too much for the point cloud to bear. The large uncertainties of these two parameters (along with the much larger uncertainties of all the correlated parameters) causes the vertical and horizontal point cloud TPU to swell to 37.5m and 23.1m (1σ) respectively. In this case, one would be justified in saying the calibration failed as both the proposed solution for the calibration parameters and the location of the laser points have poor confidences. Even a calibration of just the two prism/scanner angles yields a point cloud that would not satisfy an IHO Order 1 survey (0.889m – 1σ vertical TPU versus the depth requirement of 0.5m). Note: see Section 7.3 for a breakdown of the relative contributions to the TPU by the calibration parameters.

It is reasonable to wonder why the point cloud uncertainties are so large when previous examples (see Figure 116) have shown the point cloud is capable of absorbing large calibration parameter uncertainties. One must understand that the confidences reported by the LSA are merely the confidence in the choice of the calibration values that lead to the best possible fit to a planar surface. A high confidence in the calibration values does not necessarily imply a high confidence in the point cloud position. Recall when the adjustment of the vertical INS offset was first introduced, the calibrator was successful in fitting the points to a planar surface, but the large uncertainty in Δz_{IL} implied the calibrator was not confident in the vertical position of said planar surface (Figure 116 – A). In short, the vertical position of the planar surface is the vertical TPU of the point cloud.

To summarize, the surveyor has two options with regard to determining the values of $PS\theta_x$ and $PS\theta_y$. First, the data density can be increased. As with the other calibration

parameters, quadrupling the data density will halve the calibration uncertainties. Further, quadrupling the data density will also halve the horizontal and vertical point cloud TPU (see Section 7.3). So, if enough data are included in problem, the calibration parameters can eventually be determined to any desired degree (theoretically). The second option is to forgo the inclusion of these two parameters in the adjustment. Lacking a large enough dataset, the calibrator cannot determine their values to a high degree of accuracy, and their inclusion degrades the reported accuracy of the boresight angles, prism slope and laser/scanner angles.

A recommendation for future work is to instead express the alignments between the prism and scanner in spherical coordinates (similar to how the alignment between the laser and scanner was done). Such a model will remove the large correlation between $PS\theta_x$ and $PS\theta_y$ and may lead to an improved model confidence.

6.3.4.2 – Scanner azimuth bias. Forgoing the signature plots that have been a constant presence throughout this chapter, let it be said up front that a bias in the scanner azimuth ($PS\theta_z$) is linearly dependent on the calibration parameters that have already been discussed. Like θ_{VI} with Δx_{IL} , Δy_{IL} and $BS\theta_z$, $PS\theta_z$ can be held fixed at any value and other parameters can organize themselves to still reconstruct the correct point cloud.

Consider a lidar with 5° misalignments for the three boresight angles, a 1m forward-starboard-down INS offset, a 1° misalignment in both laser/scanner angles (ϕ_{LS}, θ_{LS}) as well as the two prism/scanner angles ($PS\theta_x, PS\theta_y$), and a 0° misalignment in both the VRF/IRF heading bias and the scanner azimuth bias. $PS\theta_z$ is then held fixed at 0° in the calibrator while the remaining 11 parameters are adjusted in the calibrator (Figure 122). The calibration module is successful in recovering the planar surface. The

11-parameter calibration is then executed a second time, this time holding $PS\theta_z$ fixed at 10° . The calibration routine is again successful in recovering the planar surface (Figure 123). To compensate for the change in $PS\theta_z$, θ_{LS} also rotates by 10° and the boresight angles reorient themselves, most notably $BS\theta_z$ nearly counter-rotates by 10° .

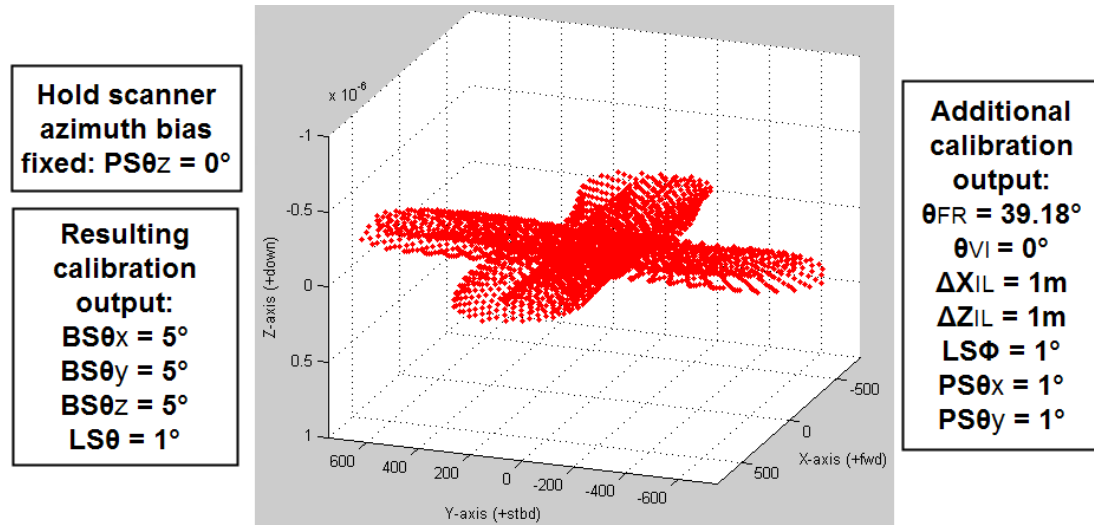


Figure 122. An 11-parameter calibration in which the scanner azimuth bias is held fixed at 0° . All units in meters.

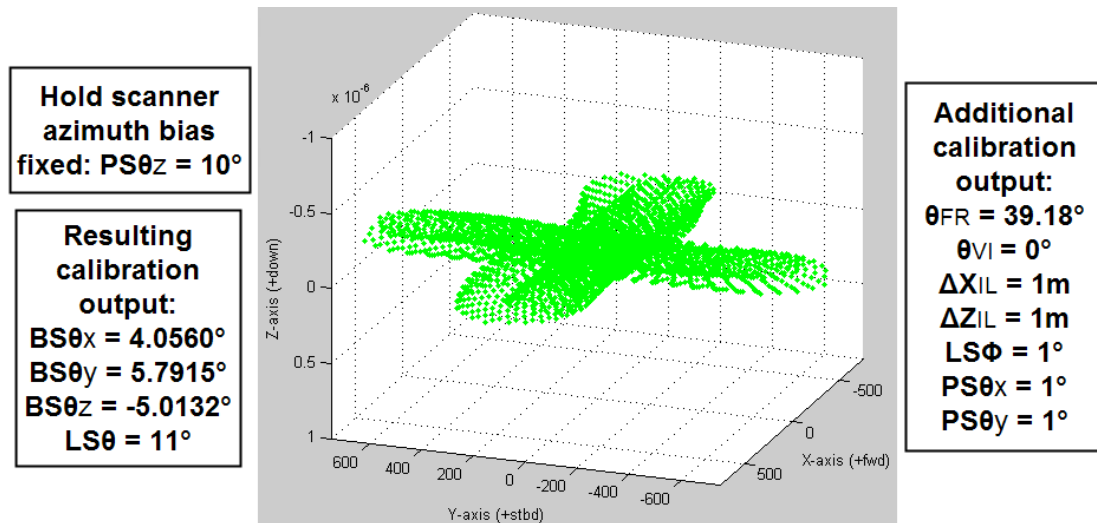


Figure 123. A second attempt at an 11-parameter calibration of the same point cloud as in Figure 122, this time holding the scanner azimuth bias fixed at 10° .

That the point cloud can be correctly reconstructed in more than one way is the epitome of an adjusted point cloud containing a linearly dependent variable. In this case, $PS\theta_z$ is dependent on θ_{LS} and the three boresight angles. To algebraically demonstrate the dependence is not as straight forward a matter as it was for θ_{VI} , as the parameters are entwined deep within the laser equation.

Consider again the following simplified excerpts of the laser equation (3.46):

$$\vec{x}_G = \mathbb{R}_V \cdot \mathbb{R}_{VI} \left(\underbrace{\mathbb{R}_{BS} \cdot \vec{L}_2}_{\text{highlighted}} \cdot \rho + \vec{x}_{IL} \right) + \vec{x}_{ECEF} \quad (6.8)$$

Here, we only want to focus on the part of the equation highlighted by the under braces.

Loosely speaking, \vec{L}_2 is of the form:

$$\vec{L}_2 = (\alpha_1 \vec{L}_0 + \alpha_2 \vec{P}_1) + \alpha_3 \vec{P}_2 \quad (6.9)$$

where the terms α_1 , α_2 , and α_3 are constants that are not of consequence for this discussion and

$$\begin{aligned} \vec{P}_1 &= \begin{bmatrix} \cos PS\theta_z & -\sin PS\theta_z & 0 \\ \sin PS\theta_z & \cos PS\theta_z & 0 \\ 0 & 0 & 1 \end{bmatrix} \mathbb{R}_{\theta_{zs}} \cdot \mathbb{R}_{PS\theta_y} \cdot \mathbb{R}_{PS\theta_x} \cdot \begin{bmatrix} -\sin \theta_{FR} \\ 0 \\ -\cos \theta_{FR} \end{bmatrix} \\ \vec{P}_2 &= \begin{bmatrix} \cos PS\theta_z & -\sin PS\theta_z & 0 \\ \sin PS\theta_z & \cos PS\theta_z & 0 \\ 0 & 0 & 1 \end{bmatrix} \mathbb{R}_{\theta_{zs}} \cdot \mathbb{R}_{PS\theta_y} \cdot \mathbb{R}_{PS\theta_x} \cdot \begin{bmatrix} 0 \\ 0 \\ -1 \end{bmatrix} \\ \vec{L}_0 &= - \begin{bmatrix} \cos \theta_{LS} & -\sin \theta_{LS} & 0 \\ \sin \theta_{LS} & \cos \theta_{LS} & 0 \\ 0 & 0 & 1 \end{bmatrix} \mathbb{R}_{\phi_{LS}}, \end{aligned} \quad (6.10)$$

where each \mathbb{R} represents a rotational matrix for the parameter indicated in the subscript.

For each equation in (6.10), notice the left-most matrix is a rotation about a z-axis.

Should $PS\theta_z$ and θ_{LS} happen to be the same angle, then all three terms in (6.9) would

have a common term that would represent the rotation of \vec{L}_2 about a z -axis. If desired, both $PS\theta_z$ and θ_{LS} could be intentionally shifted in tandem in either direction to induce a further rotation in \vec{L}_2 that isn't actually present (this would be the algebraic equivalent of holding $PS\theta_z$ fixed at an incorrect value in the LSA). Call this now incorrectly rotated vector \vec{L}_2^* . Then, back in the laser equation we have:

$$\vec{x}_G = \mathbb{R}_V \cdot \mathbb{R}_{VI} \left(\mathbb{R}_{BS} \cdot \vec{L}_2^* \cdot \rho + \vec{x}_{IL} \right) + \vec{x}_{ECF}. \quad (6.11)$$

With a now incorrect value for \vec{L}_2^* , to still produce the geometrically correct point cloud requires a method of un-rotating \vec{L}_2^* about the z -axis. Recall from (3.47) the \mathbb{R}_{BS} represents the three boresight angle rotations defined by:

$$\underbrace{\begin{bmatrix} \cos BS\theta_z & -\sin BS\theta_z & 0 \\ \sin BS\theta_z & \cos BS\theta_z & 0 \\ 0 & 0 & 1 \end{bmatrix}}_{\text{Yaw boresight angle}} \underbrace{\begin{bmatrix} \cos BS\theta_y & 0 & \sin BS\theta_y \\ 0 & 1 & 0 \\ -\sin BS\theta_y & 0 & \cos BS\theta_y \end{bmatrix}}_{\text{Pitch boresight angle}} \underbrace{\begin{bmatrix} 1 & 0 & 0 \\ 0 & \cos BS\theta_x & -\sin BS\theta_x \\ 0 & \sin BS\theta_x & \cos BS\theta_x \end{bmatrix}}_{\text{Roll boresight angle}} \quad (6.12)$$

which contains a rotation about a z -axis in the form of $BS\theta_z$. Should the pitch and roll boresight angles happen to be zero, then their associated rotational matrices would be identity matrices and drop from the equation, at which point, the yaw boresight angle could be shifted in the opposite direction that $PS\theta_z$ and θ_{LS} were first misrotated. If the pitch and roll boresight angles are non-zero, then one must solve for the three Tait-Bryan angles that will restore the system to its original geometry. Depending on the magnitude of the original bias in $PS\theta_z$, $BS\theta_x$ and $BS\theta_y$ will only be altered slightly while $BS\theta_z$ will very nearly be rotated in the opposite direction.

In the example shown in Figure 123, when the value for $PS\theta_z$ was erroneously rotated by 10° , the calibrated value for θ_{LS} also rotated by that same angle, going from 1° to 11° . Meanwhile, the boresight angles also reorganized themselves, among them, $BS\theta_z$ nearly counter-rotated by 10° , going from 5° to -5.0132° . The other seven parameters included in the calibration were unaffected.

Previously, the reasons for the linear dependence of the VRF/IRF heading bias came down to a matter of reference frame. The vehicle reference frame is abstract in design and can be oriented in any direction. Similarly, the scanner's reference frame, from the laser-prism-scanner assemblage, is also arbitrarily designated. Ideally, the scanner should be oriented in a manner that is meaningful, for example declaring the 0° azimuth to be directed towards the nose of the aircraft. However any direction can be declared the 0° angle for the scanner. Once that decision is made, that will dictate the z -axis rotation (called θ_{LS}) needed to align the laser to the scanner. Further, the boresight angles will also then be decided given these angles represent a transformation from the scanner's reference frame to the vehicle's.

The take home message for the surveyor is they have a choice of which parameter between the scanner azimuth bias and the laser/scanner θ -angle that they want to include in the calibration (since including both is not possible). By fixing θ_{LS} at 0° , the implication becomes that the “forward” direction of the scanner is the incoming direction of the laser. Such a decision is a bit capricious given the ideal system geometry will have the laser pointing normal to the scanner (i.e. $\phi_{LS} = 0$), which would render θ_{LS} meaningless. The alternative is to set $PS\theta_z = 0$, which would imply that the scanner has

no encoding bias. Whichever direction the scanner declares to be “forward” will be “forward,” and the laser and vehicle reference frames will be rotated accordingly.

Calibration trials were consecutively executed in which first θ_{LS} and then $PS\theta_z$ were held fixed. In each case the confidence in the adjusted parameters were comparable, respectively 1.240° and 1.221° (1σ). The difference, however, comes in the calibration parameters contribution to the point cloud propagated uncertainty. When the scanner azimuth bias is adjusted, the maximum calibration parameters’ contribution to the TVU is 1.14m (1σ); but when the laser/scanner θ -angle is adjusted, the maximum TVU drops to 0.009m (1σ) – see Section 7.3 for further details. For this reason, $PS\theta_z$ should be held fixed while θ_{LS} is included in the calibration.

6.3.5 – Laser Range Bias and Scale Factor

The final two parameters to discuss are more radiometric in nature, having to do with how the signal from the returning laser emission is interpreted as a range.

Nevertheless, the presence of either a laser range bias, ρ_0 , or scale factor, ρ_1 (pictured in Figure 30) would result in a geometric misalignment of the point cloud, which this dissertation is seeking to address. They are briefly discussed here, but the surveyor should give due consideration to whether attempting to determine these two corrective factors via this calibrator rather than seeking to better understand the signal processing algorithms used to derive the laser range is the best course of action. The calibrator provides the option to disable these parameters.

For a level flight, with no other non-zero misalignments (boresight angles, laser/scanner angles, etc.), errors in either ρ_0 or ρ_1 will lead to a biased point cloud that is still coplanar and vertically shifted from the true values. To cause the point cloud to

diverge from this planar structure, and thus make calibration possible, different maneuvers are required for each of the parameters. For the laser range scale factor, the vehicle must experience a change in acquisition altitude (Figure 124). The greater the change in altitude, the better the ability of the calibrator to determine the value of this parameter. It should be noted a vehicle roll or pitch will produce a very slight vertical dispersion of the biased point cloud, but this dispersion is about four orders of magnitude less than that induced by a change of altitude. To determine the laser range bias, the vehicle must undergo some change in aspect, either pitch or roll (Figure 125).

The heaving signature plot for ρ_1 looks very similar to the plots for both θ_{FR} (Figure 88) and Δz_{IL} (Figure 89), suggesting there may be some correlation. Likewise, the signature plots for ρ_0 resemble those for θ_{FR} (Figure 115). The relationship among these variables should be intuitive since a bias in all four of the parameters results in a vertical shift of the biased point cloud.

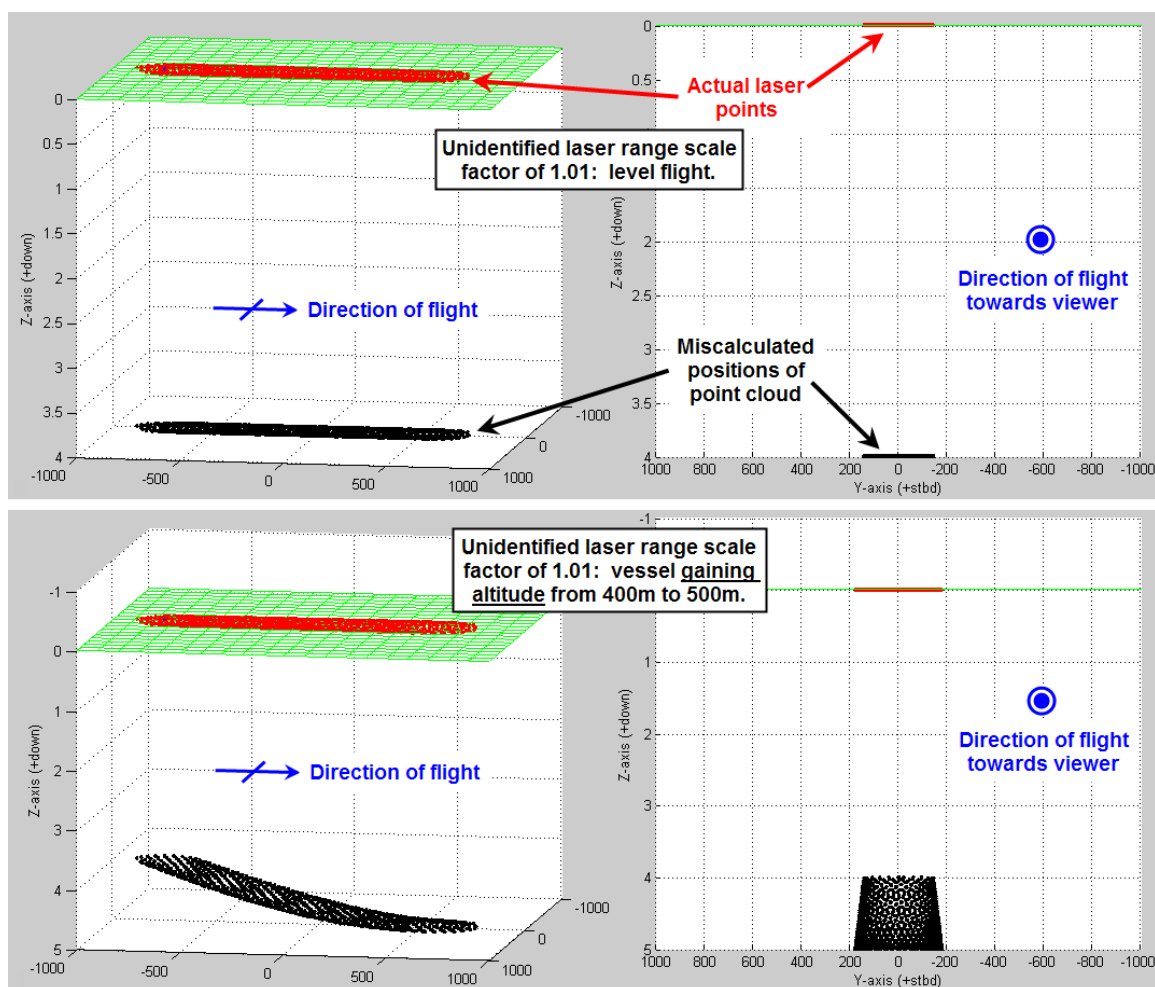


Figure 124. Visualization of a point cloud generated from a lidar with an unidentified laser range scale factor of 1.01 (top), and a point cloud from the same system as it experiences an increase in altitude (bottom). The red points indicate the true laser strikes, while the black are the miscalculated biased points. All units in meters.

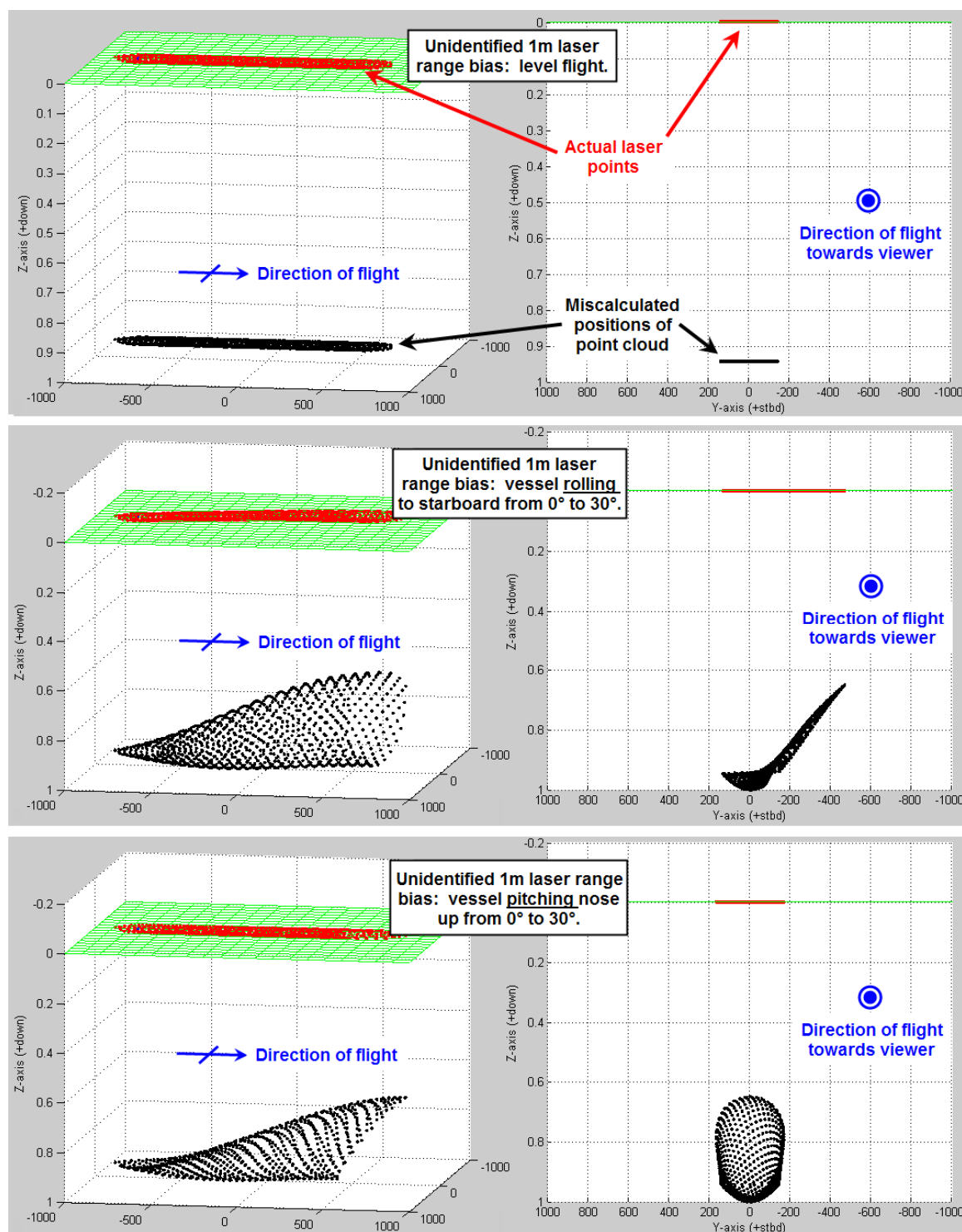


Figure 125. Signature analysis plots for a lidar with a 1m laser range bias for a level flight (top) and in the presence of a rolling (middle) and pitching (bottom) vehicle. The red points indicate the true laser strikes, while the black are the miscalculated biased points. All units in meters.

Calibration results including either one, the other, or both of the radiometric parameters ρ_0 and ρ_1 are shown in Figure 126, with a baseline trial including neither parameter shown in column 1. Note that the uncertainty in the prism slope increases whenever the range scale factor is included in the calculation (column 1 vs. columns 2 and 4). The uncertainty in the vertical offset of the INS vector increases only slightly with the inclusion of the laser range scale factor (column 1 vs. column 2), but much shows a large jump in uncertainty when the laser range bias is adjusted (column 1 vs. columns 3 and 4). This increase in the uncertainties of θ_{FR} and Δz_{IL} confirms the correlation among these parameters with ρ_0 and ρ_1 .

Calibration parameter	Uncertainty (1σ)			
Trial #	1	2	3	4
Boresight roll angle	0.018°	0.019°	0.019°	0.019°
Boresight pitch angle	0.018°	0.019°	0.019°	0.019°
Boresight yaw angle	3.036°	3.043°	3.052°	3.381°
Prism slope	0.004°	0.006°	0.004°	0.017°
VRF/IRF heading bias	3.035°	3.041°	3.051°	3.380°
IMU x-offset	0.083m	0.083m	0.084m	0.084m
IMU z-offset	0.007m	0.009m	0.123m	0.280m
Laser/Scanner Φ -angle	0.021°	0.217°	0.027°	0.022°
Laser/Scanner θ -angle	1.191°	1.243°	1.236°	1.244°
Laser range scale factor	-	2.9E-05	-	6.9E-05
Laser range bias	-	-	0.126m	0.300m
Max. contribute to THU	0.100m	0.109m	0.167m	0.166m
Max. contribute to TVU	0.009m	0.010m	0.026m	0.026m

Figure 126. Table of confidences of an 11-parameter calibration trial including the laser range bias and scale factor (1σ uncertainties shown). Parameters marked by a ‘-’ were not included in a given calibration trial. The maximum contribution to the propagated uncertainty of the point cloud is included for reference. The crossing pattern shown in Figure 101 was used to generate the data at 51Hz (with the exception of the final column).

Given the final goal is the uncertainty of the point cloud (not the uncertainty of the calibration parameters), the last two rows of Figure 126 are of great interest. The baseline flight had a horizontal uncertainty (1σ) of 0.100m; the inclusion of the two radiometric parameters increased this uncertainty to 0.166m. However, the more critical parameter (from a hydrographic perspective) is the vertical uncertainty. Including ρ_0 and ρ_1 increases the calibration parameters' contribution to the point cloud uncertainty from 0.009m to 0.026m. As usual, these uncertainties can be improved by increasing the data volume included in the calibration. For example, if the preceding 11-parameter calibration were conducted with a laser operating at 10KHz (rather than 51Hz), the THU would drop to 0.012m and the TVU to a paltry 0.002m (1σ).

It is interesting to note that the uncertainty of the vertical INS offset vector is 0.28m in the full 11-parameter calibration, but this vertical uncertainty does not translate to the point cloud TPU. This is another example of covariance working in the surveyor's favor. The relatively large uncertainty in Δz_{IL} is coupled with relatively large uncertainties in the prism slope and laser range bias. The large covariances simply imply the calibration module is unsure which of the three parameters to adjust to produce the geometrically correct point cloud. The calibrator is confident, however, in the positioning of the point cloud.

The correlations for the proposed acquisition pattern (Figure 101) for the final proposed 11-parameter calibration are shown in Figure 127. While the figure appears very busy with many correlations several groups of parameters can be clustered together:

- As just discussed, ρ_0 , ρ_1 , Δz_{IL} and θ_{FR} have a high correlation because they all induce a vertical translation in the biased point cloud.

- $BS\theta_z$, θ_{VI} , Δx_{IL} have high correlations as demonstrated when they become linearly dependent with the inclusion of Δy_{IL} .
- If θ_{LS} should be approximately 0° , there will be a high correlation among ϕ_{LS} and $BS\theta_y$ and among θ_{LS} and $BS\theta_x$. However, if θ_{LS} is closer to 90° or 270° (i.e. oriented towards port or starboard), then the pairings will swap (ϕ_{LS} with $BS\theta_x$ and θ_{LS} with $BS\theta_y$).

The above correlations will exist regardless of the amount of data acquired and represent a best case scenario as far as flight strategies are concerned. That is, if the calibration flights experienced no vehicle roll, then the correlations would be worse. These large correlations should not concern the surveyor. They only serve to illustrate the reasons behind some of the larger uncertainties of the calibration parameters. It is thanks to these large correlations that the point cloud positions do not also have large uncertainties.

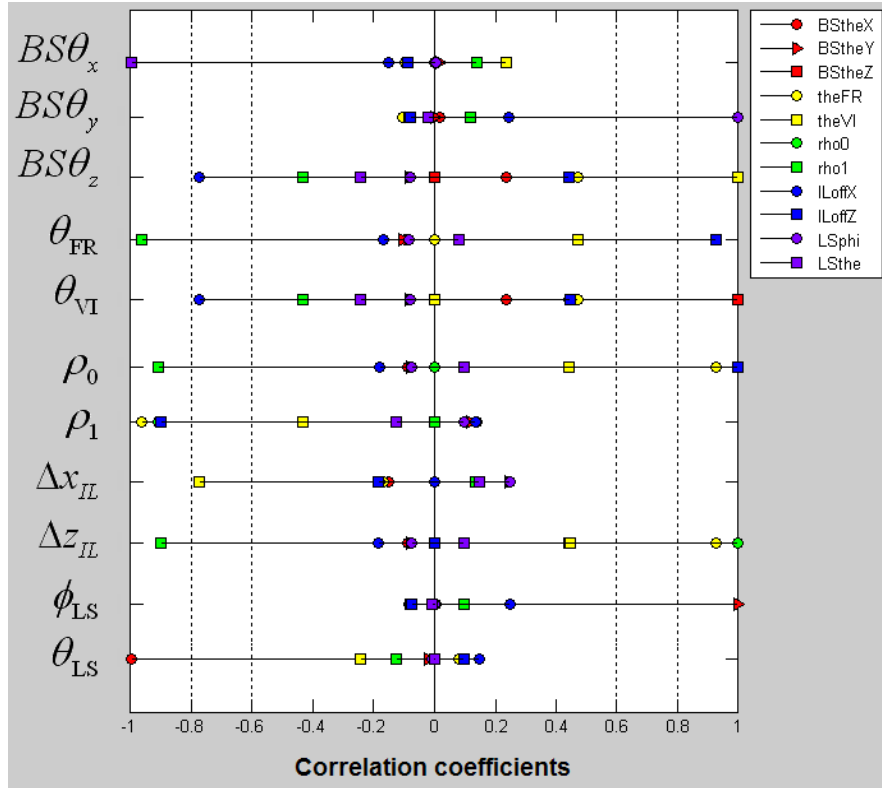


Figure 127. Correlation coefficients of the final 11-parameter calibration using the crossing flight pattern of Figure 101.

6.3.6 – Advice on Setting Weights within the LSA

This discussion of the calibration algorithm closes with some advice on setting up the initial settings for the least squares: the initial guesses and the initial uncertainties. It should go without saying that the closer the initial guesses are to the actual calibration values, the better the calibration will perform. “Better” being used in the context of the calibration routine will converge to the correct values. It is entirely possible that even with a properly acquired dataset, the LSA will fail to converge. Either the algorithm will iterate off to an infinite solution, or it may converge to values the surveyor finds to be inconvenient (e.g., a boresight angle being reported as -2874° versus 6° – though both are equally correct answers).

In addition to providing good initial estimates for the parameters, one should also make sure the uncertainty of the observations are suitably small. If the user claims the uncertainty in the scanner azimuth is 90° , then the calibrator will have little hope for success.

The final and possibly trickiest values to initialize are the estimates of the uncertainties for the calibration parameters. Presumably, since the parameters are being calibrated, the user doesn't know their value, so associating an uncertainty on an unknown quantity may seem a strange exercise. The best practice is to start with relatively small uncertainties (say 0.1° for the angles and 0.1m for the distances). Small uncertainties will prevent any one calibration value from wildly iterating to compensate for a poor initial guess. Other than testing the user's patience, small weights will never cause the algorithm to crash. After three to five iterations, the calibration parameters should begin to properly "align" themselves, not necessarily achieving their correct values, but achieving an approximately coplanar point cloud. At this point it is safe to increase the uncertainty (decrease the weight) on the parameters that are iterating slowly. One can look at the output uncertainties of the LSA to determine which weights need to be relaxed.

Typically, the parameters that represent rotations about a vertical axis present the most trouble: $BS\theta_z$, θ_{VI} and θ_{LS} . These parameters in particular require the closest monitoring of their weights. If any parameter is ever converging too slowly then the weights can always be decreased (increase the standard deviations). While no input uncertainty can be too small (for a successful convergence of the LSA), it is possible to

input an uncertainty that is too large. Should that parameter start to iterate to absurd values, then the calibration should be rerun with a smaller uncertainty.

Selecting the best combination of weights and initial guesses is a quasi-art form that is the nemesis of anyone who seeks a “one button solution” for the calibration. Again, the calibrator was intentionally designed without an automatic termination statement. It will iterate a fixed number of times and then stop. The onus is on the user to stop with the calibrator and interpret the results and assess whether the calibrator is on the right track (i.e., do the values appear to be converging). It may be necessary to hold some values fixed to erroneous values just so the calibrator can focus on refining the initial estimates of the other parameters. As those parameters start to converge, the previously fixed parameters can be allowed to iterate as well. Every attempt has been made to make the calibration interface as intuitive as possible, but it is still just a tool. Much like a hammer and saw can be used to build a bird house, simply setting the tools on a pile of lumber will not achieve anything. Likewise, one cannot expect to dump a few million soundings on the calibrator and expect it to magically produce a set of calibration values. The “one button solution” does exist, provided a skillful choice of the initial estimates and uncertainties are entered; otherwise, the surveyor must settle for a “four-or-five button solution.” Likely, for each user, and the collection of users as a whole, there will be an initial learning curve while they collectively come to understand which parameters have the greatest effect on the point cloud and which can be fixed with some flexibility. With experience a set of routine values to be used for initial estimates will likely reveal themselves.

6.4 – Impacts of Survey Site Selection on the Calibration Module

A potential hitch to the aforementioned calibration is the need for a flat piece of real estate of suitable size (the crossing pattern requires at least $2\text{km} \times 2\text{km}$). Short of surveying next to a dried lake bed, such a location can be difficult to locate. This section presents two options for a planar surface which are likely to be available for all airborne platforms which perform a bathymetric survey: the airport runway and the sea surface. Each has its own merits and limitations which will be discussed in the following sections.

6.4.1 – Calibration on a Narrow Runway

One planar surface that is likely available to all airborne platforms is the airport runway. The drawback is that the average runway is only 50m wide. The CZMIL system has a swath width of 300m, thus relying on so narrow a calibration surface will greatly reduce the number of points that can be used in the adjustment.

With the reduction in point density associated with a 50m-wide runway, one must ask how the confidence in the calibration values will be affected. In terms of the raw number of data points, the full crossing pattern dataset acquired at 51Hz has 3,800 observations; depending on how the runway is oriented, only 200-300 points will lie within a narrow swath (Figure 128).

Even with this diminished dataset, a successful calibration is still possible (Figure 129); however, the uncertainties of the calibration parameters will get worse (larger) compared to the full dataset. Likewise, the point cloud TPU is also expected to grow. Results of the calibration over a runway are summarized in Figure 130. For reference, the uncertainty of the 11-parameter calibration for the full crossing flight pattern dataset (Figure 126 – column 4) is included as Trial 1.

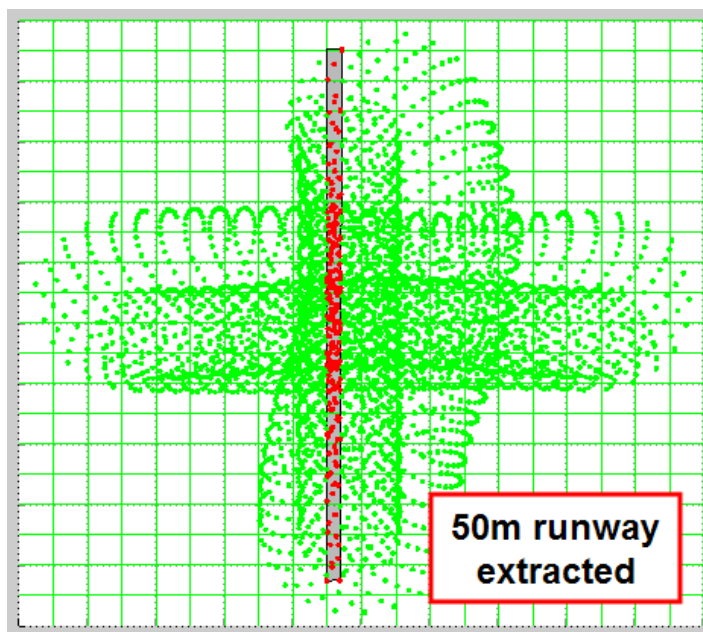


Figure 128. From the crossing flight pattern, a swath of data 50m wide, to simulate an airport runway, is extracted using the simulator's subset tool.

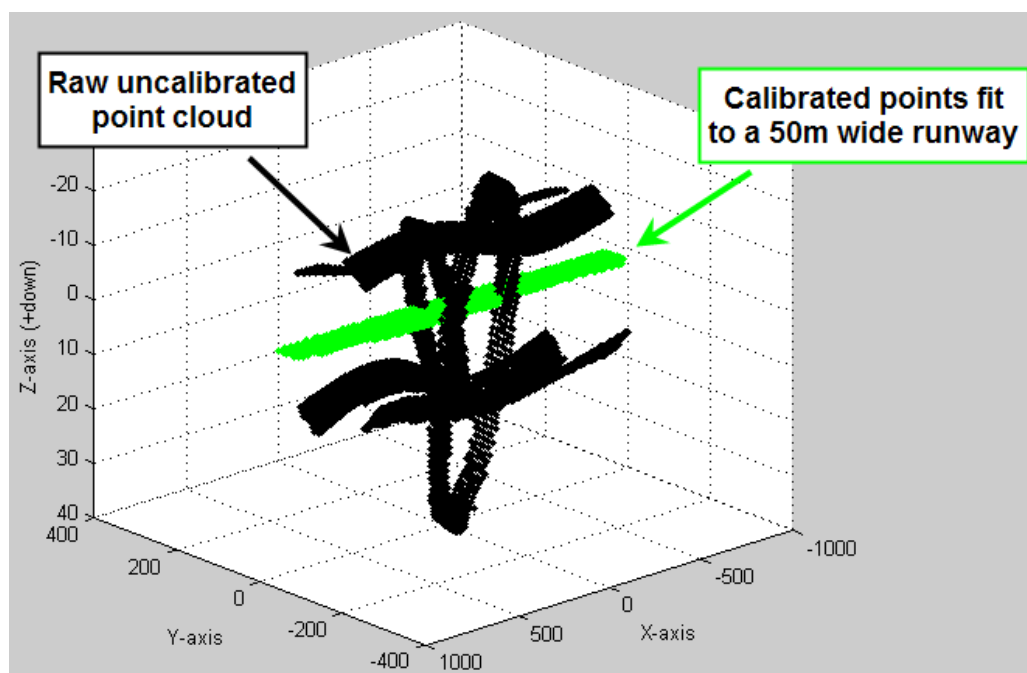


Figure 129. Both the uncalibrated (black) and calibrated point cloud (green) based on the data limited to the width of an airport runway. All units in meters.

Calibration parameter	Confidence (1σ) in calibration solution and point cloud TPU.		
Trial #	1	2	3
Laser repetition rate	51Hz	51Hz	10000Hz
Dataset: All or Runway?	All	Runway	Runway
Boresight roll angle	0.019°	0.133°	0.010°
Boresight pitch angle	0.019°	0.116°	0.008°
Boresight yaw angle	3.381°	18.735°	1.398°
Prism slope	0.017°	0.077°	0.006°
VRF/IRF heading bias	3.380°	18.763°	1.400°
IMU x-offset	0.084m	0.354m	0.026m
IMU z-offset	0.280m	1.215m	0.089m
Laser/Scanner Φ -angle	0.022°	0.129°	0.009°
Laser/Scanner θ -angle	1.244°	8.792°	0.639°
Laser range scale factor	6.9E-05	3.0E-04	2.2E-05
Laser range bias	0.300m	1.299m	0.095m
Max. contribute to THU	0.166m	0.739m	0.052m
Percent change	-	444.0%	31.2%
Max. contribute to TVU	0.026m	0.088m	0.007m
Percent change	-	334.0%	28.3%

Figure 130. Table of confidences of an 11-parameter calibration trial over a 50m runway with ground control (1σ uncertainties shown). The maximum contribution to the propagated uncertainty of the point cloud is included for reference. Percent changes are references to the full dataset.

As expected, the reduction in data volume associated with the narrow runway has reduced the confidence in the calibration values. Every calibration parameters' uncertainty has increased by four to seven times, the largest uncertainties being associated with the yaw boresight angle and VRF/IRF heading bias (both exceeding $18^\circ - 1\sigma$). In spite of these large uncertainties, one cannot cast aspersions on the results of the calibration without also considering the induced uncertainty of the point cloud position. The horizontal TPU increases by over 400%, as compared to using the full dataset, to a value of 0.739m (1σ). Larger horizontal TPU is typical when there are large uncertainties in the calibration parameters that involve rotations about a vertical axis ($BS\theta_z$, θ_{VI} , θ_{LS}). The calibration parameters' contribution to the point cloud vertical TPU increases by

over 300%. That said, the vertical TPU is only 0.088m (1σ). One must remember this uncertainty is based on a point cloud of only 300 data points. When the system is simulated at a full 10KHz, the added data density brings the point cloud THU and TVU down to 0.052m and 0.007m, respectively (Figure 130 – Trial 3). The vertical uncertainty is only a small fraction of that induced by the GPS positioning alone and is likely good enough for most applications.

There is a simpler way of increasing the data density without increasing the number of flight lines, rather than having the two flight lines flying perpendicular to the runway, they could instead be rotated by 45° . This will increase the number of points on the runway without too greatly sacrificing the necessary geometry to determine the calibration values.

In summary, limiting the point cloud to a narrow runway will yield a set of calibration values with a larger uncertainty (and an associated point cloud with a larger TPU) as compared to having the full dataset available. But even with the four basic flight lines of the crossing pattern at a full sampling rate of 10KHz, this limited dataset is good enough to yield a high confidence in the point cloud positions. Thus an airport runway is a feasible calibration site.

6.4.2 – Calibration on a Dynamic Sea Surface

In some cases, an airport runway may not be an available option for calibration: the survey site may be far removed from where the aircraft is staged; clearance may be difficult to obtain to repeatedly occupy the airspace immediately over the runways; or a surveyor may just be dissatisfied with such a small percentage of the acquired data going

to the calibration. There is, however, another option for a planar surface: the ocean surface itself.

The nature of a bathymetric survey means ample access to an ocean, sea or lake. Further, most bathymetric lidars already have the technology and algorithms in place to log the position where the laser pulse strikes the water surface. However, when proposing to use the ocean's surface as a proxy for a flat planar surface, the "flatness" of the ocean must be considered. For a given location, an instantaneous measurement of the ocean surface is subject to both wave and tidal influence. Meteorological considerations aside, even mean sea level (as a geopotential surface) will track with the undulations of the local geoid. Provided the calibration area is confined to a small region (less than 10km×10km), the relief of the geoid can be assumed to be flat (Zilkowski, 1990); however the waves and tidal effects are not so easily controlled. The potential impacts of using the dynamic ocean surface as a planar surface for the purposes of a geometric calibration require further investigation.

6.4.2.1 – Wave effects on calibration uncertainty. The casual observer will remark that the ocean is not flat. The sea surface is a dynamic landscape of waves and sea swell. Fortunately, a lidar's laser footprint is intentionally expanded to a diameter of several meters at the water surface in order to satisfy eye safety requirements (while still maintaining a satisfactory pulse energy to provide reasonable signal-to-noise ratios; Guenther, 2007). Recall from Section 4.2.2.5, the relatively large laser footprint means any high frequency waves (Figure 51, left) will be removed in the averaging that occurs across the system's field-of-view. Conversely, long period swell and shorter period gravity waves (Figure 51, right) will lead to an aliasing of the measured sea surface

height. From shot-to-shot, adjacent footprints will report differing heights. This inconsistent vertical component to the point cloud coordinates suggests the ocean surface may not be ideal for representing a single, constant planar surface. However, in much the same way that high frequency waves are averaged out within a single footprint, the vertical deviations exhibited by the laser points during long period swell may be averaged out with a sufficiently large temporal and spatial sampling. For the calibration algorithm to work, it is not necessary that every point be coplanar; instead, the points must just describe a planar surface.

To generate a test dataset, the simulator introduced a 1m swell (50m wavelength) beneath the crossing flight plan, using (4.21) and (4.22). With the weighted least squares adjustment, a priori estimates of the uncertainties of all the measured quantities (laser range, scanner azimuth, etc.) must be provided. The inclusion of waves will adversely affect the previously used value for the estimated uncertainty of the measured laser range, thus far limited to just the manufacturer's specifications of the hardware (0.01m). Since the adjustment model is fitting points to a planar surface, the uncertainties must report the confidence in the points describing that planar surface. That is, even with an error-free range measurement, the oscillating waves will prevent the laser points from ever laying on the theoretical mean sea surface (at least, it is unlikely).

To account for the changing height of the planar surface (see Figure 50) the uncertainties of the laser range were modified using (4.27). Instead of the customary 0.01m for σ_ρ , the new uncertainty is given by:

$$\begin{aligned}
\sigma_{\rho^*}^2 &= \sigma_{\rho}^2 + \left(\frac{h_w^2}{8} + \frac{h_s^2}{8} \right) \sec^2 20^\circ \\
&= (0.01)^2 + \left(\frac{0^2}{8} + \frac{1^2}{8} \right) \sec^2 20^\circ = 0.142 \text{m}^2 \\
\sigma_{\rho^*} &= 0.376 \text{m}.
\end{aligned} \tag{6.13}$$

Note, this uncertainty will be calculated automatically by the calibrator, but it requires the user to input the estimated wave and swell height (Figure 77 – blue). In spite of the dynamic conditions, the calibration of the point cloud is still achieved (Figure 131). The results of said calibration are shown in Figure 132 where, again, the uncertainty of the 11-parameter calibration for the full crossing flight pattern dataset in a wave-free environment (Figure 126 – column 4) is included as Trial 1.

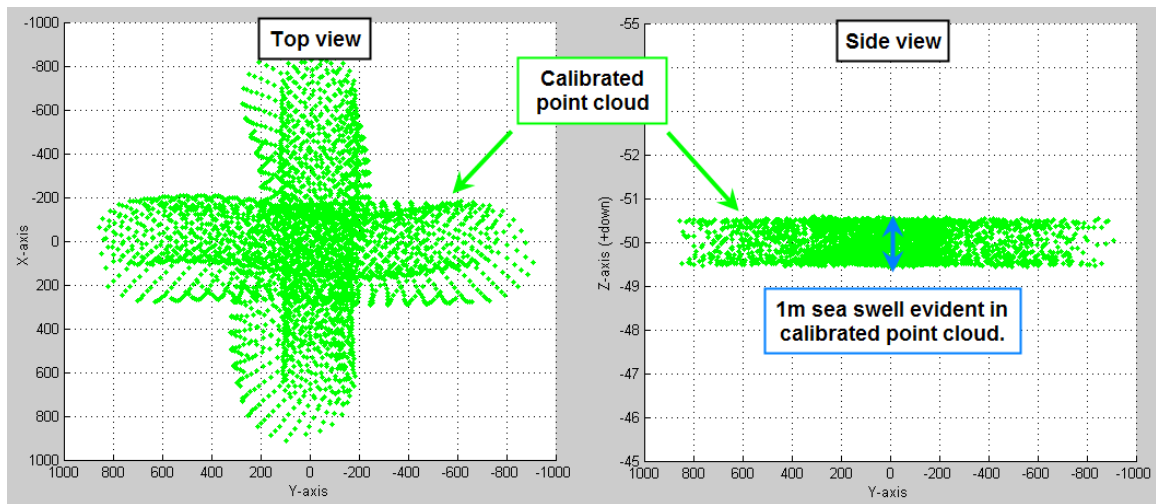


Figure 131. Calibrated point cloud when acquired over a dynamic sea with a 1m swell height. All units in meters.

The changing values of the laser range induced by the wave action led to an increase in the uncertainty of all the calibration parameters, typically increasing by 300% as compared to the wave-free surface (Trial 2 vs. Trial 1). The point cloud uncertainty also increased by ~300%, yielding a horizontal TPU of 0.556m and a vertical TPU of 0.089m (1σ). As usual, these uncertainties can be improved through the acquisition of additional

data. To confirm, the repetition rate was quadrupled and, as anticipated, the uncertainties of the calibration parameters and point cloud were all reduced by 50% (Trial 3). If this pattern holds true, then the full 10KHz dataset would be suspected to lead to significantly smaller values. This implies that a wavy sea surface does hinder the calibration, but it does not prevent it. Naturally, the smaller the amplitude of the waves, the smaller the hindrance.

Calibration parameter	Confidence (1σ) in calibration solution and point cloud TPU.		
Trial #	1	2	3
Laser repetition rate	51Hz	51Hz	204Hz
Swell height	0m	1m	1m
Boresight roll angle	0.019°	0.064°	0.032°
Boresight pitch angle	0.019°	0.064°	0.032°
Boresight yaw angle	3.381°	14.0299°	3.814°
Prism slope	0.017°	0.056°	0.028°
VRF/IRF heading bias	3.380°	14.024°	3.802°
IMU x-offset	0.084m	0.321m	0.124m
IMU z-offset	0.280m	0.944m	0.476m
Laser/Scanner Φ -angle	0.022°	0.074°	0.036°
Laser/Scanner θ -angle	1.244°	5.364°	1.748°
Laser range scale factor	6.9E-05	2.4E-04	1.2E-04
Laser range bias	0.300m	1.012m	0.515m
Max. contribute to THU	0.166m	0.556m	0.293m
Percent change	-	334.2%	176.2%
Max. contribute to TVU	0.026m	0.089m	0.041m
Percent change	-	337.0%	156.4%

Figure 132. Table of confidences of an 11-parameter calibration trial over a dynamic sea surface (1σ uncertainties shown). The maximum contribution to the propagated uncertainty of the point cloud is included for reference. Percent changes referenced to the swell-free trial.

For comparative purposes, the calibration accuracies associated with a narrow runway are compared to those over a dynamic sea surface (Figure 133). When contrasting a 1m sea swell to a narrow runway, the confidence of all the calibration parameters is generally better for the sea surface. This suggests having a larger amount of data spread over a wider area (even if the points themselves have a higher uncertainty)

makes for a better calibration than a confined (though with a high confidence) dataset.

Though looking at the big picture, the induced point cloud vertical TPU is comparable for both methods ($0.088\text{m} - 1\sigma$). The induced horizontal TPU for the sea surface is better than the narrow runway (0.556m as compared to 0.739m). When the height of the swell is increased to 2m , the narrow runway then yields a better estimate of both the calibration parameters and the point cloud positions. Thus for larger sea states exceeding 1m , the surveyor desiring to do an 11-parameter calibration would be better served performing it on land. Different results may be achieved if fewer parameters are being calibrated, see Gonsalves (2010) for further examples.

A drawback to using the ocean surface is the requirement for ground control is still present (unless Δz_{IL} and ρ_0 are withheld from the calibration). This implies a GPS tide buoy will need to be installed (or some other floating platform) during the calibration session.

Calibration parameter	Confidence (1σ) in calibration solution and point cloud TPU.		
	Runway	1m	2m
Swell height			
Boresight roll angle	0.133°	0.064°	0.125°
Boresight pitch angle	0.116°	0.064°	0.125°
Boresight yaw angle	18.735°	14.0299°	37.383°
Prism slope	0.077°	0.056°	0.109°
VRF/IRF heading bias	18.763°	14.024°	37.371°
IMU x-offset	0.354m	0.321m	0.761m
IMU z-offset	1.215m	0.944m	1.816m
Laser/Scanner Φ -angle	0.129°	0.074°	0.143°
Laser/Scanner θ -angle	8.792°	5.364°	14.431°
Laser range scale factor	$3.0\text{E-}04$	$2.4\text{E-}04$	$4.6\text{E-}04$
Laser range bias	1.299m	1.012m	1.949m
Max. contribute to THU	0.739m	0.556m	1.070m
Max. contribute to TVU	0.088m	0.089m	0.171m

Figure 133. Table of confidences of an 11-parameter calibration trial over a narrow runway versus a dynamic sea surface (1σ uncertainties shown). The maximum contribution to the propagated uncertainty of the point cloud is included for reference. Swell entries are highlighted in bold when they are larger than their runway counterparts.

6.4.2.2 – *Tidal effects on calibration uncertainty.* In contrast to the relatively high frequency sea waves whose deviations from the theoretical planar survey average out with sufficient spatial and temporal sampling, the problems introduced by tides increase with the duration of the sampling period. The longer the sampling session continues the greater the opportunity for tides to adversely affect the calibration. There are three approaches for contending with the changing tides. First, the tides may be disregarded. If the calibration flights involve a minimal amount of time, then the tidal effects may be negligible. Second, over an abbreviated window the change in tides can be viewed as nearly linear. A parameter representing the linear change in tides could then be included in the least squares adjustment. Third, if tidal data are available during the time of the calibration (a likely scenario in the case of most surveys intended for nautical charting), then the vertical influence may just be subtracted from the laser spot's coordinates. With the values reduced to a common datum, the adjustment may then proceed without further consideration to tides. Each method of coping with the tides will be further explored.

Recall from Section 4.2.2.6 the tides are simulated using equation (4.29):

$$z(t) = \frac{R}{2} \sin\left(\frac{2\pi}{T}t + \phi\right), \quad (6.14)$$

where:

R = peak-to-peak tidal range

T = tidal period

ϕ = phase of the tides

z = tidal value

t = time.

For this simulation, a semi-diurnal tide ($T = 12\text{hr}$) with a tidal range of 4m is considered.

To experience the tide at its maximum rate of change, the phase of the tides will be set to zero. Recall the simulator is programmed to allow six minutes to elapse between flight

lines, so the full crossing flight pattern will last approximately twenty minutes. During this time, the tides will continue to rise. Because the data is being sampled over such a small portion of the tidal signal, a modification to the laser range uncertainty like that shown in (6.13) is not necessary. A view of the four survey lines are shown under the effect of tides are shown in Figure 134. Notice over the course of the survey, there's a net increase in sea level by 0.18m. The vertical separation of the flight lines are a result of the tidal increase during the six minutes that are allocated for the vehicle to set up for each subsequent survey line.

Results of each calibration attempt in the presence of tides are summarized in Figure 135. In the first case, it is assumed that the tidal values are known during the time of acquisition. In such a case, the vertical offsets due to the tides are removed to reduce the points to a single datum. This represents the best possible scenario, as the results of the calibration are now equivalent to surveying on land (Trial 1).

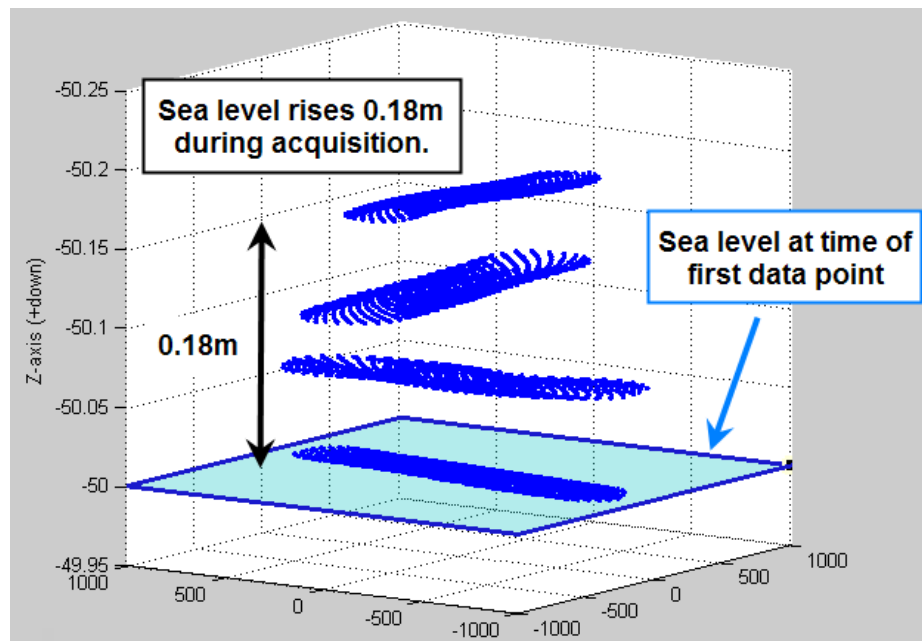


Figure 134. Crossing pattern point cloud in the presence of a tidal effect. The vertical offsets among the lines are a result of the tidal increase during the vehicle turns. All units in meters.

Calibration parameter	Confidence (1σ) in calibration solution and point cloud TPU (reported as a percentage of the baseline, "Trial 1", confidence).		
Trial #	1	2	3
Tidal Model	Tides Known	Tide Ignored	Linear Tide
Boresight roll angle	0.019°	100.0%	100.0%
Boresight pitch angle	0.019°	100.0%	100.0%
Boresight yaw angle	3.381°	138.3%	100.3%
Prism slope	0.017°	99.9%	100.0%
VRF/IRF heading bias	3.380°	138.3%	100.3%
IMU x-offset	0.084m	118.8%	100.3%
IMU z-offset	0.280m	99.8%	100.1%
Laser/Scanner Φ -angle	0.022°	100.0%	100.0%
Laser/Scanner θ -angle	1.244°	100.8%	100.0%
Laser range scale factor	6.9E-05	100.0%	100.0%
Laser range bias	0.300m	99.8%	100.0%
Linear Tide rate	-	-	1.0459 m/hr
Max. contribute to THU	0.166m	0.166m	0.166m
Percent change	-	100.0%	100.1%
Max. contribute to TVU	0.026m	0.026m	0.027m
Percent change	-	100.0%	101%

Figure 135. Table of confidences of an 11-parameter calibration trial in the presence of tides (1σ uncertainties shown). Three methods are shown: “Tides Known” implying the tide values were known at the time of each sounding and removed; “Tides Ignored” assumes there is no tidal effect and attempts to calibrate anyway; and “Linear Tide” adds an extra parameter to the adjustment, to estimate the linear rate at which the tide is changing. The maximum contribution to the propagated uncertainty of the point cloud is included for reference.

In the second column, the point cloud is calibrated where the effects due to tides are erroneously believed to be zero. In such a case, the uncertainty of some of the calibration parameters will increase; however, the overall uncertainty of the point cloud will remain unchanged Figure 135 – Trial 2. The reason for this lack of increase in point cloud TPU can be best understood when the calibrated point cloud is viewed (Figure 136). Because the survey lines were evenly distributed over the same spot, the most planar-like surface the LSA could produce occurs when each flight line is “flattened” as much as possible. Thus every line is fit to the correct sea surface, only with a vertical offset. If the survey lines were acquired in a more careless manner, say four parallel lines

with the same heading northerly heading being collected from east to west, then the tidal effect would be misconstrued as a sloping plane (in this example, the water surface would slope up from east to west).

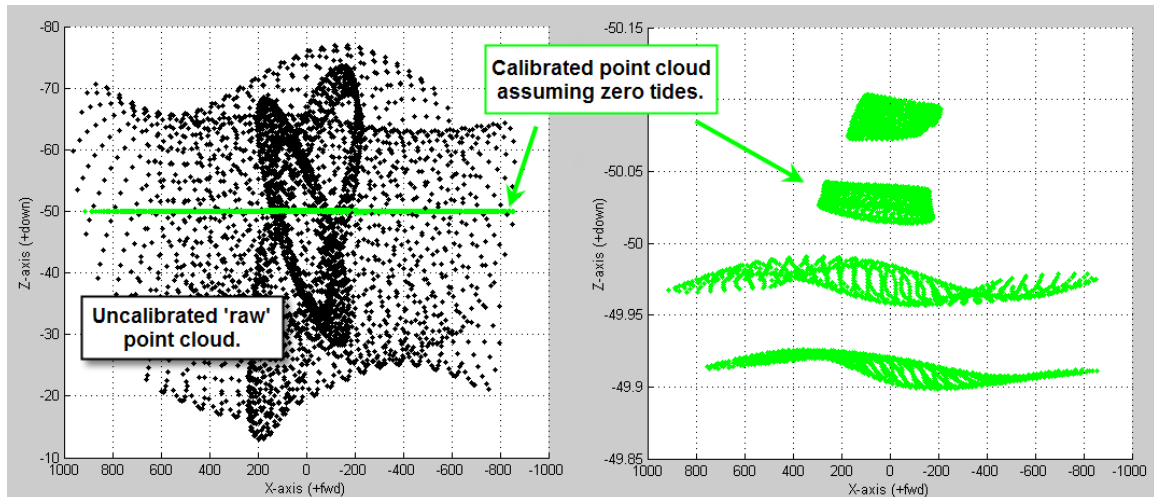


Figure 136. Side view of attempts to calibrate a point cloud in the presence of tides in which a tidal signature is erroneously believed to not be present. The biased points are shown in black while the calibrated points are shown in green. All units in meters.

If tides are acknowledged to exist in the calibration area, but the tidal curve is not known, the tides can be approximated using the least squares. Over a sufficiently short interval, the behavior of a tidal curve is approximately linear. This linear rate of change in the water levels can be determined during the adjustment. An example of approximating the sinusoidal tide with the linear model is shown in Figure 137. Notice in contrast to Figure 136 the point cloud was properly reconstructed without any vertical offsets among the survey lines by including a tidal parameter in the adjustment. The uncertainties in the calibration parameters were also equivalent to those if the tides were known in advance and removed from the point cloud (Figure 135 – Trial 3 vs. Trial 1). Again, the uncertainty of the point cloud is equivalent to when the tides are either removed or ignored. This only serves to emphasize that over the short sampling period

necessary to acquire data for the calibration, the tidal level is not given the opportunity to change appreciably.

As a side note, notice that when calibrated the tidal rate was estimated to be 1.046m/hr. This value is unsurprising when we consider (6.14) gives the height of the tide at any time, so its derivative would give the rate of change of the tide. That is,

$$\left. \frac{\partial z}{\partial t} \right|_{t=0} = \frac{R}{2} \cos\left(\frac{2\pi}{T} \cdot 0 + \phi\right) \frac{2\pi}{T} = \frac{4}{2} \frac{2\pi}{12} \approx 1.047 \text{ m/hr.} \quad (6.15)$$

Thus the LSA can serve as a linear approximation of a tide gauge over extremely short time intervals.

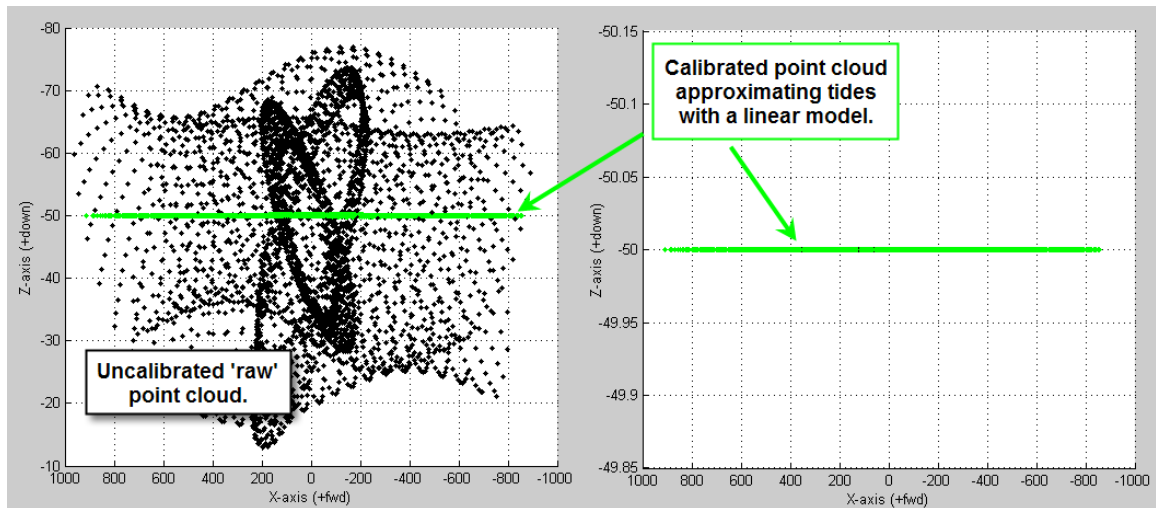


Figure 137. Side view of attempts to calibrate a point cloud in the presence of tides in which the tidal signature is approximated with a linear model. The biased points are shown in black while the calibrated points are shown in green. All units in meters.

6.5 – Summary of Key Results

The following is a bulleted list of the key results, concepts and contributions presented within this chapter. When possible, the relevant section(s) that offer a more detailed explanation are indicated.

▪ In Chapter III, 15 system parameters, which would require calibration, were proposed to describe the laser equation. Results of the signature analysis for all the parameters are summarized in Figure 138 (Sections 6.1.1 through 6.3.5).

Calibration Parameter	Abbrev.	Best determined by:	Correlated with:	Linearly Dependent?	Notes:
Boresight roll angle	BStheX	Reciprocal headings, increased pitch	LSthe	YES - 1	
Boresight pitch angle	BStheY	Reciprocal headings	LSphi	YES - 1	
Boresight yaw angle	BStheZ	Increased roll or pitch	theVI, lLoffX, lLoffY	YES - 1 YES - 2	Tends to have a large variance, but does not adversely affect point cloud.
Prism slope	theFR	Increased roll or pitch, different acquisition heights.	BStheY, lLoffZ, rho0, rho1		
VRF/IRF heading bias	theVI	Large amounts of roll or pitch, or large IMU lever arms	BStheZ, lLoffX, lLoffY	YES - 2	Tends to have a large variance, but does not adversely affect point cloud.
IMU x-offset	lLoffX	Increased vessel roll	BStheZ, theVI, lLoffY	YES - 2	Of lLoffX and lLoffY, one should be measured manually and treated as an observed value.
IMU y-offset	lLoffY	Increased vessel pitch	BStheZ, theVI, lLoffX	YES - 2	The other should be included in the adjustment.
IMU z-offset	lLoffZ	Increased roll or pitch	theFR, rho0, rho1		Requires ground control to determine.
Laser/Scanner Φ -angle	LSphi	Reciprocal headings, increased pitch	BStheY		
Laser/Scanner θ -angle	LSthe	Reciprocal headings	BStheX	YES - 1	Tends to have a large variance, but does not adversely affect point cloud.
Laser range scale factor	rho1	Different acquisition heights	theFR, lLoffZ, rho0		
Laser range bias	rho0	Increased roll or pitch	theFR, lLoffZ, rho1		Requires ground control to determine.
Prism/Scanner x-axis	PStheX	Requires copious data; do not adjust.	theFR, LSphi, BStheX, BStheY, PStheY		Extremely difficult to determine; requires excessive amounts of data or vessel roll/pitch.
Prism/Scanner y-axis	PStheY	Requires copious data; do not adjust.	theFR, LSphi, BStheX, BStheY, PStheX		Extremely difficult to determine; requires excessive amounts of data or vessel roll/pitch.
Scanner azimuth bias	PStheZ	Do not adjust	BStheX, BStheY, BStheZ, LSthe	YES - 1	Set to zero and treated as observed value in LSA.

Figure 138. Table summary of the 15 proposed calibration parameters: including the vehicle maneuver that yields the most confident result in the calibration, which other parameters have a high correlation, identifies the 2 groups of parameters that are linearly dependent, and other calibration notes.

▪ The correlations listed in Figure 138 exist regardless of the flight configuration chosen.

- Among the 15 calibration parameters, there are two sets of linearly dependent parameters: $BS\theta_x, BS\theta_y, BS\theta_z, \theta_{LS}$ and $PS\theta_z$; and $BS\theta_z, \theta_{v1}, \Delta x_{IL}$ and Δy_{IL} . Among each group of parameters, one must be withheld from the calibration. For the first group, based upon both the point cloud TPU and the reported confidence of the calibration solution, it is recommended $PS\theta_z$ be set to 0° while the other four parameters are adjusted (Section 6.3.4.2). For the second group either Δx_{IL} or Δy_{IL} should be measured manually while the other is included in the adjustment (Section 6.3.3.2). This brings the total number of proposed calibration parameters to 13.

- Two parameters, $PS\theta_x$ and $PS\theta_y$, were found to be extremely difficult to determine to a high degree of confidence using the proposed calibration methodology. In this case, the high uncertainty of the parameters leads to a high uncertainty of the point cloud. It was discussed that reformulating these rotations in spherical coordinates might improve the ability to determine these calibration values, but lacking this development, it is recommended these two parameters be withheld from the calibration routine. This brings the final total number of proposed calibration parameters to 11 (Section 6.3.4.1).

- The confidence of the calibration solution can always be improved by doing one of three things: including a greater number of points in the adjustment, performing more dynamic vehicle maneuvers during the calibration acquisition (e.g., roll the vehicle 10° rather than 5°), or surveying over a broader region (Section 6.2.1.3). Generally speaking, quadrupling the data density will halve the calibration parameters' uncertainty (Section 6.3.2).

- Through repeated examples, it was demonstrated that large uncertainties in the calibration parameters do not necessarily imply a large point cloud TPU, particularly if

said parameters have a large correlation coefficient (Section 6.2.2). This is particularly true with regard to parameters that involve a rotation about a vertical axis ($BS\theta_z$, θ_{VI} , and θ_{LS} – Sections 6.3.2 & 6.3.3.1), but also with parameters that reflect a vertical displacement of the biased point cloud in their signature plots (Δz_{IL} and ρ_0 – Sections 6.3.3.3 & 6.3.5).

- The proposed flight pattern (of those presented in this dissertation) that leads to the highest confidence in the calibration parameters is shown in Figure 101. It requires four lines of data, run at two different altitudes. On two of the lines, the pilots must intentionally induce a change in vehicle heading/roll, while for the other two a change in vehicle pitch/altitude must be achieved. The greater the magnitude of the change in the vehicle attitude, the better the calibration will be (Section 6.3.2).
- Were one to erroneously believe the VRF/IRF heading misalignment to be 0° , the correct point cloud geometry could almost be recovered by over-correcting the yaw boresight angle. Under such a scheme the laser points would experience a 0.003m vertical offset for every 10° of change in vehicle attitude for every 1m of INS offset for every 1° of θ_{VI} that is ascribed to $BS\theta_z$ (Section 6.3.3.1).
- A single ground control point is required if the vertical offset of the INS vector, Δz_{IL} , is to be adjusted. The inclusion of a ground control point also mitigates the of covariance terms between the calibration parameters and the nuisance planar parameters, which will lead to an improved point cloud TPU (Section 6.3.3.2).
- While limiting the calibration site to a narrow runway will diminish its performance (as compared to the full dataset), the 11 proposed calibration parameters can

still be determined to satisfactory levels. A narrow runway is an acceptable location for calibration (Section 6.4.1).

- If the sea surface is chosen as a calibration site, the wave action, manifesting itself as an uncertainty in the laser range measurement will lead to a less confident solution than a wave-free equivalent. However, in seas up to 1m, the calibration is both valid and more successful than the narrow runway equivalent. As the sea state grows larger, the confidence will diminish (Section 6.4.2.1). Given the calibration works in the presence of waves implies the calibrator does not require data be acquired over a flat surface but over an approximately flat surface. This suggests the requirements for the calibration may potentially be relaxed further to regions like open fields, or the grassy patches sometimes adjacent to runways (though they will naturally not describe as flat a surface as a water mass – further testing is required).

- Due to the short duration of the time required to perform the calibration, tidal effects will not hamper the calibration. Ideally, the stage of the tide should be known throughout the calibration exercise and removed from the point cloud. If the tides are not known, then they can be approximated within the calibration by a linear model (Section 6.4.2.2).

- Because neither the presence of waves nor tides was sufficient to derail the calibration, the water surface is also an acceptable location for a calibration. Due to the sloping geoid, the site over the water should be limited to no larger than a 10km×10km region (Section 6.4.2).

- The final point to stress is that a successful calibration of the point cloud has been successfully demonstrated using the least squares approach. But the user must be

cautioned to not focus exclusively on the reported uncertainties (variances) of the calibration parameters. Certainly small variances imply a confident solution which will likely lead to a confident point cloud. The converse is not necessarily true, large variances in the calibration parameters do not necessarily imply a large uncertainty in the point cloud. The ultimate goal of the surveyor is not to produce calibration parameters with low variances (though that would be nice). The ultimate goal is to produce a point cloud which has a high confidence in its reported positions. The covariances of the calibration parameters must be retained and propagated (along with the variances) to determine the total propagated uncertainty (TPU) of the point cloud positions. It is only after assessing the point cloud TPU that one can assess whether the results of the attempted calibration were satisfactory.

This leads to the next chapter where the determination of the point cloud TPU is developed.

CHAPTER VII

TOTAL PROPAGATED UNCERTAINTY

7. TOTAL PROPAGATED UNCERTAINTY
7.1 BACKGROUND
7.1.1 The General Law of the Propagation of Variances
7.1.1.1 Derivation.
7.1.1.2 A simplified uncertainty propagation example
7.1.1.3 The full-form uncertainty model
7.1.2 Covariance and its Impact on Propagated Uncertainty
7.2 TOTAL PROPAGATED UNCERTAINTY VISUALIZATION MODULE
7.2.1 Propagated Uncertainty Called from Simulator
7.2.1.1 Examining the effects of various IMUs
7.2.1.2 Further exploration of the plotting tools
7.2.1.3 Vehicle altitude versus point cloud uncertainty
7.2.1.4 Vehicle attitude versus point cloud uncertainty
7.2.2 Propagated Uncertainty Called from Calibrator
7.2.2.1 Covariance example #1: redistributing the uncertainty
7.2.2.2 Covariance example #2: overestimating the uncertainty
7.2.2.3 A few more notes on variance and the TPU module
7.3 RELATIVE CONTRIBUTIONS TO TPU OF OBSERVED AND CALIBRATED PARAMETERS' UNCERTAINTIES
7.3.1 Uncertainty of Simple 5-Parameter Calibration
7.3.2 Uncertainty of Prism/Scanner Alignments
7.3.3 Uncertainty of Scanner Azimuth Bias
7.3.4 Uncertainty of Final Calibration with and without Ground Control
7.3.5 Final Assessment of the Calibrator's Performance
7.4 SUMMARY OF KEY RESULTS

Figure 139. Chapter VII outline.

The previous chapter focused on the methodology for determining the best estimate of the calibration parameters' values. Since a least squares adjustment was performed, uncertainty bounds were also provided for each parameter. This chapter takes the topic of uncertainty management further. Both the newly-derived calibration parameters' uncertainties coupled with the uncertainties of the raw measurements can be combined to assess the uncertainty of the reported positions of the laser points. The Total Propagated Uncertainty (TPU) of the laser points is the ultimate metric in assessing the quality of the point cloud.

This chapter has four key goals:

- To provide the mathematical framework of how a total propagated uncertainty (TPU) model is constructed (Sections 7.1.1 – 7.1.1.3).
- To discuss covariance and how it impacts the TPU calculation (Sections 7.1.2, 7.2.2.1 & 7.2.2.2).
- To present a “user’s guide” for the TPU visualization module (Section 7.2).
- To provide a suite of examples to illustrate the behavior of uncertainty in the face of a number of scenarios likely to be encountered by the surveyors: What benefits are to be gained from upgrading an IMU (Section 7.2.1.1)? How does flying at different heights affect uncertainty (Section 7.2.1.3)? How far can the aircraft roll or pitch before certain beams have an unacceptable uncertainty (Section 7.2.1.4)? What return on investment will be gained by doubling the accuracy (halving the uncertainty) of the measured laser range (Section 7.2.1)? Do the forward/aft beams have a higher confidence than the port/starboard beams (Section 7.2.1.2)? To improve the confidence in my point cloud, should I upgrade my equipment or invest more time in the calibration (Section 7.3)?

The focus of this chapter is on how one determines the total propagated uncertainty (TPU) in the calculated position (both horizontal and vertical) of a single posting within the point cloud . Only with such information can a surveyor make informed decisions about the data. Throughout this chapter features of the TPU visualization module are demonstrated so the user may understand the interpretive tools at their disposal. A reoccurring theme throughout the chapter is that it is equally important to understand both the root causes and the symptoms of uncertainties in the

point cloud. A TPU model for the point cloud is not the end, but the beginning of a comprehensive uncertainty management strategy.

7.1 – Background

Please note that this background section presents the mathematical derivation of the total propagated uncertainty of any function. Throughout, the principles are demonstrated through simple examples (some lidar-related). This material is provided both for completeness and for the benefit of the uninitiated with regard to uncertainty modeling. Those already possessing a firm understanding of propagated error may wish to skip ahead to Section 7.2 which returns the focus to the CZMIL system.

One of the ancillary benefits of using a least squares adjustment for the calibration routine is the output of a fully populated variance-covariance matrix for the calibration parameters. The variance-covariance matrix provides an estimate of the confidence in each adjusted parameter's value, as well as the covariance of each parameter pair (i.e., a measure of each parameter's dependence of every other parameter). When combined with the manufacturer reported uncertainties of the system's components (the laser range, the GPS position, etc.), and the laser location equation (3.46), all the ingredients are present to derive a shot-by-shot uncertainty model of the final point cloud.

7.1.1 – The General Law of the Propagation of Variances

7.1.1.1 – Derivation. When a quantity is calculated as a function of some observations, it is reasonable to expect that uncertainties, or errors, in the observations will percolate through and induce an error in the calculated quantity. For example the area, A , of a circle of radius r is given by: $A = \pi r^2$. Clearly, if the radius of the circle is incorrectly measured, then the area of the circle will be miscalculated. More specifically,

if one were capable of measuring the radius with a one standard deviation (1σ) confidence of 0.01 meters; how would one determine the associated 1σ uncertainty for the area?

Such a simple uncertainty propagation can be achieved through a differential (Anton, Bivens, & Davis, 2002):

$$\begin{aligned}\frac{dA}{dr} &= 2\pi r \\ dA &= 2\pi r dr \\ \Delta A &= 2\pi r \Delta r\end{aligned}\tag{7.1}$$

Studying (7.1), we see the uncertainty in the calculated area cannot be determined given only the uncertainty in the measured radius. Both the uncertainty of the radius and the value of the radius itself must be provided.

But the preceding was a discussion of a single function of one variable. What is needed here is a more robust method of propagating all the uncertainties of all the measured or computed values through the laser equation to the final laser spot's position – for every laser shot. The general law of the propagation of variances does exactly that; using an a priori knowledge of the uncertainties of the measured quantities, the estimated uncertainties of the calibrated values, and the laser geolocation equation relating all these parameters, the predicted uncertainties in the computed positions of the laser points can be calculated. This is achievable by first considering a simple system of linear equations and then building from there. For a further discussion of error propagation of random errors, both the works of Fornasini (2008) and Kirkup and Frenkel (2006) are instructive; however, the following discussion follows the works of Dieck (2007) and Ghilani and Wolf (2006).

Begin with two linear equations:

$$z_1 = a_1x_1 + a_2x_2 \quad (7.2)$$

$$z_2 = b_1x_1 + b_2x_2 \quad (7.3)$$

where:

z_i = calculated quantities (like laser point coordinates)

x_i = measured quantities (like laser range or azimuth angle)

a_i, b_i = constants.

Suppose several attempts are made to measure each x , but there is some variability in the measurements. If:

x_{T1} = the true value of x_1

x_{T2} = the true value of x_2

x_1^i = the i^{th} measured value for x_1

x_2^i = the i^{th} measured value for x_2

ε_1^i = correction to the i^{th} observation of x_1

ε_2^i = correction to the i^{th} observation of x_2

then,

$$\varepsilon_1^i = x_{T1} - x_1^i \quad (7.4)$$

$$\varepsilon_2^i = x_{T2} - x_2^i. \quad (7.5)$$

Defining the true value of z_1 and z_2 as z_{T1} and z_{T2} respectively, then from (7.2):

$$z_{T1} = a_1x_{T1} + a_2x_{T2}. \quad (7.6)$$

For each attempt to compute z_{T1} , (7.4) is substituted into (7.6):

$$z_{T1} = \begin{cases} a_1(x_1^i + \varepsilon_1^i) + a_2(x_2^i + \varepsilon_2^i) \leftarrow 1^{st} \text{ Observation} \\ a_1(x_1^{ii} + \varepsilon_1^{ii}) + a_2(x_2^{ii} + \varepsilon_2^{ii}) \leftarrow 2^{nd} \text{ Observation} \\ a_1(x_1^{iii} + \varepsilon_1^{iii}) + a_2(x_2^{iii} + \varepsilon_2^{iii}) \leftarrow 3^{rd} \text{ Observation.} \end{cases} \quad (7.7)$$

Then rearranging terms:

$$z_{T1} = \begin{cases} (a_1x_1^i + a_2x_2^i) + (a_1\varepsilon_1^i + a_2\varepsilon_2^i) \\ (a_1x_1^{ii} + a_2x_2^{ii}) + (a_1\varepsilon_1^{ii} + a_2\varepsilon_2^{ii}) \\ (a_1x_1^{iii} + a_2x_2^{iii}) + (a_1\varepsilon_1^{iii} + a_2\varepsilon_2^{iii}). \end{cases} \quad (7.8)$$

Following similar reasoning, from (7.3) and (7.5):

$$z_{T2} = \begin{cases} (b_1x_1^i + b_2x_2^i) + (b_1\varepsilon_1^i + b_2\varepsilon_2^i) \\ (b_1x_1^{ii} + b_2x_2^{ii}) + (b_1\varepsilon_1^{ii} + b_2\varepsilon_2^{ii}) \\ (b_1x_1^{iii} + b_2x_2^{iii}) + (b_1\varepsilon_1^{iii} + b_2\varepsilon_2^{iii}). \end{cases} \quad (7.9)$$

With each observation, a calculated value for z_1 can be computed.

$$\begin{aligned} z_1^i &= a_1x_1^i + a_2x_2^i \\ z_1^{ii} &= a_1x_1^{ii} + a_2x_2^{ii} \\ z_1^{iii} &= a_1x_1^{iii} + a_2x_2^{iii} \end{aligned} \quad (7.10)$$

Subtracting the calculated values for z_1 given in (7.10) from the true values in (7.8), we

get the corrections for the calculated values. That is, True – Observed = Correction:

$$\begin{aligned} z_{T1} - z_1^i &= \left((a_1x_1^i + a_2x_2^i) + (a_1\varepsilon_1^i + a_2\varepsilon_2^i) \right) - (a_1x_1^i + a_2x_2^i) \\ \Delta z_1^i &= (a_1\varepsilon_1^i + a_2\varepsilon_2^i) \end{aligned} \quad (7.11)$$

where Δz_1^i = the correction to the calculated value of z_1 for the i^{th} observation. So, for

repeated observations:

$$\begin{aligned} \Delta z_1^i &= (a_1\varepsilon_1^i + a_2\varepsilon_2^i) \\ \Delta z_1^{ii} &= (a_1\varepsilon_1^{ii} + a_2\varepsilon_2^{ii}) \\ \Delta z_1^{iii} &= (a_1\varepsilon_1^{iii} + a_2\varepsilon_2^{iii}) \end{aligned} \quad (7.12)$$

and

$$\begin{aligned}
\Delta z_2^i &= (b_1 \varepsilon_1^i + b_2 \varepsilon_2^i) \\
\Delta z_2^{ii} &= (b_1 \varepsilon_1^{ii} + b_2 \varepsilon_2^{ii}) \\
\Delta z_2^{iii} &= (b_1 \varepsilon_1^{iii} + b_2 \varepsilon_2^{iii})
\end{aligned} \tag{7.13}$$

Needed now are two definitions from descriptive statistics. First, the variance of a random variable x , written σ_x^2 , is a measure of the variable's dispersion about some mean or true value, μ_x . For a sufficiently large sample, n , it is defined by:

$$\sigma_x^2 = \frac{1}{n} \sum_{j=1}^n (\mu_x - x_j)^2 \tag{7.14}$$

where x_j are the individual observations of x . Second, the covariance of two random variables x and y , written $\text{cov}(x, y)$ or $\sigma_{x,y}$, which quantifies how two variables vary about their respective means with respect to each other. That is, if there is some correlation between x and y , then should observation x_j deviate far from its mean, then y_j would be expected to do the same. The form of the definition for the covariance is similar to that of the variance. For a sufficiently large sample, n :

$$\text{cov}(x, y) = \frac{1}{n} \sum_{j=1}^n ((\mu_x - x_j)(\mu_y - y_j)). \tag{7.15}$$

The topic of covariance will be revisited later in this chapter; for now we focus on the variance.

Note the quantity within the parentheses of the (7.14) is subtracting an observed value from a true value (True – Observed), which from (7.11) is how the correction to z is defined (making the assumption that the mean value is a proxy for the true value). Thus (7.14) can be rewritten in variance parlance as:

$$\sigma_{z_1}^2 = \frac{1}{n} \sum_{j=1}^n (\Delta z_1^j)^2. \quad (7.16)$$

Writing out the summation and substituting the expressions given in (7.12) and (7.13)

yield:

$$\begin{aligned} n\sigma_{z_1}^2 &= (\Delta z_1^i)^2 + (\Delta z_1^{ii})^2 + (\Delta z_1^{iii})^2 + \dots \\ &= (a_1 \varepsilon_1^i + a_2 \varepsilon_2^i)^2 + (a_1 \varepsilon_1^{ii} + a_2 \varepsilon_2^{ii})^2 + (a_1 \varepsilon_1^{iii} + a_2 \varepsilon_2^{iii})^2 + \dots \end{aligned} \quad (7.17)$$

and

$$n\sigma_{z_2}^2 = (b_1 \varepsilon_1^i + b_2 \varepsilon_2^i)^2 + (b_1 \varepsilon_1^{ii} + b_2 \varepsilon_2^{ii})^2 + (b_1 \varepsilon_1^{iii} + b_2 \varepsilon_2^{iii})^2 + \dots. \quad (7.18)$$

Multiplying out the right-hand side of (7.17):

$$\begin{aligned} n\sigma_{z_1}^2 &= a_1^2 (\varepsilon_1^i)^2 + 2a_1 a_2 \varepsilon_1^i \varepsilon_2^i + a_2^2 (\varepsilon_2^i)^2 + \dots \\ &\quad a_1^2 (\varepsilon_1^{ii})^2 + 2a_1 a_2 \varepsilon_1^{ii} \varepsilon_2^{ii} + a_2^2 (\varepsilon_2^{ii})^2 + \dots \\ &\quad a_1^2 (\varepsilon_1^{iii})^2 + 2a_1 a_2 \varepsilon_1^{iii} \varepsilon_2^{iii} + a_2^2 (\varepsilon_2^{iii})^2 + \dots, \end{aligned} \quad (7.19)$$

and collecting like terms produces:

$$\begin{aligned} n\sigma_{z_1}^2 &= a_1^2 \left((\varepsilon_1^i)^2 + (\varepsilon_1^{ii})^2 + (\varepsilon_1^{iii})^2 + \dots \right) + \\ &\quad 2a_1 a_2 \left(\varepsilon_1^i \varepsilon_2^i + \varepsilon_1^{ii} \varepsilon_2^{ii} + \varepsilon_1^{iii} \varepsilon_2^{iii} + \dots \right) + \\ &\quad a_2^2 \left((\varepsilon_2^i)^2 + (\varepsilon_2^{ii})^2 + (\varepsilon_2^{iii})^2 + \dots \right). \end{aligned} \quad (7.20)$$

Putting the preceding equation back into sigma notation:

$$n\sigma_{z_1}^2 = a_1^2 \sum_{j=1}^n (\varepsilon_1^j)^2 + 2a_1 a_2 \sum_{j=1}^n (\varepsilon_1^j \varepsilon_2^j) + a_2^2 \sum_{j=1}^n (\varepsilon_2^j)^2 \quad (7.21)$$

and, finally, dividing through by n yields:

$$\sigma_{z_1}^2 = a_1^2 \left[\frac{1}{n} \sum_{j=1}^n (\varepsilon_1^j)^2 \right] + 2a_1 a_2 \left[\frac{1}{n} \sum_{j=1}^n (\varepsilon_1^j \varepsilon_2^j) \right] + a_2^2 \left[\frac{1}{n} \sum_{j=1}^n (\varepsilon_2^j)^2 \right]. \quad (7.22)$$

With the assumption that ε_1 and ε_2 are random variable (i.e. there are no systematic biases in the measurements of x_1 or x_2), then the bracketed items in (7.22) are (from left to right) the definitions of the variance of x_1 , the covariance of x_1 and x_2 , and the variance of x_2 – or symbolically:

$$\sigma_{z_1}^2 = a_1^2 \sigma_{x_1}^2 + 2a_1 a_2 \sigma_{x_1, x_2} + a_2^2 \sigma_{x_2}^2. \quad (7.23)$$

Following similar reasoning for z_2 produces:

$$\sigma_{z_2}^2 = b_1^2 \sigma_{x_1}^2 + 2b_1 b_2 \sigma_{x_1, x_2} + b_2^2 \sigma_{x_2}^2. \quad (7.24)$$

The previous two equations can now be combined into a single matrix equation:

$$\begin{bmatrix} \sigma_{z_1}^2 & \sigma_{z_1, z_2} \\ \sigma_{z_1, z_2} & \sigma_{z_2}^2 \end{bmatrix} = \begin{bmatrix} a_1 & a_2 \\ b_1 & b_2 \end{bmatrix} \begin{bmatrix} \sigma_{x_1}^2 & \sigma_{x_1, x_2} \\ \sigma_{x_1, x_2} & \sigma_{x_2}^2 \end{bmatrix} \begin{bmatrix} a_1 & b_1 \\ a_2 & b_2 \end{bmatrix} \quad (7.25)$$

To confirm this, multiply out the right-hand side of (7.25)

$$\begin{aligned} \begin{bmatrix} \sigma_{z_1}^2 & \sigma_{z_1, z_2} \\ \sigma_{z_1, z_2} & \sigma_{z_2}^2 \end{bmatrix} &= \begin{bmatrix} a_1 & a_2 \\ b_1 & b_2 \end{bmatrix} \begin{bmatrix} \sigma_{x_1}^2 & \sigma_{x_1, x_2} \\ \sigma_{x_1, x_2} & \sigma_{x_2}^2 \end{bmatrix} \begin{bmatrix} a_1 & b_1 \\ a_2 & b_2 \end{bmatrix} \\ &= \begin{bmatrix} (a_1^2 \sigma_{x_1}^2 + a_1 a_2 \sigma_{x_1, x_2} + a_1 a_2 \sigma_{x_1, x_2} + a_2^2 \sigma_{x_2}^2) & (a_1 b_1 \sigma_{x_1}^2 + a_2 b_1 \sigma_{x_1, x_2} + a_1 b_2 \sigma_{x_1, x_2} + a_2 b_2 \sigma_{x_2}^2) \\ (a_1 b_1 \sigma_{x_1}^2 + a_2 b_1 \sigma_{x_1, x_2} + a_1 b_2 \sigma_{x_1, x_2} + a_2 b_2 \sigma_{x_2}^2) & (b_1^2 \sigma_{x_1}^2 + b_1 b_2 \sigma_{x_1, x_2} + b_1 b_2 \sigma_{x_1, x_2} + b_2^2 \sigma_{x_2}^2) \end{bmatrix} \begin{bmatrix} a_1 & b_1 \\ a_2 & b_2 \end{bmatrix}. \end{aligned} \quad (7.26)$$

Which, with further multiplication, is equal to:

$$\begin{bmatrix} (a_1^2 \sigma_{x_1}^2 + a_1 a_2 \sigma_{x_1, x_2} + a_1 a_2 \sigma_{x_1, x_2} + a_2^2 \sigma_{x_2}^2) & (a_1 b_1 \sigma_{x_1}^2 + a_2 b_1 \sigma_{x_1, x_2} + a_1 b_2 \sigma_{x_1, x_2} + a_2 b_2 \sigma_{x_2}^2) \\ (a_1 b_1 \sigma_{x_1}^2 + a_2 b_1 \sigma_{x_1, x_2} + a_1 b_2 \sigma_{x_1, x_2} + a_2 b_2 \sigma_{x_2}^2) & (b_1^2 \sigma_{x_1}^2 + b_1 b_2 \sigma_{x_1, x_2} + b_1 b_2 \sigma_{x_1, x_2} + b_2^2 \sigma_{x_2}^2) \end{bmatrix}. \quad (7.27)$$

Matching up each element of (7.27) with the left-hand side of (7.26), the first row/first column gives:

$$\sigma_{z_1}^2 = a_1^2 \sigma_{x_1}^2 + 2a_1 a_2 \sigma_{x_1, x_2} + a_2^2 \sigma_{x_2}^2, \quad (7.28)$$

which is an exact match of (7.23). Further (7.24) is produced by matching elements in the second row/second column position. Thus (7.25) is a successful matrix representation of the system of variance equations. As a bonus, the off-diagonal elements yield a formula for the covariance among the two variables z_1 and z_2 :

$$\sigma_{z_1, z_2} = a_1 b_1 \sigma_{x_1}^2 + a_2 b_1 \sigma_{x_1, x_2} + a_1 b_2 \sigma_{x_1, x_2} + a_2 b_2 \sigma_{x_2}^2. \quad (7.29)$$

If one were to make the simplifying assumption that all the observations are independent of one another, then $\sigma_{x_1, x_2} = 0$. With this assumption of independence, (7.23) and (7.24) reduce to a simple sum of squares error formula:

$$\sigma_{z_1}^2 = a_1^2 \sigma_{x_1}^2 + a_2^2 \sigma_{x_2}^2 \quad (7.30)$$

$$\sigma_{z_2}^2 = b_1^2 \sigma_{x_1}^2 + b_2^2 \sigma_{x_2}^2. \quad (7.31)$$

Depending on the context of the problem, the assumption of independence of variables may or may not be valid. From a lidar perspective, it is reasonable to assume the uncertainty in the laser range measurement is independent from the uncertainty in the scanner azimuth; however there is a likely a coupling of the INS-sensed pitch and INS-sensed roll values. If one were to concede non-zero covariances, the challenge then becomes how to calculate their values.

Generalizing the discussion to an arbitrary number of variables, consider the system of linear equations:

$$\begin{aligned} z_1 &= a_{11}x_1 + a_{12}x_2 + \cdots + a_{1n}x_n \\ z_2 &= a_{21}x_1 + a_{22}x_2 + \cdots + a_{2n}x_n \\ &\vdots \\ z_m &= a_{m1}x_1 + a_{m2}x_2 + \cdots + a_{mn}x_n \end{aligned} \quad (7.32)$$

The covariance matrix of the z variables, \mathbb{C}_z , will have the form:

$$\mathbb{C}_z = \begin{bmatrix} \sigma_{z_1}^2 & \sigma_{z_1, z_2} & \cdots & \sigma_{z_1, z_m} \\ \sigma_{z_2, z_1} & \sigma_{z_2}^2 & \cdots & \sigma_{z_2, z_m} \\ \vdots & \vdots & \ddots & \vdots \\ \sigma_{z_m, z_1} & \sigma_{z_m, z_2} & \cdots & \sigma_{z_m}^2 \end{bmatrix} \quad (7.33)$$

and will be defined by:

$$\underbrace{\begin{bmatrix} a_{11} & a_{12} & \cdots & a_{1n} \\ a_{21} & a_{22} & \cdots & a_{2n} \\ \vdots & \vdots & \ddots & \vdots \\ a_{m1} & a_{m2} & \cdots & a_{mn} \end{bmatrix}}_{\mathbf{A}} \underbrace{\begin{bmatrix} \sigma_{x_1}^2 & \sigma_{x_1, x_2} & \cdots & \sigma_{x_1, x_n} \\ \sigma_{x_2, x_1} & \sigma_{x_2}^2 & \cdots & \sigma_{x_2, x_n} \\ \vdots & \vdots & \ddots & \vdots \\ \sigma_{x_n, x_1} & \sigma_{x_n, x_2} & \cdots & \sigma_{x_n}^2 \end{bmatrix}}_{\mathbb{C}_x} \underbrace{\begin{bmatrix} a_{11} & a_{21} & \cdots & a_{m1} \\ a_{12} & a_{22} & \cdots & a_{m2} \\ \vdots & \vdots & \ddots & \vdots \\ a_{1n} & a_{2n} & \cdots & a_{mn} \end{bmatrix}}_{\mathbf{A}^T}. \quad (7.34)$$

Should the equations in (7.32) be non-linear, then a Taylor series expansion can be applied similar to (5.30). In such a case, the matrix \mathbf{A} in (7.34) will take the form of the Jacobian:

$$\mathbf{A} = \begin{bmatrix} \frac{\partial z_1}{\partial x_1} & \frac{\partial z_1}{\partial x_2} & \cdots & \frac{\partial z_1}{\partial x_n} \\ \frac{\partial z_2}{\partial x_1} & \frac{\partial z_2}{\partial x_2} & \cdots & \frac{\partial z_2}{\partial x_n} \\ \vdots & \vdots & \ddots & \vdots \\ \frac{\partial z_m}{\partial x_1} & \frac{\partial z_m}{\partial x_2} & \cdots & \frac{\partial z_m}{\partial x_n} \end{bmatrix} \quad (7.35)$$

7.1.1.2 – A simplified uncertainty propagation example. Rather than overwhelming the reader with the uncertainty model of the fully-developed laser equation, a simpler model is presented for the sake of illustrating the implementation of the above equations. In this simplified laser scanner, the vehicle is assumed stationary, and the laser has two degrees of freedom: the azimuth angle, θ , and the nadir angle, ϕ , (Figure 140). With the inclusion of the laser range, ρ , the ground coordinate is given by the spherical-to-rectangular coordinate transformation:

$$\begin{aligned}
 x_g &= \rho \cos \theta \sin \phi \\
 y_g &= \rho \sin \theta \sin \phi \\
 z_g &= \rho \cos \phi
 \end{aligned}
 \tag{7.36}$$

Consider the following measurements with associated 1σ uncertainties:

$$\begin{aligned}
 \rho &= 425 \pm 0.01 \text{ meters} \\
 \theta &= 45^\circ \pm 0.12^\circ \text{ (} 0.785 \pm 0.002 \text{ radians)} \\
 \phi &= 20^\circ \pm 0.06^\circ \text{ (} 0.349 \pm 0.001 \text{ radians)}
 \end{aligned}$$

where the goal is to determine the uncertainties in x , y , and z .

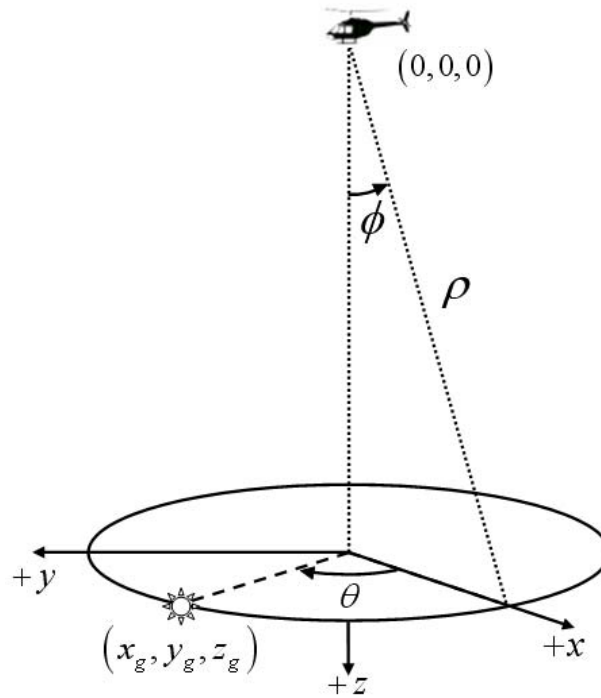


Figure 140. A simplified laser scanner with only three inputs, a laser range ρ , azimuth angle θ and elevation angle ϕ .

With the assumption of the simpler, covariance-free, independent variable model, (7.30) can be used.

$$\sigma_{x_g}^2 = \left(\frac{\partial x}{\partial \rho} \sigma_\rho \right)^2 + \left(\frac{\partial x}{\partial \theta} \sigma_\theta \right)^2 + \left(\frac{\partial x}{\partial \phi} \sigma_\phi \right)^2
 \tag{7.37}$$

Substituting the respective partial derivatives yields:

$$\sigma_{x_g} = \sqrt{(\cos \theta \sin \phi (0.01))^2 + (-\rho \sin \theta \sin \phi (0.002))^2 + (\rho \cos \theta \cos \phi (0.001))^2} \quad (7.38)$$

$$= 0.349 \text{ meters.}$$

Similarly,

$$\sigma_{y_g} = \sqrt{\left(\frac{\partial y}{\partial \rho} \sigma_\rho\right)^2 + \left(\frac{\partial y}{\partial \theta} \sigma_\theta\right)^2 + \left(\frac{\partial y}{\partial \phi} \sigma_\phi\right)^2}$$

$$= \sqrt{(\sin \theta \sin \phi (0.01))^2 + (\rho \cos \theta \sin \phi (0.002))^2 + (\rho \sin \theta \cos \phi (0.001))^2} \quad (7.39)$$

$$= 0.349 \text{ meters}$$

and

$$\sigma_{z_g} = \sqrt{\left(\frac{\partial z}{\partial \rho} \sigma_\rho\right)^2 + \left(\frac{\partial z}{\partial \theta} \sigma_\theta\right)^2 + \left(\frac{\partial z}{\partial \phi} \sigma_\phi\right)^2}$$

$$= \sqrt{(\cos \phi (0.01))^2 + (0)^2 + (-\rho \sin \phi (0.001))^2} \quad (7.40)$$

$$= 0.146 \text{ meters.}$$

Working with points in space, uncertainties are not usually deconstructed into separate components. Instead the errors are expressed as a horizontal and vertical uncertainty (or fully combined into a radial uncertainty). From the example above:

$$\text{Vertical TPU} = 0.146 \text{ meters}$$

$$\text{Horizontal TPU} = \sqrt{0.349^2 + 0.349^2} = 0.494 \text{ meters}$$

$$\text{Radial TPU} = \sqrt{0.349^2 + 0.349^2 + 0.146^2} = 0.515 \text{ meters}$$

Alternatively, the uncertainties can be expressed in matrix form:

$$\underbrace{\begin{bmatrix} \sigma_x^2 & \sigma_{x,y} & \sigma_{x,z} \\ \sigma_{y,x} & \sigma_y^2 & \sigma_{y,z} \\ \sigma_{z,x} & \sigma_{z,y} & \sigma_z^2 \end{bmatrix}}_{\mathbb{C}_z} = \underbrace{\begin{bmatrix} \frac{\partial x}{\partial \rho} & \frac{\partial x}{\partial \theta} & \frac{\partial x}{\partial \phi} \\ \frac{\partial y}{\partial \rho} & \frac{\partial y}{\partial \theta} & \frac{\partial y}{\partial \phi} \\ \frac{\partial z}{\partial \rho} & \frac{\partial z}{\partial \theta} & \frac{\partial z}{\partial \phi} \end{bmatrix}}_{\mathbf{A}} \underbrace{\begin{bmatrix} \sigma_\rho^2 & \sigma_{\rho,\theta} & \sigma_{\rho,\phi} \\ \sigma_{\theta,\rho} & \sigma_\theta^2 & \sigma_{\theta,\phi} \\ \sigma_{\phi,\rho} & \sigma_{\phi,\theta} & \sigma_\phi^2 \end{bmatrix}}_{\mathbb{C}_x} \underbrace{\begin{bmatrix} \frac{\partial x}{\partial \rho} & \frac{\partial y}{\partial \rho} & \frac{\partial z}{\partial \rho} \\ \frac{\partial x}{\partial \theta} & \frac{\partial y}{\partial \theta} & \frac{\partial z}{\partial \theta} \\ \frac{\partial x}{\partial \phi} & \frac{\partial y}{\partial \phi} & \frac{\partial z}{\partial \phi} \end{bmatrix}}_{\mathbf{A}^T} \quad (7.41)$$

where the Jacobian matrix, \mathbf{A} , has the form:

$$\mathbf{A} = \begin{bmatrix} \cos \theta \sin \phi & -\rho \sin \theta \sin \phi & \rho \cos \theta \cos \phi \\ \sin \theta \sin \phi & \rho \cos \theta \sin \phi & \rho \sin \theta \cos \phi \\ \cos \phi & 0 & -\rho \sin \phi \end{bmatrix}. \quad (7.42)$$

From a programming stand-point, putting the uncertainties in a matrix representation offers greater flexibility and yields a simpler partial derivative.

One final observation can be made of this simplified model. Revisiting equation (7.37):

$$\sigma_{x_g}^2 = \underbrace{\left(\frac{\partial x}{\partial \rho} \sigma_\rho \right)^2}_{\text{Laser range induced error}} + \underbrace{\left(\frac{\partial x}{\partial \theta} \sigma_\theta \right)^2}_{\text{Azimuth angle induced error}} + \underbrace{\left(\frac{\partial x}{\partial \phi} \sigma_\phi \right)^2}_{\text{Nadir angle induced error}} \quad (7.43)$$

it follows that (assuming independence of the observations) the variance in the x -position is a linear sum of the contributions by the individual observations. In this respect, by comparing the magnitudes of the individual components being summed, it is possible to determine which parameter is most affecting the final uncertainty.

For example, the fraction of the vertical uncertainty in the previous example that can be attributed exclusively to the uncertainty of the measured laser nadir angle can be found. That is:

$$\left(\frac{\partial z}{\partial \phi} \sigma_\phi \right)^2 / \sigma_{z_g}^2 = ? \quad (7.44)$$

In the full laser equation, closed form expressions for x , y , and z as shown in (7.36) are not available. So, for demonstrative purposes, (7.36) is expressed as a series of rotational matrices:

$$\begin{bmatrix} x_g \\ y_g \\ z_g \end{bmatrix} = \begin{bmatrix} \cos \theta & -\sin \theta & 0 \\ \sin \theta & \cos \theta & 0 \\ 0 & 0 & 1 \end{bmatrix} \begin{bmatrix} \cos \phi & 0 & \sin \phi \\ 0 & 1 & 0 \\ -\sin \phi & 0 & \cos \phi \end{bmatrix} \begin{bmatrix} 0 \\ 0 \\ \rho \end{bmatrix}. \quad (7.45)$$

When expressed as a product of matrices of one variable, computing the partial derivatives is a simple exercise. In this case, computing the partial with respect to the nadir angle yields:

$$\begin{bmatrix} \frac{\partial x_g}{\partial \phi} \\ \frac{\partial y_g}{\partial \phi} \\ \frac{\partial z_g}{\partial \phi} \end{bmatrix} = \begin{bmatrix} \cos \theta & -\sin \theta & 0 \\ \sin \theta & \cos \theta & 0 \\ 0 & 0 & 1 \end{bmatrix} \begin{bmatrix} -\sin \phi & 0 & \cos \phi \\ 0 & 0 & 0 \\ -\cos \phi & 0 & -\sin \phi \end{bmatrix} \begin{bmatrix} 0 \\ 0 \\ \rho \end{bmatrix}. \quad (7.46)$$

Next, substituting the measured values for ρ , θ and ϕ gives:

$$\begin{bmatrix} \frac{\partial x_g}{\partial \phi} \\ \frac{\partial y_g}{\partial \phi} \\ \frac{\partial z_g}{\partial \phi} \end{bmatrix} = \begin{bmatrix} 282.4 \\ 282.4 \\ -145.4 \end{bmatrix}. \quad (7.47)$$

To compute the contribution to the total vertical error, from (7.44) we have:

$$\begin{aligned} \left(\frac{\partial z}{\partial \phi} \sigma_\phi \right)^2 / \sigma_{z_g}^2 &= \frac{(-145.4 * 0.001)^2}{(0.146)^2} \\ &= \frac{0.0211}{0.0213} = 98.99\% \end{aligned} \quad (7.48)$$

Roughly 99% of the vertical error can be exclusively attributed to the uncertainty of laser nadir angle. Under this scenario, should the lidar manufacturer wish to improve the total vertical uncertainty (TVU) of this posting, their efforts should be focused on refining their ability to measure the laser's nadir angle – the laser range and azimuth are “good

enough.” Then again, the gross error must also be kept in context: if the survey specifications call for 0.500m of vertical confidence, then a 0.146m TVU is small enough to proceed without further system modifications.

7.1.1.3 – The full-form uncertainty model. Much like the discussion of the computation of the partial derivatives of the full-form laser equation discussed in Chapter III, the complexity of the calculation of the contribution to the total uncertainty by a given variable is largely a function of whether or not \vec{L}_2 , the laser vector exiting the prism, is a function of a particular variable. Here, one of the simpler derivatives is computed to illustrate the process. Recalling the laser equation as stated in (3.46):

$$\vec{x}_G = \mathbb{R}_V \cdot \mathbb{R}_{VI} \left(\mathbb{R}_{BS} \cdot \vec{L}_2 \cdot \left(\frac{\rho - \rho_0}{\rho_1} \right) + \vec{x}_{IL} \right) + \vec{x}_{ECEP},$$

the propagated uncertainty associated strictly with the IMU-sensed pitch, ψ , is found. A study of the definitions of the above symbols (found in [3.47]), shows that the only item in the above stated equation that is dependent on the vehicle pitch is \mathbb{R}_V . Thus,

$$\frac{\partial \vec{x}_G}{\partial \psi} = \mathbb{R}_V \cdot \mathbb{R}_{VI} \left(\frac{\partial \mathbb{R}_{BS}}{\partial \psi} \cdot \vec{L}_2 \cdot \left(\frac{\rho - \rho_0}{\rho_1} \right) + \mathbf{0} \right) + \mathbf{0}. \quad (7.49)$$

Where, given:

$$\mathbb{R}_V = \underbrace{\begin{bmatrix} \cos \kappa & -\sin \kappa & 0 \\ \sin \kappa & \cos \kappa & 0 \\ 0 & 0 & 1 \end{bmatrix}}_{\text{Vessel yaw}} \cdot \underbrace{\begin{bmatrix} \cos \psi & 0 & \sin \psi \\ 0 & 1 & 0 \\ -\sin \psi & 0 & \cos \psi \end{bmatrix}}_{\text{Vessel pitch}} \cdot \underbrace{\begin{bmatrix} 1 & 0 & 0 \\ 0 & \cos \omega & -\sin \omega \\ 0 & \sin \omega & \cos \omega \end{bmatrix}}_{\text{Vessel roll}}, \quad (7.50)$$

$$\frac{\partial \mathbb{R}_V}{\partial \psi} = \begin{bmatrix} \cos \kappa & -\sin \kappa & 0 \\ \sin \kappa & \cos \kappa & 0 \\ 0 & 0 & 1 \end{bmatrix} \cdot \begin{bmatrix} -\sin \psi & 0 & \cos \psi \\ 0 & 0 & 0 \\ -\cos \psi & 0 & -\sin \psi \end{bmatrix} \cdot \begin{bmatrix} 1 & 0 & 0 \\ 0 & \cos \omega & -\sin \omega \\ 0 & \sin \omega & \cos \omega \end{bmatrix}. \quad (7.51)$$

7.1.2 – Covariance and its Impact on Propagated Uncertainty

From a mathematical perspective, dropping the covariance terms from the uncertainty propagation model makes for a simpler calculation. Computing the uncertainty of the parameters z_1, z_2 , etc. goes from:

$$\begin{aligned} \mathbb{C}_z &= \begin{bmatrix} \sigma_{z_1}^2 & \sigma_{z_1, z_2} & \cdots & \sigma_{z_1, z_m} \\ \sigma_{z_2, z_1} & \sigma_{z_2}^2 & \cdots & \sigma_{z_2, z_m} \\ \vdots & \vdots & \ddots & \vdots \\ \sigma_{z_m, z_1} & \sigma_{z_m, z_2} & \cdots & \sigma_{z_m}^2 \end{bmatrix} \\ &= \begin{bmatrix} a_{11} & a_{12} & \cdots & a_{1n} \\ a_{21} & a_{22} & \cdots & a_{2n} \\ \vdots & \vdots & \ddots & \vdots \\ a_{m1} & a_{m2} & \cdots & a_{mn} \end{bmatrix} \begin{bmatrix} \sigma_{x_1}^2 & \sigma_{x_1, x_2} & \cdots & \sigma_{x_1, x_n} \\ \sigma_{x_2, x_1} & \sigma_{x_2}^2 & \cdots & \sigma_{x_2, x_n} \\ \vdots & \vdots & \ddots & \vdots \\ \sigma_{x_n, x_1} & \sigma_{x_n, x_2} & \cdots & \sigma_{x_n}^2 \end{bmatrix} \begin{bmatrix} a_{11} & a_{21} & \cdots & a_{m1} \\ a_{12} & a_{22} & \cdots & a_{m2} \\ \vdots & \vdots & \ddots & \vdots \\ a_{1n} & a_{2n} & \cdots & a_{mn} \end{bmatrix}, \end{aligned} \quad (7.52)$$

to a matrix-free system of equations:

$$\begin{aligned} \sigma_{z_1}^2 &= \left(\frac{\partial z_1}{\partial x_1} \sigma_{x_1} \right)^2 + \left(\frac{\partial z_1}{\partial x_2} \sigma_{x_2} \right)^2 + \cdots + \left(\frac{\partial z_1}{\partial x_n} \sigma_{x_n} \right)^2 \\ \sigma_{z_2}^2 &= \left(\frac{\partial z_2}{\partial x_1} \sigma_{x_1} \right)^2 + \left(\frac{\partial z_2}{\partial x_2} \sigma_{x_2} \right)^2 + \cdots + \left(\frac{\partial z_2}{\partial x_n} \sigma_{x_n} \right)^2 \\ &\vdots \\ \sigma_{z_m}^2 &= \left(\frac{\partial z_m}{\partial x_1} \sigma_{x_1} \right)^2 + \left(\frac{\partial z_m}{\partial x_2} \sigma_{x_2} \right)^2 + \cdots + \left(\frac{\partial z_m}{\partial x_n} \sigma_{x_n} \right)^2. \end{aligned} \quad (7.53)$$

Not only is (7.53) a more straight-forward calculation, but it relieves the modeler of the responsibility of estimating the many covariance terms (a non-trivial exercise).

Covariances can be omitted from an uncertainty calculation, provided a proper argument is made for the independence of the respective parameters. Using a lidar-related example: the uncertainty of the laser range measurement is independent of the uncertainty of scanner's encoded azimuth. The laser and scanner were likely constructed

by different manufacturers and the accuracy of one device has nothing to do with the other, thus their covariance is zero. On the other hand, there may be some cross-talk within the IMU that leads to a non-zero covariance between the measured pitch and roll of the vehicle. The difficulty is in determining the value of this covariance. While the INS manufacturers are relatively forthcoming with their systems' capabilities of measuring a vehicle's roll, pitch or yaw (typically reported as a standard deviation or variance), the covariances are not so readily advertised. At the time of this writing, representatives of Applanix have been contacted with regard to accessing the covariances among their INS' reported pitch, roll and heading. Their initial response was that while they felt the information to compute the covariances may be available, no such information was available to the user.

With regard to propagated uncertainty, covariances are ignored at the risk of an incomplete and inaccurate model. Depending on the signs of the covariances (and their associated partial derivatives), an inclusion of these terms could lead to either larger or smaller point cloud uncertainties. The behavior is application specific, but given the casual modeler's propensity to think in terms of their inputs' variances, and not their covariances, a simple example is provided to demonstrate the effects of covariance on propagated uncertainty (and the consequences of overlooking it).

Consider an unorthodox method of computing the area of a rectangle (Figure 141). The area of a rectangle is given by the product of its length and width. To measure the dimensions, a 10-meter measuring tape is affixed to one corner and then wrapped along the rectangle's length and width, terminating at the opposite corner. The length can then be read off of the tape measure, while the width can be determined through

subtraction. For example, if the length is measured as 6 meters, then the width must be 4 meters. In the interest of replication, suppose the length is measured two more times, yielding 5.9 and 6.1m (with associated computed widths of 4.1 and 3.9m).

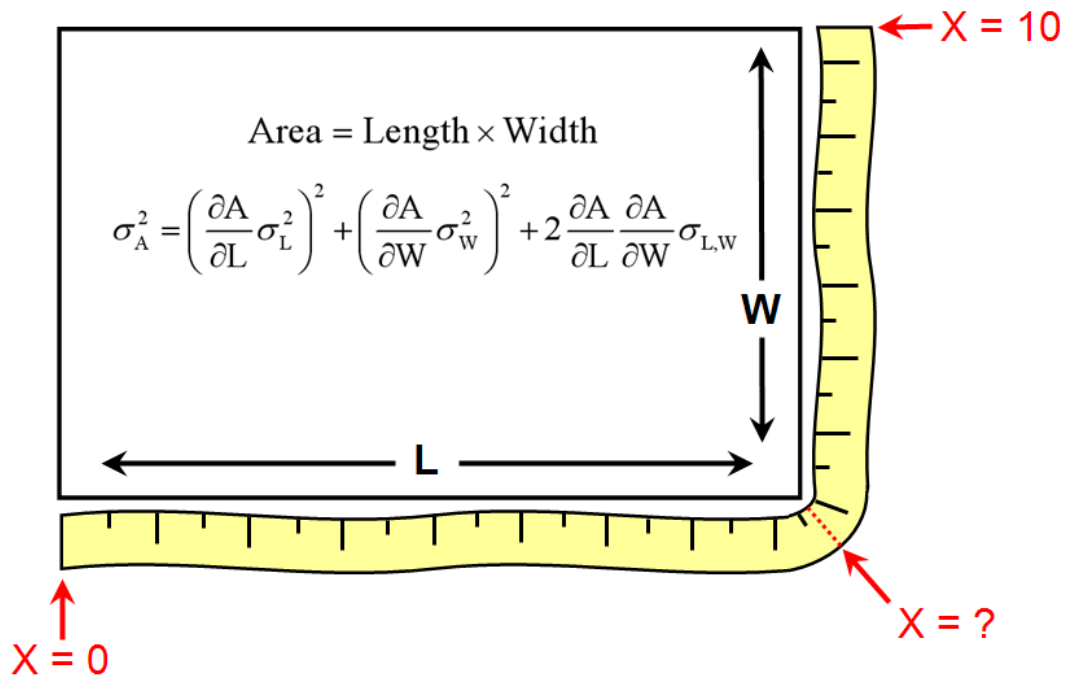


Figure 141. Determining the area (and associated uncertainty) of a rectangle whose dimensions are determined by wrapping a 10-meter tape measure along the rectangle's half-perimeter.

Determining the dimensions of the rectangle in this way, there is a clear (negative) correlation between the measured length and the calculated width of the rectangle. If one estimates the length to be a little larger than the true value by some amount, then the calculated width will be smaller than its true value by that same amount.

Though three data points does not make for a robust dataset, the uncertainty in the computed area of the rectangle can still be estimated based on the uncertainties of the two inputs. Given the area of a rectangle is the product of its length and width, the uncertainty is given by (7.34):

$$\sigma_A^2 = \begin{bmatrix} \partial A / \partial L & \partial A / \partial W \end{bmatrix} \begin{bmatrix} \sigma_L^2 & \sigma_{L,W} \\ \sigma_{L,W} & \sigma_W^2 \end{bmatrix} \begin{bmatrix} \partial A / \partial L & \partial A / \partial W \end{bmatrix}^T \quad (7.54)$$

which can be simplified to:

$$\sigma_A^2 = \left(\frac{\partial A}{\partial L} \right)^2 \sigma_L^2 + \left(\frac{\partial A}{\partial W} \right)^2 \sigma_W^2 + 2 \frac{\partial A}{\partial L} \frac{\partial A}{\partial W} \sigma_{L,W}. \quad (7.55)$$

The variance and covariance are respectively computed (for small sample sizes) using the two equations:

$$\sigma_L^2 = \frac{1}{(n-1)} \sum_{i=1}^n (L_i - \bar{L})^2 \quad (7.56)$$

$$\sigma_{L,W} = \frac{1}{(n-1)} \sum_{i=1}^n ((L_i - \bar{L})(W_i - \bar{W})). \quad (7.57)$$

Using the preceding three data points, $\sigma_L^2 = \sigma_W^2 = 0.01\text{m}^2$ and $\sigma_{L,W} = -0.01\text{m}^2$.

Assuming an independence of the input variables (i.e. assuming $\sigma_{L,W} = 0$), then

(7.55) yields:

$$\begin{aligned} \sigma_A^2 &= (4)^2 (0.01) + (6)^2 (0.01) + 2(4)(6)(0) \\ &= 0.52\text{m}^4. \end{aligned} \quad (7.58)$$

So the standard deviation, being the square root of the variance, of the area is equal to 0.72m^2 . However, this is an overly pessimistic view of the uncertainty of the computed area. The area is the product of the rectangle's length and width. Should the measured length be larger than its actual value, the width will necessarily be smaller than its actual value (by the nature of how the rectangle's width is computed). This balancing of the length and width will help temper any variability in the rectangle's area. Inclusion of the covariance in (7.55) yields:

$$\begin{aligned}\sigma_A^2 &= (4)^2 0.01 + (6)^2 0.01 + 2(4)(6)(-0.01) \\ &= 0.04\text{m}^4\end{aligned}\quad (7.59)$$

with a standard deviation of 0.2m^2 . Thus the inclusion of the covariance term reduced the calculated standard deviation of the area by 72% and the calculated variance by 92%.

The previous example should serve as a warning to how neglecting the covariance can lead to a misinterpretation of a function's overall uncertainty. Large uncertainties in a function's input do not necessarily translate to large uncertainty in a function's output (provided there is a negative covariance among the input parameters). Inversely, should there be a positive covariance, the uncertainty of the function's output may be greater than the sum of the individual contributions.

Returning to the simplified laser scanner shown in Figure 140, a covariance-free model had an uncertainty in the x-coordinate of the point cloud given by (7.37):

$$\sigma_{x_g}^2 = \left(\frac{\partial x}{\partial \rho} \sigma_\rho \right)^2 + \left(\frac{\partial x}{\partial \theta} \sigma_\theta \right)^2 + \left(\frac{\partial x}{\partial \phi} \sigma_\phi \right)^2.$$

With the inclusion of the covariances, the full uncertainty of the point cloud becomes:

$$\sigma_{x_g}^2 = \left(\frac{\partial x}{\partial \rho} \sigma_\rho \right)^2 + \left(\frac{\partial x}{\partial \theta} \sigma_\theta \right)^2 + \left(\frac{\partial x}{\partial \phi} \sigma_\phi \right)^2 + 2 \frac{\partial x}{\partial \rho} \frac{\partial x}{\partial \theta} \sigma_{\rho,\theta} + 2 \frac{\partial x}{\partial \rho} \frac{\partial x}{\partial \phi} \sigma_{\rho,\phi} + 2 \frac{\partial x}{\partial \theta} \frac{\partial x}{\partial \phi} \sigma_{\theta,\phi}. \quad (7.60)$$

Even with this simplified lidar having only three measured quantities, it is not so straightforward a matter to assess whether or not the inclusion of the covariance terms will increase or decrease the uncertainty of the point cloud. The final contribution is dependent on the signs of the covariances, the signs of the partial derivatives and their linear combination. But, regardless of whether the covariance terms help or hurt the point cloud's TPU, if they are known, they must be included in the calculation.

The discussion of covariance will be revisited later in this chapter when the TPU module as called by the lidar calibrator is presented. Generally, the covariances among parameters are not known. When attempting to assess the “success” or “failure” of a given flight configuration with regard to how well the calibration parameters can be determined, typically the reported uncertainties of the adjusted parameters are considered. The logic being large reported uncertainties in the calibration values imply a poorly designed flight plan. However, large uncertainties for the calibration values do not necessarily translate to large positional uncertainties in the point cloud. The calibrator may report a pair of parameters to have large standard deviations only because the module cannot determine which parameter is the true culprit for the geometric misalignments. In such a case, these parameters will have a relatively large covariance which may ultimately lead to a small uncertainty in the point cloud. Only with a full analysis of the variance-covariance matrix can one assess the performance of the calibration routine.

7.2 – Total Propagated Uncertainty Visualization Module

The final Graphical User Interfaces (GUIs) developed in conjunction with this dissertation – the others being the simulation module, the calibration module, and the covariances/correlation module – is now presented. The TPU module is a custom GUI developed for the purposes of giving the operator a means of visualizing the estimated uncertainties of any point cloud dataset. This module also provides a means of adjusting the uncertainties of the laser equation inputs to understand their influence on the final outputs. Depending on whether the program is called from the simulator or calibrator, it will behave slightly differently.

7.2.1 – Propagated Uncertainty Called from Simulator

A rendering of the overall propagated uncertainty module, as called from the lidar simulator, is shown in Figure 142 (along with more detailed views shown in Figure 143, Figure 144 and Figure 145).

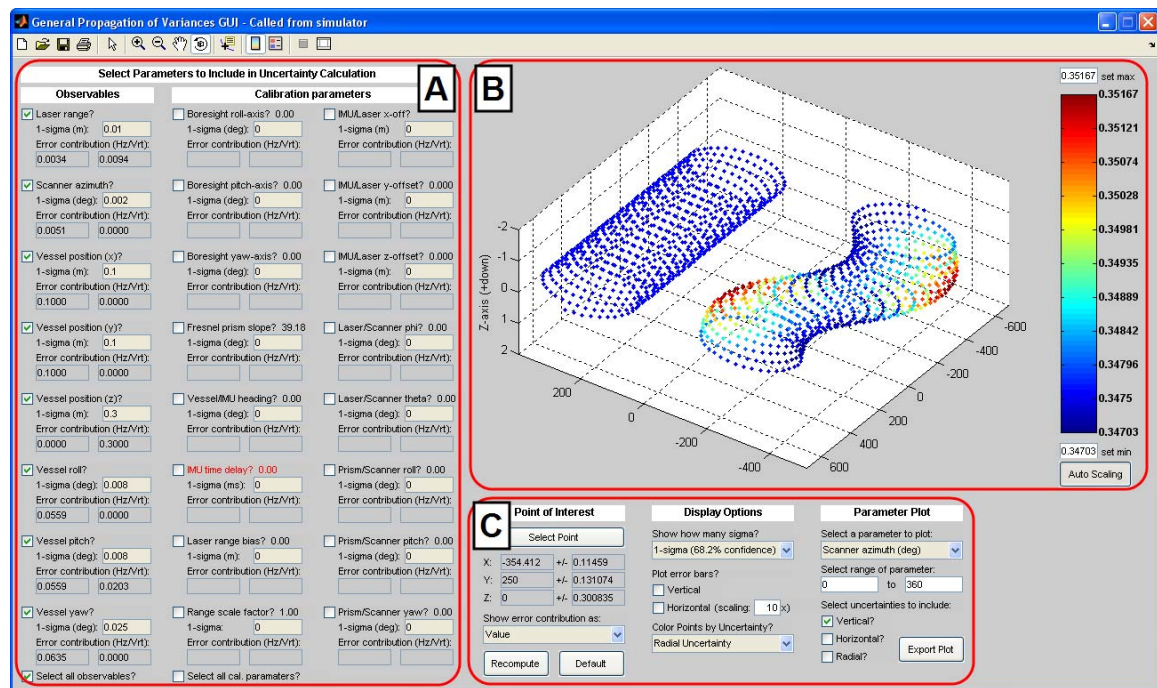


Figure 142. The total propagated uncertainty interface. Close up views of the parameter list (A), plotting window (B) and control panel (C) are shown in the following figures.

Select Parameters to Include in Uncertainty Calculation		
Observables	Calibration parameters	
<input checked="" type="checkbox"/> Laser range? 1-sigma (m): 0.01 Error contribution (Hz/Vrt): 0.0037 0.0093	<input checked="" type="checkbox"/> Boresight roll-axis? 0.00 1-sigma (deg): 0.005 Error contribution (Hz/Vrt): 0.0368 0.0054	<input type="checkbox"/> IMU/Laser x-offset? 0.000 1-sigma (m): 0 Error contribution (Hz/Vrt):
<input checked="" type="checkbox"/> Scanner azimuth? 1-sigma (deg): 0.002 Error contribution (Hz/Vrt): 0.0051 0.0000	<input checked="" type="checkbox"/> Boresight pitch-axis? 0.00 1-sigma (deg): 0.005 Error contribution (Hz/Vrt): 0.0372 0.0134	<input type="checkbox"/> IMU/Laser y-offset? 0.000 1-sigma (m): 0 Error contribution (Hz/Vrt):
<input type="checkbox"/> Vessel position (x)? 1-sigma (m): 0.1 Error contribution (Hz/Vrt):	<input checked="" type="checkbox"/> Boresight yaw-axis? 0.00 1-sigma (deg): 0.005 Error contribution (Hz/Vrt): 0.0134 0.0020	<input type="checkbox"/> IMU/Laser z-offset? 0.000 1-sigma (m): 0 Error contribution (Hz/Vrt):
<input type="checkbox"/> Vessel position (y)? 1-sigma (m): 0.1 Error contribution (Hz/Vrt):	<input checked="" type="checkbox"/> Fresnel prism slope? 39.18 1-sigma (deg): 0.01 Error contribution (Hz/Vrt): 0.0370 0.0213	<input type="checkbox"/> Laser/Scanner phi? 0.00 1-sigma (deg): 0 Error contribution (Hz/Vrt):
<input type="checkbox"/> Vessel position (z)? 1-sigma (m): 0.3 Error contribution (Hz/Vrt):	<input type="checkbox"/> Vessel/IMU heading? 0.00 1-sigma (deg): 0 Error contribution (Hz/Vrt):	<input type="checkbox"/> Laser/Scanner theta? 0.00 1-sigma (deg): 0 Error contribution (Hz/Vrt):
<input checked="" type="checkbox"/> Vessel roll? 1-sigma (deg): 0.008 Error contribution (Hz/Vrt): 0.0589 0.0087	<input type="checkbox"/> IMU time delay? 0.00 1-sigma (ms): 0 Error contribution (Hz/Vrt):	<input type="checkbox"/> Prism/Scanner roll? 0.00 1-sigma (deg): 0 Error contribution (Hz/Vrt):
<input checked="" type="checkbox"/> Vessel pitch? 1-sigma (deg): 0.008 Error contribution (Hz/Vrt): 0.0589 0.0217	<input type="checkbox"/> Laser range bias? 0.00 1-sigma (m): 0 Error contribution (Hz/Vrt):	<input type="checkbox"/> Prism/Scanner pitch? 0.00 1-sigma (deg): 0 Error contribution (Hz/Vrt):
<input checked="" type="checkbox"/> Vessel yaw? 1-sigma (deg): 0.025 Error contribution (Hz/Vrt): 0.0729 0.0000	<input type="checkbox"/> Range scale factor? 1.00 1-sigma: 0 Error contribution (Hz/Vrt):	<input type="checkbox"/> Prism/Scanner yaw? 0.00 1-sigma (deg): 0 Error contribution (Hz/Vrt):
<input checked="" type="checkbox"/> Select all observables?	<input type="checkbox"/> Select all cal. parameters?	

Figure 143. A closer view of the parameter select screen within the TPU module. Checkboxes determine whether a parameter is included in the uncertainty computation. White text boxes allow the user to set the standard deviations of the many parameters, and gray boxes display the contribution to the total uncertainty by each individual parameter. The value of the calibration parameters are displayed in the respective name fields (e.g., Fresnel prism slope = 39.18°).

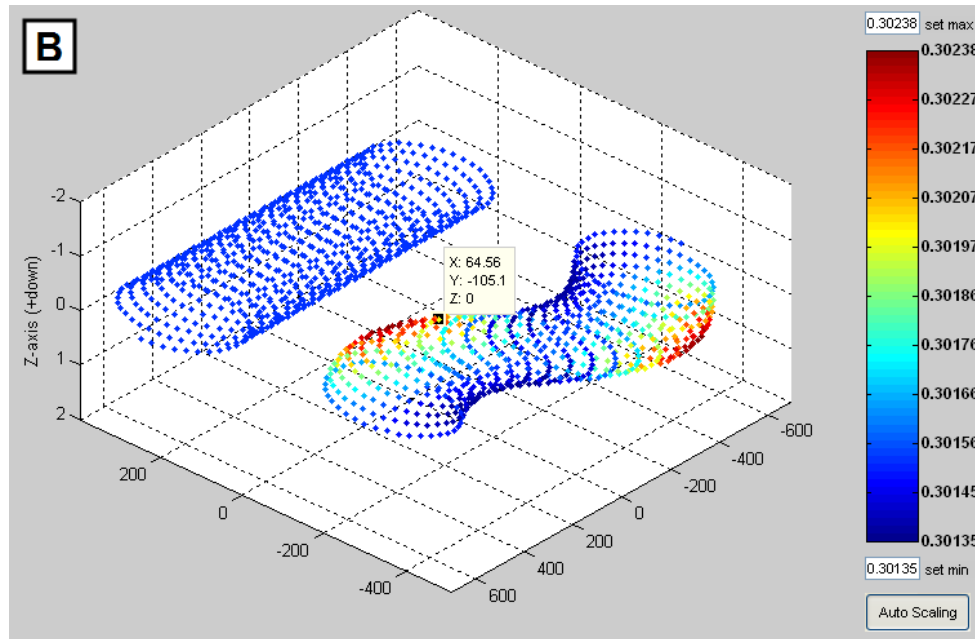


Figure 144. A closer view of the point cloud spatial view within the TPU module. Laser points are color coded by uncertainty.

C	Point of Interest	Display Options	Parameter Plot
	Select Point	Show how many sigma? 1-sigma (68.2% confidence)	Select a parameter to plot: Scanner azimuth (deg)
	X: 64.5601 +/- 0.123532	Plot error bars? <input type="checkbox"/> Vertical	Select range of parameter: 0 to 360
	Y: -105.106 +/- 0.142926	<input type="checkbox"/> Horizontal (scaling: 10 x)	Select uncertainties to include: <input checked="" type="checkbox"/> Vertical?
	Z: 0 +/- 0.301968	Color Points by Uncertainty? Vertical Uncertainty	<input type="checkbox"/> Horizontal?
	Show error contribution as: Value		<input type="checkbox"/> Radial?
	Recompute Default		Export Plot

Figure 145. A closer view of the TPU module's control panel. The first column determines the uncertainty of any selected laser point, the second column controls the display features of the point cloud shown in Figure 144, and the third column generates plots of uncertainty versus various acquisition parameters.

7.2.1.1 – Examining the effects of various IMUs. When the TPU module is called from the simulator, the only uncertainty information immediately available is that associated with the system's observables (laser range, scanner azimuth, GPS position,

and vehicle orientation), the first column of Figure 142. From the simulator, the default covariance matrix of all the input parameters, \mathbb{C}_x in (7.34) will have the form:

$$\mathbb{C}_x = \begin{bmatrix} \sigma_\rho^2 & 0 & 0 & 0 & 0 & 0 & 0 & 0 \\ 0 & \sigma_{\theta_{zs}}^2 & 0 & 0 & 0 & 0 & 0 & 0 \\ 0 & 0 & \sigma_{x_I}^2 & 0 & 0 & 0 & 0 & 0 \\ 0 & 0 & 0 & \sigma_{y_I}^2 & 0 & 0 & 0 & 0 \\ 0 & 0 & 0 & 0 & \sigma_{z_I}^2 & 0 & 0 & 0 \\ 0 & 0 & 0 & 0 & 0 & \sigma_\omega^2 & 0 & 0 \\ 0 & 0 & 0 & 0 & 0 & 0 & \sigma_\psi^2 & 0 \\ 0 & 0 & 0 & 0 & 0 & 0 & 0 & \sigma_\kappa^2 \end{bmatrix}. \quad (7.61)$$

The user is provided the ability to input any standard deviation for these observables (the white fields in Figure 142) and then recompute the propagated uncertainty. As an example of this functionality, a flight line was simulated with no installation offsets (no boresight misalignments, perfect laser-prism-scanner alignment, etc.), nor any vehicle attitude (no pitch, roll or yaw). Assuming a typical acquisition height of 400 meters, the published uncertainties of various Applanix POS AVs were applied to assess the effects on the final point cloud. Standard deviations for the laser range of 0.01m and scanner azimuth of 0.002° , based on estimates from Optech International, were also applied, producing the results shown in Figure 146.

POS Type	POS 410	POS 510	POS 610
Horizontal Pos (m)	0.1	0.1	0.1
Vertical Pos (m)	0.3	0.3	0.3
Roll and Pitch (deg)	0.008	0.005	0.0025
Heading (deg)	0.025	0.008	0.0050
Horizontal TPU 1σ (m)	0.1741	0.1513	0.1442
Vertical TPU 1σ (m)	0.3008	0.3004	0.3002

Figure 146. Table of predicted horizontal (2D) and vertical uncertainties of the CZMIL point cloud (1σ) with different models of Applanix POS AV. Specifications provided by Applanix (2009). Note: the horizontal position uncertainty of 0.1 meters for the POS was interpreted to be a one-dimensional (i.e. north-south and east-west) uncertainty.

Figure 146 reveals several interesting pieces of information. First, when equipped with a POS 410, post processed with POSpac MMS (the present configuration presently employed in USACE's CHARTS system), there is a baseline confidence of 0.174m in the horizontal direction and 0.301m in the vertical. Next, we see upgrading the POS from a model 410 to model 610 has minimal impact on the point cloud TPU, particularly the vertical uncertainty. The total horizontal uncertainty (THU) of the lidar points will improve from 0.174cm to 0.144m; whereas, the vertical estimated confidence only improves from 0.3008m to 0.3002m. The reason for this nominal reduction in uncertainty is best understood when the contribution to the error by each parameter is expressed as a percentage of the whole (much as was done in (7.48)). If independence among the measured parameters (i.e. no covariance) is assumed, then the percent contribution of an arbitrary parameter P is given by:

$$\begin{aligned} & \left(\frac{\partial x}{\partial P} \sigma_P \right)^2 / \sigma_{x_g}^2 * 100\% \\ & \left(\frac{\partial y}{\partial P} \sigma_P \right)^2 / \sigma_{y_g}^2 * 100\% \\ & \left(\frac{\partial z}{\partial P} \sigma_P \right)^2 / \sigma_{z_g}^2 * 100\%. \end{aligned} \quad (7.62)$$

It is important to note that the percent contributions can be viewed in the TPU module by toggling the “Show error contribution as:” drop-down from “value” to “percentage” in the TPU module's control panel (first column, Figure 145). Both the uncertainty values and percent contributions are shown for the POS AV 410 in Figure 147. Upgrading the INS does improve the accuracy of the calculated orientation of the vehicle; however, it does not affect the accuracy of the vehicle's calculated position. Even with values from the “poorest” performing POS shown in Figure 146, the 0.30m vertical uncertainty

associated with a post-processed GPS position still accounts for ~99.5% of the vertical uncertainty. So, under this scenario, all efforts (and dollars) should be invested in improving the GPS solution, not the vehicle orientation. For the remainder of this chapter, unless otherwise stated, the uncertainties associated with the POS AV 410 will be used.

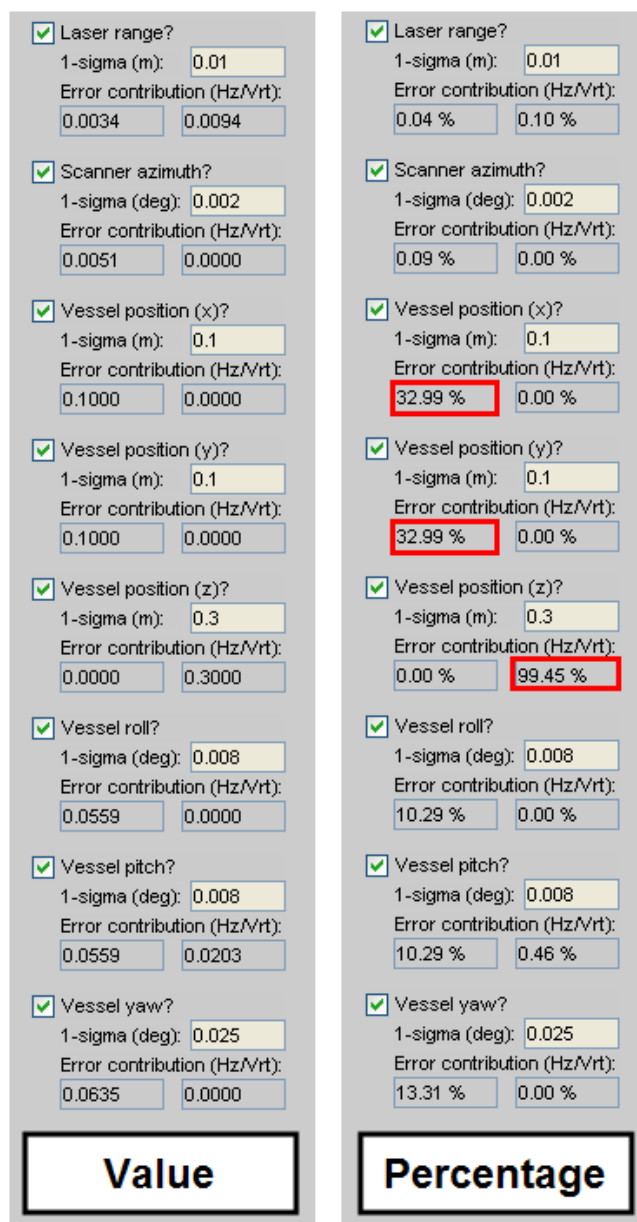


Figure 147. The net contribution to the horizontal and vertical TPU, sorted by parameter (left) and the percent contribution (right). The disproportionate contribution to uncertainty caused by GPS positioning emphasized in red.

Should the user desire, not all of the observation parameters need to be included in the uncertainty calculation. By deselecting any parameter the associated rows and columns are removed from both the covariance matrix and the Jacobian. While reducing the matrices is mathematically equivalent to setting the variance equal to zero, computationally, it is more efficient to delete the entries. Conversely the user may also include uncertainties associated with the calibration parameters. This can be done by checking the appropriate parameter and entering the standard deviation in the provided fields shown in Figure 142. All checked parameters will be incorporated into the Jacobian and covariance matrix. For example, in Figure 142, the GPS position is not adjusted; whereas, the vehicle boresight angles ($BS\theta_x, BS\theta_y$ and $BS\theta_z$) and Fresnel prism slope (θ_{FR}) are. The associated covariance matrix is thus:

$$\mathbb{C}_x = \begin{bmatrix} \sigma_\rho^2 & 0 & 0 & 0 & 0 & 0 & 0 & 0 & 0 \\ 0 & \sigma_{\theta_{zs}}^2 & 0 & 0 & 0 & 0 & 0 & 0 & 0 \\ 0 & 0 & \sigma_\omega^2 & 0 & 0 & 0 & 0 & 0 & 0 \\ 0 & 0 & 0 & \sigma_\psi^2 & 0 & 0 & 0 & 0 & 0 \\ 0 & 0 & 0 & 0 & \sigma_\kappa^2 & 0 & 0 & 0 & 0 \\ 0 & 0 & 0 & 0 & 0 & \sigma_{BS\theta_x}^2 & 0 & 0 & 0 \\ 0 & 0 & 0 & 0 & 0 & 0 & \sigma_{BS\theta_y}^2 & 0 & 0 \\ 0 & 0 & 0 & 0 & 0 & 0 & 0 & \sigma_{BS\theta_z}^2 & 0 \\ 0 & 0 & 0 & 0 & 0 & 0 & 0 & 0 & \sigma_{\theta_{FR}}^2 \end{bmatrix}. \quad (7.63)$$

7.2.1.2 – Further exploration of the plotting tools. Continuing the discussion of the TPU module, the visualization portion of the module is now explored. In this analysis, a perfectly-aligned lidar is considered (e.g., 0° boresight angles). In addition to the uncertainties of the observables, uncertainties (1σ) in the boresight values of 0.4° , 0.1° and 0.2° about the vehicle's roll, pitch and yaw axes respectively are assumed.

Figure 148 shows two simulated flight lines: one with a straight and level flight path, and a second where the vehicle rolls 10° to starboard, then 10° to port, and finally returns to level. In this case, the points are colored with respect to the horizontal uncertainty.

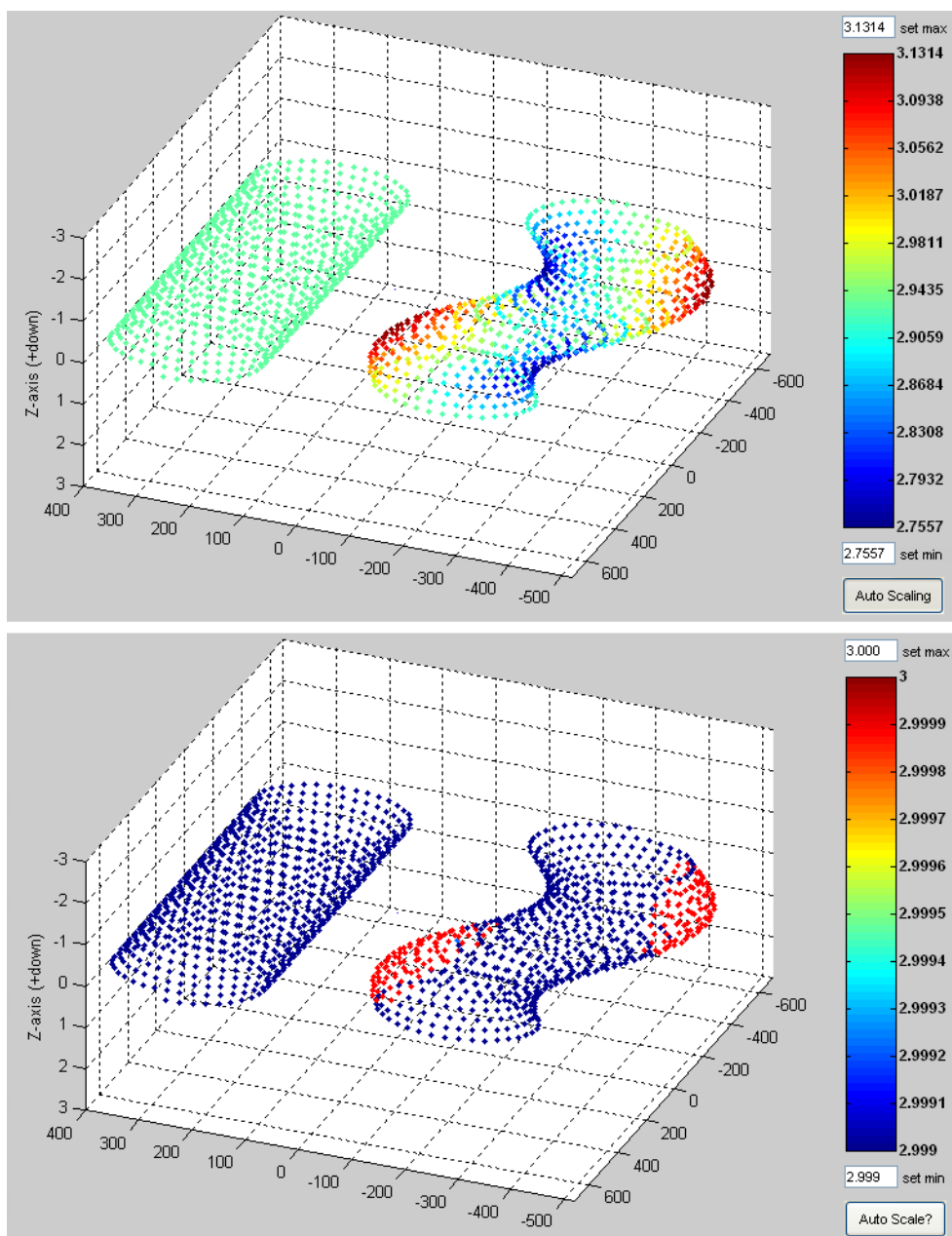


Figure 148. Point cloud colored by horizontal uncertainty (top). By adjusting the scale of the color bar the user can create a binary palette to show whether a point meets a given accuracy criteria (bottom).

Above and below the color bar to the right of the plot, fields are provided to rescale the image's color table. For example, a user only interested in whether the THU of the point cloud is greater or less than 3 meters could set the lower index to 2.999 meters and the upper index to 3.000 meters (Figure 148 – bottom). This creates a two-tone image that is exceedingly easy to interpret. With respect to the horizontal uncertainty, it appears the outer beams coinciding with the maximum roll have the maximum uncertainty.

Toggling the coloring from horizontal to vertical uncertainty (found under the “Display Options”), a different pattern is revealed (Figure 149). This time, rather than just the outer beams coinciding with the maximum vehicle roll having the maximum uncertainty, the maximum uncertainty is exhibited from all beams when the vehicle is at maximum roll. Coloring the points by radial uncertainty is also an option (not shown).

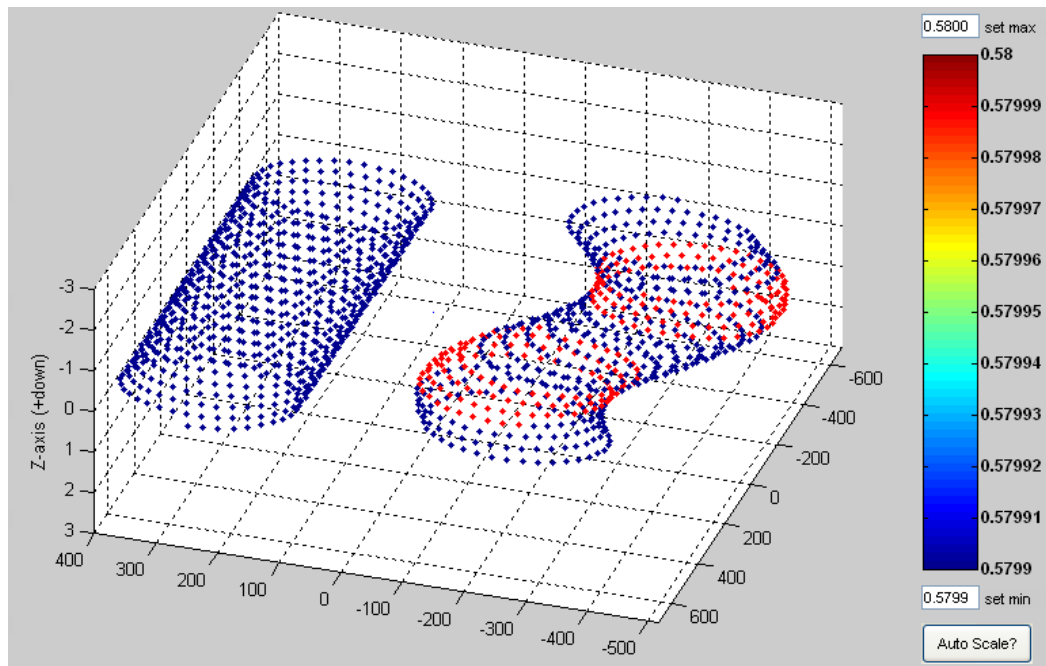


Figure 149. The same point cloud in Figure 148, this time colored by TVU. The maximum vertical uncertainty is displayed at all angles (rather than just the outer beams) when the vehicle experiences its greatest roll.

In addition to coloring the data points by uncertainty, error bars are an alternative method of visualizing the uncertainty. As shown in Figure 150, interpreting point-by-point uncertainty through the use of error bars is not as intuitive as the previous color coding, but general trends can still be determined. First, the vertical uncertainty is greater on the rolling vehicle than on the level one. Second, within the higher variability of TVU of the rolling flight line, an increase in uncertainty among the outer-most beams is seen. The error bars do not show, however, that the full swath has a larger uncertainty when the vehicle rolls, as seen in Figure 148.

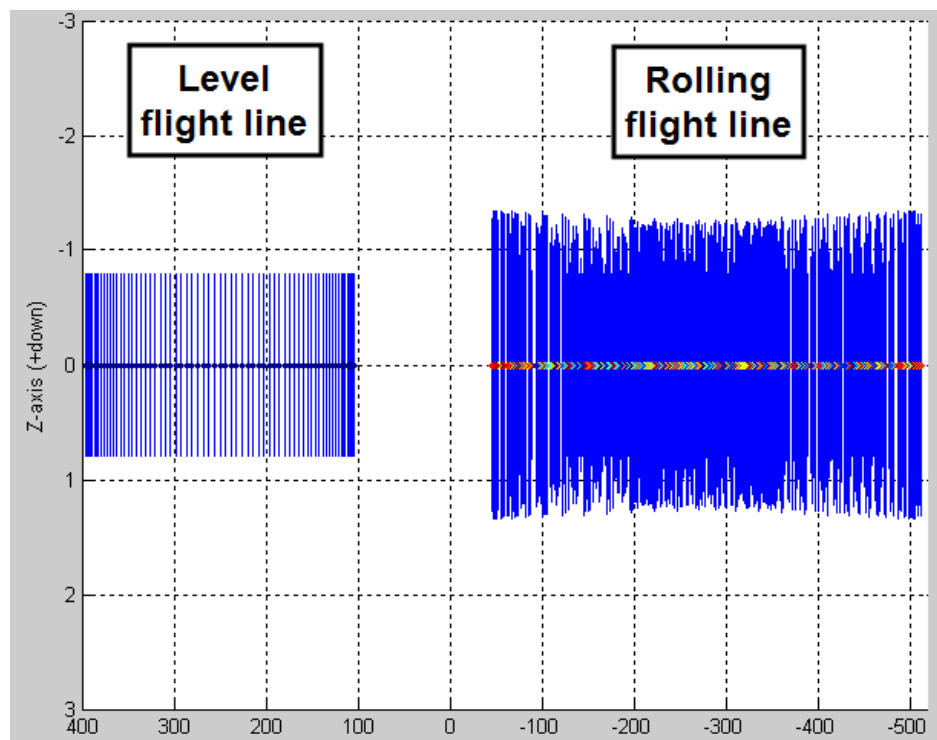


Figure 150. Dataset viewed from the front (vehicle traveling towards viewer) with vertical error bars shown with two standard deviations.

Horizontal error bars are shown in Figure 151. Because of the large disparity in scale between the lidar points themselves (spanning hundreds of meters across the swath) and the THU (on the order of centimeters), the horizontal error bars cannot typically be

seen without some amount of exaggeration. With that in mind, a horizontal error bar scaling feature has been implemented. In the figure below, the horizontal error bars are scaled by a factor of 10. Thus, while y-axis ticks indicate a 100 meter spacing for the lidar points, each tick is only 10 meters for the error bars. Recalling the uncertainty of the boresight angle in the roll axis was 0.4° , while the uncertainty in the pitch axis was only 0.1° . We can see the effects of this disparity in confidence depicted in Figure 151. The uncertainty in the across-track direction is shown to be larger than that of the along-track direction; which stands to reason with a larger uncertainty in the roll axis.

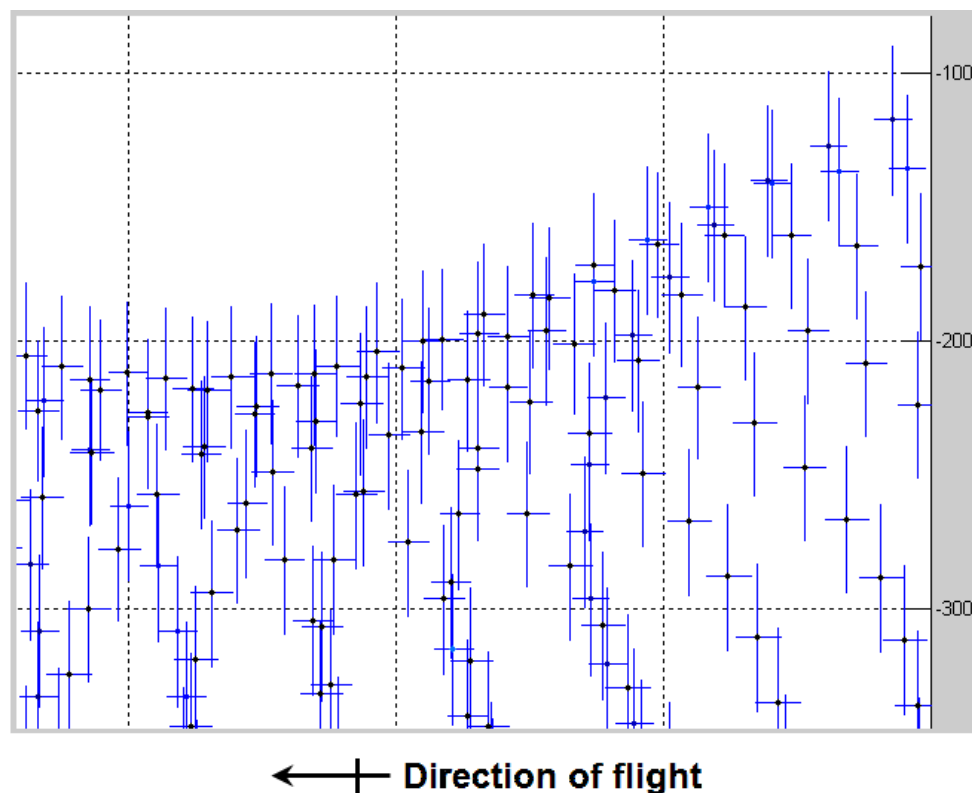


Figure 151. Horizontal TPU where horizontal error bars are exaggerated at 10 times the scale used for the data points. Fore/aft and port/starboard axes have same scale – notice larger uncertainty in direction of roll.

A last investigative tool provided by the TPU module is the ability to plot the horizontal or vertical TPU versus any of the eight observation parameters. The options for configuring this feature are located under the heading “Parameter Plot” in Figure 145. To demonstrate the application of this tool in an investigative capacity, plots of several parameters are presented below. Given the vehicle was rolling back and forth during one of the two flight lines, there may be an interesting correlation between the vehicle roll and the propagated uncertainty; see Figure 152. With respect to the horizontal, there does not appear to be a positive or negative correlation between the roll angle and the THU. While the vehicle is level there appears to be a more consistent predicted uncertainty; whereas, as the vehicle’s roll increases, there is a greater variability in the uncertainty. On the other hand, there is a distinct relationship between the vertical uncertainty and the vehicle roll. A close up of just the vertical uncertainty is shown in Figure 153.

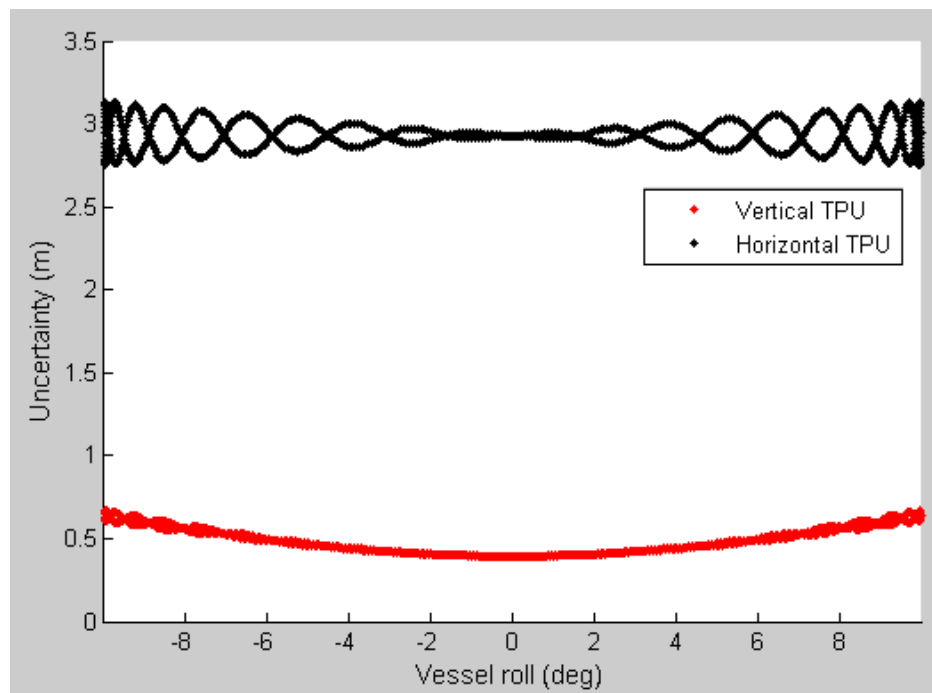


Figure 152. Horizontal (black) and vertical (red) propagated uncertainty (1σ) plotted versus the vehicle roll.

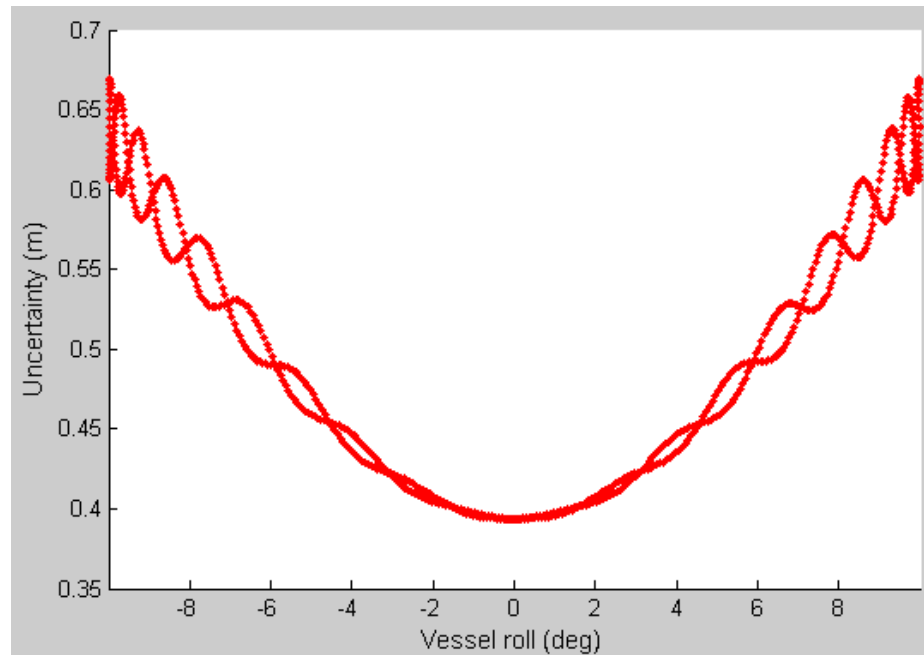


Figure 153. Vertical propagated uncertainty (1σ) plotted versus vehicle roll.

As seen above, as the vehicle roll increases, so too does the vertical uncertainty of the laser points. There does appear to be an additional signal in the above curve, which suggests there are factors beyond the vehicle roll that are contributing to the TVU. Increased TVU with increased roll agrees with the colored point cloud shown in Figure 149.

Next, a comparison of the laser range to both the vertical (Figure 154) and horizontal (Figure 155) TPU is made. Unlike the vehicle roll, it is difficult to see a correlation with respect to the TVU and laser range. A minimum uncertainty is detected when the range is 425 meters. Most likely this minimum value is associated with the fact that the range is 425 meters when the vehicle has a 0° roll. As discussed above, the minimum TVU is exhibited when the vehicle has a 0° roll. So the low point seen in Figure 154 is more likely ascribed to vehicle roll, not the range – this confounding of inputs is what makes determining the cause of the point cloud uncertainty so difficult.

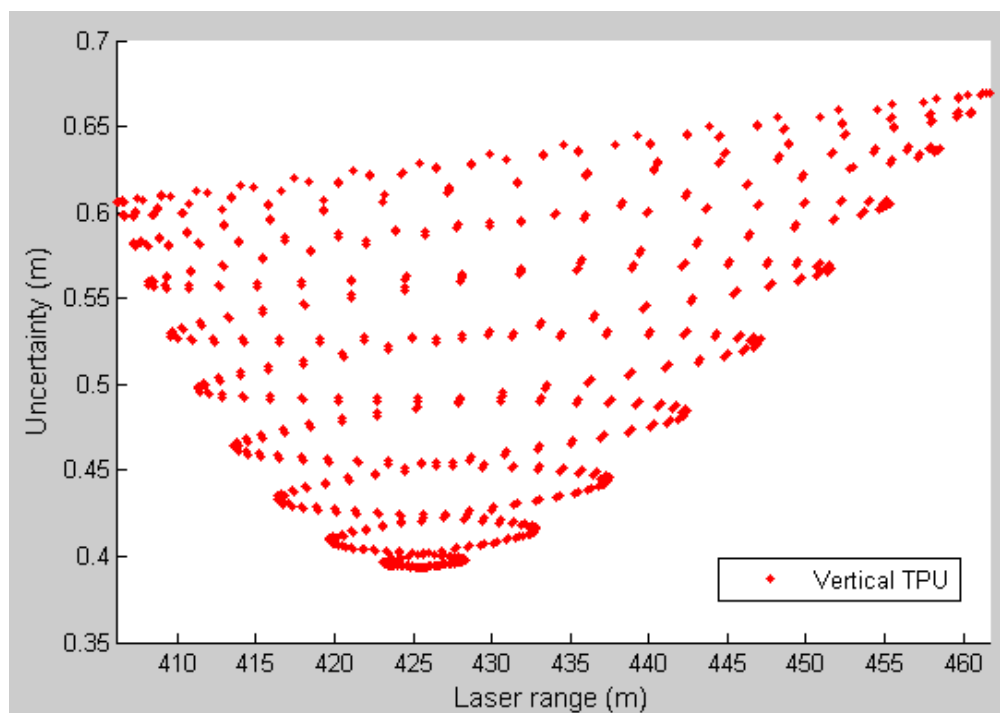


Figure 154. Vertical propagated uncertainty (1σ) plotted versus the laser range.

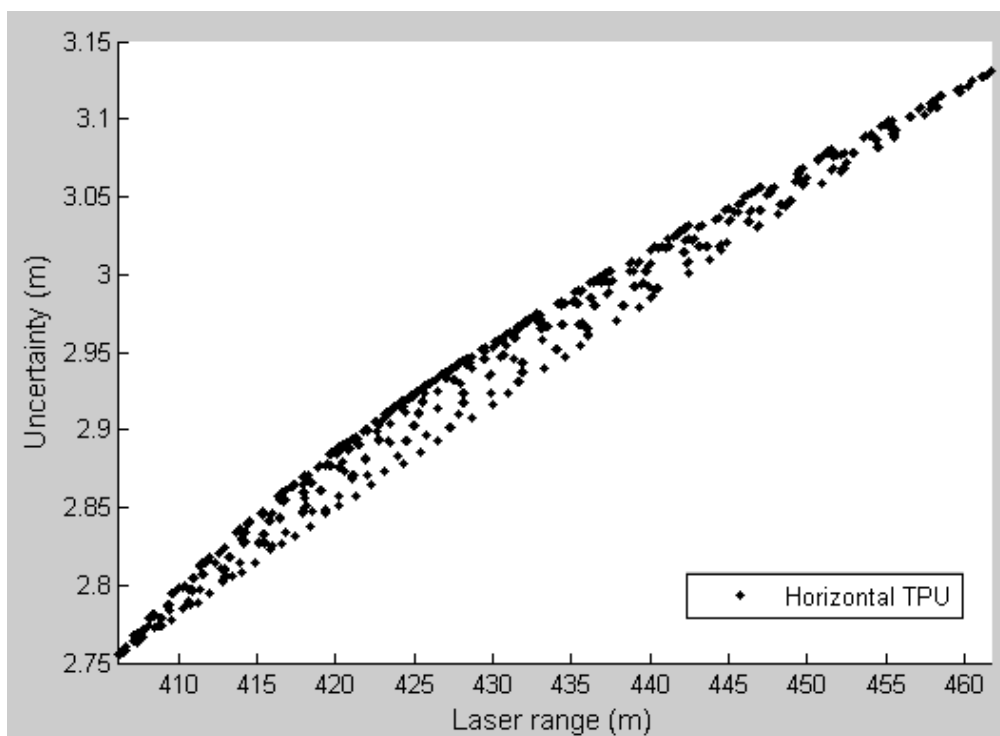


Figure 155. Horizontal propagated uncertainty (1σ) plotted versus the laser range.

The horizontal uncertainty, on the other hand, exhibits a strong correlation with the laser range (Figure 155). As the range increases, so too does the THU of the point cloud. Because the plot is not strictly linear, this suggests that other factors are contributing to the uncertainty to some extent as well. This observation of increased horizontal uncertainty with range is consistent with the color plot shown in Figure 148.

One final parameter/TPU based plot is shown in Figure 156 – this time investigating the relationship of the TPU with the scanner azimuth. Unlike the laser range and vehicle roll there does not appear to be a positive or negative correlation between the laser azimuth and TPU. The mean uncertainty at the forward, port, starboard and aft scanner angles are all the same (there appears to be a correlation in the *variability* of the uncertainty, but not the uncertainty itself).

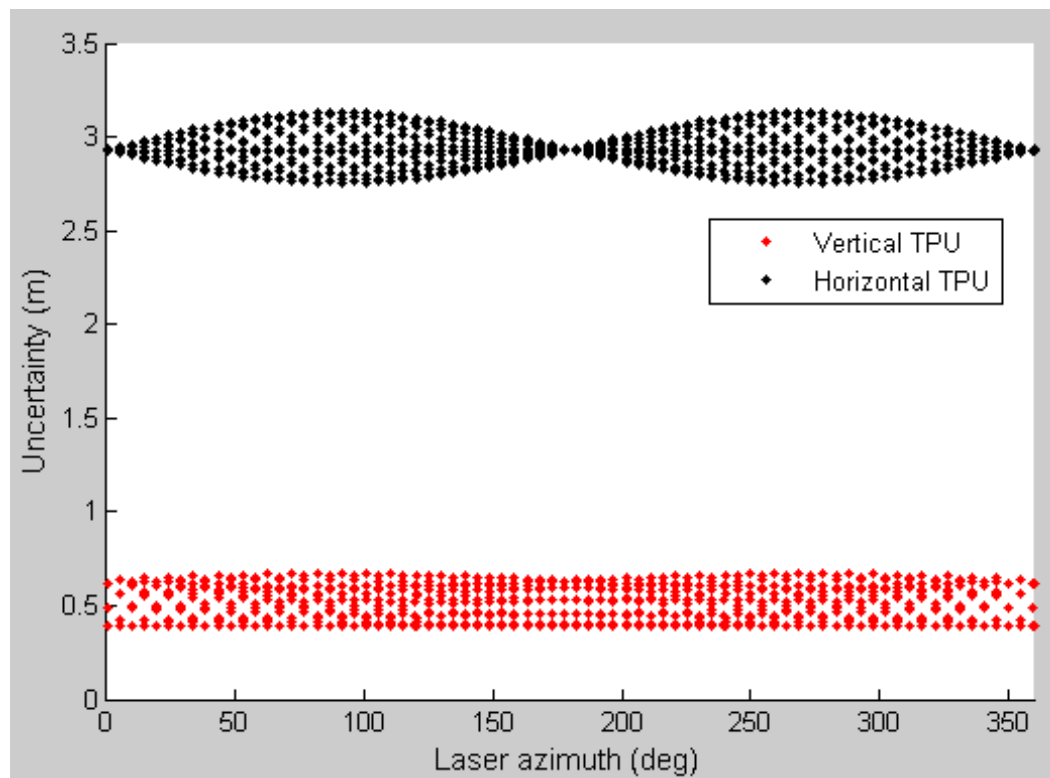


Figure 156. Vertical (red) and horizontal (black) point cloud TPU (1σ) plotted versus the laser scanner's azimuth. (0° = forward, 90° = starboard, etc.)

To generalize the previous three observations for this particular flight plan:

- The TVU is most affected by the vehicle attitude.
- The THU is most affected by the lidar range measurement.
- There was no apparent correlation with the scanner azimuth in the previous

simulation. This may have been due to the fact that there were no system misalignments (boresight, laser-to-scanner, etc.).

It is equally important to understand both the root causes and the symptoms of large uncertainties. For example, the laser may have an inordinately large ranging error, but it only manifests itself in the point cloud should the vehicle roll over 30° – in which case the laser ranging error could be considered within tolerance. As such, all three of the previous bullet points will be further investigated in the following sections.

7.2.1.3 – Vehicle altitude versus point cloud uncertainty. To further demonstrate the investigative flexibility afforded by the TPU module's controls, we will explore two open-ended questions: how does the acquisition altitude affect the point cloud uncertainty, and how does the vehicle's attitude affect the uncertainty. The former question will be discussed in this section, while the latter will be presented in the following section.

Exploring the behavior of uncertainty for different flight altitudes is an important endeavor. Should the surveyors wish to relax their spot spacing and fly at a higher altitude, they must first know whether they will exceed their uncertainty budget before they begin surveying.

To make the simulation less trivial, a few of the calibration parameters were shifted from their previous zero values. For the boresight misalignments, the laser-prism-

scanner assembly is tilted forward 5° and rolled to port by 5° . There is also a 10° yaw misalignment. Thus the longest beam will be directed forward and to port (relative azimuth of 305°) and the shortest beam will be directed starboard and aft (relative azimuth of 125°). An IMU-to-laser offset vector, in meters, of $[0.5, 0.5, 0.5]$ is also included. When these calibration values were included within the simulation, they were considered to be well-determined and error-free. Six flight lines were then simulated at altitudes of 200, 400, 600, 800, 1000, and 1200 meters (note: 400 meters is a typical operational altitude); results are shown in Figure 157.

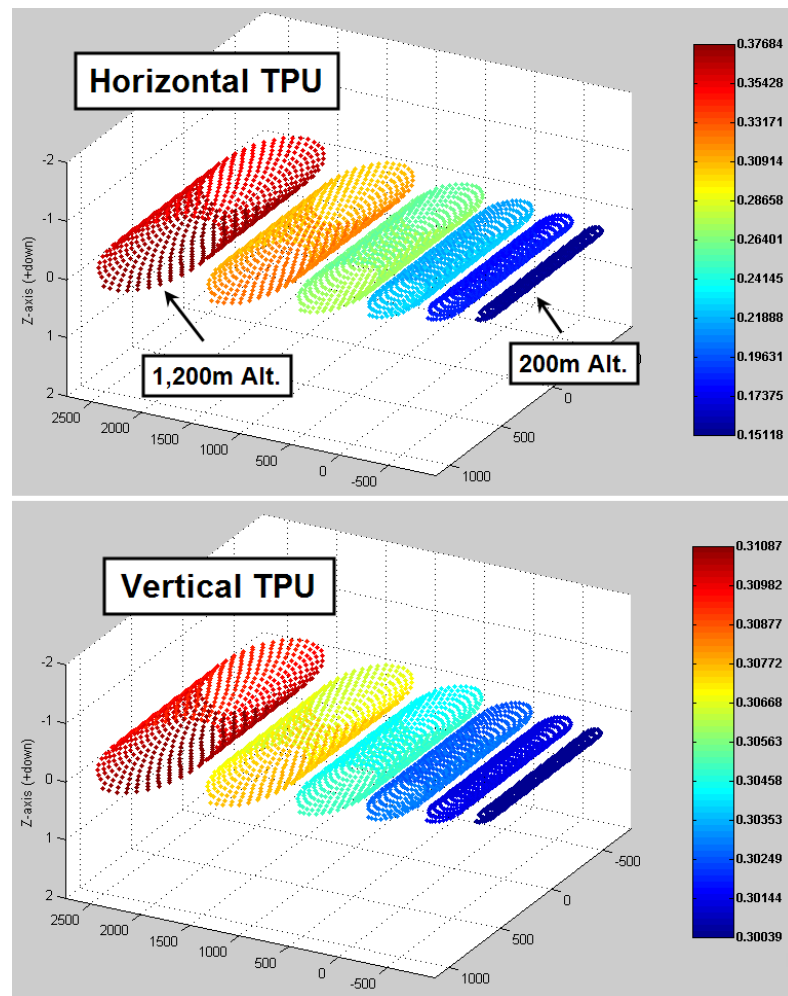


Figure 157. Horizontal (top) and vertical (bottom) point cloud TPU (1σ) plotted for various vehicle altitudes (from left-to-right: 1200, 1000, 800, 600, 400 and 200 meters).

By changing altitude, the principle parameter affected in the laser equation is an increased laser range. As discussed in the previous section, increasing the laser range has a marked effect on the point cloud's THU but inconclusive effects on the TVU.

Examining Figure 157 (top), we see that the trend of an increased laser range leading to an increased point cloud THU is repeated. As the altitude increased from 200 meters to 1,200 meters, the THU increased from 0.15m to 0.37m. Given even a Special Order hydrographic survey has a horizontal uncertainty allowance of 2 meters (IHO 2008), the aforementioned horizontal uncertainties are well within tolerance.

Examining the TVU (Figure 157 – bottom), changing the altitude has had a nearly negligible impact (increasing the uncertainty by only 1 centimeter with an increase in altitude of 1000 meters). The color banding for the TVU plot matches that of the horizontal, which suggests that (though diminished) there is also an increase in TVU with increased laser range. As far as survey specifications are concerned, the vehicle altitude has an almost negligible contribution to the total vertical uncertainty of the final point cloud.

To further examine the impact of the laser range on the point cloud uncertainty, the ranges for all six flight lines are plotted with respect to both horizontal and vertical TPU. Again, both the THU and TVU increase with an increased laser range (the TVU to a lesser extent).

Because the boresight angles are no longer zero (as in previous sections), it is reasonable to expect some shot-to-shot variation in the point cloud TPU as the scanner rotates around (Figure 158). Both the THU and TVU exhibited similar behaviors (though only the THU is plotted). The uncertainty curves were sinusoidal with minimums near a

scanner azimuth of 130° and maximums near 310° . Given the boresight misalignments, these angles are consistent with the direction of the shortest and longest laser ranges respectively. So, there is a weaker correlation between point cloud uncertainty and scanner azimuth than between scanner azimuth and laser range.

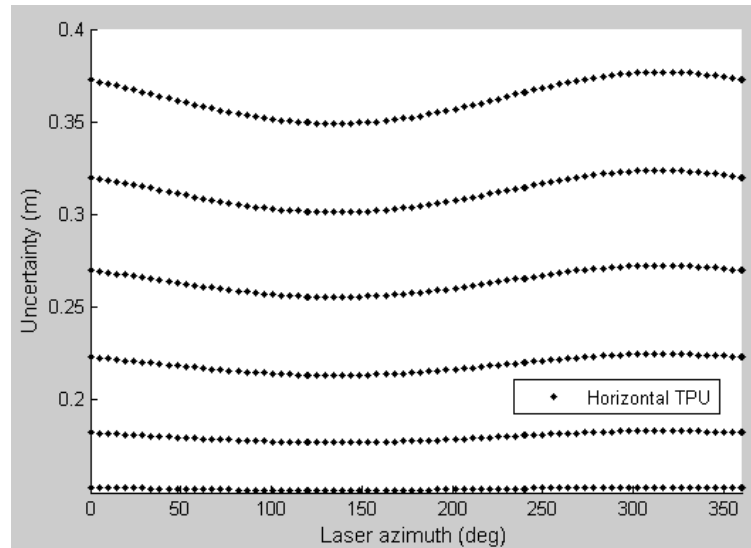


Figure 158. Horizontal point cloud TPU (1σ) plotted against scanner azimuth for flight lines of various altitudes (0° = forward, 90° = starboard, etc.). Higher altitudes are represented by curves with larger uncertainty.

Another way of visualizing the effects of a changing altitude is to simulate a single flight line with a starting altitude of 200 meters that exhibits a steady climb in altitude to 600 meters (Figure 159). As anticipated, uncertainty again increases with altitude. However, we can see that the steady increase in laser range does not form a linear relationship with the THU, but instead has a slight curve.

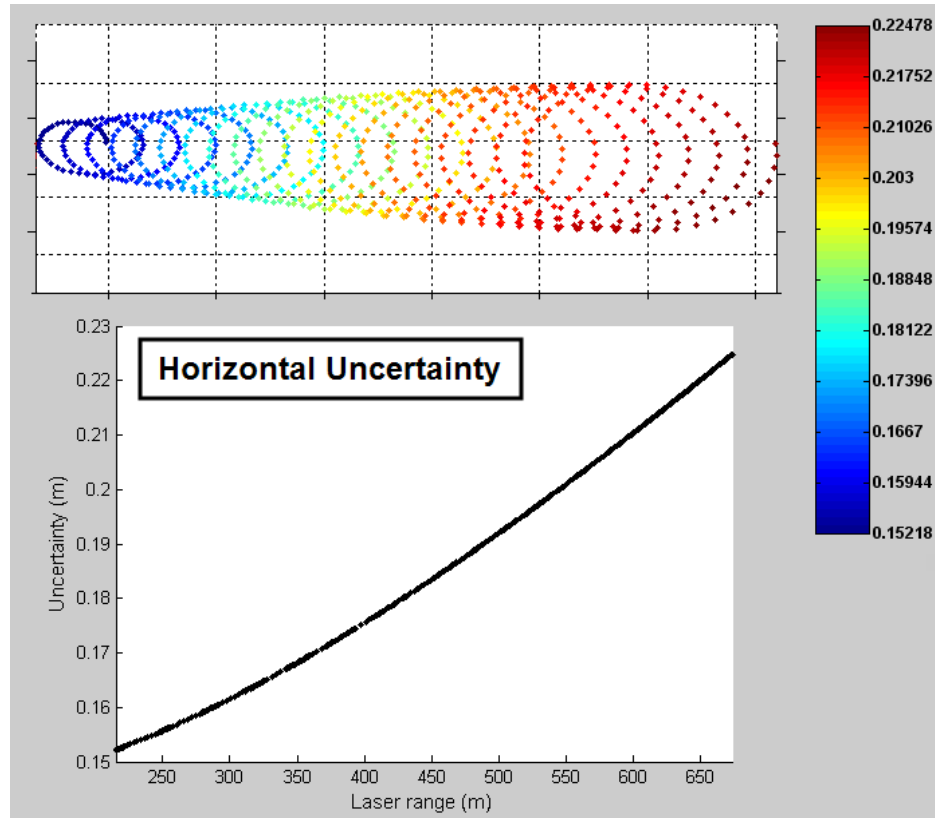


Figure 159. Horizontal point cloud TPU (1σ) for a vehicle steadily gaining altitude (200m left side to 600m right side).

7.2.1.4 – Vehicle attitude versus point cloud uncertainty. While changing the vehicle's altitude has little effect on the point cloud's propagated uncertainty (particularly from a “does it still meet survey specifications?” point-of-view), dynamic changes in the vehicle's attitude are much more likely to be encountered during daily operations. Particularly when the suggested calibration strategy is to fly as dynamic a flight line as the system, flight crew and vehicle will support. System parameters will be equivalent to those presented in the previous section: roll/pitch/yaw boresight misalignments of 5° , 5° and 10° respectively; and an INS-to-laser offset vector, in meters, of [0.5, 0.5, 0.5]. For this example, the acquisition altitude will be limited to the anticipated system acquisition altitude of 400 meters.

As a baseline comparison, the simulated vehicle will experience no dynamic motion (no roll, pitch, yaw or heave). Both the horizontal and vertical TPU exhibit a similar spatial behavior, though the THU has the larger range of values (THU ranging between 0.177m and 0.183m, compared to TVU ranging between 0.3011m and 0.3013m), Figure 160.

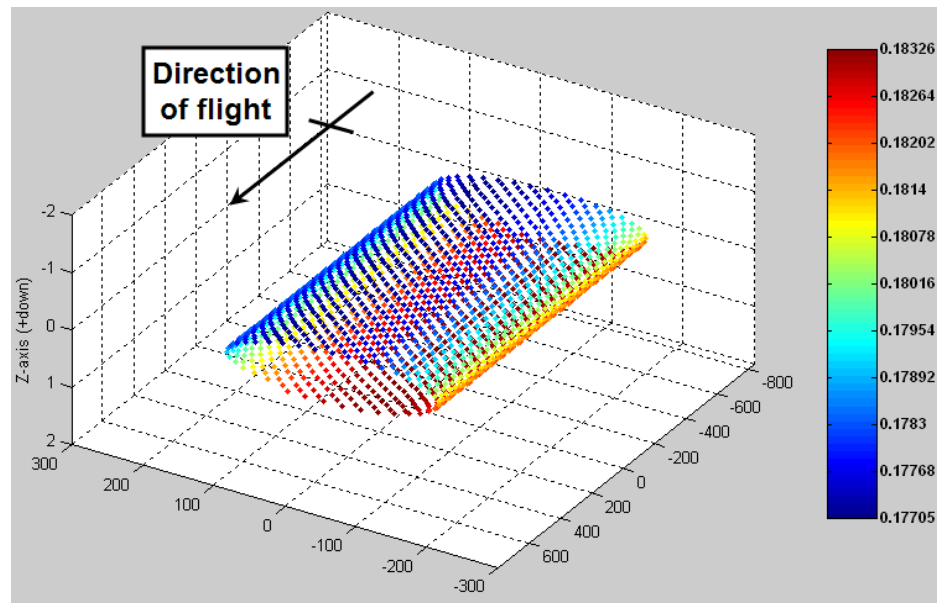


Figure 160. Horizontal point cloud TPU (1σ) for a vehicle with boresight angles tilting the laser scanner forward and to port.

One revolution to the next, the largest uncertainties are associated with the beams oriented forward and to port (Figure 161). The reason for this distribution of uncertainties is easily understood when the uncertainty is compared against the laser range (Figure 162). Both the TVU and THU display a linear correlation with the laser range, the farther the laser travels, the greater the uncertainty. Therefore, the peak and valley displayed in the laser azimuth versus uncertainty plot of Figure 161 can simply be

attributed to the differing laser range resulting from the boresight angles tilting the laser forward and to port.

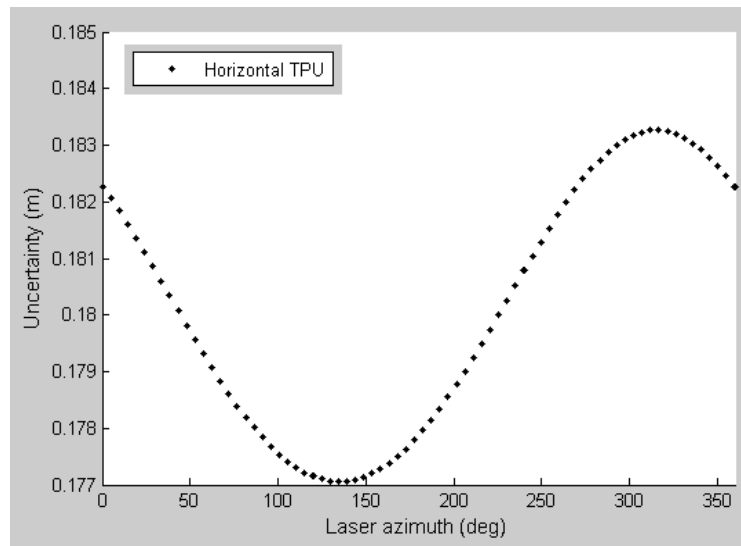


Figure 161. Horizontal point cloud TPU (1σ) compared to laser azimuth (0° = forward, 90° = starboard, etc.). Vehicle boresight angles result in tilting the laser forward and to port (towards 310°).

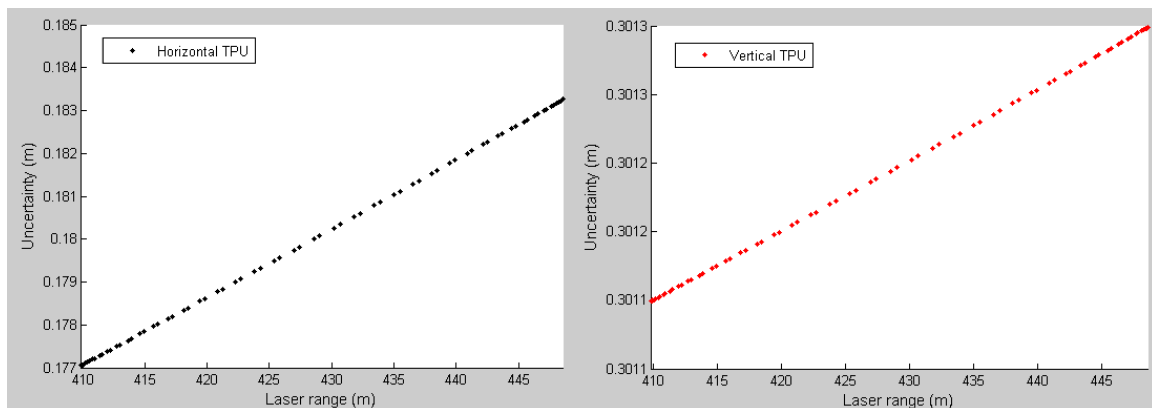


Figure 162. Horizontal (left) and vertical (right) TPU (1σ) compared to laser range for a vehicle experiencing no dynamic roll, pitch or yaw.

With a baseline established, the effects of changing the vehicle attitude is investigated. The flight line is again flown from an altitude of 400 meters, but this time the vehicle starts with a roll of 30° to port (directing the laser to starboard) and incrementally rolls to an orientation of 30° to starboard (directing the laser to port). The

THU of this flight line (along with a smaller non-rolling flight line – included for reference) is shown in Figure 163. By adding this rolling aspect to the vehicle's trajectory, the maximum THU increases from 0.183m to 0.262m and the TVU increases from 0.301m to 0.306m. As expected, the maximum horizontal and vertical TPU are calculated at the vehicle's maximum roll angles. In comparison to the previous section, a 30° roll induced a THU similar to a flight at 800 meters and a TVU similar to a flight at 1,000 meters.

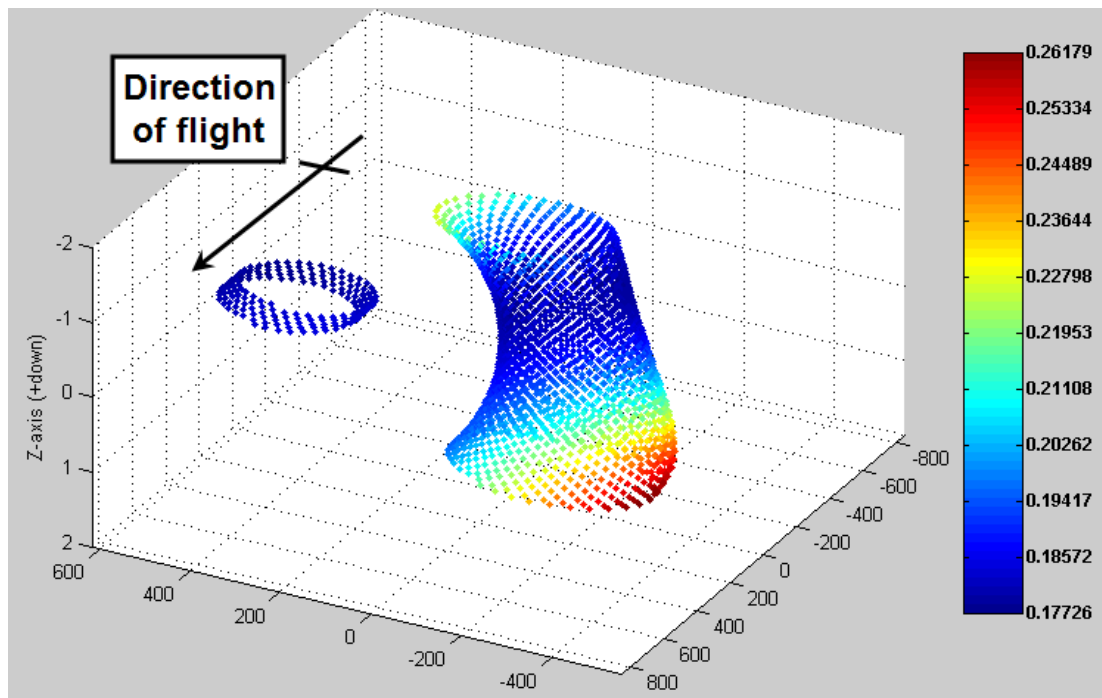


Figure 163. Horizontal point cloud TPU (1σ) for a vehicle with boresight angles tilting the laser scanner forward and to port. As vehicle proceeds forward, it rolls from 30° to port to 30° to starboard. A non-rolling flight line is shown on the left for reference.

To examine whether the point cloud uncertainty is again a linear function of laser range (as in Figure 162), the THU is again plotted versus the range (Figure 164). As before, increasing the laser range has an associated increase in point cloud uncertainty; however, unlike before, for any given laser range, there is some variability. For

reference, the THU from the baseline flight has been added to Figure 164 in red.

Through comparison to the non-rolling flight, any change in the vehicle attitude is revealed to also have an associated increase in point cloud uncertainty beyond that which would be strictly attributed to the increased laser range.

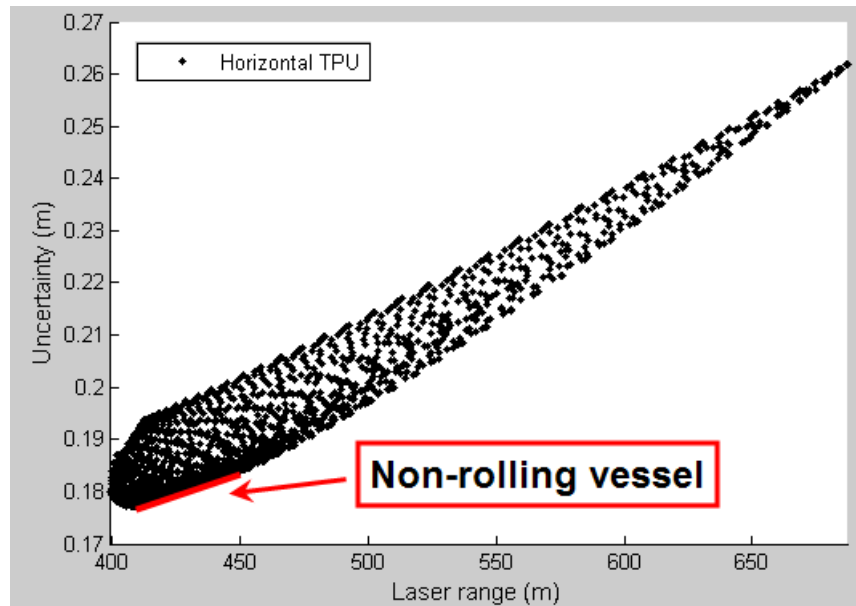


Figure 164. Total horizontal uncertainty (1σ) for a rolling vehicle (black) plotted versus laser range. Data from the non-rolling vehicle displayed in Figure 162 also shown (red).

Investigating the uncertainty signature beyond the laser range, the point cloud's horizontal uncertainty versus the vehicle orientation is shown in Figure 165. For every revolution of the laser (the “wiggles” in Figure 165), there is considerable variation in the uncertainty. Recalling that the laser is tilted via the boresight misalignments to aim an extra 5° to the port side, one observes that the port side of each revolution has the larger uncertainty (likely associated with the slightly longer laser range). Likewise a roll of X° to starboard (thus directing the laser to port) has a greater uncertainty than an equivalent

roll of X° to port. Also, as the magnitude of the vehicle's roll increases in either direction, so too does the uncertainty in the point cloud's position.

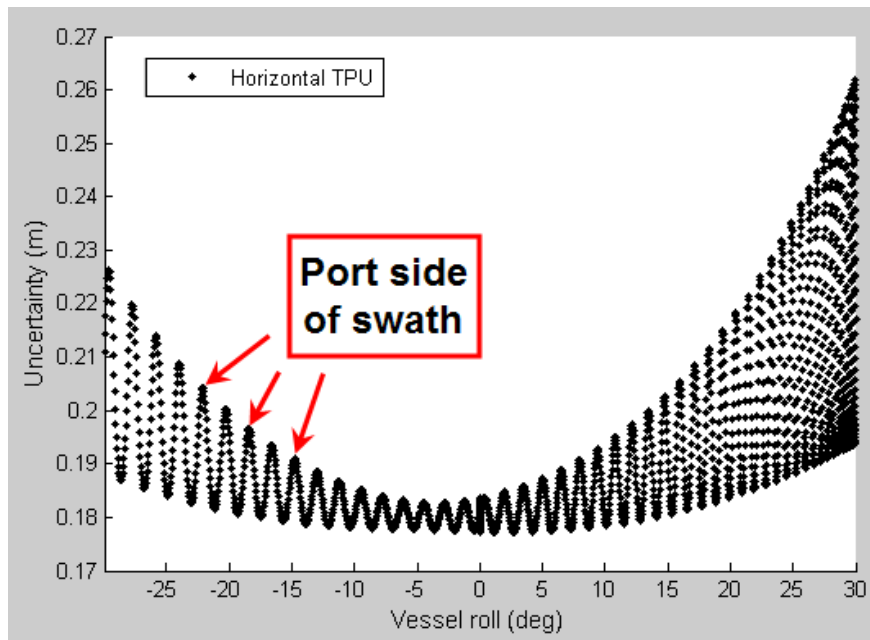


Figure 165. Total horizontal uncertainty (1σ) for a rolling vehicle plotted versus vehicle's attitude. Vehicle is rolling from 30° port (left) to 30° starboard (right) with a roll boresight angle directing the laser towards the port side.

Given that the laser scanner's central axis is tilted 5° to port, one might expect the minimum point cloud uncertainty to be observed when the vehicle is also oriented with a 5° roll to port (when the scanner's central axis is oriented towards nadir), since this will yield the shortest of the observed laser ranges. Examining Figure 165, the minimum THU is actually distributed among the vehicle's orientation between 0 and -5° roll, with the lowest observed uncertainties of all between 0 and $+5^\circ$ roll. This suggests that not only does an increased laser range lead to an increased uncertainty (minimized at a vehicle roll of -5°), but any vehicle attitude other than perfectly level also contributes to an increase of the overall uncertainty of the point cloud's reported position.

One final parameter of interest is the laser scanner's azimuth. Because of the boresight misalignments, the non-rolling vehicle displayed a larger relative uncertainty to the port side of the vehicle's nose ($\sim 310^\circ$ relative azimuth) and a smaller uncertainty off the vehicle's starboard quarter ($\sim 140^\circ$), see Figure 161. To follow up for a rolling vehicle, the horizontal TPU versus the scanner azimuth is shown in Figure 166. For the rolling vehicle, the average maximum uncertainty has shifted from 310° closer to 270° (i.e., oriented towards port). Most likely, this shift in maximum uncertainty is associated with the laser range. As the vehicle experiences a greater roll, the maximum laser range will be increasingly associated with the "outer-most" beams (e.g., regardless of the vehicle's boresight misalignments as the vehicle rolls more and more to starboard, the port-most beams will have the longest laser ranges). Conversely, the same argument can be made to describe why the laser azimuth with the smallest uncertainty is directed towards starboard (90°).

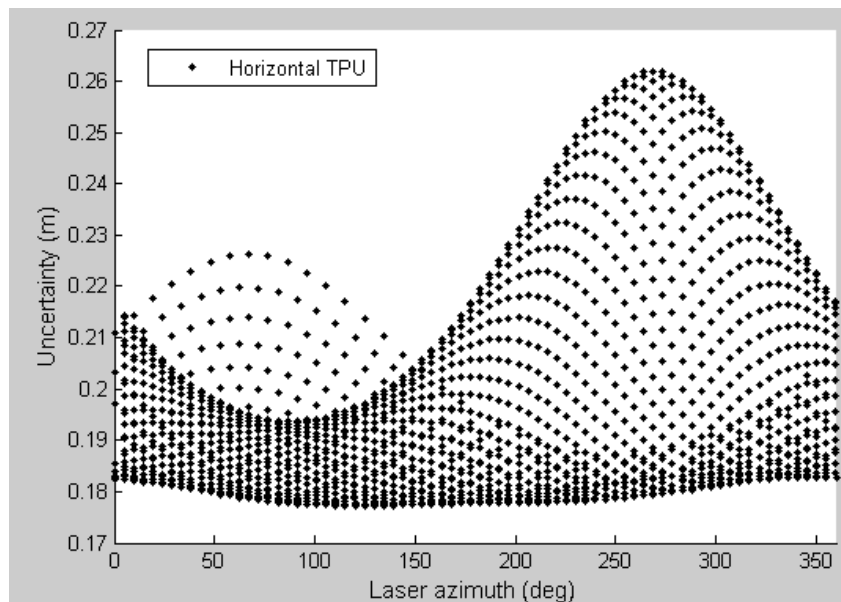


Figure 166. Total horizontal uncertainty (1σ) for a rolling vehicle plotted versus scanner azimuth (0° = forward, 90° = starboard, etc.). Recalling in a non-rolling vehicle the minimum THU was observed near 140° and maximum near 310° .

Though only the horizontal uncertainty was displayed in the previous four figures, the vertical TPU exhibited very similar trends. Earlier in this chapter, after the first simulation (Figure 149), it was postulated the THU is more closely associated with laser range, the TVU is more closely associated with vehicle attitude, and there is no discernible pattern with regard to the scanner azimuth. With the additional simulations of the varying altitudes and attitudes, refinements to these initial observations can be made:

- Both the horizontal and vertical uncertainty are closely related to the laser range: the greater the range, the greater the uncertainty. The horizontal uncertainty is more affected by the laser range than the vertical uncertainty.
- Changing the vehicle's attitude will also lead to an increase in point cloud uncertainty. Part of this increase is due to the non-level nature of the vehicle, but mostly a change in vehicle attitude will have an associated change in the laser range (which, from the previous bullet, leads to a change in uncertainty).
- The scanner azimuth is related to uncertainty, but only so far as the boresight angles steer the scanner's rotational axis away from nadir. The larger uncertainty will then be in the direction the scanner is oriented (e.g., if the scanner is tilted forward, the forward beams will have a longer range and thus a higher uncertainty).
- Even with 30° of roll, the estimated vertical uncertainty of the point cloud increased by less than one centimeter. Thus, from a geometric point-of-view, no amount of dynamic motion likely to be encountered during acquisition will render the point cloud unusable from an uncertainty perspective. There may be radiometric issues associated with beam stretching when the laser forms a low incidence angle with the water's surface, but such issues are beyond the scope of this work.

7.2.2 – Propagated Uncertainty Called from Calibrator

As stated previously, an advantage to using a least squares adjustment in the execution of the calibration routine is the output of a fully populated variance-covariance matrix. Unlike the simulator which only uses a priori assumptions about the uncertainties of the inputs to the laser equation (e.g. the manufacturer's specifications for the laser, INS, etc.), the calibrator has access to the covariance which describes the interaction among the parameters. The TPU module will have one additional section devoted to covariance if called from the calibrator (see Figure 167 and Figure 168).

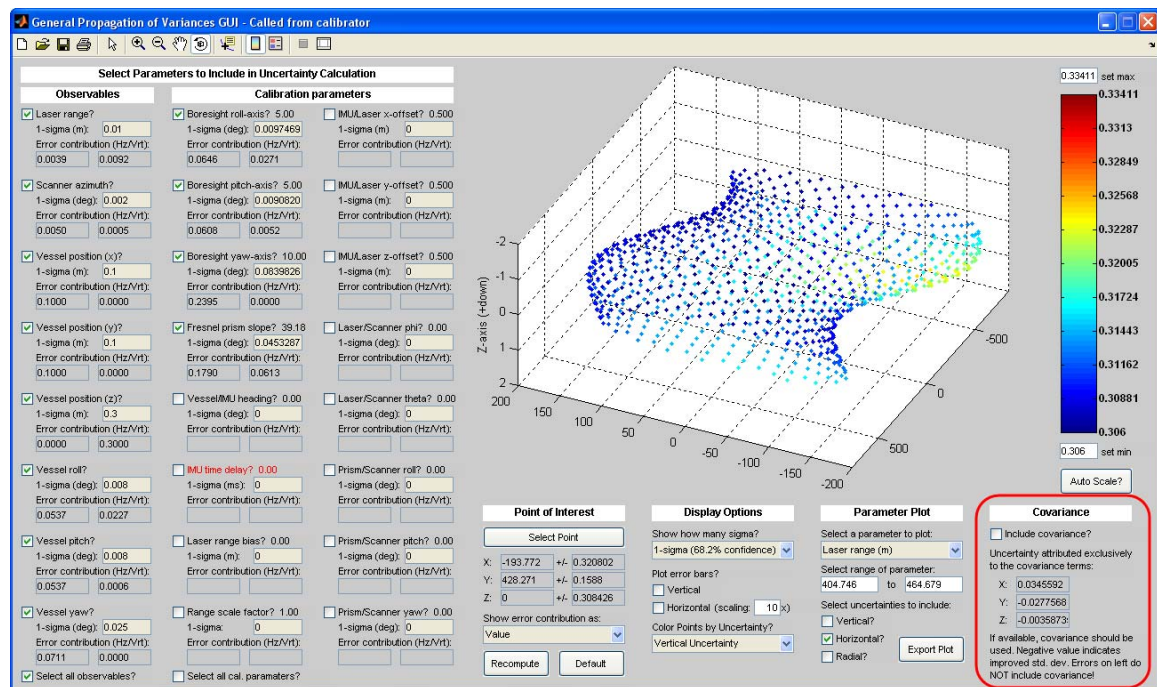


Figure 167. The TPU module's interface as called from the calibration module. An additional panel devoted to covariance is highlighted in the lower right (with a close-up view shown in Figure 168).

Covariance

☒ Include covariance?

Uncertainty attributed exclusively to the covariance terms:

X:

Y:

Z:

If available, covariance should be used. Negative value indicates improved std. dev.

Figure 168. Covariance panel within the propagated uncertainty interface, allowing the user the option of including covariance in uncertainty calculations.

Recall from (7.33) and (7.34) that the generic formula for computing the variance-covariance matrix of the point cloud, $\mathbb{C}_{x,y,z}$, is given by:

$$\mathbb{C}_{x,y,z} = \begin{bmatrix} \frac{\partial f_1}{\partial x_1} & \frac{\partial f_1}{\partial x_2} & \dots & \frac{\partial f_1}{\partial x_n} \\ \frac{\partial f_2}{\partial x_1} & \frac{\partial f_2}{\partial x_2} & \dots & \frac{\partial f_2}{\partial x_n} \\ \vdots & \vdots & \ddots & \vdots \\ \frac{\partial f_m}{\partial x_1} & \frac{\partial f_m}{\partial x_2} & \dots & \frac{\partial f_m}{\partial x_n} \end{bmatrix} \underbrace{\begin{bmatrix} \sigma_{x_1}^2 & \sigma_{x_1,x_2} & \dots & \sigma_{x_1,x_n} \\ \sigma_{x_2,x_1} & \sigma_{x_2}^2 & \dots & \sigma_{x_2,x_n} \\ \vdots & \vdots & \ddots & \vdots \\ \sigma_{x_n,x_1} & \sigma_{x_n,x_2} & \dots & \sigma_{x_n}^2 \end{bmatrix}}_{\mathbb{C}_x} \begin{bmatrix} \frac{\partial f_1}{\partial x_1} & \frac{\partial f_1}{\partial x_2} & \dots & \frac{\partial f_1}{\partial x_n} \\ \frac{\partial f_2}{\partial x_1} & \frac{\partial f_2}{\partial x_2} & \dots & \frac{\partial f_2}{\partial x_n} \\ \vdots & \vdots & \ddots & \vdots \\ \frac{\partial f_m}{\partial x_1} & \frac{\partial f_m}{\partial x_2} & \dots & \frac{\partial f_m}{\partial x_n} \end{bmatrix}^T \quad (7.64)$$

where \mathbb{C}_x is the variance-covariance matrix of the laser equation inputs (both observation and calibration parameters). The uncertainties in the observed quantities (laser range, laser azimuth, etc.) are still represented solely by their variances in the matrix \mathbb{C}_x . Since a user may only choose to adjust a few of the calibration parameters, only those parameters will have both variance and covariance entries in \mathbb{C}_x . As is the case with the simulator version of the TPU module, the user still has the opportunity to add uncertainties for the calibration parameters – such an edit will only be performed for the parameter's variance (the user may not edit the covariances).

As an example, suppose 5 of the observables ($\rho, \theta_{zs}, \omega, \psi, \kappa$) are included in a TPU calculation. Additionally, suppose the three boresight angles ($BS\theta_x, BS\theta_y, BS\theta_z$) along with the laser-to-scanner phi-angle (ϕ_{LS}) angle are adjusted by the calibrator, while the user wishes to manually enter an uncertainty for the prism slope (θ_{FR}), which is not included in the calibration routine. Under such a scenario, the variance-covariance matrix will have the form:

$$\mathbb{C}_x = \begin{bmatrix} \sigma_\rho^2 & 0 & 0 & 0 & 0 & 0 & 0 & 0 & 0 & 0 \\ 0 & \sigma_{\theta_{zs}}^2 & 0 & 0 & 0 & 0 & 0 & 0 & 0 & 0 \\ 0 & 0 & \sigma_\omega^2 & 0 & 0 & 0 & 0 & 0 & 0 & 0 \\ 0 & 0 & 0 & \sigma_\psi^2 & 0 & 0 & 0 & 0 & 0 & 0 \\ 0 & 0 & 0 & 0 & \sigma_\kappa^2 & 0 & 0 & 0 & 0 & 0 \\ 0 & 0 & 0 & 0 & 0 & \sigma_{BS\theta_x}^2 & \sigma_{BS\theta_x, BS\theta_y} & \sigma_{BS\theta_x, BS\theta_z} & 0 & \sigma_{BS\theta_x, \phi_{LS}} \\ 0 & 0 & 0 & 0 & 0 & \sigma_{BS\theta_x, BS\theta_y} & \sigma_{BS\theta_y}^2 & \sigma_{BS\theta_y, BS\theta_z} & 0 & \sigma_{BS\theta_y, \phi_{LS}} \\ 0 & 0 & 0 & 0 & 0 & \sigma_{BS\theta_x, BS\theta_z} & \sigma_{BS\theta_y, BS\theta_z} & \sigma_{BS\theta_z}^2 & 0 & \sigma_{BS\theta_z, \phi_{LS}} \\ 0 & 0 & 0 & 0 & 0 & 0 & 0 & 0 & \sigma_{\theta_{FR}}^2 & 0 \\ 0 & 0 & 0 & 0 & 0 & \sigma_{BS\theta_x, \phi_{LS}} & \sigma_{BS\theta_y, \phi_{LS}} & \sigma_{BS\theta_z, \phi_{LS}} & 0 & \sigma_{\phi_{LS}}^2 \end{bmatrix} \quad (7.65)$$

The capability of toggling the covariance terms on and off (see Figure 168) is provided. Neglecting covariance, (7.65) simplifies to the diagonal matrix:

$$\mathbb{C}_x^* = \begin{bmatrix} \sigma_\rho^2 & 0 & 0 & 0 & 0 & 0 & 0 & 0 & 0 & 0 \\ 0 & \sigma_{\theta_{zs}}^2 & 0 & 0 & 0 & 0 & 0 & 0 & 0 & 0 \\ 0 & 0 & \sigma_\omega^2 & 0 & 0 & 0 & 0 & 0 & 0 & 0 \\ 0 & 0 & 0 & \sigma_\psi^2 & 0 & 0 & 0 & 0 & 0 & 0 \\ 0 & 0 & 0 & 0 & \sigma_\kappa^2 & 0 & 0 & 0 & 0 & 0 \\ 0 & 0 & 0 & 0 & 0 & \sigma_{BS\theta_x}^2 & 0 & 0 & 0 & 0 \\ 0 & 0 & 0 & 0 & 0 & 0 & \sigma_{BS\theta_y}^2 & 0 & 0 & 0 \\ 0 & 0 & 0 & 0 & 0 & 0 & 0 & \sigma_{BS\theta_z}^2 & 0 & 0 \\ 0 & 0 & 0 & 0 & 0 & 0 & 0 & 0 & \sigma_{\theta_{FR}}^2 & 0 \\ 0 & 0 & 0 & 0 & 0 & 0 & 0 & 0 & 0 & \sigma_{\phi_{LS}}^2 \end{bmatrix}. \quad (7.66)$$

With the covariance de-selected, the modified diagonal matrix shown above is used in coloring the point cloud, rendering the error bars, and displaying the uncertainties in the parameter plots. Also, for any given point, the uncertainty attributed exclusively to the covariance of the inputs of the point cloud is displayed in the lower-right hand corner of the TPU module (Figure 168).

It should be emphasized that if the covariance terms are available, they must be included in the uncertainty propagation. To not include them is a statistically invalid approach. Given the difficult nature of quantifying the covariance among physical quantities, some may be in the habit of only thinking in terms of (the easily visualized) variance (and its related statistic the standard deviation). Even this author is guilty of more often reporting variances than covariances. The calibration module immediately reports the uncertainties in each parameter by displaying their respective standard deviations; the covariances are only shown through the separate covariance/correlation-coefficient module. The practice of discussing variance over covariance is also a matter finding a way to visually represent the data. If 10 parameters are adjusted, then the user

just wants to know the confidence in those 10 parameters; to further report the 45 ways in which these parameters interact via their covariances can be overwhelming.

Reading the preceding paragraph, one may wonder why the ability to remove the covariance terms from the uncertainty propagation is provided. This functionality is present to illustrate the impacts of covariance on the final point cloud uncertainty and, by extension, the dangers of interpreting the alleged point cloud TPU based only on the inputs' variances. Two examples are provided below to demonstrate how neglecting the covariance can lead to erroneous interpretations of the point cloud TPU.

7.2.2.1 – Covariance example #1: Redistributing the uncertainty. Consider a vehicle with boresight misalignments of 5° , 5° and 10° (roll, pitch and yaw respectively) with an IMU-to-laser offset vector (measured in meters) of $[0.5, 0.5, 0.5]$. Two flights are performed from an altitude of 400 meters at a speed of 140 knots. In one flight, the vehicle experiences both a roll oscillation of 5° (rolling to starboard, then to port, then back to level) and a similar oscillation in the heading of 5° ; the second is a reference flight in which the vehicle experiences no change in attitude (see Figure 169). Note: such a small dataset is not an ideal flight plan for determining calibration parameters; the data is just being used to demonstrate the effects of covariance.

Four parameters (the three boresight angles and the prism slope) were determined within the calibrator, at which point the TPU module was launched (Figure 170). Two quick observations: within the point cloud, there is a range in the THU from 0.32m to 0.39m. The largest uncertainty is associated with the aft pulses and the least uncertainty with the forward pulses.

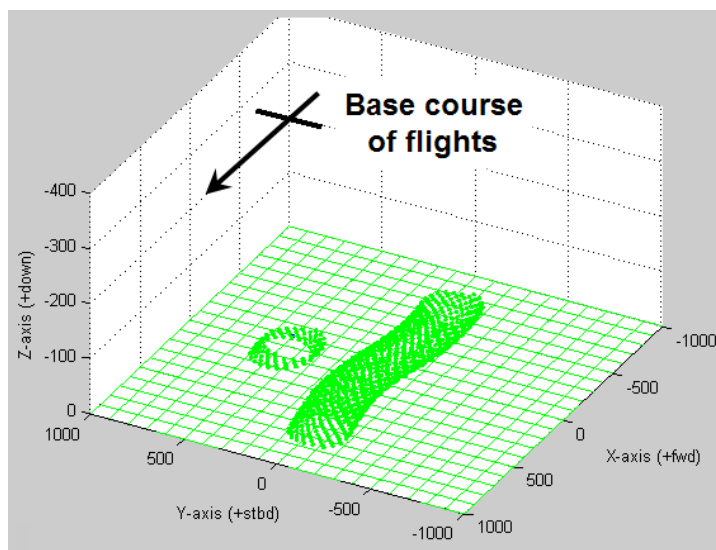


Figure 169. Flight plan used to illustrate covariance.

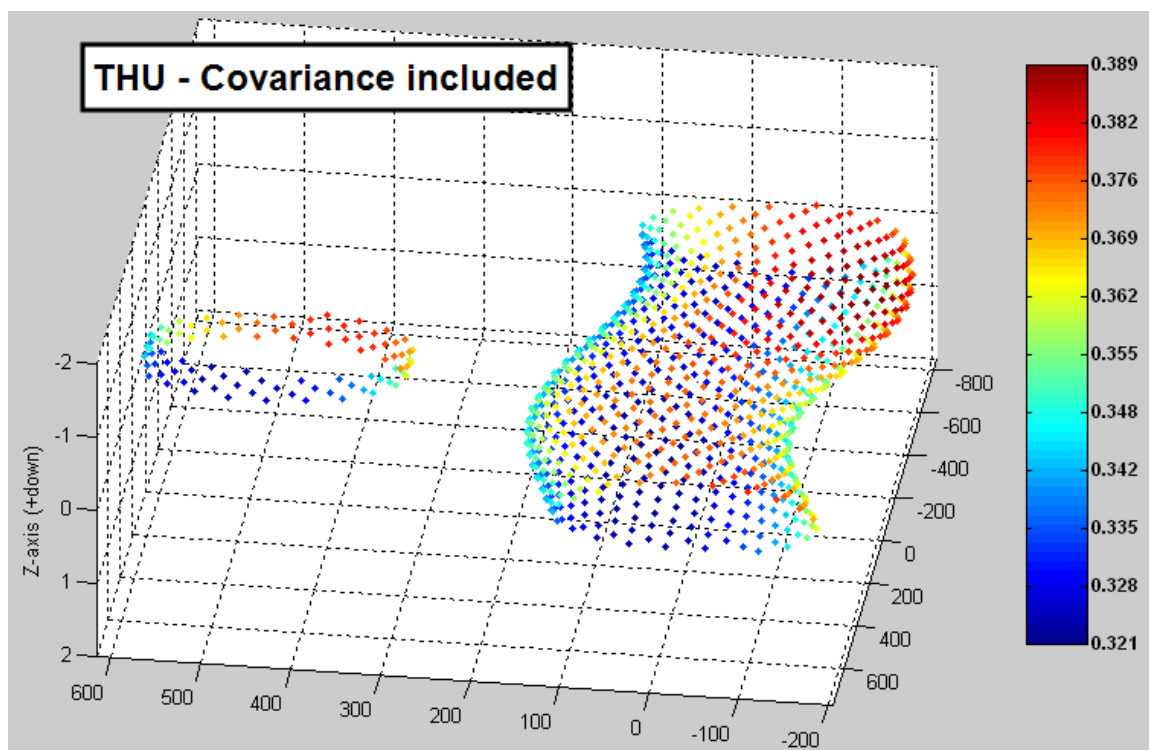


Figure 170. Horizontal propagated uncertainty (1σ) with covariance included error calculation (all units in meters).

For comparison, the point cloud is again plotted, but this time the points are colored with respect to their THU as computed without reference to the covariance terms (Figure 171). The range in magnitude of the THU has not changed, still extending between 0.32m and 0.39m. What has changed is the distribution of the uncertainties. Neglecting covariance, the points with the largest uncertainty are now located exclusively on the port side of the laser swath (a laser azimuth of 270° in Figure 172). If the covariance terms are (mistakenly) not included in the TPU calculation, the surveyor may try to design an acquisition scheme that favors the starboard side of the aircraft (thinking those to be the laser pulses with the highest confidence). This would in fact be unnecessarily complicating a flight plan for a false gain in point cloud confidence.

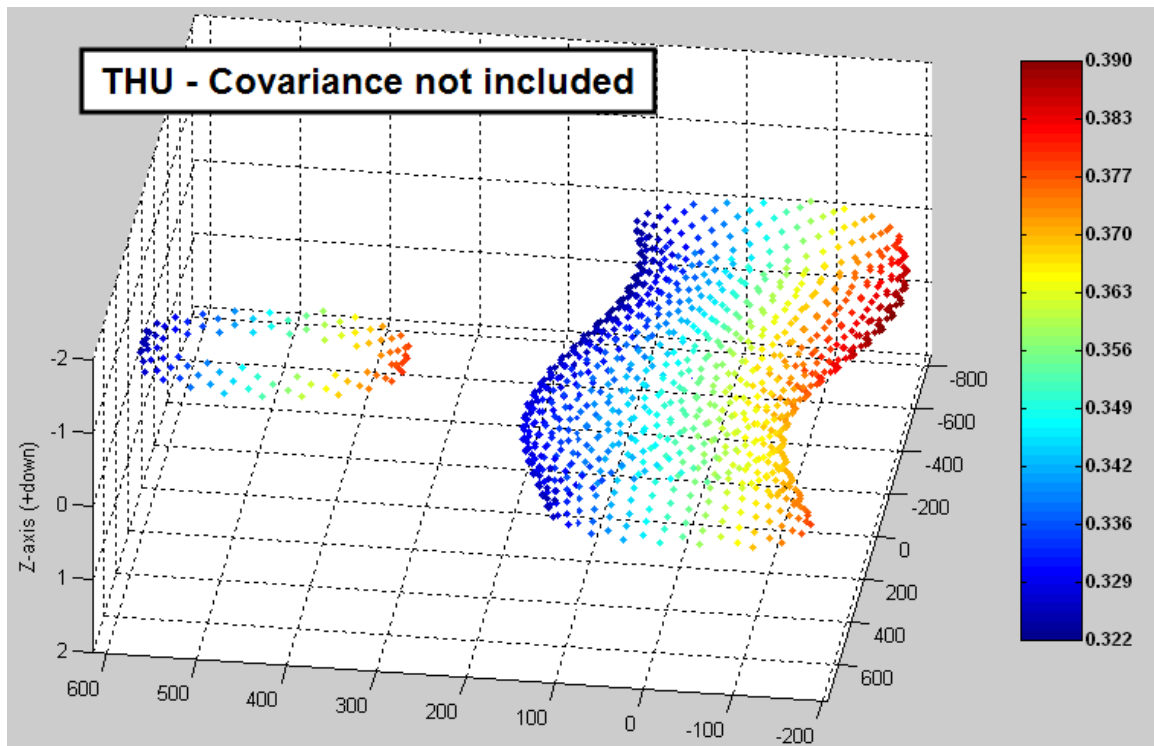


Figure 171. Horizontal propagated uncertainty (1σ) with covariance not included in error calculations (all units in meters).

Further emphasizing the complexity of covariance, notice in Figure 172 that including covariance reduces the THU for the forward beams (red arrow), whereas it increases the THU for the port beams (blue arrow). Thus a blanket statement like “including the covariances will lead to larger/smaller TPU values” is not possible. Instead the statement: “including the covariances will lead to a more accurate TPU model,” better captures the truth of the matter.

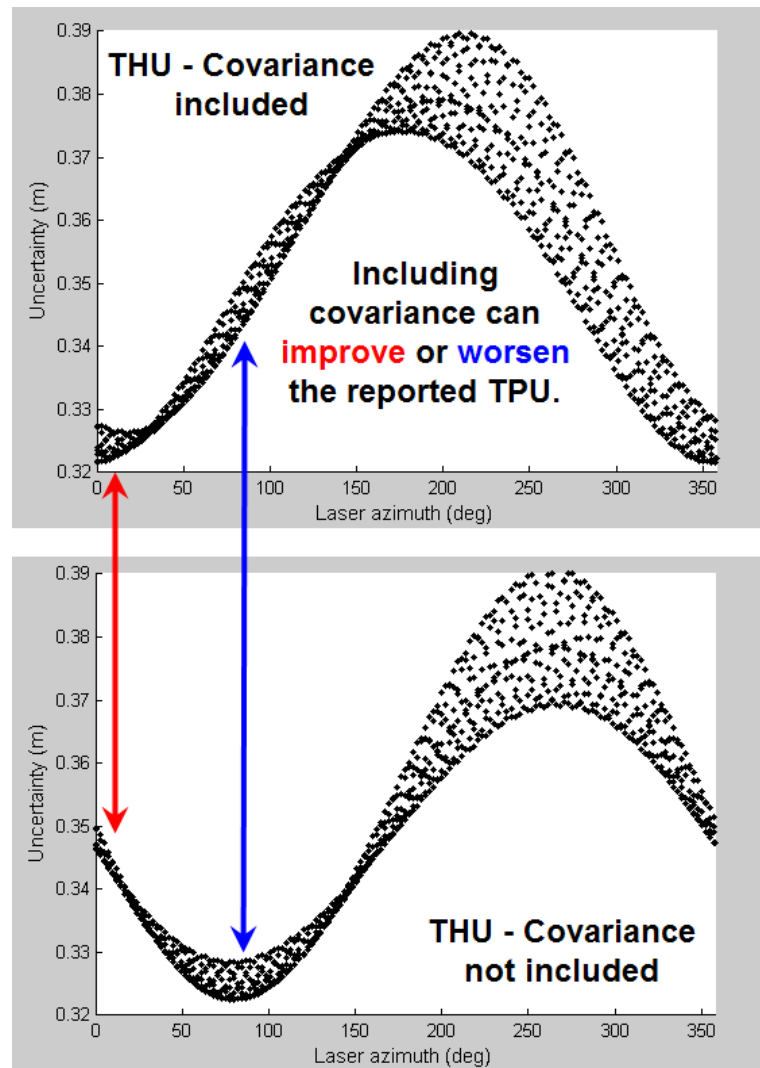


Figure 172. Horizontal TPU (1σ) versus scanner azimuth (0° = forward, 90° = starboard, etc.) for a point cloud both including (top) and not including (bottom) covariance in the computation. Depending on a points location in the scanner’s swath, including covariance can either decrease (red arrow) or increase (blue arrow) the reported TPU.

7.2.2.2 – Covariance example #2: Overestimating the uncertainty. In this example, the same vehicle and flight plan as described in Figure 169 is used. This time however, a fifth parameter (the laser-to-scanner phi-angle) is included in the calibration. The reported standard deviations of both this and the previous calibration routine are shown in Figure 173. As expected, the attempt to determine more calibration parameters with an equivalent amount of input data results in a less confident solution. The reported confidence in the roll and yaw boresight angles, as well as the prism slope remain unchanged. The pitch boresight angle's ($BS\theta_y$) standard deviation gets 15 times worse, and the laser-to-scanner phi angle (ϕ_{LS}) has an uncertainty of similar magnitude to the pitch boresight. Whether increasing the uncertainty in a parameter by 15 times means the reported calibration value is now “bad” still remains to be seen.

	Calibration #1	Calibration #2
(1-sigma calibration uncertainties)		
Boresight - roll	0.010°	0.010°
Boresight - pitch	0.009°	0.139°
Boresight - yaw	0.084°	0.084°
Prism slope	0.045°	0.045°
Laser-to-Scanner phi angle	N/A	0.156°
Point cloud THU including covariance		
Maximum value	0.39m	0.42m
Minimum value	0.32m	0.36m
Point cloud THU excluding covariance		
Maximum value	0.39m	1.66m
Minimum value	0.32m	1.44m

Figure 173. Table of reported confidences (1σ) from two calibration routines attempting to determine 4 (calibration #1) and 5 (calibration #2) parameters. In addition, the THU for each resulting point cloud is compared both with and without the inclusion of the covariances.

With the inclusion of this extra calibration parameter, the resulting point cloud THU does not change remarkably (Figure 174) from the point cloud with only four parameters calibrated (Figure 170). The net propagated uncertainty does get larger, increasing in range from 0.32-0.39m to 0.36-0.42m. This increase is again expected because there is a larger uncertainty in the input parameters. Also, the structure of the uncertainty with respect to a point's location with respect to the scanner azimuth is also the same (smaller uncertainties forward and larger uncertainties aft). It is only at this point that an operator should judge whether or not the reported confidence in the calibration values are “good enough” for their purposes.

If one were now to compute the horizontal TPU based strictly on the uncertainties of the input parameters (i.e., ignore the impact of the covariances) a very different picture is revealed (Figure 175). As in the previous example, the points with the larger uncertainties have shifted to a new location (now in the forward-portside sector of the swath). However, what is much more startling is the almost quadrupling of the reported uncertainties. The range in THU increases from 0.36-0.42m to 1.44-1.66m. It is again emphasized that the propagated uncertainty as computed from a set of inputs in which their covariances are ignored is not mathematically correct.

To understand why there is such a large jump in uncertainties with the omission of the covariance, one must examine a plot of both the calibration parameter's variance-covariance matrix (Figure 176) and correlation coefficients (Figure 177) – both generated through the covariance module within the calibrator. Not only do $BS\theta_y$ and ϕ_{LS} have the largest variance of the five parameters, but they also have the largest covariance. Between these two parameters, there are three parameters of consequence in the TPU

calculation. For example, the uncertainty in x due just to the two parameters

$BS\theta_y$ and ϕ_{LS} is given by:

$$\sigma_x^2 = \left(\frac{\partial f}{\partial BS\theta_y} \sigma_{BS\theta_y} \right)^2 + \left(\frac{\partial f}{\partial \phi_{LS}} \sigma_{\phi_{LS}} \right)^2 + 2 \frac{\partial f}{\partial BS\theta_y} \frac{\partial f}{\partial \phi_{LS}} \sigma_{BS\theta_y, \phi_{LS}}. \quad (7.67)$$

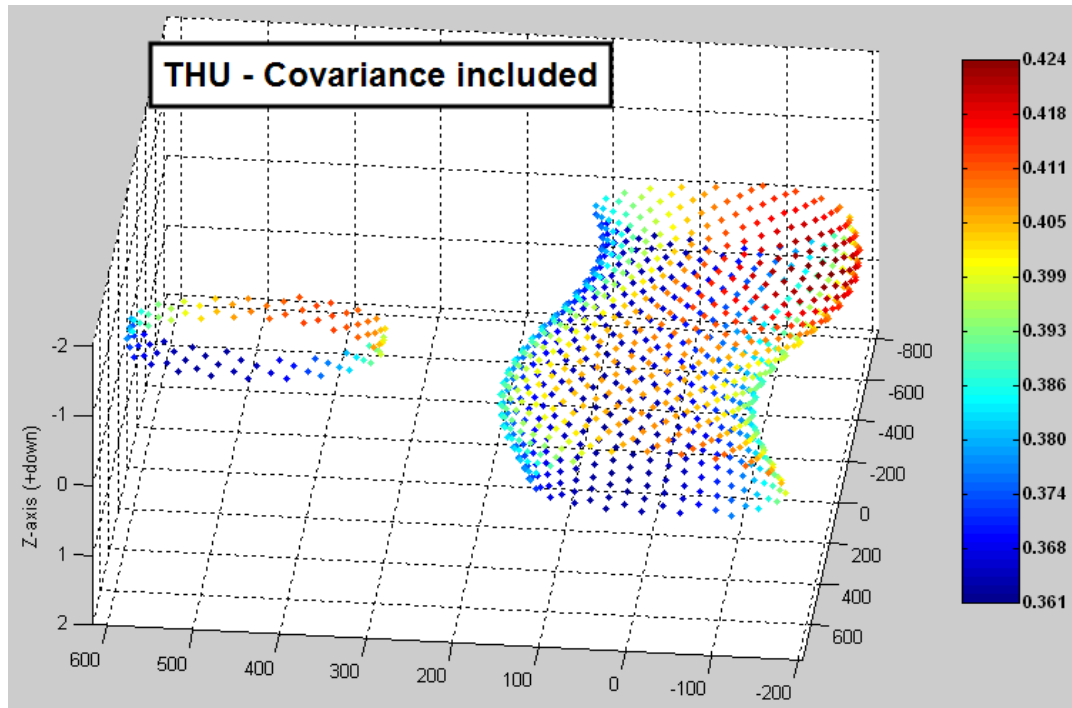


Figure 174. Horizontal TPU (1σ), in meters, when a fifth parameter (ϕ_{LS}) is included in the calibration. Covariance is included in the computation.

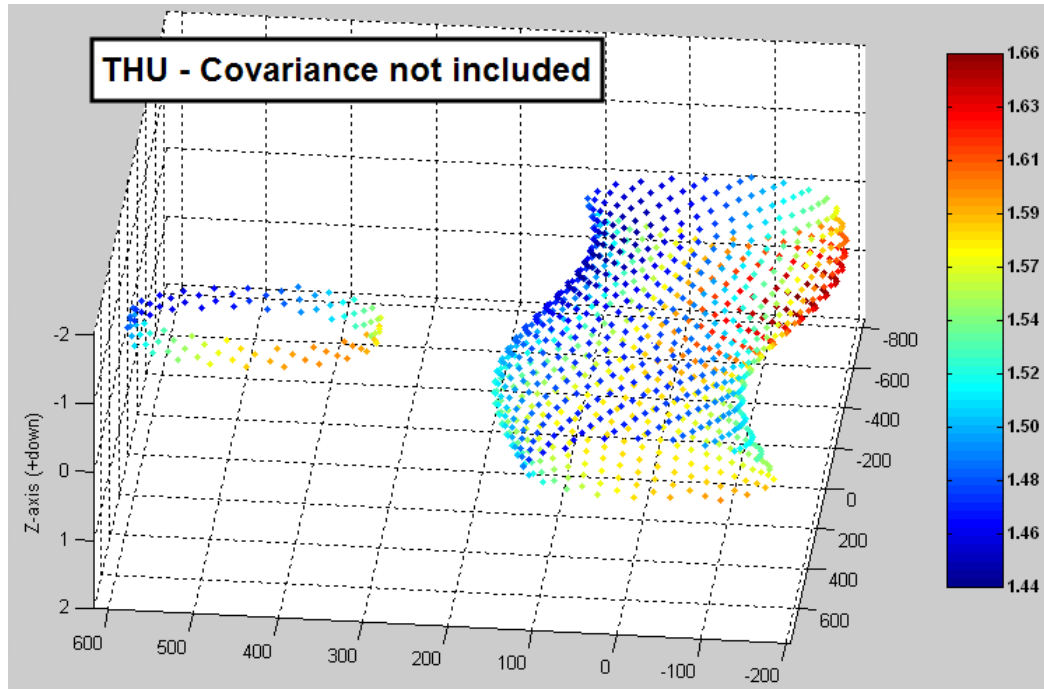


Figure 175. Horizontal TPU (1σ), in meters, when a fifth parameter (ϕ_{LS}) is included in the calibration. Covariance is not included in the computation. Notice the large increase in the reported uncertainties.

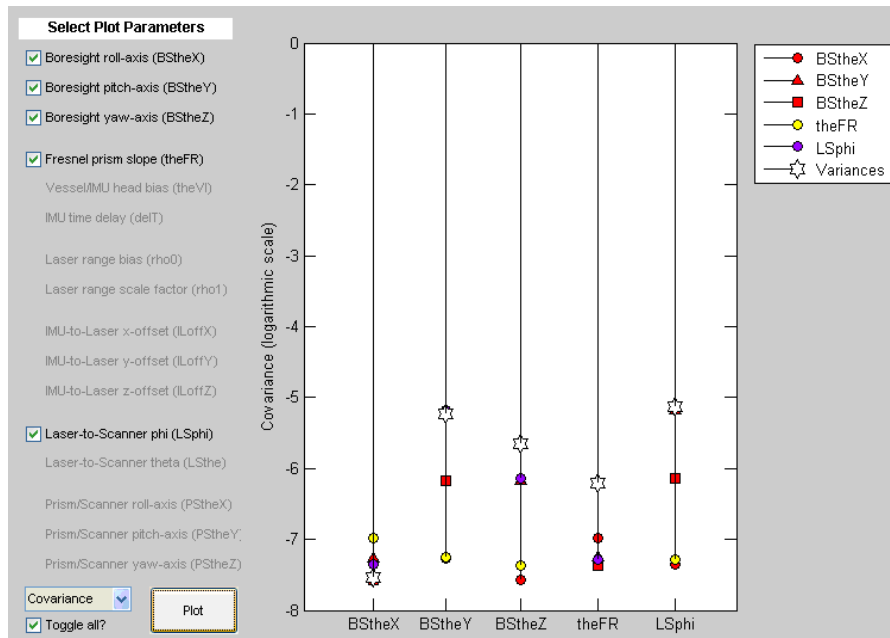


Figure 176. Visualization module of the variance-covariance matrix for the five parameter calibration run. Both the largest variances and the largest covariance are associated with the pitch boresight angle ('BStheY' – red triangle) and the laser-to-scanner phi-angle ('LSphi' – purple circle). Logarithmic scale is used.

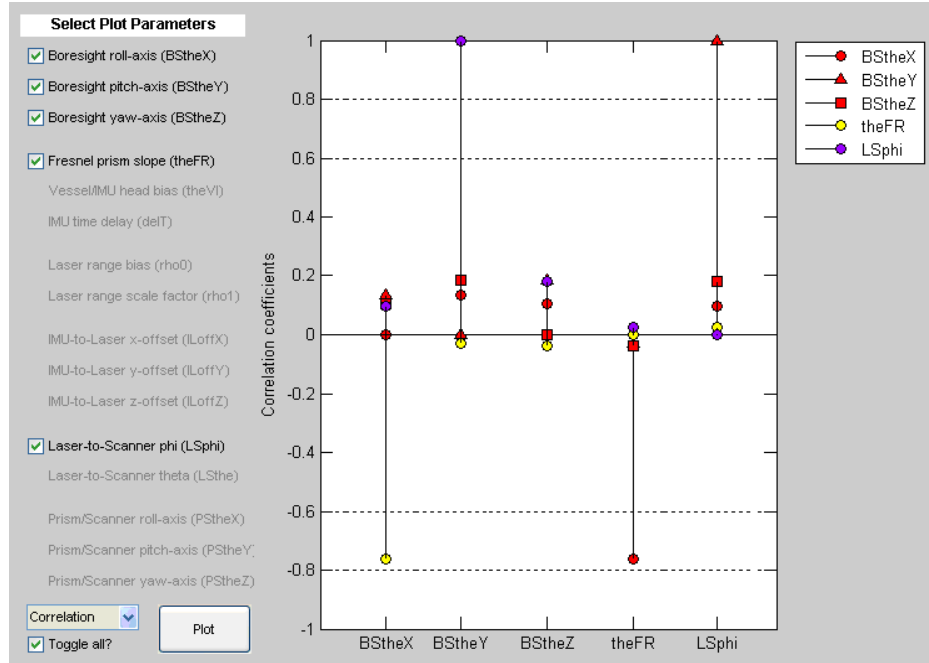


Figure 177. Visualization module of the correlation coefficients for the five parameter calibration run. There is a perfect positive correlation between the pitch boresight angle ('BStheY' – red triangle) and the laser-to-scanner phi-angle ('LSphi' – purple circle). There is also a negative correlation between the roll boresight angle ('BStheX' – red circle) and prism slope ('theFR' – yellow circle).

Only the red terms in the preceding equation are used in the TPU calculation when covariance (the blue term) is neglected. Because the variances of $BS\theta_y$ and ϕ_{LS} are so large, it is unsurprising that the TPU is also large. In order to reduce the TPU, the covariance term must be negative. Figure 177 shows the two parameters are highly, positively correlated (implying the covariance is positive). Close examination of the partial derivatives show the partial derivative with respect to the boresight angle is positive; whereas the partial derivative with respect to the laser/scanner angle is negative. Thus, as a whole, the blue term in (7.67) is negative and will reduce the final computed TPU. Figure 177 also shows a relatively large negative correlation between the roll boresight angle and the prism slope. In this case, the two corresponding partial

derivatives are positive, so their product with the negative covariance will net a negative number and also reduce the TPU.

Generally, the determination of which terms have a large impact on the TPU, can be garnered through an examination of the variances and the covariance terms with large correlation coefficients. Assuming the calibration routine yielded a geometrically correct point cloud, a large covariance indicates the calibration routine could not decide which of two parameters was the true culprit for the system misalignments. Under such a scenario, both the variances and covariance will be relatively large. They should also be complementary and work to cancel each other out in the final uncertainty model. However, to determine whether the covariance terms will positively or negatively impact the TPU, the signs of the partial derivatives must be calculated.

No information regarding the five planar parameters adjusted in the calibration routine are carried forward to the TPU module. These are nuisance parameters that have no meaning within the lidar. Unfortunately, this is a detriment to any calibration parameter that has a high correlation with a planar parameter (e.g., IMU-to-laser vertical offset or the laser range bias) at the time of calibration. While the large variances for these parameters will propagate through to the TPU module, the associated covariances will not. As discussed in Section 6.3.3.3, the use of ground control, will eliminate three of the planar parameters from the adjustment. The remaining two parameters (describing the ground normal vector) are seldom correlated with calibration parameters and can be mitigated through a well designed flight plan that successfully decouples the lidar's calibration parameters from the planar parameters.

While this forensic analysis of determining which parameters are the largest contributors to the point cloud TPU may only be of interest to some, the take-home message is the same for all: if covariance terms are available, they must be included in the TPU calculation. The previous two examples only serve to reinforce the types of misinformation about the point cloud that may be spread if covariance is ignored. The user may either completely misunderstand the distribution of the point cloud uncertainty (example #1), or may grossly over (or under) estimate the total uncertainty (example #2).

We conclude this section by revisiting a calibration trial from Section 6.3.3.1, which provides an extreme example of the pitfalls associated with disregarding the covariance. In this example, a 7-parameter calibration was performed (boresight angles, prism slope, laser/scanner angles and VRF/IRF heading alignment) in which 6 of the parameters had a correlation coefficient of either +1 or -1. These large correlations led to some inordinately large estimated uncertainties the calibration parameters, in particular: 3.7° (1σ) for both the yaw boresight angle and VRF/IRF heading misalignment and 2.2° (1σ) for ϕ_{LS} . In spite of the large parameter uncertainties, the point cloud's TPU is actually relatively small (provided the covariances are included in the computation). The THU both with and without the inclusion of covariance are shown in Figure 178 and Figure 179, respectively. The THU of the point cloud only ranges between 0.17m and 0.19m. This point cloud uncertainty is better, in fact, than that of the point cloud shown in Figure 174 which had uncertainties in its associated calibration values several times (and in some cases several orders of magnitude) smaller than the 7-parameter calibration. This is because in spite of the large uncertainties in the calibration parameters, there were also large associated covariances. Such a combination of circumstances implies that

while the calibrator was not confident in the calibration values, per se, it was confident that a geometrically correct point cloud was produced. This is reflected in the high confidence (low THU) of the final point cloud. If the covariances are neglected, the THU jumps by two orders of magnitude up to a range of 15.7m to 18.1m. For reference, this point cloud had a TVU ranging from 0.104m to 0.107m.

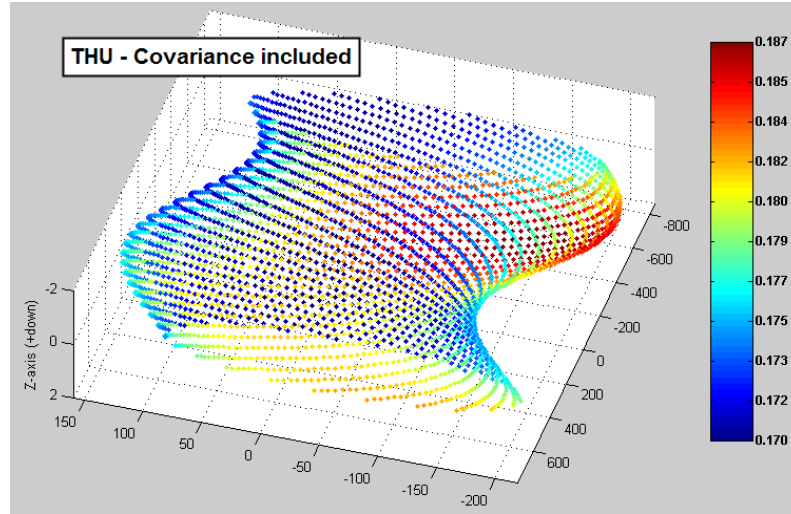


Figure 178. Horizontal TPU (1σ), in meters, for a point cloud which has both large uncertainties in its input parameters and large correlations among said parameters. Covariance is included in the computation.

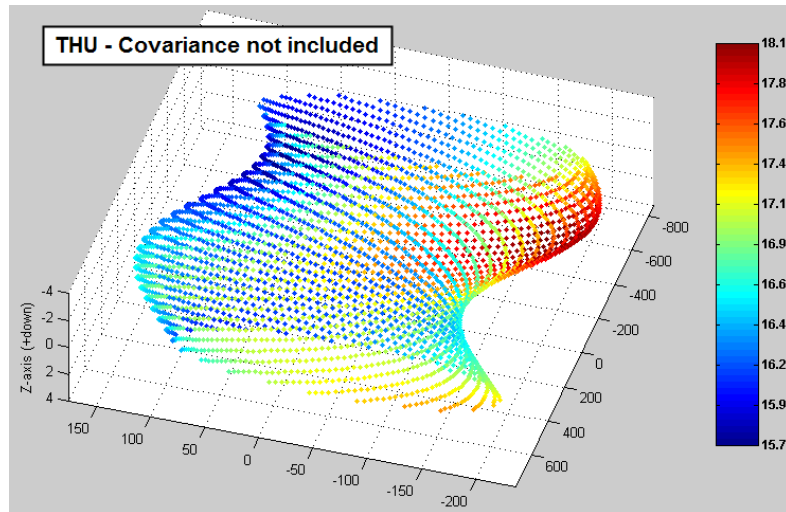


Figure 179. Horizontal TPU (1σ), in meters, for a point cloud which has both large uncertainties in its input parameters and large correlations among said parameters. Covariance is not included in the computation. Notice the large increase in the reported uncertainties.

7.2.2.3 – *A few more notes on variance and the TPU module.* On the left-hand side of the TPU module (Figure 142), every input to the laser equation is listed (both the observed and calibrated parameters). Beneath each parameter are two fields which list the purported contribution to the final point cloud THU and TVU on a point-by-point basis. These fields only reflect the contribution due to the variance of the parameters (the red terms of [7.67]); the covariances are not included. Thus the final error of the point cloud is no more than a sum of squares of the individual contributions, much like (7.43):

$$\sigma_{x_g}^2 = \underbrace{\left(\frac{\partial x}{\partial \rho} \sigma_\rho \right)^2}_{\text{Laser range induced error}} + \underbrace{\left(\frac{\partial x}{\partial \theta} \sigma_\theta \right)^2}_{\text{Azimuth angle induced error}} + \underbrace{\left(\frac{\partial x}{\partial \phi} \sigma_\phi \right)^2}_{\text{Nadir angle induced error}} . \quad (7.43)$$

Without covariance, this is how the point-by-point uncertainty is determined in the first column of Figure 145. Further, each squared term on the right-hand side of (7.43) is used to determine the percent contribution to the laser point's uncertainty.

As has been demonstrated, however, the inclusion of covariance may either add to or subtract from a particular point's uncertainty (thus changing the value of the left-hand of (7.43)). In its present state, the TPU module does not include the covariance terms when computing the percent contribution. Given that, the capabilities of displaying the percent contribution to the uncertainty has been disabled when the TPU module is called from the calibrator.

The user is also given the capability of modifying the standard deviations for both the observed and calibrated parameters. The user is not, however, given the ability to modify the covariances. This can potentially lead to an undefined TPU calculation for the final point cloud. For example, consider a function of just two variables, A and B, whose TPU would be given by:

$$\sigma_x = \sqrt{\left(\frac{\partial x}{\partial A} \sigma_A\right)^2 + \left(\frac{\partial x}{\partial B} \sigma_B\right)^2 + 2 \frac{\partial x}{\partial A} \frac{\partial x}{\partial B} \sigma_{A,B}}. \quad (7.68)$$

The first two terms are being squared and are thus clearly positive. By changing the standard deviations, the user also has the ability to make the first two terms as large or small as they desire. But the third term, the covariance term may be negative, and should the user make the first two terms sufficiently small, then the quantity under the radical may become negative (and thus imaginary). Should such a scenario be encountered, the TPU module will output a warning message that the user-defined standard deviations are too small and cease calculation of the point cloud TPU.

One final note on modifying the uncertainties of the system's observables (the laser range, azimuth, etc.): in the context of the TPU module being called from the calibrator, the observable uncertainties are used twice. As just discussed, the user has the capability of manipulating the standard deviations of all the input parameters within the TPU module; however, as part of the a priori weighting of the least squares model, those uncertainties are also used in determining the confidence of the calibration parameters. So, if a user wished to visit a “what-if” scenario and change the confidence in one of the measured parameters, they should change the value in the TPU module, but only after they rerun the calibration module with the newly proposed confidences.

For example, consider the second set of calibration values and TPU assessments shown in Figure 173, here repeated in the first column of Figure 180. Using an initial estimate in the vertical positioning of the aircraft of 0.30m, the TVU of the final point cloud ranges between 0.304 and 0.311m. Noting the GPS positioning constitutes such a large percentage of the point cloud's TPU, the system operators may wish to test whether an alternate method of determining their vehicle's position will have improved results.

Changing the vertical uncertainty of the GPS to only 0.10m in the TPU module, the point cloud's TVU drops to a range of 0.111m to 0.142m. The GPS still accounts for a large fraction of the TVU, but the values themselves are much smaller than before. An improved GPS solution, however, will also lead to an improved confidence in the calibration parameters. Using a 0.10m vertical uncertainty in the calibration module, the standard deviations in the five parameters being calibrated drops between 65 and 70% (illustrating the uncertainty in the GPS positioning not only adversely affects the point cloud, but also the calibration parameters). In turn, an improved confidence in the calibration parameters leads to an improved confidence in the point cloud positions. With the refined calibration solution, the point cloud's TVU has a further reduction to between 0.103m and 0.110m, an improvement of 1 to 3cm over neglecting to rerun the calibration routine.

7.3 – Relative Contributions to TPU of Observed and Calibrated Parameters'

Uncertainties

In the previous section, observing how much the point cloud's TPU was reduced by improving the confidence in one of the lidar's measured quantities, one may wonder exactly how much of the uncertainty in the point cloud is due to the system components and how much is due to the calibration routine. That is, for a surveyor to improve the confidence of their final point cloud, should they invest in better equipment (laser, IMU, GPS processing software) or invest more time in acquiring data to be used in their calibration procedure. First, a simpler calibration (two flight lines, five adjusted parameters) will be examined, followed by some more robust examples from Chapter VI.

Change GPS vertical (1σ) value where?			
	Unchanged	TPU module	TPU & Cal. Module
(1-sigma GPS vertical uncertainties)			
	0.3m	0.1m	0.1m
(1-sigma calibration uncertainties)			
Boresight - roll	0.010°		0.003°
Boresight - pitch	0.139°		0.047°
Boresight - yaw	0.084°		0.029°
Prism slope	0.045°		0.015°
Laser-to-Scanner phi angle	0.156°		0.053°
	Point cloud vertical TPU		
Maximum value	0.311m	0.142m	0.110m
Minimum value	0.304m	0.111m	0.103m

Figure 180. Table of changes in point cloud vertical TPU (1σ), in meters, depending on when the vertical GPS uncertainty is updated: in just the TPU module or both the TPU and calibration modules.

7.3.1 – Uncertainty of Simple 5-Parameter Calibration

For the simple example, we return to the flight plan shown in Figure 169. Only two small lines were acquired, one with the vehicle rolling and yawing by 5° , the other without any change in vehicle attitude. The reader is reminded of the paltry size of the dataset. As seen in Chapter VI, larger datasets lead to reduced uncertainties in calibration parameters (and thus, reduced TPU). When both the measured and adjusted parameters are included in the TPU calculation, the THU ranges 0.165 to 0.191m and the TVU between 0.103 and 0.110m.

		Is the parameter included in the TPU calculation?						
		51Hz					10,000Hz	
OBSERVABLES ($\pm 1\sigma$)								
Laser range ($\pm 0.01\text{m}$)	YES	-	-	YES	YES	YES	YES	-
Laser azimuth ($\pm 0.002^\circ$)	YES	-	-	YES	YES	YES	YES	-
GPS x-direction ($\pm 0.05\text{m}$)	YES	-	YES	-	YES	-	YES	-
GPS y-direction ($\pm 0.05\text{m}$)	YES	-	YES	-	YES	-	YES	-
GPS z-direction ($\pm 0.10\text{m}$)	YES	-	YES	-	YES	-	YES	-
IMU-sensed roll (0.008°)	YES	-	-	YES	YES	YES	YES	-
IMU-sensed pitch (0.008°)	YES	-	-	YES	YES	YES	YES	-
IMU-sensed yaw (0.025°)	YES	-	-	YES	YES	YES	YES	-
CALIBRATION PARAMETERS ($\pm 1\sigma$)								
Boresight roll (0.003°)	YES	YES	-	-	-	YES	YES	YES
Boresight pitch (0.05°)	YES	YES	-	-	-	YES	YES	YES
Boresight yaw (0.03°)	YES	YES	-	-	-	YES	YES	YES
Prism slope (0.015°)	YES	YES	-	-	-	YES	YES	YES
Laser-to-Scanner Φ (0.05°)	YES	YES	-	-	-	YES	YES	YES
Point cloud Horizontal TPU (1σ)								
Maximum value	0.191m	0.131m	0.071m	0.125m	0.144m	0.178m	0.144m	0.009m
Minimum value	0.165m	0.108m	0.071m	0.095m	0.119m	0.150m	0.119m	0.008m
Point cloud Vertical TPU (1σ)								
Maximum value	0.110m	0.033m	0.100m	0.032m	0.105m	0.045m	0.105m	0.002m
Minimum value	0.103m	0.014m	0.100m	0.020m	0.102m	0.025m	0.102m	0.001m

Figure 181. For a point cloud with 8 observed parameters and 5 calibrated parameters (1σ uncertainties shown), table of the horizontal and vertical TPU (1σ) of the point cloud is presented for a variety of inputs into the TPU module. For example, total uncertainty (1^{st} column), uncertainty due to calibration values (2^{nd} column), uncertainty due to GPS positioning (3^{rd} column), etc. Uncertainties for 10KHz laser are also shown (7^{th} and 8^{th} columns).

Figure 181 summarizes the point cloud uncertainty in which only certain input uncertainties are propagated to the point cloud. Some conclusions to be drawn include:

- Nearly all of the vertical uncertainty in the point cloud can be attributed to the uncertainty in the GPS positioning (column 1 vs. column 3).
- All of the other input parameters combined do not amount to half of the vertical uncertainty induced by GPS (column 6 vs. column 3).
- At 51Hz, the calibration parameters' contributions to the point cloud THU are roughly equivalent to the contributions by the observed parameters (column 2 vs. column

5). The calibration parameters' contributions to the TVU are on par with the errors induced by the observed parameters when GPS is excluded (column 2 vs. column 4).

- When the point cloud data density is increased to the anticipated laser repetition rate of 10KHz, the uncertainty of the point cloud becomes indistinguishable whether the calibration parameters' uncertainties are included or not (column 5 vs. column 7). The THU that can be ascribed exclusively to the calibration results is less than 1 centimeter, while the TVU is roughly 1 millimeter (column 8). An increase in data density pays great dividends towards improving both the confidence in the calibration parameters and the point cloud TPU.

Using robust examples with a greater number of calibration parameters and following the recommended flight pattern of Figure 101, consider first the 11-parameter calibration trial shown in Figure 121 (Trial 4) which presented a simulation acquired at 51Hz with ground control; a point cloud size of ~3800 data points. The adjusted parameters (with their associated values shown in parentheses) included the three boresight angles (5° , 5° and 5°), the prism slope (39.18°), the VRF/IRF heading bias (0°), two components of the INS offset vector (1m and 1m), the two laser/scanner angles (1° and 1°) and the two prism/scanner angles (1° and 1°). The uncertainties of both the calibration values and the point cloud are shown in Figure 182 (column 1).

7.3.2 – Uncertainty of Prism/Scanner Alignments

In comparison to the 5-parameter calibration shown in Figure 181, the uncertainties associated with the 11-parameter are much larger. The maximum horizontal uncertainty exceeds 24m while the vertical TPU is over 37m (column 1). The first observation one can always make with regard to calibration uncertainties is that the

results can be improved by more data. As seen in Chapter VI, quadrupling the data density will reduce the uncertainty of the calibration parameters by 50%. This trait carries forward to the point cloud TPU: quadrupling the data density will halve the contribution of the calibration parameters towards both the TVU and THU (column 2).

Delving further into the point cloud uncertainties, one notices a broad range from point to point. For example, the contribution to THU ranges from 0.085m to 24.6m (the TVU similarly ranges from 0.003m to 37.5m). There is no apparent correlation between the uncertainty and the vehicle's aspect (pitch, roll or heading) or altitude. There is, however, a large correlation with the scanner's azimuth (Figure 183). The beams directed forward and to port (315°) are associated with the most confident beams; whereas the aft-starboard beams (135°) have the largest uncertainty. The root cause of both these large uncertainties and the large variation can be understood if the calibration is recomputed while holding different parameters fixed.

Calibration parameter	Confidence in both calibration solution and point cloud TPU (1σ). The second column is expressed as a percentage of the first.				
	51Hz	204Hz	51Hz		
Boresight roll angle	0.273°	53.6%	0.018°	0.279°	0.034°
Boresight pitch angle	0.444°	52.3%	0.018°	0.081°	0.439°
Boresight yaw angle	3.975°	49.9%	3.036°	3.888°	3.180°
Prism slope	1.636°	49.9%	0.004°	0.051°	1.634°
VRF/IRF heading bias	3.403°	50.0%	3.035°	3.234°	3.218°
IMU x-offset	0.091m	50.0%	0.083m	0.083m	0.091m
IMU z-offset	0.007m	49.5%	0.007m	0.007m	0.007m
Laser/Scanner Φ -angle	0.398°	52.6%	0.021°	0.051°	0.395°
Laser/Scanner θ -angle	21.707°	52.7%	1.191°	22.141°	2.963°
Prism/Scanner x-axis	7.771°	51.5%	-	7.974°	-
Prism/Scanner y-axis	8.213°	51.4%	-	-	8.213°
Max. contribute to THU	24.6m	51.7%	0.100m	9.7m	23.1m
Min. contribute to THU	0.085m	49.7%	0.076m	0.083m	0.081m
Max. contribute to TVU	37.5m	49.4%	0.009m	18.9m	37.5m
Min. contribute to TVU	0.003m	49.7%	0.004m	0.004m	0.003m

Figure 182. Table of calibration results from an 11-parameter calibration including prism/scanner alignments (1σ uncertainties shown). Parameters marked by a ‘-’ were not included in a given calibration trial. The horizontal and vertical TPU are shown under various calibration configurations.

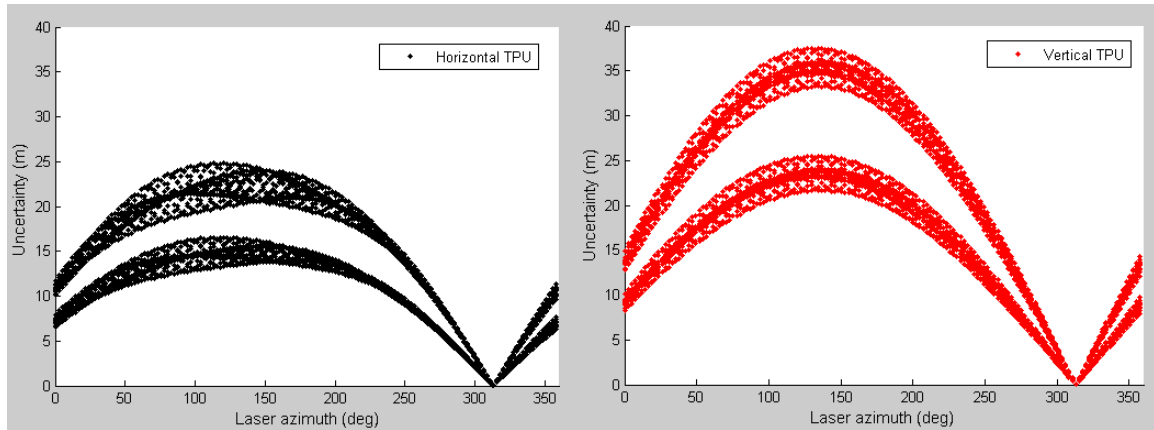


Figure 183. Horizontal (left) and vertical (right) TPU (1σ) versus scanner azimuth (0° = forward, 90° = starboard, etc.) for the calibrated point cloud depicted in Figure 182 – column 2. Each plot shows two separate bands which are representative of the two acquisition altitudes (higher altitudes yielding higher uncertainties).

As was discussed in Section 6.3.4.1, the inclusion of the prism/scanner alignments $PS\theta_x$ and $PS\theta_y$ (and their highly correlated nature) led to the inordinately large uncertainties in the values for the parameters themselves (Figure 121 – columns 2 through 4). Suspecting one of these two parameters to be the dominant factor in the point cloud's uncertainty, the calibration was performed three more times in which either one of both of the parameters $PS\theta_x$ and $PS\theta_y$ was held as constants. When neither parameter was included in the adjustment, the point cloud TPU dropped to a maximum THU of 0.100m and a maximum TVU of 0.009m (Figure 182 – column 3). The marked drop in uncertainty establishes one of these two parameters is corrupting the TPU. Alternately holding first $PS\theta_y$ (column 4) and $PS\theta_x$ (column 5) fixed, while adjusting the other, the point cloud still shows large uncertainty implying neither parameter can be included in the adjustment without greatly adversely affecting the TPU.

Of course, if a user was adamant about adjusting $PS\theta_x$ and $PS\theta_y$, it is possible to improve the point cloud TPU by increasing the amount of data adjusted. As stated, every

time the data volume is quadrupled, the point cloud uncertainty is halved. In the first entry of Figure 182, a 51Hz laser (totaling 3,828 data points) netted a maximum TVU of 37.5m (1σ). If one wished to decrease this uncertainty to 0.15m (1σ), then approximately 250,000,000 data points would be required. To achieve this data density, a lidar running at a full 10,000Hz repetition rate would need to survey non-stop for 6.96 hours over roughly the same area (for a 0.15m – 2σ , survey for 27.9 hours). If the surveyor does not have the resources to dedicate to this task, then the next best option is to remove $PS\theta_x$ and $PS\theta_y$ from the adjustment and determine their values by some other means.

7.3.3 – Uncertainty of Scanner Azimuth Bias

In Section 6.3.4.2, the scanner azimuth bias, $PS\theta_z$ was discussed in the context of the system calibration and demonstrated to be linearly dependent on θ_{LS} (along with the 3 boresight angles). This implies a decision must be made with regard to which of the two variables is included in the adjustment and which is held fixed. Figure 184 shows the results of a 9-parameter calibration and the associated point cloud uncertainties for an adjustment that contains θ_{LS} (left column) and $PS\theta_z$ (right column). Notice the uncertainties for the parameters themselves are comparable, both around 1.2° (1σ); the point cloud TPU highlights a vast disparity. When $PS\theta_z$ is adjusted rather than θ_{LS} , the maximum contribution to the point cloud horizontal uncertainty by the calibration parameters increases by over 1,000 times (0.009m to 9.331m). The vertical TPU increases by over 10 times (0.100m to 1.142m). From the perspective of determining the most confident values for the calibration parameters, either of the two parameters can be adjusted. However, if the end goal is producing the most confident reported positions of

the lidar point cloud, the scanner azimuth bias should be held at 0° while θ_{LS} is determined through the LSA.

Calibration parameter	Uncertainty (1σ)	
Trial #	1	2
Boresight roll angle	0.018°	0.088°
Boresight pitch angle	0.018°	0.108°
Boresight yaw angle	3.036°	2.845°
Prism slope	0.004°	0.004°
VRF/IRF heading bias	3.035°	3.013°
IMU x-offset	0.083m	0.082m
IMU z-offset	0.007m	0.007m
Laser/Scanner Φ -angle	0.021°	0.021°
Laser/Scanner θ -angle	1.191°	-
Scanner azimuth bias	-	1.221°
Max. contribute to THU	0.100m	9.331m
Max. contribute to TVU	0.009m	1.142m

Figure 184. Table of calibration results from an 9-parameter calibration including the scanner azimuth bias (1σ uncertainties shown). Parameters marked by a ‘-’ were not included in a given calibration trial. The horizontal and vertical TPU are shown under various calibration configurations.

7.3.4 – Uncertainty of Final Calibration with and without Ground Control

Estimated uncertainties for both the calibration parameters and the associated point cloud TPU are shown in Figure 185 for the final proposed 11-parameter calibration (11 parameters as opposed to 13 parameters because of the difficulty associated with calibrating $PS\theta_x$ and $PS\theta_y$). Significant to this table is that it contains the ultimate uncertainties that a surveyor should expect to achieve when using the proposed calibration procedure. Also considered are the effects of the inclusion of ground control and manually measuring the INS offset vector. There are several key observations to be taken from this table and they will be discussed one at a time.

Calibration parameter	Confidence (1σ) in calibration solution and point cloud TPU (reported as a percentage of the baseline, "Trial 1", confidence).						
Trial #	1	2	3	4	5	6	7
Laser repetition rate	51Hz	10KHz	51Hz	51Hz	51Hz	51Hz	51Hz
Ground Control?	YES	YES	NO	NO	NO	NO	YES
Boresight roll angle	0.019°	0.001°	100.0%	100.4%	100.4%	98.9%	98.6%
Boresight pitch angle	0.019°	0.001°	100.0%	100.4%	100.5%	97.7%	97.3%
Boresight yaw angle	3.381°	0.241°	100.0%	100.0%	90.4%	55.7%	55.6%
Prism slope	0.017°	0.001°	100.0%	98.9%	38.2%	38.9%	38.2%
VRF/IRF heading bias	3.380°	0.241°	100.0%	100.0%	90.4%	55.7%	55.6%
IMU x-offset	0.084m	0.006m	100.0%	100.4%	99.2%	-	-
IMU z-offset	0.280m	0.020m	467.4%	-	-	-	-
Laser/Scanner Φ -angle	0.022°	0.002°	100.0%	100.4%	100.5%	97.6%	972.2%
Laser/Scanner θ -angle	1.244°	0.089°	100.0%	100.4%	100.3%	98.9%	98.5%
Laser range scale factor	6.9E-05	4.9E-06	100.0%	98.9%	42.3%	42.2%	43.8%
Laser range bias	0.300m	0.021m	100.0%	98.7%	-	-	3.1%
Max. contribute to THU	0.166m	0.012m	0.202m	0.252m	0.109m	0.109m	0.109m
Percent change	-	7.1%	121.4%	151.4%	65.7%	62.9%	62.7%
Max. contribute to TVU	0.026m	0.002m	1.289m	0.281m	0.014m	0.014m	0.014m
Percent change	-	7.1%	4868%	1063%	52.4%	51.3%	38.5%

Figure 185. Table of anticipated calibration and point cloud uncertainties (1σ) for the final proposed calibration procedure. Parameters marked by a ‘-’ were not included in a given calibration trial. All uncertainties are displayed as a percentage of the baseline (Trial 1) flight. The effects of including ground control and manually determining the INS offset vector are considered.

- Trial 1 – If ground control is to be used (that is, a single point on the planar surface is identified in advance), then Trial 1 is the recommended calibration configuration. The vertical point cloud TPU (1σ) is only 0.026m. Recall, to achieve this level of accuracy, only the four flight lines (each of an approximately 20 second duration) of the crossing flight pattern shown in Figure 101 are necessary.

- Trial 2 – Demonstrates the anticipated point cloud accuracy of the recommended calibration configuration when acquisition rates are at 10KHz. The uncertainty of the calibration parameter’s values will contribute only 0.002m to the point cloud TVU (and 0.012m to the THU). The simple rule of thumb is that by quadrupling the data density, the uncertainty will be halved. More generally, if x data points are acquired to produce

an uncertainty (1σ) of s , then adjusting n times more data points will yield an uncertainty given by:

$$s^* = s \left(\frac{1}{2} \right)^{\frac{\ln n}{\ln 4}}. \quad (7.69)$$

Thus going from 51Hz data to 10KHz data will reduce the uncertainty of both the calibration parameters and the point cloud to 7.1% of the previous levels. This principle can be applied to all the other trials shown in this table if an alternative calibration configuration were to be considered.

- Trial 3 – As was seen in Section 6.3.3.3, if ground control is not included, the uncertainty in the vertical INS offset will become prohibitively large leading to excess uncertainties of the point cloud TVU (1.289m).
- Trial 4 – without ground control, including the laser range bias in the calibration will also lead to large ($0.281\text{m} - 1\sigma$) vertical uncertainties in the point cloud.
- Trial 5 – In the absence of a ground control point, the best practice is to manually measure the vertical offset of the INS and withhold ρ_0 from the calibration. Though one could still achieve comparable point cloud accuracies and adjust the laser range bias, it would require collecting about 400 times more data,

$$\text{since } 0.014 = 0.281 \left(\frac{1}{2} \right)^{\frac{\ln n}{\ln 4}} \rightarrow n = 402.9.$$

If a ground control point is not included in the calibration, then Trial 5 is the recommended configuration.

- Trial 6 – Is a repeat of Trial 5 (no ground control, no calibration of ρ_0 , manually measure vertical INS offset), but also includes manually measuring the horizontal INS

offset. Out to one-thousandth of a meter, no improvement is gained in either the horizontal or vertical point cloud uncertainty. Therefore, rather than risking an erroneous measurement of the horizontal INS offset, the user should let the LSA determine this value.

- Trial 7 – Even if ground control is being employed, the user may elect to manually measure all three INS offset vector components (rather than just the requisite one, Δy_{IL}) and treat them as fixed quantities in the calibration. This is not a recommended strategy for three reasons: First, the user may erroneously measure the offset vector. Second, at 10KHz the calibration module can determine the horizontal offset to 0.006m and the vertical offset to 0.020m. Third, in the case of ground control, while it is true the point cloud vertical uncertainty induced by the calibration parameters will be improved by 51.5% by manually setting the INS offset vector, with a 10KHz dataset, the vertical TPU contribution was already 0.002m. When the vertical uncertainties due to such factors as GPS positioning are accounted for ($\sim 0.10\text{m}$ vertical), the calibration induced point cloud uncertainty is already negligible. As such, the user can effectively eyeball one component of the INS offset vector (say Δy_{IL}) and then let the calibrator determine all the other parameters.

7.3.5 – Final Assessment of the Calibrator's Performance

In Chapter VI, it was cautioned that the success or failure of a given calibration trial should not be assessed based exclusively on the reported uncertainties of the calibration parameters. Since the ultimate goal is the production of a geometrically-correct, well-positioned point cloud, judgment of the calibration should be reserved until the total propagated uncertainty of the point cloud is assessed.

One must first appreciate the uncertainty of the point cloud that can be attributed exclusively to the random noise in the measured quantities (laser range, scanner azimuth, GPS position, etc.). In the case of the crossing flight pattern of Figure 101, the maximum horizontal TPU is 0.216m and the vertical is 0.112m (Figure 186 – column 1). As discussed in the previous section, the crossing flight pattern at a 10KHz sampling rate will induce a maximum horizontal TPU of 0.012m and a maximum vertical error of 0.002m (Figure 186 – column 2). When the errors induced by the random noise of the observed quantities are combined with the errors induced by the calibration parameters, the point cloud TPU does not change (rounded to the nearest millimeter) from the uncertainty due to the observables alone (Figure 186 – column 3). The fact that the point cloud uncertainty induced by the calibrator is negligible definitively establishes the least squares adjustment employed by the calibration module is a successful method for determining the calibration values.

For comparative purposes, the TPU of the point cloud was computed assuming the calibration values were determined using some method other than the method of least squares (e.g., manually adjusting the parameters until adjacent swaths appear to align themselves). Suppose one is able to determine the confidence of all the angular calibration parameters to within 0.05° (less than 1mrad) and all the distance parameters to within 0.01m. In such a case, the combined observation/calibration maximum point cloud horizontal TPU will be 1.153m and the maximum vertical TPU will be 0.457m (Figure 186 – column 4). In spite of the fact that many of the uncertainties of the individual calibration parameters are smaller (INS offset, laser range bias, VRF/IRF heading bias), the point cloud uncertainty grows larger (5 times the THU and 2-to-4 times

the TVU) when the calibration parameters are determined by a method other than the LSA. The LSA is the superior method because, while it may lead to large uncertainties in the calibration parameters, their covariances will keep the point cloud uncertainty small.

Parameter	Uncertainty used in TPU calculation.			
OBSERVABLES (1σ)				
Laser range	0.010m	-	0.010m	0.010m
Laser azimuth	0.002°	-	0.002°	0.002°
GPS x-direction	0.050m	-	0.050m	0.050m
GPS y-direction	0.050m	-	0.050m	0.050m
GPS z-direction	0.100m	-	0.100m	0.100m
IMU-sensed roll	0.008°	-	0.008°	0.008°
IMU-sensed pitch	0.008°	-	0.008°	0.008°
IMU-sensed yaw	0.025°	-	0.025°	0.025°
CALIBRATION PARAMETERS (1σ)				
LSA used to determine cal. values?	YES		YES	NO
Boresight roll	-	0.001°	0.001°	0.050°
Boresight pitch	-	0.001°	0.001°	0.050°
Boresight yaw	-	0.241°	0.241°	0.050°
Prism slope	-	0.001°	0.001°	0.050°
VRF/IRF heading bias	-	0.241°	0.241°	0.050°
IMU x-offset	-	0.006m	0.006m	0.010m
IMU z-offset	-	0.020m	0.020m	0.010m
Laser/Scanner Φ-angle	-	0.002°	0.002°	0.050°
Laser/Scanner θ-angle	-	0.089°	0.089°	0.050°
Laser range scale factor	-	4.9E-06	4.9E-06	0
Laser range bias	-	0.021m	0.021m	0.010m
Point cloud Horizontal TPU (1σ)				
Maximum value	0.216m	0.012m	0.216m	1.153m (increased by 530%)
Minimum value	0.120m	0.006m	0.120m	0.619m (increased by 515%)
Point cloud Vertical TPU (1σ)				
Maximum value	0.112m	0.002m	0.112m	0.457m (increased by 410%)
Minimum value	0.103m	0.000m	0.103m	0.205m (increased by 200%)

Figure 186. Table of point cloud uncertainties (1σ) induced by the observed parameters (column 1), the calibration parameters derived from the LSA (column 2), the combined observed and LSA-calibrated parameters (column 3) and the combined uncertainty when the calibration parameters are determined by a method other than the LSA (column 4). Data based on crossing flight pattern of Figure 101.

Rather than offering repeated theoretical estimates of the point cloud uncertainty, a more visual example is offered. The crossing flight pattern was simulated at 51Hz with the sensor misalignments listed in Figure 187 (column 1). Further, random noise was added to the eight observed parameters (the magnitude of the noise is shown in Figure 186— column 1). The adjustment was then performed, deriving estimated values for the calibration parameters shown in Figure 187 (column 2). Notice that the misclosures of the proposed calibration values are all within the predicted tolerances shown in Figure 185 (column 1). According to Figure 185, a dataset of this size should yield calibration values that are confident enough to produce a point cloud with a maximum calibration induced TVU of 0.026m. To test this, an independent flight line with its own trajectory was simulated again using the true calibration values of Figure 187 to determine the corresponding observations. For this particular flight, the observations were simulated as error-free so all biases in the point cloud would be attributed exclusively to the calibration values. These observations and the (incorrect) adjusted calibration values were then used to reconstruct the point cloud (Figure 188). The maximum vertical misclosure was only 0.016m, which is well within the predicted tolerance.

Value:	True	Adjusted	Error
Boresight roll	5°	5.005°	0.005°
Boresight pitch	5°	4.988°	0.012°
Boresight yaw	5°	3.138°	1.862°
Prism slope	39.181°	39.173°	0.008°
VRF/IRF heading bias	0°	-1.851°	1.851°
IMU x-offset	1m	0.978m	0.022m
IMU z-offset	1m	1.158m	0.158m
Laser/Scanner Φ -angle	1°	0.985°	0.015°
Laser/Scanner θ -angle	1°	0.943°	0.057°
Laser range scale factor	1	1.000004	4.0E-05
Laser range bias	0m	0.157m	0.157m

Figure 187. Table of the true and adjusted values of the calibration parameters used to render the point cloud in Figure 188. Misclosures of the proposed calibration values are also shown.

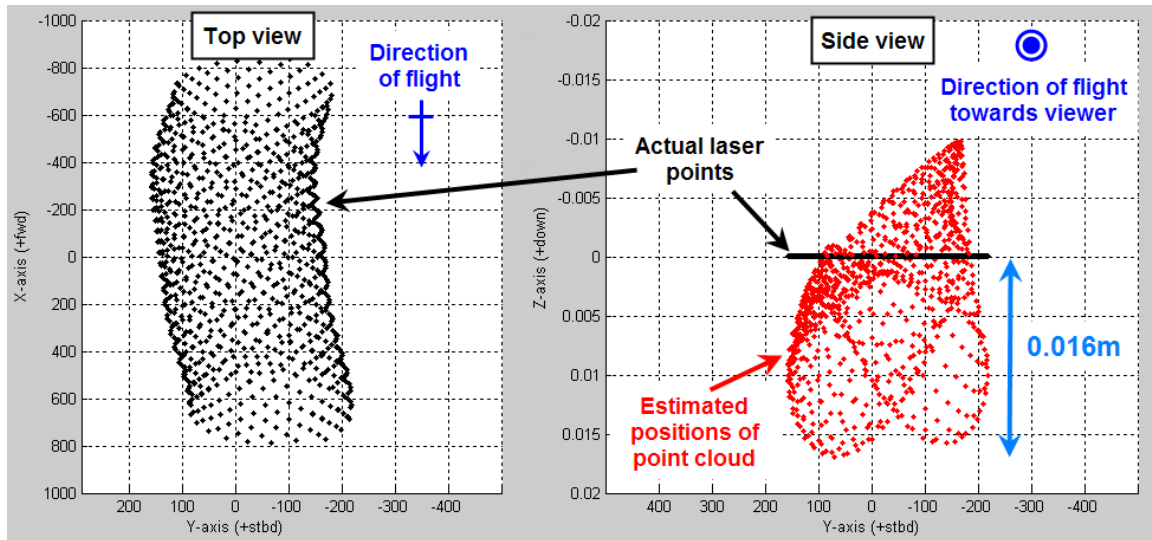


Figure 188. An independent flight line was simulated (left). Using the flight's true, error-free observations, the point cloud was reconstructed using the calibration values based on a noisy dataset (right). True laser points shown in black, biased points in red. All units in meters.

7.4 – Summary of Key Results

The following is a bulleted list of the key results, concepts and contributions presented within this chapter. When possible, the relevant section(s) that offer a more detailed explanation are indicated.

- The full mathematical frame work was presented for computing the total propagated uncertainty of a point cloud which accounts for both the uncertainty in the calibration parameters and the measured quantities (Section 7.1.1.1).
- The issue of covariance was discussed along with its history of being omitted from uncertainty models. The potentially large effects of covariance on the propagated uncertainty were presented using both simple examples (Section 7.1.2) and examples specific to lidar (Sections 7.2.2.1 & 7.2.2.2). The key message with regard to covariance is this: if covariance terms are available, they must be included in the TPU calculation. This includes the covariance terms derived during the calibration.

- The point cloud TPU was calculated for various model IMUs. The higher-end IMU only had a slight improvement on the THU and a negligible improvement on the TVU (Section 7.2.1.1).
- It is difficult to identify any single factor in what will lead to larger or smaller point cloud uncertainties. Generally speaking, increased laser ranges, increased changes in vehicle attitude, and even increased misalignments within the calibrator will lead to an increased uncertainty in the point cloud. However, even tripling the acquisition height (Section 7.2.1.3) or rolling the vehicle by as much as 30° (Section 7.2.1.4) will not lead to unacceptably large point cloud TPU. This does appear to be a conundrum in that, from the previous chapter, the greater the changes in vehicle altitude or attitude experienced, the more confident the solutions for the calibration parameters. The obvious solution is to perform the dynamic flight during calibration, but then shift to a more ‘level’ strategy when acquiring survey-grade data.
- The vertical uncertainty associated with the GPS position (even at $0.10\text{m} - 1\sigma$) dominates the point cloud TVU. The point cloud THU is derived equally from the uncertainty of the GPS position and from the other 5 observed parameters (laser range, scanner azimuth, and vehicle orientation) (Section 7.3.1).
- With sufficient data density (as is the case with a 10KHz lidar), the contribution to the point cloud TPU by the calibration parameters are nearly negligible when compared to the uncertainties associated with the observed parameters (Section 7.3.5).
- Based on uncertainty analysis, the parameters $PS\theta_x$ and $PS\theta_y$ cannot be included in the calibration as they lead to inordinately large point cloud uncertainties (Section 7.3.2).

- As was the case with the calibration parameters' reported confidence, quadrupling the number of data points adjusted will halve the contribution by the calibration parameters to the point cloud TPU (Section 7.3.2).
- As discussed in Chapter 6, θ_{LS} and $PS\theta_z$ are linearly dependent on each other, thus one must be held fixed while the other is adjusted. Based on the point cloud uncertainty $PS\theta_z$ should be held fixed (the alternative leading to point cloud uncertainties nearly 100 times larger) (Section 7.3.3).
- By analyzing the point cloud TPU, it was seen if ground control is included in the calibration area, then a total of 11 parameters can be adjusted (three boresight angles, prism slope, VRF/IRF heading bias, two INS offset components, two laser/scanner angles, and the laser range scale factor and bias). Without ground control Δz_{LL} should be measured by hand ρ_0 must be withheld from the adjustment (Section 7.3.4).
- Finally, the point cloud TPU was computed assuming the calibration parameters were determined by some means other than a least squares adjustment and thus lacked any covariance information. In such a case, the point cloud THU increased by 500% and the TVU increased by 200% to 400% as compared to what the point cloud uncertainties would be were the LSA-derived calibration uncertainties used. This represents a complete validation of the calibration methodology proposed in this dissertation.

It is equally important to understand both the root causes and the symptoms of large uncertainties. In the context of the point cloud positions, while the calibration parameters may have larger reported uncertainties than some would like, thanks to their covariances, they have little impact on the uncertainty of the final point cloud.

CHAPTER VIII

CONCLUSIONS

8.1 – Results

By all accounts, this dissertation achieved all of its stated goals. First, a laser point positioning equation was developed for a novel large aperture circular scanner such as the one to be implemented in the Coastal Zone Mapping and Imaging Lidar (CZMIL) (3.46).

Next a complete simulation of the lidar was programmed to permit the generation of test datasets that could be used in conjunction with the development of the calibration module as well as provide insight into the behavior of the soon-to-be constructed lidar. Anticipating the potential conditions necessary for calibration, the simulator incorporated such features as:

- the ability to dynamically change the attitude of the vehicle mid-flight;
- the ability to subsample a dataset to simulate conditions over a runway,
- the presence of an undulating sea surface to demonstrate the effects of beam steering on the sea floor scan pattern, as well as investigate the feasibility of using the sea surface as a proxy for the flat calibration surface. A tidal model was also incorporated.

The simulator also provided a mechanism for visualizing the behavior of a point cloud should any unidentified misalignments exist within the system (e.g., if the prism slope can only be machined to a given precision, what is the maximum vertical error that will be induced in the point cloud?). By visualizing these biases, a sensitivity analysis can easily be undertaken for all of the system parameters. Further, from the bias plots, the

optimal flight maneuvering characteristics were established for all of the proposed calibration parameters.

With simulated datasets in hand, the calibration module was created which performs a weighted constraint least squares adjustment. The model takes the uncertainties of all the measured quantities (like laser range, scanner azimuth, etc.) as well as initial estimates and uncertainty bounds for all the parameters to be calibrated. Of the 15 proposed calibration parameters, 11 can routinely be determined with a high degree of confidence.

Parameter estimation is achieved through a least squares fit to a planar surface. While a broad, flat terrestrial plane would be best, it was shown either a narrow runway or a wavy sea surface are acceptable calibration sites. Though the uncertainty of the latter two are larger, the confidence in the calibration results were still negligible when compared to the uncertainties associated with such factors as the GPS position of the vehicle.

The calibrator also included a separate module which can be used to display both the covariances and the correlation coefficients of all the adjusted parameters. In this way, the correlations (and in some cases the linear dependence) of all the proposed calibration parameters were determined with respect to one another. The correlation coefficients are of great benefit in interpreting whether an adequate geometry was achieved during the calibration acquisition (i.e., did the vehicle change heading enough?), as well as put into context any (seemingly) large variances for a pair of calibration parameters. The implication being two parameters with large variances, may only

contribute a small amount of uncertainty to the point cloud if they also have a correspondingly large covariance.

A proposed flight plan to be followed during calibration was presented. Only four flight lines are required, to be conducted at two different altitudes and crossing over a common point. During one pair of lines the pilot should induce a change in the vehicle's roll aspect and heading, while in the other pair the pilot should induce a change in vehicle pitch and altitude. Each line need total no more than 20 seconds in duration. Under such a configuration, even if limited to a 50m wide runway, the anticipated contribution to the point cloud uncertainty by the calibration parameters would be 0.052m in the horizontal and 0.007m in the vertical. Comparable results were achieved when simulated over a sea surface with waves of up to 1m in height.

The impacts of a lack of ground control were also investigated. Without a ground control point, neither the laser range bias, nor the IMU vertical offset can be reliably determined. What is more, the TVU of the point cloud will increase by a factor of 10 to 50 times. Either a single ground control point must be provided, or the two aforementioned calibration parameters must be excluded from the LSA.

Finally a module was developed for computing the total propagated uncertainty (both horizontal and vertical) of the final point cloud. Uncertainties can be computed directly from the simulator, where the user can enter any tolerances they wish for the various measured quantities (e.g., what happens if I relax my positioning from real-time kinematic to differential GPS?). Or, the TPU module can be executed after the calibration using the full variance-covariance matrix constructed during the calibration. In this case, the uncertainties induced in the point cloud are calculated based upon both

the uncertainties of the measured quantities as well as the uncertainty resulting from the calibration. The ultimate validation of the proposed calibrator's success is shown in Figure 186 in which it was shown the uncertainties induced in the point cloud by the calibration parameters were completely negligible when compared to the uncertainties induced by the measured values. That is, not only does the calibrator produce a geometrically correct point cloud, but it has a negligible impact on the point cloud uncertainty!

Regarding the MATLAB code itself, the programs are too large (16,000 lines) to paste into the appendix of this document. They were developed using MATLAB R2007b Version 7.5.0.342 without the use of any additional toolbox. The code is freely available and a digital copy can be obtained by contacting the author at michael.gonsalves@noaa.gov.

8.2 – Recommendations for Future Work

Recommendations for future work can be divided into two categories: refinements and expansions to the existing algorithms and modules. Refinements to improve the overall performance and expansions to address issues not conceived before this work was undertaken.

8.2.1 – Refinements to the Present Work

- The algorithms presented should be tested on actual datasets. Presently the constructs for reading external files do not exist.
- Based on the residuals of the observations which can be determined during the least squares adjustment, a noise filtering algorithm should be instituted to remove fliers

from the dataset which could potentially corrupt the calibration. That is, perform the adjustment once, identify and delete the fliers, then re-execute the adjustment.

- Incorporate an atmospheric refraction model or establish that the induced geometric misalignments are negligible with regard to the calibration. Determine whether the atmospheric refraction will have a greater affect when calibrating over the land or over the water.
- While a precise time protocol is recommended, incorporate a navigation time latency into the calibration module.
- Restate the prism-to-scanner alignments in spherical coordinates (similar to how the laser/scanner reference frames were related) to see if the parameters $PS\theta_x$ and $PS\theta_y$ can be calibrated.
- Incorporate three parameters to represent the biases in the INS sensed pitch, roll and yaw. Assess whether they will be linearly dependent on the previous parameters.
- Develop a method of accounting for the large uncertainty of a calibration parameter with a high correlation with a planar parameter. As presently written, such a calibration parameter will lead to an anomalously large point cloud TPU.
- Extend the TPU model for the laser points on the sea floor. As it stands, the equations for the point cloud TPU are only valid for the topographic laser and for the laser strikes on the water's surface.

8.2.2 – Expansions Beyond the Present Work

- Further develop the QC tools similar to those shown in Figure 67 which allow for the inspection of the structure of the point cloud for misalignments without having to perform a live calibration.

- Develop a method of automatically extracting the dataset over an airport runway, perhaps based on the intensity of the return, when such a region is used in the calibration.
- Rather than using the manufacturer's reported uncertainties for the GPS positions and vehicle attitude, use the output from the SBET file, which computes a shot-by-shot uncertainty.
- The framework now exists for the geometric calibration of any geometric system, provided the observation equation is known. The proposed techniques should be applied to other lidars (e.g., CHARTS or EAARL).
- Conceivably, the proposed techniques could even be extended to the calibration of ship-based acoustic systems. The problem of ray tracing would have to be addressed as the sonar pulse travels through the water column, but otherwise, the geometry exists for a successful calibration.
- Develop a new observation equation that results in the point cloud being adjusted to a control dataset rather than being adjusted to a planar surface. A low-pass filtered spatial surface could be derived from the control dataset and then the would-be calibrated datasets would be compared to the control surface (again using an LSA approach). In this way, there would be no requirements placed upon the acquisition conditions necessary for a calibration trial (other than having the reference dataset, obviously). Further with the presence of buildings, trees or other projecting features, the confidence of the calibration routine would be much higher.
- Consider the development of inputting a ground control target file, in which the user may enter several "known" points on the ground plane into the calibration routine. This would lessen the calculated uncertainty of the calibration parameters and minimize

the chance of a blunder being entered for the single ground control point that is presently accepted.

- Develop a method of real-time calibration. As the lidar is operating, a very small percentage of the data can be siphoned to a perpetually running calibration algorithm which is constantly testing whether the point cloud is well-aligned. Such a technique could reveal whether something internal to the lidar becomes misaligned should it be bumped, or whether the GPS solution or INS attitude suddenly becomes corrupt.

APPENDIX

TAIT-BRYAN ROTATIONS

A.1 – Traditional Formulation

Euler angles are a system for describing a coordinate transformation by defining three angular rotations, the proper sequence of these rotations, and the three orthogonal axes about which the rotation occurs. The present motivation is found in trying to describe the orientation of an aircraft given its pitch, roll and yaw angles. Even adhering to the standard, SAE (Grewal, Weill, & Andrews, 2007) body-fixed reference frame (right-handed Forward-Starboard-Down, see Figure A1), there are 24 possible permutations for the sequencing of the rotations. The Tait-Bryan convention specifies the order and direction of these rotations.

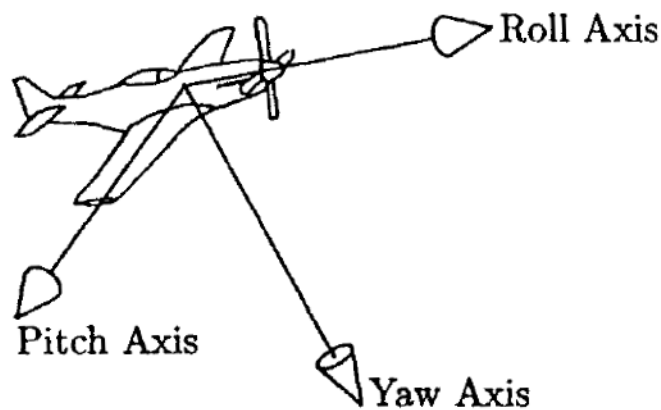


Figure A1. An aircraft's roll (x-axis), pitch (y-axis) and yaw (z-axis) axes, where the arrow indicates the positive direction (from Grewal, Weill, & Andrews, 2007).

The Tait-Bryan convention is followed throughout the geomatics, remote sensing and hydrographic communities. More importantly, it is adhered to by Applanix, the manufacturer of IMU to be deployed with CZMIL (Applanix, 2003; Applanix, 2007). The rotations described by Tait-Bryan are not only applicable in the trajectory of the

aircraft, but are also used to describe the order of rotations for rectifying the boresight misalignment angles (University of New Brunswick, 1998; Wehr, 2009). Figure A2 shows the labeling of the axes under Tate-Bryan along with the direction of a positive rotation. For reference, when located at the coordinate system's origin and looking along a positive axis, a positive rotation is perceived as a rotation in the clockwise direction. That is, a positive rotation about the x-axis can be thought of as “port-side up,” a positive rotation about the y-axis can be thought of as “nose up,” and a positive rotation about the z-axis can be thought of as “turn right.”

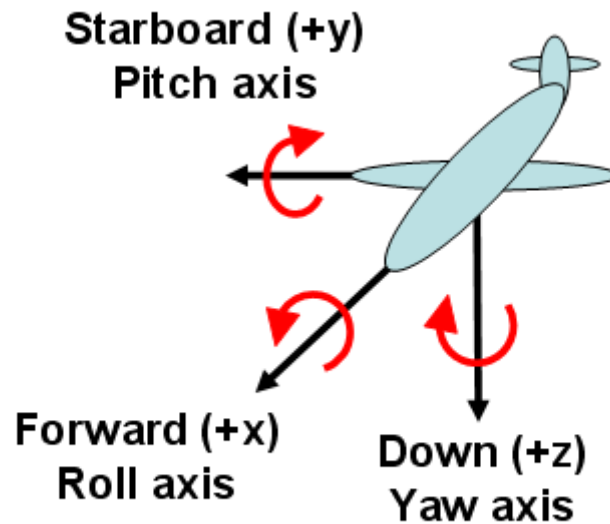


Figure A2. An aircraft's three orthogonal axes and the corresponding direction of a positive rotation.

If one has a set of vehicle orientation angles and wishes to represent the vehicle reference frame (VRF) with respect to an Earth-centered Earth fixed (ECEF) reference frame, the Tait-Bryan convention specifies the rotations are to be performed in the following order (Bryan, 1911):

- Begin with the vehicle aligned with the ECEF (Figure A3a).

- Rotate the VRF about the VRF's z-axis by the yaw angle, κ (Figure A3b).
- Rotate the VRF about the VRF's now once-rotated y-axis, y' , by the pitch angle, ψ (Figure A3c).
- Finally, rotate the VRF about the VRF's now twice-rotated x-axis, x'' , by the roll angle, ω (Figure A3d).

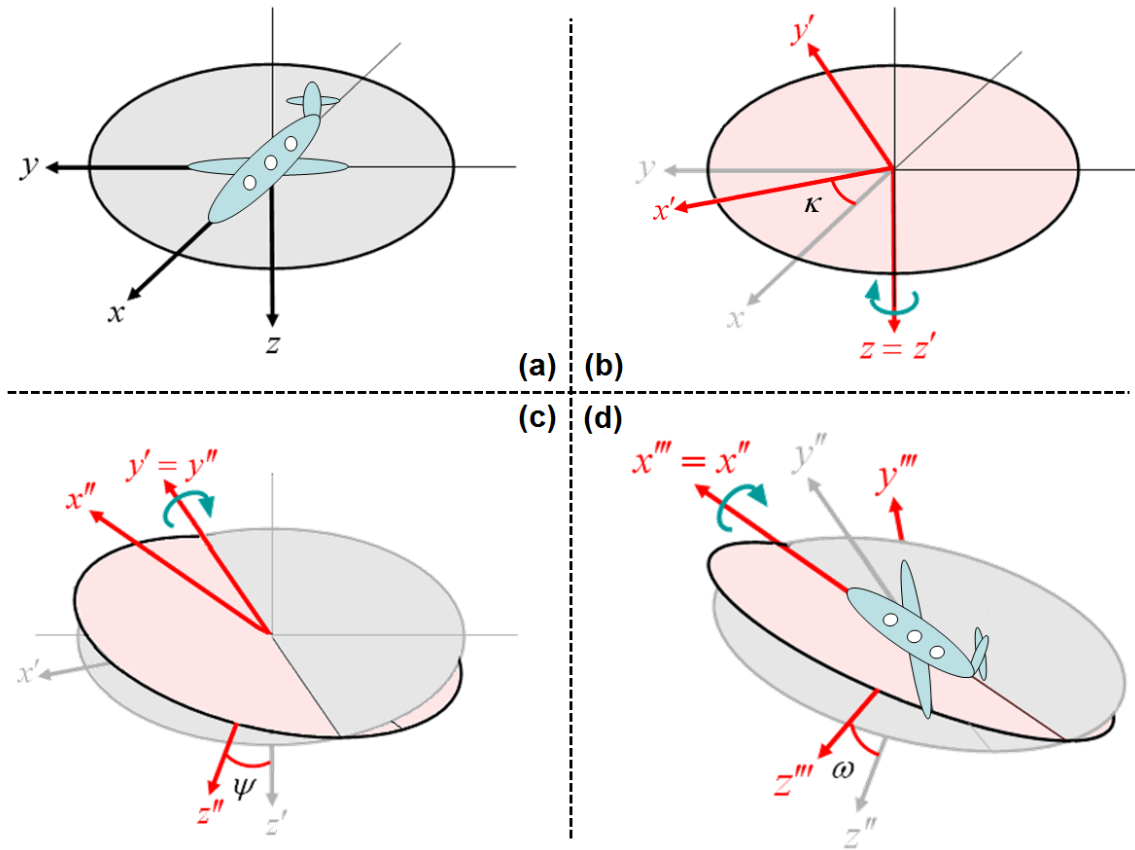


Figure A3. The Tait-Bryan rotation sequence (ECEF to VRF): (a) align vehicle to ECEF, (b) rotate yaw angle, κ , about VRF z-axis, (c) rotate pitch angle, ψ , about once-rotated VRF y-axis, (d) rotate roll angle, ω , about twice-rotated VRF x-axis.

To convert a vector, \vec{n} , from the ECEF to the VRF, three rotational matrices,

$\mathbb{R}_z, \mathbb{R}_{y'}, \mathbb{R}_{x''}$ (representing a rotation about the z axis, the once-rotated y' axis, and the twice rotated x'' axis respectively), must be applied, such that:

$$\vec{n}_{VRF} = \mathbb{R}_{x''} \mathbb{R}_{y'} \mathbb{R}_z \vec{n}_{ECEF} \quad (9.1)$$

Where the rotation describing yaw, \mathbb{R}_z , is given by a simple rotation about the vector

$\begin{bmatrix} 0 & 0 & 1 \end{bmatrix}^T$, that is:

$$\mathbb{R}_z = \begin{bmatrix} \cos \kappa & -\sin \kappa & 0 \\ \sin \kappa & \cos \kappa & 0 \\ 0 & 0 & 1 \end{bmatrix} \quad (9.2)$$

Subsequent rotations require a more general formula for rotating about an arbitrary axis.

From Fillmore (1984), the Rodrigues' Rotation Formula states to rotate a vector

$\vec{v} = \begin{bmatrix} v_x & v_y & v_z \end{bmatrix}^T$, about an arbitrary vector $\vec{L} = \begin{bmatrix} L_x & L_y & L_z \end{bmatrix}^T$, by an angle α , then:

$$\vec{v}' = \mathbb{R}_L \vec{v} \quad (9.3)$$

where:

$$\mathbb{R}_L = \begin{bmatrix} L_x \\ L_y \\ L_z \end{bmatrix} \begin{bmatrix} L_x \\ L_y \\ L_z \end{bmatrix}^T + \cos \alpha \left(\begin{bmatrix} 1 & 0 & 0 \\ 0 & 1 & 0 \\ 0 & 0 & 1 \end{bmatrix} - \begin{bmatrix} L_x \\ L_y \\ L_z \end{bmatrix} \begin{bmatrix} L_x \\ L_y \\ L_z \end{bmatrix}^T \right) + \sin \alpha \begin{bmatrix} 0 & -L_z & L_y \\ L_z & 0 & -L_x \\ -L_y & L_x & 0 \end{bmatrix} \quad (9.4)$$

To compute $\mathbb{R}_{y'}$, \vec{y}' must first be found. This is easily done, as the columns of \mathbb{R}_z

represent the vectors \vec{x}' , \vec{y}' , and \vec{z}' respectively. Re-examining (9.2):

$$\mathbb{R}_z = \begin{bmatrix} \cos \kappa & -\sin \kappa & 0 \\ \sin \kappa & \cos \kappa & 0 \\ 0 & 0 & 1 \end{bmatrix} \Rightarrow \underbrace{\begin{bmatrix} \cos \kappa \\ \sin \kappa \\ 0 \end{bmatrix}}_{\vec{x}'} , \underbrace{\begin{bmatrix} -\sin \kappa \\ \cos \kappa \\ 0 \end{bmatrix}}_{\vec{y}'} , \underbrace{\begin{bmatrix} 0 \\ 0 \\ 1 \end{bmatrix}}_{\vec{z}'} \quad (9.5)$$

So, substituting \vec{y}' for \vec{L} in (9.4), with a pitch of ψ , yields:

$$\mathbb{R}_L = \mathbb{R}_{y'} = \begin{bmatrix} \sin^2 \kappa + \cos \psi \cos^2 \kappa & \sin \kappa \cos \kappa (\cos \psi - 1) & \sin \psi \cos \kappa \\ \sin \kappa \cos \kappa (\cos \psi + 1) & \cos^2 \kappa + \cos \psi \sin^2 \kappa & \sin \psi \sin \kappa \\ -\sin \psi \cos \kappa & -\sin \psi \sin \kappa & \cos \psi \end{bmatrix} \quad (9.6)$$

Finally, we are left with computing $\mathbb{R}_{x''}$, which necessitates determining \vec{x}'' . This is fairly straightforward with the observation that:

$$\mathbb{R}_{y'} \cdot \mathbb{R}_z = \mathbb{R}_z \cdot \mathbb{R}_y \quad (9.7)$$

Which can be confirmed by substituting the respective matrices into (9.7) and multiplying out both sides. Showing just the right-hand side of (9.7) yields:

$$\begin{aligned} \mathbb{R}_z \cdot \mathbb{R}_y &= \begin{bmatrix} \cos \kappa & -\sin \kappa & 0 \\ \sin \kappa & \cos \kappa & 0 \\ 0 & 0 & 1 \end{bmatrix} \cdot \begin{bmatrix} \cos \psi & 0 & \sin \psi \\ 0 & 1 & 0 \\ -\sin \psi & 0 & \cos \psi \end{bmatrix} \\ &= \begin{bmatrix} \cos \kappa \cos \psi & -\sin \kappa & \cos \kappa \sin \psi \\ \sin \kappa \cos \psi & \cos \kappa & \sin \kappa \sin \psi \\ -\sin \psi & 0 & \cos \psi \end{bmatrix} \end{aligned} \quad (9.8)$$

Combining (9.7) and (9.8), much like in (9.5) gives the vectors \vec{x}'' , \vec{y}'' , and \vec{z}'' .

$$\begin{aligned} \mathbb{R}_{y'} \cdot \mathbb{R}_z &= \begin{bmatrix} \cos \kappa \cos \psi & -\sin \kappa & \cos \kappa \sin \psi \\ \sin \kappa \cos \psi & \cos \kappa & \sin \kappa \sin \psi \\ -\sin \psi & 0 & \cos \psi \end{bmatrix} \\ \Rightarrow &\underbrace{\begin{bmatrix} \cos \kappa \cos \psi \\ \sin \kappa \cos \psi \\ -\sin \psi \end{bmatrix}}_{\vec{x}''}, \underbrace{\begin{bmatrix} -\sin \kappa \\ \cos \kappa \\ 0 \end{bmatrix}}_{\vec{y}''}, \underbrace{\begin{bmatrix} \cos \kappa \sin \psi \\ \sin \kappa \sin \psi \\ \cos \psi \end{bmatrix}}_{\vec{z}''} \end{aligned} \quad (9.9)$$

The form of $\mathbb{R}_{x''}$ can now be determined through a substitution of \vec{x}'' into (9.4). Using the shorthand $C\kappa = \cos \kappa$, $S\kappa = \sin \kappa$, $C\kappa^2 = \cos^2 \kappa$, etc., $\mathbb{R}_{x''}$ will be the (3 x 3) matrix given by:

$$\begin{aligned}
\mathbb{R}_{x'}(:,1) &= \begin{bmatrix} C\kappa^2 C\psi^2 + C\omega(1 - C\kappa^2 C\psi^2) \\ C\kappa S\kappa C\psi^2 - C\omega C\kappa S\kappa C\psi^2 - S\omega S\psi \\ -C\kappa C\psi S\psi + C\omega C\kappa C\psi S\psi - S\omega S\kappa C\psi \end{bmatrix} \\
\mathbb{R}_{x'}(:,2) &= \begin{bmatrix} C\kappa S\kappa C\psi^2 - C\omega C\kappa S\kappa C\psi^2 + S\omega S\psi \\ S\kappa^2 C\psi^2 + C\omega(1 - S\kappa^2 C\psi^2) \\ -S\kappa C\psi S\psi + C\omega S\kappa C\psi S\psi + S\omega C\kappa C\psi \end{bmatrix} \\
\mathbb{R}_{x'}(:,3) &= \begin{bmatrix} -C\kappa C\psi S\psi + C\omega C\kappa C\psi S\psi + S\omega S\kappa C\psi \\ -S\kappa C\psi S\psi + C\omega S\kappa C\psi S\psi - S\omega C\kappa C\psi \\ S\psi^2 + C\omega(1 - S\psi^2) \end{bmatrix}
\end{aligned} \tag{9.10}$$

Thus, by Tait-Bryan, $\vec{n}_{VRF} = \mathbb{R}_{x'} \mathbb{R}_{y'} \mathbb{R}_z \vec{n}_{ECEF}$, where $\mathbb{R}_{x'}$, $\mathbb{R}_{y'}$, \mathbb{R}_z are given by equations (9.10), (9.6) and (9.2) respectively.

A.2 – Alternative Formulation

The preceding equations, however, are computationally expensive, and a simpler calculation can be performed with the observation that:

$$\mathbb{R}_{x'} \cdot \mathbb{R}_{y'} \cdot \mathbb{R}_z = \mathbb{R}_z \cdot \mathbb{R}_{y'} \cdot \mathbb{R}_x \tag{9.11}$$

In words, the preceding equation, (9.11), states that the Euler angles used in the Tait-Bryan rotations (left-hand side) can instead be performed in reverse order, provided they are rotations about the original ECEF axes, \vec{x} , \vec{y} , and \vec{z} , see Figure A4. This relation has been confirmed by the author both numerically and algebraically. A full algebraic validation is too large for this document.

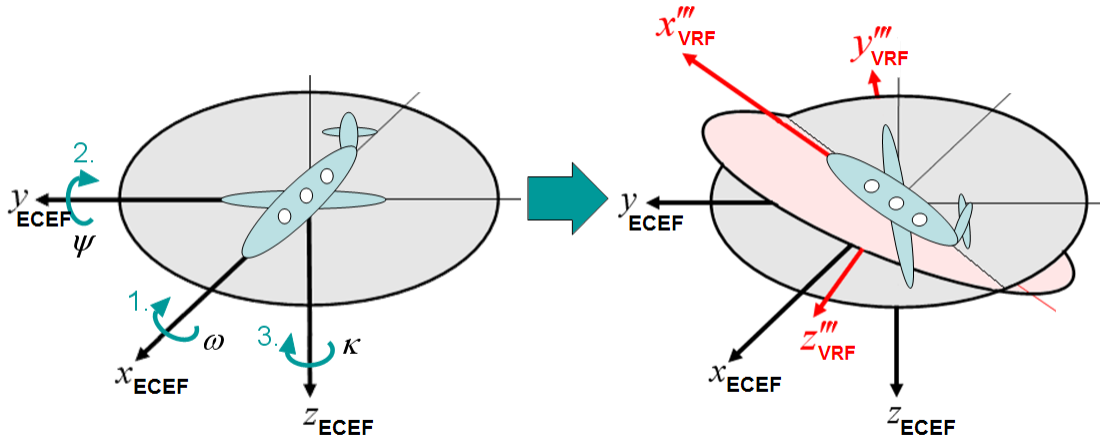


Figure A4. By reversing the order of rotations prescribed by the Tait-Bryan convention, an equivalent transformation can be performed by rotating about the fixed (non-rotating) Earth-centered Earth-fixed (ECEF) coordinate axes. Note: the right-hand side of Figure A4 is equivalent to the results shown in Figure A3.

Writing out the right-hand side of (9.11)

$$\begin{aligned}
 \mathbb{R}_z \cdot \mathbb{R}_y \cdot \mathbb{R}_x &= \begin{bmatrix} \cos \kappa & -\sin \kappa & 0 \\ \sin \kappa & \cos \kappa & 0 \\ 0 & 0 & 1 \end{bmatrix} \cdot \begin{bmatrix} \cos \psi & 0 & \sin \psi \\ 0 & 1 & 0 \\ -\sin \psi & 0 & \cos \psi \end{bmatrix} \cdot \begin{bmatrix} 1 & 0 & 0 \\ 0 & \cos \omega & -\sin \omega \\ 0 & \sin \omega & \cos \omega \end{bmatrix} \\
 &= \begin{bmatrix} \cos \kappa \cos \psi & -\cos \omega \sin \kappa + \sin \omega \cos \kappa \sin \psi & \sin \omega \sin \kappa + \cos \omega \cos \kappa \sin \psi \\ \sin \kappa \cos \psi & \cos \omega \cos \kappa + \sin \omega \sin \kappa \sin \psi & -\sin \omega \cos \kappa + \cos \omega \sin \kappa \sin \psi \\ -\sin \psi & \sin \omega \cos \psi & \cos \omega \cos \psi \end{bmatrix} \\
 (9.12)
 \end{aligned}$$

The above equation, (9.12), agrees with the coordinate transformations from a North-East-Down coordinate system to a Roll-Pitch-Yaw coordinate system presented in Grewal, Weill, and Andrews (2007). More importantly, it agrees with the original text of Bryan (1911), showing nothing has been lost in translation over the past 99 years. This convention, rotating a vector about an x-axis, then y-axis, then z-axis is employed throughout this dissertation whenever a three axis transformation is required (vehicle attitude, boresight misalignment, prism-to-scanner alignment, etc.).

REFERENCES

- Alharthy, A., & Bethel, J. (2004). Detailed building reconstruction from airborne laser data using a moving surface method. In O. Altan (Ed.) *Proceedings of the ISPRS Congress: Vol. XXXV-B3* (pp 213-218). Istanbul, Turkey: ISPRS.
- Anton, H., Bivens, I., & Davis, S. (2002). *Calculus* (7th Ed.). New York: John Wiley & Sons, Inc.
- Applanix Corporation (2003). *POS MV V3 Installation and Operation Guide*. PUBS-MAN-000032, Revision 1, Ottawa, Ontario, Canada.
- Applanix Corporation (2007). *POS AV V5 Installation and Operation Guide*. PUBS-MAN-000046, Revision 4, Ottawa, Ontario, Canada.
- Bang, K.-I., Kersting, A. P., Habib, A., & Lee, D.-C. (2009, March). Lidar system calibration using point cloud coordinates in overlapping strips, *Proceedings of ASPRS Annual Conference*, Baltimore, MD, CD-ROM.
- Besl, P. J., & McKay, N. D. (1992). A method for registration of 3D shapes. *IEEE transactions on pattern analysis and machine intelligence*, 14(2), 239-256.
- Bryan, G. H. (1911). *Stability in aviation: An introduction to dynamical stability as applied to the motions of aeroplanes*. London: Macmillan.

- Calder, B. R., & McLeod, A. (2007). Ultraprecise absolute time synchronization for distributed acquisition systems. *IEEE Journal of Oceanic Engineering*, 32(4), 772-785.
- Csanyi, N. Toth, D., Grejner-Brzezinska, & Ray J. (2005, March). Improving LiDAR data accuracy using LiDAR-specific ground targets. *Proceedings of ASPRS Annual Conference*, Baltimore, MD, CD-ROM.
- Del Mar Ventures (2007). *Fused silica*. Retrieved from <http://www.sciner.com/Opticsland/FS.htm>
- Dieck, R. H. (2007). *Measurement uncertainty: Methods and applications* (4th Ed.). Research Triangle Park, North Carolina: ISA.
- Feynman, R. P. (1963). *The Feynman lectures on physics: Volume I*. New York: Addison-Wesley.
- Fillmore, J. (1984). A note on rotation matrices. *IEEE Computer Graphics and Applications*, 4(2), 30-33.
- Fitzgibbon, A. W. (2003). Robust registration of 2D and 3D point sets. *Proceedings of the British Machine Vision Conference*. Manchester, UK: BMVC.

Fornasini, P. (2008). *The uncertainty in physical measurements*. New York: Springer.

Friess, P. (2006). Toward a rigorous methodology for airborne laser mapping.

International Calibration and Orientation Workshop EuroCOW. Castelldefels, Spain.

Fuchs, E., & Mathur, A. (2010). Utilizing circular scanning in the CZMIL system. In S. S. Shen P. E. Lewis (Eds.) *Proceedings of Algorithms and Technologies for Multispectral, Hyperspectral and Ultraspectral Imagery XVI. Vol. 7695*. Tampa, FL: SPIE.

Fuchs, E., & Tuell, G. H. (2010). Conceptual design of the CZMIL data acquisition system (DAS): integrating a new bathymetric lidar with a commercial spectrometer and metric camera for coastal mapping applications. In S. S. Shen P. E. Lewis (Eds.) *Proceedings of Algorithms and Technologies for Multispectral, Hyperspectral and Ultraspectral Imagery XVI. Vol. 7695*. Tampa, FL: SPIE

Ghilani, C. D., & Wolf, P. R. (2006). *Adjustment computations: Spatial data analysis* (4th Ed.). Hoboken, NJ: J. Wiley & Sons.

Glassner, A. (1989). *An introduction to ray tracing*. London: Academic Press.

Gonsalves, M. O. (2010). Using a dynamic ocean surface to perform a geometric calibration of a bathymetric lidar. *Proceedings of OCEANS 2010 MTS/IEEE Conference*. In press.

Gross, H., & Thoennessen, U. (2006). Extraction of lines from laser point clouds.

Proceedings of the ISPRS Commission III Symposium on Photogrammetric and Computer Vision: Vol. XXXVI (86-91). Bonn, Germany: ISPRS.

Grewal, M., Weill, L., & Andrews, A. (2007). *Global positioning systems, inertial navigation and integration* (2nd ed.). New York: J. Wiley & Sons.

Guenther, G. C. (1985). *Airborne laser hydrography: system design and performance factors* (NOAA Professional Paper Series, National Ocean Service 1). Rockville, Maryland: NOAA.

Guenther, G. C. (2007). Airborne lidar bathymetry. In D. F. Maune (Ed.), *Digital elevation model technologies and applications: The DEM users manual* (2nd ed.) (pp. 237-306). Silver Spring, MD: ASPRS.

Habib, A. F., Al-Durgham, M., Kersting, & A. P., Quackenbush, P. (2008a). Error budget of lidar systems and quality control of the derived point cloud. *Proceedings of the XXI ISPRS Congress, Commission I: Vol. XXXVII. Part B1*. (pp 203-209). Beijing, China: Institute of Photogrammetry and Remote Sensing.

Habib, A. F., Kersting, A. P., Ruifang, Z., Al-Durgham, M., Kim, C., & Lee, D. C. (2008b). Lidar strip adjustment using conjugate linear features in overlapping strips.

Proceedings of the XXI ISPRS Congress, Commission I: Vol. XXXVII. Part B1.

Beijing, China: ISPRS.

Habib, A. F., & Rens, J. V. (2008). Quality assurance and quality control of lidar systems and derived data. Retrieved November 14, 2008, from American Society for Photogrammetry and Remote Sensing website:
<http://www.asprs.org/society/committees/lidar/>

de Hilster, N. (2008, November). The MRU and SRF aligned. *Hydro International*, 12(9), 24-28.

Hughes Clark, J.E. (2003). *A reassessment of vessel coordinate systems: what is it that we are really aligning?*, Paper presented at the meeting of US Hydrographic Conference. Biloxi, MS.

International Association for the Properties of Water and Steam (1997). *Release on the refractive index of ordinary water substance as a function of wavelength, temperature, and pressure*. Erlangen, Germany: IAPWS.

Kilian, J., Haala, N., & Englich, M. (1996). Capture and evaluation of airborne laser scanner data. *International Archives of Photogrammetry and Remote Sensing*, 33(B3), 383-388.

- Kirkup, L. & Frenkel, B. (2006). *An introduction to uncertainty in measurement*. New York: Cambridge University Press.
- Lee I., & Schenk, T., (2001). Autonomous extraction of planar surfaces from airborne laser scanning data. In *Proceedings of the Annual Conference of the American Society of Photogrammetry and Remote Sensing*, St. Louis, MO: ASPRS
- Martin, J. J. (1967). *Bayesian decision problems and Markov chains*. New York: Wiley.
- May, N. C. (2008). *A rigorous approach to comprehensive performance analysis of state-of-the-art airborne mobile mapping systems*. (Unpublished doctoral dissertation). Ohio State University, Columbus.
- Morin, K. W. (2002). *Calibration of airborne laser scanners*. (Unpublished master's thesis). University of Calgary, Alberta.
- National Oceanic and Atmospheric Administration (2010). *NOAA Office of Coast Survey field procedures manual*. Silver Sprnig, MD: U.S. Department of Commerce.
- Pond, S. & Pickard, G. L. (2000). *Introductory dynamical oceanography* (2nd ed.). Boston: Butterworth-Heinemann.

Reynolds, P. F. (2009). The role of modeling and simulation. In J. A. Sokolowski & C. M. Banks (Eds.), *Principles of modeling and simulation: A multidisciplinary approach* (pp. 25-46). Hoboken, NJ: John Wiley & Sons.

Schenk, T. (2001). *Modeling and analyzing systematic errors in airborne laser scanners*. (Technical Notes in Photogrammetry No. 19). Columbus: Ohio State University.

Schmid, H.H. & Schmid, E. (1965). A generalized least squares solution for hybrid measuring systems. *The Canadian Surveyor*, 19, 27-41.

Skaloud, J., & Schaer, P. (2007). Towards automated lidar boresight self-calibration. Symposium conducted at the 5th International Meeting of Mobile Mapping Technology. Padua, Italy.

Smith, S. W. (1997). *The scientist and engineer's guide to digital signal processing*. USA: California Technical Publishing.

Tuell, G., Barbor, K., & Wozencraft, J. (2010). Overview of the Coastal Zone Mapping and Imaging Lidar (CZMIL). In S. S. Shen P. E. Lewis (Eds.) *Proceedings of Algorithms and Technologies for Multispectral, Hyperspectral and Ultraspectral Imagery XVI Vol. 7695*. Tampa, FL: SPIE.

- University of New Brunswick. (1998). *The Calibration of Shallow Water Multibeam Echo-Sounding Systems*. M. Eng. Report, Department of Geodesy and Geomatics Engineering Technical Report No. 190. Fredericton, New Brunswick, Canada: Godin, A.
- Vosselman, G., & Dijkman, S. (2001). 3D building model reconstruction from point clouds and ground plans. In M. A. Hofton (Ed.) *Proceedings of the ISPRS Workshop: Vol. XXXIV-3/W4. Land surface mapping and characterization using laser altimetry* (pp 37-43). Annapolis, MD: ISPRS.
- Vosselman, G., & Maas, H.-G. (2001). Adjustment and filtering of raw laser altimetry data. *Proceedings of the OEEPE workshop on airborne laserscanning and interferometric SAR for detailed digital elevation models*. Publication No. 40. Stockholm, Sweden.
- Wehr, A. (2009). Lidar systems and calibration. In J. Shan, & C. K. Toth (Eds.), *Topographic laser ranging and scanning* (pp. 129-172). Boca Raton, Florida: CRC Press.
- Wells, D. (1999, October 2). *Applications of partitioning in geomatics approximation and estimation*. Unpublished internal document, University of New Brunswick.
- Zilkowski, D.B. (1990, November). Minimum steps required when estimating GPS-derived orthometric heights. *Proceedings of the GIS/LIS 1990 Fall Convention*, Anaheim, California.